DGK Veröffentlichungen der DGK

Ausschuss Geodäsie der Bayerischen Akademie der Wissenschaften

Reihe C | Dissertationen | Heft Nr. 937

Bernd Uebbing

Consistently closing global and regional sea level budgets

München 2024

Bayerische Akademie der Wissenschaften

ISSN 0065-5325 ISBN 978-3-7696-5349-6

Diese Arbeit ist gleichzeitig veröffentlicht in:
bonndoc – Publikationsserver der Rheinischen Friedrich-Wilhelms-Universität Bonn
https://hdl.handle.net/20.500.11811/10452 oder https://nbn-resolving.org/urn:nbn:de:hbz:5-68773, Bonn 2022

DGK Veröffentlichungen der DGK

Ausschuss Geodäsie der Bayerischen Akademie der Wissenschaften

Reihe C Dissertationen Heft Nr. 937

Consistently closing global and regional sea level budgets

An der Landwirtschaftlichen Fakultät
der Rheinischen Friedrich-Wilhelms-Universität Bonn
zur Erlangung des akademischen Grades
Doktor der Ingenieurwissenschaften (Dr.-Ing.)
vorgelegte Dissertation

von

Bernd Uebbing

München 2024

Bayerische Akademie der Wissenschaften

ISSN 0065-5325 ISBN 978-3-7696-5349-6

Diese Arbeit ist gleichzeitig veröffentlicht in:

bonndoc – Publikationsserver der Rheinischen Friedrich-Wilhelms-Universität Bonn
https://hdl.handle.net/20.500.11811/10452 oder https://nbn-resolving.org/urn:nbn:de:hbz:5-68773, Bonn 2022

Adresse der DGK:



Ausschuss Geodäsie der Bayerischen Akademie der Wissenschaften (DGK)

Alfons-Goppel-Straße 11 ● D – 80 539 München

Telefon +49 - 331 - 6264 1685 ● E-Mail post@dgk.badw.de

http://www.dgk.badw.de

Referent: Prof. Dr.-Ing. Jürgen Kusche

Korreferenten: Prof. Dr.-Ing. Martin Horwath (TU Dresden)
Prof. Dipl.-Ing. Dr. techn. Wolf-Dieter Schuh

Tag der mündlichen Prüfung: 04. November 2022

© 2024 Bayerische Akademie der Wissenschaften, München

Alle Rechte vorbehalten. Ohne Genehmigung der Herausgeber ist es auch nicht gestattet,
die Veröffentlichung oder Teile daraus auf photomechanischem Wege (Photokopie, Mikrokopie) zu vervielfältigen

ISSN 0065-5325 ISBN 978-3-7696-5349-6

Abstract

Nowadays, human-induced climate change is the major driver of global and regional sea level change threatening the well-being and livelihoods of hundreds of millions of people living close to the coast. Consequently, accurate observations of global and regional down to coastal zone sea level are paramount for monitoring and understanding as well as predicting future risk scenarios. This includes studying the global and local drivers of integrated sea level change resulting from water mass fluxes into the ocean and volumetric expansion due to ocean temperature and salinity changes.

Starting in the early 1990, conventional satellite radar altimetry, for the first time, provided sea surface height observations with global coverage on a regular basis. However in coastal zones, the radar signals are perturbed by land surfaces, requiring extensive post-processing efforts in order to obtain valid sea level information. Since 2002, mass changes in the ocean have been observed from time-variable gravity obtained from the twin satellites of the Gravity Recovery And Climate Experiment (GRACE) mission. After 2005, the Argo program reached its global coverage goal, consisting of thousands of freely drifting floats that regularly measure profiles of temperature and salinity. Combination of at least two datasets from altimetry, GRACE and in-situ profiles allows for construction of a sea level budget, partitioning the total sea level change into mass and volumetric components.

The goals of this thesis are twofold. On the one hand, the development, implementation and assessment of an improved coastal reprocessing of radar signals for application to conventional altimetry observations. On the other hand, the construction of consistently closed global and regional sea level budgets by combining altimetry, gravity and volume expansion measurements in a joint inversion framework.

For the first objective, a novel post-processing or "retracking" method is designed and implemented for the application to conventional satellite altimetry. The Spatio-Temporal Altimetry Retracker (STAR) shifts the problem of finding the matching physical model for each radar signal to a later stage by first extracting hundreds of sub-signals, based on a novel approach. These are then processed by applying a simple and robust retracking model resulting in many equally likely estimation parameters at each along-track measurement location. The resulting point clouds of equally likely estimates are then further processed by means of a shortest-path algorithm to select final estimates at each position. Validation indicates that STAR, applied to conventional altimetry, provides sea level results with a quality comparable to Delay Doppler Altimetry (DDA).

For deriving sea level budgets as part of the second objective, first, different approaches for processing each dataset individually are investigated and assessed for the application of deriving consistent budgets. As part of this effort, an inconsistency in the standard processing of ocean mass change from GRACE has been discovered and the, subsequently, updated processing is now widely applied. The main focus of this thesis is on improving and extending a global fingerprint inversion approach that consistently integrates altimetry, GRACE and Argo data within a single estimation step. The fingerprints are composed of empirical spatial patterns that have been extracted from auxiliary datasets in a pre-processing step. Based on an existing framework, each processing step has been thoroughly assessed and, if necessary, modified in order to significantly improve the quality of derived budgets. By further extending the potential input datasets, it was possible to close the sea level budget on global and, for the first time, also on regional scales within less than 0.1 mm/yr of budget closure. In addition, the inversion results are directly linked to Earth Energy Imbalance (EEI) based on a novel rescaling approach, therefore, providing an independent measure for one of the key indicators of climate change.

Zusammenfassung

Der menschengemachte Klimawandel ist heute einer der Haupttreiber von globalen und regionalen Meerespiegeländerungen, welche Leben und Lebensunterhalt von Hunderten Millionen Menschen in Küstennähe bedrohen. Die hochgenaue Beobachtung von globalen und regionalen Meeresspiegeländerungen bis hin zur Küste ist daher von größter Wichtigkeit für die Überwachung, das Verständnis, sowie die Vorhersage zukünftiger Risiken. Dies umfasst die Unterschuchung von globalen und lokalen Treibern der Gesamtmeeresspiegeländerungen, sowie Anteilen aufgrund von Massenzuflüssen in den Ozean und Volumenänderungen durch Temperatur- und Salzgehaltvariationen.

Erst in den frühen 1990er Jahren wurde es möglich, mittels konventioneller Satellitenradaraltimetrie, die Meeresoberfläche zeitlich regelmäßig und global zu beobachten. Allerdings sind Radarsignale in Küstenregionen durch Landreflexionen gestört, was eine aufwendige Nachprozessierung erfordert. Seit 2002 ist es möglich, Ozeanmassenänderungen direkt mittels zeitvariabler Schweremessung durch die Zwillingssatelliten der Gravity Recovery And Climate Experiment (GRACE) Mission zu erfassen. Im Jahr 2005 erreichte das Argo-Programm seine globale Abdeckung mittels tausender frei im Ozean treibender Schwimmkörper, welche in regelmäßigen Abständen Profile von Temperatur und Salzgehalt messen. Die Kombination von mindestens zwei Datenprodukten aus Altimetrie, GRACE und Argo-Profilen erlaubt die Konstruktion von Meeresspiegelbudgets, welche den Gesamtanstieg in einzelne Massen- und Volumenanteile aufspalten.

Diese Arbeit hat zwei Ziele. Zum einen, die Entwicklung, Implementierung und Beurteilung einer verbesserten Methodik zur Bestimmung von Meereshöhen in Küstengebieten aus konventioneller Altimetrie. Zum anderen, die Konstruktion konsistenter und geschlossener globaler und regionaler Meeresspiegelbudgets durch Kombination von Altimetrie, Schweremessungen und Volumenänderungen in einer gemeinsamen Inversion.

Zum Erreichen des ersten Ziels wurde eine neue Postprozessierungsmethodik (“Retracker”) für die Anwendung auf konventionelle Radaraltimetrie entwickelt und implementiert. Der Spatio-Temporal Altimetry Retracker (STAR) verschiebt die Problematik, das perfekte Modell für die gemessenen Radarsignale zu finden, auf einen späteren Prozessierungschritt in dem zunächst, basierend auf einem neuen Ansatz, hunderte Subsignale extrahiert werden. Diese werden dann weiter prozessiert, indem ein einfacher und robuster Retracker angewendet wird. Dadurch ist es möglich für jede Position entlang der Satellitenbodenspur eine Vielzahl potentieller Ergebnisse abzuleiten. Diese Punktwolke an gleichwertigen Ergebnissen wird dann mit Hilfe eines Kürzeste-Pfade-Algorithmus analysiert, um an jeder Position ein finales Ergebnis zu selektieren. Validierungsergebnisse zeigen, dass STAR in der Lage ist, Meeresspiegelhöhen aus konventioneller Altimetrie mit einer Qualität vergleichbar zu Delay Doppler Altimetry (DDA) zu liefern.

Für die Ableitung von Meeresspiegelbudgets werden zunächst die individuellen Prozessierungsmethoden für jedes der genannten Datenprodukte untersucht und im Hinblick auf die Anwendung zur Ableitung konsistenter Budgets beurteilt. Als Teil dieser Arbeit wurde eine Inkonsistenz in der standardmäßigen Prozessierung der GRACE-Daten aufgedeckt und behoben. Der Hauptfokus der Arbeit liegt auf der Verbesserung und Erweiterung der globalen Fingerprintinversion, welche Altimetrie, GRACE und Argo-Daten in konsistenter Weise in einer Schätzung miteinander kombiniert. Fingerprints repräsentieren räumliche Muster, welche aus Hilfsdaten in einem Vorprozessierungsschritt als empirische räumliche Basisfunktionen extrahiert wurden. Basierend auf einer bereits existierenden Implementation wurde jeder Prozessierungsschritt sorgfältig beurteilt und verbessert, was zu signifikant besseren Ergebnissen führte. Durch eine Erweiterung der Eingangsdaten war es möglich, globale und, zum ersten Mal, regionale Meeresspiegelbudgets konsistent mit einem Restfehler von unter 0.1 mm/yr zu schließen. Des Weiteren war es möglich, mittels eines neuen Ansatzes eine direkte Verbindung herzustellen zwischen den Inversionsergebnissen und Earth Energy Imbalance (EEI), einem Schlüsselindikator für den Klimawandel.

Acknowledgments

While it has been almost nine years until I could write these final lines, I do not regret a single minute of it. I consider myself very lucky to have been able to work in this exciting field of research and finish my thesis in a way that I am satisfied with the results. Over time, I have been able to better understand the intricacies of sea level change and meet some of the world's most distinguished scientists in the field. Talking to them lead to new insights and ideas, which benefited this thesis. My work provided me with a unique perspective on global and regional sea level change, anthropogenic climate change and the resulting global and regional impacts, which are already observable today. To some extent, I might have become a little bit pessimistic about the future of humanity, since I, as a scientist, cannot understand why actions against climate change are not the number one priority on every single day; human greed is insatiable, I guess. Luckily, I also developed a great sense of (dark) humor over the years.

Reaching the finish line would not have been possible without the help and support from a lot of people. First of all, I am very thankful to my supervisor Prof. Dr.-Ing. Jürgen Kusche, who not only gave me the time to finish my thesis, but also put the trust in me, supported and motivated me along the way. During my Bachelor and Master studies, he taught me the basics in Astronomical, Mathematical and Physical Geodesy (APMG) that enabled me to start the work as a PhD student in his group. While juggling teaching, meetings, writing proposals and running a marathon before breakfast, he always had time to listen and provide guidance. If there was a problem, he always tried to solve it in the best possible way for everyone involved, thus, providing a pleasant and welcoming working environment to myself and my colleagues.

I would like to thank my two additional referees of this thesis, Prof. Dr.-Ing. Martin Horwath from the Geodetic Earth System Research Group at TU Dresden and Prof. Dipl.-Ing. Dr. techn. Wolf-Dieter Schuh from the Theoretical Geodesy group at University of Bonn. I got to know Prof. Horwath as part of a co-operation within the OMCG project, where he showed lots of knowledge on topics related to sea level change, ice mass changes and glacial isostatic adjustment. He provided valuable insights with respect to the inversion method and the collaborative work of myself and his own PhD student, while always radiating a great deal of joy about doing his work. Prof. Schuh taught me greater mathematics as a student and provided me with the statistical foundation, which benefited me a lot during the work related to my thesis. I admired his ability to quickly grasp complicated mathematical concepts and ask on-point questions, while always being fair and polite.

Furthermore, I am grateful for my colleagues, Jan Martin, Luciana, Anno, Roelof, Christina and Kristin, who agreed to proof-read parts of or even the whole thesis. Your comments on the content and the hundreds of comma errors that I made, helped me to improve the manuscript. Thanks also to my sister, Maria, who provided an outside perspective, which lead to an interesting discussion on what I am actually doing.

I am grateful for the funding that enabled me to work on the thesis topics over the years. I started working as part of the "Bangladesh Delta: assessment of the Causes of Sea-level Rise Hazards and Integrated Development of Predictive Modeling Towards Mitigation and Adaption" (BanD-AID) project, KU 1207/19-1, which was funded by the German Research Foundation (DFG) and the Belmont-Forum and provided me with the opportunity to work as part of a large international team. Afterwards, I was part of the DFG Priority Programme on Regional Sea Level & Society (SPP 1889), where I worked on the project "Reconciling ocean mass change and GIA from satellite gravity and altimetry" (OMCG), KU 1207/22-1, and its follow-up OMCG-2, KU 1207/22-2. I especially enjoyed the collaborations with Matthias Willen from TU Dresden as part of the OMCG project, which already helped to improve the inversion and will likely lead to further extensions in the near future.

The data in this thesis is mostly based on freely available satellite data, which are collected and funded by several institutions, including NASA, ESA, CNES, JPL, GSFC, NOAA, ECMWF or DLR, for which I am very thankful. I would also like to thank Torsten Mayer-Gürr and Andreas Kvas from TU Graz, who made the ITSG2018 GRACE and GRACE-FO degree and order 120 normal equations available. Furthermore, thanks to my colleagues Anno and Christina for providing me access to their SLR and Swarm normal equations, respectively. Thanks to Jens Schröter from the AWI for sharing FESOM ocean model runs. For this thesis, I utilized several open source software programs including the Generic Mapping Toolbox, Inkscape and GIMP as well as open source C++, C and Fortran compilers within a Linux environment.

Thanks a lot to all my colleagues over the years, who provided me with tons of advice and let me be part of a nice working environment over the years. Thanks to Jan Martin and Roelof for always taking the time to answer my, sometimes stupid, questions. Thanks to Cathrin for always helping me with administrative issues. Thanks to Christian for helping me with all the IT problems. I am grateful for my first office mate, Ribana, with whom I always had a good time and who helped me a lot in the beginning when everything was new to me. Similarly, thank you to Christina, my second office mate, with whom I became good friends and had a lot of fun. In addition, I am happy that I had a good time with all my other colleagues. Listing everyone individually would probably lead to a few more pages, so please, all of you should feel warmly appreciated.

I would like to thank my friends and family for supporting me throughout all the time it took to write my thesis. Thank you for your patience and always believing in me. Last but not least, I would like to thank my girlfriend, Kristin. Your support and love over the last few months of my thesis encouraged me to finally get it done.

PS: @Ehsan, who asked me when I will finish my thesis from the very first day that I started working in the group. I did it!

Contents

1 Introduction **1**
1.1 Motivation . . . 1
1.2 Sea Level Change, Measured and Modeled Contributions . . . 2
1.3 Consistency of Sea Level Budgets . . . 7
1.4 Objectives of this Thesis . . . 8
1.5 Thesis Outline . . . 10

2 Sea Level Theory: Gravity, Loading and Steric Sea Level **13**
2.1 The Gravity Field of the Earth . . . 13
2.1.1 Mathematical Representation of the Earth's Gravity Field . . . 14
2.1.2 Surface Loading . . . 15
2.2 Self-Consistent Sea Level Theory . . . 19
2.2.1 The Sea Level Equation . . . 20
2.2.2 Spectral Solution of the SLE without Rotational Feedback . . . 21
2.2.3 Incorporating Rotational Feedback into the SLE . . . 23
2.3 The Equation of State of Seawater . . . 25
2.3.1 Steric Sea Level . . . 26
2.3.2 Ocean Heat Content . . . 28
2.4 Reference System Theory . . . 29
2.4.1 Reference Frames . . . 29
2.4.2 Translation of the Reference Frame . . . 31
2.4.3 Shifting the Reference System for a Radially Symmetric Elastic Earth . . . 32

3 Observations and Model Data **35**
3.1 Radar Altimetry . . . 35
3.1.1 From Measured Distance to Sea Level Anomaly . . . 36
3.1.2 Conventional Altimetry Datasets . . . 39
3.1.3 Delay Doppler Altimetry Datasets . . . 40
3.1.4 Mean Sea Level Time Series . . . 41
3.2 Time-Variable Gravity . . . 41
3.2.1 GRACE and GRACE-FO . . . 41
3.2.2 Satellite Laser Ranging . . . 43
3.2.3 Swarm . . . 44
3.3 Temperature and Salinity Data . . . 45
3.3.1 In-Situ Profiles . . . 45
3.3.2 Ocean Model Data . . . 46
3.4 Auxiliary Data . . . 47
3.4.1 Glacial Isostatic Adjustment . . . 47
3.4.2 Terrestrial Hydrology Model Data . . . 47
3.4.3 Glacier Inventory Data . . . 48
3.4.4 GRACE Ocean and Atmosphere De-aliasing Products . . . 48
3.4.5 Ice-Altimetry Data . . . 48

4 Improving Retracking of Coastal Radar Altimetry Estimates 49
4.1 Altimeter Return Waveform . . . 49
4.2 Retracking Conventional Altimetry . . . 52
4.2.1 Physics Based Retracking Algorithms . . . 53
4.2.2 Empirical Retracking Algorithms . . . 56
4.2.3 Sub-Waveform Retracking Algorithms . . . 57
4.3 STAR-V3: Spatio-Temporal Altimetry Retracker Version 3 . . . 59
4.3.1 Partitioning of the Altimeter Waveform . . . 60
4.3.2 Retracking Individual Sub-Waveforms . . . 63
4.3.3 Analysis of the Point-Cloud . . . 63
4.4 Validation of STAR-V3 . . . 72
4.4.1 Comparison to Other Conventional Retracking Approaches . . . 72
4.4.2 Validation Against Delay Doppler Altimetry . . . 76

5 Separately Estimating Individual Sea Level Contributions 81
5.1 The Sea Level Budget Equation . . . 81
5.2 Global and Regional Mean Sea Level from Radar Altimetry . . . 82
5.2.1 Obtaining Sea Level Anomalies . . . 83
5.2.2 Averaging Sea Level Anomalies . . . 84
5.2.3 Converting Absolute to Relative Sea Level Change . . . 85
5.3 Estimating Ocean Mass Change from Time-Variable Gravity . . . 85
5.3.1 Converting Time-Variable Gravity Observations to Ocean Mass Change . . . 85
5.3.2 Effect of Individual Processing Choices on Ocean Mass Change . . . 88
5.4 Steric Sea Level from Temperature and Salinity Data . . . 92

6 Combination of Space Geodetic Observations in a Global Inversion Framework 95
6.1 Building Inversion Fingerprints . . . 95
6.1.1 Land Glaciers . . . 95
6.1.2 Ice Sheets . . . 97
6.1.3 Terrestrial Hydrology . . . 97
6.1.4 Internal Mass Variations . . . 99
6.1.5 Steric Fingerprints . . . 100
6.1.6 Glacial Isostatic Adjustment . . . 102
6.2 The Global Fingerprint Inversion . . . 105
6.2.1 Input Data Pre-Processing . . . 105
6.2.2 Functional and Stochastic Model . . . 109
6.2.3 Combining Individual Input Data Sets . . . 111
6.2.4 Formal Errors of the Inversion . . . 113
6.2.5 Differences with Respect to Previous Inversions . . . 115
6.2.6 The Base Inversion . . . 117
6.2.7 Extending the Inversion Setup . . . 117
6.2.8 Converting Inversion Steric Sea Level to Ocean Heat Content . . . 118

7 Results: Consistent Closure of the Sea Level Budget 119
7.1 The Global Mean Sea Level Budget . . . 119
7.2 Contribution of Individual Sea Level Components . . . 123
7.2.1 Total Sea Level Change . . . 123
7.2.2 Ocean Mass Change . . . 127
7.2.3 Greenland Mass Change . . . 133
7.2.4 Antarctic Mass Change . . . 136
7.2.5 Land Glacier Mass Change . . . 140
7.2.6 Terrestrial Hydrology Contribution . . . 142
7.2.7 Internal Ocean Mass Variations . . . 146
7.2.8 Steric Sea Level Component . . . 147

7.2.9 Budget Closure: Residuals with Respect to Altimetry . . . 151
7.3 Robustness of the Inversion Results . . . 153
7.3.1 Effect of Variance Component Estimation . . . 153
7.3.2 Impact of Glacial Isostatic Adjustment Correction . . . 153
7.3.3 Regularization of Individual Basins . . . 156
7.3.4 Impact of Different Altimetry Inter-Mission Bias Configurations . . . 157
7.3.5 Impact of Different Fingerprint Setups . . . 158
7.3.6 Impact of the steric fingerprint creation period . . . 160
7.3.7 Applying a 300 km ocean buffer . . . 161
7.4 Extending the Inversion with Additional Input Data . . . 162
7.4.1 Replacing GRACE RL05 with RL06 Data . . . 162
7.4.2 Including GRACE-FO Data . . . 163
7.4.3 Including Additional Altimetry Missions . . . 164
7.4.4 Introducing in-situ Steric Observations from easyCORA . . . 167
7.4.5 Closing the GRACE/GRACE-FO Gap using Swarm and SLR . . . 169
7.4.6 Combining All Available Input Data . . . 171
7.5 Regional Sea Level Budgets . . . 171
7.5.1 Major Ocean Basins . . . 171
7.5.2 Selected Regions of Interest . . . 173
7.6 Additional Inversion Output . . . 175
7.6.1 Low Degree Gravity Coefficients . . . 175
7.6.2 Ocean Heat Uptake and Earth Energy Imbalance . . . 181

8 Conclusions and Outlook **185**
8.1 Conclusions . . . 185
8.2 Outlook . . . 189

A Least Squares Estimation and Modification of Normal Equation Systems **193**
A.1 Least Squares Estimation . . . 193
A.2 Modification of Normal Equation Systems . . . 195
A.2.1 Reducing Parameters . . . 195
A.2.2 Changing the a priori Information . . . 195
A.2.3 Fixing Parameters to a priori Values . . . 196
A.2.4 Linear Transformation of Estimation Parameters . . . 196
A.2.5 Variance Component Estimation . . . 197
A.3 Autoregressive Process . . . 198

B Principal Component Analysis **201**

C Additional Global Sea Level Budget Results **203**

D Acronyms **205**

List of Figures **209**

List of Tables **213**

Bibliography **215**

Chapter 1

Introduction

1.1 Motivation

It is commonly known that sea level is rising on global scales. Regional distribution of non-uniform sea level change, natural and human-induced global and local drivers of sea level as well as socio-economic impacts from current and future sea level change are topics of ongoing research.

In the Earth system, water is transported dynamically between the atmosphere, land and ocean. These mass transports affect the Earth's gravitational field, consequently requiring close monitoring of the gravity field. The ocean changes its salinity as a result of freshwater influx and evaporation, heats up and cools down based on energy fluxes, where all of these effects lead to expansion and contraction of the water column. Measuring those variations in gravity and sea surface height within the Earth system is a key objective of geodesy.

In addition to observations, modeling the dynamic system interactions or parts of it where the physics are known will help in understanding past and present variations as well as aid in predicting future impacts. For the ocean, models simulate the transport of water, heat and salinity within the ocean. Hydrological models provide information on the terrestrial water cycle and ice sheet and glacier models can simulate ice mass change and corresponding mass fluxes. However, models are always a simplified representation of reality. No model is able to replace observational data entirely.

Consistently combining different complementary observation types together with model information plays an integral role in this thesis. Connecting the generally well represented spatial information from models together with the high quality temporal coverage from observations, which might lack spatial coverage, within a global inversion framework results in an improved representation of global and regional sea level changes. It also allows for separation of total observed sea level variations into individual mass and volume change related contributors.

On the other hand, obtaining sea level information in coastal regions, where it is most important in terms of socio-economic costs, is also the most difficult as tide gauge data from many countries is classified information. This makes altimetry an important and reliable provider of coastal sea level data. Different surface properties of the ocean and land areas or local unmodeled perturbing signals will negatively affect the retrieved parameters from satellite altimetry and, thus, require specialized processing in order to provide meaningful results. This thesis will present a novel method to retrieve high quality coastal sea level information.

Overall, the works presented in this thesis will enable retrieving accurate global, regional and coastal sea level information, which is further separated into individual contributions as part of a sea level budget in order to better understand causes of sea level change and the processes connected to it. Ultimately, predictions based on these results can aid in better mitigating future sea level impacts from human induced climate change.

1.2 Sea Level Change, Measured and Modeled Contributions

Total Sea Level Change

Total sea level, i.e. the observed variation of water level, has been changing for millions of years. Today human-induced climate change is the major driver of global and regional sea level changes (Cazenave and Llovel, 2010; Nicholls and Cazenave, 2010; Stocker et al., 2013). About ten percent of the world's population live within 100 km distance to the coast (McGranahan et al., 2007) and rising mean sea level and, especially, the associated rise in sea level extremes, such as storm floods, directly threaten their lives and livelihoods (Kirezci et al., 2020; Calafat et al., 2022). The cost of future damages as a result of rising sea levels is estimated to be around one trillion US Dollar per year (Hallegatte et al., 2013). Consequently, accurate monitoring of coastal sea level change and investigation of individual drivers of global and regional sea level is paramount for understanding the causes and assessing future risks.

Geocentric Sea Level (GSL), or absolute sea level, refers to sea level change relative to an ellipsoid, which describes a well-defined and temporally constant reference surface. However, utilizing GSL is unpractical as the Earth's surface moves and human infrastructure, such as buildings, coastal defenses or tide gauges are generally mounted on the surface. Consequently, Relative Sea Level (RSL) describes the change in sea level relative to the shift, i.e. uplift or subsidence, of the solid surface.

Sea level has always been changing throughout history. Extraction of sea level indicators from coral fossils enables retracing of RSL variations as early as several ten thousand years ago indicating periods of high and low sea level (Lambeck et al., 2010; Hibbert et al., 2016). Some tide gauge stations in Europe observe sea level change dating back to the 17th century providing long-term sea level observations (Woodworth et al., 2010). Hay et al. (2015) report a Global Mean Sea Level (GMSL) trend of 1.20 ± 0.20mm/yr over the last century (1901 till 1990). Similarly, Church and White (2006) found 1.70 ± 0.30mm/yr over 1870-2004. Today, thousands of tide gauge stations exist all over the world providing regular observations of local RSL (Holgate et al., 2013).

In contrast, GSL observed by satellite altimetry can be converted to RSL considering Glacial Isostatic Adjustment (GIA) and contemporary mass changes. Altimeters are flying on defined repeat orbits allowing for regular observation of the same location every 10 to 30 days providing a continuous record of (total) sea level change since 1993. Based on this, a trend of 3.28 ± 0.30mm/yr of GMSL change is observed between 1993 and 2021 (International-Altimetry-Team, 2021).

Nowadays, time series of GMSL are provided routinely by several groups over the world (e.g., Nerem et al., 2010; Watson et al., 2015; Ablain et al., 2019; Nerem et al., 2018). Furthermore, GMSL has been rising over the last decades as observed from globally distributed tide gauge data with an acceleration of 0.01 to 0.02 mm/yr^2 (Church and White, 2006; Jevrejeva et al., 2008; Jevrejeva et al., 2014). Over the altimetry period, acceleration is found to be even higher at the level of 0.08 mm/yr^2 ± 0.03 mm/yr^2 (e.g., Nerem et al., 2018). However, deriving accurate accelerations requires longer observation periods of 40 to 60 years compared to trend estimates (Jordà, 2014) leading to rather large errors.

Sea level change is not uniform, but rather varies regionally with areas exhibiting above average sea level rise as well as those where sea level actually falls (Cazenave and Llovel, 2010). Identifying those regions where sea level rise will have significant socio-economic impact is important (Rayner and MacKenzie, 2010). Consequently, accurate knowledge of global and regional drivers and, especially, coastal sea level change is important to better asses these risks and prepare for future extreme events (Lowe et al., 2010).

Ocean Mass Change

Ocean Mass Change (OMC) generally describes the ocean component of the dynamic mass transports within the Earth's water cycle, exchanging water between atmosphere, ocean and land. Resulting from influx of masses into the ocean and vice versa, the water masses are non-uniformly redistributed. This change in surface load also changes the geoid and the ocean will react to it, usually within a few days (Kuhlmann et al., 2011). The major drivers of OMC are due to variations in terrestrial hydrology, melting of land glaciers as well as the Greenland and Antarctic ice sheets. Furthermore, mass is transported between basins within the ocean, denoted as Internal Mass Variations (IMV) in this thesis. These are driven by ocean currents such as the Gulf Stream, the Kuroshio Current, the Agulhas and the Antarctic Circumpolar Current, leading to significant sea level changes on regional scales (Chambers and Willis, 2009). Wind driven sea level change, however, is not accounted for.

Accurately measuring these mass changes has not been possible until the launch of the Gravity Recovery And Climate Experiment (GRACE) satellite mission (Tapley et al., 2004) in 2002. GRACE enabled unprecedented resolution of global time-variable gravity changes resulting from mass redistribution in within the Earth system, which affects the satellites orbits. Under certain assumptions regarding the distribution of masses, the observed orbit variations can be inverted to infer information on mass transports. Satellite gravity missions, such as GRACE and Gravity Recovery And Climate Experiment Follow On (GRACE-FO) (Kornfeld et al., 2019) as well as in-situ gravimeter measurements on the ground, observe the integral effect of all individual mass and density variations. Changes in mass distribution will also deform the surface of the Earth, which, in turn, will lead to mass displacement below the (water) load, again, indirectly affecting the gravity (Farrell, 1972). On short time scales, such as in this thesis, it is safe to assume that observed OMC is mainly related to transports of water masses. Other physical processes underneath, such as mass transports in the Earth's mantle, are either negligible, or can be modeled. The satellite gravity observations can be utilized to infer information on the causes and drivers of mass related global and regional sea level change.

Time series of global mean OMC are derived on a regular basis (e.g. Chambers and Bonin, 2012; Chen et al., 2013; Johnson and Chambers, 2013; Rietbroek et al., 2016; Uebbing et al., 2019) providing trend estimates of 1.00 to 2.60 mm/yr depending on the applied method, processing corrections and time period (WCRP-Global-Sea-Level-Budget-Group, 2018; Horwath et al., 2022). From the individual drivers of OMC, terrestrial hydrology exhibits the largest amplitude, dominating the mass variability on seasonal to inter-annual scales (Llovel et al., 2010; Milly et al., 2010; Reager et al., 2016; Rietbroek et al., 2016). In contrast, long term trends are rather dominated by the mass components related to ice-melt of the Greenland and Antarctic ice sheets (Steffen et al., 2010; Brunnabend et al., 2012) and land glaciers (Marzeion et al., 2012; Chen et al., 2013; Marzeion et al., 2020). IMV trend influence is negligible for the global ocean, but can become the dominant contributor on regional scales.

Steric Sea Level Change

Besides mass changes, sea level in the ocean will also vary due to volume changes. These are caused by expansion of the water column, defined from the ocean floor to the sea surface. These are caused by variations in temperature and salinity, which will modify the density of seawater leading to a change in volume while the water column mass remains constant (J. A. Church et al., 2010). Consequently, volumetric, or "steric", sea level changes will not cause gravity variations, but the geometric effects are observed by altimetry. Ocean temperature is also directly related to changes in Ocean Heat Content (OHC), which in turn connects to Earth Energy Imbalance (EEI), since the world's oceans store about 93% of the Earth's excess energy as heat (Stocker et al., 2013; Trenberth et al., 2016). EEI refers to the imbalance between the incoming and outgoing radiation

at the top of atmosphere (e.g., Trenberth et al., 2016; Trenberth et al., 2019; von Schuckmann et al., 2020; Hakuba et al., 2021).

Steric sea level change is not directly observed from space, but rather by an array of in-situ floaters as part of the Argo program. The program includes thousands of floats, freely drifting in the ocean and measuring profiles of temperature and salinity, which are then transmitted via satellite connection (Roemmich et al., 2009). However, in-situ profile coverage is not always optimal. In another approach, subtracting OMC derived from GRACE/GRACE-FO from altimetry observed total sea level change will also allow derivation of steric sea level change (Lombard et al., 2007). The latter approach is associated with relatively large errors. As a result, model based estimates from global and regional ocean models and reanalysis, which assimilate in-situ observations (Zuo et al., 2019), are often substituted for actual observations, especially on regional scales (e.g. Legeais et al., 2018).

Since 2005, steric expansion of the ocean contributes by about 1.00 to 1.50 mm/yr accounting for about 40% of GMSL change (WCRP-Global-Sea-Level-Budget-Group, 2018; Horwath et al., 2022) and varies significantly on spatio-temporal scales. Apart from seasonal variations between the hemispheres, global and regional phenomena such as El Niño Southern Oscillation (ENSO) or the Indian Ocean Dipole (IOD) significantly impact steric sea level variations (Boening et al., 2012).

Sea Level Budgets

A sea level budget describes the separation of total sea level change into mass and steric contributions based on globally and regionally averaged time series and corresponding trend estimates (e.g., Cazenave et al., 2009; Chambers et al., 2017; Kusche et al., 2016; Rietbroek et al., 2016; Dieng et al., 2017; WCRP-Global-Sea-Level-Budget-Group, 2018; Hakuba et al., 2021; Horwath et al., 2022). This requires at least two of the three components to be either derived from observational or model data in order to construct a budget. In theory, the sum of mass and steric contributions should equal the total sea level. However, in practice this is never the case resulting in a budget closure error, which serves as a quality indicator for the constructed budget. Accurately closed contemporary sea level budgets are important for predicting future total, mass and steric sea level variations (Gregory et al., 2013).

Commonly, individually processed total GMSL from satellite altimetry is combined with global mean OMC from GRACE and global mean steric sea level, either based on Argo data or ocean reanalysis, in a post-processing step based on time series and trends (e.g. Cazenave et al., 2009; Chambers et al., 2017; Dieng et al., 2017; WCRP-Global-Sea-Level-Budget-Group, 2018; Hakuba et al., 2021; Horwath et al., 2022). Another approach to sea level budgets considers spatial patterns, so called “fingerprints”, derived a-priori from auxiliary data in combination with observed temporal variability (Riva et al., 2010; Rietbroek et al., 2012; Jensen et al., 2013; Rietbroek, 2014; Kusche et al., 2016; Rietbroek et al., 2016; Uebbing et al., 2019). Here, both approaches are investigated with a focus on the fingerprint method. Commonly, budgets are constrained by the availability of observational data, especially OMC tied to the GRACE mission, although recently first attempts have been made to extend these budgets backwards in time based on sparsely available observational data (Frederikse et al., 2020).

The global fingerprint inversion framework (Rietbroek, 2014; Rietbroek et al., 2016) represents the basis for evaluating, further developing and extending the method as part of this thesis. It allows separation of sea level change into individual mass and steric contributions by fitting a combination of along-track satellite altimetry data and GRACE gravity data to a predefined set of fingerprints in order to estimate temporally varying scaling factors (Fig. 1.1). The combination of datasets enables further partitioning of mass changes down to basin scale contributions related to ice melting of land glaciers and from the Greenland and Antarctic ice sheets, terrestrial hydrology

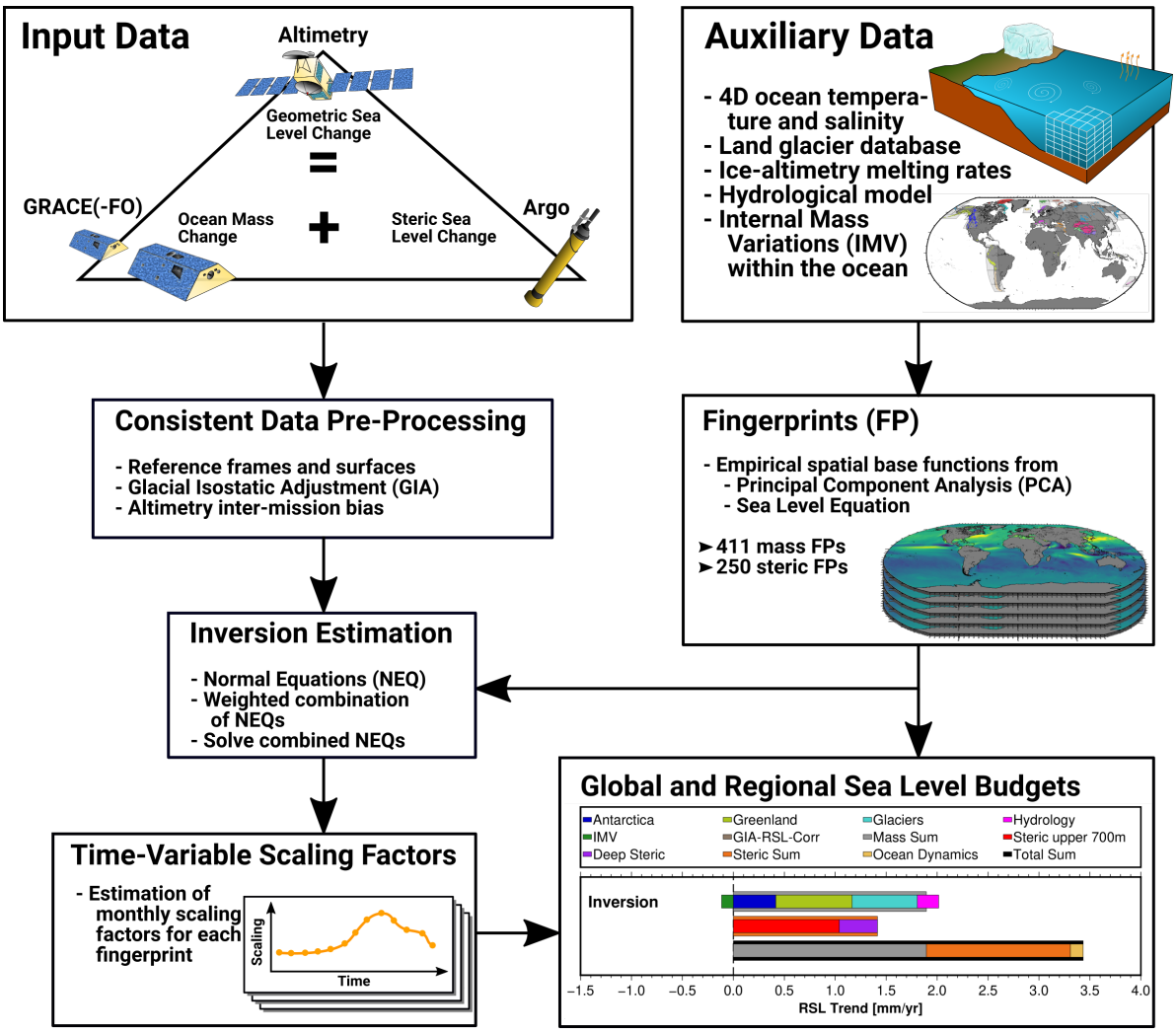


Figure 1.1: General overview of the global fingerprint inversion framework. The sea level budget shown is the same as in section 7.1.

contributions and IMV within the ocean itself. For steric sea level, the water column is split into a shallow (upper 700 m) part and a deep ocean (below 700 m) contribution.

Each fingerprint is generally associated with a specific contributor to sea level change, e.g. a certain melting basin in Greenland or a spatial pattern related to steric change. Recombining the estimated time-variable scaling factors with the corresponding fingerprints enables reconstruction of spatio-temporal sea level variability for each considered contributor down to basin scale (Fig. 1.1). This offers the possibility to reconstruct even budget subsets, e.g., for the Greenland ice sheet or ocean mass in general. Besides global mean sea level budgets, the inversion method also allows relatively easy extraction of regional sea level budgets, since the fingerprints are defined and evaluated spatially (Rietbroek et al., 2016).

In contrast to global mean sea level budgets, regional budgets are more difficult to derive since additional influences from local effects such as wind driven sea level (Dangendorf et al., 2014) or sedimentation (Chang et al., 2019) play a role. So far, published regional sea level budgets are largely limited to the northern hemisphere and to the North Atlantic Ocean, in particular (Fig. 1.2). These budgets are derived over relatively arbitrarily defined regional bounds (e.g. Frederikse et al., 2016; Rietbroek et al., 2016; Frederikse et al., 2017b) leading to limited agreement (Fig. 1.2). In contrast, Kusche et al. (2016) derived a regional sea level budget for the Bay of Bengal defined according to internationally agreed sea region boundaries allowing for better comparability.

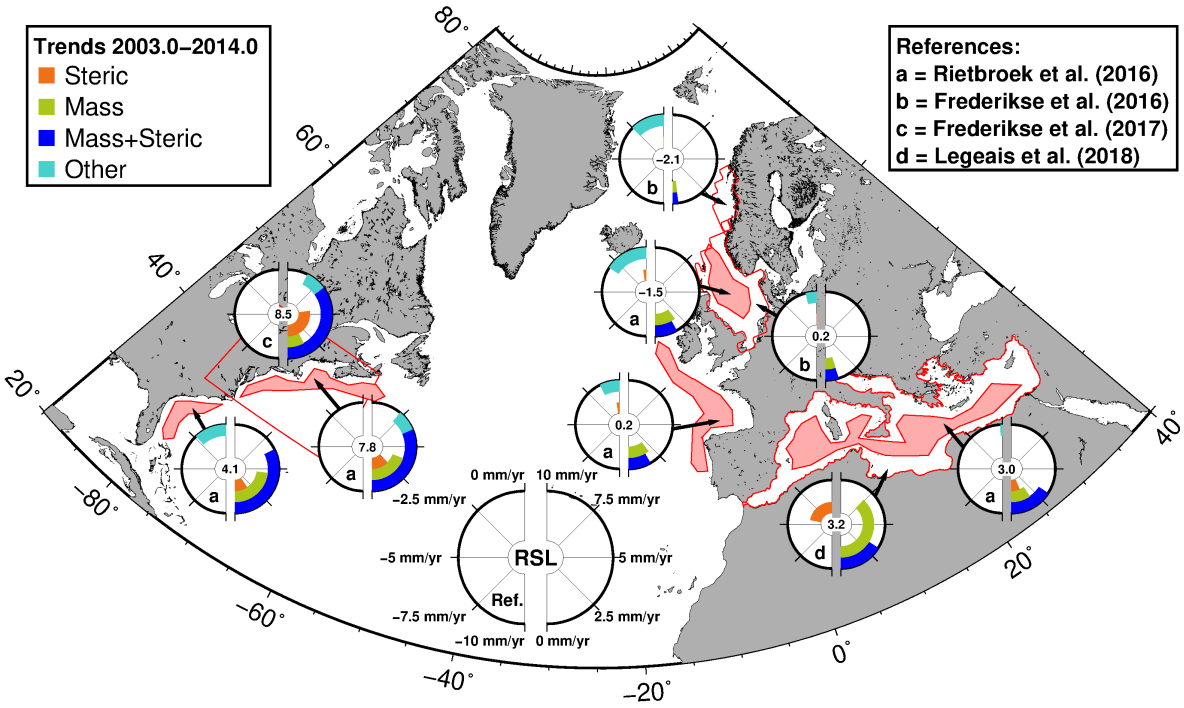


Figure 1.2: Published regional sea level budgets in the northern Atlantic Ocean region.

Coastal Sea Level Change

While tide gauges provide coastal sea level information at a single location, accurate coastal altimetry observations are needed in order to monitor and react early with respect to potential increased risks for the people and infrastructure close to the coast. Predicting future risks related to coastal sea level requires combination of accurate observational data from altimetry and regional high resolution modeling (Ponte et al., 2019). This applies especially to extreme sea level events that increase in frequency and magnitude with rising mean sea levels (Calafat et al., 2022). Variations of sea level in coastal waters result from small effects including shape of the coastlines, fresh water input in estuaries and harbors, changes in ocean circulation, waves and other coastal processes superimposed on signals originating thousands of kilometers away (Woodworth et al., 2019). Observing and identifying these effects and their interaction with land subsidence is fundamental for understanding and predicting risks (Wu et al., 2022). Coastal sea level trends, on average, significantly exceed those of the GMSL (Holgate and Woodworth, 2004), which was also recently confirmed in several case studies investigating open ocean variations relative to coastal ones utilizing specialized coastal analysis methods (Gouzenes et al., 2020; Marti et al., 2021).

Over the open ocean, the signal measured by altimetry is well understood (Brown, 1977; Hayne, 1980) and sea level parameters, such as sea surface height, wave height and wind speed, are retrieved operationally from well defined standard methods (Amarouche et al., 2004). In coastal regions, the return signal, which is to be analyzed, or “retracked”, is prone to signal disturbances due to the different surface reflection characteristics of land and ocean as well as land topography. Retrieval of coastal sea level information requires specialized algorithms (Gommenginger et al., 2011). In addition, atmosphere and tidal corrections are significantly quality-impacted as either required measurements are also perturbed by land influence or model based correction errors increase (Andersen and Scharroo, 2011).

Nowadays, various algorithms to handle these land perturbed radar signals from conventional altimetry have been proposed (e.g. Hwang et al., 2006; Passaro et al., 2014; Uebbing et al., 2015;

Roscher et al., 2017; Buchhaupt et al., 2018), all of which either try to better model or extract relevant sub-signals from the measured perturbed radar signal. However, trying to model every possible disturbance is futile and the estimates from many methods, available today, rapidly degrade over the last few kilometers to the coast. Since about ten years ago, Delay Doppler Altimetry (DDA) (Raney, 1998) has become available, which, depending on the coastal geometry, can significantly reduce the impact of perturbing signals from land providing improved height estimates due to increased along-track resolution. However, long-term records of (coastal) sea level change still also require improvements in conventional altimetry data processing. Therefore, this thesis will introduce a new approach, i.e. the Spatio-Temporal Altimetry Retracker (STAR) method (Roscher et al., 2017), and further expand it resulting in significantly improved estimates, similar to DDA quality, up to less than 1 km off the coast.

1.3 Consistency of Sea Level Budgets

Consistency of individual data sets utilized for deriving sea level budgets is likely the most important aspect. In this thesis, consistency means utilizing and combining different datasets for constructing sea level budgets. This includes considering the same time frame, applying the corrections to each dataset in a way these correspond physically, but also smaller aspects, such as evaluation at the same (grid-)points, applying the same weights and averaging over the same basins. Combining individual steric and mass components, which have been processed independently but inconsistently, leads to an error, which will directly transfer to the budget misclosure error. Inconsistencies can occur at almost all processing steps. Obvious inconsistencies, which are easily identified include different time frames, observational corrections in terms of atmospheric or tidal effects, reference systems and geocenter motion and other physical phenomena, such as GIA. However, even small inconsistencies that are not directly considered can have significant impact. Combining time series, which have been averaged over different "global" basins in combination with individual averaging methods and weighting schemes will lead to significantly different results from the same dataset (Sect. 5.2). In addition, differences in handling of errors and covariance information, e.g., when estimating trends, will directly impact the results leading to largely inconsistent time series, trends and other estimates. These can then neither be combined, e.g., in terms of sea level budgets, nor compared to other self-derived or published results.

While the issues mentioned above seem obvious, one or more of these inconsistencies can be found in published sea level budgets. The publications mentioned in the following, serve as an example for individual, mostly small, inconsistencies and are not meant to represent an exhaustive overview. A common issue that arises in the combination of GRACE and altimetry data is the different "global" coverage of both satellite products. While GRACE covers the whole globe, OMC estimates derived from spherical harmonics are generally limited to a 300 km buffered ocean area in order to remove potential leakage effects from the much stronger terrestrial hydrology signal close to the coast. Altimetry estimates, on the other hand, cover different latitude regimes depending on the utilized missions. Most GMSL estimates are based on the Jason reference mission, which only covers the global oceans up to $\pm 66°$ of latitude. Combining the aforementioned OMC and GMSL time series or similarly derived ones as part of a sea level budget is inconsistent leading to avoidable budget closure errors and interpretation mistakes (e.g., done in Cazenave et al., 2009; Chambers et al., 2017; Dieng et al., 2017). Similar inconsistencies occur when combining time series from altimetry and steric products. Other publications (e.g., WCRP-Global-Sea-Level-Budget-Group, 2018) collect published estimates of GMSL, OMC and steric in form of an ensemble and utilize the ensemble mean hoping this will iron out most of the processing differences. Generally however, this is not the case resulting in potentially large budget closure errors.

Others (e.g., Royston et al., 2020; Hakuba et al., 2021) pay more attention to consistent processing. However, small inconsistencies still occur such as removing a monthly climatology from the steric dataset, while the mass and altimetry have a static mean removed or substituting incon-

sistently processed estimates for individual components, such as the deep ocean steric contribution (e.g., Royston et al., 2020). Most of the inconsistencies mentioned mostly affect the overall budget (mass + steric) directly derived from combination of different datasets. Sub-budgets, such as a mass related sea level budget, are generally a combination of the same observation or model data types and, therefore, less prone to inconsistencies (WCRP-Global-Sea-Level-Budget-Group, 2018; Horwath et al., 2022). Comparisons, while associated with error bounds, are influenced by inconsistencies due to different signal contents of the estimates to be compared. For example, Rietbroek et al. (2016) applied a GRACE background correction to their altimetry data, thereby introducing small residual atmospheric signals. Bad data quality, e.g., due to older processing standards, inconsistently processed datasets or missing sea level components in the budget will generally lead to attributing observed changes to the wrong contribution (e.g., large deep ocean contribution in Rietbroek, 2014).

This thesis emphasizes consistency of datasets and tries to be as consistent as possible when comparing to other results or combining estimates from different datasets individually or as part of the fingerprint inversion. Even though small inconsistencies can have large impacts, such as the weights applied during basin averaging, these are usually not documented in detail and, thus, perfect consistency is not always possible.

1.4 Objectives of this Thesis

From the previous sections open research questions arise, which will be addressed in this thesis. These include

- Can existing conventional altimetry processing schemes be improved to provide higher quality sea surface height, wave height and wind speed in open ocean and, especially, coastal regions?
- What causes the spread in published global sea level, OMC and steric sea level estimates?
- Is the processing of individual altimetry, gravity and steric datasets consistent?
- What caused previous global fingerprint inversion results to diverge from other published estimates?
- Is it possible to reduce the global sea level budget closure error based on consistent data processing?
- Can regional sea level budgets be closed up to a reasonable error based on datasets available today?

Based on these questions, this thesis has two major goals. On the one hand, the development, implementation and assessment of an improved coastal retracking procedure for application to conventional altimetry, called STAR. On the other hand, the construction of consistently closed global and regional sea level budgets from individually processed satellite datasets and, in particular, from a global fingerprint inversion framework, which allows for consistent combination of various observational datasets. The inversion enables separation not only limited to mass and steric contributions, but also further partitioning of mass changes down to basin scale as well as separating the steric effect based on different ocean depth levels. In order to achieve these major goals, the tasks have been split into the following five objectives.

1) Improved retrieval of coastal sea level estimates by implementing a novel sub-waveform retracking approach:

In altimetry retracking there are generally two concepts: (1) finding the perfect model for the radar return signal that can handle land perturbations (e.g., Halimi et al., 2013) or (2) extracting relevant sub-signals that are then processed individually allowing to ignore the

perturbed parts of the signal (e.g. Hwang et al., 2006; Passaro et al., 2014; Uebbing et al., 2015; Boergens et al., 2016). This thesis concentrates on the second point. Consequently, the hypothesis of this first objective is, that instead of trying to find the perfect waveform-model that can explain every shape of altimetry waveform, the problem can be postponed to a later stage, where additional information can be utilized for finding improved Sea Level Anomaly (SLA), Significant Wave Height (SWH) and Backscatter Coefficient (σ°) over open ocean and coastal areas. This is achieved by, first, generating a significant number of sub-waveforms, which are then each retracked with a simple, but, robust retracker, resulting in individual point-clouds for each of the three parameters. These point-clouds along the satellite groundtrack can then be further analyzed by means of a shortest-path algorithm, assuming similarity between neighboring points. In order to select a final estimate at each along-track altimetry position, prior information can be incorporated into the point-cloud analysis. The results from implementing this approach will be validated against other state-of-the-art conventional altimetry retrackers, as well as highly accurate estimates from coastal DDA. A first version of this approach has been published in Roscher et al. (2017). This thesis will build on that, eliminate disadvantages and extend the STAR algorithm to provide further improved retracking results in open ocean as well as coastal areas.

2) Analyze and improve the processing of individual satellite altimetry and time-variable gravity data in the context of deriving consistent sea level budgets:

This objective aims at examining, understanding and assessing state-of-the-art processing procedures for satellite altimetry, time-variable satellite gravity and steric datasets in order to derive GMSL, global mean OMC and steric sea level change, respectively. To understand differences in published estimates, based on the same data and the same time period, different processing steps are reviewed in terms of impact on the desired results and consistency in the context of deriving sea level budgets from combining, at least, two of these datasets. Special focus is put on the derivation of consistent OMC estimates, since individual processing choices will significantly affect the resulting OMC estimate. Works in the context of this thesis uncovered a common inconsistency in the widely applied GRACE processing, which, after correction, led to significantly improved global mean OMC. Results from this work have been published in Uebbing et al. (2019).

3) Improve and expand the Rietbroek (2014) inversion methodology:

In order to facilitate consistent estimation of high quality sea level budgets, the parameterization and individual processing components of the global fingerprint inversion method by Rietbroek (2014) will be assessed, improved and expanded. For this, the fingerprint basis of the inversion will be updated based on newly available auxiliary data as well as new fingerprints accounting for IMV, a previously neglected component, will be introduced. Negative impacts on the derived sea level budget from co-estimating GIA and altimetry Inter-Mission Bias (IMB) are evaluated and the inversion scheme will be adapted accordingly. Furthermore, the two-step processing scheme, where the residuals from the first step are introduced as another set of fingerprints, will be abandoned as this adversely affects the other components. Also, due to general residual reduction from other improvements, this will no longer be necessary.

4) Investigate possibilities for including additional datasets in the inversion:

In the outlook of Rietbroek (2014) it was hypothesized that inclusion of additional input datasets would benefit the inversion in terms of separability of individual mass and steric components. This will be investigated by assessing the earlier input data and expanding these by introducing multi-mission along-track altimetry data, including non-repeat orbit missions, which has not been possible before. This requires restructuring of parts of the inversion processing as well as an improved implementation optimized in terms of run-time as the design matrix needs to be constructed on a monthly basis. Adapting the inversion

to handle individually distributed data points will also enable a relatively easy inclusion of in-situ steric profile data. Furthermore, usage of Satellite Laser Ranging (SLR) and Swarm time-variable gravity data, in combination with the previously mentioned steric in-situ data, will be investigated in order to overcome the inversion's limitation of requiring GRACE data for separating the total sea level on a monthly basis. This will not only allow filling of individual missing GRACE months, but also extending the analysis to the gap between the GRACE and GRACE-FO missions as well as being a first step for future extension backwards in time before the GRACE era.

5) Consistent closure of global and regional sea level budgets:

Based on the improved inversion framework from (3) and (4), consistently closed global and regional sea level budgets will be produced. These are analyzed in terms of validity of individual mass and steric components by comparing and assessing these in context of published results as well as against independent validation data. Regions of interest are to be defined according to international standards. The residuals with respect to altimetry data and the corresponding budget closure error will be investigated also in terms of an often observed bias (e.g., Barnoud et al., 2021) between the GRACE and GRACE-FO era, likely related to Jason-3 altimetry data.

Parts of the work in this thesis have been published over the years. However, not all of those fit in the context of coastal sea level change and sea level budgets and are, consequently, not further discussed in this thesis. A first retracker dealing with retrieval of inland water surface heights has been published in Uebbing et al. (2015). The first version of the coastal altimetry STAR retracking method has been developed in collaboration with Prof. Dr. Ribana Roscher and was published in Roscher et al. (2017). This thesis eliminates identified weaknesses and further improves the method in terms of an efficient C++ implementation as well as providing significantly improved results. When applied to Reduced Synthetic Aperture Radar (RDSAR) data, the obtained quality of the individual estimates are comparable to state-of-the-art DDA over the open ocean and in coastal areas. Furthermore, based on the STAR pointcloud a river retracking approach has been implemented where the results have been utilized by S. Schröder et al. (2019). Furthermore, intermediate versions of the STAR retracker have been employed as part of evaluating DDA from the Cryosat-2 and Sentinel-3A mission along the German coast (Fenoglio et al., 2019). A similar extensive validation study confirmed the high quality of STAR in coastal regions (Fenoglio et al., 2021).

A first regional sea level budget for the Bay of Bengal has been published in Kusche et al. (2016). An error in the processing of GRACE data in term of global mean OMC has been uncovered in Uebbing et al. (2019) and, consequently, the standards of processing have been adapted. Uebbing et al. (2019) also utilized OMC extracted from an intermediate inversion solution for additional reference. Finally, Uebbing et al. (2017) successfully transferred the inversion concept for deriving soil moisture based on along-track altimetry backscatter information.

1.5 Thesis Outline

Chapter 2 introduces the theoretical concepts related to sea level theory. First, the mathematical representation of the Earth's gravity field is introduced including the description of surface loading effects (Sect. 2.1), which is the basis for the self-consistent sea level theory (Sect. 2.2). Conversion of temperature and salinity into steric sea level change and OHC is described in section 2.3. The reference systems relevant for this thesis are introduced in section 2.4.

Chapter 3 introduces the observation and model data employed in this thesis. Section 3.1, describes altimetry missions, principle and basic data handling. Time-variable gravity data from GRACE/GRACE-FO, SLR and Swarm is introduced in section 3.2. Next, temperature and salinity

observations from in-situ profile floats and ocean model reanalysis are explained (Sect. 3.3). The auxiliary data, relevant for building the inversion fingerprints, is introduced in section 3.4.

Chapter 4 introduces the basic concepts of altimeter retracking (Sect. 4.1), followed by a description of commonly used physical and empirical retrackers as well as sub-waveform approaches (Sect. 4.2). The STAR retracking method developed in this thesis is then described in section 4.3 and a validation of STAR retracking results is presented in section 4.4.

Chapter 5, first, introduces the general concepts of sea level budgets (Sect. 5.1). Then, published altimetry based computations of GMSL are examined (Sect. 5.2). Processing steps and their effect on time series and trends of global mean OMC as well as improved processing concepts, developed as part of this thesis, are presented in section 5.3. Steric estimates from different temperature and salinity datasets are compared in section 5.4.

Chapter 6 describes the inversion framework. First, the derivation of the mass and steric related fingerprints is introduced (Sect. 6.1), followed by explanations of the input data pre-processing, the functional and stochastic models as well as general processing and handling of the inversion data (Sect. 6.2).

Chapter 7 presents consistently closed global and regional sea level budgets. First, a global budget is presented, which is as consistent as possible to budgets published in the past (Sect. 7.1). Then, individual mass and steric contributors are analyzed in section 7.2. The robustness of the inversion method with respect to parameterization and processing options is examined in section 7.3. Section 7.4 augments the inversion with additional datasets and analyzes their effect on the global mean sea level budget. Closure of regional sea level budgets is presented in section 7.5. Additional useful outputs, that can be extracted from the inversion as a byproduct, are investigated in section 7.6.

Finally, chapter 8 summarizes the major findings from this thesis and provides an outlook to further utilize and extend the developed coastal retracker and the global fingerprint inversion.

Chapter 2

Sea Level Theory: Gravity, Loading and Steric Sea Level

Sea level is, to a large extent, driven by gravity and loading changes, deformations of the ocean basins due to loading effects, and steric (volumetric) sea level changes. Consequently, a corresponding theoretical background is necessary in order to understand and model contemporary and future sea level changes. Sea level theory summarized in this chapter includes the mathematical and physical background of mass and steric related sea level change, the passive sea level theory and the involved observational reference frames. In combination, this provides the basis for partitioning the total sea level change into individual contributions as part of the sea level budget. However, this section does not cover ocean internal barotropic and baroclinic dynamics or responses to wind or pressure changes, where the latter are corrected by applying the inverse barometric correction. Wind driven impact on sea level can be assumed to be negligible on global scales, however, these can become relevant for regional studies (Sect. 7.5.2).

Total sea level change consists of various individual mass and steric contributions as well as influences from varying ocean circulation or wind-driven changes (Sect. 1.2). Mass (gravity + loading) and steric sea level are the major contributor to total sea level change on monthly scales, wind-driven changes are often associated with short time scales. Ocean circulation varies on short and long time scales and is directly connected to heat transport and, thus, steric variations within the ocean (Winton et al., 2013). However, the impact from ocean circulation changes as well as short-time wind-driven effects on sea level budgets for time scales considered in this thesis is small.

This chapter, first, introduces the theoretical backgrounds for the Earth's gravity field (Sect. 2.1) including the elastic deformation of the Earth surface and corresponding gravity changes. The passive self-consistent sea level response provides the change in sea level resulting from surface load changes, e.g. melting of land ice and is introduced in section 2.2. Conversion of temperature and salinity profiles to steric sea level change is described in section 2.3 including the connection between thermo-steric sea level and ocean heat content. Finally, section 2.4 describes the reference frames and corresponding conversions utilized throughout this thesis.

2.1 The Gravity Field of the Earth

The Earth's gravitational field is generally not static but varies over spatial and temporal scales. These changes can be almost static over time, such as large scale ocean circulations. This includes secular effects from convection of material in the Earth's mantle or changes to the lithosphere and plate boundaries, as well as visco-elastic effects of GIA due to ice loads during the last glacial maximum. On monthly to decadal time scales, the gravitational change is mostly driven by the movement of water within the Earth system (Sect. 1.2). On sub-monthly to sub-daily scales gravity mostly varies due to tides caused by time-variable forces from the Sun and Moon, as well as instantaneous events, such as Earth quakes or eruptions of volcanoes and dry air mass variability.

2.1.1 Mathematical Representation of the Earth's Gravity Field

The mathematical basics for representing the Earth's gravity field are based on Heiskanen and Moritz (1967) with the notation adjusted to this thesis where necessary.

The gravitational potential of a point mass Φ at a distance l from the Earth is given by

$$\Phi = \frac{GM}{l}, \tag{2.1.1}$$

with $GM = 3986004415 \cdot 10^5\ \mathrm{m^3\,s^{-2}}$ representing the product of the Earth's mass M with the gravitational constant $G = (6.672 \pm 4) \cdot 10^{-11}\ \mathrm{m^3\,s^{-2}\,kg^{-1}}$. While equation (2.1.1) is valid for point masses, the potential at point $\boldsymbol{r}$ for a distribution of masses within the (non-rotating) Earth system becomes

$$\Phi(\boldsymbol{r}) = G \oint_{V_{\mathrm{earth}}} \frac{\rho(v')}{|\boldsymbol{r} - \boldsymbol{r}'|} dv', \tag{2.1.2}$$

with contributions from each volume element dv' at position $\boldsymbol{r}'$. The gravity acceleration on an other body at distance l, such as a satellite, is derived from the potential by computing its gradient vector

$$\boldsymbol{g} = \nabla\Phi. \tag{2.1.3}$$

Computing the second derivative of the gravitational potential outside the attracting body yields Laplace's equation

$$\Delta\Phi = \nabla^2\Phi = 0. \tag{2.1.4}$$

The solutions for this second order differential equation are harmonic basis functions. Expressing Laplace's equation in spherical coordinates of longitude λ and co-latitude θ, which relates to the latitude φ by $\theta = 90° - \varphi$, and radial distance r to the origin of the Earth-fixed coordinate system, leads to a solution for the exterior of the attracting body, which is given in terms of spherical harmonic functions

$$\Phi(\lambda, \theta, r) = \sum_{n=0}^{\infty} \frac{Y_n(\lambda, \theta)}{r^{n+1}}. \tag{2.1.5}$$

By further separating the longitude and latitude dependent terms it can be shown that the general solution for the surface spherical harmonics $\widetilde{Y}_n(\lambda, \theta)$ can be expressed as

$$\widetilde{Y}_n(\lambda, \theta) = \sum_{m=-n}^{n} C'_{nm} \widetilde{Y}_{nm} = \sum_{m=0}^{n} \left[c'_{nm} \cos(m\lambda) + s'_{nm} \sin(m\lambda)\right] \tilde{P}_{nm}(\cos(\theta)), \tag{2.1.6}$$

where c'_{nm} and s'_{nm} are the spherical harmonic coefficients and $\tilde{P}_{nm}(\cos(\theta))$ are the associated Legendre functions of degree n and order m. The surface spherical harmonic base functions $\widetilde{Y}_{nm}$ are given by

$$\widetilde{Y}_{nm} = \begin{cases} \cos(|m|\lambda)\tilde{P}_{nm}(\cos(\theta)) & m \geq 0 \\ \sin(|m|\lambda)\tilde{P}_{n|m|}(\cos(\theta)) & m < 0, \end{cases} \tag{2.1.7}$$

and

$$C'_{nm} = \begin{cases} c'_{n|m|} & m \geq 0 \\ s'_{n|m|} & m < 0. \end{cases}$$

The Legendre functions can be derived using a stable recursion formula (see e.g., Heiskanen and Moritz, 1967). Converting equation (2.1.5) from a unit sphere to be applied to a spherical Earth of mass M and radius a and inserting equation (2.1.6) leads to the representation of the Earth's gravity potential

$$\Phi(\lambda, \theta, r) = \frac{GM}{a} \sum_{n=0}^{\infty} \left(\frac{a}{r}\right)^{n+1} \sum_{m=0}^{n} \left[c_{nm} \cos(m\lambda) + s_{nm} \sin(m\lambda)\right] P_{nm}(\cos(\theta)), \tag{2.1.8}$$

with the dimensionless Stokes coefficients c_{nm} and s_{nm}, and the fully normalized Legendre functions $P_{nm}(\cos(\theta)) = \eta_{nm}\tilde{P}_{nm}(\cos(\theta))$, which are generally used in the context of gravity field determination in physical geodesy. The normalization factor η_{nm} is given by

$$\eta_{nm} = \sqrt{(2-\delta_{0m})\,(2n+1)\,\frac{(n-m)!}{(n+m)!}}, \tag{2.1.9}$$

with the Kronecker delta function

$$\delta_{nm} = \begin{cases} 1 & \text{if } n = m \\ 0 & \text{else.} \end{cases}$$

This is based on the orthogonality relation between the individual surface spherical harmonics Y_{nm} by integrating over the unit sphere Ω

$$\oint_{\Omega} Y_{nm}(\omega)Y_{n'm'}(\omega)d\omega = 4\pi\delta_{nn'}\delta_{mm'}. \tag{2.1.10}$$

In practice, the Stokes coefficients of the gravitational potential Φ are provided at the surface of the Earth, which is rotating with angular speed Ω_E, inducing an additional centrifugal potential Λ. When the rotation axis is perfectly aligned with the Z-axis of the terrestrial reference frame, Λ is given by

$$\Lambda(r,\theta) = \frac{1}{2}\Omega_E^2(r\sin(\theta))^2 = \frac{1}{2}\Omega_E^2 r^2(1-\tilde{P}_2(\cos\theta)). \tag{2.1.11}$$

The sum of the gravitational and centrifugal potential describes the gravity potential. An equipotential surface is defined as a surface where the gravity potential is the same at every location. The geoid, N, is a special equipotential surface, which is aligned with the shape of the mean sea surface when the ocean shape is only affected by the gravity potential, i.e. in the absence of dynamic influences, such as currents. The geoid height undulation above the ellipsoid can be approximated by following Bruns formula (Heiskanen and Moritz, 1967)

$$N = \frac{\Phi + \Lambda - \tilde{U}}{\gamma}, \tag{2.1.12}$$

with the normal potential $\tilde{U}$ of the chosen ellipsoid (e.g. GRS80), also including Λ and the associated normal gravity γ. In this thesis, the geoid undulation is represented as a time-variable deviation from a temporal mean state, which means that $\tilde{U}$ is commonly replaced by a multi year mean gravity field and γ with the mean gravity g, resulting in computation of geoid perturbations δN. This can be expressed in terms of Stokes coefficient anomalies $\Delta c_{nm} = c_{nm} - \bar{c}_{nm}$ after reducing the mean values $\bar{c}_{nm}$ at each time t as

$$\delta N(\lambda,\theta,r,t) = a\sum_{n=0}^{\infty}\left(\frac{a}{r}\right)^{n+1}\sum_{m=0}^{n}\left[\Delta c_{nm}\cos(m\lambda) + \Delta s_{nm}\sin(m\lambda)\right]P_{nm}(\cos(\theta)). \tag{2.1.13}$$

2.1.2 Surface Loading

Following from Stokes' theorem, a harmonic exterior potential $\widetilde{\Phi}$ outside a body with a surface Ω is directly and uniquely determined by its values on Ω, but there exists an infinite number of mass distributions, which generate the same $\widetilde{\Phi}$ (Heiskanen and Moritz, 1967). This means that it is possible to compute the corresponding gravitational potential Φ from a given mass distribution of the Earth, but explicitly solving the inverse problem is generally impossible. However for the Earth and short time scales of a few years, the majority of time-variable gravity changes originate from water transport between ocean, air, ice, and land hydrology as well as within each of the subsystems as part of the global water cycle. Consequently, it is generally assumed that the observed (water) mass changes occur in a thin layer with height h_w at the Earth's surface (Fig. 2.1). It is

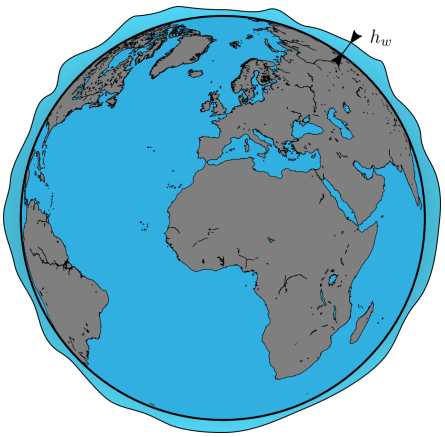


Figure 2.1: Thin shell approximation. All mass changes are expressed as a change in surface density $\sigma(\omega')$, where the Equivalent Water Height (EWH), h_w, is spatially and temporally variable under assumption of a fixed reference density, ρ_w, of seawater.

possible to adapt equation (2.1.2) for a spherical thin shell as

$$\delta\Phi(\boldsymbol{r}) = G \oint_{|r'|=R} \frac{\sigma(\omega')}{|\boldsymbol{r} - \boldsymbol{r}'|} a^2 d\omega', \tag{2.1.14}$$

where the density $\rho(v')$ is replaced by the surface density $\sigma(\omega') \approx \rho_w h_w$ (in $\mathrm{kg\,m^{-2}}$). The deformation and potential change of an elastic Earth is described by a system of three linear partial differential equations. The momentum equation describes the deformation and stress change with respect to a reference state (indicated by subscript 0)

$$\nabla \cdot \boldsymbol{\sigma} + \nabla(\rho_0 g_0 \boldsymbol{s} \cdot \boldsymbol{e}_r) - \rho_0 \nabla \delta\Phi - \delta\rho g_0 \boldsymbol{e}_r = 0, \tag{2.1.15}$$

with the stress tensor $\boldsymbol{\sigma}$, density ρ, gravitational acceleration g, displacement vector $\boldsymbol{s}$ and the perturbed gravitational potential $\delta\Phi$. This relates to a change in density $\delta\rho$ by Poisson's equation (e.g., Farrell, 1972)

$$\Delta\Phi = -4\pi G \delta\rho. \tag{2.1.16}$$

Finally, the density change $\delta\rho$ is related to the displacement $\boldsymbol{s}$ by the continuity equation

$$\delta\rho = \nabla \cdot (\rho \boldsymbol{s}). \tag{2.1.17}$$

In general, the Earth is assumed to be a Spherically-symmetric Non-rotating Elastic Isotropic (SNREI) body (e.g., Pagiatakis, 1990; Sabadini and Vermeersen, 2004). According to the Love-Shida hypothesis, the deformation response of a radially symmetric Earth induced by a point load must also be axially symmetric (Love, 1909). The solution of the momentum, Poisson and continuity differential equations of the Earth's surface response to an axially-symmetric surface load consists of a radial (U) and horizontal (V) component, which is given by (Farrell, 1972)

$$\boldsymbol{s}(r, \alpha) = \sum_{n=0}^{\infty} \left[U_n(r) P_n(\cos\alpha) \boldsymbol{e}_r + V_n(r) \frac{dP_n(\cos\alpha)}{d\alpha} \boldsymbol{e}_\alpha \right], \tag{2.1.18}$$

in accordance with the Love-Shida hypothesis. The deformation $\boldsymbol{s}$ depends only on the radial distance and the angle α between the position of the point load and the location of interest. Applying Bruns formula given by equation (2.1.12), the corresponding potential change is expressed as geoid height variation

$$\delta N(r, \alpha) = \sum_{n=0}^{\infty} \frac{\delta\Phi_n(r)}{g} P_n(\cos\alpha). \tag{2.1.19}$$

In the following, the radius is always set to $r = a$ since the deformations and potential changes are considered to occur at the Earth's surface and, consequently, this dependency is omitted in the notation for ease of reading. According to Farrell (1972), the elastic deformation of a sphere due

to an axially symmetric point load Φ'^p can be written for each degree n in terms of dimensionless load Love numbers h'_n, l'_n, and k'_n as

$$\begin{bmatrix} U_n \\ V_n \\ \Phi_n \end{bmatrix} = \Phi'^p_n \begin{bmatrix} \frac{h'_n}{g} \\ \frac{l'_n}{g} \\ 1 + k'_n \end{bmatrix}. \tag{2.1.20}$$

From equation (2.1.20) it becomes clear that the potential change and the deformation are forced by the potential of the point load Φ'^p. For a point load of 1 kg, the direct potential contribution Φ'^p following from equation (2.1.14) can be written as

$$\delta\Phi'^p(\boldsymbol{r}, \alpha) = \frac{G}{|\boldsymbol{r} - \boldsymbol{r}'|} = G \sum_{n=0}^{\infty} \frac{|\boldsymbol{r}'|^n}{|\boldsymbol{r}|^{n+1}} P_n(\cos\alpha), \tag{2.1.21}$$

where the distance $|\boldsymbol{r} - \boldsymbol{r}'|$ between observed ($\boldsymbol{r}$) and source ($\boldsymbol{r}'$) position is expressed as an infinite series of Legendre Polynomials $P_n(\cos\alpha)$. For the Earth's surface, $|\boldsymbol{r}| = |\boldsymbol{r}'| = a$ and after substituting $G = \frac{ga^2}{M}$ this becomes

$$\delta\Phi'^p(a, \alpha) = \sum_{n=0}^{\infty} \Phi'^p_n P_n(\cos\alpha), \tag{2.1.22}$$

with $\Phi'^p_n = \frac{ag}{M}$. Further substituting equation (2.1.22) into equations (2.1.18) and (2.1.19) allows to derive Green's functions G_x for the Earth's deformation and potential change response to an imposed unit load (see also Farrell, 1972)

$$\begin{aligned} \mathsf{G}_U(\alpha) &= \frac{a}{M} \sum_{n=0}^{\infty} h'_n P_n(\cos\alpha), \\ \mathsf{G}_V(\alpha) &= \frac{a}{M} \sum_{n=1}^{\infty} l'_n \frac{dP_n(\cos\alpha)}{d\alpha}, \\ \mathsf{G}_N(\alpha) &= \frac{a}{M} \sum_{n=0}^{\infty} (1 + k'_n) P_n(\cos\alpha). \end{aligned} \tag{2.1.23}$$

In this thesis, the load Love numbers are chosen based on the Preliminary Reference Earth Model (PREM, Dziewonski and Anderson, 1981) up to a finite maximum degree $N_{\max}$. For a large $N_{\max}$, the load Love numbers become nearly constant and can be written as (comp. Eq. (37) in Farrell, 1972)

$$\begin{aligned} \lim_{n\to\infty} h'_n &= h'_\infty \\ \lim_{n\to\infty} n l'_n &= l'_\infty \\ \lim_{n\to\infty} n k'_n &= k'_\infty \end{aligned} \tag{2.1.24}$$

Making use of the superposition principle, the Green's functions for the axially symmetric surface point load can be generalized to derive the deformation and potential change of geographically varying changes of surface loads by applying a Kummer transformation (comp. Eqs. (39) and (45) in Farrell, 1972). The corresponding Green's functions of the surface mass elements are then convoluted with the mass $\sigma(\omega')a^2 d\omega'$ extracted from equation (2.1.14). For the radial deformation this results in

$$U(\lambda, \theta) = \int_\Omega \mathsf{G}_U(\alpha)\sigma(\lambda', \theta')a^2 d\omega' \tag{2.1.25}$$

According to the addition theorem for spherical harmonics, the Legendre polynomial can be further expressed as

$$P_n(\cos(\alpha)) = \frac{1}{2n+1} \sum_{m=-n}^{n} Y_{nm}(\lambda,\theta) Y_{nm}(\lambda',\theta'). \tag{2.1.26}$$

Similarly, the surface density can be expanded to spherical harmonics

$$\sigma(\lambda,\theta) = a\rho_\omega \sum_{n=0}^{\infty} \sum_{m=-n}^{n} T_{nm} Y_{nm}(\lambda,\theta), \tag{2.1.27}$$

with the dimensionless spherical harmonic coefficients of the surface density T_{nm} and the average density of sea water $\rho_w = 1025\,\mathrm{kg\,m^{-3}}$. The choice of ρ_w is related to the thin shell approximation introduced above (Fig. 2.1), where the mass changes in the thin layer at the Earth's surface are considered to be explained by the transport of water masses. Substituting equation (2.1.26) into equation (2.1.23), the result together with equation (2.1.27) can then be used to rewrite equation (2.1.25) to

$$U(\lambda,\theta) = \frac{a^4\rho_w}{M} \int_\Omega \sum_{n=0}^{\infty} \sum_{m=-n}^{n} \frac{h'_n}{2n+1} Y_{nm}(\lambda,\theta) Y_{nm}(\lambda',\theta') \sum_{n'=0}^{\infty} \sum_{m'=-n'}^{n} T_{n'm'} Y_{n'm'}(\lambda',\theta') d\omega'. \tag{2.1.28}$$

Considering only the non-zeros according to the orthogonality relation equation (2.1.10) and replacing the mass of the Earth with $M = \frac{4}{3}\pi a^3 \rho_e$, with the mean Earth density $\rho_e = 5517\,\mathrm{kg\,m^{-3}}$, equation (2.1.28) is reduced to

$$U(\lambda,\theta) = \frac{3a\rho_w}{\rho_e} \sum_{n=0}^{\infty} \sum_{m=-n}^{n} \frac{h'_n}{2n+1} T_{nm} Y_{nm}(\lambda,\theta). \tag{2.1.29}$$

When introducing the surface gradient operator $\nabla_\Omega = \boldsymbol{e}_\lambda \frac{\partial}{\sin\theta \partial\lambda} + \boldsymbol{e}_\theta \frac{\partial}{\partial\theta}$, the reduced form of the North- and East-component vector of the horizontal deformation, $\mathbf{V}$ can be written as

$$\mathbf{V}(\lambda,\theta) = \frac{3a\rho_w}{\rho_e} \sum_{n=0}^{\infty} \sum_{m=-n}^{n} \frac{l'_n}{2n+1} T_{nm} \left[\frac{\partial Y_{nm}(\lambda,\theta)}{\sin\theta \partial\lambda} \boldsymbol{e}_\lambda + \frac{\partial Y_{nm}(\lambda,\theta)}{\partial\theta} \boldsymbol{e}_\theta \right]. \tag{2.1.30}$$

The potential change is derived similar to the radial deformation resulting in

$$\delta\Phi(\lambda,\theta) = \frac{3ag\rho_w}{\rho_e} \sum_{n=0}^{\infty} \sum_{m=-n}^{n} \frac{1+k'_n}{2n+1} T_{nm} Y_{nm}(\lambda,\theta). \tag{2.1.31}$$

Rewriting the deformation of a SNREI Earth according to the Love-Shida hypothesis from equation (2.1.18) in spherical harmonics

$$\boldsymbol{s}(\lambda,\theta) = \sum_{n=0}^{\infty} \sum_{m=-n}^{n} \left[U_{nm} Y_{nm}(\lambda,\theta) \boldsymbol{e}_r + V_{nm} \nabla_\Omega Y_{nm}(\lambda,\theta) \right], \tag{2.1.32}$$

and considering the analytical solution to the Laplace equation (Eq. (2.1.8)) allows to relate the surface density coefficients T_{nm} to the corresponding radial (U_{nm}) and horizontal (V_{nm}) deformation coefficients as well as to the residual Stokes coefficients (δC_{nm}) by

$$U_{nm} = \frac{3a\rho_w}{\rho_e} \frac{h'_n}{2n+1} T_{nm}, \tag{2.1.33}$$

$$V_{nm} = \frac{3a\rho_w}{\rho_e} \frac{l'_n}{2n+1} T_{nm}, \tag{2.1.34}$$

and

$$\delta C_{nm} = \frac{1+k'_n}{2n+1}\frac{3\rho_w}{\rho_e}T_{nm}. \tag{2.1.35}$$

From equation (2.1.31) it is possible to derive the thickness of the water layer h_w (Fig. 2.1), which exerts the same gravitational attraction that is related to a surface load induced gravitational potential change $\delta\Phi$, defined as Equivalent Water Height (EWH)

$$h_w(\lambda,\theta) = \frac{a\rho_e}{3\rho_w}\sum_{n=0}^{\infty}\sum_{m=-n}^{n}\frac{2n+1}{1+k'_n}\delta C_{nm}Y_{nm}(\lambda,\theta). \tag{2.1.36}$$

Furthermore, it is possible to directly relate the uplift and vertical deformation coefficients to the Stokes coefficients by substituting equation (2.1.35) into equations (2.1.33) and (2.1.34)

$$U_{nm} = a\frac{h'_n}{1+k'_n}\delta C_{nm} \tag{2.1.37}$$

$$V_{nm} = a\frac{l'_n}{1+k'_n}\delta C_{nm}. \tag{2.1.38}$$

When the solid part of the Earth is rigid, the load Love numbers become zero for all degrees. While the surface deformation on a rigid Earth is indeed zero, which is obvious from equations (2.1.33) and (2.1.34), there is still a direct non-zero potential change following from equation (2.1.35) related to the rigid Earth Stokes coefficients δC^r_{nm}

$$\delta C^r_{nm} = \frac{1}{2n+1}\frac{3\rho_w}{\rho_e}T_{nm}. \tag{2.1.39}$$

2.2 Self-Consistent Sea Level Theory

The gravitationally self-consistent sea level theory describes ocean mass variations due to changes in surface loading. As part of the Earth's water cycle, water masses are transported between land, ocean and atmosphere. Over land, water masses are stored irregularly in lakes, groundwater reservoirs, glaciers and as part of the ice sheets in Greenland and Antarctica. The exchange between land based water reservoirs is therefore limited. In the ocean, water masses are distributed and balanced rather easily and, thus, the sea surface adapts to a new equipotential surface.

This adaption of the sea surface to the geoid occurs rather quickly, within a few days (Kuhlmann et al., 2011), assuming the ocean is nearly at rest, which is generally interpreted as the passive sea level response of the ocean to an external load. In this thesis, the focus is on monthly variations in ocean (mass) changes and, therefore, the ocean is assumed to react to load changes following the passive sea level response, thus, neglecting short-term variations. Furthermore, passive sea level refers to sea level variations due to the modeled surface load changes and does not include dynamic effects, e.g., resulting from changes in ocean transport from increased freshwater inflow; this effect is later somehow mitigated by accounting for the Internal Mass Variations (IMV) contribution (Sect. 6.1.4).

Mathematically, the passive sea level response due to a forcing by a surface load is described by the Sea Level Equation (SLE) (e.g. Farrell and Clark, 1976) whereas the physical principles go back to Woodward (1888). For solving the SLE forced by an (visco-)elastic loading due to melting of land ice one generally employs an iterative approach (Farrell and Clark, 1976; Sabadini and Vermeersen, 2004). In this thesis, the SLE is solved by employing a spherical harmonic approach based on Dahlen (1976). The theory described in this section closely follows Rietbroek (2014) since the (improved) sea level inversion, developed in this thesis, is based on his work and the passive sea level response assumption is still valid.

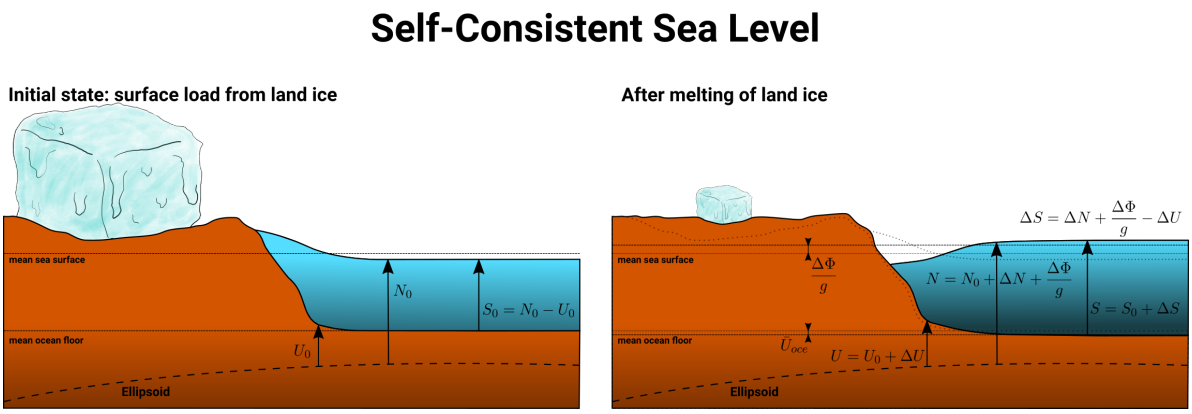


Figure 2.2: Principle of self consistent sea level (based on Rietbroek, 2014). Left: Initial situation with a surface load deforming the solid Earth and attracting the ocean. Right: After unloading (e.g. due to melting), (1) the deformed solid Earth rebounds at the location of the load and subsides over the open ocean where the additional water mass from the former ice exerts stress on the ocean floor. (2) The mean sea surface adapts to the new equipotential surface, which differs from the geoid by $\Delta\Phi$ due to the total mass change within the ocean. (3) The volume change of the ocean basin, U_{oce}, describes the volume offset between the ocean floor in the initial and the deformed state.

2.2.1 The Sea Level Equation

On the Earth, mass is conserved on a global scale and the total surface load anomalies, T, in EWH at time t is given by

$$T(\lambda, \theta, t) = S(\lambda, \theta, t) + H(\lambda, \theta, t). \tag{2.2.1}$$

The Sea Level Equation (SLE) describes the physical relationship between the passive sea level anomalies, S, and the prescribed (continental) surface load anomalies, H.

Starting from a reference state of equilibrium (Fig. 2.2, left), the (ice-)load is located on land and no melting occurs. The load exerts stress on the Earth surface leading to a deformation and advection of mantle material away from the load resulting in an uplift U_0 of the sea floor. The sea surface adapts to the geoid N_0 relative to the ellipsoid with an additional attraction of the water by the mass of the (ice-)load. Consequently, the RSL in the equilibrium state S_0 is derived from $S_0 = N_0 - U_0$. Changes in RSL are especially important in coastal regions and are directly measured by tide gauges, which are attached to the Earth's surface. Similarly, gravity satellite missions are generally also sensitive to RSL. In contrast, satellite altimetry measures the GSL variations in terms of geoid height by observing the change in relative sea level, i.e. the ocean mass change in terms of EWH, and, in addition, the geometric effect of the uplift, which then cancels out.

After melting of the ice-load (Fig. 2.2, right), the Earth surface is deformed by ΔU and the ocean adapts itself to the new geoid $N = N_0 + \Delta N + \frac{\Delta\Phi}{g}$. Here, ΔN refers to the change of the equipotential surface due to the change in loading. The term $(\frac{\Delta\Phi}{g})$ ensures mass conservation, since the additional melt-water causes a uniform upward shift in sea level changing the overall ocean mass and the total volume of the ocean basin, U_{oce}, by deforming the sea floor. Both effects are small and the resulting sea surface can still be considered as an equipotential surface with a potential difference of $\Delta\Phi$ with respect to the geoid. The effects described above are represented

by the SLE as

$$S(\lambda,\theta,t) = O(\lambda,\theta)\int_{\Omega} \mathsf{G}_{N-U}(\alpha-\alpha')\left[S(\lambda',\theta',t)+H(\lambda',\theta',t)\right]d\omega' + \frac{\Lambda_{N-U}(S,H,\lambda,\theta)}{g}+\frac{\Delta\Phi}{g}. \tag{2.2.2}$$

The change in surface loading is captured by convolution of the Green's function $\mathsf{G}_{N-U}(\alpha-\alpha')$, adapted from equation (2.1.23), with the change in total surface load

$$\mathsf{G}_{N-U}(\alpha) = \frac{a}{M}\sum_{n=0}^{\infty}(1+k'_n-h'_n)P_n(\cos\alpha). \tag{2.2.3}$$

From $(1+k'_n-h'_n)$ follows that the reference system can be chosen freely as the combination of the load Love numbers is frame independent (section 2.4.3). Horizontal deformations are generally smaller than the vertical ones and can be safely neglected in the context of sea level (Rietbroek, 2014). The convolution in equation (2.2.2) is restricted to the ocean by multiplying with the ocean function, $O(\lambda,\theta)$, given by

$$O(\lambda,\theta) = \begin{cases} 1 & \text{ocean} \\ 0 & \text{elsewhere.} \end{cases} \tag{2.2.4}$$

The ocean function used in this thesis is shown in Fig. 5.3.

The second term in equation (2.2.2) describes the effect on the sea level due to the rotational feedback as a consequence from the change in loading (see section 2.2.3). As described above, the last term ensures global mass conservation. The sea level, S, occurs on both sides of the differential equation (2.2.2). Due to the self-gravitation effect of S, this either requires an iterative approach (Farrell and Clark, 1976; Sabadini and Vermeersen, 2004) or solving the equation explicitly for S (Rietbroek, 2014) as will be shown in the following.

2.2.2 Spectral Solution of the SLE without Rotational Feedback

In order to solve the SLE in the spectral domain, the first step is the expansion of the variables into a series of spherical harmonics, which are truncated at a reasonably large $N_{\max}$

$$\begin{aligned} S(\lambda,\theta) &= \sum_{n=0}^{N_{\max}}\sum_{m=-n}^{n} S_{nm}Y_{nm}(\lambda,\theta), \\ H(\lambda,\theta) &= \sum_{n=0}^{N_{\max}}\sum_{m=-n}^{n} H_{nm}Y_{nm}(\lambda,\theta), \\ aT_{nm} &= S_{nm}+H_{nm}, \end{aligned} \tag{2.2.5}$$

where S_{nm} and H_{nm} are given in units of meter of EWH, while T_{nm} is dimensionless and multiplied by the Earth's radius a in accordance with section 2.1.2.

Since there is no sea level over land utilizing S would create an artifact of mass change and corresponding geometry changes. Consequently, the SLE is explicitly restricted to the ocean domain by defining the quasi-spectral sea level $\tilde{S}$ (Blewitt and Clarke, 2003), which is a band limited quantity that relates to the relative sea level, S, by

$$\begin{aligned} S(\lambda,\theta) &= O(\lambda,\theta)\tilde{S}(\lambda,\theta) \\ \tilde{S}(\lambda,\theta) &= \sum_{n=0}^{N_{\max}}\sum_{m=-n}^{n} \tilde{S}_{nm}Y_{nm}(\lambda,\theta). \end{aligned} \tag{2.2.6}$$

By definition, S is zero valued over land but since the maximum degree is limited $N_{\max} \ll \infty$, there will be significant truncation effects in the spectral domain. Therefore, introducing the quasi-spectral sea level $\tilde{S}$ leads to a much smoother surface at the coast, which is more suitable to represent an equipotential surface. Only for $N_{\max} \to \infty$ the two will be equal over the ocean. However, the values over land deviate significantly from zero, which implies that $\tilde{S}$ cannot be used to represent an actual surface load.

Expanding the ocean function into spherical harmonics and utilizing the 'product to sum' operator (Rietbroek, 2014, appendix B), it is possible to write equation (2.2.6) as a matrix-vector operation in the spectral domain

$$\boldsymbol{s} = \mathbf{O}\tilde{\boldsymbol{s}}, \tag{2.2.7}$$

where the ocean function is converted to a symmetric matrix, $\mathbf{O}$, of size $(N_{\max}+1)^2 \times (N_{\max}+1)^2$. For this, the spherical harmonic coefficients are stacked in vectors

$$\begin{aligned} \boldsymbol{s}^T &= \left[S_{00} \cdots S_{nm}\right]^T, \\ \tilde{\boldsymbol{s}}^T &= \left[\tilde{S}_{00} \cdots \tilde{S}_{nm}\right]^T, \\ \boldsymbol{o}^T &= \left[O_{00} \cdots O_{nm}\right]^T. \end{aligned} \tag{2.2.8}$$

Consequently, the SLE can be written in matrix form as

$$\mathbf{P}\tilde{\boldsymbol{s}} = \mathbf{G}_{N-U}(\boldsymbol{s} + \boldsymbol{h}) = \mathbf{G}_{N-U}(\mathbf{O}\tilde{\boldsymbol{s}} + \boldsymbol{h}), \;\; n > 0, \tag{2.2.9}$$

with the projection matrix

$$\mathbf{P} = \left[\begin{array}{c|ccc} 0 & 0 & \cdots & 0 \\ \hline 0 & 1 & \cdots & 0 \\ \vdots & \vdots & \ddots & \vdots \\ 0 & 0 & \cdots & 1 \end{array}\right], \tag{2.2.10}$$

which ensures for the degree 0 coefficient to be exactly zero.

The matrix $\mathbf{G}_{N-U}$ includes the corresponding Green's functions from equation (2.2.3) on the main diagonal

$$\mathbf{G}_{N-U} = \left[\begin{array}{c|ccc} 1 & 0 & \cdots & 0 \\ \hline 0 & \frac{\rho_w}{\rho_e}(1 + k'_1 - h'_1) & \cdots & 0 \\ \vdots & \vdots & \ddots & \vdots \\ 0 & 0 & \cdots & \frac{3\rho_w}{\rho_e}\frac{1+k'_{N_{\max}}-h'_{N_{\max}}}{2N_{\max}+1} \end{array}\right] \tag{2.2.11}$$

where setting the degree 0 entry to one will turn out convenient for enforcing mass conservation (Rietbroek, 2014). The requirement for this is given by

$$0 = S_{00} + H_{00} = \int_\Omega O(\lambda,\theta)\tilde{S}(\lambda,\theta)d\omega + H_{00}. \tag{2.2.12}$$

In the spectral domain the integral term can be solved utilizing the orthogonality property from equation (2.1.10) and write this as the inner product of the spectral sea level and ocean function vectors

$$\int_\Omega O(\lambda,\theta)\tilde{S}(\lambda,\theta)d\omega = \boldsymbol{o}^T\tilde{\boldsymbol{s}}. \tag{2.2.13}$$

After sorting the quasi-spectral sea level $\tilde{\boldsymbol{s}}$ to the left side of equation (2.2.9) leads to

$$\left[\mathbf{P} - \mathbf{G}_{N-U}\mathbf{O}\right]\tilde{\boldsymbol{s}} = \mathbf{G}_{N-U}\boldsymbol{h} \tag{2.2.14}$$

The benefit of setting the degree 0 entry to one in equation (2.2.11) becomes obvious when writing the first row of equation (2.2.14) explicitly, which indicates that the mass conservation constraint is always fulfilled

$$\begin{aligned} -\left[\mathbf{O}\right]_{1^{st}row}\tilde{\boldsymbol{s}} &= H_{00} \\ -\boldsymbol{o}^T\tilde{\boldsymbol{s}} = -S_{00} &= H_{00}. \end{aligned} \tag{2.2.15}$$

The quasi-spectral sea level without accounting for rotational feedback (2nd term in Eq. (2.2.2)) is then derived from inverting equation (2.2.14), resulting in

$$\tilde{\boldsymbol{s}} = \mathbf{G}_{\tilde{S}}\mathbf{G}_{N-U}\boldsymbol{h}, \tag{2.2.16}$$

with

$$\mathbf{G}_{\tilde{S}} = \left[\mathbf{P} - \mathbf{G}_{N-U}\mathbf{O}\right]^{-1}. \tag{2.2.17}$$

The inversion $\mathbf{G}_{\tilde{S}}$ is quite stable (Rietbroek, 2014). An iterative solution to equation (2.2.2) generally converges after just a few iterations, additionally indicating stability. However, these approaches often require transformation between the spatial and spectral domain, which requires to pay attention to the choice of suitable spatial representations.

2.2.3 Incorporating Rotational Feedback into the SLE

The rotational feedback term Λ_{N-U} in equation (2.2.2) accounts for the misalignment of the Earth's rotation axis with the reference system's z-axis, caused by the change in the inertia tensor, forced by the surface load. This leads to a small rotational potential acting as a tidal load, deforming the Earth and changing the geoid (see section 2.1.2). For small surface load changes, such as those considered here, the rotational feedback mechanism can be linearized, which allows to perform a spectral inversion similar to equation (2.2.16) given by

$$\mathbf{P}\tilde{\boldsymbol{s}} = (\boldsymbol{\Xi}_{N-U})(\mathbf{O}\tilde{\boldsymbol{s}} + \boldsymbol{h}). \tag{2.2.18}$$

The rotational feedback is limited to the $\tilde{S}_{20}$, $\tilde{S}_{21}$ and $\tilde{S}_{2-1}$ coefficients, forced by the corresponding loading coefficients and the degree 0 term. Consequently, the transformation matrix $\boldsymbol{\Xi}_{N-U}$ is a (3×4) matrix, which can be derived by splitting the transformation into 4 individual transformations

$$\boldsymbol{\Xi}_{N-U} = \left[\mathbf{T}_{\tilde{S}\leftarrow\Lambda}\boldsymbol{\Phi}_{\Lambda\leftarrow m}\boldsymbol{\Gamma}_{m\leftarrow J}\boldsymbol{\Psi}_{J\leftarrow T}\right]. \tag{2.2.19}$$

The first term $\boldsymbol{\Psi}_{J\leftarrow T}$ transforms the change in surface load to the corresponding variation of the Earth's inertial tensor. Following Munk and MacDonald (1960), the Euler-Liouville equations are linearized by assuming that the Earth's axis of angular momentum, $\boldsymbol{\omega}$, is perturbed by a small torque $[m_1, m_2, m_3]^T$. This slightly shifts the axis from, originally, being perfectly aligned with the z-axis

$$\boldsymbol{\omega} = \Omega_E \begin{bmatrix} m_1 \\ m_2 \\ 1 + m_3 \end{bmatrix}, \tag{2.2.20}$$

with the mean rotational speed of the Earth Ω_E. In other words the ocean and ice load redistribution will create a response in polar motion and in the length of day. This shift will induce a change of the Earth's inertial tensor

$$\mathbf{J} = \begin{bmatrix} A & 0 & 0 \\ 0 & A & 0 \\ 0 & 0 & C \end{bmatrix} + \begin{bmatrix} \delta J_{11} & \delta J_{12} & \delta J_{13} \\ \delta J_{12} & \delta J_{22} & \delta J_{23} \\ \delta J_{13} & \delta J_{23} & \delta J_{33} \end{bmatrix}, \tag{2.2.21}$$

where A and C are the Earth's principal moments of inertia. The first order terms of the linearized Euler-Liouville equations only contain contributions from δJ_{13}, δJ_{23}, and δJ_{33} (Wu and Peltier, 1984; Milne and Mitrovica, 1998). Based on equations (43a)-(43c) in Milne and Mitrovica (1998) and accounting for the different normalization and the Condon-Shortely phase, $(-1)^m$, the change in the Earth's inertial tensor from an arbitrary surface load $\sigma(\lambda,\theta)$ can be written as a matrix vector operation under consideration of equations (2.1.27), (2.1.10) and (2.2.5)

$$\begin{aligned}\begin{bmatrix}\delta J_{13}\\ \delta J_{23}\\ \delta J_{33}\end{bmatrix} &= \pi a^4 \rho_w \begin{bmatrix}0 & 0 & -\frac{4}{\sqrt{15}} & 0\\ 0 & 0 & 0 & -\frac{4}{\sqrt{15}}\\ \frac{8}{3} & -\frac{8}{3\sqrt{5}} & 0 & 0\end{bmatrix}\begin{bmatrix}aT_{00}\\ aT_{20}\\ aT_{21}\\ aT_{2-1}\end{bmatrix}\\ &= \mathbf{\Psi}_{J\leftarrow T}\begin{bmatrix}S_{00}+H_{00}\\ S_{20}+H_{20}\\ S_{21}+H_{21}\\ S_{2-1}+H_{2-1}\end{bmatrix}.\end{aligned} \tag{2.2.22}$$

For an elastic Earth, the linearized Euler-Liouville equations relate the change in polar motion to the changed inertial tensor (Nakada and Okuno, 2003; Mitrovica et al., 2005; Peltier and Luthcke, 2009)

$$\begin{bmatrix}m_1\\ m_2\\ m_3\end{bmatrix} = \begin{bmatrix}\Omega_E\frac{1+k_2'}{A\sigma_c} & 0 & 0\\ 0 & \Omega_E\frac{1+k_2'}{A\sigma_c} & 0\\ 0 & 0 & -\frac{1+k_2'}{C}\end{bmatrix}\begin{bmatrix}\delta J_{13}\\ \delta J_{23}\\ \delta J_{33}\end{bmatrix} = \mathbf{\Gamma}_{m\leftarrow J}\begin{bmatrix}\delta J_{13}\\ \delta J_{23}\\ \delta J_{33}\end{bmatrix}, \tag{2.2.23}$$

with Chandler frequency σ_c. Equation (2.2.23) is only valid for slowly varying phenomena with periods significantly longer than σ_c. Capturing higher frequency effects requires the application of either the non-linear theory, i.e. numerical integration of the Euler Liouville equations, or correction from utilizing observed Earth orientation parameters. For the global sea level inversion this assumption is not always fulfilled since individual sea level changes resulting from corresponding land surface loads exhibit annual periods or below. The remaining effect is expected to be small.

Variations in the axis of rotation, $\boldsymbol{\omega}$, will induce corresponding changes in the centrifugal potential $\delta\Lambda(\theta) = \Lambda(\theta) - \Lambda'(\lambda',\theta')$ with respect to a reference state $\Lambda(\theta)$. When inserting equation (2.1.11) and accounting for equation (2.1.26) this can be written as

$$\delta\Lambda(\lambda,\theta) = \frac{1}{2}\Omega_E^2 a^2(1-P_2(\cos\theta)) - \frac{|\boldsymbol{\omega}|^2 a^2}{3}\left(1-\frac{1}{5}\sum_{m=-2}^{2} Y_{2m}(\lambda,\theta)Y_{2m}(\lambda',\theta')\right), \tag{2.2.24}$$

with the new position of the rotation axis at

$$\lambda' = \arctan\left(\frac{m_2}{m_1}\right), \qquad \theta' = \arctan\left(\frac{\sqrt{m_1^2+m_2^2}}{m_3}\right). \tag{2.2.25}$$

For small torques, as considered in this work, the quadratic terms (e.g. Milne and Mitrovica, 1998, Eqs. (33a)-(33d)) can be ignored and the resulting centrifugal potential based on the first order terms written in matrix-vector form is approximated by

$$\begin{bmatrix}\delta\Lambda_{00}\\ \delta\Lambda_{20}\\ \delta\Lambda_{21}\\ \delta\Lambda_{2-1}\end{bmatrix} \approx (a\Omega_E)^2\begin{bmatrix}0 & 0 & \frac{2}{3}\\ 0 & 0 & -\frac{2}{3\sqrt{5}}\\ -\frac{1}{\sqrt{15}} & 0 & 0\\ 0 & -\frac{1}{\sqrt{15}} & 0\end{bmatrix}\begin{bmatrix}m_1\\ m_2\\ m_3\end{bmatrix} = \mathbf{\Phi}_{\Lambda\leftarrow m}\begin{bmatrix}m_1\\ m_2\\ m_3\end{bmatrix}. \tag{2.2.26}$$

The changed potential acts as a tidal load on the Earth leading to surface deformations and a change in geoid. Computing the resulting effect on quasi-spectral sea level, $\tilde{S}$, from subtracting the

uplift deformation from the geoid change requires the use of body Love numbers. In contrast to load Love numbers, body Love numbers describe the solution of a boundary value problem where the load does not exert surface pressure on the Earth. Furthermore, the degree 0 component is negligible small and omitted ensuring global mass conservation. Consequently, the effect of the rotational feedback on the quasi spectral sea level is limited to degree 2 and can be written as

$$\begin{bmatrix} \tilde{S}_{20} \\ \tilde{S}_{21} \\ \tilde{S}_{2-1} \end{bmatrix} = \frac{1+k_2-h_2}{g} \begin{bmatrix} 0 & 1 & 0 & 0 \\ 0 & 0 & 1 & 0 \\ 0 & 0 & 0 & 1 \end{bmatrix} \begin{bmatrix} \delta\Lambda_{00} \\ \delta\Lambda_{20} \\ \delta\Lambda_{21} \\ \delta\Lambda_{2-1} \end{bmatrix} = \mathbf{T}_{\tilde{S}\leftarrow\Lambda} \begin{bmatrix} \delta\Lambda_{00} \\ \delta\Lambda_{20} \\ \delta\Lambda_{21} \\ \delta\Lambda_{2-1} \end{bmatrix}. \tag{2.2.27}$$

The terms of $\tilde{S}_{21}$ and $\tilde{S}_{2-1}$ are the most dominant terms since the m_1 and m_2 components are relatively large compared to m_3.

After building the transformation matrix $\boldsymbol{\Xi}_{N-U}$ from equation (2.2.19), it is possible to combine the SLE from equation (2.2.9) and the rotational feedback effect on sea level from equation (2.2.18) resulting in

$$\mathbf{P}\tilde{\boldsymbol{s}} = (\mathbf{G}_{N-U} + \boldsymbol{\Xi}_{N-U})(\mathbf{O}\tilde{\boldsymbol{s}} + \boldsymbol{h}), \tag{2.2.28}$$

where the rotational feedback affects only the corresponding degree 2 terms and is zero otherwise. Following equation (2.2.16) this is then rewritten in order to solve for $\tilde{\boldsymbol{s}}$

$$\tilde{\boldsymbol{s}} = \mathbf{G}^{\dagger}_{\tilde{S}}(\mathbf{G}_{N-U} + \boldsymbol{\Xi}_{N-U})\boldsymbol{h}, \tag{2.2.29}$$

with

$$\mathbf{G}^{\dagger}_{\tilde{S}} = [\mathbf{P} - (\mathbf{G}_{N-U} + \boldsymbol{\Xi}_{N-U})\mathbf{O}]^{-1}. \tag{2.2.30}$$

2.3 The Equation of State of Seawater

While variations of mass fluxes in and out of the ocean account for about 50% of the sea level change (Chap. 7), the other half is forced by variations in ocean temperature T and salinity S, leading to volumetric expansion of the seawater. These effects are commonly denominated as thermo- and halo-steric sea level change, respectively (e.g., Landerer et al., 2007). Steric changes are related to numerous phenomena on global and regional scales, including sea level change driven by ocean dynamics and currents. In addition, temperature information allows monitoring variations of the heat content of the ocean. Ocean Heat Content (OHC) is primarily forced by the excess heat energy due to the Earth Energy Imbalance (EEI) and the resulting atmosphere-ocean heat flux (e.g., Trenberth et al., 2016). EEI describes the proportion of radiation by the sun to the energy radiated by the Earth at the top of atmosphere, where about 93% of the heat energy accumulate in the world's oceans (e.g., Stocker et al., 2013; Trenberth et al., 2016). Consequently, (thermo-)steric sea level change is closely related to changes in OHC.

Considering a column of seawater from the sea surface down to the sea floor, the height will change either due to additional water mass being added to the ocean, or due to variations in density resulting from changes in temperature and salinity. The latter only leads to a volume change of the water column from the ocean floor to the sea surface, whereas the mass within that column remains constant. An increase in ocean temperature will lead to a decrease in density and consequently to a (thermo-)steric increase in water volume. Similarly a decrease in salinity, e.g. due to fresh-water being added to the ocean, will also decrease the density in the water column and, consequently, result in (halo-)steric increase in sea level.

The Thermodynamic Equation of Seawater - 2010 (TEOS-10), as defined by IOC et al. (2010), supersedes the Equation of State (EOS-80, UNESCO, 1981; Gill, 1982) defined in the 1980s. It

represents an updated and state of the art representation of the thermodynamic properties and behavior of seawater. This includes the definition of standard sea water properties for temperature $T_{\mathrm{so}} = 0\,^{\circ}\mathrm{C}$ and salinity $S_{\mathrm{so}} = 35.165\,04\,\mathrm{g\,kg^{-1}}$ (e.g., Millero et al., 2008; IOC et al., 2010). With TEOS-10 the seawater is represented by the Gibbs function formalism (e.g., Feistel, 2003; Feistel, 2008), which mathematically equals to a thermodynamic potential and, in contrast, to the EOS-80 also allows to derive quantities such as entropy or enthalpy. The Gibbs function (Feistel, 2008) describes the specific Gibbs energy of seawater (in $\mathrm{J\,kg^{-1}}$) and consists of a pure water part g^w and a saline part g^s

$$g(S_A, T_i, p) = g^w(T_i, p) + g^s(S_A, T_i, p). \tag{2.3.1}$$

The specific Gibbs energy, g, is a function of absolute salinity, S_A, in-situ temperature, T_i, according to the International Temperature Scale - 1990 (ITS-90) and sea pressure $p = P - P_0$, where P is the absolute pressure and the reference pressure at the sea surface, $P_0 = 101\,325\,\mathrm{Pa}$. The mathematical form of the Gibbs function cannot be derived from thermodynamic principles, but rather depends on the substance, accuracy and validity range, which requires the construction based on experimental data (Feistel, 2008). While the pure water part, g^w of the Gibbs energy is defined, e.g., by Wagner and Pruß (2002), the saline part g^s for the TEOS-10 formulation has been adopted from Feistel (2008). For TEOS-10, the Gibbs function is defined in terms of an empirical 75-term expression (Millero et al., 2008).

Since the Gibbs function basically acts as a thermodynamic potential, other thermodynamic quantities can be computed by partial derivatives with respect to temperature or pressure resulting in representations for specific entropy, specific enthalpy and seawater density. The specific entropy η (in $\mathrm{J\,kg^{-1}\,K}$) is the first partial derivative of the Gibbs function with respect to temperature

$$\eta(S_A, T_i, p) = -\left.\frac{\partial g}{\partial T_i}\right|_{S_A,p}. \tag{2.3.2}$$

Specific enthalpy $q(S_A, T_i, p)$ (in $\mathrm{J\,kg^{-1}}$) can be derived from the Gibbs function (Eq. (2.3.1)) by

$$q(S_A, T_i, p) = g - (T_{0\,^{\circ}\mathrm{C}} + T_i)\eta = g(S_A, T_i, p) - (T_{0\,^{\circ}\mathrm{C}} + T_i)\left.\frac{\partial g}{\partial T_i}\right|_{S_A,p}, \tag{2.3.3}$$

where $T_{0\,^{\circ}\mathrm{C}} = 273.15K$ is the Celsius zero point. The Gibbs function is generally defined in a way so that $q(S_{\mathrm{so}}, T_{\mathrm{so}}, 0) = \eta(S_{\mathrm{so}}, T_{\mathrm{so}}, 0) \equiv 0$ for standard seawater. The density of seawater is derived by the reciprocal of the partial derivative of the Gibbs function with respect to pressure at constant absolute salinity S_A and in-situ temperature T_i

$$\rho(S_A, T_i, p) = \left(\left.\frac{\partial g}{\partial p}\right|_{S_A,T_i}\right)^{-1}. \tag{2.3.4}$$

This is generally referred to as equation of state of seawater relating pressure, temperature and salinity to seawater density.

2.3.1 Steric Sea Level

In-situ profilers (Sect. 3.3), ocean models and re-analyses generally provide practical salinity S_P, which is, e.g., directly related to measured conductivity variations, and unit-less. The thermodynamic effects from changing salinity are only known for a specified reference seawater composition. However, when the seawater composition changes, the relations are no longer valid (Wright et al., 2011). The absolute salinity, S_A, for TEOS-10 is defined in terms of a density salinity, which provides the best density estimate given the value of S_A (IOC et al., 2010; Wright et al., 2011; McDougall et al., 2012) and is given by

$$S_A = S_R + \delta S_A. \tag{2.3.5}$$

The reference composition salinity S_R is related to practical salinity by $S_R = \frac{S_{so}}{35} S_P$. In equation (2.3.5), $\delta S_A = S_A - S_R$ is the absolute salinity anomaly, which is in principal interpolated from a high resolution look up table (McDougall et al., 2012).

Besides in-situ temperature T_i, which is directly measured by ocean profilers, model data is generally provided in terms of potential temperature T_θ. This is the temperature that a small parcel of water at a given reference pressure level p_r would have in case its pressure level is changed from p in an isentropic (same entropy) and isohaline (same salinity) manner without dissipation of kinetic energy, which makes this a reversible thermodynamic process (IOC et al., 2010). Potential temperature is usually referenced to the sea surface where the reference pressure is well known and it allows comparison of temperature from different depth levels. Converting T_i to T_θ can be derived by solving the following equation for T_θ

$$\eta(S_A, T_\theta, p_r) = \eta(S_A, T_i, p), \tag{2.3.6}$$

which can, e.g., be achieved to satisfactory numerical accuracy following McDougall and Wotherspoon (2014). With TEOS-10, conservative temperature, T_Θ has been adopted as the new standard for ocean temperature, replacing the EOS-80 standard, T_θ. Conservative temperature is not a real temperature, but rather the potential enthalpy $q^0(S_A, T_i, p)$ scaled by a constant heat capacity $c_p^0 \equiv 3991.867\,957\,119\,63\,\mathrm{J\,kg^{-1}\,K}$ in order to have units of Kelvin. While the heat capacity of T_θ is allowed to vary due to changing heat capacity based on salinity when shifting from p to p_r, it is preserved by T_Θ. The relation between T_i and T_Θ is given by (IOC et al., 2010)

$$T_\Theta(S_A, T_i, p) = \frac{q^0(S_A, T_i, p)}{c_p^0}, \tag{2.3.7}$$

with q^0 defined in terms of the Gibbs function

$$q^0(S_A, T_i, p) = q^0(S_A, T_\theta, 0) = g(S_A, T_\theta, 0) - (T_0 + T_\theta)\left.\frac{\partial g}{\partial T_\theta}\right|_{S_A,0}. \tag{2.3.8}$$

The thermal expansion coefficient α (in $\mathrm{K^{-1}}$) and saline contraction coefficient β (in $\mathrm{kg\,g^{-1}}$) in terms of T_i are given by

$$\begin{aligned} \alpha_{T_i} &= -\frac{1}{\rho(S_A, T_i, p)}\left.\frac{\partial \rho}{\partial T_i}\right|_{S_A,p}, \\ \beta_{T_i} &= \frac{1}{\rho(S_A, T_i, p)}\left.\frac{\partial \rho}{\partial S_A}\right|_{T_i,p}. \end{aligned} \tag{2.3.9}$$

This provides means to derive steric sea level change after depth integrating an in-situ temperature difference $\Delta T = T_i - T_{so}$ relative to standard seawater and, correspondingly, a difference in salinity $\Delta S = S_A - S_{so}$. Consequently, total steric sea level change, h_{steric}, at a time, t, can be expressed by depth integral of density changes relative to a given reference level over the water column from the sea floor at $z = -H$ up to the sea surface (Gill and Niller, 1973)

$$h_{steric} = \int_{-H}^{0} \frac{\rho_{so}(S_{so}, T_{so}, p(z)) - \rho(S(z), T(z), p(z), t)}{\rho_{so}(S_{so}, T_{so}, p(z))} dz. \tag{2.3.10}$$

Following equation (2.3.9) this can be further split into a thermosteric component, h_{steric}^{thermo}, and a halosteric component, h_{steric}^{halo} (e.g., Landerer et al., 2007)

$$\begin{aligned} h_{steric} \approx h_{steric}^{thermo} + h_{steric}^{halo} = &\int_{-H}^{0} \frac{\rho_{so}(S_{so}, T_{so}, p(z)) - \rho(S_{so}, T(z), p(z), t)}{\rho_{so}(S_{so}, T_{so}, p(z))} dz \\ &+ \int_{-H}^{0} \frac{\rho_{so}(S_{so}, T_{so}, p(z)) - \rho(S(z), T_{so}, p(z), t)}{\rho_{so}(S_{so}, T_{so}, p(z))} dz. \end{aligned} \tag{2.3.11}$$

The sum of thermo- and halo-steric sea level is not exactly the same compared to directly deriving (combined) steric sea level change due to non-linearities in the equation of state (Landerer et al., 2007). Consequently, equations (2.3.10) and (2.3.11) provide thermo- and halosteric sea level change from either in-situ profiler observation or ocean model data, after transforming temperature and salinity to suitable temperature representation and absolute salinity.

2.3.2 Ocean Heat Content

Besides (thermo-)steric sea level changes, temperature variations within the oceans also allow to derive information on the Ocean Heat Content (OHC) describing the amount of (heat) energy stored in the ocean. This can be further related to the EEI, which is either deferred from model data or directly measured at the top of atmosphere by the Clouds and the Earth's Radiant Energy System (CERES) project that combines satellite-based radiation measurements and cloud data. Based on measured temperature and salinity, OHC, $Q(t)$ at time t (in J) is computed as

$$Q(t) = \int_{V_{oce}} q(\lambda, \theta, S_A, T_i, p, t)\rho(\lambda, \theta, S_A, T_i, p, t)dv \tag{2.3.12}$$

with the specific enthalpy $q(\lambda, \theta, S_A, T_i, p, t)$ and seawater density $\rho(\lambda, \theta, S_A, T_i, p, t)$, given by equations (2.3.4) and (2.3.3), and evaluated at each position. In the following, the dependency on the location and time is, again, omitted for better readability.

By separating the volume integral in equation (2.3.12) into an integral over depths and over the ocean area, it is possible to write

$$Q(t) = \int_{A_{oce}} \int_{-H}^{0} c_p(S_A, T_i, p)\rho(S_A, T_i, p)\Delta T_i(p)dzdA = \int_{A_{oce}} Q'(\lambda, \theta, t)dA, \tag{2.3.13}$$

where c_p is the isobaric heat capacity (in $\mathrm{J\,kg^{-1}\,K}$) and $\Delta T_i(p)$ the temperature change at pressure level p. The isobaric heat capacity describes the change of specific enthalpy with temperature at constant S_A and p. In other words, it represents the amount of heat energy transferred to a body of water and the resulting temperature increase in Kelvin, K (IOC et al., 2010). Following TEOS-10, it can be derived as the derivative of equation (2.3.1) with respect to temperature

$$c_p(S_A, T_i, p) = \left.\frac{\partial q}{\partial T_i}\right|_{S_A,p} = -(T_{0\,^\circ\mathrm{C}} + T_i) \left.\frac{\partial^2 g}{\partial T_i^2}\right|_{S_A,p}, \tag{2.3.14}$$

which represents the second derivative of the Gibbs function with respect to temperature. Solving the inner integral in equation (2.3.13) over depth results in local estimates of ocean heat content in $\mathrm{J\,m^{-2}}$. The Ocean Heat Uptake (OHU) ϕ, in $\mathrm{W\,m^{-2}}$, or the ocean heat flux at the air-sea interface, is computed from the change in OHC over time

$$\phi(\lambda, \theta, t) = \frac{d}{dt}Q'(\lambda, \theta, t). \tag{2.3.15}$$

While equation (2.3.13) allows to derive the OHC variation within the total ocean, averaging the rate in equation (2.3.15) over the global ocean results in the average ocean warming rate $\bar{\phi}$

$$\bar{\phi}_{oce}(t) = \frac{1}{A_{oce}} \int_{A_{oce}} \phi(\lambda, \theta, t)dA. \tag{2.3.16}$$

As mentioned above, the CERES project measures in- and outgoing short- and longwave radiation fluxes at the top of atmosphere $\bar{\phi}_{TOA}(t)$, which refers to the total Earth surface A_Ω. About 93% of the excess heat is stored in the oceans (e.g., Stocker et al., 2013; Trenberth et al., 2016). Consequently, the average ocean warming rate is approximately related to EEI by

$$\bar{\phi}_{oce}(t) = 0.93\frac{A_{oce}}{A_\Omega}\bar{\phi}_{TOA}(t). \tag{2.3.17}$$

From the above it is possible to directly relate changes in (thermo-)steric sea level to OHC variations by

$$\Delta Q(t) = \int_{A_{oce}} \int_{-H}^{0} \frac{c_p(S_A, T_i, p)\rho(S_A, T_i, p)}{\alpha(S_A, T_i, p)} \Delta h_{steric}^{thermo}(p) dz dA, \tag{2.3.18}$$

with the thermal expansion coefficient, c_p, given by equation (2.3.9). When one assumes an ocean averaged $\bar{c}_p$, $\bar{\rho}$, $\bar{\alpha}$ and $\bar{\Delta h}_{steric}^{thermo}$, it is possible to approximate this as

$$\bar{Q}(t) = \frac{\bar{c}_p \bar{\rho}}{\bar{\alpha}} \bar{h}_{steric}^{thermo}(t) \tag{2.3.19}$$

in order to convert a given time series of ocean average steric heights to OHC or, similarly, OHU after computing the derivative with respect to time.

2.4 Reference System Theory

Geodetic observations as well as modeled data are generally associated to a well-defined reference system. Combining data from different sources, thus, requires careful and consistent treatment of the associated reference frames. In addition, changes within the Earth structure due to varying surface loads will induce translations, impacting certain reference frames with respect to others. These translation effects are generally tied to spherical harmonic degree 1 coefficients.

For isomorphic reference frames as defined by Blewitt (2003), it can be shown that the loading deformation on an elastic SNREI Earth (section 2.1.2) and the corresponding translation effect between reference frames is achieved by substituting the degree 1 load Love numbers. While satellites generally fly in an orbit around the center of mass of the Earth, providing data in the center of mass (CM) of the Earth system frame, other data is often provided with respect to the center of figure (CF) frame, which is tied to the solid Earth crust (e.g. tide gauge data). The CM and CF frames are the two major reference frames considered in this thesis. The translation vector between these two frames is denominated "geocenter motion".

In reality, the isomorphic theory by Blewitt (2003) is only partly fulfilled. The definitions of the CM and CF frame do not require isomorphy. The International Terrestrial Reference Frame (ITRF), which is a realization of the ideal International Terrestrial Reference System (ITRS), is defined by a set of points with three-dimensional Cartesian coordinates (Altamimi et al., 2013). The ITRF is realized by combining several space geodetic techniques of Very Long Baseline Interferometry (VLBI), SLR, Global Positioning System (GPS) and Doppler Orbitography and Radio-positioning Integrated by Satellite (DORIS). By definition the ITRF origin is located at the center of mass of the whole Earth including atmosphere and ocean. The origin of the ITRF is mainly constrained by the long-term mean from SLR observations. These are sensitive to geocenter motion, which is only weakly constrained by GPS and DORIS and not at all by VLBI. The latter defines the orientation of the axes. Based on the above and the following frame definitions, the ITRF is more or less a hybrid frame, which is generally a CF frame that is tied to a mean CM frame.

2.4.1 Reference Frames

Center of Figure Frame

Assuming a uniform and infinitely dense spread of surface points, the center of surface figure (CF) frame of the Earth is defined geometrically by the three-dimensional Cartesian coordinates of surface points and their respective motion (Blewitt, 2003). The position of the CF frame origin, after a change in surface loading, is derived by integrating the surface deformation $\boldsymbol{s}(\lambda, \theta)$ based on equation (2.1.32) under the the Love-Shida hypothesis over the whole Earth (Blewitt, 2003)

$$\boldsymbol{x}_{CF} = \frac{1}{4\pi} \int_{\Omega} \boldsymbol{s}(\lambda, \theta) d\omega'. \tag{2.4.1}$$

When the radial unit vector $\boldsymbol{e}_r$ in equation (2.1.32) is expressed in terms of λ and θ it is possible to notice the correspondence to the normalized surface spherical harmonics from equations (2.1.7) and (2.1.9) as

$$\boldsymbol{e}_r = \begin{bmatrix} \cos\lambda\sin\theta \\ \sin\lambda\sin\theta \\ \cos\theta \end{bmatrix} = \frac{1}{\sqrt{3}} \begin{bmatrix} Y_{11} \\ Y_{1-1} \\ Y_{10} \end{bmatrix}. \tag{2.4.2}$$

After substitution into equation (2.4.1) this becomes

$$\boldsymbol{x}_{CF} = \frac{1}{\sqrt{3}4\pi} \int_\Omega \sum_{n=0}^{\infty} \sum_{m=-n}^{n} U_{nm} Y_{nm} \begin{bmatrix} Y_{11} \\ Y_{1-1} \\ Y_{10} \end{bmatrix} + V_{nm} \begin{bmatrix} \nabla_\Omega Y_{nm} \nabla_\Omega Y_{11} \\ \nabla_\Omega Y_{nm} \nabla_\Omega Y_{1-1} \\ \nabla_\Omega Y_{nm} \nabla_\Omega Y_{10} \end{bmatrix} d\omega', \tag{2.4.3}$$

where most terms reduce to zero due to the orthogonality relation from equation (2.1.10) and the identity for the surface gradient operator ∇_Ω

$$\oint_\Omega \nabla_\Omega Y_{nm}(\omega) \nabla_\Omega Y_{n'm'}(\omega) d\omega = 4\pi n(n+1)\delta_{nn'}\delta_{mm'}, \tag{2.4.4}$$

which for the degree 1 terms is two, in case of fully normalized surface spherical harmonics. Therefore, only degree 1 terms will remain in equation (2.4.3), which are directly linked with the components of $\boldsymbol{x}_{CF}$ as

$$\boldsymbol{x}_{CF} = \frac{1}{\sqrt{3}} \begin{bmatrix} U_{11} + 2V_{11} \\ U_{1-1} + 2V_{1-1} \\ U_{10} + 2V_{10} \end{bmatrix}. \tag{2.4.5}$$

In practice the CF frame is well suited for measurement techniques, which cannot realize the CM frame, due to being tied to the Earth's surface (Blewitt, 2003). However, the assumption of a uniform and infinitely dense coverage of points for its definition is not fulfilled and, thus, a realization of the center of surface figure frame by a number of N stations at position $\boldsymbol{r}_i$ within a network leads to a center of network (CN) frame

$$\boldsymbol{x}_{CN} = \frac{1}{N} \sum_i^N \boldsymbol{r}_i. \tag{2.4.6}$$

Differences to the CF frame result from the sparse station coverage and measurement errors of the contributing geodetic observing techniques.

Center of Mass Frame

The center of all masses within the Earth system, including solid Earth and surface loads from atmosphere, ocean, and land hydrology, define the center of mass (CM). Since no (significant) mass is added or removed from the Earth system, the CM can be considered stationary in inertial space (Blewitt, 2003). Consequently, a change in surface load as discussed in section 2.1.2 will not affect the CM position. Therefore, $\boldsymbol{x}_{CM}$ is defined as the translation vector, which ensures that the degree 1 contribution in equation (2.1.31) is zero following Klemann and Martinec (2009) and App. A.1 in Rietbroek (2014)

$$\boldsymbol{x}_{CM} = \sqrt{3}a \begin{bmatrix} C_{11} \\ C_{1-1} \\ C_{10} \end{bmatrix}, \tag{2.4.7}$$

with the Earth's radius a.

Other Reference Frames

As mentioned before, the CM and CF frames are the predominantly employed reference frames in this thesis. For completion, three more reference frames are mentioned here, following Blewitt (2003). The center of Earth (CE) frame defines the barycenter of the solid Earth and it changes its trajectory with respect to inertial space due to surface loading changes. After the surface load has been redistributed, any resulting deformation of the solid Earth is not able to change $\boldsymbol{x}_{CE}$ (Blewitt, 2003), resulting in

$$\boldsymbol{x}_{CE} = \sqrt{3}a \begin{bmatrix} C_{11} \\ C_{1-1} \\ C_{10} \end{bmatrix} - \frac{\sqrt{3}a\rho_w}{\rho_e} \begin{bmatrix} T_{11} \\ T_{1-1} \\ T_{10} \end{bmatrix}. \tag{2.4.8}$$

The center of surface height (CH) frame is defined so that the integral over all height displacements over the total surface of the Earth is zero (Blewitt, 2003), which results in

$$\boldsymbol{x}_{CH} = \sqrt{3} \begin{bmatrix} U_{11} \\ U_{1-1} \\ U_{10} \end{bmatrix}. \tag{2.4.9}$$

Similarly, the center of lateral surface figure (CL) frame defined in a way that the integral of the horizontal displacement vector field is zero (Blewitt, 2003)

$$\boldsymbol{x}_{CL} = \sqrt{3} \begin{bmatrix} V_{11} \\ V_{1-1} \\ V_{10} \end{bmatrix}. \tag{2.4.10}$$

2.4.2 Translation of the Reference Frame

When observing the deformation $\boldsymbol{s}^A(\lambda, \theta)$, according to equation (2.1.32), in reference frame A from a frame B, the deformation can be translated by the vector $\boldsymbol{t}^{A\to B}$ with respect to A. This can be written as

$$\boldsymbol{s}^B(\lambda, \theta) = \boldsymbol{s}^A(\lambda, \theta) + \boldsymbol{t}^{A\to B}. \tag{2.4.11}$$

In a local spherical frame, $\boldsymbol{t}^{A\to B}$ can by expressed in spherical harmonics of degree 1

$$\boldsymbol{t}^{A\to B} = \frac{1}{\sqrt{3}} \sum_{m=-1}^{1} t_{1m} \left[Y_{1m}\boldsymbol{e}_r + \nabla_\Omega Y_{1m} \right], \tag{2.4.12}$$

where the x-, y- and z-components of the translation vector correspond to t_{11}, t_{1-1} and t_{10}, respectively. Consequently, it is possible to write the deformation $\boldsymbol{s}^B(\lambda, \theta)$ in terms of changing degree 1 coefficients of the vertical or horizontal deformation by

$$\begin{bmatrix} U_{11} \text{ or } V_{11} \\ U_{1-1} \text{ or } V_{1-1} \\ U_{10} \text{ or } V_{10} \end{bmatrix}^B = \begin{bmatrix} U_{11} \text{ or } V_{11} \\ U_{1-1} \text{ or } V_{1-1} \\ U_{10} \text{ or } V_{10} \end{bmatrix}^A - \frac{1}{\sqrt{3}} \begin{bmatrix} t_{11} \\ t_{1-1} \\ t_{10} \end{bmatrix}^{A\to B}. \tag{2.4.13}$$

For the potential change, it is generally necessary to replace all the Stokes coefficients. However, for small translations, such as movements of the geocenter, the degree 1 variations will be significantly larger compared to the other coefficients, which allows to limit the translation to

$$\begin{bmatrix} C_{11} \\ C_{1-1} \\ C_{10} \end{bmatrix}^B = \begin{bmatrix} C_{11} \\ C_{1-1} \\ C_{10} \end{bmatrix}^A - \frac{1}{a\sqrt{3}} \begin{bmatrix} t_{11} \\ t_{1-1} \\ t_{10} \end{bmatrix}^{A\to B}. \tag{2.4.14}$$

2.4.3 Shifting the Reference System for a Radially Symmetric Elastic Earth

To derive the surface loading relations in section 2.1.2, the reference system has not been defined explicitly. While the load Love numbers of the solid Earth are most conveniently computed in the CE system, the relations for surface deformation for equations (2.1.29) and (2.1.30) as well as potential change from equation (2.1.31) are valid in most of the introduced reference frames. The set of these valid frames has been denominated by Blewitt (2003) as 'isomorphic frames'.

Further following Blewitt (2003), the transformation from one isomorphic frame to another requires a load moment vector $\boldsymbol{m}_L$. On a SNREI Earth, the transformation vector $\boldsymbol{t}^{A\to B}$, constructed from an arbitrary combination of the degree 1 surface deformation and potential change coefficients, can be written as (Blewitt, 2003, Eq. (14))

$$\begin{aligned}\boldsymbol{t}^{A\to B} &= \beta \begin{bmatrix} C_{11} \\ C_{1-1} \\ C_{10} \end{bmatrix}^A + \eta \begin{bmatrix} U_{11} \\ U_{1-1} \\ U_{10} \end{bmatrix}^A + \epsilon \begin{bmatrix} V_{11} \\ V_{1-1} \\ V_{10} \end{bmatrix}^A \\ &= \alpha^{A\to B} \frac{\boldsymbol{m}_L}{M} = \alpha^{A\to B} \frac{\sqrt{3} a \rho_w}{\rho_e} \begin{bmatrix} T_{11} \\ T_{1-1} \\ T_{10} \end{bmatrix}^A , \end{aligned} \tag{2.4.15}$$

with the load moment vector given based on Blewitt (2003)(Eq. (10))

$$\boldsymbol{m}_L = \int_\Omega a \boldsymbol{e}_r \sigma(\omega') a^2 d\omega'. \tag{2.4.16}$$

After accounting for equations (2.1.10) and (2.4.2), as well as substituting equation (2.1.27) and introducing the Earth mass M, equation (2.4.15) reduces to

$$\boldsymbol{m}_L = \frac{4\pi a^4 \rho_w}{\sqrt{3}} \begin{bmatrix} T_{11} \\ T_{1-1} \\ T_{10} \end{bmatrix} = \frac{\sqrt{3} a \rho_w M}{\rho_e} \begin{bmatrix} T_{11} \\ T_{1-1} \\ T_{10} \end{bmatrix}. \tag{2.4.17}$$

Equation (2.4.15) is valid for all the reference frames mentioned here, except for the CN frame, and it introduced the isomorphic parameter $\alpha^{A\to B}$ (Blewitt, 2003). For isomorphic frames the transformation from frame A to B is completely described by $\alpha^{A\to B}$, which implies that all the isomorphic frame origins for an elastic Earth are located on a straight line.

Following from equations (2.4.15), (2.1.34), and (2.1.35), the degree 1 coefficients are given by

$$\begin{aligned} \delta C_{1m}^A &= (1 + k_1'^A) \frac{\rho_w}{\rho_e} T_{1m}, \\ U_{1m}^A &= h_1'^A \frac{a\rho_w}{\rho_e} T_{1m}, \\ V_{1m}^A &= l_1'^A \frac{a\rho_w}{\rho_e} T_{1m}, \end{aligned} \tag{2.4.18}$$

where the refrence frame can be shifted from frame A to B based on equations (2.4.13) and (2.4.14) substituted into equation (2.4.15)

$$\begin{aligned} \delta C_{1m}^B &= (1 + k_1'^A - \alpha^{A\to B}) \frac{\rho_w}{\rho_e} T_{1m} = (1 + k_1'^B) \frac{\rho_w}{\rho_e} T_{1m}, \\ U_{1m}^B &= (h_1'^A - \alpha^{A\to B}) \frac{a\rho_w}{\rho_e} T_{1m} = h_1'^B \frac{a\rho_w}{\rho_e} T_{1m}, \\ V_{1m}^B &= (l_1'^A - \alpha^{A\to B}) \frac{a\rho_w}{\rho_e} T_{1m} = l_1'^B \frac{a\rho_w}{\rho_e} T_{1m}. \end{aligned} \tag{2.4.19}$$

From this it becomes clear that the load Love numbers are frame specific and can be transformed from one reference frame to another utilizing $\alpha^{A\to B}$ by

$$\begin{aligned} 1 + {k_1'}^B &= 1 + {k_1'}^A - \alpha^{A\to B}, \\ {h_1'}^B &= {h_1'}^A - \alpha^{A\to B}, \\ {l_1'}^B &= {l_1'}^A - \alpha^{A\to B}. \end{aligned} \tag{2.4.20}$$

Consequently, when combining equations (2.4.5), (2.4.7), (2.4.8), (2.4.9), and (2.4.10) with (2.4.19) the isomorphic frame parameter $\alpha^{A\to B}$ is derived as

$$\begin{aligned} \alpha^{A\to CM} &= 1 + {k_1'}^A, \\ \alpha^{A\to CF} &= \frac{({h_1'}^A + 2{l_1'}^A)}{3}, \\ \alpha^{A\to CE} &= {k_1'}^A, \\ \alpha^{A\to CH} &= {h_1'}^A, \\ \alpha^{A\to CL} &= {l_1'}^A, \end{aligned} \tag{2.4.21}$$

in accordance with Blewitt (2003), Table 1. Replacing A in equation (2.4.21) with any of the isomorphic reference frames, thus, yields the corresponding load Love numbers in the target system and, at the same time, shifting to the target reference frame.

Examining the difference between the CM and CE it becomes clear that the distance between the origins is independent of the frames and constant with respect to the applied surface load

$$\boldsymbol{x}_{CM} - \boldsymbol{x}_{CE} = a\sqrt{3}\frac{(1 + {k_1'}^{CE})\rho_w}{\rho_e} \begin{bmatrix} T_{11} \\ T_{1-1} \\ T_{10} \end{bmatrix} = a\sqrt{3}\frac{\rho_w}{\rho_e} \begin{bmatrix} T_{11} \\ T_{1-1} \\ T_{10} \end{bmatrix}. \tag{2.4.22}$$

Furthermore, the distance between the CM and CF origin depends on the degree one load love number ${k_1'}^{CF}$, which has a magnitude of ${k_1'}^{CF} = 0.026$ for the PREM Earth model, which is generally employed in this thesis

$$\boldsymbol{x}_{CM} - \boldsymbol{x}_{CF} = a\sqrt{3}\frac{(1 + {k_1'}^{CF})\rho_w}{\rho_e} \begin{bmatrix} T_{11} \\ T_{1-1} \\ T_{10} \end{bmatrix} = a\sqrt{3} \begin{bmatrix} C_{11} \\ C_{1-1} \\ C_{10} \end{bmatrix}. \tag{2.4.23}$$

This means the CE and the CF coincide by about $\sim 3\%$ while the CM origin is farther away.

Geocenter motion in literature is not always defined consistently (Blewitt, 2003). Sometimes the CF origin is adopted as the geocenter (e.g., Blewitt, 2003; Klemann and Martinec, 2009), while in other publications the geocenter is assumed to coincide with the CM origin (e.g., Heiskanen and Moritz, 1967; Rietbroek et al., 2009; Rietbroek, 2014; Rietbroek et al., 2016). In order to be consistent with previously published works on the inversion (Rietbroek et al., 2016), the geocenter motion, $\boldsymbol{x}_{GC}$, in this thesis is defined as

$$\boldsymbol{x}_{GC} \equiv \boldsymbol{x}_{CM} - \boldsymbol{x}_{CF}. \tag{2.4.24}$$

In context of the ITRF, geocenter motion, as considered in this thesis, represents an anomaly with respect to the SLR long-time mean.

Chapter 3

Observations and Model Data

This thesis combines space geodetic and in-situ observations together with model data in order to estimate individual sea level contributions. Consequently, chapter 2 and this one represent the basis for the inverse approach and coastal retracking improvements.

3.1 Radar Altimetry

Beginning with the launch of Topex/Poseidon in August 1992 by National Aeronautics and Space Administration (NASA) and Centre national d'études spatiales (CNES), orbit accuracy and measurement precision were in the range of 2 to 3 cm allowing for accurate and continuous monitoring of the Earth's oceans every ten days (Chelton et al., 2001). After almost ten years in orbit, Topex/Poseidon was followed by the Jason-1, Jason-2 and Jason-3 missions in 2001, 2008 and 2016, respectively (Fig. 3.1). Together, Topex/Poseidon and Jason-1/-2/-3 provide a continuous time series of global and regional sea level changes of more than 25 years. After a calibration phase of about six months, where two of the satellites flew a tandem formation on the same orbit, observing the same surface conditions just a few seconds apart, the older satellite was moved to an interleaved orbit in between the nominal orbit (see Fig. 3.2).

The Topex and Jason missions are complemented by several other altimetry missions, flying on orbits with different inclinations, reaching higher latitude regions and providing a higher spatial resolution at the cost of a lower temporal sampling (Tab. 3.1). The European Space Agency (ESA)'s missions fly on a 35 d repeat orbit with more dense spatial coverage compared to the Jason missions. The ERS-1 and ERS-2 missions were followed by the European Environmental Satellite (Envisat) mission, which provided continuous coverage, especially after failure of the on-board data storage of the ERS-2 satellite in June 2003. Afterwards, ERS-2 data has been limited to those observations close to the ground receiving stations. After an unexpected failure of the Envisat satellite in 2012 there is a time gap until the Saral/Altika mission recovered the time series in 2013. Nowadays it is continued as part of ESA's Sentinel program, where the satellite altimeters are flown on all satellites of the Sentinel-3 series with Sentinel-3A and Sentinel-3B currently in orbit. Both are flying on an interleaved orbit with respect to each other (orange and dark blue orbits in Fig. 3.2), while both carry a novel Synthetic Aperture Radar (SAR) or Delay Doppler Altimetry (DDA) altimeter that allows for significantly higher along-track accuracy compared to conventional altimetry. In addition, the Cryosat-2 mission, launched in 2010, has been originally developed for measuring the height changes over the ice sheets in Greenland and Antarctica. Cryosat-2 was the first mission to carry an altimetry instrument capable of measuring in DDA mode as well as conventional mode. Over the ocean, it also provides highly accurate Sea Surface Height (SSH) with an unprecedented spatial resolution but at the cost of a 369 d repeat cycle with a 13 d sub-cycle. The Chinese HY-2A is not further utilized in this thesis as these data are not available from the Radar Altimetry Database System (RADS) (Scharroo et al., 2013), which is the basis for the inversions input altimetry data.

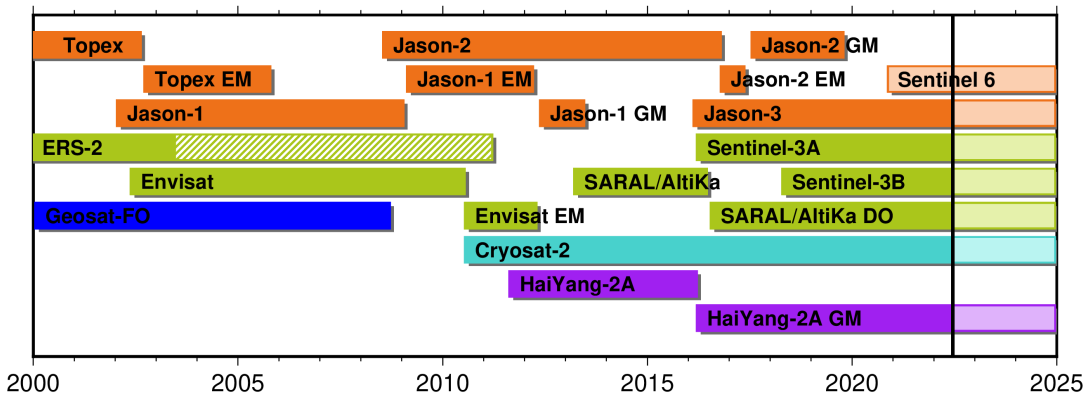


Figure 3.1: Overview of individual altimetry missions and corresponding mission phases since 2000. Colors indicate roughly the same orbits.

Table 3.1: Satellite altimetry mission overview during the GRACE/GRACE-FO era (extended from Quartly et al., 2001).

Mission	Launch	End	Altitude [km]	Inclination	Repeat [days]
Topex/Poseidon	1992-08	2006-01	1336	66.04°	9.9156
GFO	1998-02	2008-09	800	108.04°	17
Jason-1	2001-12	2009-01	1336	66.04°	9.9156
Envisat	2002-03	2013-07	784	98.54°	35
Jason-2	2008-06	2019-10	1336	66.04°	9.9156
Cryosat-2	2010-04	present	717	92.00°	369
HY-2A	2011-08	present	963	99.35°	14
SARAL/AltiKa	2013-02	present	800	98.54°	35
Jason-3	2016-01	present	1336	66.04°	9.9156
Sentinel-3A	2016-02	present	814.5	98.65°	27
Sentinel-3B	2018-04	present	814.5	98.65°	27

3.1.1 From Measured Distance to Sea Level Anomaly

The altimeter instrument on-board of the satellite emits a radar pulse, which is reflected back at the (sea) surface and the two-way travel time t is observed and converted to the raw distance r_{raw} by (Chelton et al., 2001)

$$r_{\text{raw}} = t\frac{c}{2}, \tag{3.1.1}$$

with the speed of light in vacuum $c = 299\,792\,458\,\text{m}\,\text{s}^{-1}$. Due to the radar pulse propagating through the Earth's atmosphere, the two-way travel time of the pulse is influenced by tropospheric and ionospheric delays, which will affect the travel time. The raw range measurement is always referred to a fixed position within the return window (the so called "tracking gate"), which itself is automatically positioned by the satellite, e.g., based on digital elevation model data. Consequently, a retracking correction Δr_{retr} is required to account for potential offsets of the return power measurement from this fixed position (see Sect. 4.2 for details)

$$r_{\text{retr}} = r_{\text{raw}} + \Delta r_{\text{retr}}. \tag{3.1.2}$$

The corrected range r with the atmospheric influences removed (Fig. 3.3) is then given by (Picot et al., 2018)

$$r = r_{\text{retr}} + \Delta r_{\text{dry}} + \Delta r_{\text{wet}} + \Delta r_{\text{iono}} + \Delta r_{\text{ssb}}, \tag{3.1.3}$$

where Δr_{dry} and Δr_{wet} represent the corrections for the dry and wet troposphere, respectively, Δr_{iono} is the ionospheric correction and Δr_{ssb} corrects for the sea state bias effect.

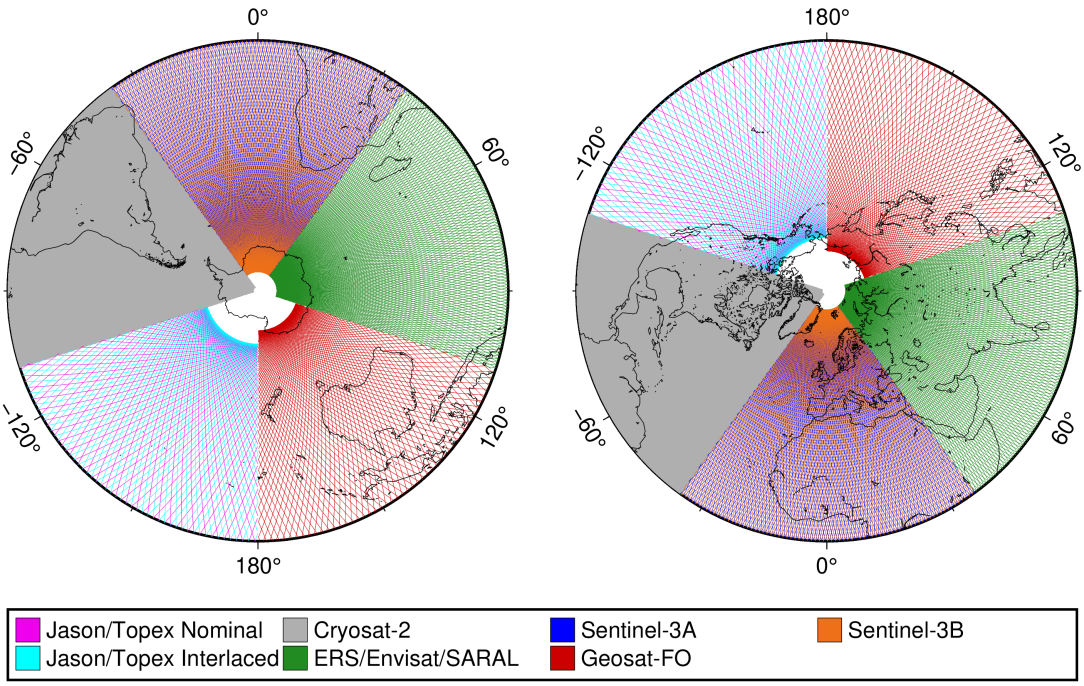


Figure 3.2: Nominal orbits for individual altimetry missions. For better visualization, only a certain longitude section of each mission, with a global coverage, is shown.

The dry troposphere correction is the range correction with the largest magnitude of about 2.1 m. It accounts for the refraction due to dry atmospheric gases and is derived from atmospheric pressure at sea level, which is proportional to vertically integrated air density. Because of scarcely available direct observations, modeled sea level pressure is used, e.g. provided by European Centre for Medium-Range Weather Forecasts (ECMWF) or U.S. National Centers for Environmental Prediction (NCEP) (Andersen and Scharroo, 2011).

The wet troposphere correction accounts for refraction resulting from water vapor content within the atmosphere rapidly varying in, both, spatial and temporal scales. It reaches magnitudes of a few millimeter in cold air and up to more than 30 cm in hot, wet air (Andersen and Scharroo, 2011). Due to the rapid variations, most modern altimeter satellites also carry a microwave radiometer in order to measure the water vapor variations simultaneously. However, the microwave radiometers are more susceptible to disturbances from land surfaces compared to the radar altimeter measurements, since the footprint diameter of the microwave radiometer (20 to 30 km) is significantly larger (Andersen and Scharroo, 2011). As a consequence, modeled wet troposphere corrections are usually applied in coastal zones and for missions without a microwave radiometer.

The frequency dependent (dispersive) ionospheric refraction of the radar signal is influenced by the total electron content (TEC) along the signal path within the ionosphere at altitudes above 100 km. The magnitude (0 to 10 cm) of the correction is largest at around 14:00h local time and smallest during the night at 02:00h. In addition, it depends on the season of the year and the solar activity increasing and decreasing with a cycle of about 11 years (Andersen and Scharroo, 2011). Since the ionospheric delay is dispersive, the TEC can be derived from comparing measurements at two different frequencies, which is why most modern altimeters not only provide measurements at the Ku-Band but also at the C-Band (or S-Band in case of Envisat). Furthermore, GPS based global ionosphere maps (GIM) allow interpolation on the altimeter tracks and provide a ionosphere correction, if no second frequency measurement is available.

The sea state bias correction accounts for the range bias towards the wave troughs arising from

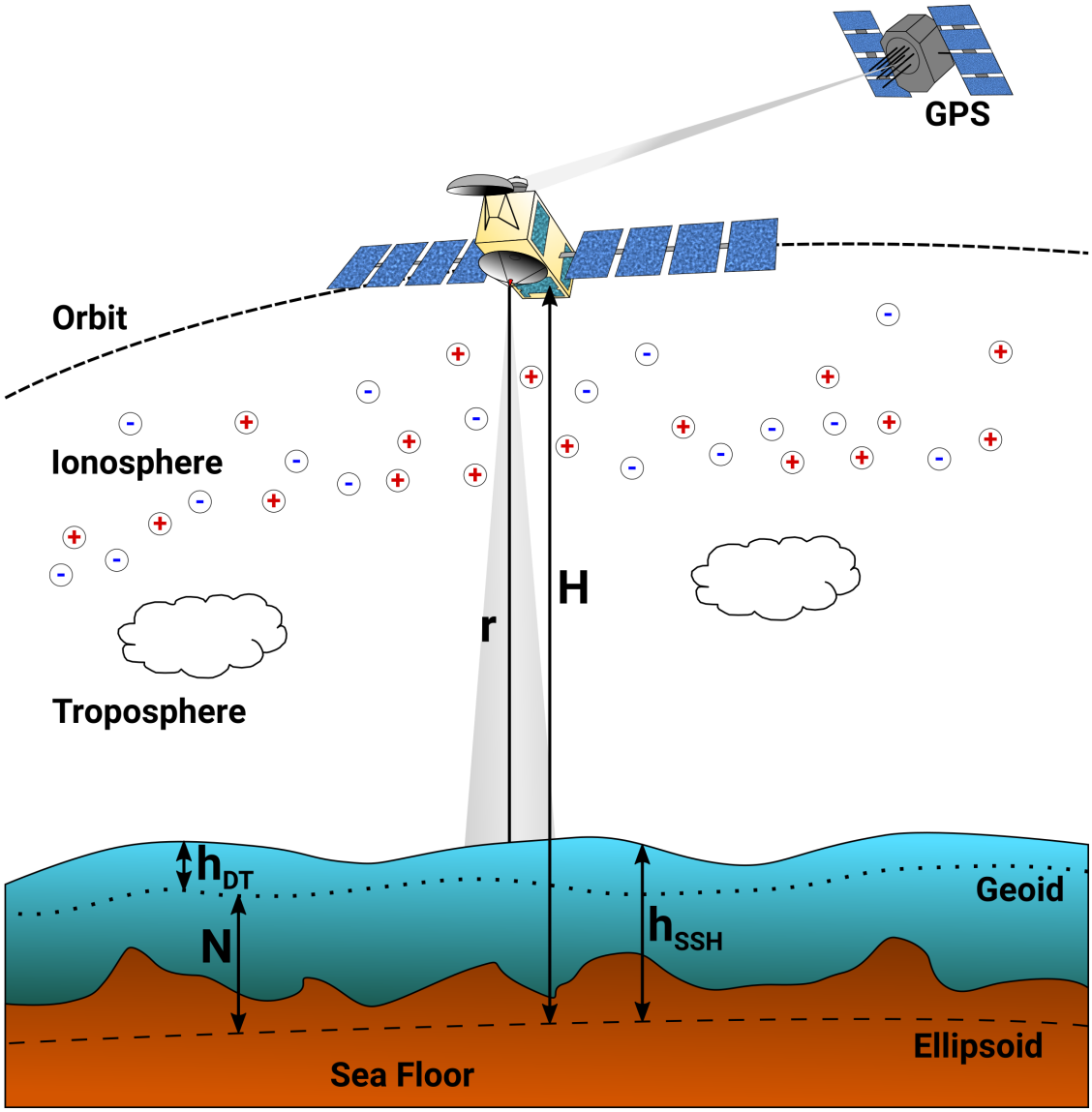


Figure 3.3: Principle of altimetry measurements, where H is the satellite altitude above the reference ellipsoid determined from different locating systems, such as GNSS, SLR or DORIS, r is the measured range, h_{SSH} is the sea surface height with respect to the reference ellipsoid and h_{DT} is the dynamic topography referred to the geoid, N.

the tracker bias, the electromagnetic bias and the skewness bias (Andersen and Scharroo, 2011). The tracker bias depends on the retracker used for estimating Significant Wave Height (SWH). The electromagnetic bias is related to the distribution of specular facets and their reflection properties within the footprint leading to a bias towards the wave troughs relative to the wave crests. The skewness bias arises from the satellite altimeter on-board tracker, which uses a median based tracking, whereas the mean is the desired parameter (Andersen and Scharroo, 2011). The sea state bias is one of the biggest contributors to altimetry error budgets (Yaplee et al., 1971), since it is usually estimated from models depending on the estimated SWH and wind speed, which can be derived from Backscatter Coefficient (σ°).

The corrected range r can be combined with the known satellite altitude H in order to derive Sea Surface Height (SSH), h_{SSH}, which is the height of the sea surface above the reference ellipsoid (Fig. 3.3)

$$h_{\mathrm{SSH}} = H - r. \tag{3.1.4}$$

The SSH estimate still includes geophysical effects from tides $\Delta r_{\mathrm{tides}}$ and deformations of the sea surface due to atmospheric pressure variations Δr_{DAC}. These time dependent effects can be modeled and removed in order to examine long term sea level changes. In addition, one usually removes a Mean Sea Surface (MSS) h_{MSS} in order to derive residual sea level change or Sea Level Anomaly (SLA), h_{SLA}, from

$$h_{\mathrm{SLA}} = h_{\mathrm{SSH}} - \Delta r_{\mathrm{tides}} - \Delta r_{\mathrm{DAC}} - h_{MSS}. \tag{3.1.5}$$

Here, the geophysical tidal effects $\Delta r_{\mathrm{tides}}$ represent the sum of the solid Earth tide Δr_{set}, pole tide Δr_{pt}, ocean tide Δr_{ot} and the loading tide Δr_{lt}

$$\Delta r_{\mathrm{tides}} = \Delta r_{\mathrm{set}} + \Delta r_{\mathrm{pt}} + \Delta r_{\mathrm{ot}} + \Delta r_{\mathrm{lt}}. \tag{3.1.6}$$

The solid Earth tide is the elastic deformation of the land and ocean bottom surfaces due to periodic tidal attraction from the Sun and the Moon. It can be computed using closed formulas by Cartwright and Tayler (1971); Cartwright and Edden (1973). The pole tide correction accounts for the effect from the change in centrifugal potential of the Earth due to variations of the axis of rotation with a period of about 435 days (Chandler Wobble). The ocean tide represents the dominant tidal signal. It is induced by gravitational attraction from the Sun and the Moon leading to variations of up to several meters in some coastal areas. It is usually determined from tidal models, which have improved considerably over the years providing accuracies of 1 to 2 cm nowadays (Andersen and Scharroo, 2011). In contrast to tide gauges mounted on the solid earth surface, altimeter measurements include the surface displacement due to the changing water mass load related to the ocean tides, which is corrected with the loading tide correction.

The dynamic atmosphere correction, $\Delta r_{\mathrm{DAC}} = \Delta r_{\mathrm{ib}} + \Delta r_{\mathrm{hf}}$, includes a long periodic Inverse Barometric (IB) component Δr_{ib}, which is usually derived from modeled hydrostatic sea level height changes due to atmospheric loading on time scales of more than 20 days. It can be derived from measured or modeled surface pressure, P_0, with 1 hPa depressing the sea surface by roughly 1 cm, as given by Andersen and Scharroo (2011)

$$\Delta r_{\mathrm{ib}} \approx -0.99484(P_0 - \bar{P}_{\mathrm{ref,oce}}), \tag{3.1.7}$$

with the global mean pressure over the total ocean area $\bar{P}_{\mathrm{ref,oce}}$ in each time step removed. In addition, Δr_{DAC} also includes a short-periodic component Δr_{hf} representing high frequency changes (periods of less than 20 days), such as wind effects.

The mean sea surface is computed by averaging all SSH values over a long time period (nowadays at least 20 years) and usually from a combination of several altimetry missions. During the estimation a least squares collocation technique can be applied in order to provide a gridded MSS product with a calibrated error estimate after carefully accounting for altimetry noise and biases (Pujol et al., 2018).

3.1.2 Conventional Altimetry Datasets

For retracking of the Jason missions, Sensory Geophysical Data Records (SGDR) have been obtained from the Archiving, Validation and Interpretation of Satellite Oceanographic data (AVISO) team[1], which is part of the French CNES. The SGDR are ordered by cycle and pass, including 254

[1] https://www.aviso.altimetry.fr (last accessed: 15.06.2022)

Table 3.2: Chosen RADS orbits and corrections.

Effect	Correction
Orbit	GDRD (where applicable GDRE) processing standards
Range	Ku-Band (Ka-Band) Ranges
Dry Troposphere	ECMWF model
Wet Troposphere	On-board radiometer (ECMWF model)
Ionosphere	smoothed 2-freq. (JPL GIM model, e.g. Komjathy et al. (2005))
Inverse Barometric	MOG2D (Carrère and Lyard, 2003)
Solid Earth Tide	Petit and Luzum (2010)
Pole Tide	Petit and Luzum (2010)
Ocean Tide	FES2014 (Lyard et al., 2021)
Loading Tide	FES2014 (Lyard et al., 2021)
Sea State Bias	CLS 2D (Labroue et al., 2004)
Inter-Mission Bias	RADS bias + Sect. 6.2.2
Mean Sea Surface	DTU15 MSS (Andersen et al., 2016)

repeat passes per cycle (~10 days). Similarly SGDR from the Envisat mission with a 35 day repeat cycle and 1002 passes are provided by ESA[2].

The Radar Altimetry Database System (RADS) (Scharroo et al., 2013) represents the altimetry data basis of the fingerprint inversion approach (Sect. 6) and comparisons of global and regional altimetric sea level estimates (Sect 5.2). RADS provides along-track 1 Hz orbits, ranges and a variety of additional corrections compared to the original SGDR products. The database is nowadays maintained by National Oceanic and Atmospheric Administration (NOAA) in cooperation with TU Delft. It is regularly updated with new missions as well as updated processing, orbits and corrections. In the context of global and regional sea level budgets, altimetry data from all missions between 2002 and 2020 is used, i.e., Topex, Jason-1/-2/-3, Envisat, Geosat-FO, Saral/Altika, Cryosat-2 and Sentinel-3. The chosen corrections that are applied unless stated otherwise are listed in table 3.2.

3.1.3 Delay Doppler Altimetry Datasets

Besides the higher resolution Synthetic Aperture Radar (SAR) mode, DDA altimeter data from the Cryosat-2 and Sentinel-3 missions can also be processed in a Reduced Synthetic Aperture Radar (RDSAR) mode similar to conventional altimetry. RDSAR data is derived by combining several of the SAR mode bursts and process the returns in order to derive 20 Hz observational data, coherent with conventional altimetry. In contrast, for SAR mode processing observations of the same ground point from individual radar bursts are stacked, allowing to make use of the Doppler effect and significantly improve the along-track resolution, whereas RDSAR processed data has similar footprint sizes as conventional altimetry. In this thesis, DDA data serves mainly as validation for the conventional altimetry retracker (Chap. 4). For this, DDA data from the Cryosat-2 and Sentinel-3 missions is extracted from the Grid Processing On Demand (GPOD) service by ESA, which is nowadays part of ESA EarthConsole (`https://earthconsole.eu/`). It offers the possibility to process DDA altimetry data either in SAR or RDSAR mode. It is possible to select and apply more sophisticated retracking algorithms compared to standard data products, leading to better quality data, especially, in coastal areas. In addition, the service also provides enhanced L2 products including the tracker range, return waveforms, corrections, etc., which allows the user to apply their own algorithms and directly compare them to other state-of-the-art SSH, SWH and σ° estimates.

[2] `https://earth.esa.int` (last accessed: 15.06.2022)

3.1.4 Mean Sea Level Time Series

For comparison and validation purposes (e.g., Sect. 5.2) time series of GMSL are acquired from different sea level processing groups. The AVISO group provides GMSL for individual satellites or a combination of missions (`https://www.aviso.altimetry.fr`). Monthly time series of GMSL are provided by the Commonwealth Scientific and Industrial Research Organisation (CSIRO) group (`https://www.cmar.csiro.au/`). The Sea Level Research Group from the University of Colorado provides global mean sea level estimates on a cycle by cycle basis (`https://sealevel.colorado.edu/`).

3.2 Time-Variable Gravity

3.2.1 GRACE and GRACE-FO

The Gravity Recovery And Climate Experiment (GRACE) mission has measured mass and corresponding gravity changes within the Earth system with an unprecedented accuracy since its launch in March 2002 (Tapley et al., 2004). GRACE is a joint mission of NASA and Deutsches Zentrum für Luft- und Raumfahrt e.V. (DLR). While originally planned to last only five years, it was possible to extend the mission lifetime to over 15 years up until the decommissioning in October 2017, after technical problems on the satellites. The mission consisted of two satellites, which were launched into the same near circular polar orbit in a tandem formation (Fig. 3.4) with an altitude of about 485 km, eccentricity of < 0.005, inclination of 89° and a separation of about 220 km between the individual satellites along the orbit. The low orbit of a few hundred kilometers is required in order to observe high resolution gravity field changes. From equation (2.1.1) it is obvious that the gravity signal magnitude is directly proportional to the inverse of the geocentric distance. Besides gravity information inferred from the spacecraft orbit positions, observed by GPS and SLR, the satellites also measure the inter-satellite distance with a K-Band ranging instrument, non-gravitational forces with on-board accelerometers and their absolute orientation in space by using star cameras for the rotation (e.g., Tapley et al., 2004). Over time, the orbits decreased, due to atmospheric drag effects, to about 380 km altitude, while the inter-satellite distance was maintained around 220 km by regular orbit maneuvers. After a gap in gravity observations of about one year, GRACE was succeeded by the Gravity Recovery And Climate Experiment Follow On (GRACE-FO) mission, which, in addition to the K-Band instrument, includes a laser ranging interferometer (LRI). The LRI instrument allows to derive even more accurate inter-satellite distances and, thus, better gravity field information (Kornfeld et al., 2019). The satellites covered the whole Earth surface roughly every 30 days, therefore, resulting in monthly gravity fields.

The general principle of the GRACE mission is shown in figure 3.4. The satellites fly on an orbit around the Earth's center of mass, consequently, providing all measurements in the CM frame (Sect. 2.4.1). Assuming an ideal scenario as in figure 3.4, initially both satellites have nearly the same velocity, $|\boldsymbol{v}_1| \approx |\boldsymbol{v}_2|$, and the distance measured by the K-Band ranging system will not vary much. When the satellites close in to the depicted surface load (Fig. 3.4, B), the first satellite will be attracted stronger by the load anomaly due to the smaller distance and the resulting acceleration, $|\boldsymbol{a}_1|$, will be larger compared to the second satellite. After the first satellite passes over the load (Fig. 3.4, C), the acceleration direction will still be directed towards the load but opposite the flight direction, consequently, decelerating the first satellite while the second satellite is still accelerated and reducing the inter-satellite distance. After both satellites passed over the load (Fig. 3.4, D), the second satellite will still be affected by an acceleration opposite to the flight direction, slowing down the second satellite compared to the first, which leads to an inter-satellite distance increase. In reality, these accelerations affect the satellites from all individual mass sources, which allows GRACE to only measure the integral effect of all mass changes affecting the satellite without discerning between individual sources. The resulting position and velocity changes are observed with GPS. The combination with the highly accurate inter-satellite K-Band ranges allows to derive monthly gravity field variations.

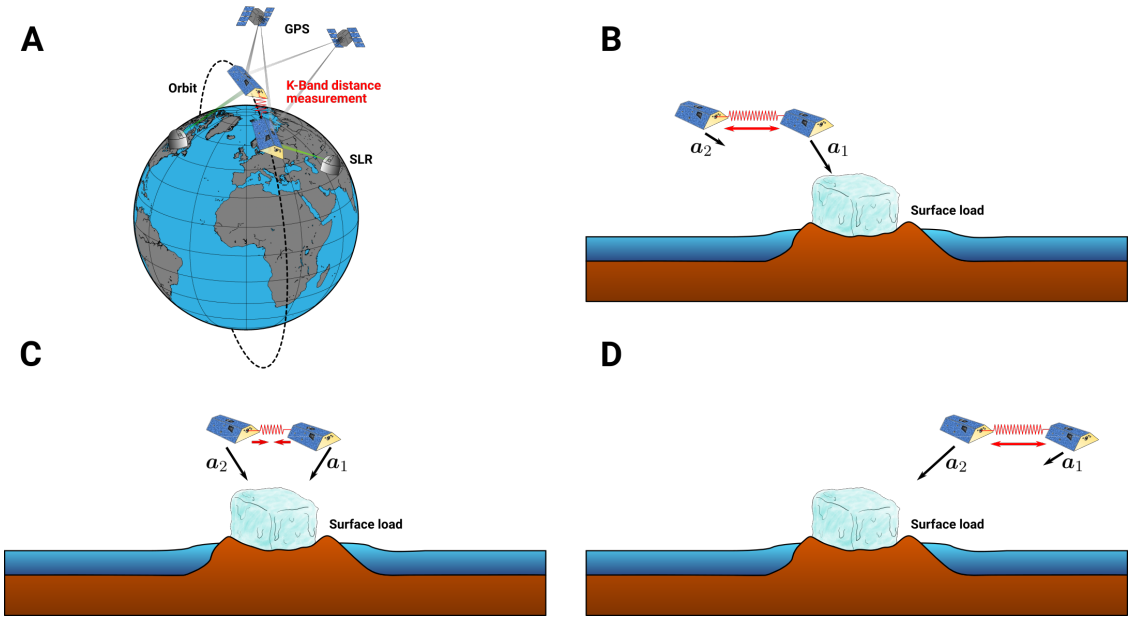


Figure 3.4: GRACE measurement principle. **A**: The two GRACE satellites fly on an orbit around the center of mass (CM, Sect. 2.4.1). Their positions are measured by GPS and SLR and the inter-satellite distance is observed with a K-Band microwave ranging instrument. In an ideal scenario when assuming no other mass anomalies relatively close on the Earth below the satellites, the velocities $|\boldsymbol{v}_1|$ and $|\boldsymbol{v}_2|$ will be nearly similar. **B**: When the satellites close in to a significant load anomaly, the first satellite will be attracted stronger due to the smaller distance to the surface load and $|\boldsymbol{v}_1|$ will increase relative to $|\boldsymbol{v}_2|$, which leads to an increase in inter-satellite distance. **C**: After the first satellite passes over the load anomaly, the direction of the corresponding acceleration vector, $|\boldsymbol{a}_1|$, is opposite to the flight direction. Consequently, the velocity $|\boldsymbol{v}_1|$ and the distance with respect to the second satellite will decrease. **D**: After both satellites passed over the surface load, the second satellite will be affected by a larger acceleration, $|\boldsymbol{a}_2|$, towards the load anomaly leading to an increase in inter-satellite distance.

Generally, GRACE and GRACE-FO gravity data is processed in different levels. Level-0 (L0) data is the raw data transmitted by the satellite. In the next step, L0 data is processed without loss of information by applying calibrations, transformation from engineering units etc., resulting in level-1A (L1A) data. Publicly available level-1B (L1B) data contains sensor data from the individual scientific instruments, which is utilized during the level-2 (L2) gravity field processing. The L2 products are the monthly spherical harmonic gravity fields. Finally, level-3 (L3) data are further processed L2 data, such as EWH variations on global and regional grids.

Spherical harmonic L2 GRACE and GRACE-FO gravity fields from the three official processing centers Deutsches GeoForschungsZentrum (GFZ), Center for Space Research (CSR) and Jet Propulsion Laboratory (JPL) are acquired from the GFZ data server (`ftp://isdcftp.gfz-potsdam.de/grace/Level-2/`). Continuously improved processing of the L1A and L1B data in combination with enhanced background models for tides, atmosphere and ocean mass signals lead to several updated data releases. In this thesis, the focus is on the newest release 06 (RL06) data as input for the inversion and for deriving individual ocean mass contributions. GRACE RL05 solutions, which are used for comparisons (Sect. 7.4), have been succeeded by the RL06 data but are still available on request from the processing centers. In this thesis, these are used for assessing earlier inversion results (e.g., Rietbroek et al., 2016) and previously published ocean mass changes

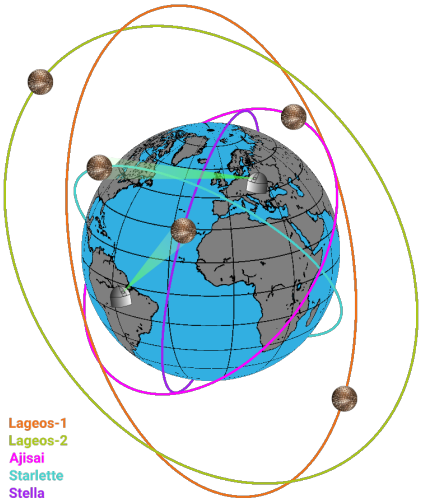


Figure 3.5: Orbits of the five satellites (Lageos-1, Lageos-2, Ajisai, Starlette, and Stella) used for SLR time-variable gravity input data utilized in this thesis.

(e.g., Johnson and Chambers, 2013). The monthly RL06 GRACE Satellite-only Model (GSM) fields contain the estimated spherical harmonics up to degree and order 60, 96 or 120 from each processing center. Corresponding monthly averaged spherical harmonics of the Atmosphere and Ocean De-aliasing Level-1B (AOD1B), that have been removed during the L2 processing, are provided (Dobslaw et al., 2017a). In addition to the official GRACE processing centers, high quality monthly spherical harmonic gravity data from the ITSG-2018 (Mayer-Gürr et al., 2018; Kvas et al., 2019) solution derived by TU Graz (`https://www.tugraz.at/institute/ifg/downloads/gravity-field-models/itsg-grace2018/`) is utilized. The fingerprint inversion (Sect. 6) expects input of monthly gravity Stokes coefficients in the form of unsolved, unfiltered GRACE and GRACE-FO Normal EQuation (NEQ) systems. For the RL05 data GRACE NEQs are provided by GFZ up to degree and order 150, while RL06 GRACE and GRACE-FO NEQs up to degree and order 120 are obtained from the ITSG-2018 solution.

As GRACE/GRACE-FO data are provided in the CM frame, the degree-1 coefficients are zero. For shifting the observations to the CF frame (Sect. 2.4.3) in order to be consistent with altimetry and other data products, auxiliary data, in the form of degree-1 coefficients, can either be directly obtained for SLR solutions, where the observing stations are naturally tied to the Earth, or from modeled solutions, which are provided by JPL as GRACE technical note 13 (TN-13) from `https://podaac.jpl.nasa.gov/gravity/grace-documentation#TechnicalNotes` based on Swenson et al. (2008) and Sun et al. (2016). For comparison, the degree-1 coefficients provided by University of Texas, CSR, are downloaded from `http://download.csr.utexas.edu/pub/slr/geocenter/`. Furthermore, TN-14 provides the c_{20} and c_{30} coefficients based on SLR, which are generally replaced during the GRACE data processing (Sect. 5.3.1), since those coefficients are relatively inaccurately estimated from GRACE data (Loomis et al., 2020).

In addition to spherical harmonics, time-variable gravity information is also provided in the form of mascons (Watkins et al., 2015). Mascons represent spherical caps of defined size, which are fitted to the gravity data. This results in scaling factors for each individual mascon and month. The results are provided on grids and stored in netCDF format. In this thesis, mascon solutions from JPL available at `http://grace.jpl.nasa.gov/` (Watkins et al., 2015; Wiese et al., 2016; Landerer et al., 2020) and from the Goddard Space Flight Center (GSFC) accessible from `https://earth.gsfc.nasa.gov` (Loomis et al., 2019a) are used. Both mascon datasets are regularly updated and cover the GRACE and GRACE-FO periods.

3.2.2 Satellite Laser Ranging

Over the last decades, Satellite Laser Ranging (SLR) has allowed to monitor the Earth's rotation and geocenter movements by measuring the range to satellites from well-defined stations around

the globe (Fig. 3.5). For this, the SLR instrument emits a laser pulse, which is then reflected back from the satellite and the two way travel time is measured. The time can then be converted to range (similar to Eq. (3.1.1)), while also accounting for atmospheric and tidal effects as well as the light-time correction. From the perspective of an inertial system, the light time correction refers to the movement of the SLR observation station during the signal run time due to Earth rotation.

Nowadays, various scientific satellite missions, e.g. GRACE/GRACE-FO, carry laser retro reflectors as part of their payload allowing for orbit observations with SLR. In addition, several specialized SLR missions consisting of a sphere covered with retro-reflectors have been launched since the 1970s starting with Starlette and Lageos-1 in 1975 and 1976, respectively. Since then, several other SLR satellites have been launched. The five mentioned here have been utilized to derive the SLR-related data utilized in this thesis. Ajisai (1986), Etalon-1/-2 (both 1989), Lageos-2 (1992) and Stella (1993). Furthermore, the LARES satellite was launched in 2012. For computing time-variable gravity changes of up to degree and order 5, as in this thesis, the satellites Lageos-1/-2, Ajisai, Starlette and Stella are utilized since they all fly on relatively low orbits. Etalon-1/-2 both fly on high altitude orbits with a perigee of about 19 000 km and, thus, are not very sensitive to gravity changes of the Earth. Since the LARES satellite was only available starting in 2012, it is often omitted from long term gravity solutions.

The monthly SLR data in this thesis has been provided by Anno Löcher and is based on Löcher and Kusche (2020). The NEQs are computed from the 5 (main) SLR satellites mentioned above and cover the time period 1993-2020 and degrees 1 to 5. Besides additional gravity information during some of the missing GRACE months and the gap between GRACE and GRACE-FO, the SLR data also yields direct observations of the Earth's geocenter motion (Sect. 2.4.3), which otherwise can only be inferred from the combination of GRACE and altimetry.

3.2.3 Swarm

The three-satellite Swarm mission represents ESA's first constellation mission for Earth observation that has been designed to observe the Earth's geomagnetic field and its temporal variations (Friis-Christensen et al., 2008). The three spacecraft have been launched into a near-polar circular orbit (inclination $\sim 87.5°$) on November 22, 2013. Swarm-A and Swarm-C fly side-by-side with initial altitudes of 480 km, while the orbit of Swarm-B is at higher altitude (530 km). The magnetometer instruments on board of each satellite allow a detailed survey of the evolution of the Earth's geomagnetic field as well as the electric field of the atmosphere.

In addition to magnetometer instruments, the Swarm satellites also carry high precision Global Navigation Satellite System (GNSS) receivers as well as accelerometers, which enable high-low satellite tracking for precise orbit determination and measurements of non-gravitational forces. Together with their low orbit height, the instrumentation allows to derive time-variable gravity information from each satellite separately and from their combination (Lück et al., 2018; Lück, 2022). However due to instrument problems, the accelerometer data from the Swarm mission requires specialized data processing before utilization (Siemes et al., 2016; Lück, 2022). As a result, it is possible to compute monthly time-variable gravity solutions up to degree and order 40. However, it is recommended to truncate at degree and order 12 when directly utilizing the gravity coefficients.

The monthly Swarm gravity field solutions in this thesis are provided by Lück (2022) and are available from 2014-08 till 2020-12 for degrees 2 to 40 in the form of NEQs. Similar to SLR, the Swarm data also provides gravity information in months, where the GRACE/GRACE-FO mission data is missing, especially during the one year gap between the two missions. Albeit its lower resolution, it can aid in estimating OMC and potentially bridge the GRACE/GRACE-FO gap.

3.3 Temperature and Salinity Data

3.3.1 In-Situ Profiles

The Argo-Program (Roemmich et al., 2009) represents an international collaboration of 30 states to deploy and maintain a consistent network of (today) more than 3800 free drifting floats spread within the world's oceans. The concept has been envisioned at the end of the 1990s requiring about 3000 floats for global coverage, which has been achieved in November 2007 (Roemmich et al., 2009). Each individual Argo float measures in-situ profiles of temperature and salinity up to an ocean depth of 2000 m, as well as pressure and biological parameters. This data is used to investigate temperature and salinity changes, steric sea level changes or ocean heat content (von Schuckmann et al., 2014). Nowadays there also exist some individual deep Argo floats, which can reach depth of 4000 m or even 6000 m but those are not part of this thesis.

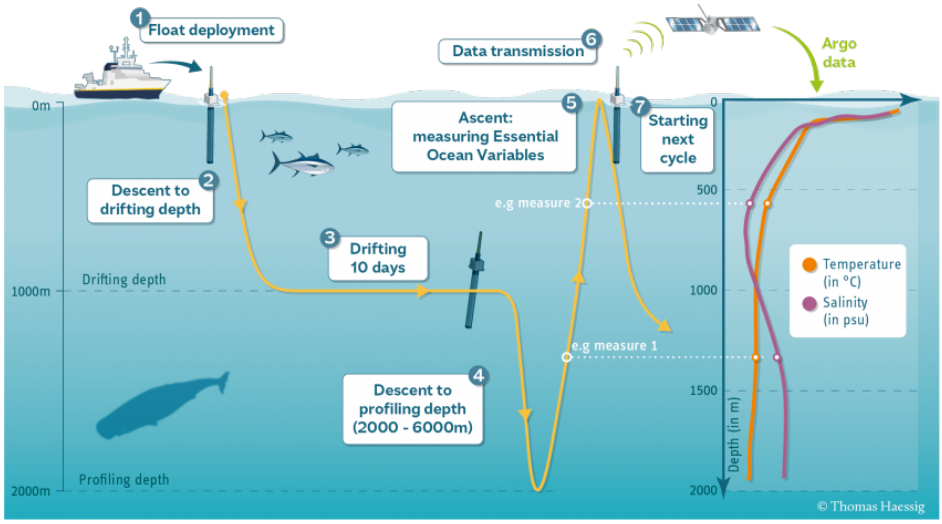


Figure 3.6: Argo measurement principle from https://argo.ucsd.edu/how-do-floats-work/ (last accessed: 27.06.2022).

Generally, the measurement cycle of an individual Argo float covers about 10 days (Fig. 3.6), leading to about 400 transmitted in-situ profiles each day. After the float has been deployed, it will sink down to its drifting depth to about 1000 m below sea surface. After 10 days, the float will dive down to its maximum measurement depth ($\sim$ 2000 m). During ascension to the sea surface, the float collects pressure, temperature and salinity profiles. At the sea surface the measured profiles, GPS position data and other quantities are transmitted to the Argo data centers via satellite communication. After transmission, the float sinks back to its drifting depth, starting the cycle anew.

For this thesis, in-situ profiles are mainly used for validation and experimentally including them as additional observables into the inversion. The Coriolis Ocean database for ReAnalysis (CORA) (Cabanes et al., 2013) is a collection of all types of in-situ temperature and salinity profile measurements including observations from Argo drifters, Conductivity, Temperature and Depth (CTD) systems, eXpendable BathyThermograph (XBT), moorings and other sources. In this work, the temperature and salinity profiles are converted to steric sea level (Sect. 2.3) and act as independent observations for validation purposes, but also as a potential additional dataset for the fingerprint inversion. The in-situ delayed mode product "INSITU_GLO_TS_REP_OBSERVATIONS_013_001_b" represents version 5.2 of the CORA dataset and collects profile data from the main global networks. In addition, CORA is nowadays merged with the EN4 profile database (Good et al., 2013) by the Met Office (https://www.metoffice.gov.uk/) and is provided by Copernicus Marine Environment Monitoring Service (CMEMS) (https://resources.marine.copernicus.eu). It includes quality controlled individual profile data from 1950 - 2019

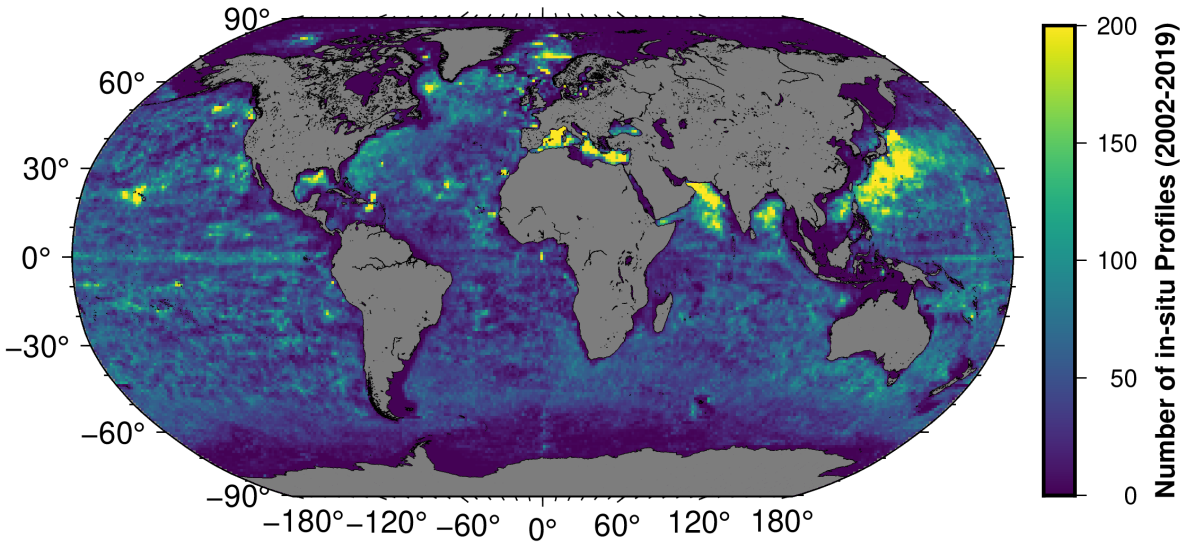


Figure 3.7: Number of in-situ profiles from the easyCORA datasets between 2002 and 2019 (216 months) at each grid point. The colorscale is capped at 200. Some grid locations may include more than 1000 measurements over the indicated time period.

intended for reanalysis and is updated on a yearly basis. In addition to gridded datasets, CORA also provides raw data as well as assimilation ready data for ocean re-analysis applications. The latter dataset (easyCORA) is utilized for including in-situ profiles as additional observables within the inversion method.

Gridded products produced by Scripps Institute of Oceanography (SIO) (Roemmich and Gilson, 2009) acquired from `http://sio-argo.ucsd.edu/` and International Pacific Research Center (IPRC) (Lebedev et al., 2007) available from `http://apdrc.soest.hawaii.edu/` are utilized for analysis of the impact on steric sea level estimates based on product choice (Sect. 5.4).

3.3.2 Ocean Model Data

Ocean models represent states of ocean and, nowadays, are coupled with additional sea-ice models. Sea level variations in these ocean models are forced by atmospheric surface (model) data or are also directly coupled with an atmospheric model. For the latter case, an ocean reanalysis model, typically, represents the ocean part of such a coupled atmosphere-ocean model, where the states are constrained by ocean observation data assimilation (Balmaseda et al., 2015). The main application of ocean model reanalysis are the climate monitoring and initialization or verification of seasonal forecasts (Zuo et al., 2019). Model quality has significantly improved over the years thanks to better understanding of the physical processes within the ocean, improved forcing data and computation resources allowing for higher spatial and temporal resolution. Today, spatial resolutions of 0.25 degree or less allow modeling of ocean transport and eddy phenomena on global and regional scales.

In this thesis, gridded 4D temperature and salinity data from several models is used and converted to steric sea level changes (Sect. 2.3). The resulting monthly maps of steric sea level change represent the basis of the steric fingerprints utilized in the inversion, but are also used for comparison and validation of the inversion output in the context of sea level budgets.

The ECMWF Ocean ReAnalysis System 5 (ORAS5) model data (Zuo et al., 2019) is utilized as a fingerprint basis throughout this thesis, unless stated otherwise. ORAS5 represents the successor of the ECMWF Ocean ReAnalysis System 4 (ORAS4) operational model (Balmaseda et al., 2013)

with improved ocean climate state and variability resulting from increased spatial resolution and updated assimilation data sets (Zuo et al., 2019). In addition, ORAS5 includes modeled eddies similar to the intermediate model Ocean ReAnalysis Pilot 5 (ORAP5) (Zuo et al., 2017). Besides the operational run, ORAS5 also provides an ensemble of a total of five runs that are generated by perturbation of initial conditions as well as assimilated observations and forcing data (Zuo et al., 2019). Utilizing the five ensembles and computing the respective ensemble mean allows to derive more robust fingerprints for the inversion. The ORAS model data has been obtained from `https://www.cen.uni-hamburg.de/icdc/data/ocean/easy-init-ocean.html`.

The Finite Element Sea Ice-Ocean Model (FESOM) (Timmermann et al., 2009), which is developed and maintained by the Alfred Wegener Institute, Bremerhaven (AWI), is realized on a triangular grid allowing for varying model resolutions down to a few kilometers for different regions. In this thesis, version 1.2 (Brunnabend et al., 2012), which has been the basis for the steric fingerprints of Rietbroek (2014) and Rietbroek et al. (2016), as well as the updated version 1.4 are used for comparison and analysis of the results. Both model results do not include any assimilated in-situ profiles or altimetry data and are based solely on atmospheric forcing data.

3.4 Auxiliary Data

This section describes the datasets that mainly serve as basis for generating fingerprints (Sect. 6.1) in this thesis.

3.4.1 Glacial Isostatic Adjustment

GIA is the effect of the adjustment of the visco-elastic Earth mantle and the elastic crust, due to the stress applied in the past, including the last glacial maximum, by mantle material shifting within the Earth's mantle resulting in mass signals visible in gravity measurements, as well as corresponding geometric height changes of the Earth's surface. Today, GIA influences on the observed uplift, geoid variation and corresponding relative sea level are not negligible and have to be considered for the gravity and altimetry measurements combined within the inversion approach.

Different GIA solutions are considered in this thesis (Sect. 6.1). The first one by A et al. (2013) has long been used in combination with GRACE RL05 data and is similar to the ICE5G model (Peltier, 2004). The ICE6G_D model (Peltier et al., 2018) represents the new standard model generally used in the context of the GRACE RL06 data. Caron et al. (2018) published an ensemble of 128000 GIA model runs, which is also considered here for comparison. Furthermore, GIA data based on Klemann and Martinec (2009) is used for consistency with Rietbroek (2014) and Rietbroek et al. (2016).

3.4.2 Terrestrial Hydrology Model Data

The WaterGAP Global Hydrological Model (WGHM) (Döll et al., 2003; Döll et al., 2014; Döll et al., 2020) provides simulated global water resources, i.e. water flows and storages, and human water use on a global 0.5 degree grid. WGHM allows to compute water storages in ten hydrological compartments including snow, soil moisture and groundwater as well as water flows, such as evapotranspiration, groundwater recharge and streamflow (Döll et al., 2020).

Integrating over all water storage compartments results in model estimates of Total Water Storage (TWS). The modeled TWS from WGHM can be compared to GRACE/GRACE-FO based TWS. Data from the Global Land Data Assimilation System (GLDAS, Rodell et al., 2004) is not considered here. GLDAS employs the same equations for the groundwater storage compartment as for the soil moisture compartment, which may create some errors. In this thesis, the WGHM version 2.2d (Döll et al., 2014; Döll et al., 2020) is used for constructing hydrological fingerprints

(Sect. 6.1), which, in contrast to WGHM-V1 (Döll et al., 2003) used in previous inversions (Rietbroek, 2014; Rietbroek et al., 2016), provides better accuracy and longer time series. Similarly, the PCRaster Global Water Balance (PCR-GLOBWB) version 2.0 model (Sutanudjaja et al., 2018) is utilized for sensitivity analysis of the inversion results with respect to fingerprint parameterization.

The dataset by Humphrey and Gudmundsson (2019) consists of an ensemble of 100 reconstructions of contemporary and past hydrological TWS changes based on a statistical model trained during the GRACE era and forced with meteorological data on daily and monthly time scales. The global gridded data is available from 1979 until 2019, trained with JPL GRACE data and forced with ERA5 atmospheric data. It has been used, e.g., to investigate a potential bias between GRACE and GRACE-FO (Landerer et al., 2020). In this thesis, it is employed as part of the validation of the hydrological component of the inversion method (Sect. 7.2.6).

3.4.3 Glacier Inventory Data

Glacier inventory data provides information on the location and extent of individual glaciers worldwide. It is used in order to construct inversion fingerprints (Sect. 6.1). Two different sets of inventory data are used. Originally, Rietbroek et al. (2016) used a combination of glacier positions from the Randolph Glacier Inventory (RGI) version 1.0 (Raup et al., 2007) and the World Glacier Inventory (NSIDC, 1999). This thesis also includes an update of the glacier inventory. The RGIv6.0 (RGI Consortium, 2017) provides significantly more glaciers and is divided into 19 regions, which are further separated into sub-regions (Sect. 6.1, Fig. 6.1), including peripheral glaciers in Greenland and Antarctica.

3.4.4 GRACE Ocean and Atmosphere De-aliasing Products

The AOD1B background model contains the modeled mass signals of the atmosphere and the ocean and is removed during estimation of the level 2 GRACE gravity fields (Dobslaw et al., 2017a; Dobslaw et al., 2017b). In the AOD1B background product, the ocean part is modeled by the Max Planck Institute Ocean Model (MPIOM, Jungclaus et al., 2013). It represents an improvement of previous model versions, e.g., utilized for GRACE RL05 data (Dobslaw et al., 2017a). It makes sense to utilize the Ocean Bottom Pressure (OBP) background model data for modeling the internal mass variations within the fingerprint inversion approach in order to capture the Internal Mass Variations (IMV). The RL06 AOD1B data contains four products: (1) the GAA product containing the mass effect of the atmosphere, (2) the GAB product contains the ocean mass contribution, (3) the GAC product is the sum of GAB and GAA and (4) the GAD product represents the OBP equivalent of GAB, i.e. including the IB effect.

In this thesis, the three hourly temporal resolution GAB product up to degree and order 180 is used for generating IMV fingerprints. For processing GRACE data directly, the official GAB or GAD products, consistent with the GRACE spherical harmonic products, are applied.

3.4.5 Ice-Altimetry Data

The ice mass balance across the large ice sheets in Greenland and Antarctica is regionally different. In order to augment the uniform melting assumptions of the Rietbroek et al. (2016) inversion, ice mass change maps based on radar (ice) altimetry (L. Schröder et al., 2019; Strößenreuther et al., 2020) are employed in this thesis. The ice-altimetry data at roughly 10 km resolution for Antarctica is utilized from 2002 starting with the Envisat mission until 2017 (L. Schröder et al., 2019) and after 2010, based on Cryosat-2 for Greenland (Strößenreuther et al., 2020). These observations can be used to derive melting patterns (Sect. 6.1), which aid in better discriminating ice and corresponding ocean mass changes from individual basins. In addition, these data sets serve as independent validation for mass changes in Greenland and Antarctica.

Chapter 4

Improving Retracking of Coastal Radar Altimetry Estimates

The global mean sea level rises with a rate of about 3.10 to 3.50 mm/yr (WCRP-Global-Sea-Level-Budget-Group, 2018) while regional rates can be significantly different. About ten percent of the world's population live close to the coast (McGranahan et al., 2007). Consequently, regional and, especially, coastal sea level change observations and predictions become more and more important for understanding the drivers of regional sea level and to enable policy makers to plan and construct reliable coastal defenses and warning systems. However, the availability of coastal sea level change observations has been sparse over the last decades and is concentrated at a small and unevenly distributed number of individual tide gauge stations worldwide (Mitchum et al., 2010). With the advent of satellite radar altimetry in the early 90's, it is possible to continuously monitor the sea level variations in the open ocean, but most conventional reprocessing methods, usually denominated as retracking, fail to provide reliable sea level change close to the coast, i.e. closer than 10 km. Only in recent years, more sophisticated retracking algorithms have become available in order to reprocess the coastal altimetry measurements in order to improve Sea Surface Height (SSH) as well as Significant Wave Height (SWH) and Backscatter Coefficient (σ°) reaching significantly closer to the coast (e.g., Hwang et al., 2006; Guo et al., 2009; Passaro et al., 2014; Roscher et al., 2017; Buchhaupt et al., 2018). Other methods focus on inland water retrieval (e.g., Uebbing et al., 2015; Boergens et al., 2016). All of these methods are based on a sub-waveform approach (see Sect. 4.2) to filter out perturbing signals from land and improve the resulting sea level estimates.

This chapter, first, introduces retracking in general, starting from the altimeter waveform (Sect. 4.1), followed by definition of basic physical, empirical and sub-waveform retrackers (Sect. 4.2). In section 4.3, the latest version of the Spatio-Temporal Altimetry Retracker (STAR) algorithm, which updates the first version introduced in Roscher et al. (2017), is described. Furthermore, the section introduces enhancements that have been made in order to significantly improve the estimated SSH, SWH and σ°. While the version from Roscher et al. (2017), which will be termed STAR-V1, already provided significantly improved coastal sea level estimates compared to other conventional altimetry coastal retracking methods, STAR-V3, introduced in this chapter, provides results from conventional altimetry, which are comparable in quality to state-of-the-art Delay Doppler Altimetry (DDA) in coastal and open ocean applications. STAR-V2, which has e.g. been used for a comparison of SWH estimates (Schlembach et al., 2020; Quartly and Kurekin, 2020), represents an intermediate step between STAR-V1 and STAR-V3 and is not further discussed here.

4.1 Altimeter Return Waveform

Nowadays, all modern satellite radar altimeter instruments are so called pulse-limited altimeters, where a short radar pulse is emitted in order to measure the range; in contrast to beam-limited altimeters, this allows for wider beam width angles Θ_B and a smaller antenna diameter (Chelton et al., 1989; Chelton et al., 2001). In addition, the pulse-limited design is associated with a smaller

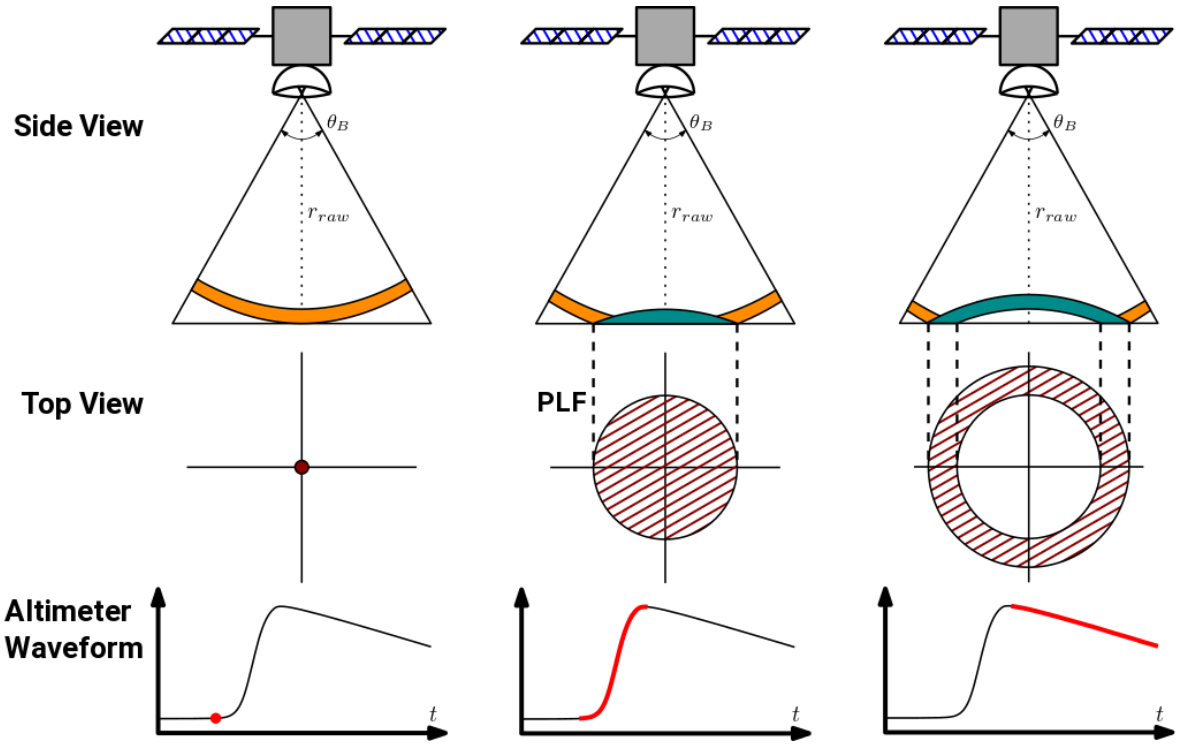


Figure 4.1: Interaction of the emitted radar pulse with the backscattering surface and the corresponding footprint and part of the return waveform measured by the altimeter. Left: the leading edge of the radar pulse hits the surface at satellite nadir. Middle: the trailing edge of the radar pulse hits the surface at satellite nadir. Right: The surface at satellite nadir is no longer illuminated, but signal is still reflected from off-nadir locations.

altimeter footprint, i.e. the surface area illuminated by the radar instrument, and it is less sensitive to antenna nadir pointing errors (Quartly et al., 2001). However, implementing a radar system, which emits only very short pulses is quite difficult due to relatively large power demands and a shortened lifetime of the instrument. Instead, all pulse-limited altimeters emit a longer pulse, which is compressed to a short effective duration by frequency modulating the signal, leading to a "chirp" signal (Chelton et al., 1989).

The altimeter emits a radar pulse with a defined (effective) pulse duration τ, which propagates spherically from the instrument on the satellite towards the Earth surface (Fig. 4.1, top left). The pulse is reflected at the surface and the instrument measures the returned energy over time forming the so called altimeter waveform (Fig. 4.2, solid black curve). Before the radar pulse reaches the surface, the recorded return signal only consists of the thermal noise T_n. Once the front edge of the pulse hits the surface at satellite nadir, the corresponding footprint is simply a point (Fig. 4.1, left column). Afterwards, the instrument begins to measure an increase in return energy, which then forms the so called leading edge of the altimeter waveform (Fig. 4.2) and the corresponding footprint becomes a circle with increasing radius, as more parts of the radar pulse hit the surface. This continues until the rear part of the radar pulse arrives at the surface at satellite nadir, where the footprint circle reaches its maximum size, forming the so called pulse limited footprint (PLF). At the same time, the return energy is at a maximum value marking the end of the leading edge (Fig. 4.1, middle). Afterwards, no more radar energy is reflected back from the surface at satellite nadir, while the outer parts of the spherical radar pulse still illuminate off-nadir locations on the surface leading to a annulus shape of the footprint. The corresponding radii of the inner and outer circle increase with time, but such that the total area remains constant, i.e. equal to the size of the PLF (Chelton et al., 1989); on the altimeter waveform this is represented by the trailing edge (Fig. 4.1, right). In theory the energy level of the trailing edge should be constant, but, in reality,

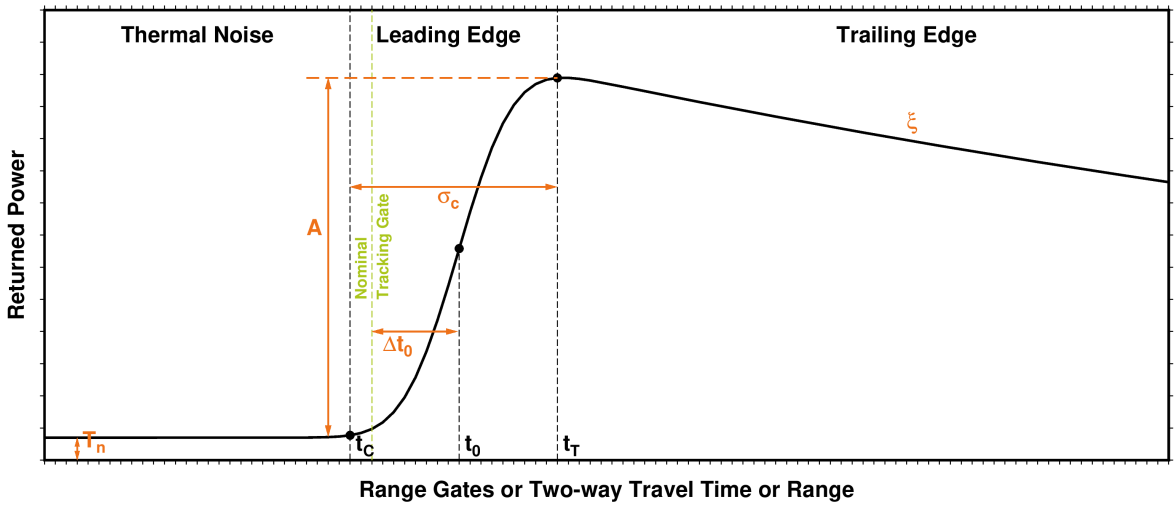


Figure 4.2: Theoretical altimeter return waveform over the ocean corresponding to the Brown (1977) model. Times t_C and t_T mark reflected signal from the wave crest and troughs, respectively; t_0, thus, indicates the average sea surface within the pulse limited footprint (PLF). The parameters of the theoretical waveform model are provided in orange: the thermal noise T_n, the amplitude A, the leading edge width σ_c, the trailing edge slope ξ and the epoch Δt_0, which is related to the mean sea level within the PLF (Fig. 4.1).

it is damped as a result of the gain pattern of the antenna on the satellite being smaller in off-nadir direction (Chelton et al., 1989).

The altimeter waveform contains information on several physical parameters related to the surface conditions along the satellite's ground track (Fig. 4.2). The thermal noise T_n represents the permanent noise level of the background radiation and electromagnetic disturbances from the satellites electronics, which largely depend on temperature. The amplitude A of the waveform, in combination with a scale factor $\Delta\sigma_{\text{scf}}$ scaling the measured waveform power of all waveforms to common levels. Besides a factor for transforming the measured power into predefined value ranges, the scaling factor includes corrections for the automatic gain control, the utilized frequencies and other mission dependent parts, which will not be further discussed here. In a level-2 or higher data product the scale factor is usually provided as a correction that is applied to the Backscatter Coefficient (σ°) (also called "sigma-naught") values derived from the estimated amplitude, by

$$\sigma^\circ = 10 \log_{10} A + \Delta\sigma_{\text{scf}}. \tag{4.1.1}$$

This rescales the normalized waveform amplitude to measured power levels. σ° can then be related to wind speed over the ocean or surface soil moisture over land. The epoch Δt_0 represents the offset between the real mid-point of the leading edge t_0 and the nominal tracking gate, which is a predefined reference point, which is related to the raw two-way travel time measurement. Thus, t_0 is an indication of the mean sea surface between the wave crests and troughs within the PLF (Fig. 4.1). It can be related to range using equation (3.1.1). Similarly the x-axis can either be viewed as two-way travel time, range or as discrete range gates with a defined separation in time Δt_{gs} or equivalently range. The leading edge width σ_c is related to Significant Wave Height (SWH), denoted as H_s, which corresponds to the crest-to-trough height of about $\frac{1}{3}$ of the largest waves in the footprint (Chelton et al., 1989). Retracking algorithms usually provide the width of the leading edge, σ_c^2, which can be converted to SWH by

$$H_s = \sqrt{4c^2(\sigma_c^2 - \sigma_p^2)}, \tag{4.1.2}$$

where c is the speed of light and σ_p is the width of the radar point target response. Finally, the trailing edge slope ξ represents the off-nadir mispointing angle. However, the number of discrete

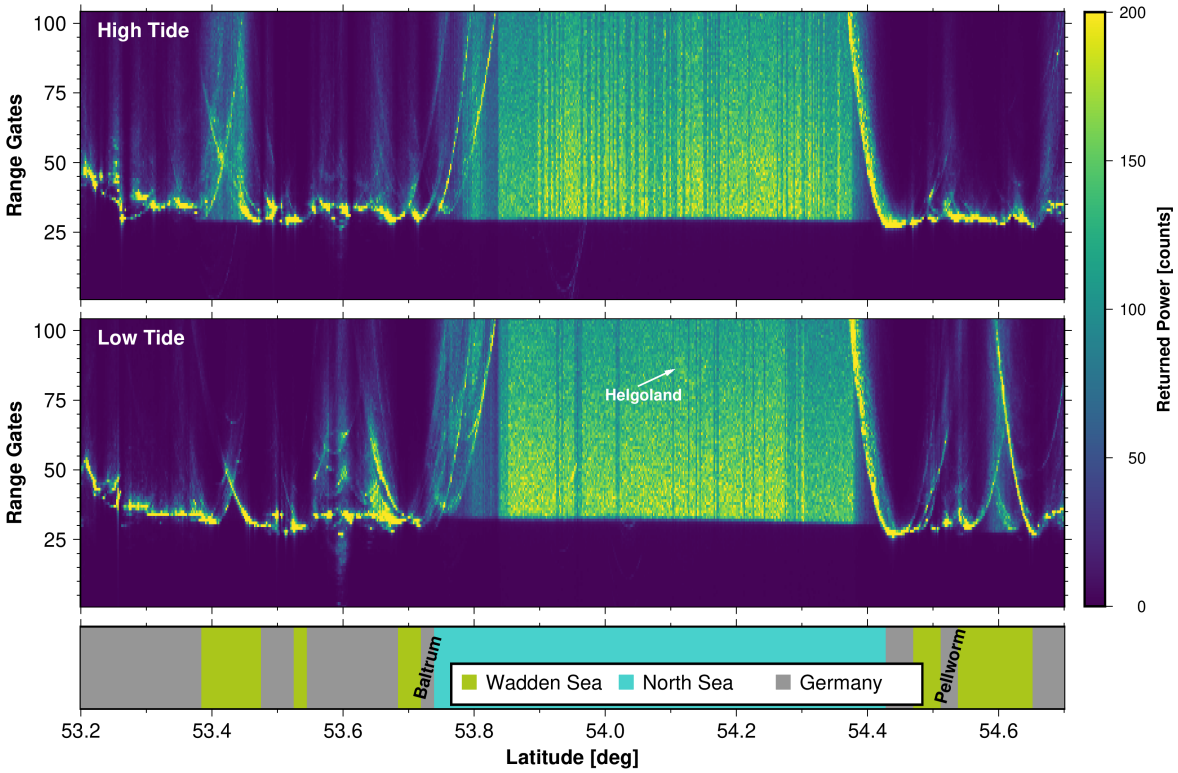


Figure 4.3: Exemplary waveforms along-track Jason-3, pass 213, passing over the North Sea.

range gates is limited meaning that only a certain range-window of the total return signal is actually observed (usually about 60 m). The range-window is permanently adjusted by a tracking algorithm on-board the satellite; erroneous adjustments will, thus, lead to either non-meaningful altimeter-waveforms or a complete "loss of lock", which often happens with older satellite missions, especially over land surfaces. Nowadays, this is less of a problem with the newer altimetry missions, due to improved tracking-algorithms using, e.g., along-track height information from an accurate Digital Elevation Model (DEM) (Gommenginger et al., 2011). Nonetheless, these algorithms are not perfect and altimeter satellites also send the waveform together with the remaining measurement information down to Earth for further reprocessing, which is called "retracking".

4.2 Retracking Conventional Altimetry

Retracking is the ground based reprocessing of the altimeter waveform measured by the satellite altimeter. On-board of the satellite, the on-board tracker tries to keep the mid-point of the leading edge at a defined position, the so called "nominal tracking gate", by adjusting the range window after each measurement to account for varying surface heights. The measured two-way travel time with respect to the nominal tracking gate is converted to range (r_{raw}, Sect. 3.1.1) and transmitted back to Earth. While this alignment of the measured return waveforms works relatively well with near perfect surface conditions over the open ocean (Fig. 4.3), it becomes significantly less reliable with perturbed signal returns within the altimeter footprint. Some areas might only be covered by water during high tide conditions, such as the Wadden sea (see e.g., the Ems river estuary at approximately 53.4° latitude, Fig. 4.3). However, islands, which are not directly crossed by the satellite but located within the surface area illuminated by the altimeter instrument can also lead to a parabolic shape in the along-track radargram (e.g. Helgoland island at 54.1° latitude, Fig. 4.3 or Kangean island, Fig. 4.5). Consequently, the measured waveforms are retracked during ground processing of the data.

The main goal of retracking is to improve the tracker range by deriving the offset Δt_0 between the nominal tracking gate and the real mid-point of the leading edge (Fig. 4.2). Furthermore, it allows to (co-)estimate additional parameters related to SWH, wind speed and antenna mis-pointing. For this task, various retracking algorithms have been developed so far, which can be roughly characterized into three classes: (1) physics based retrackers, which try to accurately model the waveform based on the mathematical representation (Eq. (4.2.1)) and fitting it to the measured waveform in an optimal way; (2) empirical retrackers, which only focus on deriving the range offset Δt_0 and not necessarily all of the other parameters and (3) sub-waveform retrackers, which only utilize a section of the total waveform in order to better deal with peaks and other disturbances of the theoretical waveform shape, e.g. by land influence (Fig. 4.3). The latter are generally combined with a physical or empirical algorithm in order to derive the desired parameters from the sub-waveform.

4.2.1 Physics Based Retracking Algorithms

The shape of the altimeter waveform over the open ocean generally follows the Brown (1977) model, which results from specular facets reflecting the radar signal on the surface. Mathematically, the returned power $P_r(t)$ of the waveform represents a convolution, which is given by (Hayne, 1980, Eq. (1))

$$P_r(t) = \mathrm{FSR}(t) * \mathrm{PTR}(t) * \mathrm{PDF}(t), \tag{4.2.1}$$

where $\mathrm{FSR}(t)$ is the average flat surface impulse response, $\mathrm{PDF}(t)$ is the density distribution of the specular points in the altimeter footprint and $\mathrm{PTR}(t)$ is the radar system point-target response.

The flat surface impulse response function $\mathrm{FSR}(t)$ can be approximated by (Hayne, 1980)

$$\mathrm{FSR}(t) = A \exp\left(-\delta t\right) I_0\left(\beta\sqrt{t}\right) U(t), \tag{4.2.2}$$

with

$$\delta = \frac{4c}{\gamma H}\cos(2\xi), \tag{4.2.3}$$

$$\beta = \frac{4}{\gamma}\sqrt{\frac{c}{H}}\sin(2\xi), \tag{4.2.4}$$

and

$$\gamma = \frac{\sin(\Theta_B)^2}{\ln 4}. \tag{4.2.5}$$

In (4.2.2), A is the amplitude of the return signal, which contains several constants and an off-nadir pointing angle ξ dependent term (Hayne, 1980, Eq. (8)), $I_0(\cdot)$ is a modified Bessel function of the second kind and $U(t)$ is a unit step function with the step at t_0 (Fig. 4.2). As in Section 3.1.1, c is the speed of light in vacuum, H is the satellite altitude and Θ_B is the antenna beamwidth. For separating the off-nadir and beamwidth dependent parts, Hayne (1980) introduced the terms δ, β and γ. The true H is often substituted by the nominal satellite altitude H_0 from the corresponding altimetry mission.

As a first order approximation, the density distribution of the specular point $\mathrm{PDF}(t)$ can be approximated as a Gaussian function and the Probability Density Function (PDF) is given by (Brown, 1977)

$$\mathrm{PDF}(\zeta) = \frac{1}{\sqrt{2\pi}\sigma_s}\exp(\frac{-\zeta}{2\sigma_s}), \tag{4.2.6}$$

Table 4.1: Conventional altimeter characteristic parameters (extended from Quartly et al., 2001).

Mission	**Band**	**Beamwidth**	**PRF [Hz]**	**Number of Range Gates**	**Nominal Tracking Gate**	**Gate Width [ns]**	**Waveform Frequency [Hz]**	**Radar Frequency [GHz]**
Topex	Ku	1.1°	4500	128	32.5	3.125	10	13.575
	C	2.7°	1200	128	35.5	3.125	5	5.3
Poseidon	Ku	1.1°	1700	60	29.5	3.125	20	13.65
GFO	Ku	1.6°	1020	128	32.5	3.125	10	13.5
Jason-1	Ku	1.28°	1800	104	31	3.125	20	13.575
	C	3.4°	300	104	31	3.125	20	5.3
Envisat	Ku	1.29°	1800	128	46.5	3.125	18	13.575
	S	5.5°	450	64	25.5	6.25	18	3.2
Jason-2	Ku	1.26°	1800	104	31	3.125	20	13.575
	C	3.38°	300	104	31	3.125	20	5.3
SARAL/AltiKa	Ka	0.61°	3800	104	39	2.0833	40	35.75
Jason-3	Ku	1.28°	1800	104	31	3.125	20	13.575
	C	3.4°	300	104	31	3.125	20	5.3
Cryosat-2*	Ku	1.38°	1900	128		3.125	20	13.575
Sentinel-3A*	Ku	1.38°	1900	128		3.125	20	13.575
Sentinel-3B*	Ku	1.38°	1900	128		3.125	20	13.575

*The number of range gates for these missions can vary for different products.

where η represents the surface elevation in meters relative to the mean sea level within the altimeter footprint and σ_s is the leading edge width. The PDF can be transferred to the two-way travel time domain by using equation (3.1.1).

The radar system point target response term $\mathrm{PTR}(t)$ corresponds to a $(\frac{\sin(x)}{x})^2$ (Gommenginger et al., 2011) function, which is also generally approximated by (Brown, 1977)

$$\mathrm{PTR}(t) = \eta_P P_T \exp\left(-\frac{1}{2}\left(\frac{t}{\sigma_p}\right)^2\right), \tag{4.2.7}$$

with the pulse compression ratio η_P, transmitted peak power P_T and the pulse width σ_p. The latter can be expressed by (Gommenginger et al., 2011)

$$\sigma_p = \begin{cases} 0.530\tau & \text{for the Envisat mission} \\ 0.513\tau & \text{else,} \end{cases} \tag{4.2.8}$$

where τ is the (effective) compressed pulse duration.

After inserting the approximations from equations (4.2.2), (4.2.6) and (4.2.7) into equation (4.2.1), Brown (1977) showed that the convolution reduces to

$$P_r(t) = \eta_P P_T \mathrm{FSR}(t) \sigma_p \frac{1}{2}\left[\mathrm{erf}(\frac{1}{\sqrt{2\pi}\sigma_c} + 1)\right], \tag{4.2.9}$$

with the combined leading edge width σ_c defined as the combination of the point-target response width σ_p and the wave height related leading edge width σ_s

$$\sigma_c = \sqrt{\sigma_p^2 + \sigma_s^2}, \tag{4.2.10}$$

where σ_c^2 is usually estimated from retracking and, consequently, σ_p^2 has to be accounted for when computing SWH from equation (4.1.2). The error function is defined as

$$\mathrm{erf}(x) = \frac{2}{\pi}\int_0^x \exp\left(-s^2\right) ds. \tag{4.2.11}$$

Several practical implementations of the physical waveform model have been published over the years. The algorithms sometimes differ only in small details, which are not always documented well. One of the most well known implementations is the Maximum Likelihood Estimation (MLE) retracker by Amarouche et al. (2004), which comes in two variations differing in the number of parameters retrieved. The MLE3 retracker only provides estimates for the epoch Δt_0, SWH and σ°, while the off-nadir angle ξ is fixed to zero; this avoids dealing with the high correlations between σ° and ξ. In contrast, the MLE4 algorithm also co-estimates the off-nadir angle. The Amarouche et al. (2004) model is the standard ocean retracking algorithm used for the official data products for the Jason-1/-2/-3 missions. For the Envisat mission a specialized algorithm is first used to retrieve the off-nadir pointing angle, which is then fixed during a second 3 parameter estimation (Gommenginger et al., 2011). Other algorithms have been published, e.g. by Deng (2003) and Halimi et al. (2013). The former aims at modeling the return waveform as accurately as possible also co-estimating the thermal noise T_n and separating the amplitude into a constant part and a part depending on the off-nadir angle.

In contrast, the Halimi et al. (2013) model is a basic 3-parameter model, which is similar to the MLE3 algorithm and given by

$$P_r(t) = T_n + \frac{A}{2}\left[1 + \mathrm{erf}\left(\frac{t - \Delta t_0 - \alpha\sigma_c^2}{\sqrt{2}\sigma_c}\right)\right] \exp\left[-\alpha\left(t - \Delta t_0 - \frac{\alpha\sigma_c^2}{2}\right)\right]. \tag{4.2.12}$$

The thermal noise T_n can be determined from averaging the first few range gates and is subtracted from the return waveform beforehand. This leaves only the three parameters A, Δt_0 and σ_c to be

estimated. In addition, the satellite mission dependent parameter α is computed from (Amarouche et al., 2004)

$$\alpha = \delta - \frac{\beta^2}{4} \tag{4.2.13}$$

$$\alpha_{\xi=0} = \frac{4c}{\gamma H} \frac{1}{1 + H/R_e}, \tag{4.2.14}$$

with δ, β and γ given by equations (4.2.3), (4.2.4) and (4.2.5), respectively. For the three parameter model the off-nadir angle is fixed to $\xi = 0$ and a correction term is introduced to account for the curved shape of the surface; Brown (1977) originally only assumed a flat surface.

4.2.2 Empirical Retracking Algorithms

Empirical retracking algorithms can roughly be classified into two classes: (1) methods based on statistical properties of the return waveform and (2) methods that fit an empirically derived function to the return waveform (Gommenginger et al., 2011).

One of the simplest and most robust empirical retrackers is the Off-Centre of Gravity (OCOG) method by Wingham et al. (1986). It computes a rectangle with the amplitude A, the center of gravity COG and a width parameter W in a pure statistical sense while only depending on the power values $P(t_i)$ in the individual range gates $i = 1, 2, ..., N$ without any connection to the waveform shape. The three parameters are computed from

$$A = \sqrt{\sum_{i=1+n_a}^{N-n_a} P^4(t_i) \Big/ \sum_{i=1+n_a}^{N-n_a} P^2(t_i)}, \tag{4.2.15}$$

$$W = \left(\sum_{i=1+n_a}^{N-n_a} P^2(t_i) \right)^2 \Big/ \sum_{i=1+n_a}^{N-n_a} P^4(t_i), \tag{4.2.16}$$

and

$$\mathrm{COG} = \sum_{i=1+n_a}^{N-n_a} iP^2(t_i) \Big/ \sum_{i=1+n_a}^{N-n_a} P^2(t_i), \tag{4.2.17}$$

with the number of aliased bins n_a at the beginning and end of the return waveform. Aliased bins refer to those bins affected by the filtering during the L1A processing. The parameters can be interpreted as a best fitting box enclosing the leading edge and trailing edge parts of the waveform, where COG is the mid point, W is the width and A is the height of the box. The OCOG leading edge gate LEG, i.e. the left edge of the box, can then be derived from

$$\mathrm{LEG} = \mathrm{COG} - \frac{W}{2}. \tag{4.2.18}$$

The amplitude provides information on the backscatter coefficient σ°. While the algorithm is fairly easy to implement and quite robust, it only provides a limited quality of retracked ranges since it does not account for the shape of the return waveform.

A better result is achieved with a so called threshold algorithm (Davis, 1995; Davis, 1997). It was originally developed to process ice waveforms of ESA's ERS mission (Davis, 1995) and later adopted by NASA as part of the ice-ranges provided in the official Geophyiscal Data Records (GDR) products. The basic idea is to utilize the amplitude A from the OCOG method (Eq. (4.2.15)) derived from the thermal noise corrected return waveform and combine it with a user defined threshold value v_{thresh} to derive the threshold power level $P(t_{\mathrm{thresh}})$ given as

$$P(t_{\mathrm{thresh}}) = v_{\mathrm{thresh}} A. \tag{4.2.19}$$

In the next step, one searches the measured waveform for the first range gate g_k exceeding the power defined by the percentage of the amplitude $P(t) > P(t_{\text{thresh}})$. Then, the epoch Δt_0 can be linearly interpolated between the gates g_k and g_{k-1} with the known range gate separation Δt_{gs} (see, e.g., Tab. 4.1) as

$$\Delta t_0 = \left(g_{k-1} + \frac{P(t_{\text{thresh}}) - P(t_{k-1})}{P(t_k) - P(t_{k-1})} \right) \Delta t_{\text{gs}}. \tag{4.2.20}$$

For areas dominated by surface scattering, such as water bodies and solid ground Davis (1997) suggest a threshold value of 50%. In contrast, for areas with predominant volume scattering, e.g. ice and snow surfaces, a value of 10-20% should be used. For the official Jason GDR, the "ICE1" retracker corresponds to a 30% threshold retracker. Due to the robustness of this method, it is nowadays not only used over ice surfaces, but also over inland water bodies (e.g. Tourian et al., 2016), where the return waveform signal is dominated by land perturbing signals and conventional physical algorithms will not converge.

Other empirical methods such as the β-parameter retracker (Martin et al., 1983) fit an empirically derived functional model to the waveform with either 5 parameters for a single leading edge waveform or 9 parameters for a double leading edge waveform, which can occur over ice surfaces.

4.2.3 Sub-Waveform Retracking Algorithms

Instead of finding the best fitting physical or empirical model for deriving the parameters of interest, while trying to also deal with the disturbances from land or other sources, affecting the waveform, there exists a third approach. This only takes into account a certain part of the total altimeter return waveform. These, so called sub-waveform retrackers, have become relatively popular over the recent years, as they, theoretically, allow to estimate improved waveform parameters over the ocean, as well as in coastal regions or over inland water bodies. The general idea is to have a two step procedure, where, first, one or more sub-waveforms are extracted from the total waveform and then these are further processed with existing retracking algorithms. The goal is to estimate at least the epoch Δt_0 and, in some cases, also SWH and σ° from the sub-section of the total waveform to avoid possible peaks and other disturbances during the estimation step.

The first retracking algorithm of this class was the Improved Threshold Retracker (ITR) (Hwang et al., 2006), which consists of a two step procedure: (1) finding possible sub-waveforms and (2) retrieving a retracked height estimate for each sub-waveform using a 50%-threshold method (see Sect. 4.2.2). The final height is then selected based on prior information, such as a known temporal mean range. The sub-waveform is found by computing the differences between every other range gate

$$d_2(t_i) = \frac{1}{2}(P(t_{i+2}) - P(t_i)). \tag{4.2.21}$$

Then the standard deviation of the differences S_2 is computed from

$$S_2 = \sqrt{\left[(N-2) \sum_{i=1}^{N-2} d_2(t_i)^2 - \left(\sum_{i=1}^{N-2} d_2(t_i) \right)^2 \right] \Big/ [(N-2)(N-3)]}, \tag{4.2.22}$$

with the maximum number of range gates N. In the next step, all computed differences are checked whether $d_2(t_i) > \epsilon_2$ and the index i is increased until $d_2(t_{i+j-2}) > \epsilon_2$ and $d_2(t_{i+j-1}) \leq \epsilon_2$. If $j \geq 3$ a potential leading edge is found with a doubt (Guo et al., 2009). This is repeated until all range gates i have been checked. In order to finalize the selection of the preliminary leading edges, differences between neighboring range gates are computed

$$d_1(t_i) = \frac{1}{2}(P(t_{k+1}) - P(t_k)), \tag{4.2.23}$$

with $k = i, i+1, ..., i+j-1$ together with the corresponding standard deviation S_1

$$S_1 = \sqrt{\left[(N-1)\sum_{i=1}^{N-1} d_1(t_i)^2 - \left(\sum_{i=1}^{N-1} d_1(t_i)\right)^2\right] \Big/ [(N-1)(N-2)]}. \quad (4.2.24)$$

For each preliminary leading edge, the corresponding range gates are checked whether the condition $d_1(t_k) > \epsilon_1$ is fulfilled, providing a final set of identified leading edges, which can then be further processed using a threshold method (e.g., Hwang et al., 2006; Guo et al., 2009) or apply a physical model (e.g., Uebbing et al., 2015). The number and size of the sub-waveforms is controlled by the limits ϵ_1 and ϵ_2. While Hwang et al. (2006) originally used the empirically found values $\epsilon_2 = 8$ and $\epsilon_1 = 2$, in this work a percentage of the standard deviations $\epsilon_2 = 0.1S_2$ and $\epsilon_1 = 0.1S_1$ is used, similar to Fenoglio-Marc et al. (2010).

The Adaptive Leading Edge Subwaveform (ALES) retracker (Passaro et al., 2014) is an open ocean and coastal retracker and can generally be divided into two steps. First, the waveform parameters are fitted to a sub-waveform by cutting off the trailing edge completely. These estimates from the first step are then used to recompute the end of the leading edge more precisely using a altimetry mission dependent linear relation between Δt_0 and SWH, which has been found empirically from a Monte-Carlo simulation (Passaro et al., 2014). For estimation of the retracking parameters a model similar to Amarouche et al. (2004) is used. Recently, a new version ALES+ has been published, which especially improves the sea level estimation at high latitudes (Passaro et al., 2018). In addition, a modified version, TU-Darmstadt Adaptive Leading Edge Subwaveform (TALES), has been utilized with the RDSAR mode of the Cryosat-2 and Sentinel-3 altimetry missions (Dinardo et al., 2018). It uses a fast circular convolution model SINC instead of the one employed by Passaro et al. (2014). In this thesis, ALES and TALES data are used for comparison and validation in section 4.4.

The Spatio-Temporal Altimetry Retracker (STAR) (Roscher et al., 2017), originally developed for coastal applications of conventional altimetry, introduced a completely new method for detecting sub-waveforms providing a complete partitioning of the total waveform in contrast to, e.g., selected sub-waveforms following Hwang et al. (2006). STAR shifts the problem of finding a good waveform model to a later processing stage by first generating various sub-waveforms at each measurement position, which are then retracked utilizing a simple and robust three-parameter retracker (Roscher et al., 2017). This results in a number of equally likely parameter estimates for Δt_0, SWH and σ° forming a point-cloud along the satellite track. These point-clouds are then further analyzed in order to select a final estimate at each location (Roscher et al., 2017). In this thesis, the algorithm has been further improved leading to open ocean and coastal sea surface heights, which is comparable in quality to highly accurate DDA altimetry results, while also providing significantly improved SWH and σ°. For more detail see section 4.3.

In recent years, the sub-waveform approach has also been introduced to retracking over inland water bodies. Uebbing et al. (2015) combined the sub-waveform approach by Hwang et al. (2006) with the ability to handle symmetric and asymmetric peaks (Halimi et al., 2013) close to the leading edge and, thus, contained in the selected sub-waveform. This leads to significantly better results over small and medium inland water bodies. For retracking river heights, Boergens et al. (2016) developed the Multi-Subwaveform-Retracker (MSR), which computes the sub-waveforms in the same way as Hwang et al. (2006) and then finds the water return from the river by weighting the individual sub-waveforms based on the contained return power leading to a more clear Hooking parabola (Frappart et al., 2006), which is then fitted using the RANdom SAmple Consensus (RANSAC) algorithm (Fischler and Bolles, 1981).

Other specialized retracking approaches have been published and are mentioned here for completeness. For retracking over land surfaces, Berry et al. (1998) proposed a classification step before the actual retracking, introducing 10 different classes of return waveform shapes. After classifica-

Table 4.2: Comparison of major differences between STAR-V1 as described in Roscher et al. (2017), the intermediate version STAR-V2 (not further discussed in this thesis) and the version developed as a result of this thesis, STAR-V3.

	STAR-V2	**STAR-V3**
Implementation	Transfer from Matlab to parallelized C++ implementation and significant performance improvements of the code.	
Sub-waveform Detection	Expansion of sub-waveform size by 0-3 range gates. Reduction in number of weighting factors $w \in \mathcal{W} = \{0.5, 1, 2, 100\}$, i.e. discarding 0.1 used in STAR-V1. Number of iterations of sub-waveform detection reduced from 5 to 1.	
Retracking	Same as STAR-V1 but no SWH below $-0.5\,\mathrm{m}$ allowed to stabilize estimation convergence for very low wave height conditions.	
Analysis of the Point-cloud	Replacing the Dijkstra algorithm from STAR-V1 with a first version of an own shortest-path algorithm allowing for modification of edge weights and including additional a priori information based on retracking the full waveform.	Further improving the analysis by introducing the DBSCAN algorithm to structure the point-cloud, additional a priori information from retracking the full waveform and a median point-cloud value derived from the point-cloud itself and the reduced points from DBSCAN. Weighted combination of a priori information based on a MAD estimate and on distance to coast. Separate analysis of SLA, SWH and σ°.

tion a dedicated retracking algorithm is used for reprocessing the return waveforms of each class (Berry et al., 1998; Berry, 2000; Berry et al., 2007). For highly accurate ocean applications this approach might lead to biases or jumps along the track when combining results from different retracking algorithms.

4.3 STAR-V3: Spatio-Temporal Altimetry Retracker Version 3

The STAR algorithm (Roscher et al., 2017) represents a novel approach to retracking altimeter return waveforms in two major points: (1) a new approach to deriving sub-waveforms is introduced, which partitions the total waveforms into individual sub-waveforms. In contrast, disjointed sub-waveforms are derived by Hwang et al. (2006); (2) all sub-waveforms are reprocessed individually leading to a point-cloud of potential SSH, SWH and σ° estimates at every 20 Hz along-track measurement position, which is then further analyzed in order to select a final estimate for each of the three waveform parameters at each measurement position. This section generally follows the descriptions in Roscher et al. (2017), i.e. STAR-V1, by first describing the approach for partitioning the total waveform into individual sub-waveforms (Sect. 4.3.1), followed by a discussion of the retracking possibilities for each sub-waveform (Sect. 4.3.2) leading to a point-cloud of potential estimates whereas the selection of the final estimates is explained in Section 4.3.3. The main differences between STAR-V1 and STAR-V3, as well as the intermediate STAR-V2, are listed in table 4.2. The focus here is on the overall differences between STAR-V1 and V3.

4.3.1 Partitioning of the Altimeter Waveform

As part of the STAR algorithm, a novel sub-waveform partitioning has been introduced by Roscher et al. (2017), which, instead of only finding possible disjunct leading edges, always provides a full partitioning of the altimeter return waveform. The partitioning algorithm uses a sparse representation scheme, where the return power of each individual sub-waveform is represented by a linear combination of a defined set of common base waveforms, which are synthetically derived from the Brown (1977) model. Since the real surface properties SSH, SWH and σ° are expected to be correlated along the track and between neighboring tracks (Sandwell and Smith, 1997), it makes sense to utilize spatial and temporal neighborhood information in order to analyze the return signal (e.g. Halimi et al., 2016). For the STAR algorithm, the spatial and temporal information, where spatial means neighboring range gates within one waveform and temporal referring to successive return waveforms, is introduced as part of a Conditional Random Field (CRF) (Lafferty et al., 2001). This allows to distinguish the range gates relevant for deriving the sought for surface properties from range gates, which are contaminated by perturbing signals, thus partitioning the total waveform. In Halimi et al. (2016) a CRF is employed in order to derive smoothed retracking results by applying relatively strong constraints and filters to the estimated parameters. In contrast, for STAR the CRF is only used as part of the sub-waveform partitioning whereas the retracking step (Sect. 4.3.2) is performed completely separately without any constraints.

Since the basic sub-waveform detection scheme is the same for STAR-V1 and STAR-V3, the description closely follows Roscher et al. (2017). The algorithm starts with a block of L measured waveforms, each containing G range gates, which are collected in a $G \times L$ matrix with columns $\boldsymbol{x}_l$, $l = 1, \ldots, L$. Then, each waveform can be represented by a set of overlapping sub-parts, here termed "windowed waveforms" $\boldsymbol{\xi}_{l,g} \in \boldsymbol{x}_l$, which are centered at $\xi_{l,g}$ and comprising N_ξ neighboring range gates (Fig. 4.4). For partitioning the waveform into K sub-waveforms, the indices $\hat{\boldsymbol{y}}_{l,g}$ have to be identified, which define the best fitting base functions from the sparse representation set. The number of necessary base functions per waveform is unknown and co-estimated as part of the detection process.

For the sub-waveform detection, the input consists of windowed waveforms $\boldsymbol{\xi}_{l,g}$ as well as synthetic Brown (1977) echoes, which form the so called dictionary $\boldsymbol{D}$ that contains the set of empirical basis functions for the sparse representation of the measured waveforms (Fig. 4.4). With this a CRF can be constructed containing a unary, data dependent term based on $\boldsymbol{D}$, and a binary term enforcing a smooth partitioning of the total waveform. The weight w between the two terms can be varied in order to yield different sets of optimal indices $\hat{Y}^w = [\hat{\boldsymbol{y}}^w_{l,g}]$ and, thus, rougher or finer partitionings of the total waveform.

The dictionary is built for each waveblock by sampling a large number of synthetically generated Brown (1977) like waveforms, which should fulfill the following two conditions: (1) the elements should have a high approximation ability and (2) the choice of dictionary for reconstruction should be unique and stable. This leads to a selection of elements, which are most similar to the measured waveforms of the current waveblock as the sample generation utilizes threshold-retracked a priori estimates. From those 1000 samples, the ones with the lowest correlation to each other are chosen to ensure the dictionary elements are most dissimilar to each other. For the generation of synthetic waveforms, the parameters of the Brown model (Δt_0, A and σ_s) are sampled randomly based on a distribution derived from a large sample of open ocean waveforms from the Envisat and Jason-1/-2 missions. This ensures for the algorithm to be as mission independent as possible, which enables easy application to other datasets from existing and future missions.

For the CRF, the individual range gates are represented in a graph with "spatial" connections to neighboring range gates within a single waveform and "temporal" connections to the prior and following waveforms along the track (Fig. 4.4). For each range gate, represented as a windowed waveform $\boldsymbol{\xi}_{l,g}$, a solution for $\hat{Y}^w$ is derived, which assigns the best fitting elements from $\boldsymbol{D}$. After-

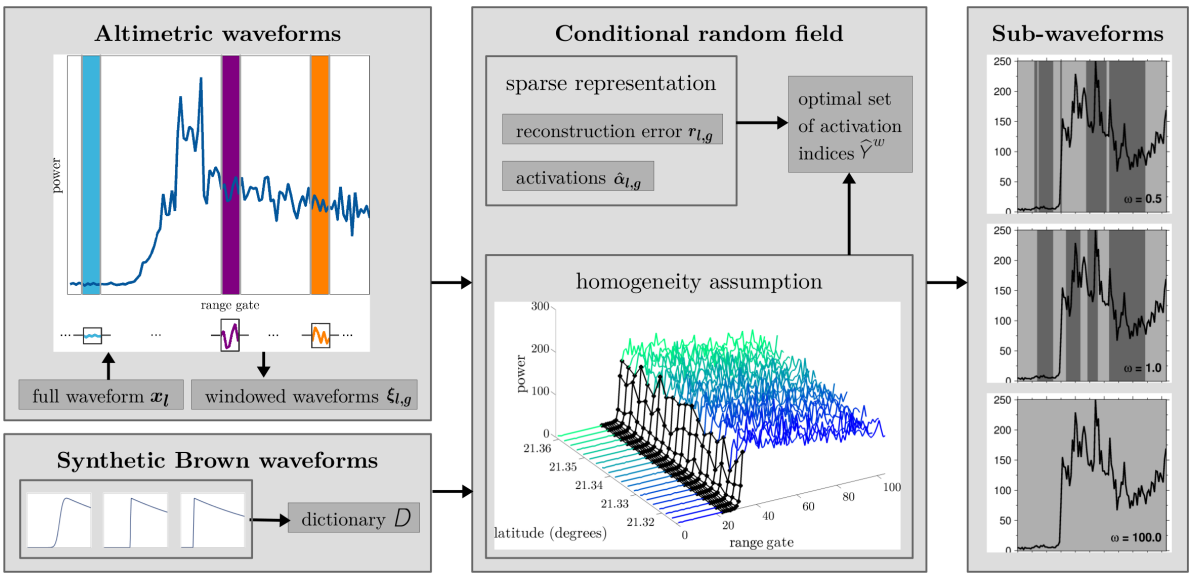


Figure 4.4: Sub-waveform partitioning: Each range gate of the measured altimeter return waveform is represented by a windowed waveform $\boldsymbol{\xi}_{l,g}$, considering the range gate itself as well as its neighbors (e.g. blue, violet, orange areas). Afterward, a conditional random field is constructed containing an unary ($\mathcal{U}(\boldsymbol{\xi}_{l,g}, \boldsymbol{y}_{l,g})$) and a binary ($\mathcal{B}(\boldsymbol{\xi}_{l,g}, \boldsymbol{\xi}_{l,q}, \boldsymbol{y}_{l,g}, \boldsymbol{y}_{l,q})$) term based on the measured waveform and the synthetic waveforms from the dictionary D. The graphical model of the conditional random field connects adjacent range gates within an individual waveform, but also between neighboring waveforms. Varying the hyperparmeter w influences the partitioning of the total waveform (Figure based on Roscher et al., 2017).

wards, all neighboring range gates within one waveform, which are represented by the same solution $\hat{\boldsymbol{y}}_{l,g}$ are grouped into one sub-waveform, therefore partitioning the total waveform into a set of adjacent, non-overlapping sub-waveforms. In mathematical terms, the CRF aims at minimizing the energy functional $\mathcal{E}(Y)$ given by

$$\mathcal{E}(Y) = \sum_{l,g} \mathcal{U}(\boldsymbol{\xi}_{l,g}, \boldsymbol{y}_{l,g}) - w \sum_{l,g,q \in \mathcal{Q}} \mathcal{B}(\boldsymbol{\xi}_{l,g}, \boldsymbol{\xi}_{l,q}, \boldsymbol{y}_{l,g}, \boldsymbol{y}_{l,q}), \tag{4.3.1}$$

with the unary term $\mathcal{U}$ and the binary term $\mathcal{B}$, which are relatively weighted with the hyperparameter w.

The unary term in equation (4.3.1) depends on the measured windowed waveforms $\boldsymbol{\xi}_{l,g}$ and the sparse representation model $\boldsymbol{y}_{l,g}$ and describes the agreement between the two. The so-called activation indices $Y = [\boldsymbol{y}_{l,g}]$ represent the modeling by indicating, which of the V synthetic waveforms from the $G \times V$ dictionary $D = [\boldsymbol{d}_v]$ are used for the sparse reconstruction modeling (Olshausen and Field, 1997) of the measured waveform signal

$$\boldsymbol{x}_l = D\boldsymbol{\alpha}_l + \boldsymbol{\epsilon}, \tag{4.3.2}$$

with the reconstruction error $\|\boldsymbol{\epsilon}\|$. Consequently, one solves for the activation vector $\boldsymbol{\alpha}_l$ containing the optimal coefficients for the corresponding dictionary elements $\boldsymbol{d}_v$ whereas most of these are zero due to the sparse representation approach. For the sub-waveform detection, only the windowed waveforms are sparsely represented by windowed synthetic waveforms from the dictionary. This allows for each range gate being reconstructed individually by a unique sparse linear combination of a subset of dictionary elements together with the corresponding $\boldsymbol{\alpha}_{l,g}$; these are the sought for activation indices $\hat{\boldsymbol{y}}_{l,g}$ defined above. Since the dictionary D is constant for one waveblock of L waveforms, the sub-dictionaries for temporally neighboring waveforms D_g, containing the rows

corresponding to a specific range gate, are identical. Mathematically, the optimal $\widehat{\boldsymbol{\alpha}_{l,g}}$ can be found from

$$\widehat{\boldsymbol{\alpha}}_{l,g} = \text{argmin} \, \|D_g \boldsymbol{\alpha}_{l,g} - \boldsymbol{\xi}_{l,g}\|_2 \qquad \text{subject to} \quad \|\boldsymbol{\alpha}_{l,g}\|_0 \leq M, \tag{4.3.3}$$

where M is equal to the maximum number of non-zero elements in $\widehat{\boldsymbol{\alpha}_{l,g}}$ and, in this case, fixed to a value of two. Then the reconstruction error of the windowed waveform $r_{l,g}$ can be computed from

$$r_{l,g} = \|D_g \widehat{\boldsymbol{\alpha}}_{l,g} - \boldsymbol{\xi}_{l,g}\|_2, \tag{4.3.4}$$

where the reconstruction errors for all possible sets of dictionary elements are collected in the vector $\boldsymbol{r}_{l,g} = [r_{l,g}]$. The optimization in equation (4.3.3) is solved using the orthogonal matching pursuit greedy algorithm (Tropp et al., 2006). Other algorithms for solving the optimization problem are also possible. The algorithm chooses the first dictionary element to be the one that maximizes the absolute value of the inner product between the dictionary element itself and the sample, which is meant to be reconstructed. In the next step, the reconstruction error $\boldsymbol{\epsilon}$ is used instead of the sample. This is repeated until the number of selected dictionary elements is greater or equal to M. An alternative approach would be to search all possible combinations of activation indices, but this would significantly increase runtime. The unary term in the energy functional of equation (4.3.1) describes the agreement between the measured signal and a specific sparse combination of dictionary elements by

$$\mathcal{U}(\boldsymbol{\xi}_{l,g}, \boldsymbol{y}_{l,g}) = \frac{1}{Z_1} \boldsymbol{r}_{l,g} + \frac{1}{Z_2} \text{abs} \left(1 - \sum_v \widehat{\boldsymbol{\alpha}}_{v,l,g} \right), \tag{4.3.5}$$

where the first term penalizes the reconstruction error for a given set of activation indices and the second term represents the difference of the estimated activations sum to 1. In addition, both terms are normalized by their respective standard deviation in order to treat all range gates equally. This allows to handle different range gate noise conditions within a waveform and neighboring waveforms.

The binary term $\mathcal{B}$ in equation (4.3.1) depends on the windowed waveforms $\boldsymbol{\xi}_{l,g}$ and $\boldsymbol{\xi}_{l,q}$, where $q \in Q$ indicates the direct neighbors within a single waveform and between adjacent waveforms of a certain range gate; $\boldsymbol{y}_{l,g}$ and $\boldsymbol{y}_{l,q}$ are the corresponding activation indices. This term prefers neighboring range gates with similar characteristics as these indicate sub-waveforms and penalizes dissimilarities, which is given by

$$\mathcal{B}(\boldsymbol{\xi}_{l,g}, \boldsymbol{\xi}_{l,q}, \boldsymbol{y}_{l,g}, \boldsymbol{y}_{l,q}) = \begin{cases} \cos\left(\boldsymbol{\xi}_{l,g}, \boldsymbol{\xi}_{l,q}\right), & \text{if} \quad \boldsymbol{y}_{l,g} = \boldsymbol{y}_{l,q} \\ 0, & \text{if} \quad \boldsymbol{y}_{l,g} \neq \boldsymbol{y}_{l,q} \end{cases} \tag{4.3.6}$$

Utilizing $\cos\left(\boldsymbol{\xi}_{l,g}, \boldsymbol{\xi}_{l,q}\right)$, which represents the normalized dot product, instead of 1 serves as a relaxation of the otherwise quite strict constraint provided by the binary term. This is helps to deal with variations of the measured waveforms, such as movements of the return waveform measurement window by the tracking algorithm on-board of the satellite.

After finding the optimal activation indices, the result is a complete partitioning of a block of L waveforms. For each new block, the dictionary is re-initialized with new synthetic waveforms using the output of a simple threshold retracker (Sect. 4.2.2) in order to adapt the dictionary to changing surface conditions along the groundtrack of the altimeter satellite. For STAR-V3 defined in this thesis, the exact same sub-waveform partitioning as in Roscher et al. (2017) is employed with a small extension: After the initial detection, the number of sub-waveforms is further increased by expanding each sub-waveform by 0-3 range gates in size, creating several additional (overlapping) sub-waveforms. This improves the number of potential SSH points in the next steps, especially close to the coast. Roscher et al. (2017) (STAR-V1) repeated the sub-waveform detection several times, by re-initializing the dictionary, to ensure the availability of certain "good" sub-waveforms close to the coast in order to become independent to some extent of the randomly generated synthetic

dictionary elements. Then they continued with all (including possible duplicate) sub-waveforms in the next step. While this lead to ensuring a more reliable quality of SSH close to the coast, this step was quite time consuming. Expanding the sub-waveforms by a few range gates, however, improves the runtime of STAR-V3 significantly leading to the same or even better results from only one iteration of the sub-waveform detection. STAR-V3 uses a neighborhood size of $N_\xi = 5$ for the windowed waveforms $\boldsymbol{\xi}$, $M = 2$ for the number of non-zero elements as in Roscher et al. (2017), but only a choice of 4 different weighting factors $w \in \mathcal{W} = \{0.5, 1, 2, 100\}$, where the smallest weight of 0.1 (Roscher et al., 2017) has been discarded due to leading to a very fine partitioning of the total waveform, which massively increased the number of duplicate sub-waveforms in combination with the expansion of the sub-waveforms as described above and, thus, provided no additional benefit anymore. The weight of 100.0 ensures that standard case of retracking the total waveform is always included as one specific case of a sub-waveform.

4.3.2 Retracking Individual Sub-Waveforms

After partitioning the altimeter return waveform into various sub-waveforms (Sect. 4.3.1), these are then individually retracked. Generally, almost every retracker can be applied to individual sub-waveforms, with some being more suitable than others. The most robust choice would be a threshold method (Sect. 4.2.2), but would not yield any SWH information. With a simple and robust three-parameter ocean retracking model, one can derive solutions for SSH, SWH, and σ°. However, the more sophisticated the applied retracker, the worse the rate of estimation convergence.

STAR-V3 employs the same basic three-parameter waveform model by Halimi et al. (2013) as STAR-V1, which has been introduced in Section 4.2. The model allows to estimate Δt_0, σ_s and A for each sub-waveform with sufficient number of observations, to avoid an ill-posed problem with more parameters than observations during the estimation. In order to better estimate the amplitude A and to deal with the thermal noise present in each waveform, the latter is first estimated from the first few range gates of the total waveform and consequently removed. In addition, the sub-waveform is reduced by the power of its first range gate before the estimation, which is later added back to the amplitude. The estimation step provides several potential solutions for SSH, SWH, and σ° for each 20 Hz measurement position along the altimetry track when applied to each individual sub-waveform, consequently forming a point-cloud of estimates for each of the three parameters (e.g. Fig. 4.5, B). In the next step, this point-cloud has to be further processed in order to select one final solution at each 20 Hz measurement position.

4.3.3 Analysis of the Point-Cloud

After partitioning all altimeter return waveforms into sub-waveforms and retracking those, the resulting point-clouds (Fig. 4.5, B) have to be further processed in order to select a final estimate of SSH, SWH and σ°. Land influence from directly crossing over the land (e.g. crossing over islands of Bali and Lombok in Fig. 4.5) or passing it with some distance (e.g. passing of Kangean in Fig. 4.5) are clearly visible in the waveforms but also in the corresponding point-cloud. Figure 4.5 (B) indicates that the potential estimates of SSH tend to cluster around the real SSH with more dense clusters over the open ocean and less density in coastal areas, where the number of outliers also increases. Therefore, the final height estimates (similar for SWH and σ°) are to be picked from the potential heights close to the real sea surface. This is achieved by, first, preparing additional prior information, which is then used in the second step for removing all potential estimates, which are classified as outliers and, third, selecting the final estimates from the remaining potential points based on a shortest-path approach. The basic algorithm is presented in algorithm 4.1, where individual steps are further described in the following.

While STAR-V1 directly utilized the point-clouds of SSH, SWH and σ°, STAR-V3 incorporates additional preprocessing and prior information. First, the SSH are converted to SLA by subtract-

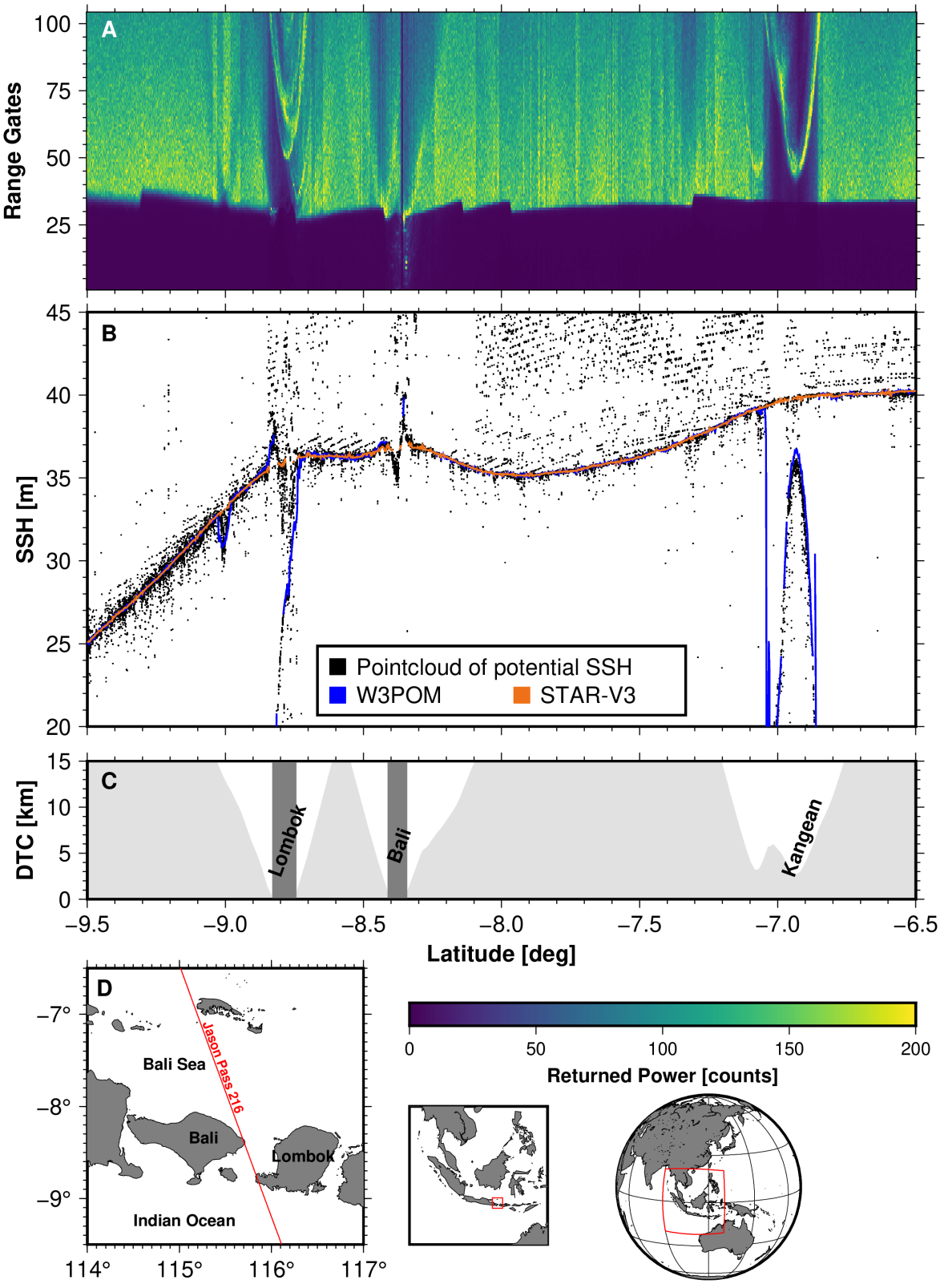


Figure 4.5: STAR-V3 point-cloud processing example for an arbitrarily chosen Jason-3 track from pass 216 and cycle 24 crossing Indonesian islands Bali and Lombok. A: Along-track waveforms. B: Point-cloud (black), conventional retracked SSH (blue) used as additional prior information and final STAR-V3 SSH (orange). C: Along-track distance to coast (DTC) as light shaded grey line and land crossings (dark gray). D: Groundtrack of Jason-3 pass 216.

Algorithm 4.1: STAR-V3 point-cloud analysis algorithm. The input and output points represent the SLA, SWH or σ° point-clouds.

Point-cloud Analysis ($\boldsymbol{y}_i$, $\boldsymbol{y}^j_{p_{\mathbf{retr}}}$, $\mathbf{DTC}_j$)

Input : i potential points $\boldsymbol{y}(t^j_i)$ at along-track position t^j (abbreviated as $\boldsymbol{y}_i$), retracking results from the full waveform $\boldsymbol{y}^j_{p_{\text{retr}}}$ for each along-track position, and along-track distance to coast DTC_j

Output: Final selection of point $\hat{\boldsymbol{y}}_j$ at each along-track position t^j.

discard all points $\boldsymbol{y}_i$ exceeding $\pm$ 10 m SLA to reduce the overall point-cloud size

`/* Prepare prior information */`

compute median value $\boldsymbol{y}^j_{p_{\text{med}}}$ from all points at their corresponding along-track position

`/* Structure the point-cloud based on clustering of points */`

apply the DBSCAN algorithm from algorithm 4.2 providing $\bar{\boldsymbol{y}}_{\text{db}}$

`/* For a moving along-track window of 15 seconds width, find the locally best fitting 1 Hz line segments with RANSAC */`

for *all blocks of 20 along-track positions* t^j **do**

- select all DBSCAN points within current window
- estimate best fitting RANSAC line $\boldsymbol{l}(\boldsymbol{t}, \boldsymbol{x}_{line})$ based on algorithm 4.3
- store RANSAC information for the central second in $\boldsymbol{y}^j_{p_{\text{line}}}$

`/* Compute MAD estimates for the a priori information. */`

Compute $\boldsymbol{d}^j_{p_{\text{retr}}}$, $\boldsymbol{d}^j_{p_{\text{med}}}$ and $\boldsymbol{d}^j_{p_{\text{line}}}$ based on equation (4.3.7)

`/* Select final estimates based on height differences, distance to coast and a priori information */`

starting point $\hat{\boldsymbol{y}}_0$ ($j = 0$) is the first point based on the weighted a priori data (Eq. (4.3.8))

initialize vector $\hat{\boldsymbol{y}}$ of final selected estimate at each along-track position t^j

for *all along-track positions* t^j **do**

- **if** *open ocean: DTC* > 10 km **then**
  - compute weighted a priori data $\bar{\boldsymbol{y}}^j_p$ from equation (4.3.8) using $\boldsymbol{y}^j_{p_{\text{retr}}}$, $\boldsymbol{y}^j_{p_{\text{med}}}$ and $\boldsymbol{y}^j_{p_{\text{line}}}$
- **else**
  - compute weighted a priori data $\bar{\boldsymbol{y}}^j_p$ from equation (4.3.8) using $\boldsymbol{y}^j_{p_{\text{med}}}$ and $\boldsymbol{y}^j_{p_{\text{line}}}$
- compute height differences $\boldsymbol{\Delta y}_{prior}(t^j_k)$ of all points $\boldsymbol{y}_k(t^j)$ to weighted a priori information $\bar{\boldsymbol{y}}^j_p$
- discard all points from $\boldsymbol{y}_k(t^j)$ that deviate more than 0.5 m from $\bar{\boldsymbol{y}}^j_p$ leaving l points $\boldsymbol{y}_l(t^j)$
- compute height differences $\boldsymbol{\Delta y}$ from $\hat{\boldsymbol{y}}_{j-1}$ to all points $\boldsymbol{y}_l(t^j)$
- derive edge weights $\boldsymbol{w}_l$ following equation (4.3.9)
- select the point with lowest weight $\min(\boldsymbol{w}_l)$ as the final estimate $\hat{\boldsymbol{y}}_j$

return $\hat{\boldsymbol{y}}$

ing the Mean Sea Surface (MSS) for each sub-waveform $k = 1 \ldots K$ at the corresponding 20 Hz measurement positions t^j ($j = 1 \ldots J$) producing a point-cloud of SLA (Fig. 4.6, black points). This is beneficial as it (1) allows to perform a very rough first reduction of the point-cloud by

discarding all potential points with SLA exceeding ±10 m and (2) it generally removes all strong bathymetry signals, which are still present in the SSH and would negatively affect the assumption of a straight line (Fig. 4.6) in the reduction step below.

STAR-V3 utilizes different kinds of prior information in order to further specify the selection of the final heights. The first prior information $y_{p_{\mathrm{retr}}}$ is based on sea level anomaly $h_{\mathrm{SLA}_{p_{\mathrm{retr}}}}$, significant wave height $H_{s_{p_{\mathrm{retr}}}}$ and sigma-naught $\sigma^{\circ}_{p_{\mathrm{retr}}}$ derived from the three-parameter ocean retracker applied to the total waveform (Sect. 4.2.2). First, outliers, e.g., for SLA larger than ±3 m are discarded and all gaps in the along-track data from $y_{p_{\mathrm{retr}}}$ are filled by linear interpolation of the 20 Hz data. Afterward, a moving average filter is applied to the interpolated $y_{p_{\mathrm{retr}}}$ to reduce the high frequency variations, which are not of interest in terms of prior information for analyzing the STAR point-cloud. The idea is to get a first rough guess on the final estimates to limit the search radius for the point-cloud analysis. The prior information based on retracking the total waveform ($y_{p_{\mathrm{retr}}}$) is only utilized over the open ocean with distance to coast of more than 10 km as coastal estimates are not reliable. This information mainly aids in dealing with rare, but severe divergence of the SLA from a more or less straight line, which can occur, e.g., during strong storm events. Under normal conditions, this prior information will not provide any additional benefit with respect to the final results of STAR-V3.

The second prior information $y_{p_{\mathrm{med}}}$ is generated from the point-cloud itself by applying a moving median filter of 2 s width followed by an additional moving average of 1 s width. This generally provides a good first estimate for locating the main dense part of the point-cloud (Fig. 4.5, B). However, it can also lead to significantly biased information close to the coast. This prior information together with the original SSH aids in case the SLA are biased by a severely wrong MSS (e.g., around the western tip of Bali at −8.5° latitude in Fig. 4.5), where the effect occurs at the same position during every cycle, or heavy rain events, which vary in time and location. Both of the aforementioned SLA artifacts result in significant divergence of SLA, violating the straight line assumption mentioned below (Fig. 4.6). The effects due to erroneous MSS often occur in coastal waters resulting from conventional retracking methods not providing good results leading to extrapolation of MSS products. Here, the median prior information can aid in selecting the correct final heights. In normal conditions, it will be in good agreement with other prior information, thus, not significantly affecting the results.

The benefit of utilizing $y_{p_{\mathrm{retr}}}$ and $y_{p_{\mathrm{med}}}$ is that it becomes possible to deal with, e.g., heavy rain event without requiring additional data flags or information on such events or deal with erroneous MSS without having to identify it first. This enables retrieval of SLA, SWH and σ° where STAR-V1 and V2 would fail.

The third prior information is based on the assumption that the dense point-cloud of the anomalies is concentrated around a straight line considering that, after removal of the MSS, the SLA are expected to be scattered around zero. From Fig. 4.6 it is obvious that the potential SLA estimates (black points) tend to cluster around the real sea level anomalies forming a relatively straight line along the track (Fig. 4.6). Consequently, it makes sense to utilize this feature as prior information, which can aid in bridging possible gaps of the main cluster in along-track coverage as well as close to the coast. The basic idea is to find an approximate line applying the RANSAC algorithm (Fischler and Bolles, 1981) within a window, covering a few seconds of data, moving along the track and discarding all points, which exceed a defined threshold distance to the line. However, applying the RANSAC algorithm (Alg. 4.3) directly, like it has been done for STAR-V1, to the black points can lead to potentially unwanted line fits, e.g. the along-track lines in the noise above the real sea surface between −8.0° to −7.0° latitude (Fig. 4.5, B).

To avoid these problems, the point-cloud is first analyzed by applying the Density-Based Spatial Clustering of Applications with Noise (DBSCAN) algorithm (Ester et al., 1996) to all equally

likely points at each along-track 20 Hz measurement position t^j, individually. A 2D application of the algorithm would lead to potentially disconnected along-track clusters, e.g. when crossing from ocean to land over the islands of Bali and Lombok or tiny gaps of one or two along-track positions when passing the island of Kangean (Fig. 4.5, B and C). Consequently, the DBSCAN algorithm (Alg. 4.2) is applied to the sub-set of i points $\boldsymbol{y}(t_i^j)$ (or short $\boldsymbol{y}_i$) at each measurement location j individually in a 1D sense, assigning each point to a cluster or classifying it as noise, thus, discarding it from further analysis. Here, the $\boldsymbol{y}_i$ is representative for the points of SLA/SSH, SWH and σ°. In order to reduce the number of points for the RANSAC algorithm below, the median values for each cluster $\bar{\boldsymbol{y}}_{\mathrm{db}}$ are computed at each along-track position (Fig. 4.6, green points). This prevents individual small clusters of noisy points from gaining too much weight during the RANSAC algorithm, as was possible with STAR-V1, while at the same time strengthening the influence on the RANSAC estimate from the main cluster.

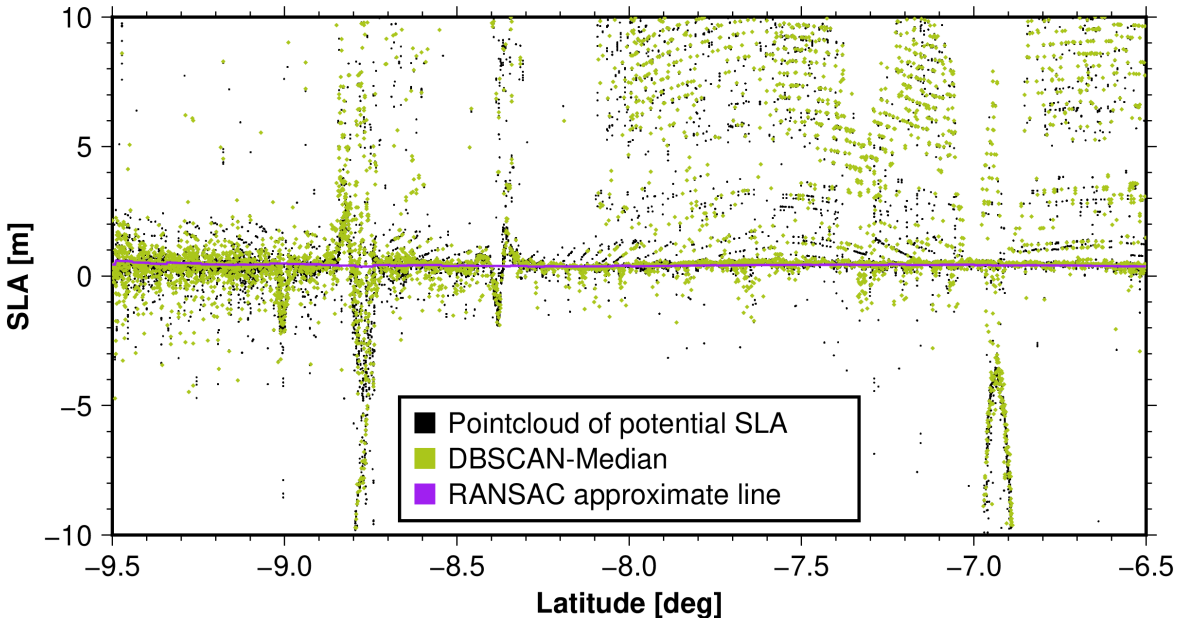


Figure 4.6: Point-cloud of SLA for the same sample track used in figure 4.5. Cluster medians from applying the DBSCAN algorithm are shown in green and the approximate line found by applying the RANSAC algorithm is plotted in purple. The black points are plotted smaller for visual reasons.

In order to identify the dense main cluster of points along the real sea surface (Fig. 4.5, B) and discard all noise clusters, which deviate too far from the real sea surface, the idea is to find an approximate line $\boldsymbol{l}(\boldsymbol{t}, \boldsymbol{x}_{line})$, with the line parameters $\boldsymbol{x}_{line}$, within the main cluster for each measurement position t^j collected in the vector $\boldsymbol{t}$. For this, a moving window of several seconds width is defined where a best fitting line is estimated from the (reduced) point-cloud of cluster-medians (Fig. 4.6, green points) by employing the RANSAC algorithm (Fischler and Bolles, 1981). STAR-V3 uses a window size of nine seconds for finding a line from the RANSAC algorithm (see algorithm 4.3), which is then stored as the approximate line for all 20 Hz along-track positions belonging to the central second of the nine second window. Afterwards the window is shifted by one second and the process is repeated until the end of the track is reached. For STAR-V1, the point-cloud of SSH (black points in Fig. 4.5, B) has been used directly and the window size has been significantly larger in order to make sure to have a majority of ocean points within the window benefiting the line identification in coastal areas. The disadvantage of this is that $\boldsymbol{l}(\boldsymbol{t}, \boldsymbol{x}_{line})$ is relatively inflexible in along-track direction. For STAR-V3 it is possible to employ a significantly smaller window due to (1) reducing the number of points using DBSCAN and (2) only utilizing measurement positions, which are not more than 2.5 km over land, identified from the distance to coast prior information (e.g. Fig. 4.5, C). The result is an improved approximate identification of

Algorithm 4.2: Slightly modified DBSCAN algorithm based (Ester et al., 1996) for reducing the number of points for finding the approximate line for the RANSAC algorithm.

DBSCAN ($\boldsymbol{y}_i$, ϵ, N_c)
Input : i potential points $\boldsymbol{y}(t_i^j)$ at along-track position t^j (abbreviated as $\boldsymbol{y}_i$), neighborhood length ϵ, and minimum points required for a cluster N_c
Output: Cluster indices $\boldsymbol{y}_c$ for each potential point i at along-track position j and corresponding number of points in each cluster $\boldsymbol{n}_{i,c}$

C=0
$\boldsymbol{y}_{i,c}$ = zeros(size($\boldsymbol{y}_i$)) `/* initialize all points as noise */`
for *all potential points* i **do**
  add point i to the list of visited points $\boldsymbol{v}$
  $\boldsymbol{y}_n$ = getNeighborPoints($\boldsymbol{y}_i$,ϵ)
  if *length*($\boldsymbol{y}_n$)>N_c **then**
    add i to the list of noise points
  else
    C=$C+1$
    expandCluster(i,C,$\boldsymbol{y}_n$, $\boldsymbol{v}$, ϵ, N_c, $\boldsymbol{y}_{i,c}$)
return $\boldsymbol{y}_c$, $\boldsymbol{n}_{i,c}$

---

expandCluster(i,C,$\boldsymbol{y}_n$, $\boldsymbol{v}$, ϵ, N_c, $\boldsymbol{y}_c$)
Input : Current index i, neighboring points $\boldsymbol{y}_n$, visited points $\boldsymbol{v}$, neighborhood length ϵ, minimum points required for a cluster N_c, and current cluster indices $\boldsymbol{y}_c$
Output: Updated $\boldsymbol{y}_n$, $\boldsymbol{v}$ and $\boldsymbol{y}_c$

$\boldsymbol{y}_c(i) = C$ `/* assign point` i `to cluster` C `*/`
$k = 0$ **while** *true* **do**
  $n_k = \boldsymbol{y}_n(k)$ `/* get` k`th neighbor */`
  if *point* n_k *has not been visited* **then**
    add index n_k to $\boldsymbol{v}$
    $\boldsymbol{y}_{nn}$ = getNeighborPoints($\boldsymbol{y}_{n_k}$,ϵ)
    if *length*($\boldsymbol{y}_{nn}$>N_c) **then**
      attach $\boldsymbol{y}_{nn}$ to $\boldsymbol{y}_n$
  if $\boldsymbol{y}_c(n_k)$==*0* **then**
    add point n_k to cluster C
  $k = k + 1$
  if k>= *length*($\boldsymbol{y}_n$) **then**
    break
return $\boldsymbol{y}_n$, $\boldsymbol{v}$, $\boldsymbol{y}_c$

---

getNeighborPoints(i, $\boldsymbol{y}_i$, ϵ)
Input : Current index i, potential points $\boldsymbol{y}_i$, and neighborhood length ϵ
Output: Neighbors $\boldsymbol{y}_n$ of point i

return *all points n, including i, within the neighborhood defined by* ϵ *of i*

the main cluster by a step wise straight line (Fig. 4.6, purple line), which can be utilized as prior information for selecting the final heights in the next step. Shifting the window by one second and

only keeping the central part of the fitted line leads to the approximation containing steps after every shift. However, these are generally small and possible (small) jumps are not a serious issue as $\boldsymbol{l}(\boldsymbol{t}, \boldsymbol{x}_{line})$ has relatively low accuracy requirements since it is used mainly to discard large outliers from the main cluster.

Algorithm 4.3: RANSAC algorithm (Fischler and Bolles, 1981) used for fitting a line to the STAR point-cloud of potential estimates.

RANSAC ($\bar{\boldsymbol{y}}_{\mathbf{db}}$, N_r, Δd)
Input : Cluster median points $\bar{\boldsymbol{y}}_{\mathrm{db}}$ of the point-cloud, number of repeated tries N_r, and distance threshold Δd
Output: Optimal parameters $\boldsymbol{x}_{line}$ from fitting a linear model to the input point-cloud.

$N_{max} = 0$ `/* Initialize maximum number of agreeing points */`
$\boldsymbol{y}_{best} = [\,]$ `/* Initialize best set of points */`
for $n \in N_r$ **do**
  randomly select a point P_1 at along-track position j_1
  randomly select a second point P_2, which is not located at j_1
  estimate the current line model $\boldsymbol{x}_{current}$
  find all points $\boldsymbol{y}_l$, which agree with the current model within Δd
  if *length*($\boldsymbol{y}_l$)>N_{max} **then**
    $N_{max} = \mathrm{length}(\boldsymbol{y}_l)$
    $\boldsymbol{y}_{best} = \boldsymbol{y}_l$
compute least squares estimate for $\boldsymbol{x}_{line}$ from $\boldsymbol{y}_{best}$
return $\boldsymbol{x}_{line}$

The a priori information now consists of three data vectors $\boldsymbol{y}_p(t^j) \in \{\boldsymbol{y}_{p_{\mathrm{retr}}}, \boldsymbol{y}_{p_{\mathrm{med}}}, \boldsymbol{l}(\boldsymbol{t}, \boldsymbol{x}_{line})\}$. In the next step, the agreement of each to the available k point-cloud points $\boldsymbol{y}_k(t^j)$ at along-track position t^j is determined by computing the Median Absolute Deviation (MAD) $\boldsymbol{d}_p(t^j)$ from the differences to the corresponding prior information $\boldsymbol{y}_p(t^j)$ by

$$\boldsymbol{d}_p(t^j) = \mathrm{median}(\mathrm{abs}(\boldsymbol{y}_k(t^j) - \boldsymbol{y}_p(t^j)))1.4826. \tag{4.3.7}$$

Here, the index p indicates the available prior information (here: $\boldsymbol{y}_{p_{retr}}$, $\boldsymbol{y}_{p_{med}}$ and $\boldsymbol{l}(\boldsymbol{t}, \boldsymbol{x}_{line})$). The MAD estimates $\boldsymbol{d}_p(t^j)$ are small for locations where a majority of potential points $\boldsymbol{y}_i$ agree well with an individual prior information and become significantly larger in case of disagreement.

For normal conditions, over the open ocean without any extreme events, such as heavy rain, all of the introduced prior information are close to each other and the magnitude of the MAD is roughly the same. Consequently, all could be utilized individually as a rough first estimate to aid the selection of final heights. However, a localized rain event of a size equal or smaller the RANSAC window will lead to non meaningful line fits and corresponding large MAD, while the prior information from the point-cloud median and retracking still work well. In contrast, the latter will introduce erroneous estimates in coastal regions leading to a large MAD, while the RANSAC line will fit well due to the large window still including open ocean points to stabilize the estimated line.

As a result, the available auxiliary data are combined by deriving a mean $\overline{\boldsymbol{y}}_p$, which is weighted with by the corresponding MAD and given by

$$\overline{\boldsymbol{y}}_p(t^j) = \frac{\sum_p^P \boldsymbol{y}_p(t^j) \frac{1}{\boldsymbol{d}_p(t^j)}}{\sum_p^P \frac{1}{\boldsymbol{d}_p(t^j)}}. \tag{4.3.8}$$

Consequently, $\overline{\boldsymbol{y}}_p$ combines the available prior data based on their MAD resulting in automatically down-weighting individual auxiliary data in certain situations in order to best aid the final estimate

selection over the open ocean and in coastal zones.

The next step is the selection of the final estimates $\widehat{\boldsymbol{y}}$ from the original point-cloud (black points in Figs. 4.5, B or, 4.6) based on the prior information of distance to coast and the best fitting $\overline{\boldsymbol{y}}_p$ derived from (4.3.8). The general idea is to find the shortest path from one 20 Hz measurement position to the next through the main cluster from a given starting position. This assumes that the SLA, SWH and σ° estimate between neighboring 20 Hz measurement locations should not change much, i.e. similar heights are preferred by the selection. Considering the point-clouds and the main cluster, it is reasonable to assume that all final points should be from this cluster, avoiding large along-track jumps as e.g. for the standard retracking (blue line in Fig. 4.4, B). The shortest-path approach is one possible solution to solving this problem, although other approaches may be feasible as well.

STAR-V1 simply applied a Dijkstra algorithm (Dijkstra, 1959) to the point-cloud of SSH. While this generally solved the problem providing a selection of final estimates of SLA, SWH and σ° , it had several disadvantages: (1) the requirement to provide a well defined start and end point, which was selected randomly, leading to some warm up (and cool down) time until (after) which the heights have been selected from the main cluster. This is especially problematic in case the start or end point is located over the ocean instead of land. (2) the requirement to construct a complete graph with nodes and edges connecting all i points at position t^j to all k points at position t^{j+1} by an edge weight defined as $w_i^k = \mathrm{abs}(\boldsymbol{y}(t_i^j) - \boldsymbol{y}(t_k^{j+1}))$, which necessitates visiting each point once, thus, increasing run-time of the algorithm. (3) problems while dealing with gaps along the track within the main cluster, leading to jumps and unphysical distortions of the final "shortest" path, such as preferring the blue over the orange path in Fig. 4.7; (4) a complexity of $O(V^2)$ in the worst case, with V representing the number of vertices (black points). In order to prevent choosing the blue path over the orange one (Fig. 4.7) with the standard Dijkstra algorithm of STAR-V1 can only be achieved by removing the red point, classifying it as an outlier, e.g. due to the distance to $\boldsymbol{l}_{V1}(\boldsymbol{t}, \boldsymbol{x}_{line})$, thus, requiring quite strict selection criteria.

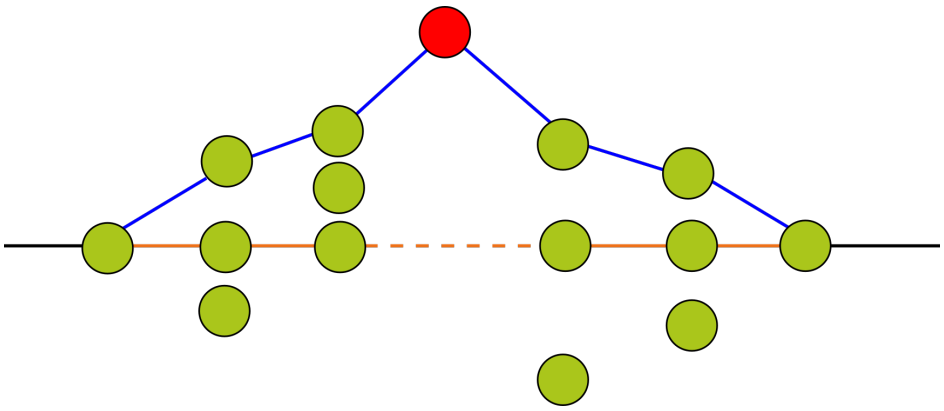


Figure 4.7: Effect of a leverage point on the selection of final heights for STAR.

The point selection algorithm for STAR-V3 is designed to overcome the caveats of the STAR-V1 approach. In the beginning, the first point is selected to be a virtual point at the 20 Hz measurement position $j = 0$ with the same height as the approximate line at $\overline{\boldsymbol{y}}(t^0)$. It is only required to start the algorithm and by selecting a point on the approximate line, one can minimize any possible warm up time, as was potentially the case with selecting a random point for STAR-V1. Over land surfaces, the approximate line may be significantly wrong, but since STAR is designed as an ocean and coastal retracker this is not really a problem. If one is interested in the land or inland water surface heights, a generally different approach for analyzing the point-cloud needs to be pursued. Secondly, the differences $\boldsymbol{\Delta y}_{prior}(t_k^{j+1}) = \mathrm{abs}(\boldsymbol{y}(t_k^{j+1}) - \overline{\boldsymbol{y}}_p(t^{j+1}))$ to weighted mean prior information $\overline{\boldsymbol{y}}_p$ are computed for all points $k = 1 \ldots K$ at position $j + 1$, which have not been

removed by any of the mentioned preprocessing steps. In order to further reduce the number of potential estimates for the final selection, all points k with an absolute difference value of more than a pre-defined threshold T_{prior} are discarded. It is important to note that depending on the threshold value T_{prior}, the resulting final estimates might include more noisy points if a rather large T_{prior} is defined or no values (NaN) in case one chooses a very small threshold forcing the final estimates to be very close to the approximate line. For 20 Hz SLA measurements one usually finds a noise level of about 10 to 20 cm and based on this the threshold should be chosen between 30 to 50 cm, roughly corresponding to two-sigma criteria retaining about 90% to 95% of the values. Similar considerations can be made for SWH and σ°. On the one hand, this ensures that the final estimates will likely be chosen from the main cluster and, on the other hand, no unrealistic jumps between two consecutive 20 Hz measurements of more than T_{prior} can occur. In case all points $\boldsymbol{y}_k$ get discarded at this step, the current height is set to the corresponding approximate value $\overline{\boldsymbol{y}}_p(t^{j+1})$, while marking the point at position $j+1$ as an outlier and the algorithm continues.

After discarding all points deviating from $\overline{\boldsymbol{y}}_p$ by more than T_{prior}, the height (similar for SWH and σ°) differences $\Delta\boldsymbol{y}(t_l^{j+1}) = \text{abs}(\widehat{\boldsymbol{y}}(t^j) - \boldsymbol{y}(t_l^{j+1})$ between the selected estimate at position j and all l remaining points $\boldsymbol{y}(t_l^{j+1})$ at position $j+1$ are derived. Simply utilizing these direct point differences $\Delta\boldsymbol{y}(t_l^{j+1})$ for the edge weights, as has been done for STAR-V1, will lead to significant influence of single leverage points (red point, Fig. 4.7). These leverage points leading to the selection of estimates along an unphysical path (blue path, Fig. 4.7). In order to avoid this and prefer smaller steps between successive 20 Hz positions, the edge weights $\boldsymbol{w}_l$ in STAR-V3 are chosen as

$$\boldsymbol{w}_l = \Delta\boldsymbol{y}(t_l^{j+1})(1 - \frac{1}{M_c} n_l) + \Delta\boldsymbol{y}_{prior}(t_l^{j+1}), \tag{4.3.9}$$

with

$$M_c = \max(\boldsymbol{n}_l^{(j+1)}). \tag{4.3.10}$$

Here, $\boldsymbol{n}_l$ contains the number of points associated with the same cluster as the point l, provided as an output of the modified DBSCAN algorithm (Alg. 4.2). This way it is possible to introduce a weighting related to the cluster size at each measurement position. In general, the majority of points are clustering around the true SLA (or SWH or σ°). Choosing the weights $\boldsymbol{w}_l$ in this way reduces the impact of individual leverage points on its along-track neighbors, while effectively down-weighting unrealistic final estimate selections (blue path in Fig. 4.7). The latter usually belong to rather small clusters of outliers. Based on empirical analysis, it is assumed that larger clusters are more likely to include the desired point selection than smaller ones. The second term in equation (4.3.9) further limits the selection to those points that do not stray too far from the auxiliary prior information.

The final point selected at position $j+1$ is then chosen as the one with the lowest weight $\boldsymbol{w}_l$, its index is stored and the algorithm continues along the track until a final point is selected for each 20 Hz measurement position. This then results in the final STAR-V3 estimates (orange line, Fig. 4.4, B).

For physical consistency, ensuring that SLA, SWH and σ° are based on the same sub-waveform retracking output, the analysis can be limited to the SLA point-cloud, where the final estimates of SWH and σ° are then selected based on the chosen SLA points. This might lead to individual noisy estimates of SWH and σ° in the corresponding along-track selections. To avoid this, it is possible to separately analyze the SWH and σ° point-clouds in a similar way resulting in a selection, which is generally less noisy along the track. However, the latter represents a rather unphysical approach, since estimates of SLA, SWH and σ° at each along-track position may result from a different sub-waveform. In this thesis, the second approach is used since experiments showed that the differences between the two approaches is mostly limited to a few noisy SWH or σ° estimates along the track.

4.4 Validation of STAR-V3

In this section, the quality of STAR-V3 results are investigated. For this, STAR-V3 is, first, validated against other state-of-the-art conventional altimetry retracking methods at two study sites with challenging coastal conditions based on Roscher et al. (2017). This enables a general quality assessment of the results and of the improvements between V1 and V3. In a second step, STAR-V3 is applied to RDSAR data from the Cryosat-2 mission and then compared to higher accuracy DDA data based on earlier validations published in Fenoglio et al. (2021).

4.4.1 Comparison to Other Conventional Retracking Approaches

For the first part of the validation, the quality of STAR-V3 is evaluated at the same study sites that have been used in Roscher et al. (2017). The first study site is in the Gulf of Trieste where the Jason-2 pass 196 covers regions of open ocean, as well as coastal regions at the Italian coast after crossing the Isla di Sant' Andrea and the Croatian coasts where it runs almost parallel to the shoreline before finally crossing to land (Fig. 4.8, left). At the second study site at the coast of Bangladesh, the Jason-2 pass 053 crosses from the deep ocean parts of the Bay of Bengal onto the coastal shelf and then over a region, which includes temporally variable sandbanks, followed by crossing Sandwip Island and after a short open water passage it finally crosses the coastline of the Bangladesh mainland (Fig. 4.8, right).

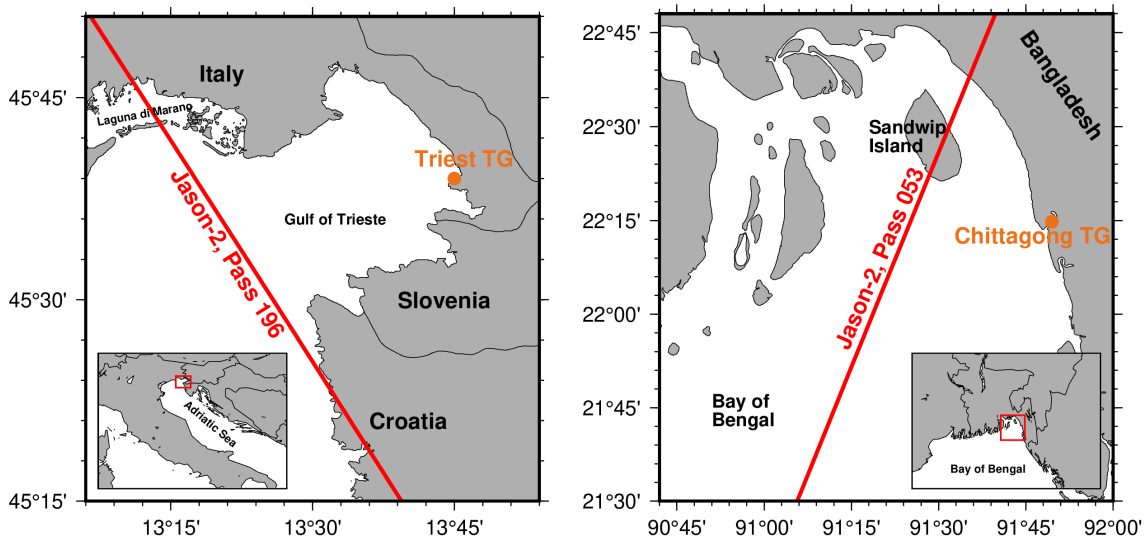


Figure 4.8: Study sites for comparing STAR-V3 to STAR-V1 as well as other retracking methods as presented in Roscher et al. (2017). The Jason-2 tracks are shown in red and the tide gauge locations are presented in orange. Left: Study site at the Gulf of Trieste. Right: Study site at the coast of Bangladesh.

In this thesis, the along-track comparison for STAR-V3 is limited to the Jason-2 mission. Roscher et al. (2017) already showed that the algorithm also works for other missions, such as Envisat, and provided results of similar quality as for Jason-2. For both study sites (Fig. 4.8) STAR-V3 is compared to STAR-V1 and the ocean and coastal retracking methods employed in Roscher et al. (2017). The input SGDRs from the Jason-2 mission include an ocean model based on Amarouche et al. (2004) as well as an empirical 30% threshold method (Sect. 4.2.2), called ICE1. The weighted three parameter ocean model (W3POM) based on Halimi et al. (2013) is the model used as part of the STAR processing. In addition, two sub-waveform methods are examined including the Improved Threshold Retracker (ITR, Hwang et al., 2006) and the Adaptive Leading Edge Subwaveform (ALES) retracker (Passaro et al., 2014).

Figure 4.9 compares the percentage of cycles, which provide valid SSH and lead to a correlation with tide gauge data of at least 0.9 for the study in the Gulf of Triest and at the coast of Bangladesh (Roscher et al., 2017). For each of the investigated retracking methods the time series of tide gauge and altimetry are correlated at each 20 Hz measurement location and the largest difference is iteratively eliminated until the correlation is at least 0.9. This enables a direct comparison of each retracker, while also accounting for possible differences in available cycles. Over the open ocean

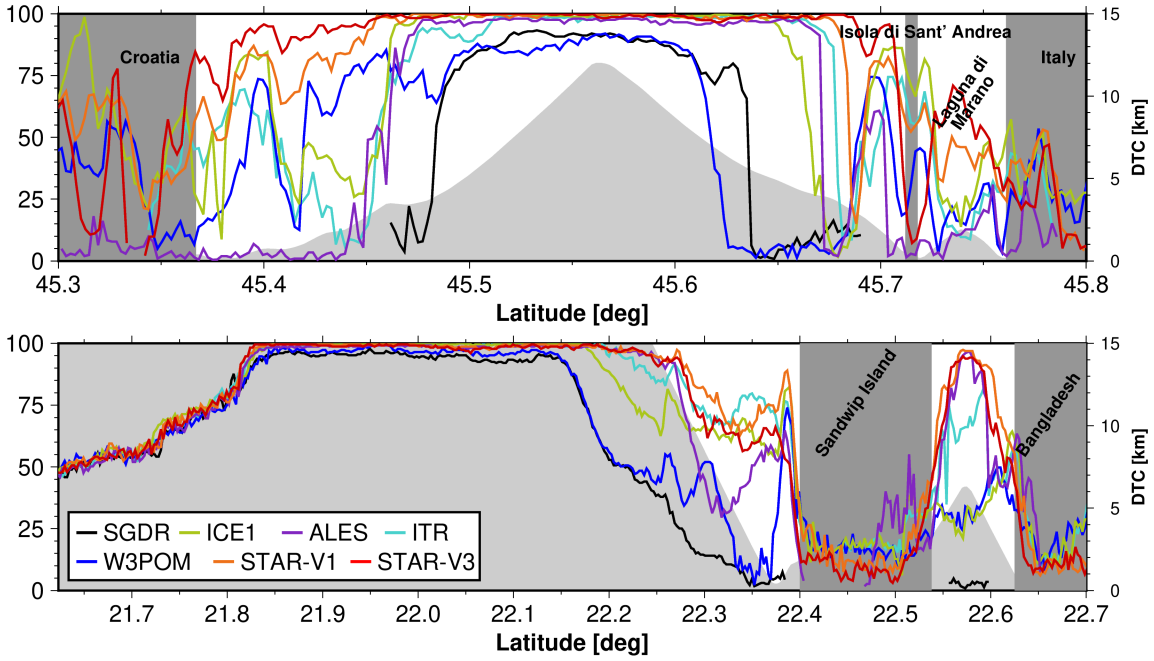


Figure 4.9: Percentage of cycles retained to achieve a correlation of at least 0.9 with hourly tide gauge data from a total number of 227 available cycles. Top: Study site at the Gulf of Trieste. Bottom: Study site at the coast of Bangladesh. The distance to the nearest coastline (DTC) is provided in light gray. Results based on Roscher et al. (2017) and extended for STAR-V3.

in the two investigated study sites, all methods agree well with about 95-100% of retained cycles. STAR-V3 generally does not show any improvement or degradation in these open ocean regions indicating that the additional prior information does not lead to a negative impact compared to STAR-V1. For the standard SGDR input data and the W3POM the level is slightly lower due to divergence of the parameter estimation during some of the cycles. The transition from the deep ocean to the coastal shelf at the coast of Bangladesh is clearly visible showing a significant decline in agreement.

For the Croatian coast Roscher et al. (2017) found a declining number of retained cycles closer towards the coast for all methods, with STAR-V1 showing the smallest decline. STAR-V3 is able to retain more cycles of good quality data. The comparison with tide gauge data indicates about 10-20% more retained cycles compared to STAR-V1, reaching levels of 90% and more up to about 1 km off the Croatian coast. From figure 4.8 one can see that the altimetry track runs roughly parallel to the coast for a while, which leads to constant land influence on the measured waveforms. However, STAR-V3 allows to extract meaningful SSH in this difficult situation.

All methods except STAR-V3 exhibit a significant decline in retainable cycles at about 3 to 4 km before the Isola di Sant' Andrea, which has also been noticed in Roscher et al. (2017). With STAR-V3 it is possible to derive good quality results in 80-90% of the cycles up to 1 km off the coast. Over the Laguna di Marano, which is connected to the Gulf of Trieste via small channels STAR-V3 also shows improved agreement with the Trieste tide gauge data. For the Bangladesh study site, the results from STAR-V1 and STAR-V3 agree rather well. Over the sandbank area

between 22.25 to 22.35 °N (Roscher et al., 2017) some differences become visible. Here, STAR-V3 shows a slightly lower level of retained cycles compared to STAR-V1 and the ITR algorithm. This can be explained by the fact that STAR-V3 utilizes SLA instead of SSH for analyzing the point-cloud of potential heights. Due to the bad quality of the MSS at this location, resulting from problems in providing meaningful data by standard methods (black line), the derived SLA is biased and, thus, does not fulfill the straight line assumption (Sect. 4.3.3). This cannot be fully compensated by the median based auxiliary a priori data (Alg. 4.1). Consequently, cycles with large jumps in SSH occur, which are then discarded by the STAR processing. In addition, STAR-V1 has been slightly over-tuned on this region. Over the strip of open water between Sandwip Island and the Bangladesh main land STAR-V3 and STAR-V1 perform well.

The basis waveforms for the sub-waveform detection are computed based on randomly generated dictionary elements (Sect. 4.3.1). For repeated applications of STAR to the same track segment, this leads to small differences in the sub-waveform partitioning and, consequently, selected final heights. This means that processing the same altimetry track twice will basically never result in the exact same heights at all 20 Hz positions. This is not problematic as long as the resulting variability in the final heights is smaller than the general 20 Hz error level of about 10 cm over the open ocean; the coastal region error level is generally larger. This has been examined for STAR-V1 in Roscher et al. (2017) and figure 4.10 shows those results in comparison to STAR-V3. The general variability over the open ocean of STAR-V1 and -V3 is found to be in the order of about 2 cm, well below the error level of 20 Hz, showing no significant differences between both versions. In the coastal regions at the Croatian coast, as well as around the Isola di Sant' Andrea STAR-V3 is found to provide a significantly improved repeatability comparable to the open ocean region. In contrast, STAR-V1 showed considerable variability in the order of 20 cm and more in the coastal zones. Investigations for other cycles and study sites showed similar results.

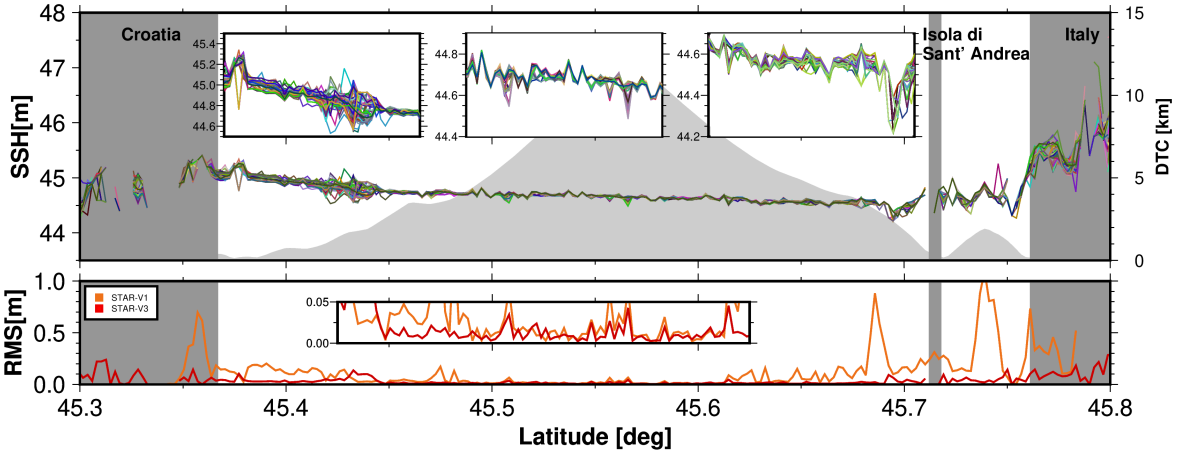


Figure 4.10: Repeatability of STAR-V1 and STAR-V3. Top: SSH obtained from 1000 runs of STAR-V3 on cycle 69, pass 196 at the Trieste study site. Zoomed sub-plots allow to closer examine the SSH repeatability in coastal and open ocean regions. The colors are generated randomly. Bottom: Comparison of the root mean square difference (RMS) derived from 1000 runs of STAR-V1 and STAR-V3; a zoomed sub-plot shows a more detailed view over the open ocean. Results based on Roscher et al. (2017) and extended for STAR-V3.

Generally, the focus of STAR is on improved retrieval of SSH. Nonetheless, the retracker also generates point-clouds of SWH and σ°, which can be analyzed analogously. Figure 4.11 shows along-track SWH from some arbitrarily selected pass and cycle, as well as comparison to the SWH gauge at the FINO3 research platform located in the open ocean of the North Sea. Without impact from land as in coastal areas this enables a quality assessment of the retrieved SWH. As described

in section 4.3, in this thesis, the SWH (and σ° below) are derived from a separate analysis of their respective point-clouds. Since not all retracking algorithms allow for retrieval of SWH, these are excluded here. It can be seen that STAR-V3 provides SWH with a significantly reduced noise level compared to other retrackers but it still follows the major variations along the satellite track well (Fig. 4.11, A). The SWH extracted from the ERA-Interim reanalysis and interpolated on the altimetry track agree well with the retracked estimates. When comparing the FINO3 gauge wave heights to the retracked heights (Fig. 4.11, B), the STAR-V3 SWH performs similar to the wave heights based on the SGDR and STAR-V1 retrackers. All of the aforementioned retrackers are slightly outperformed by the ERA-Interim reanalysis data, which likely also assimilates the FINO3 data. The W3POM retracker results include some significant outliers during some cycles.

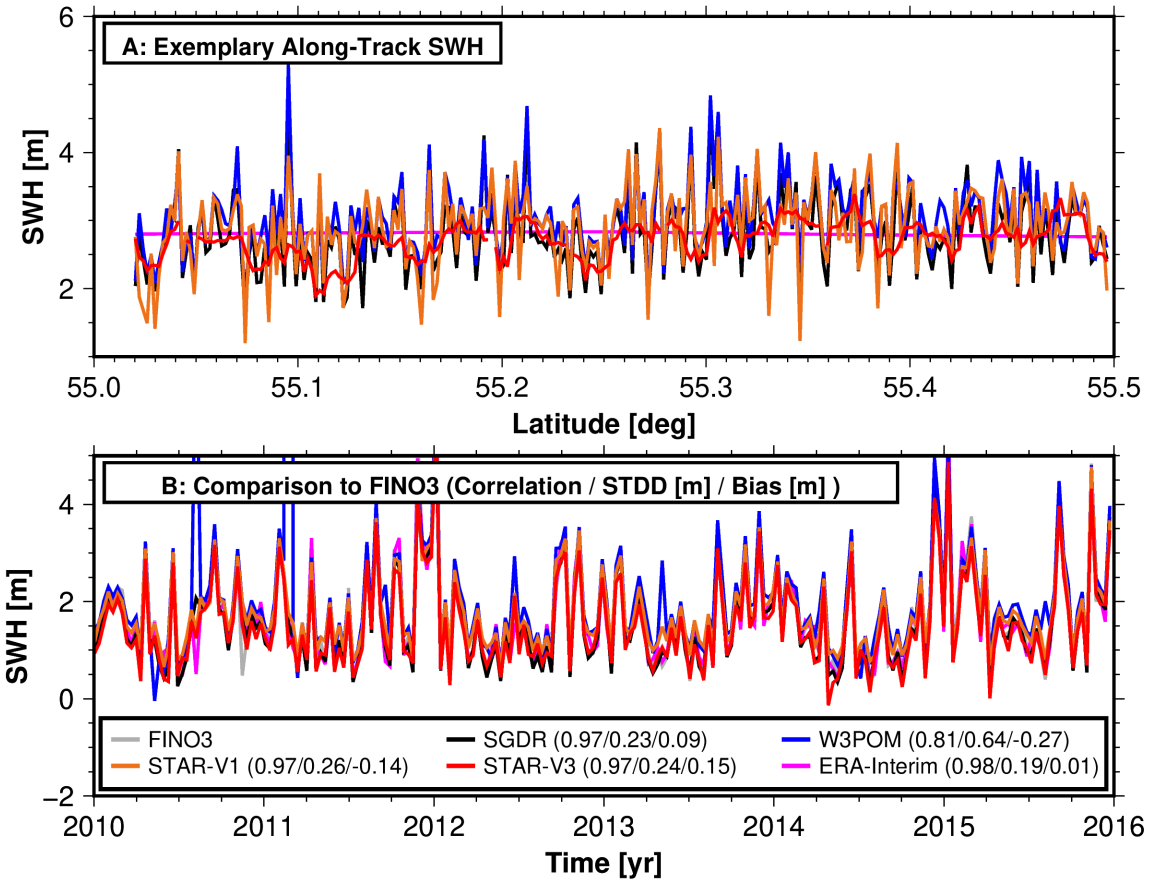


Figure 4.11: Comparison of SWH estimates. A: Comparison along the arbitrarily chosen cycle 127 of Jason-2 pass 094. SWH from four different retracking approaches that provide SWH, including STAR-V1 and STAR-V3, and re-analysis data from ERA-Interim is examined. B: Validation against SWH measured at a gauge of the FINO3 research platform in the North Sea.

Similar to the SWH, the σ° estimates are converted to wind speed based on the empirical algorithm by Lillibridge et al. (2014) adapted for Ku-Band. Figure 4.12 (A) shows an along-track comparison of wind speed. STAR-V1 is slightly noisier compared to STAR-V3. W3POM, STAR-V3 and, to some extent, the ICE1 based wind speed exhibit the least along track noise from all considered retrackers. However, there is an obvious bias between the individual methods. W3POM, STAR-V1 and STAR-V3 are relatively close, since all three use the W3POM model for estimation. ICE1 and SGDR wind speed is biased by several meters per second while the ITR result is located somewhere in between, similar to the wind speed extracted from the ERA-Interim reanalysis (Fig. 4.12, A). These biases are generally constant and related to the waveform model employed by each retracker. Therefore, they can be easily corrected to a reference σ° or wind speed level. When

comparing the 10 m wind speed to the wind speed measured at 33 m height at the FINO3 station (Fig. 4.12, B), the latter has to be corrected to also resemble wind speed at 10 m height following a simple approach proposed by Hsu et al. (1994). Based on the statistics (Fig. 4.12, B), all retrackers achieve high correlation with the gauge station with STAR-V3 and the ERA re-analysis data performing best. Among the retrackers, STAR-V3 also achieves a slightly better standard deviation of the differences compared to the other retrackers. The smallest bias is found for the re-analysis data. Again, this might be related to the data also being assimilated in the re-analysis.

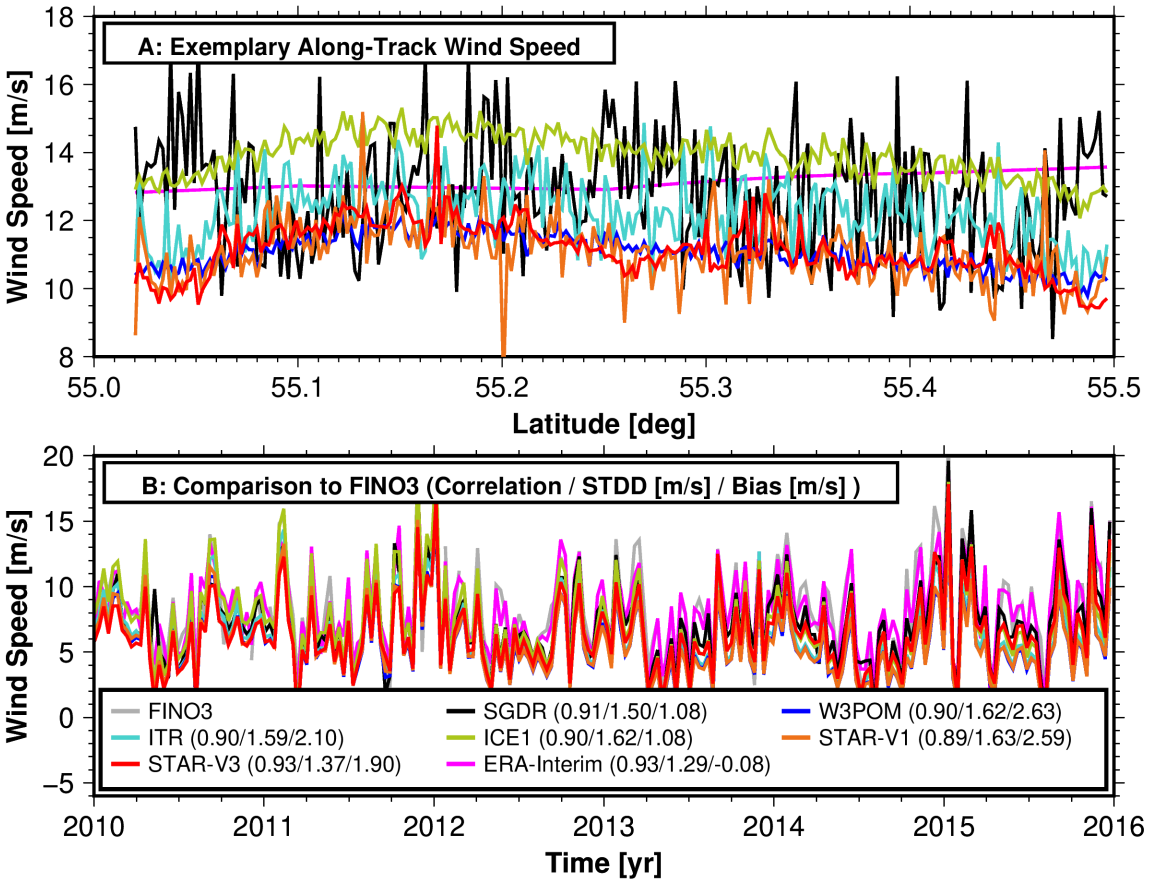


Figure 4.12: Comparison of wind speed derived from SWH and σ° estimates. A: Comparison along the arbitrarily chosen cycle 127 of Jason-2 pass 094. σ° from six different retracking approaches, including STAR-V1 and STAR-V3, and re-analysis data from ERA-Interim is examined. B: Validation against σ° measured at a gauge of the FINO3 research platform in the North Sea.

So far the selection of final estimates of SWH and σ° follows in principle the same algorithm developed and tuned for the SLA point-cloud. As mentioned before, the focus in this thesis is on the height estimation. However, in future extensions specialized analysis algorithms for the SWH and σ° point-clouds can be implemented.

4.4.2 Validation Against Delay Doppler Altimetry

Delay Doppler Altimetry (DDA) or SAR mode altimetry allows to construct conventional altimetry like waveforms from the SAR measurement, generally denoted Low Resolution Mode (LRM) or Reduced Synthetic Aperture Radar (RDSAR). Applying conventional altimetry retrackers to the RDSAR waveforms, then, enables a direct along-track comparison with the higher quality SAR mode data derived from the same instrument along the same track (e.g., Fenoglio et al., 2019; Fenoglio et al., 2021).

Computing the along-track SLA difference enables a first assessment of the RDSAR retracked SLA against the SAR mode data. Figure 4.13 compares RDSAR SLA from the TALES retracker (Buchhaupt et al., 2018) and STAR-V3 with the GPOD-SAR-SAMOSA+ (Dinardo et al., 2018) retracked results from the Cryosat-2 mission along the European Atlantic coast. When comparing the results from TALES (Fig. 4.13, A) to STAR-V3 (Fig. 4.13, B) it can be seen that while the agreement over the open ocean is generally good, the differences between RDSAR and SAR SLA are largest at the coasts. STAR-V3 shows significantly better consistency with SAR data at the coasts compared to TALES. The standard deviation of the differences over each location (Fig. 4.13) for STAR-V3 is found to be 3.12 cm, which is about 1.4 cm lower than for TALES. While the STAR algorithm includes a rather strict outlier removal, the number of valid points is still about 3 % higher compared to TALES. Both RDSAR methods are biased by about 4.5 mm with respect to the SAR SLA. This can result from the processing of the measured return energy into SAR and RDSAR waveforms as well as a general retracker bias.

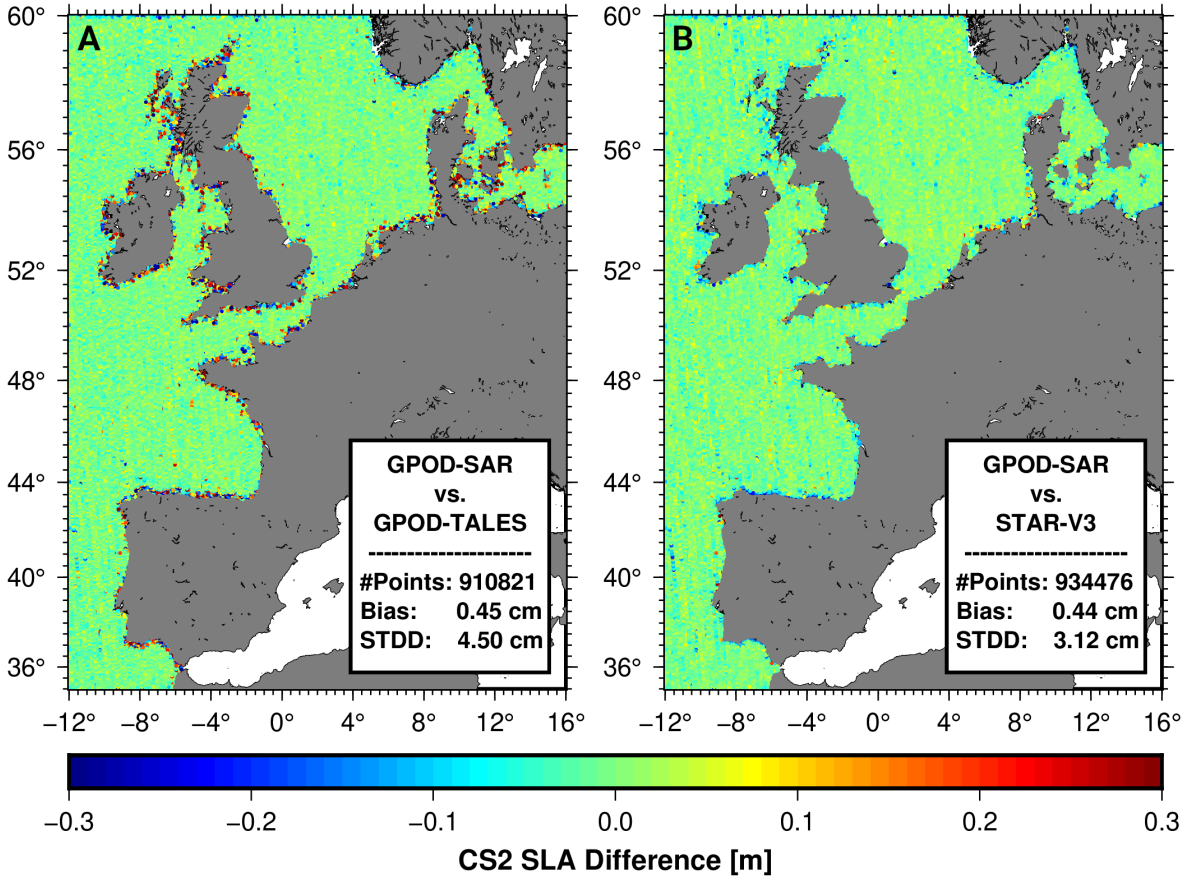


Figure 4.13: Comparison of RDSAR 1 Hz SLA from the TALES (Buchhaupt et al., 2018) and STAR-V3 retrackers against high-quality SLA derived from SAMOSA+ (Dinardo et al., 2018) retracked SAR-mode data along the European Atlantic coast from 2010-07 until 2018-12.

When separating 20 Hz coastal and open ocean points at 10 km distance to coast, STAR-V3 clearly outperforms the TALES retracker (Tab. 4.3). The 20 Hz data exhibits a generally higher noise level in, both, RDSAR and DDA, which leads to generally higher standard deviations compared to the 1 Hz data in figure 4.13. Especially in the coastal zone, STAR-V3 provides a significantly reduced noise level of 13.22 cm compared to 31.66 cm derived from TALES.

Results from comparing the two RDSAR retrackers to tide gauge data at the station Helgoland are presented in figure 4.14. Both, STAR-V3 and the SAR-SAM+ results show a correlation of

Table 4.3: Comparison of standard deviation of the differences (STDD) in cm for 20 Hz SLA between the RDSAR retrackers TALES and STAR-V3 against SAMOSA+ DDA for coastal and open ocean region. The same points are utilized for the computation for both retrackers.

Retracker	Open Ocean STDD	Coastal STDD
TALES	11.00	31.66
STAR-V3	6.65	13.22

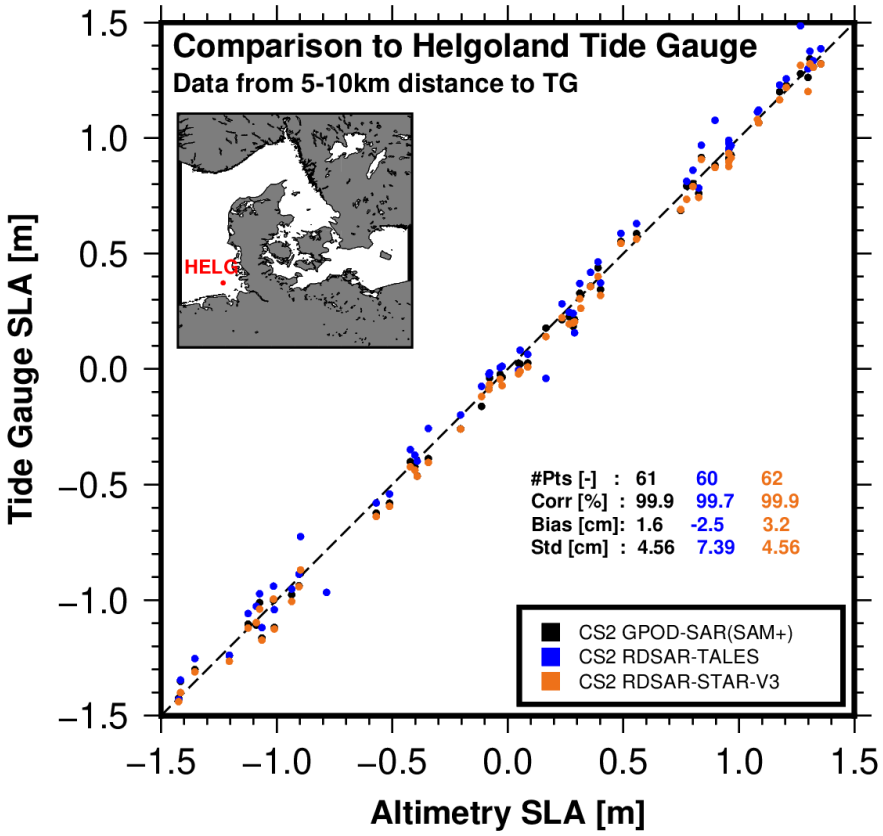


Figure 4.14: Comparison of the SAR-SAM+ retracker and the two RDSAR retrackers TALES and STAR-V3 against the tide gauge station on Helgoland.

99.9 with the tide gauge data and a standard deviation of 4.56 cm, however STAR-V3 includes one more point from an altimeter crossing where the SAR mode data does not provide valid points. The TALES results are missing two data points and show a significantly higher standard deviation of 7.39 cm.

In order to further assess the quality of the retracked 20 Hz heights in coastal areas, the variability within defined bins of 200 m distance to coast is computed (Fig. 4.15). Here, the data is taken from the region covered by the Bundesamt für Seeschifffahrt und Hydrographie (BSH, Dick et al., 2001) model defined within the bounds indicated by the red square in figure 4.15. The retracked heights from the STAR-V3 retracking show the same variability as the SAR mode SLA up to about 3 km off the coast. While the variability increases roughly linear from about 23 cm to 38 cm with decreasing distance to coast for the SAR mode data, the RDSAR STAR-V3 variability stays at the level of 23 cm right up to the coast. For the RDSAR TALES retracker the general variability is found at a level of 25 to 30 cm, which increases from about 4 km up to a level of 75 cm at the coast. The BSH model data shows an almost constant level of variability in the range of 18 cm.

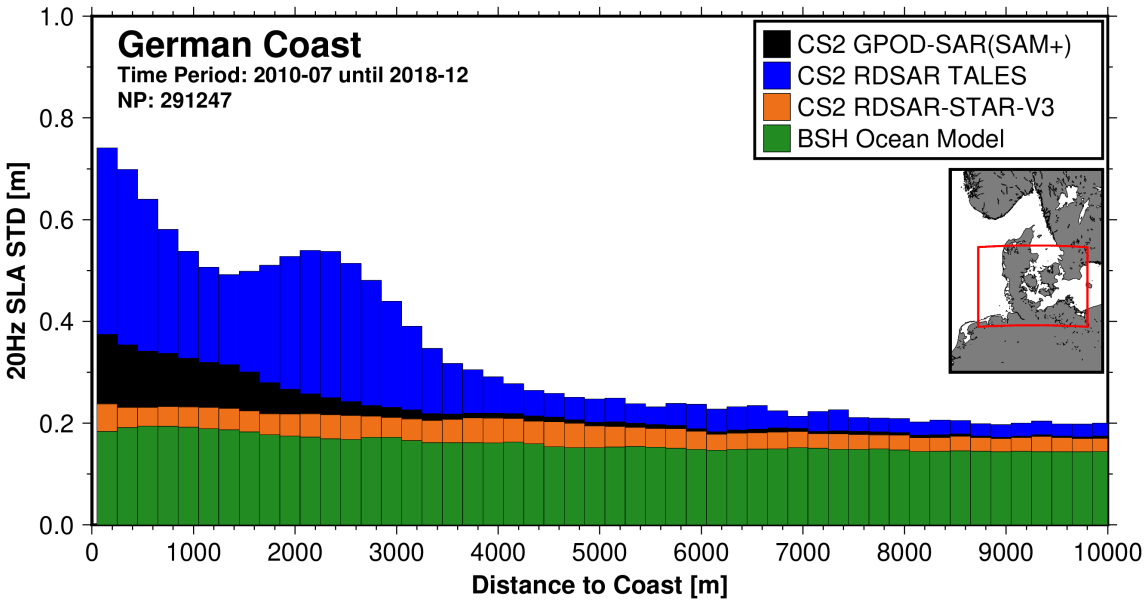


Figure 4.15: 20 Hz SLA variation depending on the distance to coast. STD is computed in 200 m steps over the period 2010-07 until 2018-12 for the GPOD-SAR-SAM+ retracker, the RDSAR TALES and STAR-V3 methods as well as ocean model data from the Bundesamt für Seeschifffahrt und Hydrographie (BSH). The region utilized for the comparison is defined by the red square.

Although the comparisons to SAR data in this thesis are limited, it is possible to conclude that STAR-V3 provides almost SAR mode quality results from RDSAR or, if transferred assuming same performance, conventional altimetry. A more comprehensive comparison is provided in Fenoglio et al. (2021), who use an intermediate version between STAR-V2 and STAR-V3 (Tab. 4.2), where it was not yet possible to deal with erroneous MSS. However, the effect on the results in the North Sea region investigated in Fenoglio et al. (2021), which generally contains high quality data, is negligible and can be safely transferred to STAR-V3. Besides results from Cryosat-2 that are presented here, validations against Sentinel-3 data show a similar performance of STAR (Fenoglio et al., 2019; Fenoglio et al., 2021).

Chapter 5

Separately Estimating Individual Sea Level Contributions

This chapter deals with deriving mass, steric and total sea level estimates from space geodetic techniques, usually resulting in global or regionally averaged time series. It is then possible to combine two or more of the individually obtained sea level contributions forming a sea level budget. This approach is generally applied in published literature (e.g., Cazenave et al., 2009; Boening et al., 2012; Dieng et al., 2017; WCRP-Global-Sea-Level-Budget-Group, 2018; Royston et al., 2020; Horwath et al., 2022). In contrast, the inversion method (Chapter 6) combines all datasets with their respective covariance information in a joint estimation.

Processing contributions to the sea level budget individually can easily lead to inconsistencies in the data coverage or evaluation steps, which then directly transfer into the budget closure error of the resulting sea level budget. This explains the sometimes significant budget misclosures found in published sea level budgets (e.g., Rietbroek et al., 2016; WCRP-Global-Sea-Level-Budget-Group, 2018). Consequently throughout this thesis, special focus will be put on the consistency of datasets and processing steps when deriving sea level budgets.

5.1 The Sea Level Budget Equation

Sea level change is not uniform neither on spatial nor temporal scales. Spatially, variations are related to transport of water masses due to ocean currents or wind forcing influenced by bathymetry and land masses, ocean heat uptake resulting from warming of the oceans, salinity changes from evaporation or freshwater input as well as land ice and water mass variations and their corresponding gravitational attraction. Temporally, long-term sea level trend signals are superimposed by seasonal variations, inter-annual and decadal changes, accelerations, e.g. from increased melting rates, and significant events such as Earth quakes or vulcano eruptions (e.g., Nerem et al., 2018).

The conventional method of deriving a sea level budget focuses on extracting and combining the long-term trends from individual mass and steric contributions. This allows to examine the spatial and temporal drivers of sea level change and better predict future sea level change on global and regional scales. Globally, sea level is mainly driven by water mass exchange between ocean, land and atmosphere either by hydrology or melting of glaciers and ice sheets (e.g., Cazenave et al., 2009; J. Church et al., 2011; Leuliette and Willis, 2011; Chambers et al., 2017; Dieng et al., 2017; Nerem et al., 2018). Furthermore, warming of the oceans is driven by global temperature increase resulting from EEI variations resulting in steric sea level change (e.g. von Schuckmann et al., 2016). On regional scales, local phenomena such as IMV, GIA and surface loading induced land uplift or a singular steric or mass related sea level driver can dominate the RSL budget.

The sea level budget can be written as a function of time, t (based on, e.g., Chambers et al.,

2017; WCRP-Global-Sea-Level-Budget-Group, 2018; Horwath et al., 2022)

$$\bar{\mathrm{S}}(t)_{\mathrm{total}} = \bar{\mathrm{S}}(t)_{\mathrm{OMC}} + \bar{\mathrm{S}}(t)_{\mathrm{steric}}, \tag{5.1.1}$$

where $\bar{\mathrm{S}}_{OMC}$ refers to the global mean OMC and $\bar{\mathrm{S}}_{\mathrm{steric}}$ contains the global mean temperature and salinity related changes. The bar indicates averaging over the global ocean. Both contributions can be further separated into sub-contributions, which also depend on location (λ, ϕ). The following assumes that the separation is additive and individual components are independent from one another. However, in reality interconnections exist, e.g. between glacier melt and fresh water flux leading to changes in ocean salinity. Based on the assumption further separating the OMC leads to (modified from, WCRP-Global-Sea-Level-Budget-Group, 2018)

$$\begin{aligned}\mathrm{S}(t,\lambda,\phi)_{\mathrm{OMC}} =& \mathrm{S}(t,\lambda,\phi)_{\mathrm{Greenland}} + \mathrm{S}(t,\lambda,\phi)_{\mathrm{Antarctica}} + \mathrm{S}(t,\lambda,\phi)_{\mathrm{Glaciers}} + \\ & \mathrm{S}(t,\lambda,\phi)_{\mathrm{Hydrology}} + \mathrm{S}(t,\lambda,\phi)_{\mathrm{IMV}} + \mathrm{S}(t,\lambda,\phi)_{\mathrm{GIA}} + \\ & \mathrm{S}(t,\lambda,\phi)_{\mathrm{Snow}} + \mathrm{S}(t,\lambda,\phi)_{\mathrm{rest}}.\end{aligned} \tag{5.1.2}$$

This represents the effects from ice melt from land glaciers, Greenland and Antarctica, terrestrial hydrology variations, IMV from transport of masses within the ocean, GIA changes as well as snow mass changes. In this thesis, changes in snow are theoretically included in the employed WGHM model. Since the focus of this thesis is not only on the global mean sea level budget, but also the investigation of regional budgets the IMV and GIA mass terms are explicitly added, although being defined as having zero RSL trend when averaged over the global ocean.

While others (e.g., J. Church et al., 2011; Chambers et al., 2017; Nerem et al., 2018) often only consider thermo-steric sea level change, as it is the dominating contribution on global scales, this thesis utilizes the integral steric change, $\mathrm{S}_{\mathrm{steric}}$, as the sum of thermo- and halo-steric contributions

$$\mathrm{S}(t,\lambda,\phi)_{\mathrm{steric}} = \mathrm{S}(t,\lambda,\phi)_{\mathrm{thermo}} + \mathrm{S}(t,\lambda,\phi)_{\mathrm{halo}}. \tag{5.1.3}$$

The remainder, $\mathrm{S}(t,\lambda,\phi)_{\mathrm{rest}}$, in equation (5.1.2) contains so-far unconsidered effects such as water vapor related sea level change, wind driven sea level changes pushing water masses in or out of a region and other local effects, such as sedimentation.

5.2 Global and Regional Mean Sea Level from Radar Altimetry

Averaging altimetry observed GSL globally and converting it to RSL (Sect. 5.2.3) allows to estimate time series of Global Mean Sea Level (GMSL). Figure 5.1 shows GMSL time series from three different groups over 2002-2020 with corresponding trends for the period 2005-01 till 2015-12; the datasets (Sect. 3.1.4) are produced by CSIRO (Watson et al., 2015), AVISO (Ablain et al., 2015; Ablain et al., 2019) and the University of Colorado (Nerem et al., 2018). In addition, an own implementation following the processing as described by the University of Colorado[1] is shown. All time series are based only on Topex/Poseidon and Jason-1/-2/-3 data, which provide continuous sea level observations since 1993. Although, these time series, theoretically, contain the same data input, one can observe significant differences between the individual curves and the derived trend estimates. The major inconsistencies result from different Inter-Mission Bias (IMB) corrections and the applied global averaging methods (see Sects. 5.2.1 and 5.2.2). When combining different altimetry missions, a certain variation can be expected, especially, when considering that the Topex/Jason mission coverage is limited to $\pm 66°$ latitude (Fig. 3.2). However, for the same data basis these variations of 0.2 mm/yr are rather related to processing choices.

In general, computing a time series of global or regional mean sea level change requires three main processing steps: (1) converting the observed ranges to SLA, (2) averaging the SLA over the region of interest and (3) potentially converting to relative sea level change for comparison to tide gauges or combination with independently obtained ocean mass or steric sea level change.

[1] https://sealevel.colorado.edu/index.php/data-processing-methods (last accessed: 12.01.2022)

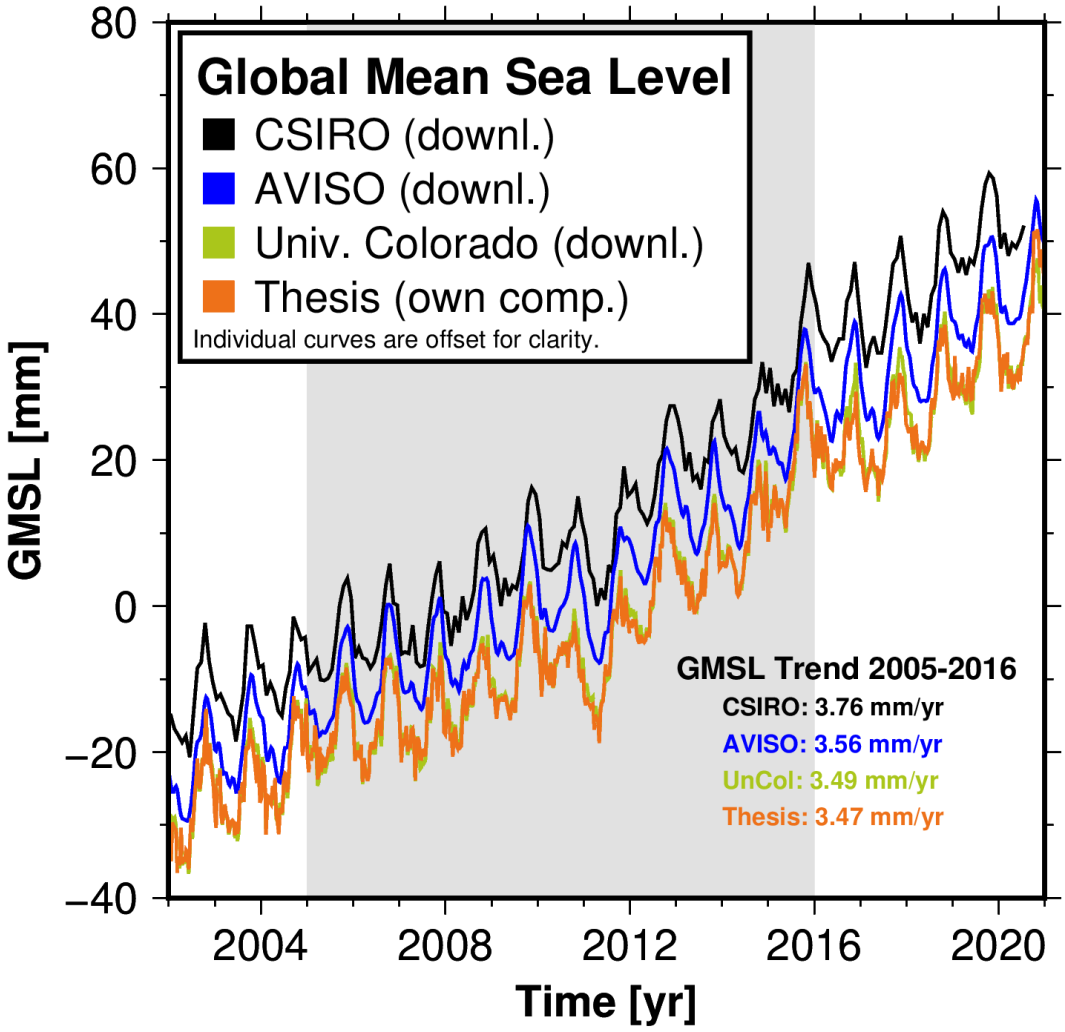


Figure 5.1: Impact of processing choices on the GMSL time series based on the reference missions Topex/Poseidon and Jason-1/-2/-3. The trend estimates refer to the period 2005-01 until 2015-12. The individual time series are offset for clarity.

5.2.1 Obtaining Sea Level Anomalies

SLA is obtained from observed satellite altimetry ranges extracted from level 2 along track datasets (Sect. 3.1.1). Following equation (3.1.5), this requires applying several atmospheric and tidal corrections, as well as subtracting a mean sea surface and applying retracking (Chapter 4). For GMSL applications, one would rather apply standard retracking approaches for comparability, instead of selecting advanced methods, e.g., for coastal regions (Chapter 4).

While this first step of computing a time series of regionally averaged sea level change seems relatively straight forward, individual corrections can significantly impact the resulting time series. This includes the applied IMB, where jumps between the individual altimetry missions directly affect the resulting trend estimate (Sect. 7.3). The differences observed in table 5.1 result from different approaches for computing the biases as well as varying atmospheric and tidal corrections. For comparison to other altimetry-based time series and combination with independently processed ocean mass or steric sea level change, the applied corrections should be as consistent as possible. Due to the uncertainties in the applied corrections, sea level estimates will be associated with a certain noise floor of about 0.2 to 0.3 mm/yr, which mainly results from the wet troposphere correction, since it is associated with the largest uncertainty (Legeais et al., 2018).

Table 5.1: Inter-mission biases for the Jason-1/-2/-3 reference missions relative to Topex/Poseidon as provided by different groups. Values for AVISO are taken from https://www.aviso.altimetry.fr (last accessed: 27.07.2022), U. Colorado https://sealevel.colorado.edu/ and extracted from the RADS Jason-data files.

Group	Jason-1 IMB [cm]	Jason-2 IMB [cm]	Jason-3 IMB [cm]
AVISO	1.16	1.39	-1.58
U. Colorado	8.64	-1.44	-4.43
RADS	8.50	-1.50	-4.30

Besides official along-track data products, third party data products, such as the RADS database (Sect. 3.1.2), often provide choice of various corrections and different retrackers in order to obtain SLA. Furthermore, not all retrackers are available from public databases and applying specialized approaches requires the use of official level 2 SGDR products (Sect. 3.1.2), which include the waveforms and all the necessary information. Some groups also provide already gridded level 4 SLA data sets. However, these datasets are potentially inconsistent since the user can not influence the applied corrections and retracking algorithms. Furthermore, not all gridded datasets are suitable for computing global or regionally mean sea level change as the temporal and spatial gaps are generally filled by statistical interpolation methods (Pujol et al., 2016).

5.2.2 Averaging Sea Level Anomalies

For the next step, the (along-track) SLA data is spatially averaged over a region of interest in order to obtain a time series of mean sea level change. While this step seems rather simple, each sea level group applies their own averaging approach, which is often poorly documented. Differences can lead to trend variations in the range of several tenths of millimeters per year (Fig. 5.1) for the GMSL time series considered in this thesis; impact on regional averages can become even larger.

The University of Colorado group (Nerem et al., 2018) directly utilized the along-track SLA discarding coastal data from regions with an ocean bathymetry of less than 120 m as well as SLA exceeding 2 m. These data are then averaged globally for each cycle individually while applying inclination dependent weighting, w_j^{incl}, defined as

$$w_j^{\text{incl}} = \sqrt{\max[0.01, (1.0 - \left(\frac{\sin(\phi_j)}{\sin(\phi_{\text{ref}})}\right)^2)]}, \tag{5.2.1}$$

where ϕ_{ref} is the chosen reference inclination. Unless stated otherwise, $\phi_{\text{ref}} = 66.04°$ is set to the maximum inclination of the Jason altimetry missions. This weighting scheme is also used for the GMSL processing applied in this thesis. In contrast, the AVISO group first collects the along-track SLA of each cycle into bins of 1×3 degrees latitude by longitude, respectively, which are then averaged for one cycle. Next, they compute a globally weighted average, where the weights are selected to be proportional to the area covered by the bins. In practice, this is implemented as cosine of latitude weight, w_j^{lat},

$$w_j^{\text{lat}} = \cos(\phi_j). \tag{5.2.2}$$

Finally after adjusting the periodic signals, the AVISO time series is smoothed with a two-month low-pass filter. The averaging process by CSIRO is not clearly documented. Following J. A. Church et al. (2004), Church and White (2006) and Watson et al. (2015) a cosine of latitude based weighting scheme is employed. In addition, the cycles are averaged to monthly mean sea level estimates. Information on outlier definition are neither provided by AVISO nor CSIRO.

5.2.3 Converting Absolute to Relative Sea Level Change

For the final step, GSL is usually converted to RSL in order to represent the sea level variation with respect to the changing surface of the Earth. Besides mass and steric related influences, the height change observed by altimetry contains the geometric uplift effect of the solid Earth. Uplift consists of a long-term visco-elastic part and a part driven by contemporary mass changes. The former is caused by glaciation periods in the past, which deformed the surface leading to mantle material being redistributed to other regions. After melting of the ice, the surface slowly rebounds, which is denoted as Glacial Isostatic Adjustment (GIA). The second part of the uplift is due to elastic effects caused by contemporary mass changes from the melting of land glaciers and the Greenland and Antarctic ice sheets, as well as hydrological mass variations and redistribution of mass within the ocean itself.

The geoid and uplift impact of GIA is generally modeled and, consequently, the geometric effect observed by altimetry can be accounted for. However, GIA models posses an uncertainty resulting in varying sea level corrections. On a global scale, this leads to trend effects in the range of approximately -0.30 to -0.20 mm/year, depending on the employed GIA model. The effect directly translates into corresponding estimates of GMSL. Thus, this represents another source of potential mismatch between individual estimates and other components of the sea level budget. Furthermore, tectonic motion in active volcano regions can become significant for RSL on regional scales.

The elastic uplift from contemporary mass changes also contributes to RSL. Frederikse et al. (2017) estimate these from a forward model approach and GRACE data. Similarly, the global fingerprint inversion method (Chap. 6) provides these as part of the output. This contemporary mass changes are often assumed to be small or included when applying a literature based GIA correction of -0.3 mm/yr (e.g., Chambers et al., 2017). In fact, on global scales, the contribution is in the range of -0.10 to -0.15 mm/year (Sec. 7.1 and Frederikse et al., 2017a), which is about half of the GIA effect. Similarly, these uplift effects also translate directly into derived trend estimates, potentially adding to the inconsistencies when combined and compared with other data.

5.3 Estimating Ocean Mass Change from Time-Variable Gravity

High resolution time-variable gravity information collected by the GRACE missions and its successor GRACE-FO have been available since April 2002 on a monthly basis, except for an 11 month gap between the two missions. Besides providing information on mass changes occuring over land due to hydrological variations and melting of the glaciers and ice sheets, the gravity missions also allow to directly infer ocean mass and ocean bottom pressure changes. Similar to GMSL from altimetry, individual processing choices when deriving Ocean Mass Change (OMC) will significantly affect the result.

OMC can be directly derived from spherical harmonics or from monthly mascon solutions as described in Section 5.3.1. The effect of specific choices of corrections during the computation is discussed in Section 5.3.2. The OMC solutions based on spherical harmonics and mascons are evaluated together with the mass component of the fingerprint inversion in Section 7.2.2.

5.3.1 Converting Time-Variable Gravity Observations to Ocean Mass Change

The following describes processing of monthly time-variable gravity fields provided in the form of either spherical harmonics or mascons in order to derive global (and regional) OMC consistent with satellite altimetry as described in Uebbing et al. (2019). A general overview on converting GRACE/GRACE-FO data to global and regional OMC is provided in Figure 5.2. Similar processing steps apply to SLR and Swarm time-variable gravity data.

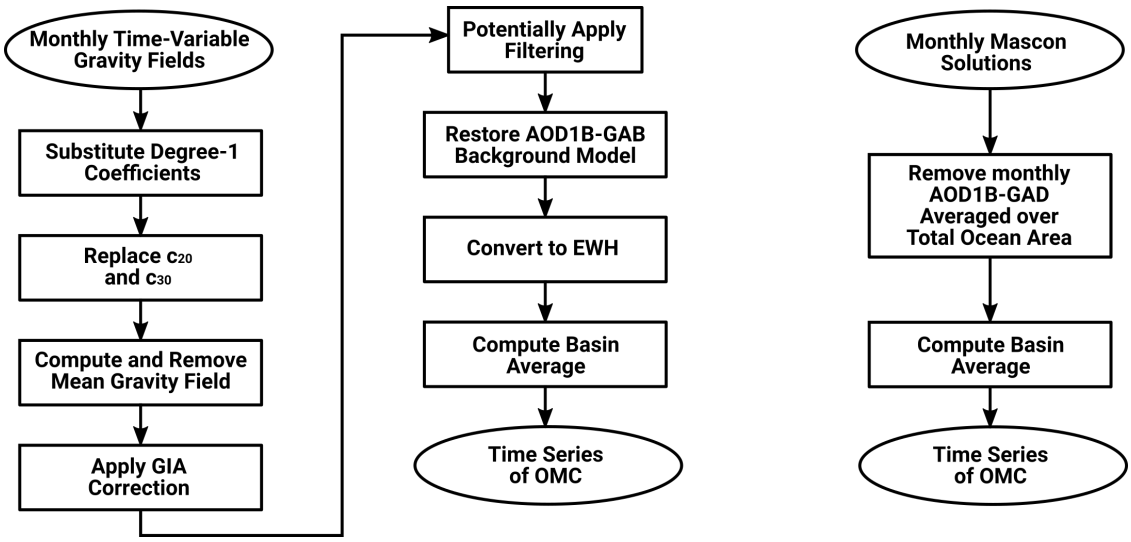


Figure 5.2: Overview of individual processing steps for deriving OMC from RL06 monthly time-variable gravity data given either as spherical harmonics or in the form of mascons.

Spherical Harmonic Approach

Directly processing the time-variable gravity fields provided in spherical harmonics to OMC follows the approaches by Chambers and Bonin (2012) and Johnson and Chambers (2013) with relevant updates in Uebbing et al. (2019). Here, the processing (Fig. 5.2) focuses on RL06 data, but, differences for the slightly outdated RL05 data will be noted.

First, one constructs a global surface mass change representation from the GRACE level-2 data GSM_{L2} (Sect. 3.2.1), representing gravity potential Stokes coefficients (Eq. 2.1.8). The spherical harmonics are available for different maximum degrees, where the data up to degree and order 60 is used here for direct estimation of OMC from GRACE/GRACE-FO data. Spherical harmonic gravity data is provided in the CM frame (Sect. 2.4.1) and, thus, missing the degree-1 coefficients, which represent the part of the mass redistribution related to a relocation of the Earth's center-of-mass. These have to be augmented by external information, which is either model-based (Swenson et al., 2008; Sun et al., 2016) or extracted from SLR data (Sect. 3.2.1). The choice of degree-1 correction will significantly affect the resulting OMC trend (see Sect. 5.3.2). Similar, the c_{20} coefficients are replaced by estimates obtained from SLR and after August, 2016 also the c_{30} coefficients (Loomis et al., 2020) with values published in TN-14 (Sect. 3.2.1). As an additional step for the RL05 processing (not required for RL06, since included), the pole tide correction (Wahr et al., 2015) needs to be applied, which modifies the c_{21} and s_{21} coefficients. Note that this is not considered when strictly following the RL05 processing described in Johnson and Chambers (2013).

For deriving OMC anomalies, a static field is subtracted from each monthly gravity field. Here following Johnson and Chambers (2013), the mean GRACE field over the time period 2005-01 till 2010-12 is selected. For reasons of consistency, this applies to all gravity data relevant processing in this thesis, including SLR, Swarm and the inversion input gravity data (Sect. 6.2.1). In the next step, the GIA effect is accounted for by subtracting a trend correction from each monthly field. Variations between individual GIA models will directly translate into the final OMC trends (Sect. 5.3.2). At this point, it is possible to further smooth and/or decorrelate the GRACE data in order to average out correlated noise. However following Chambers and Willis (2009) and Johnson and Chambers (2013), no additional filtering is applied in this thesis. Afterwards, Stokes coefficients are converted to EWH following Equation (2.1.36). When strictly following the Johnson and Chambers (2013) processing, one could then compute the final basin average up to degree and order 60

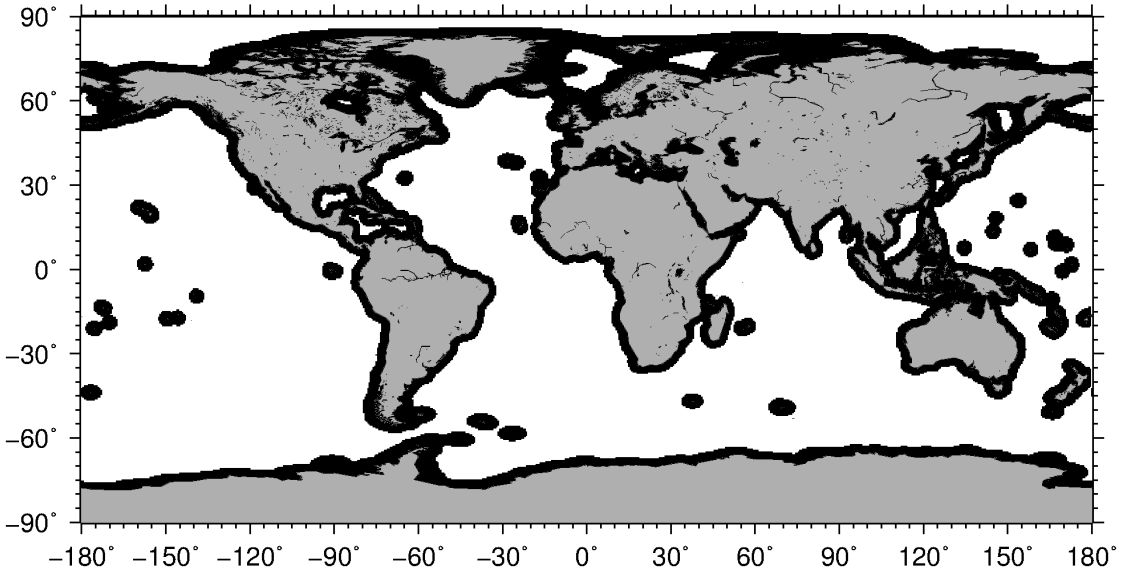


Figure 5.3: Ocean mask including a 300 km buffer zone along the coastlines.

without any restoration of the AOD1B background model.

In fact Uebbing et al. (2019) found that the AOD1B background model needs to be restored correctly in order to derive OMC consistent with satellite altimetry. This is done before computing the basin average over the ocean and after a potential filtering step (Flechtner et al., 2015). For this, the AOD1B GAD product is added back to the monthly gravity fields. The GAD product represents Ocean Bottom Pressure (OBP), where the underlying ocean model is forced with atmospheric pressure and wind (Flechtner et al., 2015). Residual atmospheric effects need to be removed from the GAD product (details in Sect. 5.3.2) in order to produce OMC consistent with the inverse barometric correction generally applied to altimetry data (Eq. (3.1.7), Sect. 3.1.1). Utilizing the GAD product works for, both, RL05 and RL06 data. Furthermore, with the RL06-AOD1B data, the GAB product already accounts for these effects and it is possible to directly restore the AOD1B-GAB product, instead.

For computing a time series of global mean OMC, the last step (Fig. 5.2) is to average the spherical harmonic EWHs by multiplying with an ocean kernel in the spectral domain (Eq. 5.3.1); this includes latitudes beyond ±66° (Fig. 5.3). Furthermore, the kernel is augmented by a buffer zone of typically a few hundred kilometers in order to avoid contamination from much stronger land hydrological signals, which effectively shrinks the considered ocean area. In this thesis, a buffer zone of 300 km is utilized, unless stated otherwise. For gridded data, the basin average is derived by computing a weighted mean over all grid points inside the area of interest, where, generally, an area-weighting is chosen, e.g. cosine of latitude weights (Eq. 5.2.2) for a regular grid. With gravity fields available in the spherical domain, basin averages, $\beta(t)$, can also be derived directly from

$$\beta(t) = \frac{1}{b_{00}} \sum_n \sum_m d_{nm}(t) b_{nm}. \tag{5.3.1}$$

This effectively multiplies each spherical harmonic coefficient of the data, d_{nm}, at time t, such as spherical harmonic fields of EWH, with the corresponding basin coefficient, b_{nm}. The basin coefficients can be derived from converting a gridded zero-one mask into the spherical harmonic domain. After summing over all degrees n and orders m, the result is normalized by the b_{00} coefficient, which is proportional to the basin area on the sphere. Applying the described processing to monthly gravity fields results in a time series of global mean OMC, which can then be further processed, e.g., by computing trends.

Mascon Approach

The mascon solutions considered in this thesis (Sect. 3.2.1) are provided on grids with 0.5° spatial resolution. The individual grid cells represent TWS over land and OBP over the ocean, both, expressed in EWH. Over the ocean this is equivalent to restoring the AOD1B GAD product without further considering the effect from atmospheric surface pressure, which is not consistent with altimetry data. Consequently, it is necessary to remove the ocean mean of the GAD product, averaged over the total ocean area (compare Sect. 5.3.2, integral term in Eq. (5.3.4)), for consistency with the IB corrected satellite altimetry. Afterwards, a weighted average of the grid points over global or regional ocean basins is computed, resulting in a time series of OMC of the considered basin (Fig. 5.2). Due to the grid structure, the weights are selected based on Eq. (5.2.2).

In contrast to the spherical harmonic approach, mascons are usually already processed to grids of EWH, where ocean grid points refer to OBP (Fig. 5.2). Modifying other corrections, such as degree-1 coefficients, requires to evaluate those on a grid and apply the differences. Both mascon products considered in this study utilize the degree-1 corrections from TN-13 (Sect. 3.2.1), c_{20} and c_{30} from TN-14 (Sect. 3.2.1) and the ICE6G_D (Peltier et al., 2018) GIA model. The GSFC group removes a mean field between 2004 and 2010, which is slightly different from the time period considered by the JPL group and the spherical harmonic processing above. Furthermore, there are small differences with respect to the level-1 processing by the GSFC and JPL groups, which lead to corresponding differences between the two products, but are not further examined here.

5.3.2 Effect of Individual Processing Choices on Ocean Mass Change

Computing global and regional OMC is significantly influenced by the choice of corrections in each of the processing steps introduced in Section 5.3.1. While Uebbing et al. (2019) focused the investigations on RL05 data at the time, this thesis extends the analysis with focus on the nowadays available RL06 data and the corrections, which predominantly affect the resulting OMC. The results are relevant not only for GRACE/GRACE-FO data, but also apply to Swarm and SLR processing and affect those in the same order of magnitude.

GIA Correction

GIA is the visco-elastic response of the Earth's mantle to ice mass load from a past glacial maximum. Differences in the GIA correction directly translate into global and regional OMC trends. While the correction for satellite altimetry is expressed in geoid height, where the errors of the GIA models lead to relatively small height errors, the same errors are significantly exacerbated when interpreting time-variable mass changes as EWH (Tamisiea, 2011). In fact, the GIA signal results from mantle material flowing beneath the Earth's crust with densities much different from water. Table 5.2 lists trend effects from various GIA models for the global mean OMC.

Table 5.2: GIA effect on global mean ocean mass change. All GIA trends reported here in EWH represent "apparent mass change" computed for a 300 km buffered ocean (Fig. 5.3).

GIA model	**Apparent OMC** $[\frac{mm}{yr}]$
A et al. (2013)	-1.129
ICE6G_C, Peltier et al. (2015)	-1.145
ICE6G_D, Peltier et al. (2018)	-1.019
Paulson et al. (2007)	-1.244
Caron et al. (2018)	-1.322
Klemann and Martinec (2009)	-0.783

Since EWH is computed assuming an elastic Earth, the GIA values reported in table 5.2 are not physically meaningful and represent an "apparent mass change" (Chao, 2016). The GIA correction is modeled as a strictly linear trend and, thus, OMC amplitudes and phases are not affected. Variations between the models are mainly driven by different mantle viscosities of the 1D models. Especially below the Antarctic continent investigations suggest a significantly different viscosity compared of other regions on the Earth (Whitehouse et al., 2012; van der Wal et al., 2015; Martín-Español et al., 2016; Barletta et al., 2018).

It is obvious that correctly accounting for GIA effects is important, when analyzing not only OMC, but also other mass contributions, e.g. from terrestrial hydrology. When the OMC is supposed to be compared to other estimates, or utilized together with satellite altimetry in order to derive sea level budgets, the corresponding GIA corrections should be consistently based on the same model, in order to avoid impacts on the comparisons or closure of the budget.

Substitution of Degree-1 Coefficients

For the RL05 data, the contribution from substituted degree-1 coefficients was found to be in the order of ~ 0.17 mm/yr over the full GRACE era and with corrections from different providers being in good agreement (Uebbing et al., 2019). Considering RL06 data, the effects have become larger. Inconsistencies in the applied degree-1 corrections affect OMC estimates in the range of several 0.1 mm/yr (Tab. 5.3).

Table 5.3: Effect of choosing different degree-1 substitutes for deriving OMC. The trends in EWH for the period 2005-01 until 2015-12 for a 300 km buffered ocean (Fig. 5.3) represent the direct impact on OMC derived from gravity fields including only the degree-1 coefficients. All trends represent the full degree-1 signal.

Degree-1 Provider	**Degree-1 OMC** $[\frac{mm}{yr}]$
RL06 SLR (Cheng et al., 2010)	-0.104
RL06 SLR (Löcher and Kusche, 2020)	0.389
RL06 TN-13 (Swenson et al., 2008; Sun et al., 2016)	0.692
RL05 TN-11 (Swenson et al., 2008)	0.272
Base Inversion (Tab. 6.2, Sect. 6.2.6)	0.304

The trend effect on global mean OMC from substituting degree-1 coefficients from different providers is listed in table 5.3 and directly propagates to the derived OMC estimates. Substitutes from RL06 SLR data provided by CSR and an in-house solution computed by Anno Löcher (Löcher and Kusche, 2020) are compared to the official RL06 TN-13 coefficients and the RL05 TN-11 coefficients. Furthermore, the degree-1 coefficients are extracted from the base inversion solution (Sect. 6.2.6). While the effect from the RL05 correction data agrees well with the inversion output and, to some extent, the in-house SLR solution, the available CSR-SLR coefficients and, especially, the official TN-13 substitutes introduce significant trend effects. For the exemplary time period (2005-01 till 2015-12) the TN-13 solution will introduce almost twice the trend effect, increasing derived OMC by ~ 0.4 mm/yr, compared to the discontinued old TN-11 correction while the CSR-SLR coefficients introduce a trend, which is about the same order of magnitude smaller. Consequently, using only publicly available degree-1 substitutes can introduce trend differences of up to ~ 0.8 mm /yr, which is a major concern with respect to consistency and interpretation of OMC results.

As an in-depth analysis of the Swenson et al. (2008) and Sun et al. (2016) methods is out of scope of this thesis, the reasons for these significant trend differences remain unclear. Nonetheless, it is important to use consistent degree-1 substitutes in order to compare to other solutions and for

generating and analyzing sea level budgets. Unless stated otherwise, the inversion based degree-1 coefficients are used for generating sea level budgets and comparison.

Restoring the AOD1B Product

Satellite gravity missions measure the full mass signal, i.e. the integrated effect of atmospheric, ocean and land hydrology variations, which is equal to OBP over the ocean and can be compared to bottom pressure recorders (Dobslaw et al., 2013). During the level-1 processing, modeled mass changes from atmosphere and ocean with 3 h resolution (6 h for RL05), provided by the AOD1B product, are removed before accumulating and solving the time-variable gravity normal equations. The model simulation neither represent reality nor the necessarily best estimate on spatial and temporal scales. In contrast to land applications, the AOD1B ocean part has to be restored for deriving OMC and OBP. For restoring the reduced signals, the processing centers provide four monthly averaged products (Flechtner et al., 2015; Dobslaw et al., 2017b): (1) the GAA product containing the modeled atmospheric mass changes, (2) the GAB product including the dynamic mass contribution to OBP but with the static atmosphere portion removed (this is not removed for RL05 and prior), (3) the sum of GAA and GAB denoted as GAC and (4) the GAD product containing simulated OBP. The difference between GAC and GAD is due to small upper-air density anomalies and the GAD is set to zero over the continents (Dobslaw et al., 2017b). While all these modeled products are provided without error information, model imperfections still exist.

For deriving OBP, the GAD product can be restored directly in the corresponding processing step

$$\mathrm{OBP} = \mathrm{GSM} + \mathrm{GAD}, \tag{5.3.2}$$

where GSM represents the original level-2 Stokes coefficients, GSM_{L2}, processed as described in Section 5.3.1, including corrections for degree-1, c_{20}, c_{30} and GIA. The OBP derived by (5.3.2) can be compared to OBP recorders (Sect. 7.2.2). But, it does not represent the ocean mass component in the context of sea level budgets in combination with satellite altimetry, since altimetry is corrected for the Inverse Barometric (IB) effect (Eq. 3.1.7, Sect. 3.1.1). The IB correction accounts for the ocean reacting to surface pressure variations, but not to mean surface pressure change averaged over the total ocean. The corresponding averaging kernel is defined to be the total ocean area (Andersen and Scharroo, 2011) without any buffer zones (Fig. 5.3), although this is not always the case (Mathers and Woodworth, 2006; Ponte, 2006).

Consistently correcting the time-variable gravity data with respect to altimetry and the applied IB correction, requires removal of the surface pressure component, $\widehat{\mathrm{GAA}}$, from the GAD product, which is not directly available to the user

$$\mathrm{OMC} = \mathrm{GSM} + \mathrm{GAD} - \frac{1}{A_{oce}} \int_{\Omega_{ib}} \widehat{\mathrm{GAA}}(\omega) d\omega, \tag{5.3.3}$$

where the integral is evaluated over the total ocean area used in the altimetry IB correction. Since the GAD product is theoretically defined as the sum of the GAB and $\widehat{\mathrm{GAA}}$, it has been suggested to utilize the ocean mean of the GAD product instead (Chambers and Bonin, 2012; Feng and Zhong, 2015). However, this requires the total ocean mean of GAB to be exactly zero, which is enforced by keeping the total ocean mass constant at each time step of the ocean model run after removing a temporal average (Dobslaw et al., 2017b; Flechtner et al., 2015). This allows to compute an altimetry-IB consistent correction

$$\mathrm{OMC} = \mathrm{GSM} + \mathrm{GAD} - \frac{1}{A_{oce}} \int_{\Omega_{ib}} GAD(\omega) d\omega. \tag{5.3.4}$$

Similarly, it is possible to directly utilize the GAB product for RL06 data (Dobslaw et al., 2017b)

$$\mathrm{OMC} = \mathrm{GSM} + \mathrm{GAB}, \tag{5.3.5}$$

which significantly simplifies the restoration of the AOD1B background model for deriving OMC.

Theoretically, equations (5.3.2), (5.3.4) and (5.3.5) are valid for all degrees and orders, including degree-1 and degree-0. Restoring the GAB (or GAD) degree-1 coefficients depends on the choice of degree-1 substitutes (Tab. 5.3). Coefficients from SLR generally contain the complete degree-1 (ocean) mass signal, while the methods by Swenson et al. (2008) and Sun et al. (2016) are usually derived relative to the AOD1B background model. The degree-0 coefficient does not affect OMC computation, since it introduces a constant value, which is then, again, removed when averaging over the ocean.

In the past, different implementations of the restoration have led to significant inconsistencies, which severely impacted the estimated OMC trends. When strictly following the Johnson and Chambers (2013) processing, one would compute the ocean average in (5.3.4) not over the full ocean area but rather over the ocean basin reduced by a 300 km buffer zone (Fig. 5.3), which would be equal to not restoring any AOD1B background model at all, since the ocean mean GAD value cancels out (Uebbing et al., 2019).

Table 5.4: Effect on OMC of averaging over an ocean basin including a 300 km buffer when restoring the GAD product instead of using the full ocean basin applied for the altimetry IB correction. The trends are provided in EWH for the period 2005-01 until 2015-12 for a 300 km buffered ocean (Fig. 5.3).

AOD1B Release	**Trend Effect** $[\frac{mm}{yr}]$
RL05	-0.365
RL06	-0.115

The effect on OMC from restoring the AOD1B-GAD incorrectly is in the range of about 0.1 mm/yr for RL06 data while it was found to be 0.3 to 0.4 mm/yr for RL05 data (Uebbing et al., 2019). The trend effect directly translates to the budget closure error when combining gravity and altimetry data in the context of sea level budgets. This has been the case for several published budgets (e.g., Dieng et al., 2015; Piecuch and Quinn, 2016; Chambers et al., 2017), which utilized a publicly available global mean OMC time series, which was computed by strictly following the Johnson and Chambers (2013) processing. Nowadays, it is much more convenient to utilize the GAB product for deriving altimetry consistent OMC when dealing with spherical harmonic level-2 data. However, the GAD ocean mean is still required for transforming the OBP included in mascon products over the ocean to OMC, which can then be regionally averaged.

Pole Tide Correction

The pole tide correction (Wahr et al., 2015), which modifies the c_{21} and s_{21} coefficients is usually removed by the processing centers. However in the past, the removal of the mean pole has been handled differently by each processing center leading to a remnant pole tide signal, which varied for each center. For the RL06 data this is no longer relevant since all processing centers nowadays consistently account for the effect following the updated IERS conventions (Petit and Luzum, 2010) during their processing. Nonetheless, for older datasets based on RL05 data or prior releases, the correction has to be applied in order to correctly account for the pole tide impact in the order of $\sim$ 0.1 mm/yr of global mean OMC between individual processing centers (Uebbing et al., 2019). Note that the pole tide is not considered when strictly following the Johnson and Chambers (2013) processing.

5.4 Steric Sea Level from Temperature and Salinity Data

Steric sea level change is computed from individual in-situ profiles of temperature and salinity variations within a water column from the sea surface down to the sea floor. Profiles can be provided as gridded data based on models (e.g., Timmermann et al., 2009), ocean re-analysis (e.g., Zuo et al., 2019) or in-situ profiles gridded using objective analysis (e.g., Hosoda et al., 2010). Furthermore, individual in-situ profiles (e.g., Cabanes et al., 2013) can be analyzed directly. Each of the aforementioned data sets have certain limitations, which become relevant depending on the area and time period of interest, especially, in the context of deriving sea level budgets.

Systematic deployment of Argo floats started in 2000 and reached the target number of about 3000 floats by 2005 with, nowadays, 3000-3800 floats in operation depending on season[1]. Float coverage before 2005 has been sub-optimal, with only isolated profile data or profiles along defined shipping routes, which limits the effective (global) use of profiles to time periods after 2005. Theoretically, the Argo program aims at a homogeneous global coverage of in-situ profiles, but in reality, it is limited by several factors (Figs. 3.7 and 5.4). Shallow ocean regions, such as the North Sea or the Indonesian Sea, are not covered at all, or with only some sporadic profiles. Other regions, e.g. the Bay of Bengal, allow retrieval of in-situ profile data with high spatial and temporal coverage (Fig. 3.7). Since the Argo buoys float freely in the ocean, they are prone to follow the large and small scale current systems, which leads to accumulation of floats and, thus, corresponding observations in some regions. The availability of data in the Arctic and Antarctic ocean varies with season and sea-ice coverage. Therefore, relying on in-situ profile data alone to infer steric sea level change information may prove difficult, even on global scales (Fig. 5.4, A).

From figure 5.4 it becomes clear that the steric sea level strongly depends on the choice of dataset and the corresponding processing, each of which has its own (dis-)advantages. Directly utilizing selected in-situ profiles will provide actual observations, which is desired when assimilating the data in re-analysis or introducing them as additional input into the inversion (Sect. 7.4.4). Nonetheless, it is limited to the relatively sparse observation positions making it less useful in the context of deriving global or regional steric sea level changes, unless comparisons are limited to the floater positions. Gridded Argo data obtained from objective analysis, such as the SIO and IPRC datasets used here, allow for regional data analysis where possible (Fig. 5.4, B), especially in regions with good Argo coverage (Fig. 3.7). However, each producer applies their own approach in spatio-temporal gap filling, data editing and bias correction (Boyer et al., 2016). Ocean model and re-analysis data (Fig. 5.4, C) provides the best data availability, these datasets are limited with respect to the model itself, which will influence the reported temperature and salinity profiles at each position. Furthermore, the model implements certain ocean dynamics that do not necessarily reflect reality, such as shallow and deep currents that redistribute heat. In addition, re-analysis data are not entirely independent as these assimilate other ocean data, e.g. satellite altimetry, besides in-situ profiles.

Converting gridded or in-situ temperature and salinity profiles to steric sea level change, generally, follows equation (2.3.10). In this thesis, the Gibbs Sea Water Toolbox[2] is utilized, which implements the functional relationships introduced in section 2.3. Depending on the data product, temperature may be provided as in-situ, potential, or conservative temperature and, thus, has to be converted, first. Afterwards, the density quotients from equation (2.3.10) can be integrated over the whole water column or chosen sub-layers of the ocean. Generally, the steric change is derived with respect to standard sea level (Sect. 2.3), but this can be shifted to a mean steric sea level by subtraction of an appropriate climatology. While thermo-steric effects dominate on global scales, significant regional halo-steric variations exist, e.g. in the Arctic oceans (Lyu et al., 2022). As most products provide gridded information, global and regional averages are readily derived applying an

[1] https://argo.ucsd.edu/ (last accessed: 21.01.2022)
[2] http://www.teos-10.org/ (last accessed: 25.01.2022)

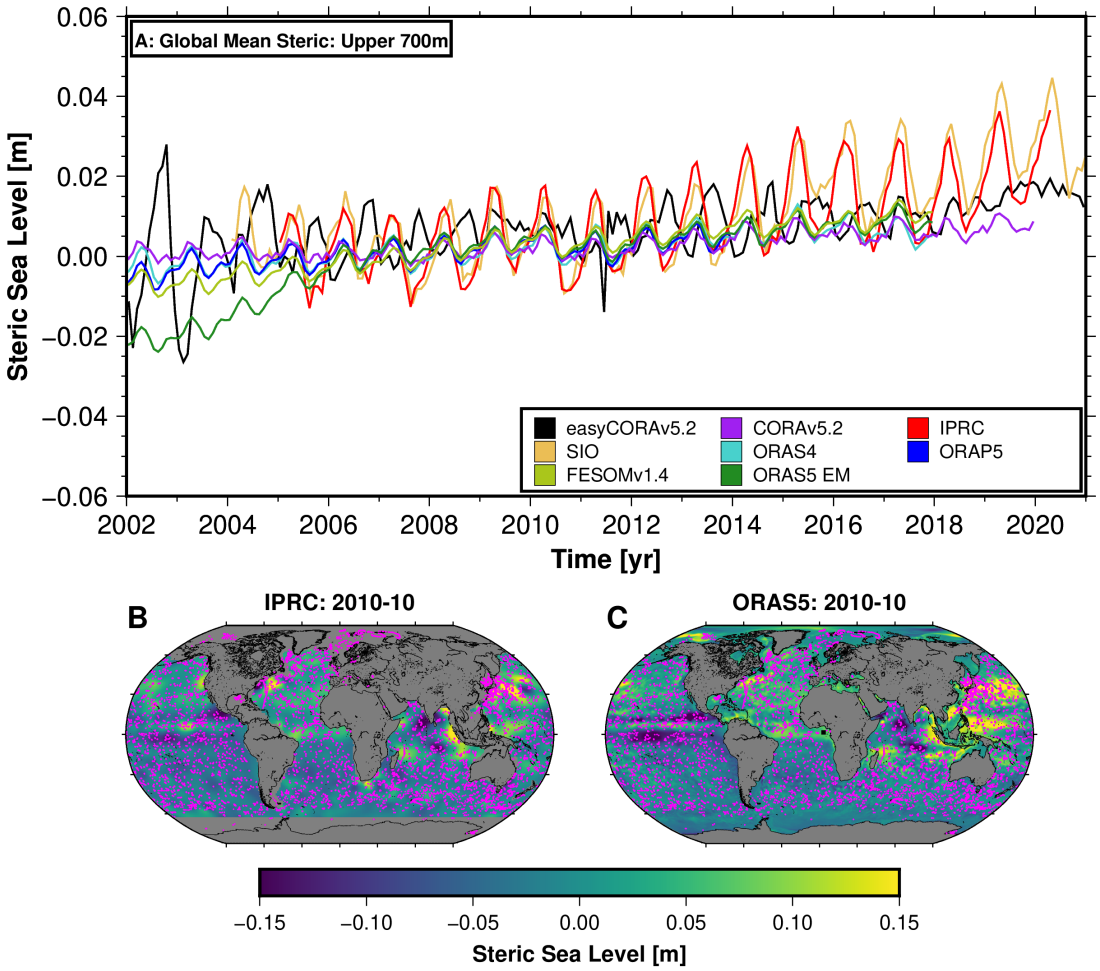


Figure 5.4: Steric sea level derived from different datasets. A: Comparison of global mean steric sea level from the upper 700 m based on individual products utilizing in-situ profile data. All time series have been derived converting gridded 4D temperature and salinity data to steric sea level following equation (2.3.10). B: Exemplary steric sea level of the objective analysis IPRC product from 2010-10. C: Exemplary steric sea level from the ORAS5 re-analysis for 2010-10. Both, B and C are overlayed with the quality controlled easyCORA in-situ profile positions for the corresponding month.

appropriate weighting scheme, e.g. cosine of latitude weights (Eq. (5.2.2)) for an equidistant grid.

When directly dealing with measured in-situ profile data, it is necessary to apply float-dependent calibration parameters and carefully remove outliers. Calibration parameters are not always delivered for each float and are usually only available in delayed mode data. In this thesis, in-situ profiles of temperature and salinity are extracted from the easyCORA dataset, which, besides Argo, includes data from CTD and XBT sensors (Sect. 3.3). The data are already calibrated and a first quality check has been applied (Cabanes et al., 2013). However before the data are used for comparison or introduced into the inversion (Sects. 6.2.1 and 7.4.4), further, relatively strict quality checks are applied. This significantly reduces the number of available monthly in-situ profiles by about 40 to 50%. First, the pressure levels of the delayed mode data are checked for outliers and unrealistic values. Floats which report positions over land areas are removed. Profiles which do not provide temperature and salinity information in the upper 10 m of the ocean are discarded. Similarly, extremely short profiles with less than three depth levels of data, or those that include huge jumps in depth, or with non-continuous depth levels are removed. Furthermore, deep Argo

floats with data from below 3000 m are discarded and those profiles, which provide data significantly above the sea surface. Finally, the quality flags for temperature and salinity observations are checked to remove further profiles containing too many bad measurements.

Standard errors for single temperature measurements are reported with 0.01 to 0.1 °C and 0.01 psu for salinity observations. In addition a depth error of 2.5 m is assumed based on reported pressure errors of Argo floats. A Monte-Carlo simulation is performed with 1000 runs, varying temperature, salinity and depth/pressure values based on their reported errors in order to derive standard deviation error estimates for the thermo- and halo-steric sea level changes for each profile. The monthly output contains the floater positions, estimated thermo- and halo-steric sea level change for depth ranges 0 to 700 m and below 700 m and the corresponding errors. Furthermore, a quality measure between 0 and 1 indicates the percentage of the total profile that has been used after applying the quality checks above. Due to the strict selection of profiles due to potentially bad data, as described before, the percentage is usually above 90%.

Chapter 6

Combination of Space Geodetic Observations in a Global Inversion Framework

For investigating individual drivers of global and regional sea level rise, total sea level change is split into mass and steric components using independent observation or model data. Generally, sea level budgets consist of a combination of individually analyzed data products, which are only combined at the very end of the processing chain based on linear trend estimates. This often and easily leads to inconsistencies, which can severely affect the closure of the budget. One of the main ideas behind the global inversion method (Rietbroek, 2014; Rietbroek et al., 2016) was to jointly analyze GRACE and altimetry data in order to derive an overall more consistent sea level budget.

A general overview of the inversion framework can be found in figure 1.1. The inversion fits temporally varying scaling factors utilizing GRACE and altimetry data to a predefined fixed set of spatial patterns; these patterns are called "fingerprints" and serve as empirical spatial basis functions. They are supposed to model, e.g., the melting in a certain glacier basin and represent the corresponding spatial effect on global and regional sea level change. The underlying assumption of the fingerprint inversion is that different contributors can be combined linearly.

In this chapter, Section 6.1 will introduce the generation and sources of the inversion fingerprints. Section 6.2 deals with the basic inversion setup in this thesis with focus on the differences to Rietbroek et al. (2016) and including an introduction of a base inversion (Sect. 6.2.6) and corresponding extensions.

6.1 Building Inversion Fingerprints

The predefined spatial patterns, or fingerprints, for the global inversion are generally based on two approaches. Mass contributions to sea level change usually originate from land-based sources and are represented by spatial patterns derived using the SLE (Eq. (2.2.2)). Steric contributions, e.g., are already confined to the ocean by default and the most dominant spatial patterns can be extracted from a Principal Component Analysis (PCA) (see Appendix B). The individual subsections provide more detail on the derivation of fingerprints for each driver of total sea level change.

6.1.1 Land Glaciers

Land glaciers store large amounts of fresh water in the form of ice and are usually located in high mountain range regions on every continent. Due to the limited resolution of the gravity observations it is not possible to separate each individual glacier. Consequently, neighboring glaciers are

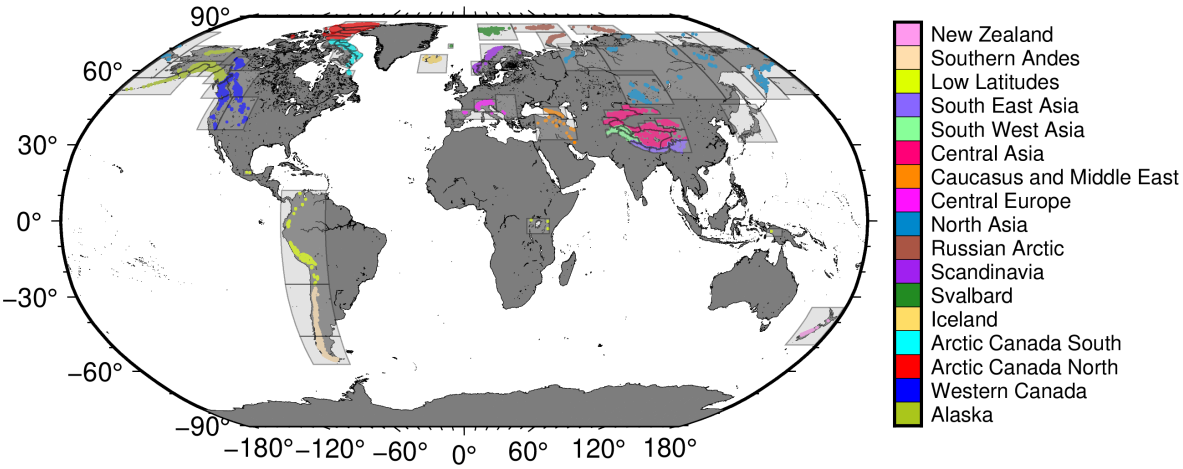


Figure 6.1: Glacier locations and sub-regions extracted from the Randolph Glacier Inventory version 6 (RGI Consortium, 2017). The glaciers in each of the 68 sub-regions, indicated by shaded outlines, are the basis for generating corresponding sea level fingerprints.

grouped and treated as one melting region.

In the past (Rietbroek et al., 2016; Rietbroek, 2014), the glacier database for the inversion has been created by combining glaciers positions from the Randolph Glacier Inventory (RGI) version 1.0 (Raup et al., 2007) and the World Glacier Inventory (NSIDC, 1999), leading to the formation of glacier clusters. For these, each glacier was interpreted as a unit load and, subsequently, added for each glacier region, resulting in combined cluster surface loads. This included two assumptions (1) all glaciers are approximately the same size and (2) the temporal melting rate of each glacier within the cluster is the same. While the first effect can be mitigated using area dependent disk-loads, the second effect will not be true since the changes of individual glaciers are related to their geometry, local precipitation and seasonal temperature variations (Huybers and Roe, 2009).

In this thesis, the RGIv6.0 (RGI Consortium, 2017) is employed, instead (Sect. 3.4.3). In contrast to RGIv1.0 the updated version provides significantly more glaciers and is divided into 19 regions, which are further separated into sub-regions (Fig. 6.1) including peripheral glaciers in Greenland and Antarctica. Since the latter cannot be separated from the melting signal of the neighboring ice sheets, those two regions will be ignored and are, thus, not shown in Fig. 6.1. In addition, RGIv6.0 also provides an estimate of each individual glacier area allowing to derive weighted cluster surface loads $T^{\text{sub-region}}(\lambda,\theta)$ for each sub-region from

$$T^{\text{sub-region}}(\lambda,\theta) = \sum_{n,m}^{\infty} T^{\text{sub-region}}_{n,m} Y_{n,m}(\lambda,\theta), \tag{6.1.1}$$

$$\text{with } T^{\text{sub-region}}_{n,m} = \frac{1}{N_{1\text{Gt}}} \frac{1}{\sum_j w_j} \sum_{j\in\text{sub-region}}^{J} w_j Y_{n,m}(\lambda_j,\theta_j), \tag{6.1.2}$$

where w_j is the area weight, i.e. the glacier area, associated to each glacier and $N_{1\text{Gt}}$ normalizes the surface load to 1 Gt. Each individual glacier is represented by a point mass load at its location, which can be represented by the spherical harmonic coefficients $Y_{n,m}(\lambda_j,\theta_j)$.

Fingerprints are then created by applying the sea level equation to the derived surface loads for each sub-region, yielding 68 fingerprints of self-consistent sea level. In contrast, Rietbroek et al. (2016) only utilized 16 glacier fingerprints, while also assuming the same size for each individual glacier. The RGIv6.0 based glacier regions have also been analyzed in Wouters et al. (2019). The

division into individual sub-regions mitigates the effect of the second assumption above, as each of the 68 sub-regions is adjusted individually, but it still holds within each of the sub-regions.

6.1.2 Ice Sheets

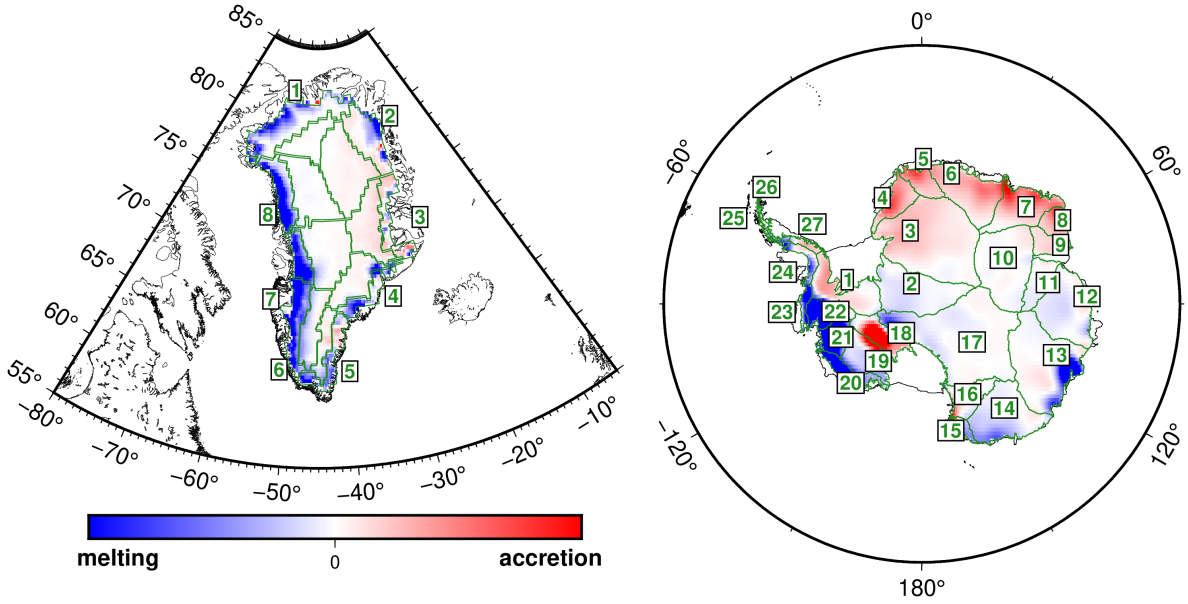


Figure 6.2: Drainage basins for Greenland and Antarctica, which are the basis for generating corresponding sea level fingerprints. The Greenland basins are extracted from Wouters et al. (2008) while the Antarctic basins are based on Zwally and Giovinetto (2011). The background net ice mass loss and accretion patterns are derived based on ice-altimetry data by L. Schröder et al. (2019) and Strößenreuther et al. (2020)

The fingerprints for the Greenland and Antarctic ice sheets are derived based on the eight drainage basins of Wouters et al. (2008) and the 27 basins from Zwally and Giovinetto (2011), respectively (Fig. 6.2). For Greenland each of the 8 basins is again sub-divided into sections below and above 2000 m elevation. Each basin is associated with a surface load, which conserves mass globally and leads to a self-consistent sea level response after applying the SLE (Sect. 2.2). In the past (Rietbroek et al., 2016; Rietbroek, 2014), a uniform surface load distribution over the whole basin area has been assumed. However, mass changes within the basins can vary considerably on a spatial scale (Fig. 6.2).

For the updated inversion introduced in this thesis, the total load within each basin is not distributed uniformly but according to the trend pattern derived from ice-altimetry (L. Schröder et al., 2019; Strößenreuther et al., 2020). While the effect on self-consistent sea level patterns is small, it allows a more realistic modeling of the mass variations in each of the individual Greenland and Antarctic basins in combination with the observations from GRACE and altimetry (Sects. 7.2.3 and 7.2.4). Similar to the glacier basins, the ice sheet fingerprints are normalized to 1 Gt. The choice of background pattern should be related to what the fingerprints represent. In this thesis, ice-altimetry height trends have been used. When interpreting these as mass change patterns a uniform density over the basin is implicitly assumed.

6.1.3 Terrestrial Hydrology

While melting of land glaciers and the Greenland and Antarctic ice sheets is usually confined to a defined basin area, terrestrial hydrology contributions to sea level change can not always be attributed to a certain area, such as a river catchment basin. An early version of the inversion

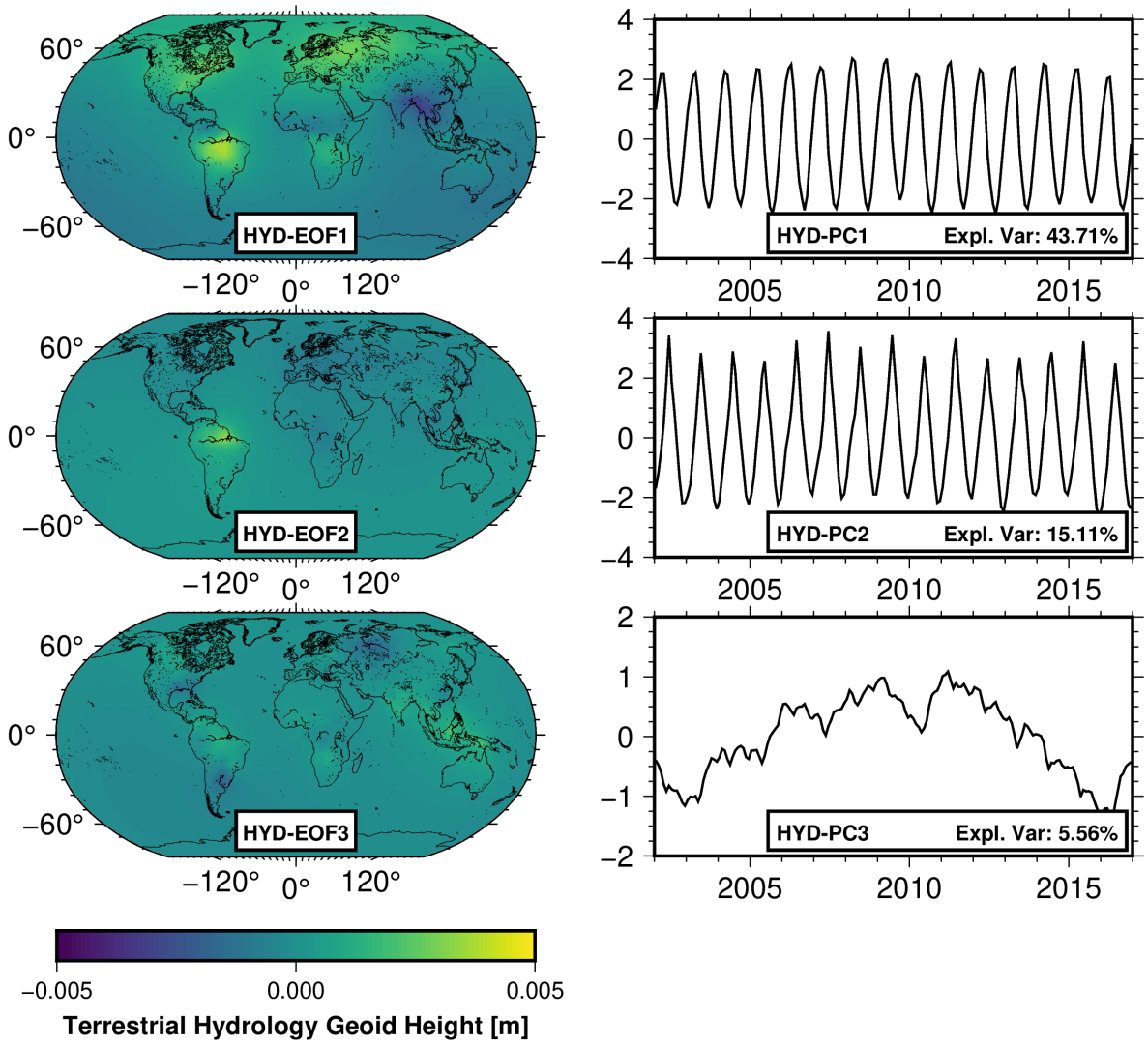


Figure 6.3: First three Empirical Orthogonal Function (EOF)s, Principal Component (PC)s and corresponding explained variances based on the WGHM model (Sect. 3.4.2). The EOFs are utilized as fingerprints within the inversion approach where the PCs are readjusted based on the gravity and altimetry observations.

approach (Jensen et al., 2013) utilized hydrological river catchment basins, assuming constant mass changes within each basin and generated fingerprints similar to the glacier and ice sheet fingerprints assuming uniform mass changes. However, this approach had two major issues: (1) assuming constant mass changes over the whole basin area is far from reality and (2) all areas between the 33 largest considered catchments are completely ignored. Consequently, hydrological model output from the WGHM is used for deriving fingerprints of sea level change related to variations in the terrestrial water cycle. In this thesis, an updated version of the hydrological mode, i.e. WGHMv2.2d (Döll et al., 2020), incorporating improved model physics and input forcing is employed including model data from 2002-2017 (Sect. 3.4.2); Rietbroek et al. (2016) utilized an earlier WGHM version (Döll et al., 2003) limited to model data from 2002-2009.

Summing over all available water storage compartments at each grid location of the WGHM results in modeled TWS, which can also be observed from satellite gravity. Not all models are suitable for this approach as some models either cover only certain regions or do not represent all compartments equally well; the Global Land Data Assimilation System (GLDAS) model (Rodell et al., 2004) utilizes the same equations for ground water representation as for soil moisture. The

WGHM model also provides TWS information in regions covered by land glaciers and over Greenland. However, the model is not suited to simulate accurate ice mass changes and the model estimates in these regions will be erroneous. Consequently, those regions, which are represented by the glacier and ice sheet fingerprints (Sects. 6.1.1 and 6.1.2), are removed, i.e. set to zero, in the model output before further processing. In addition, the data is detrended at each grid point, since the time series at some grid points exhibit large unrealistic trends.

The TWS model output from the WGHM model is decomposed using PCA (Appendix B). For the next step, only the spatial variations stored in the EOFs is of interest. This results in one fingerprint for each mode of the PCA decomposition. The number of selected EOFs for the fingerprints is defined by the ∼99% threshold of variance explained.

So far the EOFs do not contain any values over the ocean, since the hydrological model only provides information over land areas. Consequently, the spatial TWS information of each EOF is interpreted as a surface load and used as input for the SLE (Sect. 2.2) in order to derive the corresponding passive sea level response. For the ∼99% threshold this results in 100 fingerprints; in Rietbroek et al. (2016) the threshold was reached at 60 fingerprints, due to the significantly shorter model time series. The first three fingerprint modes are shown in Fig. 6.3. While the variations in the ocean are of one order of magnitude smaller compared to the land surface, they, nonetheless, introduce corresponding large scale sea level variations, which cannot be neglected in order to close the sea level budget.

6.1.4 Internal Mass Variations

The Internal Mass Variations (IMV) contribution is characterized by transports of water masses within the ocean due to currents and other effects, without considering additional water mass input from hydrology or melting of land glaciers or the Greenland and Antarctica ice sheets. It basically represents dominant Ocean Bottom Pressure (OBP) signals and their temporal evolution, e.g., around Australia or other shallow and ocean shelf regions (Fig. 6.4). Similarly, some mass signals in shallow oceans associated with ENSO events can be seen in the second PC (Fig. 6.4). IMV can theoretically be derived from every ocean model, but one has to account for the artificial fluctuations in total ocean mass induced by the Boussinesq approximation underlying basically every ocean model (Stewart, 2008; Dobslaw et al., 2017b). These fluctuations have been accounted for by removing a homogeneous shell of mass at every time step for the modeled ocean variation as part of the AOD1B background model applied during estimating the level 2 (RL06) GRACE gravity fields (Dobslaw et al., 2017a; Dobslaw et al., 2017b).

The first idea would be to utilize the GAD product, which directly corresponds to the OBP output of the MPIOM (Sect. 3.4.4). However, the inversion approach couples gravity and altimetry observations in a combined estimation. This means the observations and the corresponding modeling of individual contributions to the sea level budget have to be consistent, requiring additional removal of the mean GAD value over the total ocean area in order to achieve consistency with standard altimetry solutions. This was the approach that had to be taken with AOD1B data up to release 05. Starting with AOD1B release 06, it is possible to utilize the GAB product instead, which accounts for the inverse barometric effect (Sect. 3.4.4), in consistence with altimetry. Furthermore, it only represents the modeled internal mass variations within the ocean resulting in a zero trend, when averaging over the total ocean area, i.e. it includes no mass transport in or out of the ocean. The latter is covered by other fingerprints. In previous inversions (Rietbroek, 2014; Rietbroek et al., 2016), the AOD1B-GAC product has been subtracted from altimetry in order to achieve consistency with the monthly GRACE L2 spherical harmonics (cf. Sect. 6.2.5).

Since the inversion is performed on a monthly basis, the three hourly AOD1B-GAB data (Sect. 3.4.4) is averaged to monthly mean GAB from 1990 onward. In the next step, a PCA is performed (Appendix B) in order to extract the most dominant modes of IMV. The resulting EOFs (Fig. 6.4)

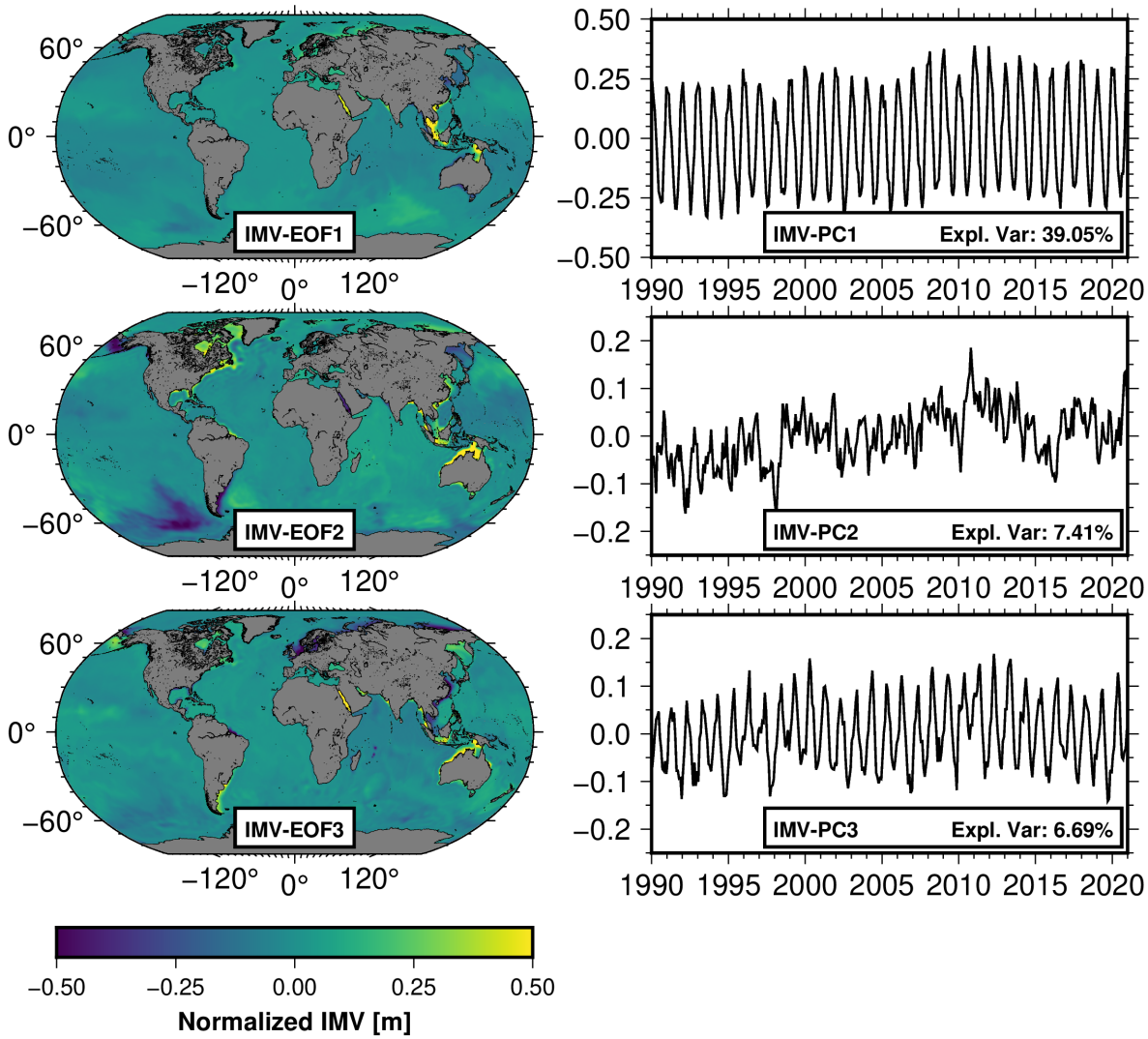


Figure 6.4: First three EOFs, converted from EWH to geoid height, PCs and corresponding explained variances based on the AOD1B-GAB product (Sect. 3.4.4). The EOFs are utilized as fingerprints within the inversion approach where the PCs are readjusted based on the gravity and altimetry observations.

can be directly interpreted as sea level fingerprints in EWH, which is then converted to geoid height and uplift according to the self-consistent sea level theory (Sect. 2.1.2) underlying the inversion approach.

6.1.5 Steric Fingerprints

Steric sea level change is caused by variations in temperature and salinity leading to density anomalies in the water column from the sea surface down to the sea floor, thus, expanding or contracting the water volume. In first approximation, this represents a purely geometric effect, which is not visible in gravity observations; in reality the density variations also cause baroclinic transports of water masses, causing OBP variations, modeled by the IMV fingerprints. In particular, the steric effects can only be linearly separated from the IMV changes as a first order approximation.

In general, there are two available data sources to identify modes of steric sea level variations: (1) observational data from individual Argo floats, which are then inter- and extrapolated on a grid using objective analysis (e.g., Ishii and Kimoto, 2009) and (2) ocean model data or ocean model reanalysis data, where the latter also assimilates in-situ profile observations. An earlier inversion (Rietbroek, 2014) utilized gridded observation data from Argo down to 1500 m (Ishii and Kimoto,

2009). However, this lead to several disadvantages: (1) The limited observation depth does not provide comprehensive information of the total water column leading to significant residual deep ocean steric signals; (2) the objective analysis method used for gridding the in-situ information can lead to significant errors in regions, where there is no data at all or only sparse temporal sampling of temperature and salinity are available (Fig. 3.7); and (3) this would introduce interdependencies when utilizing in-situ steric profile data as additional input in the inversion (Sect. 7.4.4). In Rietbroek et al. (2016), the steric data was replaced with FESOM version 1.2 model (Brunnabend et al., 2012) data for the full ocean depths. The benefit of FESOM data are variable-sized finite elements, allowing to obtain steric sea level with higher resolution in areas of interest and closer to the coast. Since FESOM does not assimilate observational data, it tends to distribute most steric variability in the upper part of the ocean. Furthermore, version 1.2, in combination with the employed forcing, significantly overestimated the steric sea level trend.

Generally, processes in the upper 1000 m of the ocean are much better understood compared to the deeper ocean. Therefore, most studies focus on the upper 1000 m or upper 700 m of the ocean, with the latter having historical reasons due to ship-based eXpendable BathyThermograph (XBT) measurements, with a maximum observation depth of 700 m. In this thesis, the total steric signal is split into the upper 700 m of the ocean and the "deep" part including everything below 700 m. This not only allows for a better comparison with published studies when interpreting the results (Sect. 7.2.8), but also enables the utilization of in-situ profile data, which not always cover the whole water column, but mostly the upper ocean.

The steric EOFs are based on ocean model data providing modeled temperature and salinity on a defined grid in monthly time steps. For this, the underlying ocean model (Sect. 3.3.2) can either assimilate data, such as ORAS4 (Balmaseda et al., 2013) or ORAS5 (Zuo et al., 2019), or run solely based on atmospheric and other forcing data, e.g. the FESOM model (Wang et al., 2014). Due to the high spatio-temporal variability of steric sea level change, the model data should cover most of the investigated time periods. Otherwise there might be biases in the residuals (cf. Sects. 7.3.6, 7.4.2 and 7.4.3). In this thesis, the ORAS5 model-based fingerprints are utilized, unless stated otherwise.

Comparing the global mean steric sea level change from figure 6.5, the differences of ORAS5 compared to the other models are obvious. The model behavior is significantly influenced by the start of the assimilation of in-situ data, at the end of the 1990s, and by a switch in atmospheric forcing data and in-situ assimilation datasets in 2008 and 2015 (Zuo et al., 2019, Fig. 3). In addition after 2015, salinity sensors on several floats experienced unusually high drift rates resulting in impacts on the steric sea level (Wong et al., 2020). Consequently, it is necessary to apply an additional trend correction during the computation of the steric sea level change from the temperature and salinity ORAS5 data. The trend jumps are corrected to be on the same level as the ORAS5 model during 2005-2015, which is in line with the other models. Since the data that went into the PCA was not detrended, the resulting EOFs include spatial patterns related to linear trends. The correction, applied to the model data before the PCA, avoids propagation of the erroneous trend patterns into the fingerprints. Otherwise, those would lead to unreasonably high steric trend estimates from the fingerprint inversion.

In order to derive steric fingerprints, the modeled temperature and salinity data is first converted to steric sea level change (Sect. 2.3.1). In this thesis, the ensemble mean from five runs of ORAS5, including a base run and four runs with perturbed starting conditions and forcing data (Zuo et al., 2019), is used as basis for the steric fingerprints. During the process a mean steric sea level signal, which in principle is equal to the Mean Dynamic Topography (MDT) (Becker, 2012) is removed, producing steric sea level anomalies, which are consistent with altimetry observations. The resulting monthly steric sea level change is then decomposed into EOFs, capturing the spatial variations and PCs referring to the temporal evolution by applying PCA. The EOFs of steric

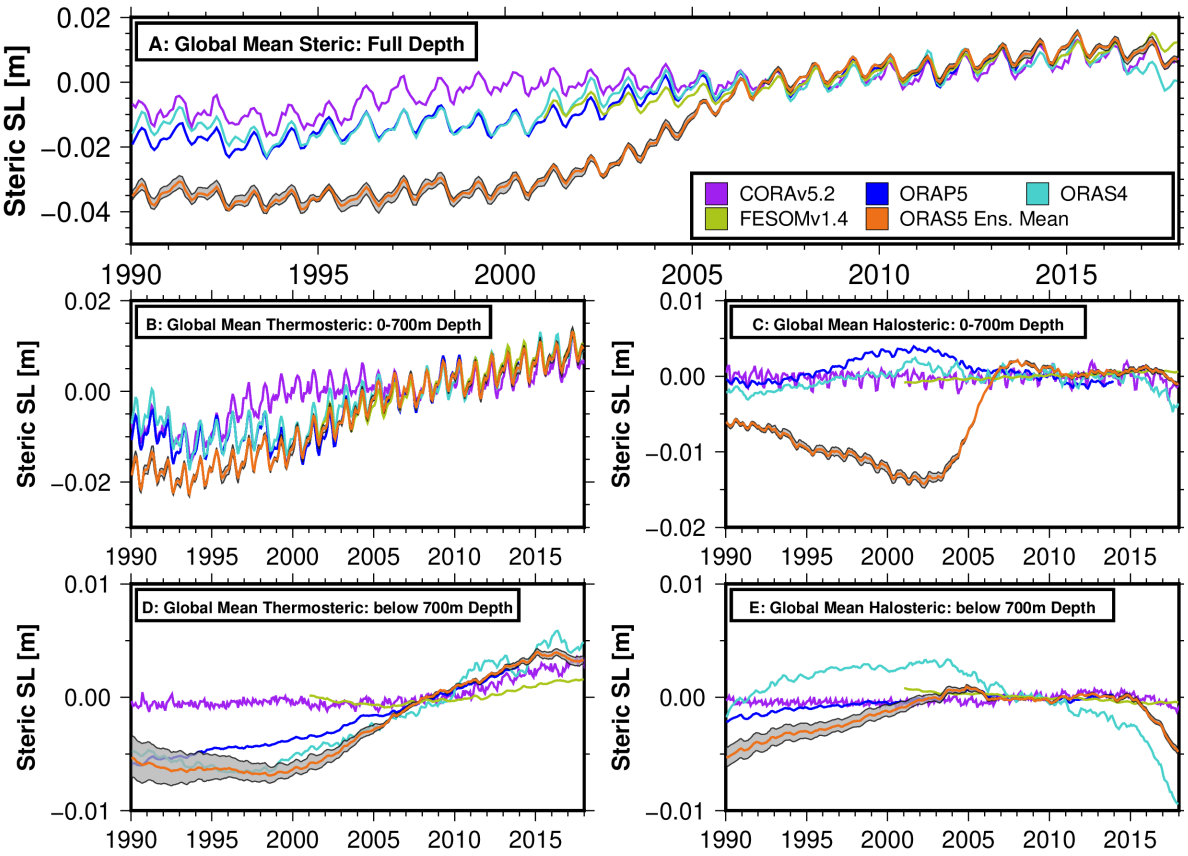


Figure 6.5: Global mean steric sea level model comparison. A: Sum of thermo- and halosteric sea level for the whole water column. Thermosteric (B) and halosteric (C) SL from the upper 700 m depth of the water column. Thermosteric (D) and halosteric (E) SL from the water column below 700 m depth.

sea level anomaly variations are then directly utilized as steric fingerprints within the inversion (Fig. 6.6 and 6.7). The number of utilized fingerprints is defined by the percentage of explained variance by each of the EOFs resulting from the PCA (Appendix B). For the steric contribution the number of fingerprints is limited to 200 for the upper 700 m, corresponding to roughly 99% of explained variance, and 50 for the deep steric effect; the latter being more uncertain and, thus, only major spatial variations from the first 50 EOFs, roughly referring to 80% explained variance, are considered. From a physical perspective, the small scale heat anomalies in the deep ocean are not causing corresponding small-scale sea level anomalies.

6.1.6 Glacial Isostatic Adjustment

The effect of GIA acts differently on GRACE-observed mass changes, expressed in EWH, and geometric altimetry observations (Tamisiea, 2011). These secular GIA influences on the observed uplift, geoid variation and corresponding relative sea level are not negligible. Instead, these have to be considered for the gravity and altimetry measurements combined within the inversion approach. When expressing the GIA as a change of sea level, e.g. observed by altimetry in the CF frame, the degree-1 terms are generally included. In contrast, the GIA solution applied to GRACE data in the CM frame does not consider degree 1.

For the correct modeling within the inversion framework it is also necessary to consider the degree 0 contribution to RSL from GIA induced changes in the volume of the ocean basin, which lead to uniform uplift shift, which is observed by altimetry. Consequently, it is necessary to account for these when modeling the GIA effect on altimetry. An altimeter will measure changes in terms of self-consistent sea level theory (Sect. 2.2) where the quasi-spectral RSL change, $\tilde{S}$ (Sect. 2.2),

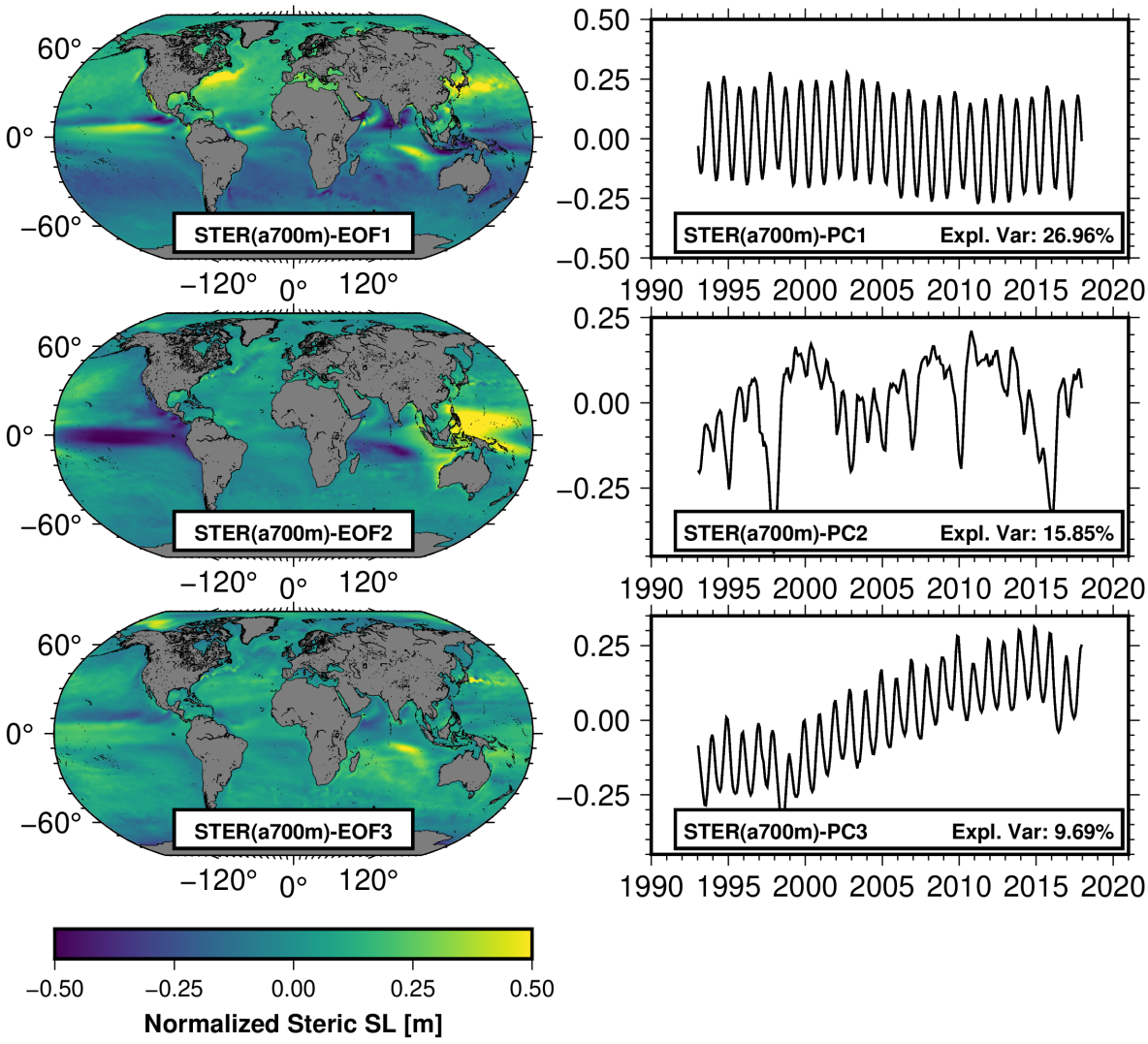


Figure 6.6: First three EOFs, PCs and corresponding explained variances based on the ORAS5 ensemble mean steric sea level change of the upper 700 m ocean depth (Sect. 3.3.2). The EOFs are utilized as fingerprints within the inversion approach where the PCs are readjusted based on the gravity and altimetry observations.

is given by

$$\tilde{S} + U = N + \frac{\Delta\phi}{g}, \tag{6.1.3}$$

where N and U represent the geoid and uplift related sea level change, respectively. The small term $\frac{\Delta\phi}{g}$ ensures mass conservation. It is assumed that the ocean mean of the GIA induced RSL is zero. This makes sense since present day mass flux in and out of the ocean from the employed ice history model forcing for the GIA models is zero by definition (e.g. A et al., 2013; Peltier et al., 2018). This means that the mass content within the total ocean does not change due to GIA. This relation can be expressed as

$$\tilde{S}^{(\mathrm{GIA})}_{oce} = 0 = \frac{1}{A_{oce}} \int_{oce} \tilde{S}^{(\mathrm{GIA})} d\omega, \tag{6.1.4}$$

the uniform shift $\left(\frac{\Delta\phi}{g}\right)^{(\mathrm{GIA})}$ can be interpreted as the degree 0 coefficient of the quasi spectral sea

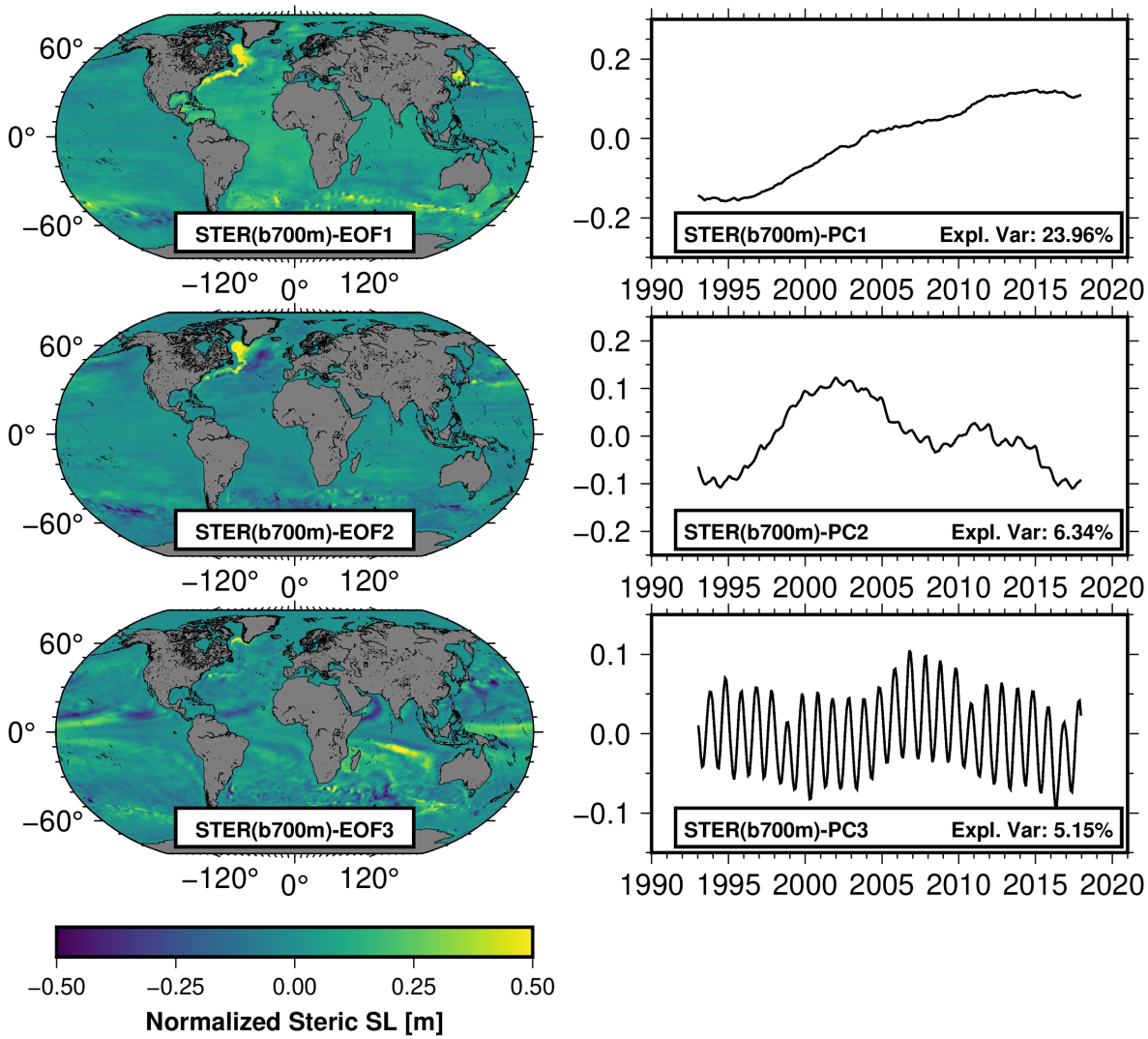


Figure 6.7: First three EOFs, PCs and corresponding explained variances based on the ORAS5 ensemble mean steric sea level change from below 700 m ocean depth (Sect. 3.3.2). The EOFs are utilized as fingerprints within the inversion approach where the PCs are readjusted based on the gravity and altimetry observations.

level $\tilde{S}^{(\mathrm{GIA})}$. Substituting (6.1.3) and solving for the shift term yields

$$\left(\frac{\Delta\phi}{g}\right)^{(\mathrm{GIA})} = -\frac{1}{A_{oce}}\int_{oce}(N^{(\mathrm{GIA})} - U^{(\mathrm{GIA})})d\omega. \tag{6.1.5}$$

In the spherical harmonic domain, the correction is easily derived from the spherical harmonic geoid height N_{nm} (or equivalently Stokes coefficients C_{nm}) and present day uplift, U_{nm}, representations of published GIA models of degree n and order m as

$$\widetilde{S}_{00}^{(\mathrm{GIA})} = -\frac{1}{O_{00}}\sum_{n=1}^{n_{max}}\sum_{m=-n}^{n} O_{nm}(aC_{nm}^{(\mathrm{GIA})} - U_{nm}^{(\mathrm{GIA})}). \tag{6.1.6}$$

Two different GIA solutions are mainly considered in this thesis. The first one by A et al. (2013) has been used in combination with GRACE RL05 and RL06 data and is similar to the ICE5G model (Peltier, 2004), both utilizing the ICE5G loading history and viscosity model VM2. The other model is the ICE6G_D model (Peltier et al., 2018) based on the updated ICE6G loading history and viscosity model (VM5a). The latter is considered as the new standard model widely

used in the context of the GRACE RL06 data. In this thesis, the GIA model data are corrected as described above. The corresponding trend patterns for gravity and altimetry observations are then introduced into the inversion as time dependent fingerprints.

Rietbroek (2014) and Rietbroek et al. (2016) also tried to improve the GIA correction by simultaneously solving for residual GIA signals from the five major driving regions (Laurentide, Fennoscandia, Antarctica, Greenland and complementary sources). This was based on an GIA model by Klemann and Martinec (2009). In contrast, this study considers only the total GIA effect, which is removed from the altimetry and GRACE datasets before solving the combined normal equations as part of the inversion estimation step. Detailed investigation of earlier inversion results have shown that it is not possible to reliably separate GIA related mass changes from other sources, such as melting of ice, which occur in the same regions. Consequently, in the new base inversion (Sect. 6.2.6) the GIA fingerprint of the modeled total effect merely acts as a correction that is applied before the estimation. However, reconstructions of present day GIA based on GRACE data have been published in the recent years (e.g., Gunter et al., 2014; Sun and Riva, 2020).

6.2 The Global Fingerprint Inversion

6.2.1 Input Data Pre-Processing

In order to combine gravity, altimetry data and potentially other datasets, as part of the global fingerprint inversion approach, it is necessary to adapt the individual datasets to be as consistent as possible. In the context of sea level budgets, one generally utilizes sea level anomalies for altimetry data and combines these with model or in-situ profile based steric sea level observations and OMC derived from satellite gravimetry.

Gravity Observations

The time-variable gravity inversion input (Sect. 3.2) in this thesis is provided as Stokes coefficients relative to some a priori static field, $\delta\widehat{c}_{nm}$, stored in the form of unsolved, unfiltered original normal equation systems, including the full covariance information. While this thesis mainly focuses on GRACE and GRACE-FO gravity observations of degree and order 120, the same procedures apply to the inputs from SLR and Swarm time-variable gravity normal equations.

In a first step, the AOD1B ocean mass signal is restored in order to achieve consistency with the ocean mass observed by altimetry (compare Sect. 5.3 and Uebbing et al., 2019). Furthermore, the individual static mean field is restored and, instead, the GRACE mean field over the period 2005-2010 is removed from all gravity datasets to avoid biases and other inconsistencies. Both of these operations change the a priori information of the input normal equations (App. A.2.2), yielding the consistently corrected Stokes parameters, δC_{nm}. The covariance information is unaffected by these operations. Finally, the Stokes coefficients are scaled with the Earth radius, a, in order to convert to geoid heights, as used for the design matrix defined in equation (6.2.2).

Altimetry Observations

Along-track altimetry from the RADS database (Sect. 3.1.2) represents the second major input data set of the fingerprint inversion. Altimetry observes the sum of the steric and mass related sea level signals. The measured ranges are converted to SLA (Sect. 3.1.1) and corrected for the corrections listed in table 3.2. This is consistent with the processing performed by Nerem et al. (2018), except for the applied IMB between individual altimetry missions. Similar to Rietbroek (2014), large outliers in the SLA are removed from the input dataset. While Rietbroek (2014) also applied a mask of maximum sea ice extent to avoid a high latitude seasonality effect and potentially

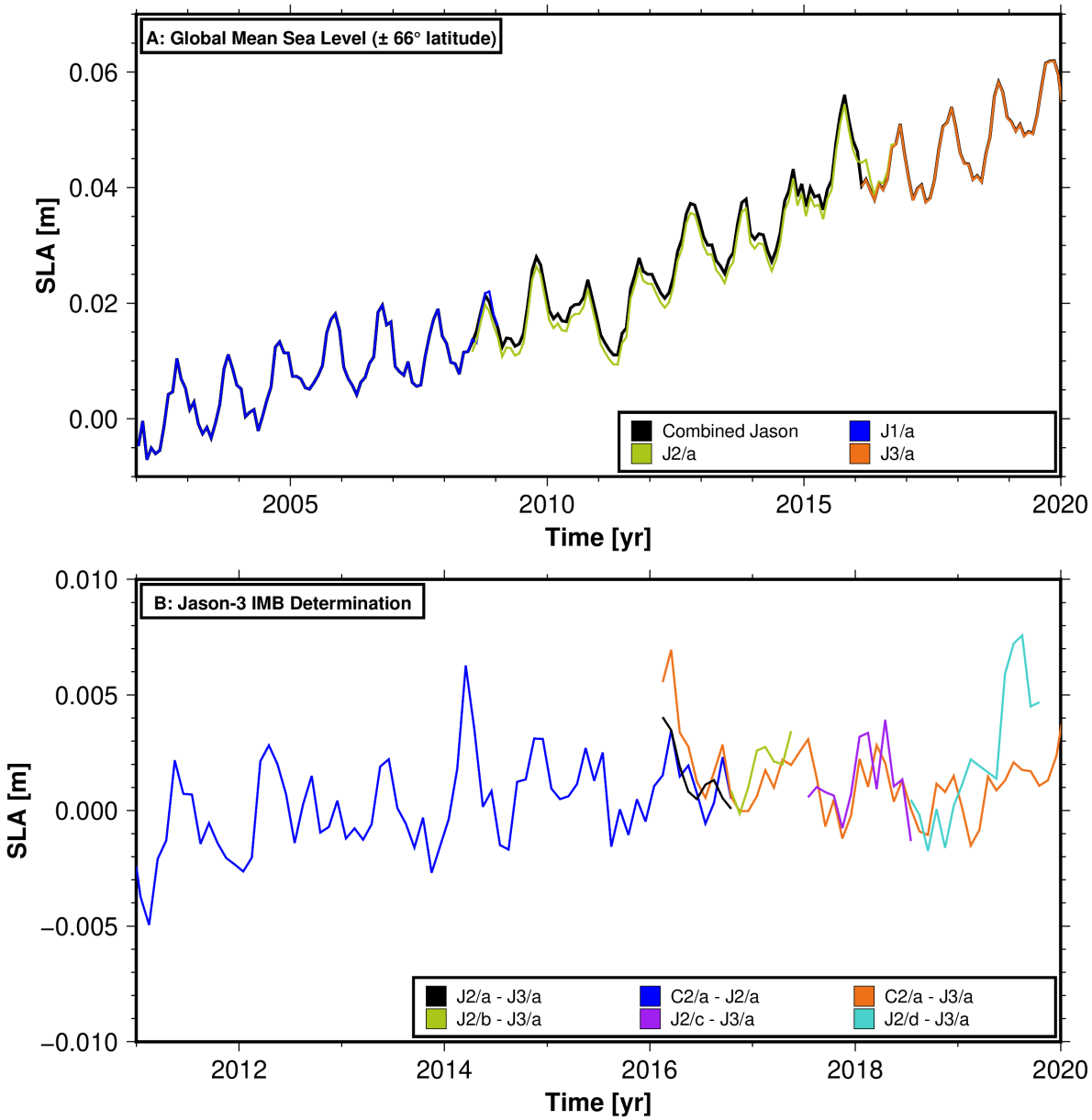


Figure 6.8: IMB effect for the nominal Jason missions. A: Combined Jason global mean sea level time series and individual nominal mission phases. B: Differences between various missions in order to derive the Jason-3 IMB. All global mean sea level values are computed between ±66° latitude and weighted following inclination weighting based on equation (5.2.1).

bad data, this is not done here. Data influenced by sea ice can be excluded relatively reliably from the RADS data. For consistency with other studies (e.g., Nerem et al., 2018), the seasonality effect from the coverage of the Arctic and Antarctic oceans is also included in this thesis. However, the number of additional observations from this is small, thus, effects on the inversion results from these particular data are expected to be small. Furthermore, section 7.4.3 will show the benefits of adding high latitude altimetry data for deriving regional sea level budgets in these regions. In this thesis, the Jason-1, Jason-2 and Jason-3 missions serve as the basis of the altimetry data in all of the inversions.

A closer look at the global mean sea level time series derived from the along-track RADS sea level anomaly data revealed that some missions still showed a significant bias, despite applying the RADS IMB correction. These remaining biases will later show up in the inversion altimetry

residuals introducing jumps, which in turn lead to artificial residual trend signals (Sect. 7.3.4). Consequently, it makes sense to remove these obvious IMB-related biases beforehand. For this, the Jason-1 mission IMB is fixed. In a first step, the IMB between Jason-1 mission phase a (J1/a) and Jason-2 phase a (J2/a) is computed from the tandem period where both satellites flew in the same orbit a few seconds apart for 6 months. The remaining bias between the two missions is found to be constant and small (~ 1.5 mm). For the Jason-3 mission, the IMB from the J2/a and J3/a tandem period is dominated by a strong trend caused by the Jason-3 mission in the first few months (black line, Fig. 6.8, B). A similar trend is also found when comparing Jason-3 to Cryosat-2 (orange line, Fig. 6.8, B). Instead, comparing Jason-2 and Cryosat-2 (blue line, Fig. 6.8, B) does not show such trends. For these comparisons, the Cryosat-2 data is limited to the Jason spatial coverage ($\pm 66°$ latitude). Therefore, the additional IMB between Jason-2 and Jason-3 is derived from the differences of mission phases b and c of the Jason-2 mission and is found to be in the sub-millimeter range. Considering this, the combined Jason time series based on J1/a, J2/a and J3/a can then be constructed without including the trend from the J2/a and J3/a tandem period.

In a second step, this combined Jason time series is then utilized as the basis for computing the IMBs with all other missions considered in this thesis. For some missions, such as Topex/Poseidon phase b (TX/b), J1/b or J2/d the IMB is not always constant and tends to show a trend towards the end of life of the respective mission (e.g., blue line, Fig. 6.9, A). This is likely related to reduced orbit maneuvers due to lack of fuel towards the end of mission-lifetime and the resulting loss of satellite altitude. Where necessary, these trends are captured by introducing a linear and quadratic term in addition to the constant IMB offset. The reason for seasonal offsets (Fig. 6.9) is likely that not all missions are covering the same areas of the ocean at the exact same time, due to different orbits. Therefore, these seasonal effects are expected to occur and not corrected here. However, some months from certain missions, such as Geosat Follow On (G1/a) or the first few months of Sentinel-3/a (S3/a), show strong deviations from the Jason combined time series (e.g., red line, Fig. 6.9). Those months will be excluded as input into the inversion.

Co-estimation of the IMB biases in the inversion, even only a constant one, would require respective fingerprints. In the simplest case, this would be represented by a constant fingerprint over the ocean, i.e. the ocean function $O(\lambda, \theta)$ from Eq. (2.2.4). However, such fingerprints tend to absorb more than just a constant bias signal, but will also influence the estimation for individual sea level contributors. Rietbroek (2014) and Rietbroek et al. (2016) co-estimate the IMBs, modeled as a 3D vector for each mission. This approach also tends to absorb other signals and makes it difficult to compare the results due to the inconsistency with other published results, which all rely on a globally constant IMB (cf. Sect. 7.3.4). Consequently, co-estimation of the IMB is no longer considered for the inversion presented in this thesis. The effect from co-estimating the IMB on the budget is shown in section 7.3.4.

Temperature and Salinity In-Situ Profile Observations

Temperature and salinity data from in-situ profiles are converted to steric sea level heights for the upper 700 m following Section 2.3.1. Profile data from below 700 m is sparse and not further considered as input in this thesis. The input data is generated based on the easyCORA dataset (Sect. 3.3.1). Each measurement technique of the easyCORA dataset is associated with a nominal error according to table 6.1 based on the data documentation.

While the easyCORA dataset already has been extensively quality-checked for the individual profiles, additional quality checks are applied in order to filter the data before further processing. Converting to steric sea level change requires, both, temperature and salinity. Consequently, all profiles that do not provide one of the two are discarded immediately. Furthermore, profiles that only include three or less depth levels, that do not provide data in the upper 10 m or that provide data with negative depth, i.e. above the water surface, are removed. In the next step, the profiles

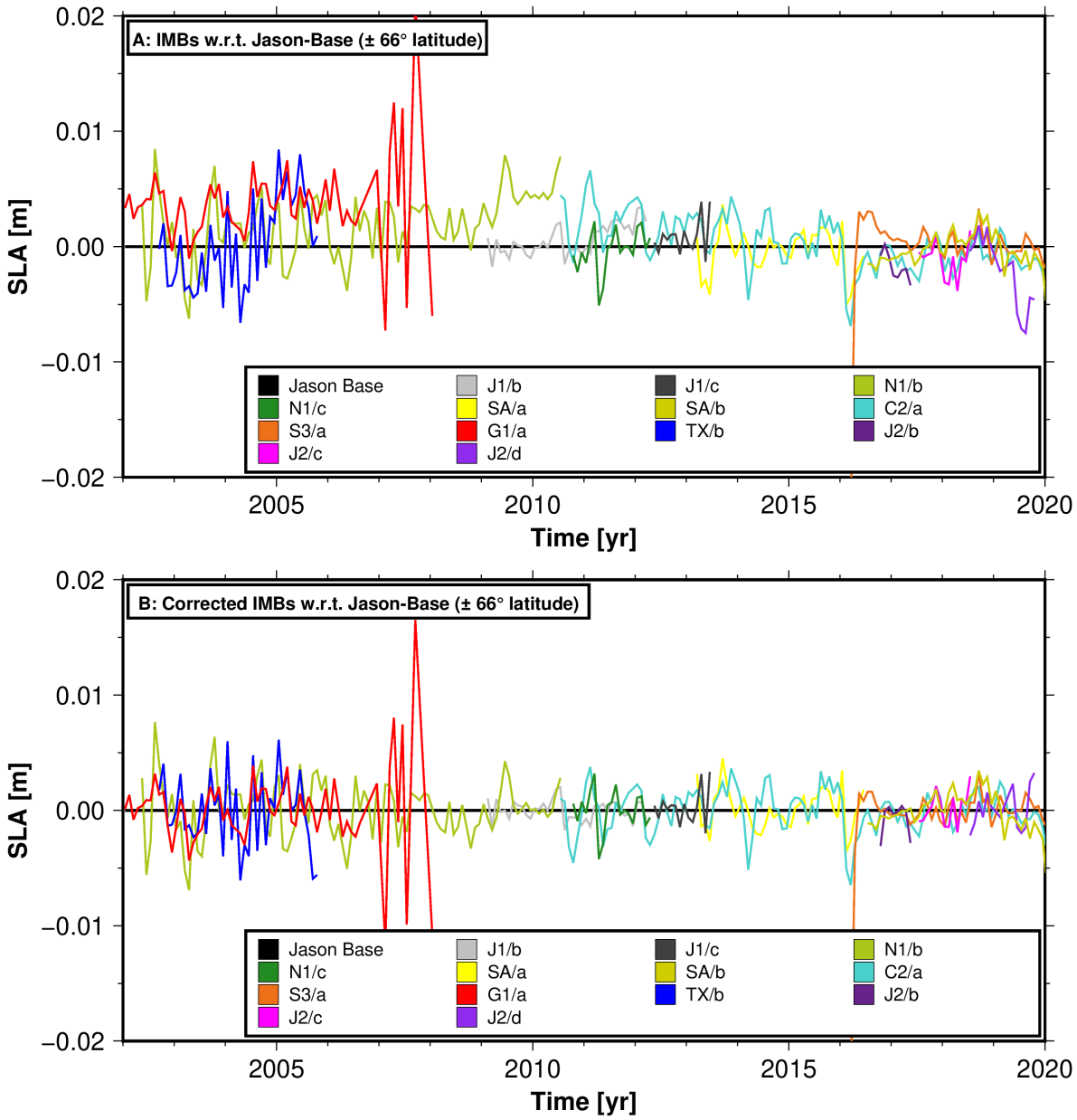


Figure 6.9: IMB effect in addition to the RADS-based IMB correction from all missions considered in this thesis with respect to the combined Jason time series. A: Only RADS IMB corrections applied. B: After applying additional IMB corrections. All global mean sea level values are computed between ±66° latitude and weighted following inclination weighting based on equation (5.2.1).

maximum depth has to be within the limits of the ORAS5 model bathymetry, especially for profiles, which provide data to less than 700 m depth. The last check on the temperature and salinity profiles is whether the profile includes more than three consecutive NaN values, which indicates large gaps that are difficult to interpolate.

After computing steric anomalies relative to the same ORAS5 mean field utilized during the creation of the steric fingerprints, these are checked for outliers, i.e. more than 2 m of thermo- or halosteric sea level anomaly. In the final step for each of the remaining profiles, a Monte Carlo simulation (e.g., Binder and Heermann, 2010) is run, varying the temperature, salinity and pressure measurements based on their nominal errors in order to derive a rough error estimate for the steric sea level input at each profile position. This is also called bootstrapping, which is not to be confused with the bootstrap-fingerprints, e.g, utilized in Rietbroek (2014).

Table 6.1: Nominal errors of the easyCORA profile data.

Technique	Nominal Temperature Error [°C]	Nominal Salinity Error [psal]
Argo	0.01	0.01
XBT	0.1	0.01
Other	0.1	0.01

6.2.2 Functional and Stochastic Model

Gravity Observation Equations

The mass fingerprints are all stored as geoid height spherical harmonics (Eq. (2.1.13)) up to degree and order 150. Since the ITSG2018 GRACE data, introduced in this thesis, is limited to degree and order 120 only corresponding coefficients are fitted. However, the higher degrees are scaled by the same factors and can still be utilized for evaluation. The functional model connecting the mass related fingerprints to the corrected corresponding Stokes coefficients, scaled to geoid heights, can be written as

$$\begin{bmatrix} a\delta c_{20} \\ \vdots \\ a\delta c_{nm} \end{bmatrix} = \mathbf{A}_{\text{grav}} \begin{bmatrix} \boldsymbol{x}_{\text{ice}} \\ \boldsymbol{x}_{\text{glac}} \\ \boldsymbol{x}_{\text{hydr}} \\ \boldsymbol{x}_{\text{IMV}} \end{bmatrix} + \boldsymbol{e}_{\text{grav}}. \tag{6.2.1}$$

Here, the parameter vector, $\boldsymbol{x}$, corresponds to the scaling coefficients for the melting of the ice sheets in Greenland and Antarctica ($\boldsymbol{x}_{\text{ice}}$) and land glaciers ($\boldsymbol{x}_{\text{glac}}$), as well as changes in terrestrial hydrology ($\boldsymbol{x}_{\text{hydr}}$) and internal ocean mass variations ($\boldsymbol{x}_{\text{IMV}}$). The design matrix, $\mathbf{A}_{\text{grav}}$, includes the spherical harmonic coefficient of each fingerprint in its columns ordered in the same way as the satellite gravity Stokes coefficients

$$\mathbf{A}_{\text{grav}} = \begin{bmatrix} \delta N_{20}^{\text{Greenland}_1} & \delta N_{20}^{\text{Greenland}_2} & \cdots & \delta N_{20}^{\text{IMV}_{max}} \\ \vdots & \vdots & & \vdots \\ \delta N_{nm}^{\text{Greenland}_1} & \delta N_{nm}^{\text{Greenland}_2} & \cdots & \delta N_{nm}^{\text{IMV}_{max}} \end{bmatrix}. \tag{6.2.2}$$

The full error covariance of the input gravity Stokes coefficients, $\boldsymbol{\Sigma}_{\text{stokes}} = \mathbf{N}_{\text{stokes}}^{-1}$, is part of the corresponding stochastic model.

Since the gravity input is available in the form of monthly normal equations for the Stokes coefficients and the fingerprints are linearly related to those, the original normal equations can easily be converted to the solution space of the fingerprints after accounting for the necessary pre-processing steps (Sect. 6.2.1). Following appendix A.2.4, this can be written as

$$\begin{aligned} \mathbf{N}_{\text{grav}}^{\text{GFI}} &= \mathbf{A}_{\text{grav}}^T \mathbf{N}_{\text{stokes}} \mathbf{A}_{\text{grav}}, \\ \boldsymbol{n}_{\text{grav}}^{\text{GFI}} &= \mathbf{A}_{\text{grav}}^T \boldsymbol{n}_{\text{stokes}}, \\ [\boldsymbol{v}_0^T \mathbf{P} \boldsymbol{v}_0]_{\text{grav}}^{\text{GFI}} &= [\boldsymbol{v}_0^T \mathbf{P} \boldsymbol{v}_0]_{\text{stokes}}, \end{aligned} \tag{6.2.3}$$

which generally reduces the size of the solution space for GRACE and GRACE-FO, which contain data up to degree and order 120. Similarly, it can also increase the solution space, e.g., for SLR input data, which is only provided up to degree and order 5.

Altimetry Observation Equations

After deriving the h_{SLA} (Sect. 3.1.1), while accounting for the small additional IMB (Sect. 6.2.1), the observation equation for the altimetry input data, representing geocentric sea level change, into the inversion can be written as

$$\begin{bmatrix} h_{\mathrm{SLA}_1} \\ \vdots \\ h_{\mathrm{SLA}_J} \end{bmatrix} = \mathbf{YB} \begin{bmatrix} \boldsymbol{x}_{\mathrm{ice}} \\ \boldsymbol{x}_{\mathrm{glac}} \\ \boldsymbol{x}_{\mathrm{hydr}} \end{bmatrix} + \mathbf{KC} \begin{bmatrix} \boldsymbol{x}_{\mathrm{steric}}^{\mathrm{700m}} \\ \boldsymbol{x}_{\mathrm{steric}}^{\mathrm{deep}} \\ \boldsymbol{x}_{\mathrm{IMV}} \end{bmatrix} + \boldsymbol{e} = \mathbf{D} \begin{bmatrix} \boldsymbol{x}_{\mathrm{ice}} \\ \boldsymbol{x}_{\mathrm{glac}} \\ \boldsymbol{x}_{\mathrm{hydr}} \\ \boldsymbol{x}_{\mathrm{steric}}^{\mathrm{700m}} \\ \boldsymbol{x}_{\mathrm{steric}}^{\mathrm{deep}} \\ \boldsymbol{x}_{\mathrm{IMV}} \end{bmatrix} + \boldsymbol{e}_{\mathrm{altim}}, \tag{6.2.4}$$

where

$$\mathbf{D}_{\mathrm{altim}} = \begin{bmatrix} \mathbf{YB} & \mathbf{KC} \end{bmatrix}. \tag{6.2.5}$$

The matrix $\mathbf{B}$ is similar to the design matrix, $\mathbf{A}_{\mathrm{grav}}$, of the gravity input. Altimetry is observing geocentric sea level, which is the relative sea level but also the change of the volume of the ocean basin, i.e. $\tilde{S} + U$ (Sect. 2.2). In addition, altimetry observes in the CF frame and, thus, requires terms for degree 1 in order to be consistent with the gravity observations in the CM frame (Sect. 2.4.1). The degree zero term of the quasi spectral sea level, $\tilde{S}_{00}$, is added in order to enforce mass conservation following equations (2.2.11) and (2.2.12). Consequently, $\mathbf{B}$ is given as

$$\mathbf{B} = \begin{bmatrix} \tilde{S}_{00}^{Greenland_1} & \tilde{S}_{00}^{Greenland_2} & \cdots & \tilde{S}_{00}^{Hydrology_{max}} \\ \delta N_{10}^{Greenland_1} & \delta N_{10}^{Greenland_2} & \cdots & \delta N_{10}^{Hydrology_{max}} \\ \vdots & \vdots & & \vdots \\ \delta N_{nm}^{Greenland_1} & \delta N_{nm}^{Greenland_2} & \cdots & \delta N_{nm}^{Hydrology_{max}} \end{bmatrix}. \tag{6.2.6}$$

The matrix $\mathbf{Y}$ evaluates each of the fingerprint patterns of the design matrix, $\mathbf{B}$, stored in spherical harmonics, at the actual along-track altimetry measurement locations

$$\mathbf{Y} = \begin{bmatrix} Y_{00}(\lambda_1, \theta_1) & \cdots & Y_{nm}(\lambda_1, \theta_1) \\ \vdots & \vdots & \vdots \\ Y_{00}(\lambda_J, \theta_J) & \cdots & Y_{nm}(\lambda_J, \theta_J) \end{bmatrix}. \tag{6.2.7}$$

Note that the matrix notation is used here for convenience; in praxis the individual fingerprints are simply evaluated at all along-track positions, since the number of rows of $\mathbf{Y}$ can easily grow to more than one or two million, which would require unnecessary large amounts of storage.

The steric fingerprints, which consist of the steric model EOFs, are stacked in the columns of the design matrix $\mathbf{C}$. Generally, the steric contribution is split into a part of the upper 700 m of the ocean and a deep ocean contribution (Sect. 6.1.5). This enables further splitting the steric sea level estimate and facilitate the use of additional in-situ profile input data. In contrast to the gravity observation equations, the IMV contribution to altimetry, which is originally also derived from a PCA of ocean model data, is utilized here directly without, first, converting to spherical harmonics in order to benefit from the higher resolution of the EOF grids in combination with the better spatial coverage of altimetry. Similarly to $\mathbf{Y}$, the matrix $\mathbf{K}$ represents the interpolation of the gridded fingerprints to the actual along-track altimetry measurement positions.

The stochastic model for the altimetry input data consists of a diagonal matrix, $\boldsymbol{\Sigma}_{\mathrm{altim}}$, which contains variances for each of the 1 Hz observations on the main diagonal. Variances are extracted from the RADS data and derived from the standard deviation of the 20 Hz measurements, which are averaged into 1 Hz. The normal equation system for the altimetry observations is then constructed

from

$$\begin{aligned} \mathbf{N}_{\text{altim}}^{\text{GFI}} &= \mathbf{D}^T \boldsymbol{\Sigma}_{\text{altim}}^{-1} \mathbf{D}, \\ \boldsymbol{n}_{\text{altim}}^{\text{GFI}} &= \mathbf{D}^T \boldsymbol{\Sigma}_{\text{altim}}^{-1} \boldsymbol{l}_{\text{altim}}, \\ [\boldsymbol{v}_0^T \mathbf{P} \boldsymbol{v}_0]_{\text{altim}}^{\text{GFI}} &= \boldsymbol{l}_{\text{altim}}^T \boldsymbol{\Sigma}_{\text{altim}}^{-1} \boldsymbol{l}_{\text{altim}}, \end{aligned} \tag{6.2.8}$$

where the initial residuals $\boldsymbol{v}_{0_{\text{altim}}}$ are equal to the observations without assuming prior information. These normal equations are built for each individual altimetry mission on a monthly basis. Rietbroek (2014) and Rietbroek et al. (2016) relied only on repeat missions phases. These can be easily averaged into bins with fixed positions, which have the benefit of needing to construct the design matrix, $\mathbf{D}$, only once. As part of this thesis, the algorithm for the construction of the design matrix has been significantly improved in run-time, allowing also to utilize non-binned data by building a new design matrix for the actual measurement positions for each month in relatively short time. This enables inclusion of missions with very long repeat orbits, such as Cryosat-2 or even non-repeat missions, e.g., Jason-1 phase C, which flew on a geodetic drifting orbit.

In-Situ Profile Observation Equations

After pre-processing the easyCORA in-situ profile data as described in Section 6.2.1, the observation equation for the steric sea level change at P positions of the upper 700 m can be directly written as

$$\begin{bmatrix} h_{\text{steric}_1} \\ \vdots \\ h_{\text{steric}_P} \end{bmatrix} = \mathbf{L}\mathbf{C}_{\text{steric}}^{700\text{m}} \left[\boldsymbol{x}_{\text{steric}}^{700\text{m}}\right] + \boldsymbol{e}_{\text{steric}} = \mathbf{F} \left[\boldsymbol{x}_{\text{steric}}^{700\text{m}}\right] + \boldsymbol{e}_{\text{steric}}, \tag{6.2.9}$$

where the projection matrix, $\mathbf{L}$, interpolates the steric fingerprints to the float positions and $\mathbf{C}_{\text{steric}}^{700\,\text{m}}$ is the block of the altimetry design matrix related to the upper 700 m steric sea level change.

The covariance matrix, $\boldsymbol{\Sigma}_{\text{cora}}$, contains the variances derived from the Monte Carlo simulation performed during the pre-processing (Sect. 6.2.1) on the diagonal. This assumes that individual profiles are uncorrelated and the results of the Monte Carlo simulation are only based on the nominal errors. Consequently, it is expected that the variance factor (appendix A.1) is underestimated and will require rescaling as part of the Variance Component Estimation (VCE) (Sect. 6.2.3). The normal equation system for the profile data can then be constructed similar to altimetry from

$$\begin{aligned} \mathbf{N}_{\text{cora}}^{\text{GFI}} &= \mathbf{F}^T \boldsymbol{\Sigma}_{\text{cora}}^{-1} \mathbf{F}, \\ \boldsymbol{n}_{\text{cora}}^{\text{GFI}} &= \mathbf{F}^T \boldsymbol{\Sigma}_{\text{cora}}^{-1} \boldsymbol{l}_{\text{cora}}, \\ [\boldsymbol{v}_0^T \mathbf{P} \boldsymbol{v}_0]_{\text{cora}}^{\text{GFI}} &= \boldsymbol{l}_{\text{cora}}^T \boldsymbol{\Sigma}_{\text{cora}}^{-1} \boldsymbol{l}_{\text{cora}}. \end{aligned} \tag{6.2.10}$$

These normal equations are built from all in-situ profiles observed during one month.

6.2.3 Combining Individual Input Data Sets

When only considering the a priori stochastic information, the individual input data sets can be combined based on common parameters of their respective normal equation systems. This assumes that all systems are weighted equal. Variance Component Estimation (VCE) (App. A.2.5) allows to derive weights based on the corresponding stochastic modeling in order to scale the error covariances and weight the individual input data sets upon combination. For combining sea level observations from altimetry with ocean mass change from GRACE, it makes sense to derive weights utilizing VCE. While GRACE data is provided with the full error covariance information, only a

diagonal error matrix is considered for altimetry (Sect. 6.2.2). The assumption of no correlations for altimetry does not hold in reality and, therefore, the altimetry observations will have more impact in the combination without VCE. With VCE the altimetry observations can be down-weighted relative to GRACE, i.e., in this case, scaling the variances, for an improved weighted combination.

However, constructing sea level budgets based on individually processed datasets (e.g., Sect. 5), normally does not consider these weights (e.g., Cazenave et al., 2009; Chambers et al., 2017; Dieng et al., 2017; Royston et al., 2020; Hakuba et al., 2021). In order to derive inversion results consistent with these published estimates it makes sense to disable the VCE for comparison, while for other inversion applications, such as combining several input data sets (IS030, Tab. 7.15), it makes sense to enable VCE.

After building the normal equation systems for the individual input datasets, these are combined using VCE following appendix A.2.5. The variance components for weighting the monthly normal equation systems from each input dataset are estimated without applying any eventually considered constraints, while fixing possible common parameters to their reference values. This means those parameters are not utilized for VCE. For the standard inversion (Sect. 6.2.5, IS002 in Tab. 7.12), the variance components for the Jason nominal altimetry missions and GRACE/GRACE-FO are shown in figure 6.10.

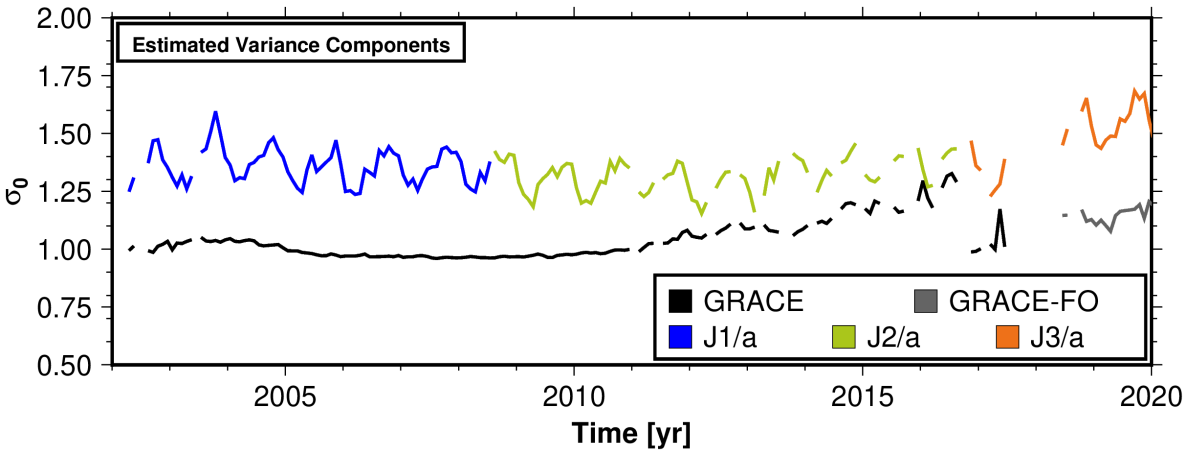


Figure 6.10: Square roots of the estimated VCE components from the standard inversion run (Sect. 7.1) for the contributions of GRACE/GRACE-FO and Jason-1/-2/-3 mission phase (a). Gaps are due to missing GRACE data where no inversion solution is derived.

For GRACE the variance factor varies closely around 1 until about 2011 (Fig. 6.10), indicating a good (co-)variance modeling of the input data. After 2011, the satellite started to experience battery problems requiring shutdown of the microwave K-Band Ranging System (KBR) and the on-board accelerometers. In the following, battery issues became more severe and, starting in the end of 2016, the accelerometer failed on one of the satellites, requiring a transplant of those measurements from one satellite to the other. This also affected the overall data quality and is reflected in the input normal equations and the variance component. Similarly for GRACE-FO, the satellite experienced some accelerometer problems right after the start, which also explains the slight down-weighting of the corresponding variance factor. The Jason altimetry input data generally indicates a higher variance factor level of about 1.25 to 1.5, which varies with a clear annual cycle. This relates to several factors: (1) the altimetry errors are generally assumed to be uncorrelated utilizing only the errors extracted from RADS with a mean level of about 8 cm. This is increased to about 11 cm on average considering the variance factors; (2) the seasonal cycle might be related to the varying coverage of the Jason missions, where regions in the Arctic and Antarctic covered by sea ice are excluded. The effect of coverage is further investigated in the context of expanding

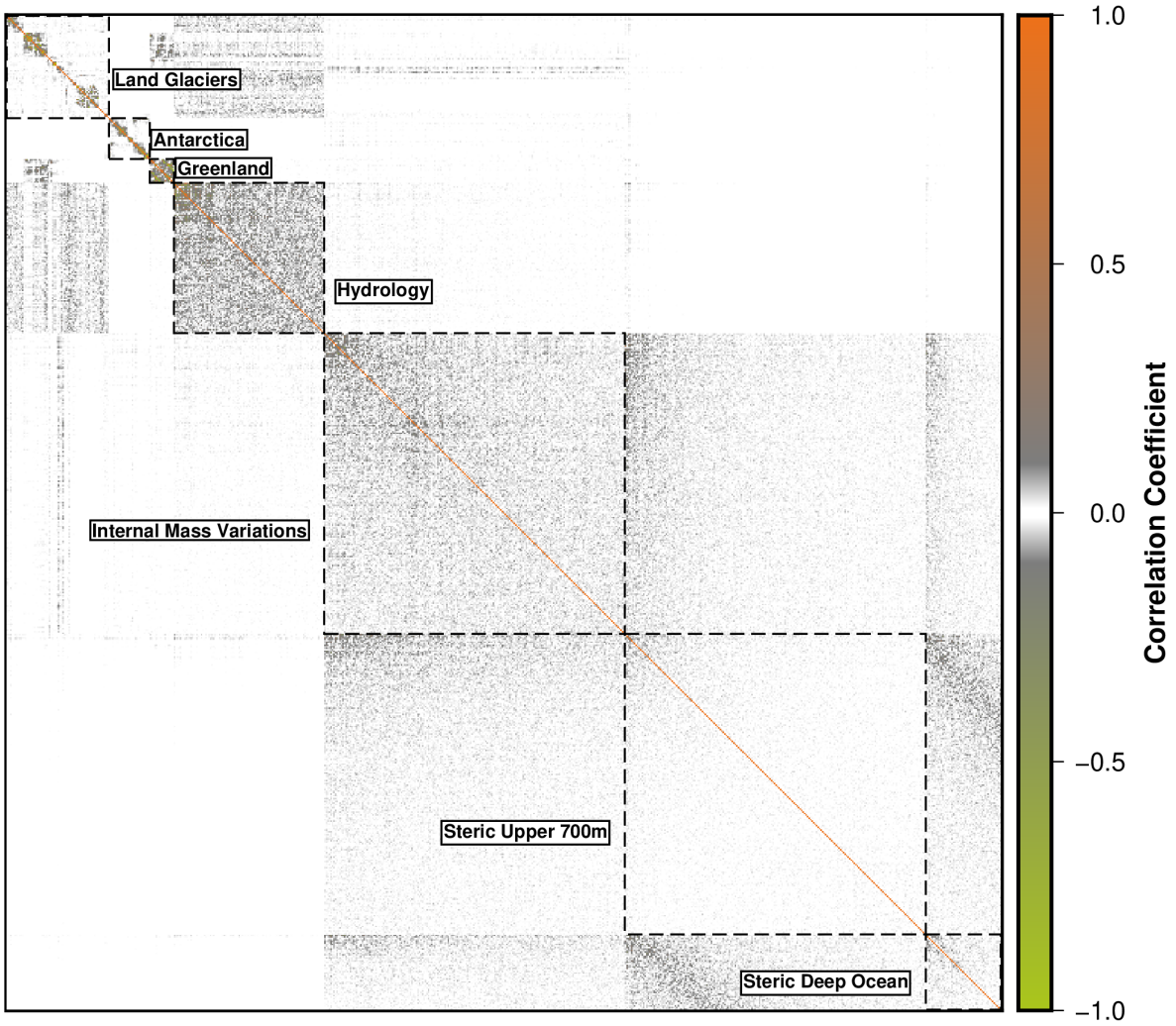


Figure 6.11: Exemplary formal error correlation of the estimated parameter scales for 2006-06 for the standard inversion run including only non-overlapping Jason-1/-2/-3 altimetry data and GRACE/GRACE-FO data.

the inversion by including additional altimetry missions (Sect. 7.4.3).

6.2.4 Formal Errors of the Inversion

The inversion propagates the error covariance information from the individual input datasets to the final estimates following the laws of error propagation (e.g., Koch, 1999; Niemeier, 2008). This allows to provide maps of formal error estimates for each individual location as well as further propagation into derived estimates, such as trends and sea level budgets. However, most published sea level budgets are comprised from individually processed input data sets without taking into account the covariance information. For consistency with published estimates, the time series of individual mass, steric and total sea level contributions and corresponding trend estimates will also be computed assuming uncorrelated and same accuracy values, unless stated otherwise.

Figure 6.11 provides the correlations between individual parameters of an arbitrary monthly solution (here: 2006-06). Generally, the individual groups of contributions are nearly uncorrelated or show only weak correlations, e.g., between the upper 700 m and deep ocean steric parameters and the IMV contributions. These weak correlations are due to similar signal content to a certain extent; the first few fingerprints of the IMV, shallow- and deep-steric contributions include a pattern related to the annual and semi-annual seasonal cycle. However, the different spatial structure

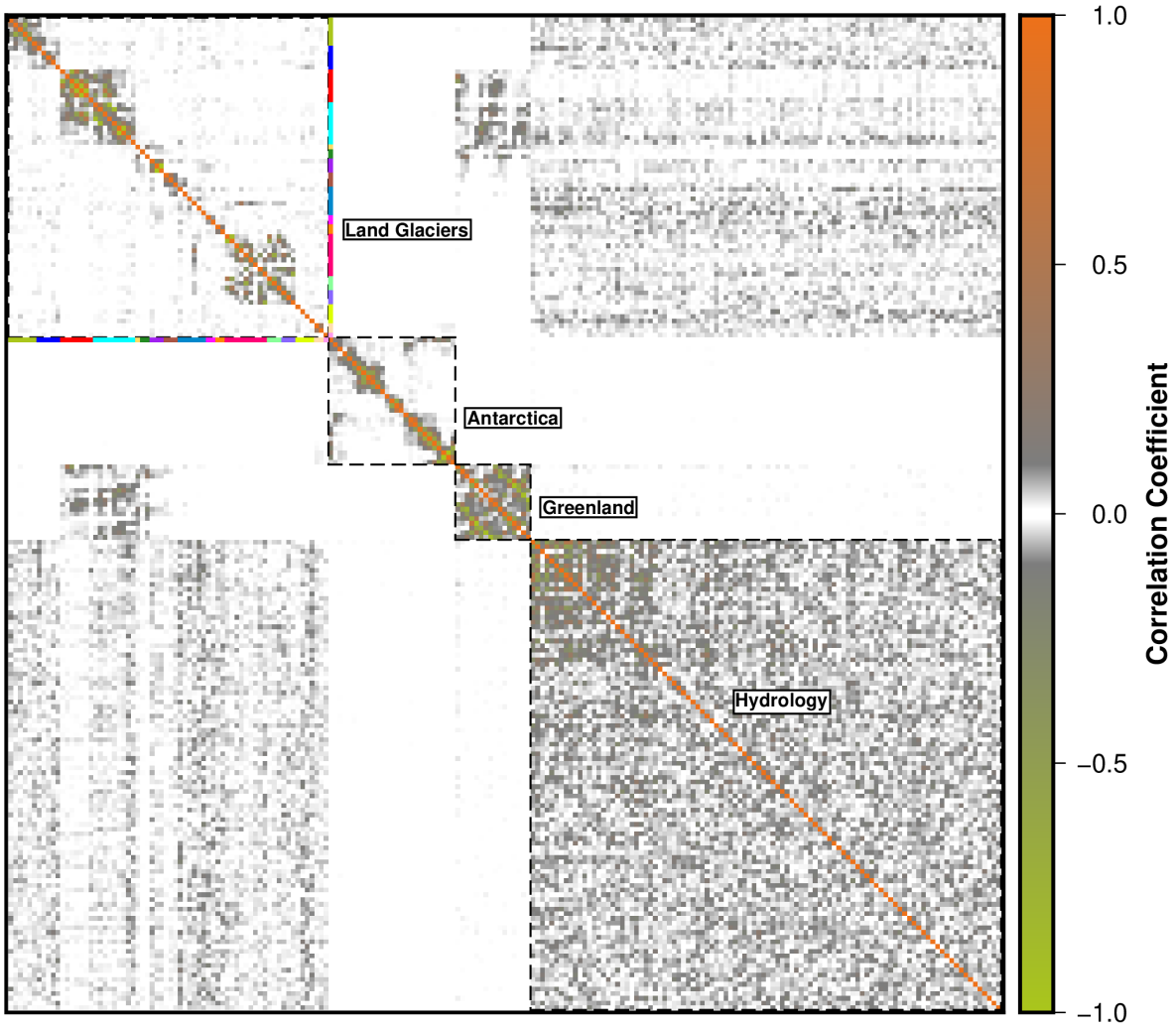


Figure 6.12: Exemplary formal error correlation of the estimated mass parameters from glaciers, Antarctica, Greenland and Hydrology for 2006-06; i.e. same as figure 6.11. IMV and steric patterns are omitted for clarity. The colors alongside the land glacier sub-matrix refer to figure 6.1.

of the fingerprints and the relatively high spatial resolution of the along-track altimetry data still enable a separation of the signals. The upper left part which displays the contributions of land glaciers, Antarctica, Greenland, and terrestrial hydrology is additionally shown in figure 6.12. Weak correlations can be identified between the hydrological contribution and the land glacier regions, despite the glacier areas being set to zero in the hydrological model data (Sect. 6.1.3). However, these are still linked by mass exchanges between hydrological catchments and glaciers, e.g., land glacier melt feeding rivers. Similarly, the glacier regions of Arctic Canada North and South, as well as Iceland and Svalbard (Fig. 6.1) are located spatially close to the Greenland ice sheet, which explains the (weak) connection observed from figure 6.12.

In addition some larger correlations are observed within individual contribution groups. Nearly all Greenland basins, which are sub-divided into sections below and above 2000 m elevation (Fig. 6.2, left) indicate a notable negative correlation ($\sim 0.5 - 0.6$) between the high and low elevation counterparts (Fig. 6.12). This is expected to a certain extent as the ice accumulated in the high elevation regions eventually flows through the lower elevation regions towards the ocean. In addition, these basins are relatively small and the GRACE resolution is not sufficient to clearly separate them. The small basins 25 and 26 located on the Antarctic peninsula (Fig. 6.2, right) are connected by negative correlation of about -0.7. These basins are both relatively small and

the available GRACE/GRACE-FO spatial resolution is not sufficient to separate them. Similarly, some individual small glacier regions of the Arctic Canada North and South clusters are difficult to separate leading to large negative correlations. An option to mitigate the problem is to constrain those small regions to respond similar (as, e.g, done by Rietbroek, 2014) or even combine neighboring glacier areas into one larger sub-region. However, the share of these small regions to the overall contribution of the corresponding sea level component is negligible. Thus, the small correlation effects on the overall sea level budget from a hand full of tiny basins can be safely ignored.
Since these correlations do not prevent solving the combined inversion normal equations, this is seen as a rather small issue. Summation of the individual basins will be the same. However, one has to be careful not to over-interpret the highly correlated sub-basins. For a better separation, higher resolution data, such as ice-altimetry observations, would be required.

6.2.5 Differences with Respect to Previous Inversions

This section focuses on the changes that have been introduced into the inversion approach since the earlier versions employed by Rietbroek (2014) and Rietbroek et al. (2016). Thus, the base (or reference) inversion of this thesis (Sect. 6.2.6) represents the basis for the extensions and experiments presented in the following chapter. The changes made to the inversions utilized by Rietbroek et al. (2016) can be divided into roughly three parts: (1) the update of the input data, (2) the extension and update of the fingerprints used to model individual sea level contributions and (3) updates of the processing and interpretation of the results. An overview over the most important changes with respect to Rietbroek et al. (2016) is provided in table 6.2.

The first major difference is related to the updated input data. Nowadays, the inversion utilizes the state-of-the-art ITSG-2018 RL06 GRACE and GRACE-FO data. The original inversion (Rietbroek, 2014) was derived using altimetry data from the Open Altimeter Database (OpenADB, `https://openadb.dgfi.tum.de`) by the Technical University Munich, which was later switched to the RADS database for Rietbroek et al. (2016). An updated version of the RADS database is used as part of the inversions in this thesis. Previously, the AOD1B background model, which has been removed during the GRACE L2 processing, has not been restored to the GRACE data but, instead, the altimetry data was additionally corrected utilizing the AOD1B-GAC product (Rietbroek, 2014; Rietbroek et al., 2016). However, this effectively removed a portion of the ocean (mass) signal from the inversion. This made it difficult to correctly account for the effect in the resulting sea level budget, making it less comparable to other published estimates. The GAC product does not exactly correspond to ocean mass change, but also includes atmospheric contributions. Consequently, the processing has been adapted (e.g., Uebbing et al., 2019) by correctly restoring the missing ocean mass signal in the GRACE/GRACE-FO data using either the AOD1B-GAD product as described in Sect. 5.3 or the AOD1B-GAB product, which is used for the RL06 data. This results in correct ocean mass estimates in the derived sea level budget, which can be directly compared to individually processed or other published ocean mass values.

The second major changes have been made to the modeling of individual sea level contributions and the corresponding fingerprint representation. Generally, all of the fingerprints used in Rietbroek (2014) and Rietbroek et al. (2016) have been revised (Sect. 6.1). The glacier fingerprints have been significantly extended by upgrading from RGIv1 to RGIv6 (Sect. 6.1.1). For Greenland and Antarctica the 16 and 27 uniform basins have been augmented with background patterns derived from ice altimetry melting rates (Sect. 6.1.2) in order to better distribute the observed mass changes within the individual basins. The hydrological fingerprints have been recomputed from an updated WGHM version over an extended time frame (Sect. 6.1.3). Additionally, IMV fingerprints (Sect. 6.1.4) have been introduced in order to capture OBP signals from mass displacements within the ocean that have not been accounted for in earlier versions. The steric fingerprints have been replaced with EOFs from the ORAS5 reanalysis product due to incapabilities of the Argo- and model-based data sets used before (Sect. 6.1.5).

Table 6.2: Comparison of the inversion setup by Rietbroek (2014) / Rietbroek et al. (2016) and the base inversion in this thesis.

		Rietbroek et al. (2016)	**Base Inversion**
Input Data			
	Altimetry	J1/a, J1/b, J2/a; corrected for AOD1B-GAC effect	J1/a, J2/a, J3/a
	GRACE(-FO)	GFZ RL05a	ITSG-2018 RL06 with AOD1B-GAB restored
Fingerprints			
	Greenland	16 basins, uniform patterns	16 basins, melting rate background patterns
	Antarctica	27 basins, uniform patterns	27 basins, melting rate background patterns
	Glaciers	16 basins, uniform patterns	68 basins, uniform patterns
	Hydrology	WGHMv1 (until 2009); 60 EOFs	WGHMv2 (until 2017) 100 EOFs
	IMV	not accounted for	200 EOFs based on AOD1B-GAB product
	Steric	FESOMv1.2 (Brunnabend et al., 2012) (200 EOFs)	ORAS5; separated into upper 700 m (200 EOFs) and 700 m to seafloor (50 EOFs)
	Bootstrap	100 EOFs	none
	GIA	5 patterns based on Klemann and Martinec (2009)	removed a-priori; not co-estimated
Processing			
	IMB	co-estimated	applied a-priori
	Estimation	two-step; common parameters followed by monthly solutions	one-step; each month individually, no common parameters
	Iterations	two; 2nd for bootstraps	one
	VCE	always	optional

The inversion in Rietbroek (2014) and Rietbroek et al. (2016) has been a two-step approach consisting of two runs, which incorporated an additional set of so called "bootstrap" fingerprints during the second estimation run. These have been derived from gridding the residuals with altimetry from the first estimation step and decomposing those grids by applying PCA, consequently, using the EOFs as fingerprints. The main motivation for utilizing these fingerprints was to capture remaining significant unmodeled signal present in the residuals and improve the overall budget retrieval during the second estimation run. However, it was not possible to clearly attribute these signals to either steric or mass related sea level changes. Furthermore, some components of the budget were prone to significant change between the two estimation runs. Consequently, the concept of bootstrap patterns is no longer used in this thesis. Nowadays, the representation of individual sea level components using the improved set of fingerprints has significantly reduced the residual signal making that step unnecessary. Instead, the residuals with altimetry from the first estimation are introduced directly as additional sea level component in the budget output (Sect. 7.1). These are denominated as "ocean dynamics", as the major spatial signatures are related to unmodeled eddies and ocean currents, but also certainly still include, both, residual mass and steric signals.

While earlier inversions (Rietbroek, 2014; Rietbroek et al., 2016) tried to co-estimate the residual GIA effect relative to a global given model (Klemann and Martinec, 2009) for five regions of the world (Laurentide, Fennoscandia, Antarctica, Greenland and complementary sources) as part of the inversion output, this has been removed from the inversion used in this thesis. Instead, the GIA is accounted for by applying a given GIA model as correction to the input data before

running the estimation step. This was necessary due to the fact that the estimated GIA values were identified to significantly underestimate the GIA effect compared to other published values, leading to unrealistic effects on the mass budget (Sect. 7.3.2).

The third group of inversion changes refers to the processing and interpretation of the results. While most of the altimetry IMB is removed by applying the RADS internal IMBs, the small remainder will show up in the altimetry residuals as constant biases of the residual time series introducing non-physical trends. Previous inversions (Rietbroek, 2014; Rietbroek et al., 2016) tried to co-estimate the IMB by modeling it as a 3D reference system shift. However, co-estimating this turned out to absorb sea level trend signal; this effect is significantly stronger when trying to co-estimate a constant shift. Therefore, for the base inversion, the remaining IMBs are applied a-priori to the altimetry data as described in Section 6.2.1.

Co-estimating the IMB as a mean value over time as well as the GIA component as a temporal trend requires data from all months. Thus, the previous inversions employed a two-step solver for the combined normal equation systems, where the first step reduced all the monthly fingerprint scaling parameters (App. A.2.3) and then only estimated the temporal mean and trend parameters. These were then fixed for each monthly NEQ system, when estimating the monthly fingerprint scales during the second step. Since neither the IMB, nor the GIA effect are co-estimated any longer, the first step is unnecessary for the base inversion presented in this thesis.

The VCE introduces a weighting of the individual observation groups on the NEQ level. In order to avoid potential consistency conflicts, when comparing inversion results and individual budget estimates to other published values, this has been made optional. Unless stated otherwise, the results presented in this thesis are always computed with VCE enabled. Finally, the interpretation of the inversion results and, consequently, the computation of the residual with altimetry has been modified.

6.2.6 The Base Inversion

The base inversion (Tab. 6.2, right column) describes the overall setup, which includes all revised fingerprints and updated processing as well as state of the art input data. The overall configuration is still relatively similar to Rietbroek (2014) and Rietbroek et al. (2016), e.g. the input data is limited to Jason-altimetry and GRACE gravity data.

The fingerprints are selected to model all relevant sea level signals observed by the GRACE and altimetry data. The number of EOFs in Rietbroek et al. (2016) was chosen to include about 99% of the signal variance. Similarly, the number of EOFs for the base inversion is adapted. Only for the deep ocean steric contribution the first 50 EOFs only cover about 80% of the signal. This is to exclude some potential small scale noise signals present in the steric reanalysis model data, which is not well constrained due to a limited availability of assimilated deep ocean observational data. Furthermore, during the overlap period of the individual Jason missions flying in a tandem formation (Sect. 3.1) only the latest mission is used starting from the first full month of available data in order to be consistent with the selection of missions in Nerem et al. (2018).

6.2.7 Extending the Inversion Setup

Starting from the base inversion, several extensions of the inversion framework are investigated and evaluated (Sects. 7.3 and 7.4). This includes additional input datasets from other mission phases of the Jason mission, but also data from altimetry satellites flying on different orbits, such as those of Envisat or Cryosat-2, allowing to achieve better high latitude spatial data coverage (Fig. 3.2).

One caveat of the inversion is the dependency on the availability of GRACE/GRACE-FO data in order to be able to separate the mass and steric sea level in combination with altimetry, leading

to missing months and a general data gap for the time between the two GRACE missions. It is investigated, whether introducing additional time-variable gravity information from SLR and Swarm can aid in filling those gaps. SLR data supports the mass signal in the low degree gravity coefficients up to degree and order 5, which are not well determined in the GRACE/GRACE-FO data and often replaced with SLR estimates (Loomis et al., 2019b; Landerer et al., 2020; Loomis et al., 2020).

In this context, including in-situ profiles of temperature and salinity data, converted to steric sea level change, can aid in improving the separation of steric and mass sea level changes as well as constraining the sea level budget in the GRACE gaps. However due to the limited data coverage of the deep ocean, the profiles in this thesis are restricted to the upper 700 m of the ocean (Sect. 3.3.1).

6.2.8 Converting Inversion Steric Sea Level to Ocean Heat Content

The general idea is to utilize the rescaled steric inversion results to improve retrieval of OHC. In the standard approach applied in literature (Johnson et al., 2016; Hakuba et al., 2019; Meyssignac et al., 2019; von Schuckmann et al., 2020; Hakuba et al., 2021; Marti et al., 2022, e.g.,), steric sea level trend estimates are simply scaled with a globally constant factor of $0.52\,\mathrm{W/m^2/mm/yr}$ (Kuhlbrodt and Gregory, 2012). In this thesis, for the first time, a novel approach is proposed, which rescales spatial OHC-EOFs based on the output of the fingerprint inversion.

For this new approach, first, OHC has been derived from the ORAS5 model data following section 2.3.2. The model OHC is then approximated by projecting onto the steric fingerprints ($\mathbf{U}_{\mathrm{ster}}$) utilized in the inversion based on equation (B.0.7)

$$\mathbf{D}_{\mathrm{ohc}} = (\mathbf{U}_{\mathrm{ster}}^T \mathbf{U}_{\mathrm{ster}})^{-1} \mathbf{U}_{\mathrm{ster}}^T \boldsymbol{Q}_{\mathrm{model}}. \tag{6.2.11}$$

The PCs, $\mathbf{D}_{\mathrm{ohc}}$, are then rescaled element wise by

$$\widetilde{d}_{\mathrm{ohc}} = \frac{d_{\mathrm{inv}}}{d_{\mathrm{ster}}} d_{\mathrm{ohc}}, \tag{6.2.12}$$

with the elements, d, of the corresponding PC matrices from the inversion ($\mathbf{D}_{\mathrm{inv}}$), i.e. the steric rescaling factors, the ORAS5 model data ($\mathbf{D}_{\mathrm{ster}}$) and the OHC ($\widetilde{\mathbf{D}}_{\mathrm{ohc}}$). Utilizing the rescaled PCs, the corresponding OHC is then constructed following equation (B.0.5)

$$\mathbf{Q}_{\mathrm{resc}} = \mathbf{U}_{\mathrm{ster}} \widetilde{\mathbf{D}}_{\mathrm{ohc}}. \tag{6.2.13}$$

In other words, instead of rescaling ocean-mean steric sea level trend estimates with a constant factor, the hypothesis is that one can derive improved rescaling factors as per major steric sea level related mode in the ocean.

In the next step, the grids of OHC are averaged over the region of interest, resulting in a time series of mean OHC. OHU can now be derived from OHC (Eq. (2.3.15)) in two ways, depending on the desired output. For the first approach, the basin time series of OHC (in $\mathrm{J\,m^{-2}}$) is used for deriving a trend over the chosen time period of interest. The trend ($\mathrm{J/m^2/yr}$) is then converted to $\mathrm{W\,m^{-2}}$ by division with the seconds in one year, resulting in an estimate of OHU.

In the second approach, the basin time series of OHC are filtered using a derivative filter and divide by the number of seconds in one year resulting in a time series of OHU. Since the derivative filter is a high pass filter, the time series will be noisy and an additional smoothing filter is applied to reduce that noise. Due to boundary effects, considering only the valid part of each filtered time series leads to a reduced number of points. Finally, an average over the desired time period can be computed. In a perfect world, both approaches should result in the same estimate of OHU, but due to the filtering effects this is not the case. Results from both approaches will be presented in section 7.6.2.

Chapter 7

Results: Consistent Closure of the Sea Level Budget

This chapter presents results for the global and regional sea level budgets derived from the improved fingerprint inversion, developed in this thesis. Special focus is on the consistency of estimates and potential impacts from inconsistencies. Unless stated otherwise, all sea level related estimates from the inversion are consistent in terms of applied corrections, evaluated at the Jason-1/-2/-3 nominal orbit positions and weighted employing inclination weights (Eq. (5.2.1)). The main time period chosen for comparisons is 2005-01 till 2015-12. Before 2005, the coverage of global in-situ steric profile data was insufficient, which consequently limits steric related data quality. Starting with 2016, degradation effects of the GRACE data increase, e.g. from replacing accelerometer data from one satellite with a transplant from the other due to an instrument failure (Bandikova et al., 2019). However, global sea level budget estimates for different time periods for the two major inversions utilized in this thesis are also provided in table C.1.

First, the global sea level budget is discussed in section 7.1, followed by validation and discussion of the individual sea level contributors in section 7.2. In section 7.3, impacts on the sea level budget from individual processing choices and extensions since the Rietbroek et al. (2016) inversion are examined, together, with different selections of fingerprint sub-sets, such as steric parameterizations based on different model data. Section 7.4 investigates the results from expanding the basic inversion setup of Jason-altimetry and GRACE input data with additional altimetry missions and GRACE-FO. Furthermore, the section examines the possibility from considering additional input data, such as time-variable gravity from SLR and Swarm or steric observations from easyCORA in-situ profile data. Regional budgets of sea level change are examined in section 7.5 for selected areas of interest. Finally, section 7.6 presents side results, such as degree-1 coefficients or EEI, produced by the inversion in addition to sea level budget estimates.

7.1 The Global Mean Sea Level Budget

On global scales, the sea level budget provides insights into drivers of contemporary global mean sea level rise, which is a major indicator of ongoing climate change. The global mean sea level budget is derived by globally averaging all individual sea level components for each month and deriving a trend from the resulting time series over a chosen period (here 2005-01 till 2015-12). This section presents the inversion results for individual contributors in the context of the overall budget. Discussions and validations of each component can be found in section 7.2.

An overview on the global mean relative sea level budget is provided in figure 7.1. The geocentric sea level from altimetry has been processed following section 5.2. For consistency, it is converted to relative sea level by applying the same GIA correction as in the inversion as well as correcting for the contemporary surface loading induced elastic uplift effect from the individual mass contributors as derived from the inversion. The OMC from the ITSG-2018 GRACE/GRACE-FO gravity

fields is derived following Section 5.3. The degree-1 coefficients during the GRACE processing are substituted with those extracted from the inversion solution (cf. Sect. 5.3.2 and Sect. 7.6.1). The ORAS5 temperature and salinity data has been converted to steric sea level change based on section 5.4 and has been further split into a contribution of the upper 700 m and the deep ocean part below 700 m.

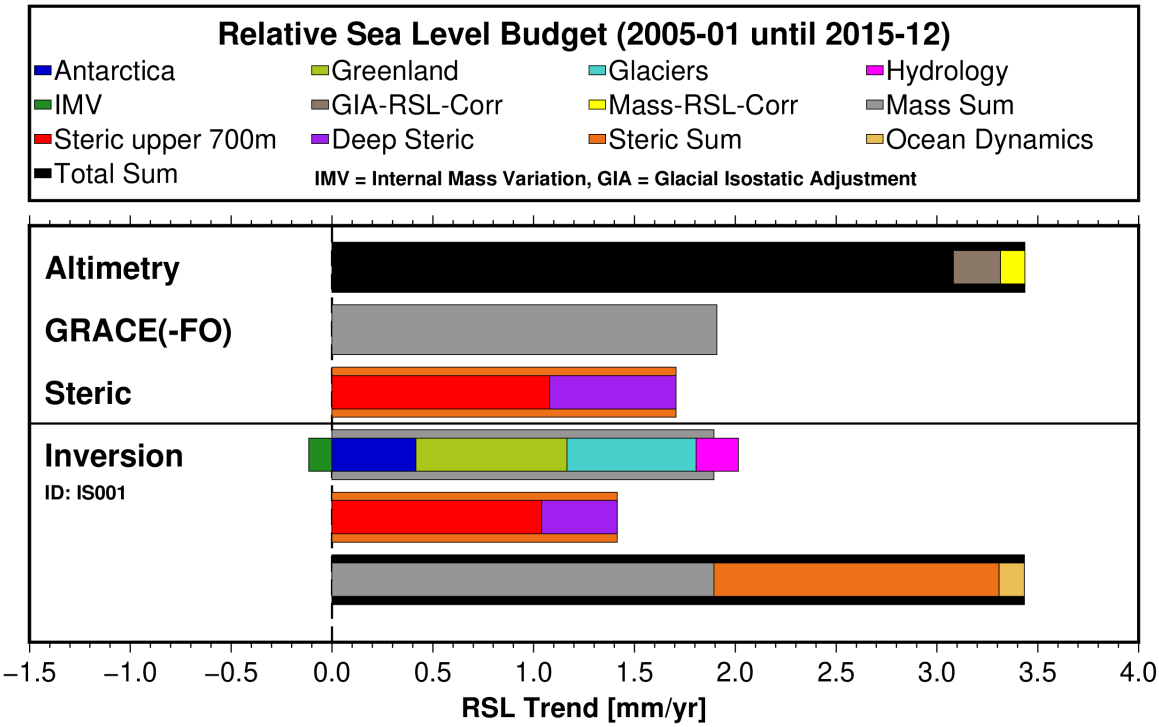


Figure 7.1: Global mean relative sea level budget overview from the base inversion (Tab. 6.2) for 2005-01 till 2015-12 with budget closure of 0.12 mm/yr. Individual components and integrated sums are compared with along-track Jason-1/-2/-3 altimetry (Sect. 5.2), GRACE/GRACE-FO ocean mass from the ITSG-2018 (Sect. 5.3) and steric sea level based on the ORAS5 re-analysis (Sect. 5.4). All datasets are evaluated at the inversion-input altimetry positions and averaged utilizing inclination weights (Eq. (5.2.1)). The trends are also reported in Table 7.1.

Besides partitioning the total sea level change into mass and steric contributions, the inversion method (Chap. 6) allows to further split the mass component into contributions from individual fractions related to the global water mass transport, even down to basin scales. Figure 7.1 (and Tab. 7.1) show the integrated effect for defined groups of individual basins, including the melting regions of the Greenland and Antarctic ice sheets, land glaciers, hydrological effects and IMV within the ocean. In addition, the inversion allows to further split the steric component into contributions from the upper 700 m and the deep ocean due to distinctly different spatial patterns, which translate to altimetry observations.

The total inversion results agree well with the individual altimetry processed data with a residual or budget closure error of 0.12 mm/yr. Spatially, the residuals are dominated by unmodeled eddies (cf. Sect. 7.2.9) and, hence, denoted as "ocean dynamics" in this thesis. Similarly, the OMC component agrees within 0.02 mm/yr with the independently and consistently processed GRACE/GRACE-FO spherical harmonic data. In contrast, the steric sea level from the ORAS5 re-analysis differs significantly from the inversion reconstructed steric change, especially for the deep ocean (Fig. 7.1 and Tab. 7.1).

Table 7.1: Sea level component trends and (semi-)annual amplitude and phase for the time frame 2005-01 till 2015-12. Datasets are evaluated at the Jason-1/-2/-3 nominal orbit positions and averaged with inclination weighting (Eq. (5.2.1)). The errors are derived assuming temporal correlations by considering an autoregressive process (App. A.3) in order to derive more realistic errors compared to simply propagating the formal errors.

Sea Level Component	Trend [mm/yr]	Annual Amplitude [mm]	Annual Phase [doy]	Semi-Annual Amplitude [mm]	Semi-Annual Phase [doy]
Steric upper 700 m	1.04 ± 0.09	3.86 ± 0.28	79.0 ± 4.7	1.71 ± 0.18	290.7 ± 3.1
Steric deep	0.38 ± 0.04	0.20 ± 0.15	180.7 ± 44.4	0.40 ± 0.11	301.0 ± 7.8
Steric sum	1.41 ± 0.07	3.83 ± 0.27	82.1 ± 4.1	2.09 ± 0.20	292.6 ± 2.7
Greenland	0.75 ± 0.01	0.37 ± 0.03	295.3 ± 4.9	0.07 ± 0.02	53.0 ± 7.4
Antarctica	0.42 ± 0.01	0.14 ± 0.03	36.5 ± 13.1	0.08 ± 0.02	24.8 ± 7.8
Glaciers	0.64 ± 0.01	1.26 ± 0.05	299.9 ± 2.1	0.17 ± 0.03	49.2 ± 5.2
Hydrology	0.21 ± 0.09	8.70 ± 0.31	283.5 ± 2.0	1.00 ± 0.21	4.8 ± 6.1
IMV	-0.11 ± 0.04	1.41 ± 0.16	141.7 ± 6.6	0.70 ± 0.14	61.9 ± 5.9
Mass sum	1.89 ± 0.13	9.12 ± 0.43	281.3 ± 2.7	1.23 ± 0.28	29.9 ± 6.6
Ocean Dynamics	0.12 ± 0.02	0.41 ± 0.06	355.6 ± 8.8	0.06 ± 0.05	31.2 ± 23.9
Total	3.43 ± 0.17	5.76 ± 0.49	296.3 ± 4.9	1.02 ± 0.30	278.1 ± 8.6
GIA	-0.23 ± 0.00	-	-	-	-
Elastic Uplift	-0.12 ± 0.01	0.53 ± 0.03	94.5 ± 2.7	0.08 ± 0.02	308.8 ± 5.7
ORAS5 upper 700 m	1.08 ± 0.13	3.55 ± 0.14	83.4 ± 2.3	1.80 ± 0.08	302.3 ± 1.2
ORAS5 deep	0.63 ± 0.01	0.07 ± 0.04	28.3 ± 34.3	0.02 ± 0.03	312.3 ± 37.6
ORAS5 sum	1.71 ± 0.12	3.59 ± 0.14	82.5 ± 2.2	1.82 ± 0.08	302.4 ± 1.2
GRACE/GRACE-FO	1.91 ± 0.13	9.59 ± 0.41	278.8 ± 2.4	1.28 ± 0.26	39.5 ± 5.8
Altimetry J1/2/3	3.44 ± 0.23	5.27 ± 0.47	302.1 ± 5.3	1.07 ± 0.29	279.5 ± 5.8

Figure 7.2 shows the temporal evolution of the individual sea level components. Table 7.1 provides the corresponding (semi-)annual amplitudes and phase estimates. The total sea level change and the OMC show a strong annual amplitude, which is roughly in phase with each other (296 d and 281 d, respectively). Steric sea level change is shifted by about 6 to 7 months with respect to OMC. In contrast, the annual amplitude of the residual component is relatively weak (Fig. 7.2, A). After 2015 and over the GRACE-FO period, the annual cycle of the steric component becomes less distinct (Fig. 7.2, A), while the mass trend is also reduced (cf. Sects. 7.3.6, 7.4.2 and 7.4.3).

The melting of the Greenland and Antarctic ice sheets and land glaciers dominate the OMC trend and the inter-annual variability is predominantly driven by the hydrological component (Fig. 7.2, B). IMV over the total global ocean is constrained to have a zero trend since it represents transports of mass within the ocean. However, on regional scales ocean mass transports can induce significant trends. Here, individual contributors are evaluated on the Jason altimetry mission nominal track positions, which do not cover the total ocean leading to the IMV trend estimate being not exactly zero (Tab. 7.1). With the degradation of the GRACE input data after August 2016, the time series show small jumps indicating difficulties with the separation of individual mass components (Fig. 7.2, B). Similarly, jumps can be detected in the steric time series, which is related to different relative weighting of the GRACE and altimetry observations (Fig. 7.2, C).

The steric seasonal and interannual variations are clearly dominated by the temperature and salinity changes in the upper 700 m. Contributions to the global steric trend from the deep ocean are close to zero between 2003 and 2011, but start to rise afterwards, resulting in the trend estimate

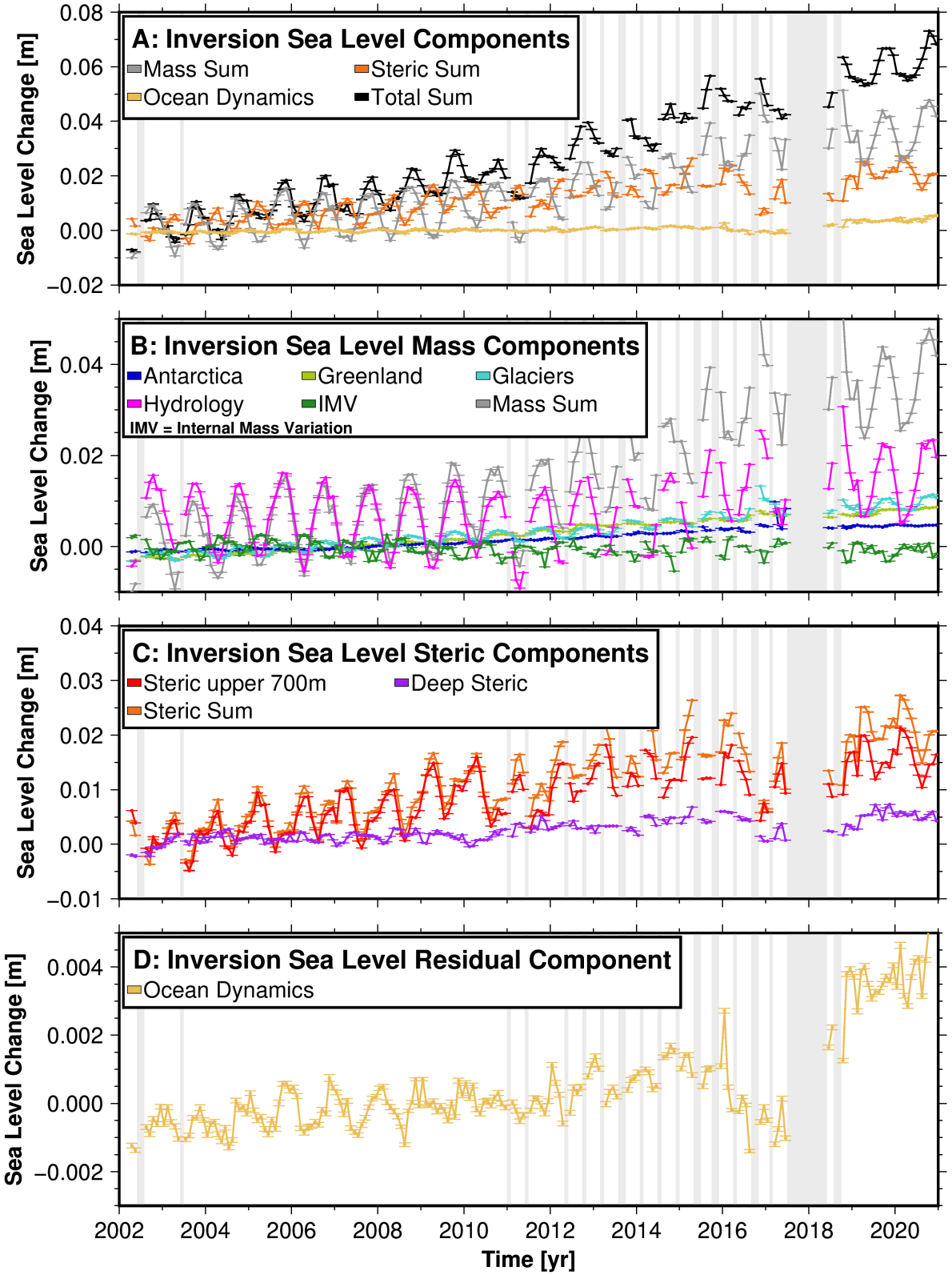


Figure 7.2: Global mean sea level budget time series. A: Global mean sea level, OMC and steric sea level change together with the budget closure error. B: Global OMC budget including integrated contributions from Antarctica, Greenland, land glaciers, hydrology and IMV. C: Global steric sea level budgets including contributions from the upper 700 m and from the deep ocean. D: The residual component.

of 0.38 mm/yr. From the ORAS5 deep steric model data, the (semi-)annual amplitudes are close to zero and corresponding phases show relatively large uncertainties (Tab. 7.1). The inversion solution finds slightly larger annual amplitudes and a significantly different phase, which are still connected to relatively large uncertainties. But, for the semi-annual amplitude and phase, the inversion finds significant differences with respect to the ORAS5 model data indicating measured signals, which are not covered in the model (Tab. 7.1).

Obviously the potential of modeling geophysical signals, which contribute to the sea level budget, depends on the employed set of fingerprints (Sect. 7.3.5). However, it is not entirely limited to the predefined (model) signals, but, will modify and deviate from the model input when necessary. This is most obvious from the deep steric contribution (Fig. 7.1) that is considered highly uncertain, even in re-analysis data.

Nonetheless, the inversion is not able to close the sea level budget completely. Instead the residual of total sea level change between altimetry and the inversion results in a budget misclosure of 0.12 mm/yr. It does not include any major signal but is linked to ocean regions with large eddy activity (Fig. 7.22 and Sect. 7.2.9). These eddies are observed by altimetry, but are not modeled by the fingerprints.

7.2 Contribution of Individual Sea Level Components

This section further investigates individual sea level budget components by comparing with additional datasets and other published estimates. A special focus is put on consistency and corresponding effects of inconsistencies on the reported estimates.

7.2.1 Total Sea Level Change

Total sea level change represents the sum of all individual OMC and steric sea level contributions and is observed by satellite altimetry. On global scales, spatially averaging total sea level results in estimates of GMSL. Since this thesis mainly focuses on monthly data and estimates, this also applies to the GMSL data. Mismatch of GMSL curves and corresponding trend estimates from different processing centers has been shown in figure 5.1. Despite utilizing the same input altimetry missions, processing choices regarding corrections or retracking play a huge role, but, also the choice of averaging region and corresponding data point selection and weighting (Sect. 5.2). Since own global altimetry processing in this thesis closely follows Nerem et al. (2018), this is chosen as the reference processing. The inversion input altimetry data has the same corrections applied with similar data selection and the resulting sea level budgets are also evaluated at the 1 Hz Jason along-track positions and globally averaged employing inclination weighting (Eq. (5.2.1)).

Consequently after removing the seasonal (annual+semiannual) signals (Fig. 7.3), the inversion based explained GMSL estimate is found close to the individually processed altimetry data time series, following Nerem et al. (2018). The major difference between the GMSL solutions is from the trend estimate (Tab. 7.2). But, the signal content of the individual GMSL curves is also different (Fig. 7.3), which is also evident from variations in the estimated seasonal amplitudes and phases (Tab. 7.2). The largest trend of 3.76 mm/yr is found from the CSIRO solution (Watson et al., 2015), followed by 3.56 mm/yr from the AVISO estimate (Ablain et al., 2015; Ablain et al., 2019) and 3.47 mm/yr and 3.43 mm/yr from the Nerem et al. (2018) based individual solution and the explained inversion GMSL, respectively. At the same time, the CSIRO time series is noisier compared to the other solutions (Fig. 7.3). The AVISO time series shows annual and semiannual amplitudes, which are larger relative to the other solutions (Tab. 7.2). Although the input data for the inversion should generally be the same as used for the Nerem et al. (2018) based computation, the small differences between the two are likely due to additional necessary data filtering applied during the inversion processing. Trend differences with respect to CSIRO and AVISO solutions are

Table 7.2: GMSL trends and (semi-)annual amplitude and phase for the time frame 2005-01 till 2015-12. Datasets are evaluated at the Jason-1/-2/-3 nominal orbit positions and averaged with inclination weighting (Eq. (5.2.1)). The errors are derived assuming temporal correlations by considering an autoregressive process (App. A.3) in order to derive more realistic errors compared to simply propagating the formal errors.

GMSL Source	Trend [mm/yr]	Annual Amplitude [mm]	Annual Phase [doy]	Semi-Annual Amplitude [mm]	Semi-Annual Phase [doy]
CSIRO (downl.)	3.76 ± 0.23	5.24 ± 0.57	316.5 ± 6.3	1.51 ± 0.33	303.9 ± 6.4
AVISO (downl.)	3.56 ± 0.05	6.39 ± 0.23	305.0 ± 2.1	1.62 ± 0.20	292.7 ± 3.5
Univ. Colorado (downl.)	3.49 ± 0.09	5.49 ± 0.40	298.4 ± 4.2	1.39 ± 0.34	285.6 ± 7.2
Univ. Colorado (own comp.)	3.47 ± 0.17	5.08 ± 0.48	290.5 ± 5.5	1.36 ± 0.25	281.23 ± 8.6
Inversion	3.43 ± 0.17	5.76 ± 0.49	296.3 ± 4.9	1.02 ± 0.30	278.1 ± 8.6

likely related to small differences in applied corrections, different conversions to RSL by applying GIA and contemporary mass uplift corrections as well as different global averaging strategies (see also Sect. 5.2).

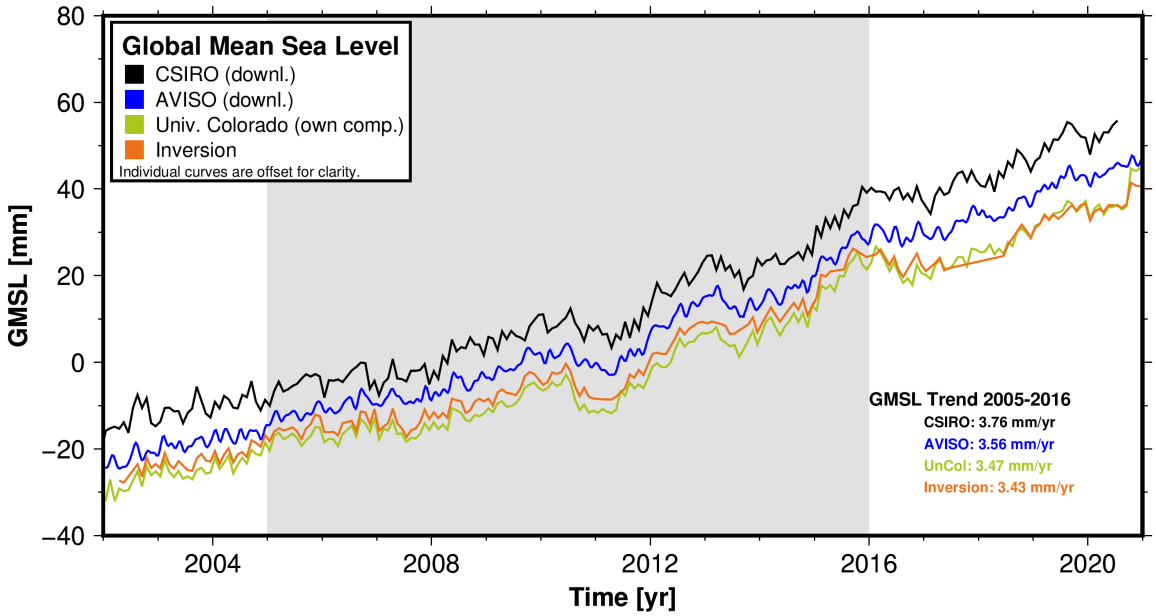


Figure 7.3: Comparison of GMSL derived from the inversion (sum over all components) with other independently computed or published time series. These include GMSL from CSIRO, AVISO and from the University of Colorado (Nerem et al., 2018, and Sect. 5.2). The seasonal signal has been reduced. The trend estimates refer to the same period 2005-01 till 2015-12 as in figure 5.1. Individual curves are offset for clarity.

The inversion GMSL trend of 3.43 mm/yr can be directly compared with the result by WCRP-Global-Sea-Level-Budget-Group (2018), who report 3.5 mm/yr for the same time period, computed from an ensemble mean containing six GMSL time series. For the slightly different period of 2005-01 till 2016-08, Horwath et al. (2022) find a GMSL rate of 3.80 mm/yr, which is derived from a combination of several altimetry missions. It agrees quite well with the 3.80 mm/yr found from the multi-mission altimetry inversion solution (IS030, Tabs. 7.15 and 7.16). This explains why the estimate is found larger compared to the 3.60 mm/yr and 3.66 mm/yr found from the inversion and the

independent processing following Nerem et al. (2018), respectively. For 2004-01 till 2015-12, Dieng et al. (2017) report GMSL of 3.27 mm/yr, which is close to the 3.33 mm/yr, when evaluating the inversion sea level. In comparison to Cazenave et al. (2009) for 2003-01 till 2007-12 (2.5 mm/yr), the inversion estimate is found larger (2.74 mm/yr). When comparing to 2.50 mm/yr from the earlier inversion solution by Rietbroek (2014), the updated version leads to an estimate of 2.38 mm/yr for the 2003-01 till 2011-01 time period, which is slightly lower. In contrast, comparison to 2.74 mm/yr from Rietbroek et al. (2016) reveals a larger inversion total sea level change of 2.90 mm/yr from this thesis' solution for the period 2002-04 till 2014-06. Including the GRACE-FO era 2005-01 till 2019-12 a total sea level change of 3.74 mm/yr is found, which is significantly smaller compared to 4.05 mm/yr found by Hakuba et al. (2021) for the same period. In contrast, Hakuba et al. (2021) utilize gridded multi-mission altimetry for deriving their GMSL estimate. Overall, the inversion total sea level change agrees well to other estimates with small deviations that are likely related to differences in corrections, employed missions, or averaging procedures, as already mentioned above.

The trend map of total (relative) sea level change (Fig. 7.4) shows the sum of the mass and steric contributions at each grid point. While GMSL rise is found with a magnitude of about 3.5 mm/yr, regional sea level rise can exceed this by a factor of up to five, e.g., locally at major currents or in the equatorial Pacific ocean. At the same time, there are regions, such as the northern central Pacific or the western Antarctic ocean, where the sea level between 2005-01 and 2015-12 is actually falling (Fig. 7.4). Deep ocean regions around the equator are generally dominated by (thermo-) steric sea level change and sea level variations in shallow regions and coastal shelves are predominantly driven by OMC (Figs. 7.4, 7.7 and 7.19).

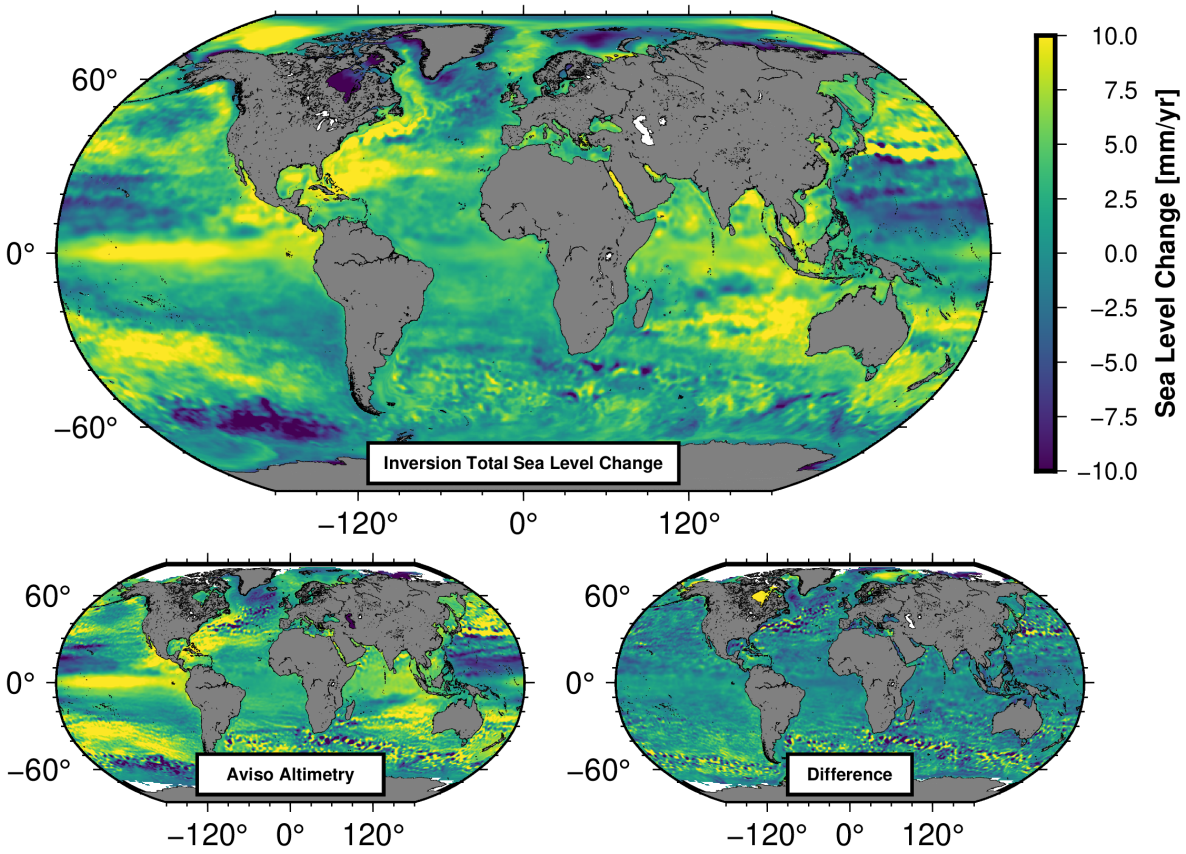


Figure 7.4: Spatial trend maps of total (relative) sea level change for the period 2005-01 till 2015-12. The total contribution represents the sum over all individual mass and steric sea level inversion components. For comparison a map of AVISO gridded sea level trends and the difference to the inversion is shown.

Inversion results agree well with corresponding trend maps from gridded AVISO altimetry data[1] for the same time period (Fig. 7.4). Small, but significant, differences are found mainly in the major current regions of the Gulf Stream, Agulhas, Kuroshio and Antarctic circum polar currents. This is expected, since the inversion does not explicitly model those currents and, consequently, the small scale and high frequency current signals show up in the residuals with altimetry, when computing the budget closure. In addition, differences related to the different processing of the inversion total sea level change and the gridded AVISO products lead to corresponding signal differences, when subtracting both datasets. Section 7.2.9 will show that these residuals are dominated by the current and eddy signals and do not contain any other major signal when directly compared at the along-track altimetry measurement positions. Generally, the small difference scales indicate the ability of the inversion approach to correctly reconstruct the total sea level change from individual mass and steric contributions.

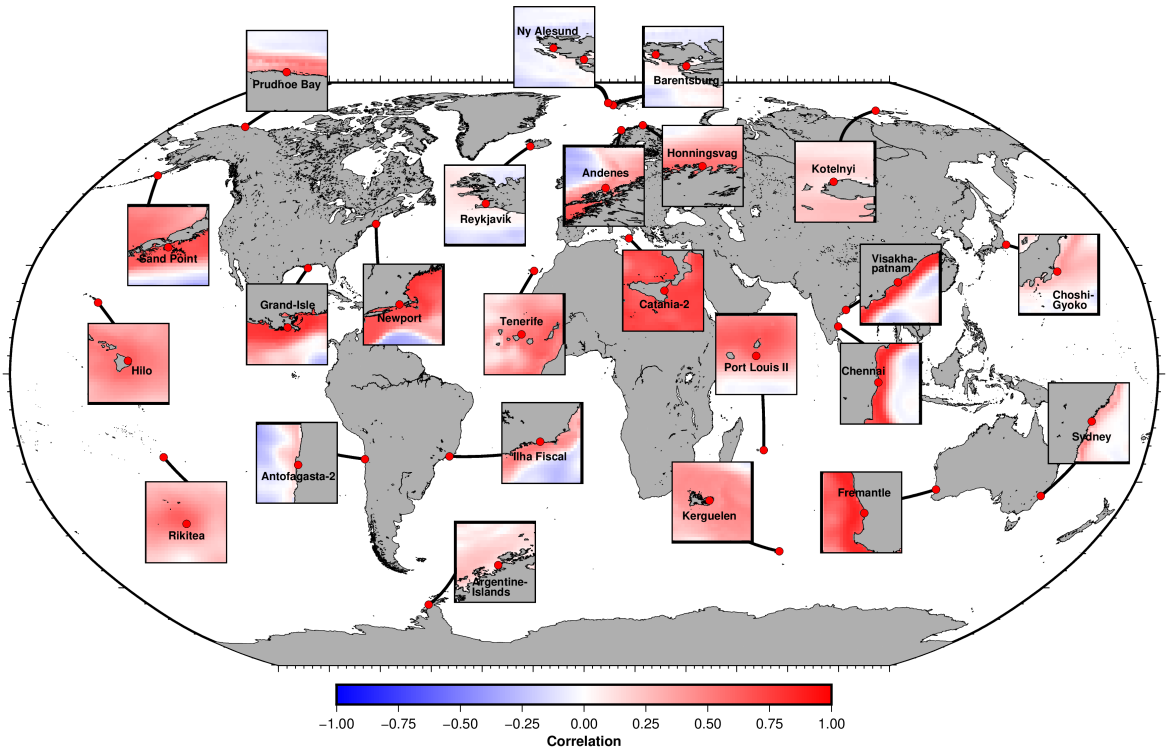


Figure 7.5: Correlation with tide gauge data for selected globally distributed tide gauges. The correlations are derived by correlating the tide gauge time series with those computed at each individual grid point close to the gauge.

In order to further assess the quality of the inversion total sea level change, a set of 24 tide gauges with good data availability and relatively evenly distributed over the globe has been extracted from the Permanent Service for Mean Sea Level (PSMSL, Holgate et al., 2013)[2]. Correlations are computed between the monthly tide gauge time series, corrected for inverse barometric effects, and time series from the inversion at individual grid points around the tide gauge in a three degree radius (Fig. 7.5). For consistency and comparability missing GRACE months have been removed in the AVISO gridded data. In general, good agreement is found with correlations well above 0.5 for 20 out of 24 tide gauges, while most even show correlations between 0.75 and above 0.9 indicating a well reconstructed total sea level rise (Fig. 7.5). For some tide gauges in the Arctic (Ny Alesund, Barentsburg and Reykjavik) and Antarctic (Argentine Islands) seas, the correlations are found weak or even slightly negative (Fig. 7.5). This is, on the one hand, related to the inversion input

[1]The Ssalto/Duacs altimeter products were produced and distributed by CMEMS http://www.marine.copernicus.eu (last accessed: 26.05.2022).

[2]https://www.psmsl.org/ (last accessed: 20.05.2022)

data being limited to only Jason-mission data, where the orbit does not cover regions exceeding 66° of latitude due to the mission orbit inclination. On the other hand, local phenomena, such as seasonal ice coverage or impacts from currents, are not well captured within the inversion and will affect the reconstructed sea level compared to the tide gauge measurements.

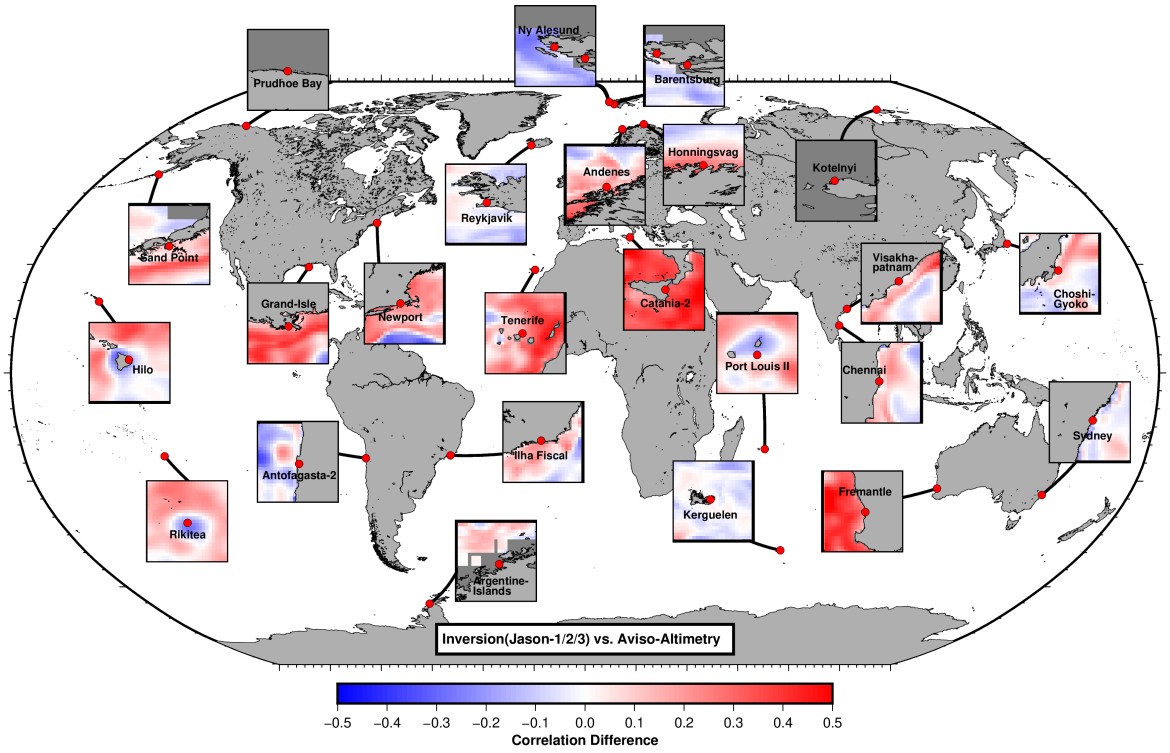


Figure 7.6: Correlation improvement of inversion gridded total sea level change relative to gridded monthly mean AVISO altimetry data at selected tide gauge stations. Red colors indicate better agreement of inversion and tide gauge data while blue indicates better correspondence to the AVISO altimetry data.

When computing the correlations for the same stations with AVISO gridded altimetry data and then subtracting them from the correlations between the tide-gauge data and the inversion solution, allows to identify tide gauges where one solution outperforms the other (Fig. 7.6). In contrast to the inversion, AVISO grids do not provide data in the ice covered regions of the Arctic and Antarctic, which prohibits comparisons at some of the tide gauges, either partially at some grid points or entirely (Prudhoe Bay and Kotelnyi). Generally for 18 out of 24 of tide gauges, a better correspondence with the inversion total sea level is found compared to the AVISO gridded data (Fig. 7.6). At other locations both datasets roughly provide the same quality of data, e.g., Hilo, Rikitea, Port Louis II or Kerguelen. Overall, the inversion is able to provide the same or even slightly better gridded sea level quality compared to state of the art gridded sea level products.

7.2.2 Ocean Mass Change

Ocean Mass Change (OMC) represents the integral effect of all individual mass contributions that modify the in- and outflow into the ocean and the water transport within. This leads to regions of mass accretion especially in coastal and shallow regions, such as the United States East coast, parts of the North Sea, the Mediterranean sea, the Indian and Bangladesh coastal shelf, as well as the ocean North of Australia and the Indonesian Sea (Fig. 7.7). Mass increase is found in the eastward extensions of the Kuroshio current and North-East Antarctica (Fig. 7.7). Strong mass loss signals are detected in the Hudson Bay and around the Greenland coast, the northern Barents Sea, along the US Alaska West coast and in the ocean at the coast of West Antarctica and of the

Antarctic Peninsula (Fig. 7.7).

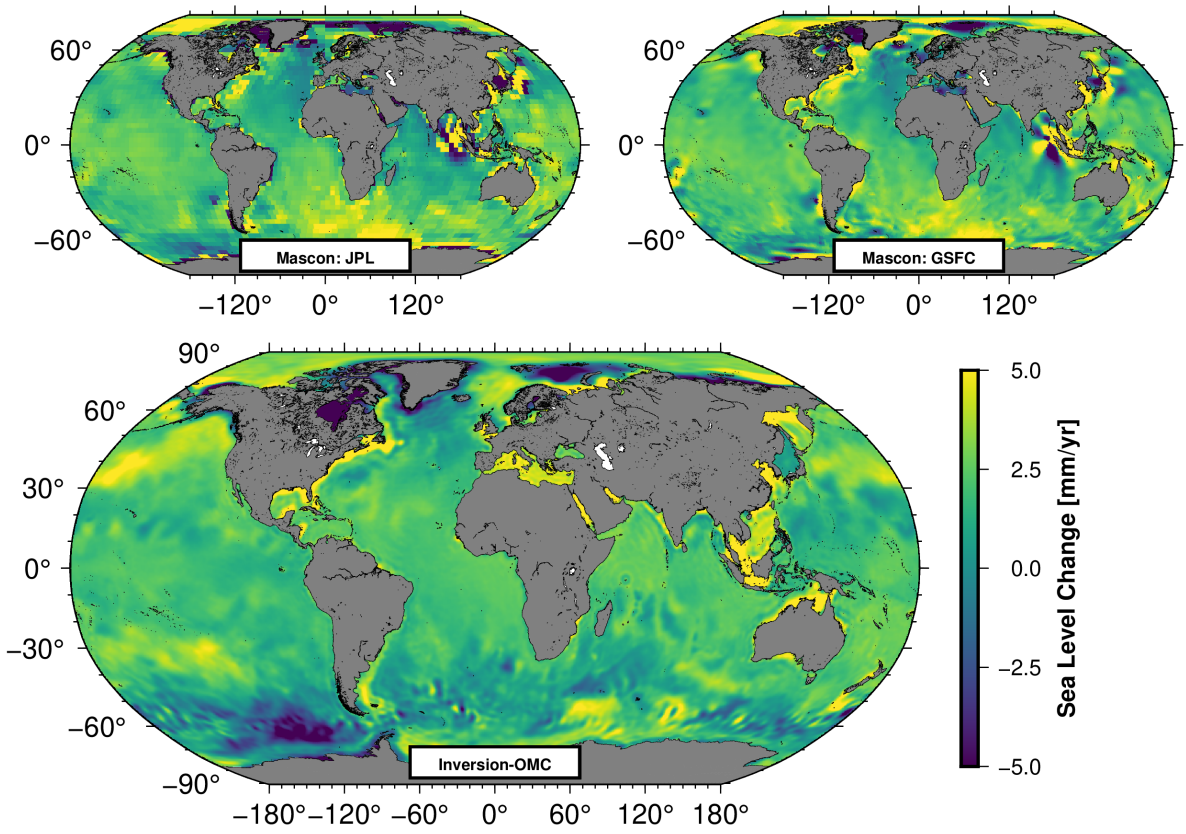


Figure 7.7: Spatial trend maps of OMC derived from the inversion and two mascon solutions by JPL and GSFC for the period 2005-01 till 2015-12. The OMC contribution represents the integrated effect from the melting of land glaciers and the ice sheets in Greenland and Antarctica, terrestrial hydrology, IMV, and GIA.

In addition to spatial trend maps based on the inversion result, figure 7.7 also includes trends from two mascon solutions by JPL and GSFC. The spherical harmonic GRACE solution is excluded, since it shows strong leakage effects due to applying no filtering when following the processing outlined in section 5.3. Comparing the two mascon solutions reveals regional differences, especially around Sumatra, which is related to treatment of the artifact caused by the 2004 earth quake (Han et al., 2006). But, the two solutions also do not agree in other regions, such as the major current regions (Gulf Stream, Agulhas or Kuroshio) at the South American west coast, around Australia or in the (Ant-)Arctic oceans. In addition, both mascon solutions suffer from hydrological and ice mass influence along the coast lines, e.g., around Greenland (Fig. 7.7). The inversion solution does not have this drawback and is able to provide OMC information closer to the coast, since the hydrological component is explicitly considered and modeled as part of the sea level budget.

Averaging the inversion OMC on global scales results in time series of global mean OMC that can be compared with other methods. These methods include computation of OMC from GRACE/GRACE-FO and independent estimates based on time-variable gravity derived from SLR and Swarm. The seasonal cycle from all solutions agrees well (Fig. 7.8) with some anomalies found for the SLR solution, which are likely related to the limited maximum degree and order. While the individual solutions agree well during the GRACE era of the de-seasoned OMC time series, significant biases and trend differences are observed following the degradation of the GRACE solutions after 2016 and during the available GRACE-FO period.

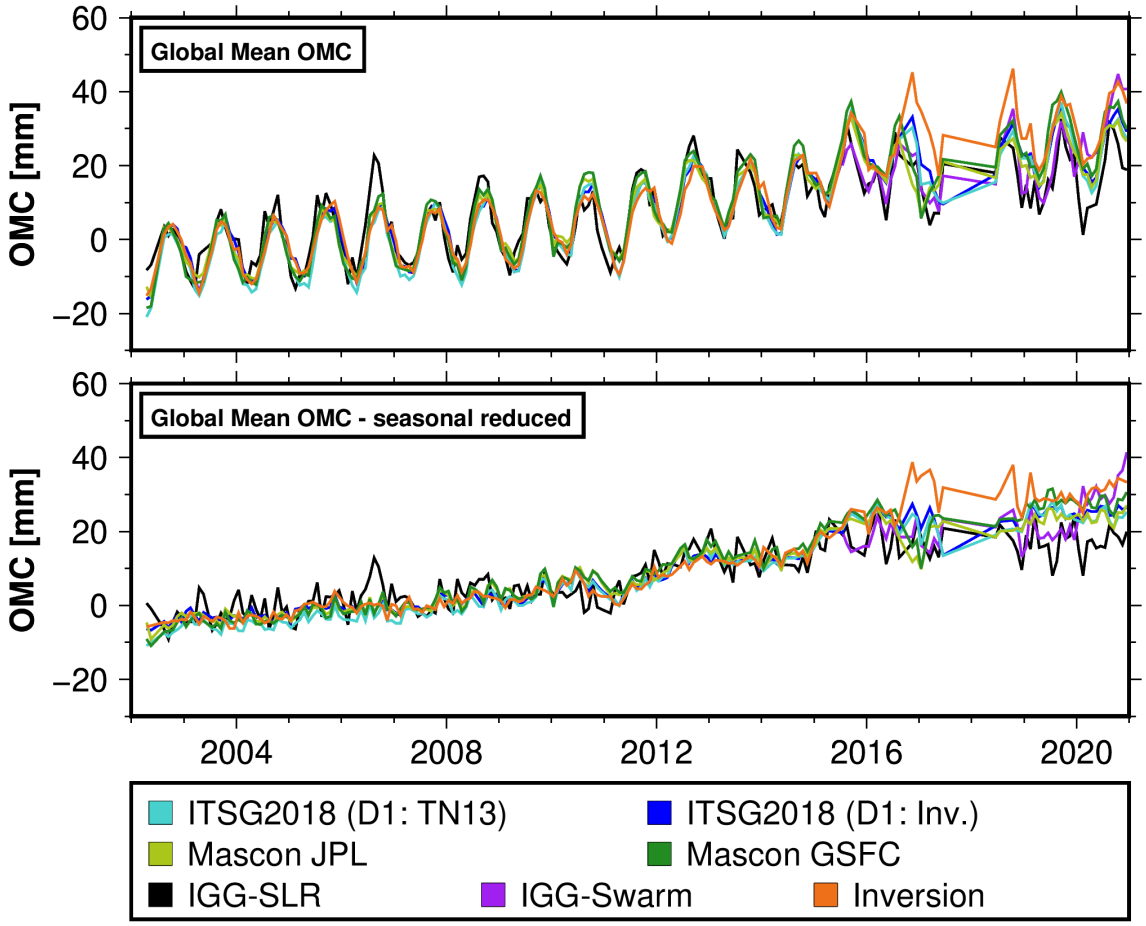


Figure 7.8: Comparison of global mean OMC time series from different data sources. This includes two ITSG2018 GRACE/GRACE-FO solutions with different degree-1 substitutes (Sect. 7.6.1), two mascon solutions from JPL and GSFC, Institut für Geodäsie und Geoinformation (IGG) SLR and Swarm-based time-variable gravity fields and the inversion OMC output. Top: Full OMC signal. Bottom: Annual and semiannual signals removed. All time series are made consistent with the available GRACE/GRACE-FO months.

Based on table 7.3 for 2005-01 till 2015-12, the inversion based global mean OMC trend (1.89 mm/yr) fits well to the ITSG2018 solution with degree-1 substitutes extracted from the inversion (1.91 mm/yr). Substituting the official TN13 degree-1 coefficients, instead, for the ITSG2018 compared to the GSFC mascon solution leads to trend estimates of 2.18 mm/yr and 2.20 mm/yr, respectively, while only 2.02 mm/yr are derived from the JPL mascon solution (Tab. 7.3). A lower trend of 1.58 mm/yr is found from the SLR data most likely due to the lower maximum degree and order, since a higher order solution utilizing additional EOFs (Löcher and Kusche, 2020) provides better results.

Trends for the available GRACE-FO period (2018-06 till 2020-12) differ more significantly (Tab. 7.3). Although 2.5 years is a rather short time span for deriving trends, which prohibits in depth analysis of the geophysical processes, this time period can still serve as an indication on the agreement between individual OMC solutions. The resulting span of trends is rather large, ranging from 0.11 mm/yr from the SLR solution to 6.72 mm/yr from Swarm (Tab. 7.3). The GRACE-FO based solutions including the inversion find OMC trends between 1.00 to 2.00 mm/yr (Tab. 7.3). The inversion estimate is influenced by the limited available time frame of the hydrological and steric fingerprints and the inability of extrapolating the highly spatio-temporal variable signals (Sect. 7.3.6).

Table 7.3: Comparison of global mean OMC trends from different data sources for the time periods 2005-01 till 2015-12 of the GRACE era and 2018-06 till 2020-12 for the GRACE-FO period. The errors are derived assuming temporal correlations by considering an autoregressive process (App. A.3) in order to derive more realistic errors compared to simply propagating the formal errors.

OMC Source	**OMC trend** mm/yr	
	2005-01 - 2015-12	2018-06 - 2020-12
ITSG2018 (D1: TN13)	2.18 ± 0.13	1.07 ± 0.92
ITSG2018 (D1: Inv.)	1.91 ± 0.13	1.50 ± 0.52
Mascon-JPL	2.02 ± 0.11	1.87 ± 0.57
Mascon-GSFC	2.20 ± 0.12	2.01 ± 0.81
IGG-SLR	1.58 ± 0.18	0.11 ± 1.18
IGG-Swarm*		6.72 ± 1.78
Inversion	1.89 ± 0.13	1.12 ± 0.88

* Swarm data only covers a small portion of the first period.

Table 7.4: Effect on the OMC trend estimate (2005-01 till 2015-12) from choosing different "global" ocean regions for averaging. Here shown exemplary for the ITSG2018 GRACE solution processed following section 5.3.1. The errors are derived assuming temporal correlations by considering an autoregressive process (App. A.3) in order to derive more realistic errors compared to simply propagating the formal errors.

Selected Region	**OMC trend** mm/yr
0 km coastal buffer (w^{lat})	1.40 ± 0.09
300 km coastal buffer (w^{lat})	1.88 ± 0.13
Jason-altimetry positions (w^{lat})	1.82 ± 0.13
Jason-altimetry positions (w^{incl})	1.91 ± 0.13

The chosen ocean basin and weighting scheme (Sect. 5.3.1) significantly affects the global mean OMC estimate. Table 7.4 shows the effect from selecting three different basins and two weighting schemes. Computing the basin average in the spherical harmonic domain (Eq. (5.3.1)) is, theoretically, equivalent to averaging grid cells, while applying latitude-weighting (Eq. (5.2.2)) for each grid point. When utilizing data up to the coast, i.e. applying a 0 km coastal buffer zone, the OMC estimate derived from ITSG2018 is in the order of 1.40 mm/yr, which is significantly smaller compared to the 1.88 mm/yr when applying a 300 km coastal buffer zone commonly used in literature (e.g., Johnson and Chambers, 2013). The difference is mostly driven by leakage effects from the ice sheets and terrestrial hydrology signals due to the limited GRACE/GRACE-FO spatial resolution. When evaluating the OMC on all Jason altimetry positions, which are limited by the satellite inclination and by additionally excluding all coastal positions, the resulting estimate is slightly smaller than the one from a 300 km buffer zone, but larger than from a 0 km zone. When the weighting scheme is adapted to the limited inclination from the Jason coverage, the estimate of 1.91 mm/yr is well within the error bounds of the 300 km buffered ocean estimate, but still not the same. Consistency with respect to the averaging region and weighting scheme is therefore important, especially, in combination with other sea level estimates in the context of sea level budgets.

When comparing the inversion based estimate and own processing of GRACE/GRACE-FO based estimates from table 7.3 to those reported in literature, some discrepancies are observed. WCRP-Global-Sea-Level-Budget-Group (2018) report an global mean OMC estimate of 2.30 mm/yr, which represents an average over an ensemble of spherical harmonic based GRACE solutions from different processing centers. The ensemble members are derived following the Johnson and Chambers (2013) processing scheme, a forward modeling estimate (update from Chen et al., 2013) and

Table 7.5: Standard deviation of the differences in cm EWH between the monthly averaged OBP gauge data and different solutions of GRACE-based OBP evaluated at the in-situ OBP gauge positions (Fig. 7.9).

OBP-Gauge	Mascon-JPL	Mascon-GSFC	Inversion	ITSG2018
A: Atlantic Bermuda	5.5	5.5	5.9	13.5
B: Bay of Bengal	4.7	2.4	1.6	12.6
C: Hawaii	1.2	1.2	1.7	9.6
D: Central Pacific	1.2	1.3	1.3	12.0
E: Tasman Sea	1.8	1.6	1.5	8.3
F: Philippine Sea	1.7	1.9	1.6	10.8
G: North Santo-Domingo	1.3	1.3	1.6	12.2

three mascon solutions, which all together provide a range of 1.76 to 2.61 mm/yr. The ensemble mean contains inconsistencies with respect to the periods of individual estimates. However, no information is provided on the ocean basin used for averaging. For 2005-01 till 2016-08, Horwath et al. (2022) report 2.69 mm/yr and 2.47 mm/yr for global mean OMC, where the ice sheet contribution is derived from ice altimetry and GRACE, respectively. The inversion based estimate is found to be 2.08 mm/yr for the same time period. Dieng et al. (2017) find OMC of 2.24 mm/yr for 2004-01 till 2015-12, where the inversion estimate of 1.81 mm/yr is significantly lower for the same period. This is connected to the processing effects due to strictly following Johnson and Chambers (2013), where the AOD1B has not been restored correctly (cf. Sect. 5.3.2). Similar issues are found with OMC estimates of Cazenave et al. (2009), Dieng et al. (2015) and Chambers et al. (2017). Compared to OMC of 1.16 mm/yr (2003-01 till 2011-12) from Rietbroek (2014), the inversion in this thesis agrees quite well with an estimate of 1.08 mm/yr. However, this is rather a coincidence as the individual mass contributors, especially from land glacier melt and terrestrial hydrology, are different (cf. Sects. 7.2.3, 7.2.4, 7.2.5 and 7.2.6). Similar issues explain discrepancies to Rietbroek et al. (2016), who found OMC of 1.08 mm/yr over 2002-04 till 2014-06, which is significantly smaller compared to this thesis's inversion estimate (1.43 mm/yr). Including the GRACE-FO period, Hakuba et al. (2021) report OMC of 2.38 mm/yr for 2005-01 till 2019-12, which is slightly smaller compared to 2.46 mm/yr found by the inversion. Disagreement between published estimates and consistently derived ones in this thesis is mainly related to processing issues (Sect. 5.3.2), when deriving the integrated effect directly from GRACE/GRACE-FO and disagreement of individual sub-contributions, when providing an integrated estimate as shown in the following sections.

Converting OMC to OBP, by restoring the time-variable total ocean average of the AOD1B-GAD product, allows direct comparison to in-situ OBP gauges at their respective locations. Naturally, these gauges are heavily influenced by high frequency local signals but monthly averages can serve as an independent validation of space-based OBP estimates. Here, 7 gauges distributed over all major ocean basins (Fig. 7.9) are extracted from the PSMSL database. Each of the gauges utilized for comparison provides at least 5 years of data during the GRACE era. Time series for three characteristic regions (Fig. 7.9) indicate different performance in retrieving space-based OBP, depending on the methodology applied to the GRACE data. The spherical harmonic processing, as described in section 5.3, provides a very noisy time series when evaluated at a single location and would require additional filtering, which is why it is not included within the figure. Table 7.5 provides standard deviation of the differences in cm EWH of individual space-based OBP time series with the respective gauge.

The Atlantic Bermuda station (Fig. 7.9, A) is located in close vicinity to the Gulf Stream and indicates a high amplitude signal and temporal variability due to the currents and eddies in this region. Both mascon solutions as well as the inversion result find a significantly smaller amplitude and different temporal evolution. These two processing approaches act as a kind of

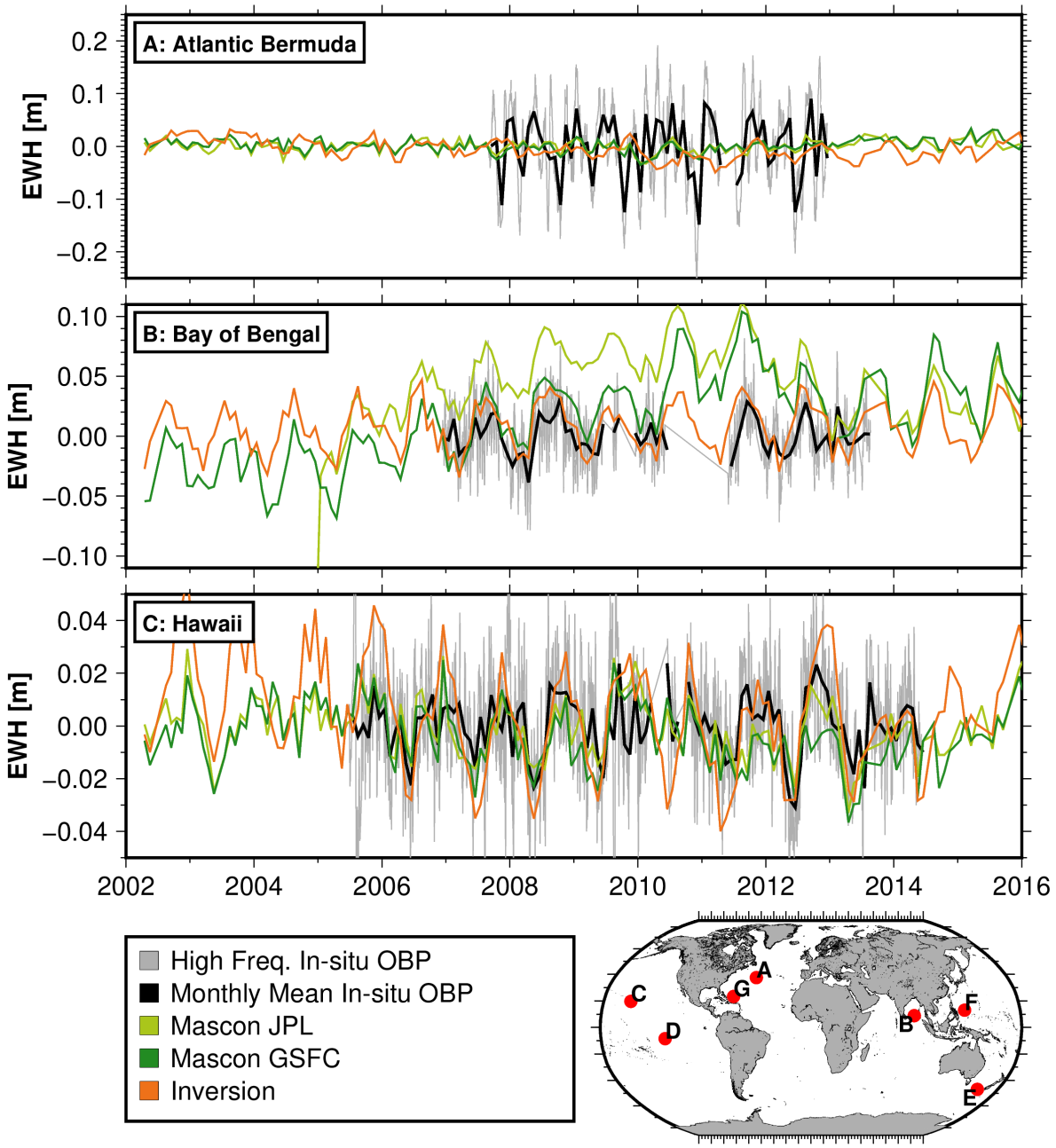


Figure 7.9: Comparison of OBP from selected gauge stations, including at least five years of data, with OBP derived from the inversion and individually processed GRACE data. Conversion from OMC to OBP is based on section 5.3 and mainly refers to adding back the total ocean mean AOD1B-GAD values. Time series from three representative stations are shown. A: The Atlantic Bermuda station is located in the Gulf Stream region, observing high amplitude time-variable signal. B and C: The Bay of Bengal and Hawaii stations show a clear seasonal signal overlayed by higher frequency variations.

low-pass filter removing high frequency signals, which limits the signal retrieval and analysis. This is also represented in the standard deviations with the gauge data, where magnitudes of about 5.5 to 5.9 cm are found for the mascon and inversion results, while the unfiltered GRACE spherical harmonic solution leads to more than 13.5 cm. In the Bay of Bengal (Fig. 7.9, B), the high frequency gauge data shows a clear annual signal after monthly averaging. While the inversion solution shows relatively good agreement, both mascon solutions are biased significantly. This is related to remaining artifact signals in the gravity data resulting from the Sumatran Earth quake

at the end of 2004, which can clearly be identified in the JPL mascon solution. The inversion is able to filter these highly localized signals due to the global scale of the individual fingerprints, providing significantly better agreement with the gauge data (Tab. 7.5). The Hawaii station (Fig. 7.9, C) also shows an annual signal, which is recovered relatively well by mascon as well as inversion based OBP. Here, the two mascon solutions provide slightly better agreement of 1.2 cm compared to the inversion (1.7 cm). For the other station positions (Fig. 7.9), the inversion provides similar quality OBP estimates than the mascon solutions (Tab. 7.5). Together the three regions and the other station-metrics indicate the limits of the space-based OBP and OMC retrieval, especially with respect to spatial and temporal resolution.

7.2.3 Greenland Mass Change

Ice melt from the Greenland ice sheet is the main contributor to global OMC. The sea level contribution is mainly driven by the melt below 2000 m elevation, which is not compensated by the accretion of snow and ice above 2000 m elevation in the central regions of Greenland (Fig. 7.10 and Fig. 7.11). Significant melting of more than 1.5 m/yr EWH is found for the Jacobshavn glacier in the West of Greenland (Fig. 7.10, basin-07), the Helheim and Kangerdlugssuaq glaciers in the East (−1.0 to −0.5 m/yr, Fig. 7.10, basin-04), but also at the Petermann glacier in the North (∼ 0.25 m/yr, Fig. 7.10, basin-01) as well as the Zachariae and Nioghalvfjerdsbrae (79°N) glaciers in the North-East (∼ 0.25 m/yr, Fig. 7.10, basin-02).

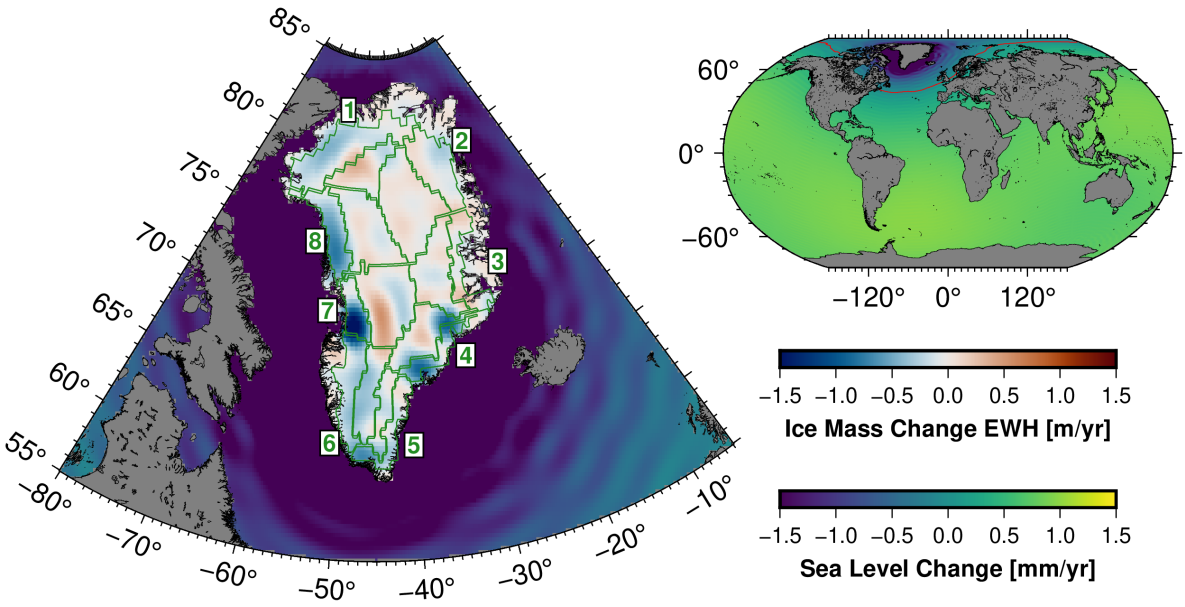


Figure 7.10: Spatial trend map of inversion-based ice mass change over the Greenland ice sheet together with corresponding spatial trend map of induced sea level change for the period 2005-01 till 2015-12. Left: Detailed view of Greenland ice mass change and surrounding sea level effect. Right: Global trend pattern due to Greenland ice melt. The red line indicates the zero contour of no relative sea level change.

The corresponding relative sea level change results from a smooth distribution of the melt water input over the total ocean. However, the Greenland ice-melt driven sea level close to the Greenland mainland actually decreases by more than 1.5 mm/yr (Fig. 7.10) due to the missing gravitational attraction of the ice mass and the elastic rise of the Earth's surface (Sect. 2.2). In figure 7.10, this is indicated by the red zero sea level change contour line. South of the line, melting of the Greenland ice sheets will lead to a rise in relative sea level. From the inversion, the melting of the Greenland ice sheet between 2005-01 and 2015-12 contributes 0.75 mm/yr (Tab. 7.1) and 0.73 mm/yr (2005-01 till 2016-08 as in Horwath et al., 2022), which is well in line with other recently published

estimates of 0.75 mm/yr (WCRP-Global-Sea-Level-Budget-Group, 2018) computed from averaging six published Greenland melting rates. In Horwath et al. (2022), 0.72 mm/yr and 0.81 mm/yr are derived for the same time frame from ice altimetry and GRACE, respectively. From combining ice-altimetry derived mass changes with peripheral glacier mass loss, Horwath et al. (2022) report a sea level contribution of 0.92 mm/yr, which is significantly larger compared to other estimates. Utilizing an approximate conversion, the Greenland mass changes from table 7.6 can be converted to sea level change of 0.77 mm/yr, 0.48 mm/yr and 0.60 mm/yr for TU Dresden, JPL and GSFC mascons, respectively. For the slightly different time period of 2004-01 till 2015-12, Dieng et al. (2017) find 0.82 mm/yr, which is larger compared to 0.74 mm/yr extracted from the inversion for the same time frame. Rietbroek (2014) report 0.66 mm/yr for the time frame 2003-2011 and Rietbroek et al. (2016) provide 0.73 mm/yr for the time period 2002-04 till 2014-06, both of, which is well in line with the inversion results of 0.65 mm/yr and 0.70 mm/yr, respectively. For 2005-01 till 2019-12, a mass change of 0.67 mm/yr is found from the inversion, which is significantly smaller compared to the 0.81 mm/yr found by Hakuba et al. (2021) and likely related to filtering and averaging processing steps.

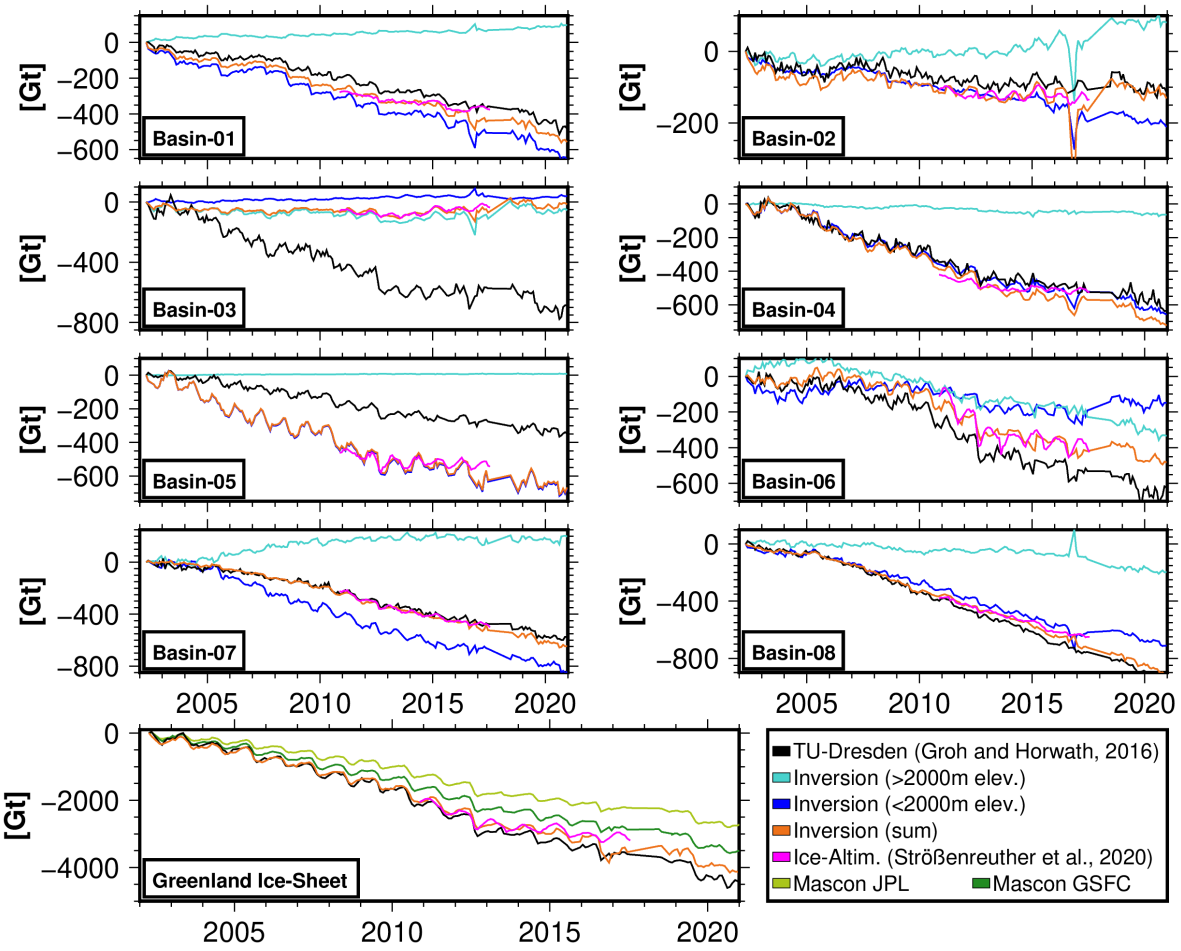


Figure 7.11: Time series of inversion results from individual Greenland basins compared to external GRACE based results from TU Dresden (Groh and Horwath, 2016) and ice-altimetry-based mass changes derived from Strößenreuther et al. (2020). The integrated Greenland mass change is additionally compared to two GRACE mascon solutions from JPL and GSFC.

Figure 7.11 compares the mass changes in each of the eight Greenland basins to external data from GRACE/GRACE-FO spherical harmonic and mascon solutions as well as ice altimetry based mass changes derived from Strößenreuther et al. (2020). The latter is limited to the time period of the Cryosat-2 mission (Fig. 3.1). All basins show overall mass loss. Above 2000 m elevation, basins

Table 7.6: Greenland ice mass loss trends in Gt/yr for the period 2005-01 till 2015-12 for the Greenland ice sheet and eight sub-basins (e.g., Fig. 6.2) from the inversion compared to external GRACE/GRACE-FO data from TU Dresden (Groh and Horwath, 2016) and mascon solutions from JPL and GSFC. Furthermore, ice mass change based on ice-altimetry data (Strößenreuther et al., 2020) from 2011-01 till 2015-12 is shown. The errors are derived assuming temporal correlations by considering an autoregressive process (App. A.3) in order to derive more realistic errors compared to simply propagating the formal errors.

	Inversion	**TU Dresden**	**JPL Mascon**	**GSFC Mascon**	***Ice-Altim.**
Basin-01	-29.0 ± 1.32	-26.1 ± 1.02			-15.55 ± 2.35
Basin-02	-6.07 ± 0.76	-5.29 ± 0.81			-0.18 ± 2.11
Basin-03	-1.76 ± 0.69	-47.15 ± 1.55			5.08 ± 3.92
Basin-04	-45.90 ± 1.00	-37.48 ± 1.06			-14.16 ± 3.51
Basin-05	-39.95 ± 1.39	-23.41 ± 0.57			-11.51 ± 3.40
Basin-06	-42.28 ± 1.89	-50.53 ± 1.97			-46.71 ± 9.93
Basin-07	-41.63 ± 0.83	-38.11 ± 0.75			-42.91 ± 2.75
Basin-08	-52.99 ± 0.64	-58.16 ± 0.46			-44.45 ± 1.56
Greenland	-259.63 ± 4.75	-286.19 ± 5.16	-181.94 ± 3.18	-221.14 ± 3.12	-170.39 ± 26.33

*Ice-altimetry is only available for the Cryosat-2 period starting end of 2010.

01, 02 and 07 show mass gain. But, this cannot compensate the mass loss of the lower part (below 2000 m elevation) of the basin. For half of the basins (basins 01, 02, 07 and 08), the inversion derived mass change agrees well to the one provided by TU Dresden based on Groh and Horwath (2016). However, for basins 03 and 05 larger disagreements of 45 Gt/yr and 17 Gt/yr, respectively, to the inversion results can be observed while basins 04 and 06 show smaller mass differences of about 8 Gt/yr (Tab. 7.6). Basin 04 includes the strong mass loss signals from the Helheim and Kangerdlugssuaq glaciers, which will be sensitive to leakage effects due to smoothing during the spherical harmonic processing. In basin 03, the inversion detects only minimal mass changes, while the GRACE based estimate from TU Dresden indicates a large mass loss over time. Additional comparison to ice altimetry data (Strößenreuther et al., 2020) converted to mass change reveals better agreement with the inversion. The lower elevation parts of basins-03 and basin-05 are much smaller compared to other sub-basins. This makes it difficult to separate individual basin mass changes, e.g. from the spherical harmonic approach employed by TU Dresden or from the inversion, since the GRACE/GRACE-FO spatial resolution is not sufficient. In contrast, ice-altimetry comes with a much higher spatial resolution and is, thus, less impacted by the basin size. Furthermore, the inversion retrieval, based on fingerprints, is additionally constrained by the observed sea level effect outside of the basins. In contrast, the spherical harmonics approach is based on a simple basin average, where the signal outside the basin is mostly ignored.

Introducing a priori background patterns, as it is done in this thesis, supports in better separating mass changes, significantly reducing the inter-basin correlations. In contrast, Rietbroek (2014) assumed uniform basin-wide mass changes, which lead to compensation effects between corresponding basins above and below 2000 m elevation (e.g., basin 01, 03 and 06 in Rietbroek, 2014). Section 7.3.5 further investigates the effect on the sea level budget from incorporating background patterns or not.

For the total mass loss of the Greenland ice sheet, the inversion result agrees well to the one by TU Dresden until about 2013, where the two begin to differ (Fig. 7.11), which leads to a trend difference of about 26 Gt/yr (Tab. 7.6). Additional comparison of mass loss derived from mascon solutions by JPL and GSFC shows significantly less mass loss (-182 Gt/yr and -221 Gt/yr, respectively; Tab. 7.6) from Greenland compared to the inversion and the TU Dresden solution. In

addition, the mascon solutions themselves show disagreeing trends over time, which amounts to a difference of ~ 750 Gt at the end of 2020.

In summary, the inversion is able to correctly recover Greenland mass changes in agreement with independent GRACE/GRACE-FO based estimates from TU Dresden as well as high-resolution ice-altimetry observations converted to mass changes. All these three solutions show discrepancies with respect to available mascon solutions. The reasons are currently unknown, but, likely related to processing inconsistencies (cf. Sect. 7.2.4). The corresponding contribution to the global mean sea level budget is in line with other recent published estimates confirming the inversions ability to retrieve the Greenland related mass changes.

7.2.4 Antarctic Mass Change

Antarctic ice melt contributes about 22% to the global mean OMC. Similar to Greenland, the melt is not uniform over the whole of Antarctica. Some basins experience rapid mass loss (e.g., basins 21 and 22, Fig. 7.12), while a slight mass accretion is found for others (basins 04-08, Fig. 7.12) and some show close to zero mass change (e.g., basin-10, Fig. 7.12).

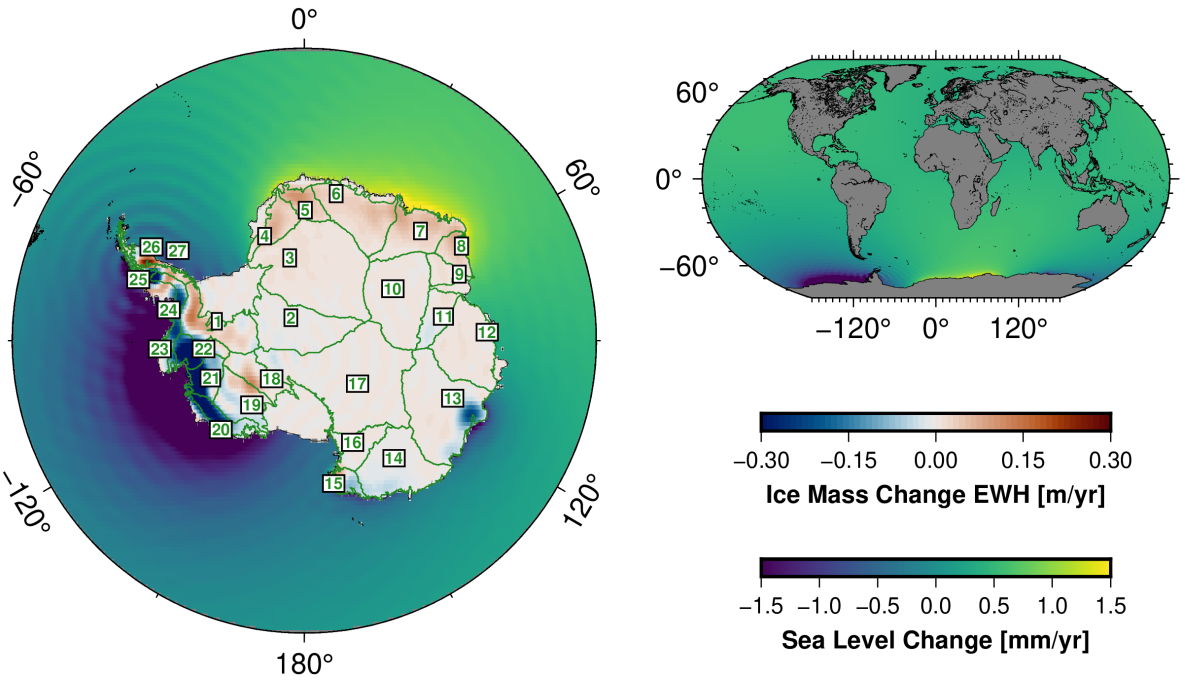


Figure 7.12: Spatial trend map of inversion-based ice mass change over the Antarctic ice sheet together with corresponding spatial trend map of induced sea level change for the period 2005-01 till 2015-12. Left: Detailed view of Antarctic ice mass change and surrounding sea level effect. Right: Global trend pattern due to Antarctic ice melt.

The resulting pattern of corresponding sea level change is related to the distribution of melting. Close to the basins of significant mass loss of the West Antarctic Ice Sheet (WAIS, Fig. 7.12, basins 18-23), in the Bellingshausen and Amundsen Sea as well as parts of the Ross Sea, an actual decrease of sea level is detected due to the loss of attraction from the melted ice mass and elastic uplift (Fig. 7.12). In the northern part of the East Antarctic Ice Sheet (EAIS, Fig. 7.12, basins 02-07), an increase in sea level is observed due to the mass accretion in this region. For the time period 2005-01 till 2015-12, the inversion finds the Antarctic contribution to global mean sea level rise at 0.42 mm/yr (Tab. 7.1), which is in line with the 0.42 mm/yr found by Horwath et al. (2022) and also WCRP-Global-Sea-Level-Budget-Group (2018). The latter computed this as an average

Table 7.7: Antarctic ice mass loss trends in Gt/yr for the period 2005-01 till 2015-12 for the whole Antarctic ice sheet, the Antarctic Peninsula, the East Antarctic Ice Sheet (EAIS) and the West Antarctic ice sheet (WAIS). The inversion result is compared to external data from TU Dresden (Groh and Horwath, 2021) and ice mass change based on ice-altimetry data (L. Schröder et al., 2019) as well as two mascon solutions and to own processing of GRACE data with different substitutes for degree-1. The errors are derived assuming temporal correlations by considering an autoregressive process (App. A.3) in order to derive more realistic errors compared to simply propagating the formal errors.

	Antarctica	Peninsula	EAIS	WAIS
Inversion	-143.98 ± 3.68	-19.88 ± 1.50	34.60 ± 3.47	-158.71 ± 4.26
TU Dresden	-105.66 ± 5.81	-33.35 ± 1.18	82.13 ± 5.55	-154.43 ± 5.35
Ice-Altim.	-226.06 ± 7.66	-7.11 ± 1.72	-63.66 ± 5.38	-155.29 ± 6.17
JPL Masc.	-80.23 ± 5.46			
GSFC Masc.	-107.68 ± 5.66			
GRACE D1: TN-13	-121.22 ± 4.52			
GRACE D1: Inv.	-143.24 ± 3.50			

of several published rates ranging from 0.31 to 0.47 mm/yr. In contrast, when applying an approximate conversion to the mass loss estimates from table 7.7, a significantly smaller contribution is found from the TU Dresden estimate (0.28 mm/yr, Groh and Horwath, 2021) in line with the JPL and GSFC mascon solutions (0.22 mm/yr and 0.29 mm/yr, respectively). At the same time, the sea level estimate from considering mass loss derived from ice-altimetry (L. Schröder et al., 2019) indicates a sea level rise of 0.61 mm/yr due to detected mass loss on the EAIS, which is not confirmed by the other approaches (Tab. 7.7). For the period 2004-01 till 2015-12, utilized by Dieng et al. (2017), they find a contribution of 0.33 mm/yr, which is slightly smaller than the 0.37 mm/yr found from the inversion for the same period. The estimates for the investigation periods of Rietbroek (2014) and Rietbroek et al. (2016) show differences of 0.10 mm/yr and 0.05 mm/yr, respectively, when evaluated from the inversion introduced in this thesis. The sea level contribution from the inversion (0.42 mm/yr) fits well to the Antarctic driven sea level rise by Hakuba et al. (2021) (0.45 mm/yr) for 2005-12 till 2019-12.

Parts of the discrepancy of Antarctic sea level estimates (Fig. 7.13) can be attributed to the choice of degree-1 substitutes during the processing of the GRACE/GRACE-FO data. Section 5.3 showed the significant impact of degree-1 coefficients on global mean OMC. As the inversion allows to extract corresponding degree-1 coefficients as additional output from the results, those are further investigated in section 7.6.1. The analysis reveals a significant discrepancy in the Z-component, which is associated to the c_{10} coefficient that in turn significantly contributes to the Antarctic mass change due to the associated spatial pattern. In order to test this theory, two GRACE time series of Antarctic mass change have been computed (Fig. 7.13), generally following the introduced processing scheme (Fig. 5.2) with the modifications of the utilized degree-1 substitute, not adding back the AOD1B and applying an additional filtering step utilizing a DDK3 filter (Kusche, 2007; Kusche et al., 2009). From figure 7.13 and table 7.7 it is obvious that the choice of degree-1 substitutes heavily impacts the resulting Antarctic mass change and the corresponding sea level contribution. The spherical harmonic analysis employing the inversion derived coefficients leads to an Antarctic sea level contribution of 0.42 mm/yr, which agrees well with the inversion output (Tab. 7.7).

Figure 7.13 exemplary examines some individual basins of mass accretion, mass loss and close to zero mass change in order to investigate the ability of the inversion to recover those variations. After a period of nearly no mass change up to 2009 significant extreme snow fall events in 2009

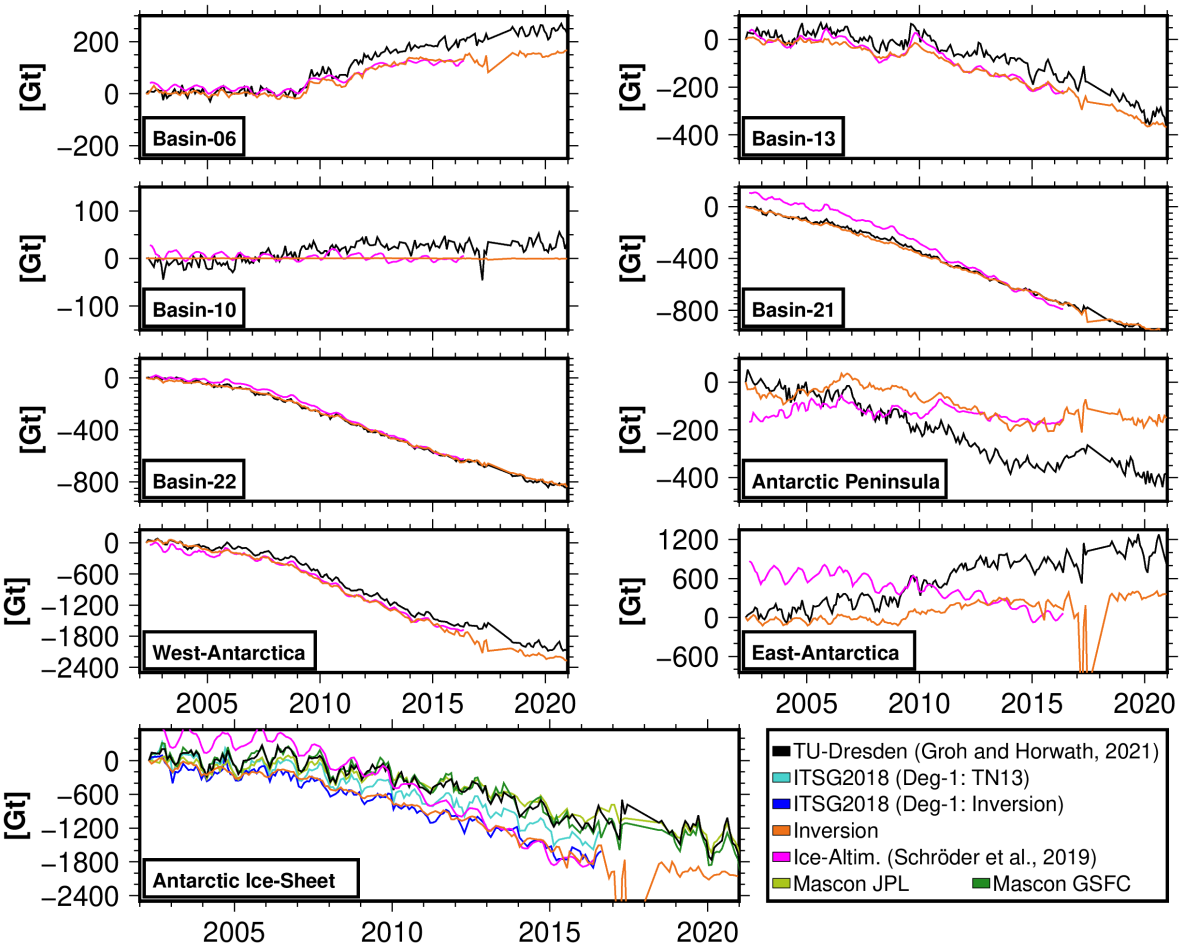


Figure 7.13: Time series of inversion results from selected Antarctic basins compared to external GRACE based results from TU Dresden (Groh and Horwath, 2016) and ice-altimetry-based mass changes derived from L. Schröder et al. (2019). The basins are selected to include mass increase (basin 06), small mass variations (basin 10), a large basin with regionally concentrated mass change (basin 13), and general mass losses (basins 21 and 22). Additionally, the cumulative effect of the West- and East-Antarctic as well as the Antarctic Peninsula is shown. The integrated Antarctic mass change is additionally compared to two GRACE mascon solutions from JPL and GSFC.

and 2011 in Dronning Maud Land have lead to a significant mass increase (Lenaerts et al., 2013). This is well observed, e.g. in basin 06 by the inversion (16.42 Gt/yr), the TU Dresden mass change (22.38 Gt/yr) and the ice-altimetry solution (13.65 Gt/yr) with the TU Dresden result indicating larger mass increase compared to the other two (Fig. 7.13 and Tab. 7.8). Basin 10 covers most of the low precipitation zone (Gunter et al., 2014), where little to no mass change is expected. This is largely confirmed by the inversion solution (0.02 Gt/yr) as well as the ice-altimetry result (−0.67 Gt/yr), while the TU Dresden time series (4.42 Gt/yr) indicates a small increase in mass over time (Fig. 7.13 and Tab. 7.8). Basin 13 is dominated by the mass loss at the Totten glacier, while the rest of the basin is relatively stable in terms of mass balance (Fig. 7.12). Here, the three solutions from the inversion, TU Dresden and ice-altimetry agree well (Fig. 7.13 and Tab. 7.8) indicating the good quality of the inversion results. Basins 21 and 22, which comprise large mass losses, are also generally retrieved well from all three methods (Fig. 7.13 and Tab. 7.8). However, the ice-altimetry time series for basin 21 differs significantly to the inversion and TU Dresden mass changes before 2011, which is related to the polar gap of the available altimetry missions (Fig. 3.2). The basin is located close to the south pole and a significant improvement is observed after Cryosat-2 data is available at the end of 2011 and the polar gap becomes smaller. The Antarctic

Table 7.8: Antarctic ice mass loss trends in Gt/yr for the period 2005-01 till 2015-12 for the 27 Antarctic basins (e.g., Fig. 6.2). From the inversion compared to external GRACE/GRACE-FO data from TU Dresden (Groh and Horwath, 2021) and ice mass change based on ice-altimetry data (L. Schröder et al., 2019). The errors are derived assuming temporal correlations by considering an autoregressive process (App. A.3) in order to derive more realistic errors compared to simply propagating the formal errors.

	Inversion	**TU Dresden**	**Ice-Altim.**
Basin-01	9.94 ± 0.33	0.06 ± 0.83	2.88 ± 0.68
Basin-02	-3.22 ± 0.42	2.18 ± 0.40	-4.01 ± 0.53
Basin-03	7.56 ± 0.67	18.74 ± 0.60	-54.41 ± 2.11
Basin-04	10.85 ± 0.43	12.70 ± 0.42	4.40 ± 0.78
Basin-05	11.27 ± 0.49	9.54 ± 0.47	-1.19 ± 0.17
Basin-06	16.42 ± 1.35	22.38 ± 1.66	13.65 ± 1.71
Basin-07	16.58 ± 1.27	19.31 ± 1.71	10.85 ± 2.07
Basin-08	6.06 ± 0.44	6.76 ± 0.39	2.98 ± 0.44
Basin-09	0.93 ± 0.19	1.11 ± 0.24	-0.08 ± 0.27
Basin-10	0.02 ± 0.01	4.42 ± 0.45	-0.67 ± 0.49
Basin-11	-2.07 ± 0.22	-0.00 ± 0.25	-0.09 ± 0.28
Basin-12	1.90 ± 0.53	4.29 ± 1.08	-3.75 ± 1.59
Basin-13	-18.79 ± 1.48	-15.34 ± 1.54	-20.99 ± 3.54
Basin-14	-7.94 ± 1.49	-9.51 ± 1.56	-5.96 ± 1.93
Basin-15	-2.21 ± 0.21	-4.02 ± 0.32	-1.49 ± 0.49
Basin-16	-0.30 ± 0.21	1.54 ± 0.20	-0.02 ± 0.28
Basin-17	-2.46 ± 0.42	8.04 ± 0.93	-2.90 ± 1.08
Basin-18	4.00 ± 0.52	14.84 ± 0.27	14.27 ± 0.47
Basin-19	-3.24 ± 0.22	-0.64 ± 0.51	-5.73 ± 0.40
Basin-20	-42.32 ± 1.69	-40.84 ± 1.86	-29.20 ± 2.16
Basin-21	-57.48 ± 0.68	-60.04 ± 1.10	-74.06 ± 2.04
Basin-22	-55.38 ± 1.02	-56.06 ± 0.99	-59.57 ± 1.34
Basin-23	-14.23 ± 0.79	-11.75 ± 0.56	-3.88 ± 1.02
Basin-24	-14.20 ± 0.74	-14.53 ± 0.78	-4.80 ± 0.85
Basin-25	-23.63 ± 2.06		-2.94 ± 0.49
Basin-26	16.24 ± 1.75		0.22 ± 0.62
Basin-27	1.71 ± 0.61	0.73 ± 0.31	0.42 ± 0.20

Peninsula basins (24-27) are relatively small, making it difficult to separate mass changes using the GRACE/GRACE-FO data. But also ice-altimetry is heavily influenced by lower quality retrievals due to large mountain ranges in these basins. Consequently, a comprehensive assessment of the peninsula is not possible without further data sources. In East-Antarctica (Fig. 7.13), the inversion result becomes noisy after 2016, which is likely related to the degradation of the GRACE input data after 2016. In contrast, the time series from TU Dresden is less affected.

Similar to the Greenland ice sheet, the introduction of a priori background patterns, which further localize the mass changes, instead of assuming uniform basin-wide mass changes, has reduced inter-basin correlations leading to improved separability, in contrast to, e.g., Rietbroek et al. (2016).

In summary, the inversion is able to recover mass changes from the WAIS as well as the EAIS, while the Antarctic Peninsula is difficult to asses. The Antarctic sea level budget contribution is in line with other published estimates, especially when considering the significant impact of the degree-1 substitutes on the resulting mass loss rate estimates.

7.2.5 Land Glacier Mass Change

Mass loss from land glaciers is found to be the second largest global OMC contributor with 0.64 mm/yr, which equals about one third of the integrated OMC (Tab. 7.1). While most glaciers loose mass (Tab. 7.9), the largest losses are found from the glaciers in Alaska (−43.75 Gt/yr), the Canadian Arctic (−77.14 Gt/yr) and the Southern Andes (−32.02 Gt/yr) region (Figs. 6.1, 7.14 and Tab. 7.9). Small rates of mass gains are detected in some sub-basins in the Central Asian Himalayan region as well as from particular glaciers in the Canadian Arctic region (Fig. 7.14).

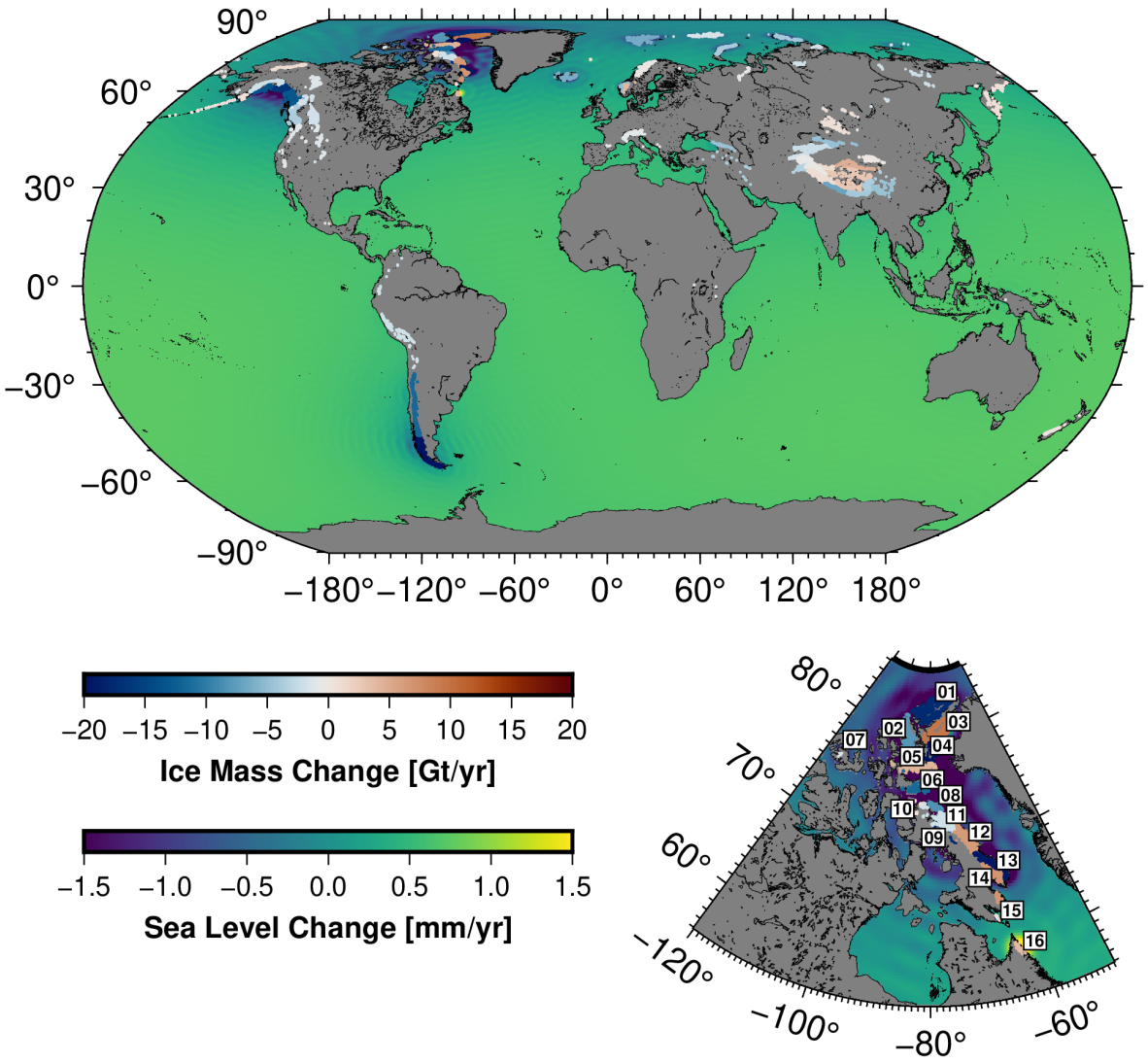


Figure 7.14: Spatial trend maps of sea level change induced by melting from individual glacier mass regions for the period 2005-01 till 2015-12. The general regions (Fig. 6.1) are further divided into sub-basins where all glaciers of an individual sub-basin are attributed with a uniform ice mass change. Over the ocean, resulting sea level trends are shown. In addition, a zoomed version of the Arctic Canadian glaciers shows ice mass change trends of the sub-basins.

In the following, the inversion results are compared to other published glacier related sea level change estimates, most of which are based on GRACE/GRACE-FO data, while others are derived from glacier models (e.g., Marzeion et al., 2012; Horwath et al., 2022). The corresponding spatial distribution of sea level change, again, indicates sea level fall close to the glaciers of significant mass loss due to elastic uplift and the vanishing attraction of the ice mass (Fig. 7.14). The globally averaged trend of 0.64 mm/yr derived from the inversion method is about 0.1 mm/yr smaller compared

Table 7.9: Trend, annual amplitude and phase of the major glacier regions defined by RGIv6.0 and shown in figure 6.1. The values are derived for the period 2005-01 till 2015-12. The errors are derived assuming temporal correlations by considering an autoregressive process (App. A.3) in order to derive more realistic errors compared to simply propagating the formal errors.

	Trend [mm/yr]	**Amplitude [Gt]**	**Phase [doy]**
Alaska	-43.75 ± 2.23	119.58 ± 5.82	103.6 ± 2.8
Western Canada	-8.91 ± 1.72	85.56 ± 4.79	110.8 ± 3.2
Arctic Canada North	-48.34 ± 1.14	18.27 ± 2.98	113.8 ± 9.4
Arctic Canada South	-28.80 ± 0.96	39.59 ± 3.51	115.1 ± 5.1
Iceland	-6.18 ± 0.31	8.67 ± 0.88	108.8 ± 5.8
Svalbard	-5.98 ± 0.61	9.65 ± 1.46	126.4 ± 8.7
Scandinavia	-1.29 ± 0.51	21.66 ± 1.70	102.5 ± 4.5
Russian Arctic	-9.49 ± 0.65	10.67 ± 2.42	106.7 ± 13.0
North Asia	-3.45 ± 0.82	40.30 ± 3.15	88.4 ± 4.5
Central Europe	-1.66 ± 0.61	17.61 ± 1.94	139.7 ± 6.4
Caucasus and Middle East	-8.32 ± 1.55	19.25 ± 3.86	158.9 ± 11.8
Central Asia	-4.38 ± 2.38	13.26 ± 5.14	137.2 ± 22.6
South West Asia	-2.68 ± 1.21	66.88 ± 2.82	131.2 ± 2.5
South East Asia	-15.67 ± 0.96	37.45 ± 3.30	184.6 ± 5.2
Low Latitudes	-3.65 ± 0.88	26.41 ± 2.78	83.3 ± 6.0
Southern Andes	-32.02 ± 1.09	35.40 ± 4.02	289.7 ± 6.5
New Zealand	0.11 ± 0.15	0.65 ± 0.62	239.6 ± 54.8

to WCRP-Global-Sea-Level-Budget-Group (2018) and Horwath et al. (2022) who report trends of 0.77 mm/yr and 0.78 mm/yr, respectively. Similarly, Dieng et al. (2017) report 0.78 mm/yr. While the estimate from Horwath et al. (2022) is based solely on an updated global glacier model (Marzeion et al., 2012), the estimate by WCRP-Global-Sea-Level-Budget-Group (2018) results from averaging several estimates ranging from 0.61 to 0.84 mm/yr based on different approaches. Consequently, the inversion result can be attributed to the lower end of that spectral range.

While a global glacier model provides mass loss for each individual glacier, the inversion assumes uniform mass loss from each of the 68 utilized glacier (sub-)regions, which can induce unintended smoothing effects and signal loss (Fig. 7.14 and Tab. 7.9). In addition, the inversion does not consider the Greenland and Antarctic peripheral glaciers, as both can not be separated from the ice sheet mass loss. Consequently those signals might be absorbed within the Greenland and Antarctic ice sheet contributions. This is not necessarily bad, since the ice sheet estimates from WCRP-Global-Sea-Level-Budget-Group (2018) and Horwath et al. (2022) are largely based on GRACE/GRACE-FO data, which can not separate the glacier signals from the ice sheets due to its spatial resolution and, thus, might include parts of the peripheral glacier mass loss twice. Based on the glacier model, Horwath et al. (2022) found the sea level effect from the peripheral glaciers in Greenland in the order of 0.2 mm/yr. A slightly larger glacier contribution (0.72 mm/yr) is found for 2005-01 till 2019-12 from the inversion compared to 0.64 mm/yr (Hakuba et al., 2021).

Rietbroek (2014) found a sea level contribution from glaciers of 0.43 mm/yr and Rietbroek et al. (2016) reported 0.38 mm/yr. Both estimates are significantly smaller compared to the inversion results of 0.59 mm/yr and 0.60 mm/yr, respectively derived for the same time period. This is mainly related to utilizing only 16 glacier regions based on the RGIv1.0 in contrast to the 68 glacier sub-regions (excluding the peripheral glaciers) that are employed nowadays. This lead to some misattribution of glacier related sea level change to other contributors. While the low number of glacier regions was largely uncorrelated (Fig. 4.20 in Rietbroek, 2014), some of the 68 basins utilized today exhibit strong negative correlations, especially in the Canadian Arctic (Fig. 6.12). As

Table 7.10: Trend, annual amplitude and phase of the Arctic Canadian glaciers. The individual glaciers are marked in figure 7.14. The errors are derived assuming temporal correlations by considering an autoregressive process (App. A.3) in order to derive more realistic errors compared to simply propagating the formal errors.

	Trend [mm/yr]	**Amplitude [Gt]**	**Phase [doy]**
Arctic Canada Northern Glaciers			
01 N Ellesmere Island	-17.63 ± 0.56	5.53 ± 1.30	111.0 ± 13.5
02 Axel Heiberg and Meighen Is	-7.98 ± 0.34	5.72 ± 0.87	94.6 ± 8.7
03 NC Ellesmere Island	9.52 ± 0.65	2.58 ± 1.74	255.3 ± 38.7
04 SC Ellesmere Island	-23.64 ± 0.93	1.94 ± 2.58	111.9 ± 76.5
05 S Ellesmere Island (NW Devon)	4.30 ± 0.62	6.67 ± 2.28	147.0 ± 19.9
06 Devon Island	-11.52 ± 0.63	4.49 ± 2.19	33.7 ± 28.5
07 Melville Island	-1.39 ± 0.13	1.60 ± 0.48	170.5 ± 17.5
Arctic Canada Southern Glaciers			
08 Bylot Island	-8.37 ± 0.52	12.82 ± 2.11	153.8 ± 9.6
09 W Baffin Island	-17.61 ± 0.79	14.16 ± 2.82	172.1 ± 11.7
10 N Baffin Island	0.75 ± 0.54	2.76 ± 1.87	286.5 ± 38.8
11 NE Baffin Island	-1.94 ± 0.47	9.13 ± 1.88	356.8 ± 12.1
12 EC Baffin Island	6.33 ± 0.91	9.57 ± 3.02	82.7 ± 18.1
13 SE Baffin Island	-19.43 ± 1.11	15.94 ± 4.34	286.8 ± 15.7
14 Cumberland Sound	6.79 ± 1.24	30.95 ± 4.91	103.3 ± 9.1
15 Frobisher Bay	0.84 ± 0.37	5.44 ± 1.24	70.7 ± 13.1
16 Labrador	3.83 ± 0.29	2.44 ± 0.97	106.4 ± 22.8

reported above, the inversion finds some neighboring glacier regions to indicate largely contrasting mass changes, which might point to the inability to separate those closely neighbored glaciers, in turn explaining the significant correlations. This is closer examined for the Canadian Arctic (Fig. 7.14 and Tab. 7.10).

While a significant mass loss of -17.6 Gt/yr is reported for basin 01, a mass increase of 9.5 Gt/yr is found for the neighboring basin 03 (Fig. 7.14 and Tab. 7.10). Both are linked by a strong negative correlation (Fig. 6.12). Similarly, basins 03-04, 04-05 and 05-06 are linked by negative correlations (Fig. 6.12), alternating between mass loss and (smaller) mass increase. Similar effects can be observed, e.g., between basins 13 and 14 for the Arctic Canadian Southern glaciers. This clearly indicates that, based on the inversion input data, a clear separation of all those small sub-basins is not possible resulting from the inherent GRACE/GRACE-FO spatial resolution. Further issues arise from missing altimetry observations, due to the coverage limits of the Jason missions utilized for the standard inversion, and also sea ice coverage, when considering higher latitude missions (Sect. 7.4.3). This means that these sub-regions can not be analyzed individually, but rather as a sum over all relevant sub-regions. For future inversion runs, one may either consider constraints during estimation or combination of sub-regions or additional high resolution observational data, e.g. from ice-altimetry to reliably separate these small neighboring high latitude regions.

7.2.6 Terrestrial Hydrology Contribution

The terrestrial hydrology component is the most variable driver of global OMC with a dominating seasonal signal (Fig. 7.2, B), but its sea level trend of 0.21 mm/yr contributes only 11% to the OMC budget over 2005-01 till 2015-12. The hydrological mass change is driven by natural variability, climate change and human activity (Rodell et al., 2018). While natural variability dominates variations, e.g. in the Amazon, central Africa and Eastern Australia, human activities are mainly

the reason for mass loss signals from groundwater extraction for agriculture irrigation, e.g., in the Midwestern United States, California and northern India (Fig. 7.15).

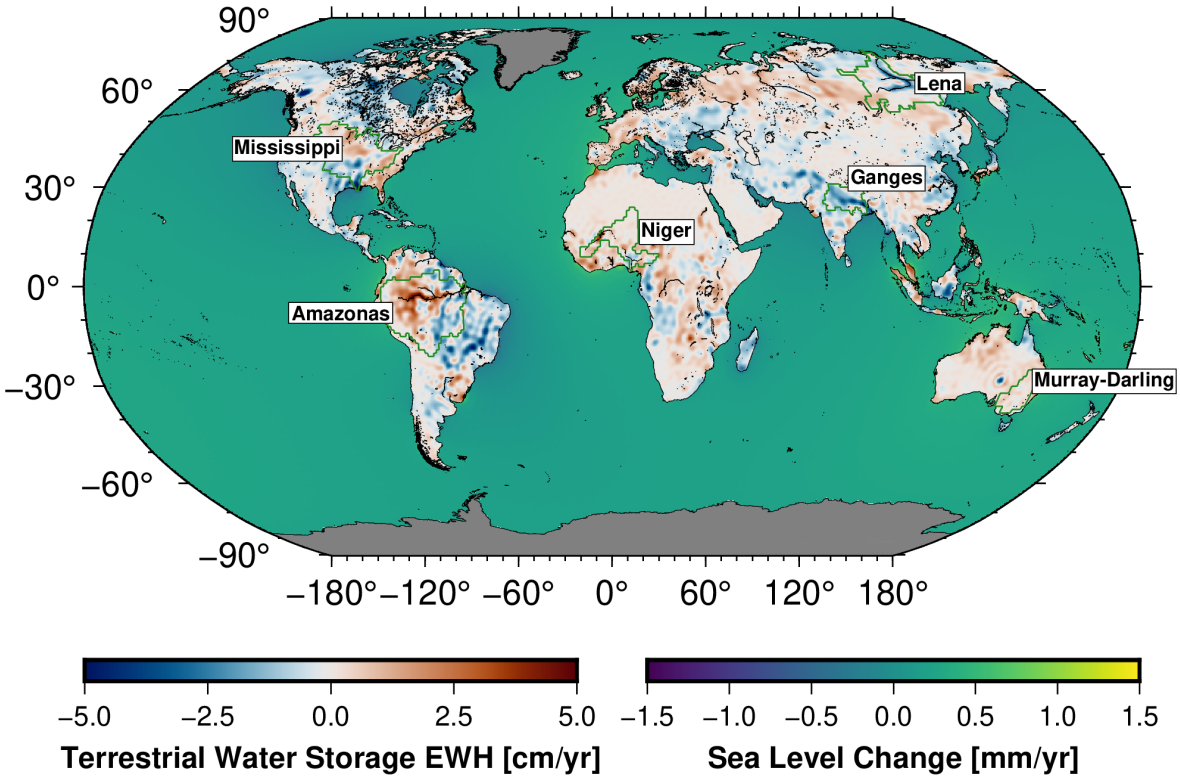


Figure 7.15: Trend maps of hydrological mass changes over the continents for the period 2005-01 till 2015-12. The ice sheets in Greenland and Antarctica, as well as glaciated regions have been removed before deriving the fingerprints. In addition, the resulting sea level change trend pattern is shown over the ocean.

The spatial pattern of hydrologically driven sea level change does not show regions of strong sea level rise or fall since the hydrological masses are not concentrated within a relatively small area, such as Greenland ice mass changes, but rather spread over the land masses. Consequently, the mass attraction effect is also distributed over the continents leading to weaker mass attraction signals (Fig. 7.15). The sea level change of 0.21 mm/yr fits well to 0.25 mm/yr found by Dieng et al. (2017). In contrast, Horwath et al. (2022) provide an estimate of 0.57 mm/yr, which is significantly larger compared to the inversion providing 0.38 mm/yr for the exact same time period. A range of −0.30 to 0.30 mm/yr is mentioned by WCRP-Global-Sea-Level-Budget-Group (2018) where the final estimate of −0.27 mm/yr is selected as the mean of Reager et al. (2016) and Scanlon et al. (2018), which is close to the result of −0.29 mm/yr reported by Rietbroek et al. (2016). For 2003-2011, Rietbroek (2014) found −0.20 mm/yr. The inversion introduced in this thesis provides estimates of −0.30 mm/yr and −0.06 mm/yr for the time periods of Rietbroek (2014) and Rietbroek et al. (2016), respectively. Including the GRACE-FO period (2005-01 till 2019-12), Hakuba et al. (2021) report terrestrial hydrology driven sea level change of 0.46 mm/yr, which is significantly smaller than the 0.73 mm/yr resulting from the inversion. However, the latter is largely influenced by a bias after 2016 (Fig. 7.17).

The large spread of published and computed hydrology related sea level estimates illustrates the variability and strong time dependence of the trends from terrestrial water changes. Due to this, even small inconsistencies when combining estimates from different time frames can have impacts. For example, the two periods 2002-04 till 2014-11 and 2002-04 till 2014-12 are utilized for the mean from Reager et al. (2016) and Scanlon et al. (2018), respectively. These are then

combined in WCRP-Global-Sea-Level-Budget-Group (2018) introducing an inconsistency. While Horwath et al. (2022) removed the ice sheets in Greenland and Antarctica from the WGHM data they used, they consider the effect on global budgets from the double accounting of glacier areas as insignificant. In combination with generally unreliable model only trends, this leads to a significantly larger estimate for the same time frame as reported above. This also means that at least parts of the glacier signal may be included twice in the Horwath et al. (2022) budget. In addition, significant differences between the models themselves and observation based estimates, e.g. from GRACE/GRACE-FO, demonstrate that relying only on model estimates for deriving terrestrial mass changes and corresponding sea level variations is not a good choice.

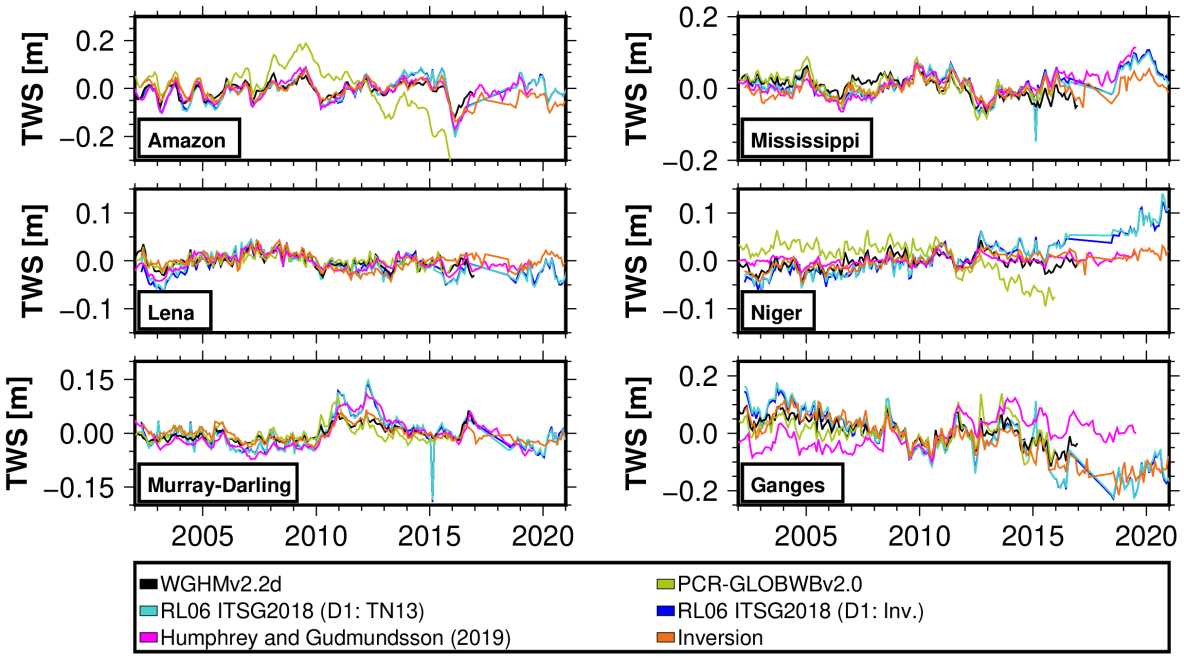


Figure 7.16: Comparison of inversion-based mass change in selected hydrological basins with mass changes from the WGHMv2.2d and the PCR-GLOBWBv2.0 model, ITSG2018 GRACE/GRACE-FO-based mass changes with two settings for degree-1 substitution, and a machine learning based time series by Humphrey and Gudmundsson (2019).

To better assess the quality of the inversion hydrology component, a set of representative catchments is further analyzed (Fig. 7.16). The ability of the inversion to reconstruct mass changes seems to be directly tied to the time period of available model data for the fingerprint computation, which is represented by the WGHM availability until 2017 (Fig. 7.16, black line). After 2017, this leads to an extrapolation of hydrological mass changes based on past signals from the fingerprint period, which does not necessarily reflect all of the spatio-temporal variability. This is especially evident when looking at the biases in the Amazon, Mississippi, Niger and Lena catchments during the GRACE-FO time period, which is well beyond the available original model period. Similar problems affect the estimates of Rietbroek (2014) and Rietbroek et al. (2016) who utilized an earlier WGHM version, which was only available up to 2009 (Rietbroek, 2014). In addition, the rescaled scaling factor for the hydrological fingerprint associated to the first EOF derived from the WGHM shows a jump in the beginning of 2016 (Fig. 7.17), which introduces a bias to the hydrological component (Fig. 7.16) and, thus, the corresponding global mean OMC (Fig. 7.8). The bias is continued towards the GRACE-FO era. This also impacts the residual component (Fig. 7.2, D). The reasons for this are currently unknown, but likely related to some real world signal that can not be fit to the WGHM-EOFs due to the available WGHM period being limited up to 2017 (cf. Sect. 7.3.6). It is expected to alleviate this problem with an updated model version available for a longer period.

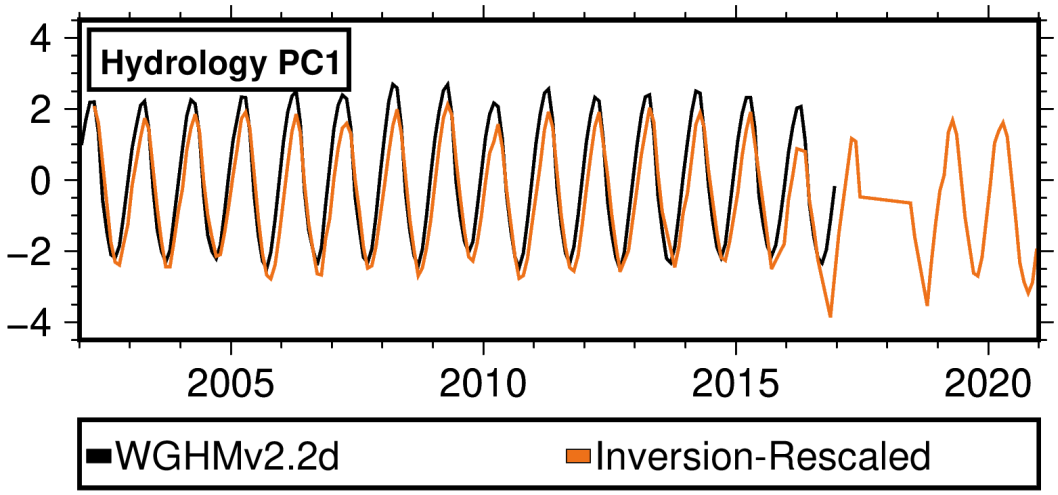


Figure 7.17: Comparison of original WGHM PC and inversion scaling factor for the first EOF mainly representing the annual signal. Besides a small phase-shift between the model and the rescaled factor, the inversion result introduces a jump in the beginning of 2016.

Table 7.11: Mass trends from 2005-01 till 2015-12 in mm/yr EWH from different solutions for selected hydrological catchments (Fig. 7.15) ordered by basin-size. The solutions include the hydrological models PCR-GLOBWB and WGHM, a statistical-based approach (H2019, Humphrey and Gudmundsson, 2019), ITSG2018 GRACE solution with different degree-1 substitutes and the inversion hydrological component. The errors are derived assuming temporal correlations by considering an autoregressive process (App. A.3) in order to derive more realistic errors compared to simply propagating the formal errors.

	PCR-GLOB	**WGHM**	**H2019**	**ITSG2018** (D1: TN13)	**ITSG2018** (D1: Inv.)	**Inversion**
Amazon	-18.74 ± 5.96	0.44 ± 1.83	3.10 ± 3.08	7.39 ± 1.99	6.76 ± 2.00	3.30 ± 1.46
Mississippi	-2.42 ± 2.61	-5.39 ± 1.91	2.32 ± 3.01	-0.25 ± 1.96	0.57 ± 1.86	-0.05 ± 1.25
Lena	-1.47 ± 0.47	-1.85 ± 0.95	-2.78 ± 1.22	-4.49 ± 0.76	-2.68 ± 0.74	-3.01 ± 1.01
Niger	-9.52 ± 1.90	0.65 ± 1.09	0.90 ± 0.66	5.52 ± 0.61	6.05 ± 0.64	2.85 ± 0.64
Murray-D.	0.19 ± 2.49	2.80 ± 1.79	8.02 ± 4.07	7.42 ± 2.20	6.63 ± 2.21	2.32 ± 1.21
Ganges	-0.82 ± 3.63	-5.50 ± 2.18	13.02 ± 3.40	-9.64 ± 2.52	-8.37 ± 2.41	-11.98 ± 1.51

For the GRACE era, the inversion results agree relatively well with the GRACE based estimates, while especially the PCR-GLOBWB model shows discrepancies in the Amazon and Niger catchments (Fig. 7.16 and Tab. 7.11). The dataset by Humphrey and Gudmundsson (2019) has been used to investigate potential biases between GRACE and GRACE-FO (Landerer et al., 2020). Here, the monthly ensemble means trained on the JPL mascon data and forced by ECMWF-ERA5 serve as additional validation in order to better assess the hydrology output of the inversion. This dataset generally agrees with the GRACE output (e.g., 2011-2013 in the Murray-Darling basin, Fig. 7.16), except for the Ganges catchment where it differs significantly to the other hydrological datasets (Fig. 7.16 and Tab. 7.11). However, the statistical model basis has been trained on the GRACE data, so good agreement during this period is expected. For the Niger basin, the GRACE-FO data indicates a significant mass increase, which is not confirmed by the inversion results as well as the Humphrey and Gudmundsson (2019) dataset. Again, significant impact of up to 1 mm/yr EWH is found with respect to the choice of degree-1 substitutes during the GRACE/GRACE-FO processing (see also Sect. 7.6.1).

In summary, the inversion is able to reconstruct the hydrological mass changes during the

GRACE era while not being strictly bound by the WGHM model input signals, but still, somewhat restricted by it (Fig. 7.16, Ganges and Lena catchments before 2005). The results from the GRACE-FO period indicate a bias effect, which is likely related to the extrapolation of time period available for the fingerprint creation.

7.2.7 Internal Ocean Mass Variations

In addition to mass influx from the continents, the ocean itself transports water masses via barotropic and baroclinic flow, as part of the global current systems. Integrated over the total global ocean area, the transport is defined to be zero. Therefore, this contribution can be neglected for global sea level budgets, but only if computed over the whole ocean. It is also not considered in any of the sea level budget studies published so far, since these mostly focus on global estimates, where this contribution is assumed to be zero. Consequently, a comprehensive literature comparison is impossible here.

However, any sub-basin of the total ocean will have a non-zero IMV contribution, e.g. when considering a 300 km coastal buffer or limiting the observational coverage to the ±66° latitude coverage of the Topex and Jason missions. This part of the sea level budget will become quite important when investigating regional sea level drivers (Sect. 7.5).

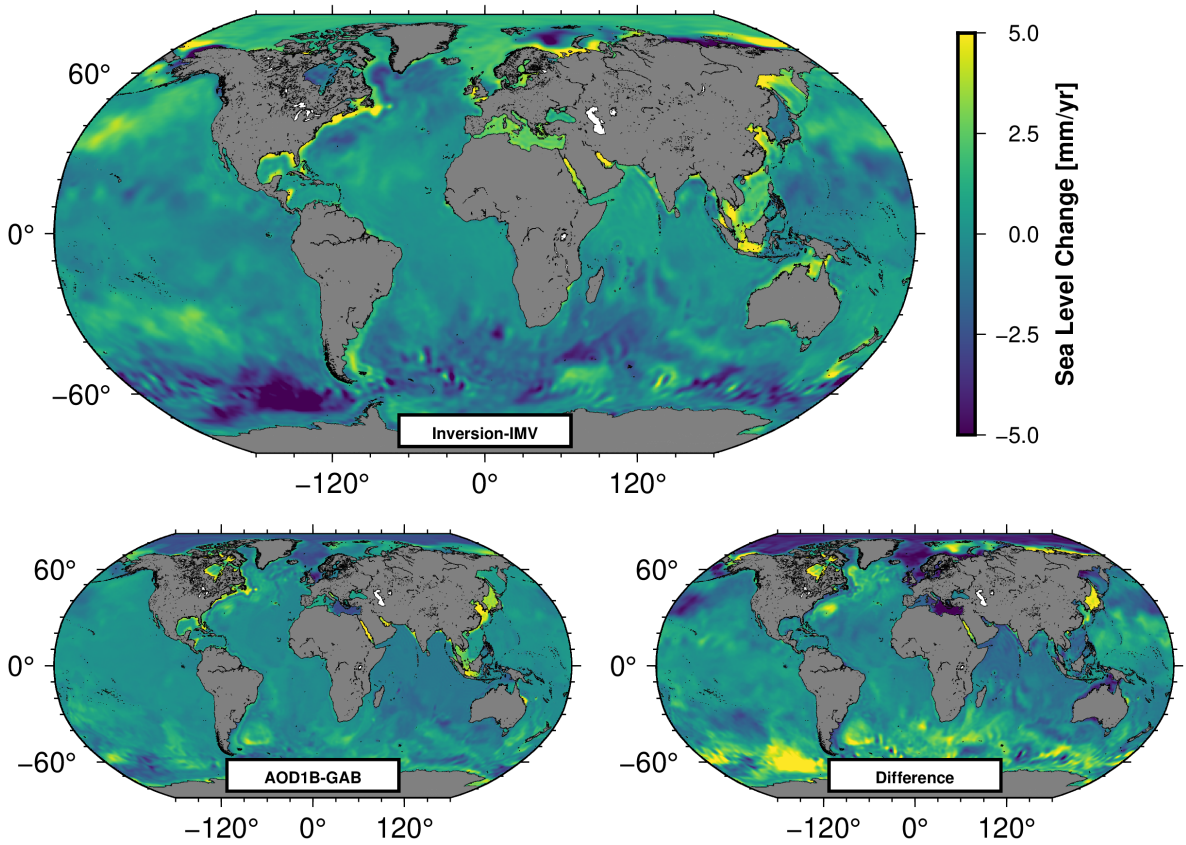


Figure 7.18: Trend map of IMV within the ocean for the period 2005-01 till 2015-12. On a global scale, the IMV-related sea level change is zero as it is not driven by mass inflow from the continents.

The spatial trend distribution of the inversion IMV component is shown in figure 7.18. Strong positive trends of IMV are found at the US East coast, the Chinese East coast, the Java Sea and coastal regions of the Barents Sea north of Finland and Russia. All these regions are coastal shelf zones or, generally, rather shallow seas. In contrast, deep ocean areas of the Antarctic circum polar current and especially the ocean off the coast of west Antarctica shows strong negative IMV trends

indicating transport of water from this region further northward.

In principle, the IMV component represents the mass that has been removed as part of the AOD1B background model (Sect. 5.3). The inversion fingerprints are based on the AOD1B-GAB product, which is the output from the MPIOM model (Jungclaus et al., 2013). The model is only forced with atmospheric data and does not assimilate any observations (Dobslaw et al., 2017b). Consequently, the inversion IMV result can be interpreted as a GAB product re-scaled by actual observations. When comparing the IMV output with the original AOD1B-GAB, some regional differences become evident (Fig. 7.18). From the difference of the two, the original GAB model seems to underestimate the regional IMV around Antarctica and regional mass gains in the Arctic. In addition relative to the GAB model, the inversion detects mass gain in the Mediterranean Sea, the North Sea and the Baltic Sea, while significant mass loss is found, e.g., in the Japanese Sea. This again underlines the necessity of considering the IMVs within the ocean, as these can become the dominating mass signal when considering regional sea level budgets (Sect. 7.5). From the differences this also means that the AOD1B background models applied during GRACE processing are not perfect and might introduce or remove unrealistic signals in the estimation of the L1B to L2 gravity processing.

7.2.8 Steric Sea Level Component

Steric sea level change results from volume expansion of the water column due to density changes resulting from variation in temperature and salinity. While global mean steric sea level is clearly rising (Figs. 5.4, 6.5 and 7.2), regional differences in ocean heating and heat transport result in a diverse spatial pattern of rising and falling steric sea level change. Besides observing the integrated steric sea level change from the combination of GRACE/GRACE-FO and altimetry data, the inversion method allows to additionally split the steric change into an upper ocean shallow component referring to the first 700 m and a deep ocean component (below 700 m depth). The corresponding spatial patterns are sufficiently independent from each other (Sect. 6.1.5). The resulting spatial sea level change trend map (Fig. 7.19) shows strong variations from the upper 700 m, while the deep ocean sea level change is relatively uniform with some more variation in the major current regions (e.g., Gulf Stream, Aghulas, Kuroshio or Antarctic Circumpolar Currents). Consequently, the combined shallow and deep ocean steric sea level change is clearly dominated by the shallow part (Fig. 7.19). Besides variability in major current regions, the spatial pattern is also affected by ocean phenomena such as ENSO, Atlantic Meridional Overturning Circulation (AMOC) or IOD.

In literature (e.g., Chambers et al., 2017; WCRP-Global-Sea-Level-Budget-Group, 2018), global mean steric sea level change estimates are often based on thermosteric variations only, since the salt content of the ocean remains basically constant over multidecadal timescales (Gregory and Lowe, 2000). However, on regional scales and, especially, at high latitude regions, halosteric sea level changes often dominate (Rhein et al., 2013). Consequently, for comparison on global scales steric and thermosteric changes are treated the same and compared directly. The global mean steric sea level trend of 1.41 mm/yr for 2005-01 till 2015-12 is found slightly larger compared to 1.30 mm/yr, which was computed as an ensemble mean from 11 reanalysis datasets ranging from 1.00 to 1.50 mm/yr (WCRP-Global-Sea-Level-Budget-Group, 2018). The authors also differentiate between individual depth levels. For the upper 700 m they report an estimate of about 1.00 mm/yr, which corresponds well to the 1.04 mm/yr found in this thesis. While others previously reported no significant steric sea level change from the deep ocean (e.g., Llovel et al., 2014), deep ocean steric contributions of about 0.35 mm/yr and 0.38 mm/yr are found in good agreement from WCRP-Global-Sea-Level-Budget-Group (2018) and the inversion method. This strengthens the confidence in the ability of the inversion method to actually separate the steric changes from these two depth regions without further input data. For 2005-01 till 2016-08, Horwath et al. (2022) report a steric trend of 1.26 mm/yr based on one dataset. This trend is smaller compared to 1.40 mm/yr found from the inversion for the same time period. Similarly for 2004-01 till 2015-12, Dieng et al. (2017) report only 1.14 mm/yr from an ensemble of estimates compared to 1.37 mm/yr from the inversion.

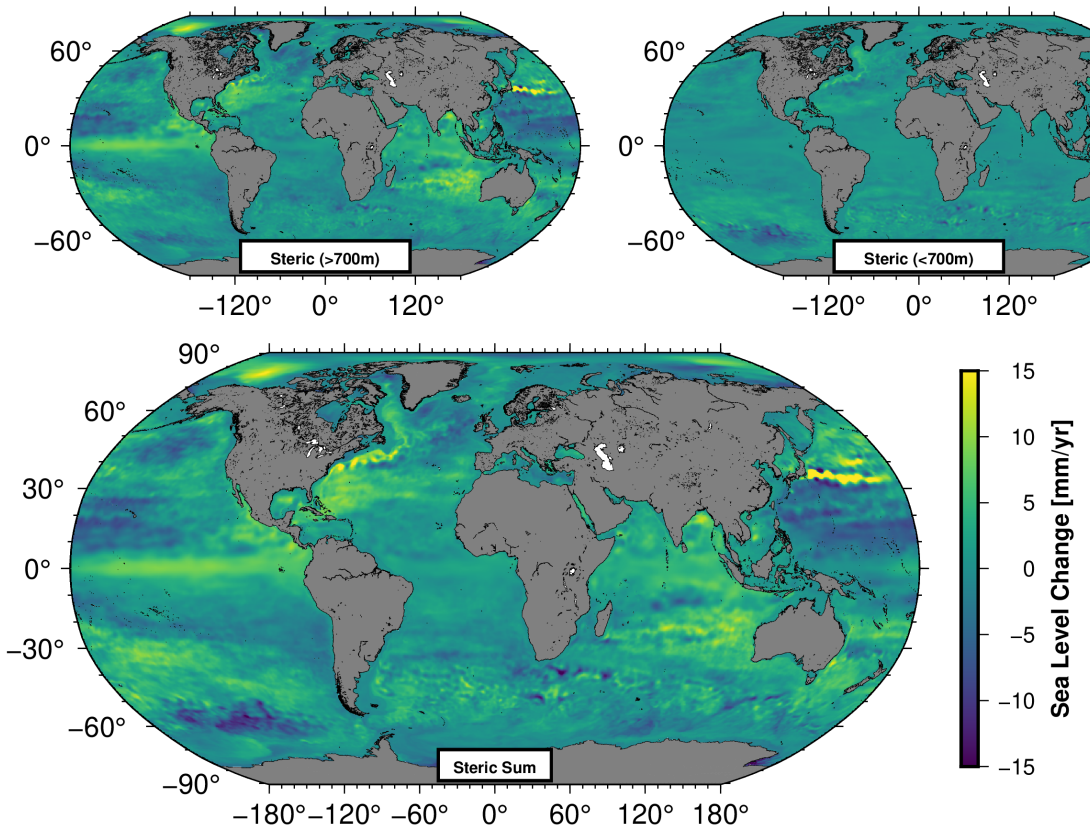


Figure 7.19: Steric sea level change trend maps for the period 2005-01 till 2015-12. The inversion is able to further split the steric change into a contribution from the upper 700 m and the deep ocean.

When examining the time frame of 2003-01 till 2011-12 used in the Rietbroek (2014) inversion, the steric sea level change of 1.20 mm/yr fits well to the inversion from this thesis (1.22 mm/yr). However, the Rietbroek (2014) estimate is comprised of an upper 700 m component (0.17 mm/yr) based on fingerprints from a steric reanalysis by Ishii and Kimoto (2009), while the remaining "deep" ocean part represents the bootstrapped effect. The latter is co-estimated in a second inversion run, where the bootstrap patterns are derived from the residuals of the first iteration. Consequently, the good fit of the estimates is likely a coincidence. The steric sea level estimate from Rietbroek et al. (2016) also agrees well with the inversion in this thesis (1.38 mm/yr and 1.36 mm/yr, respectively). Extending the period to include GRACE-FO leads to 1.09 mm/yr steric sea level rise from the inversion, which is smaller compared to 1.35 mm/yr from Hakuba et al. (2021), which is composed of a 0 to 2000 m estimate of 1.23 mm/yr and an assumed 0.12 mm/yr deep ocean contribution taken from another publication that utilized a different time period for computation. Reasons for this are the issues reported for the mass estimates, especially, the hydrological mass contribution, which introduced a bias in 2016. As both types of fingerprints strongly depend on the time frame from which the fingerprints have been created, a similar effect from "extrapolating" beyond that time period is expected for the steric component, which might introduce biases and trend errors (Sect. 7.3.6).

In order to validate the inversion's ability to separate shallow (upper 700 m) and deep (below 700 m) steric contributions, the inversion results from the shallow part together with ocean models and re-analyses are compared to in-situ profiles extracted from the easyCORA dataset (Fig. 7.20). The easyCORA profiles have been thoroughly quality checked leading to removal of up to more than 40% of data in some months (Sect. 6.2.1). Before 2005, the coverage of the Argo network, even in combination with ship-based XBT measurements, was not sufficient to derive meaningful global mean steric change. Afterward, the comparison shows a good agreement of the seasonal

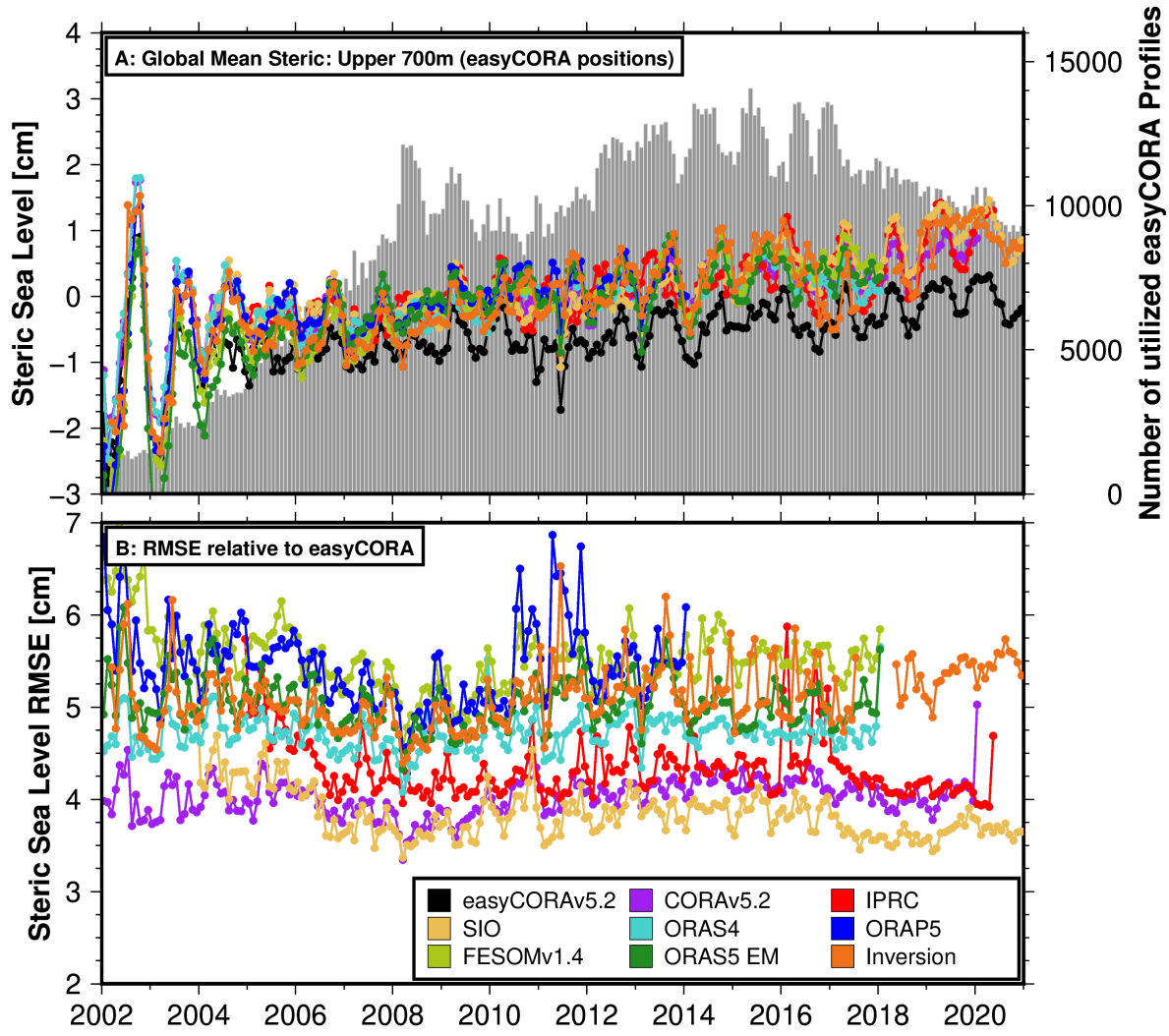


Figure 7.20: Comparison of model, re-analysis and inversion-based steric sea level change from the upper 700 m with in-situ profile data extracted from the easyCORA dataset. A: Globally averaged steric sea level evaluated at the easyCORA positions of each month. B: Monthly Root Mean Square Error (RMSE) relative to the easyCORA time series.

signal, while significant trend difference between the in-situ measurements and the output from the models, re-analyses and inversion are observed (Fig. 7.20, A). Reasons for the trend effect remain largely unknown as an in-depth investigation is out of the scope of this thesis, but could be related to the different temporal sampling of the in-situ and the (monthly) model data introducing high-frequency signals into the in-situ estimate. When computing the RMSE relative to the easyCORA in-situ dataset on a monthly basis (Fig. 7.20), the three datasets (SIO, IPRC and gridded CORA data), which are derived directly from in-situ profile data based on objective analysis, show the best agreement with the in-situ profile data. For the IPRC data, a decline in RMSE is found between 2004 and 2007 likely related to the increasing number and better coverage of in-situ profiles. The inversion performs quite similar to the ORAS5 model data, which is expected due to the utilized steric fingerprints being derived from it. In addition, the quality of the inversion based steric solution seems to correlate with the quality of the available GRACE data showing more noisy months, particularly, towards the end of the GRACE mission life cycle and the beginning of the GRACE-FO mission (Fig. 7.20, B). Overall, the results show that the inversion is well able to separate shallow and deep ocean steric contributions based only on GRACE/GRACE-FO and altimetry input data. Similar comparisons and validations for the deep ocean part are not feasible due to limited spatial and temporal coverage of available in-situ profiles. Especially the ocean below 2000 m is only ob-

served by some individual specialized deep-Argo floats. Potential improvements from introducing the easyCORA data as additional observations are investigated in section 7.4.4.

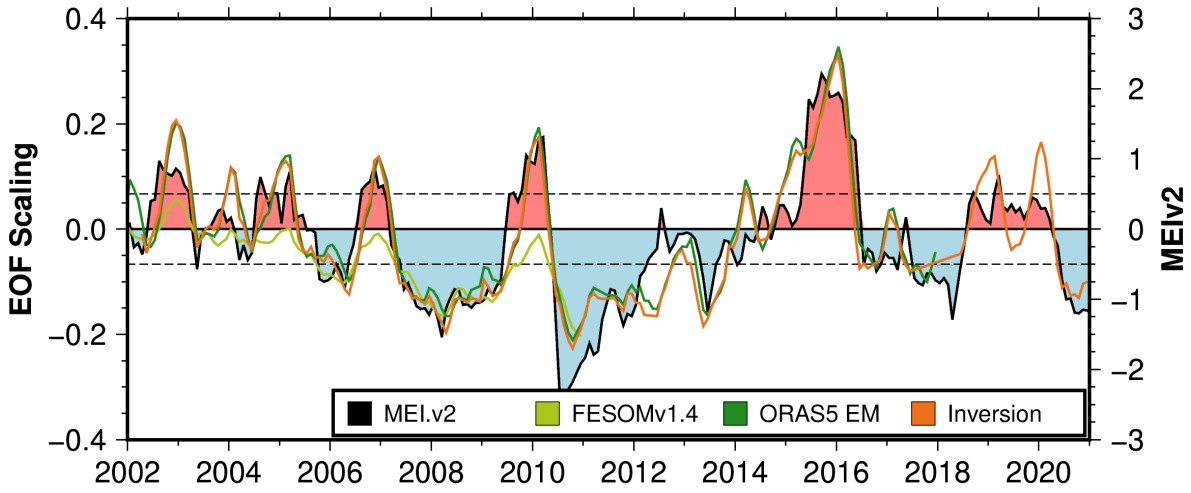


Figure 7.21: Comparison of the multi variate ENSO index (MEI.v2) against the scaling factor of the EOF, which is generally associated with the ENSO phenomenon from the inversion as well as the ORAS5 and FESOM models. Dashed lines roughly indicate warm (El Niño) and cold (La Nina) events.

Although the PCA method is generally a purely mathematical approach, individual EOFs can often be associated with specific physical phenomena. While the first EOF generally corresponds to the annual cycle, others can also be at least partly connected to strong well defined physical signals. The ENSO phenomenon is usually well represented in steric model data, as these models are utilized for routinely monitoring these effects (Zuo et al., 2019). Since the ENSO signal is so dominant, it can be easily extracted from the steric model data using PCA. In case of the EOFs (fingerprints) utilized in the inversion, the second fingerprint is associated with a strong ENSO pattern (Fig. 6.6). The corresponding scaling factor can, thus, be compared to the ENSO-index. Figure 7.21 shows the Multivariate ENSO Index Version 2 (MEI.v2, Kobayashi et al., 2015) together with scaling factors for corresponding EOFs from the ORAS5 and FESOM model as well as the rescaled inversion scaling factor. It is important to keep in mind that due to the purely mathematical approach, the ENSO-EOFs still include other signals outside the Pacific ocean region utilized in the definition of MEI.v2 (Fig. 6.6). Extracting a clear ENSO signal from the FESOM model seems to be more difficult compared to the ORAS5 model (Fig. 7.21). The reason for this is likely connected to the shorter time period of available FESOM model data limiting the capabilities to separate individual signals using PCA. In addition, FESOM is a free run model, i.e. it does not include assimilated observational data, leading to a reduced ability for correctly representing the observation based ENSO index. The rescaled inversion solution closely follows the ORAS5 model scaling indicating good agreement between observations and model with respect to the ENSO signal. Both follow the MEI.v2 closely while also exhibiting a small temporal lag for detecting El Niño signals compared to the MEI.v2 (Fig. 7.21). Although the ORAS5 model data, which is the basis for the steric fingerprints is limited to the end of 2017, the inversion is able to recover a ENSO signal during the GRACE-FO time period. However, the recovered signal is less close to the MEI.v2, but still indicating correct El Niño and La Nina time periods. This illustrates that the quality of separating the sea level change is tied to the input data quality, on the one hand, but also to representation ability of the fingerprints. For highly spatio-temporal variable signals, such as steric sea level change or hydrology (Sect. 7.2.6), it is necessary to have a good signal basis for the fingerprints to avoid severe extrapolation effects (Sect. 7.3.6). Other physical phenomena, such as IOD or AMOC are usually spread over several EOF and, thus, can not be directly analyzed from the corresponding fingerprint scaling factors.

7.2.9 Budget Closure: Residuals with Respect to Altimetry

Budget closure refers to the residual with altimetry observational data compared to the total sea level, which is reconstructed from the sum over all individual mass and steric sea level contributors. For the inversion, this is computed at each along-track position by subtracting the total sea level, expressed in GSL change, from the corresponding input altimetry data. For earlier inversions (Rietbroek, 2014; Rietbroek et al., 2016), those residuals would then be gridded, decomposed using PCA and a second inversion iteration run with the additional "bootstrapped" patterns would be run. While this lead to smaller residuals after the second run, it did not completely remove those and the resulting bootstrapped sea level component did not provide any additional meaning in terms of steric or mass related sea level contributions. Furthermore, results for the other components from the second run differed from the first one. Due to this, and the fact that nowadays the residuals are considerably smaller, the second inversion iteration is no longer meaningful and the residuals are interpreted and utilized as they are after the first run.

When plotting the global mean of the residuals against time (Fig. 7.2, A and D, "ocean dynamics" component), it is found that these are generally centered around zero with a small amplitude of about 0.5 mm (Tab. 7.1) up to 2016. Afterwards, the residuals, first, show a negative bias of about 1 mm, followed by a larger positive bias of about 4 mm for the GRACE-FO period (Fig. 7.2, D). As already mentioned, these biases likely occur due to a bias in the hydrological component as well as impacts from misrepresenting the steric and hydrological sea level change. Both components include strong spatio-temporal variability and extrapolation outside the original fingerprint creation period becomes increasingly uncertain and biased (cf. Sect. 7.3.6). However, the small magnitude of the residuals indicates a consistent closure of the budget, where individual sea level contributors are represented well.

The inversion residuals include a small trend of about 0.12 mm/yr for the period 2005-01 till 2015-12. This indicates a well closed sea level budget and is generally better compared to other published sea level budgets. For the same period, WCRP-Global-Sea-Level-Budget-Group (2018) report budget closures of −0.10 mm/yr, 0.28 mm/yr and 0.55 mm/yr depending on the composition choice for the sum over all mass components. While the budget closure using only GRACE based OMC and thermo-steric sea level change is working quite well, the sum of the individual components does not match the GRACE estimate and introduces trend effects, which directly map into the budget closure error. Similarly for 2005-01 till 2016-08, Horwath et al. (2022) report three different budget closures (−0.29 mm/yr, −0.14 mm/yr and 0.07 mm/yr), which clearly depend on the selection, or not-selection, of individual mass components. For this thesis' inversion, closure of 0.11 mm/yr is found for that period. While the GRACE only based estimate in WCRP-Global-Sea-Level-Budget-Group (2018) provided the best budget closure, it shows the largest deviation in Horwath et al. (2022) indicating general differences in how OMC should be processed (see also Sect. 5.3).

A single budget closure estimate of 0.22 mm/yr for 2004-01 till 2015-12 is reported by Dieng et al. (2017) almost twice of what is found from the inversion (0.13 mm/yr for the same period). Including the GRACE-FO, Hakuba et al. (2021) report budget closure of 0.45 mm/yr when not considering the deep ocean contribution mentioned in section 7.2.8, which reduces to 0.33 mm/yr in case this is simply subtracted for 2005-01 till 2019-12. The inversion provides budget closure of about 0.19 mm/yr for the same period, which is heavily affected by the bias effects reported above. When comparing to earlier inversions it is necessary to incorporate the bootstrap component into the budget closure evaluation. After two inversion runs, Rietbroek (2014) report 0.05 mm/yr of budget closure. However, this has to be combined with the bootstrapped estimate, which is interpreted and reported as deep ocean steric contribution of 1.03 mm/yr resulting in 1.08 mm/yr for the period 2003-01 till 2011-12, which is 1.0 mm/yr larger compared to the 0.08 mm/yr found from this thesis' inversion. Similarly the budget closure in Rietbroek et al. (2016) is expressed as "other" component with a magnitude of 0.22 mm/yr for 2002-04 till 2014-06, which is about twice

compared to 0.11 mm/yr found from this thesis. Overall, the inversion introduced in this thesis provides consistent budget closure, which is at the same level or even better compared to other published estimates for their respective time periods even, when influenced by small biases due to an insufficiently long fingerprint data basis.

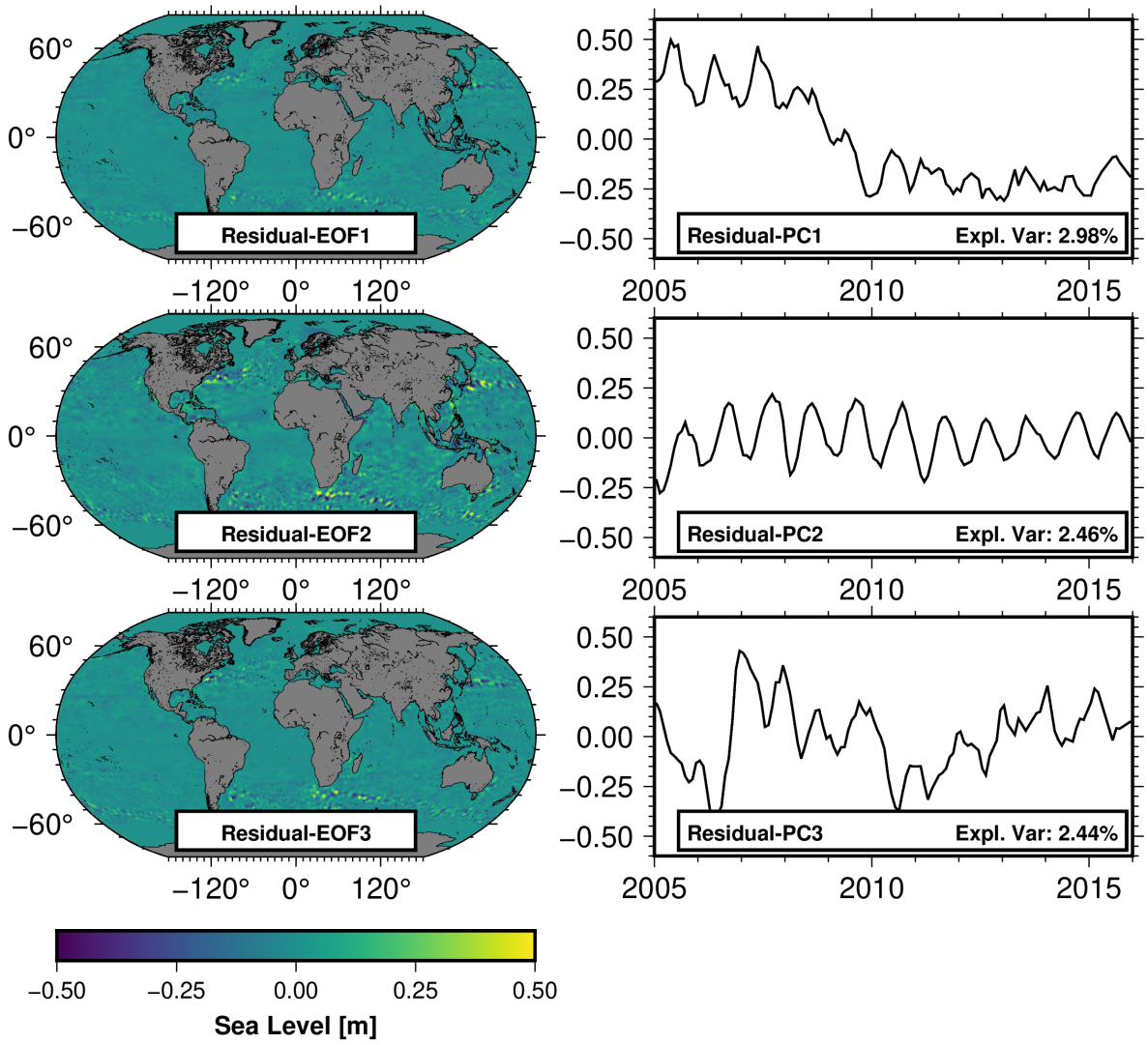


Figure 7.22: First three EOFs, PCs and corresponding explained variances based on the residuals of total sea level change between the inversion and altimetry. From the explained variance and the corresponding patterns, the residuals include no significant large signals anymore and are dominated by eddy signatures, especially in the major current regions.

When the residuals, which are originally computed at the measured along-track altimetry positions, are gridded it is possible to also spatially investigate the remaining unmodeled signal content. For analysis these spatio-temporal maps of inversion residual sea level are further decomposed over 2005-01 till 2015-12 using PCA (Sect. B). This allows to extract the major spatial and temporal signals from the data. The first three EOF and corresponding PC are shown in figure 7.22. Spatially all three presented EOFs mostly contain signals in the major current regions of the Western Boundary Currents or the Antarctic circum polar current. Corresponding PC indicate a predominantly seasonal temporal behavior superimposed with some small long term signals (Fig. 7.22). These signals are predominantly caused by seasonal eddy kinetic energy variations resulting from wind and ocean stratification variability (Rieck et al., 2015; Yamaguchi and Suga, 2019).

The variance explained by each EOF and PC combination is in the range of about $2.5-3.0\%$ for the first three modes, which indicates that there is no dominant spatial or temporal signal left in the residuals. These rather contain the high frequency variations from eddies and currents, which are not modeled by the inversion and, thus, not captured by any of the other fingerprints. Parts of this signals are absorbed in the steric variations, which are based on the ORAS5 model that includes currents and eddies to a certain extent. However, no modeled eddy and current matches reality. So it is expected to find residual dynamic ocean signal in the altimetry residuals. Therefore, the residual component and, consequently, budget closure in the sea level budgets in this thesis (e.g., Fig. 7.1 or Tab. 7.1) is generally denoted "ocean dynamics". Due to the rapid varying signal in the affected regions, regional differences with respect to the impact of the ocean dynamics sea level component are expected (Sect. 7.5). The residual trend signal is likely related to misinterpretation of steric trends, which can not be properly modeled and then ends up in the residual component. In addition, local effects and errors in the modeling will lead to residual trend signal.

However, the consistently closed sea level budget and small residuals could also be indicating an over-fitting of the signals by introducing a large number of fingerprints, which absorb and distribute signals erroneously. This is somehow alleviated by the good agreement of individual components to independent oceanic and land based validation data (Sects. 7.2.1-7.2.8), which did not indicate large discrepancies. As a consequence, the sea level budget presented in this thesis seems to be consistently closed and meaningful.

7.3 Robustness of the Inversion Results

Results from the inversion method, to a certain extent, depend on the fingerprint configuration and the processing choices, such as corrections or regularizing certain contributors. This section investigates the robustness of the inversion results with respect to these individual processing choices and fingerprint configurations.

7.3.1 Effect of Variance Component Estimation

The base inversion (IS001) has the VCE turned off in order to be consistent with how sea level budgets are generally produced in literature from individually processed datasets. Since the combination is usually done on the basis of time series without considering relative error information (e.g. Cazenave et al., 2009; Dieng et al., 2017; WCRP-Global-Sea-Level-Budget-Group, 2018; Hakuba et al., 2021; Horwath et al., 2022), it has made sense to deactivate this for the comparisons done in sections 7.1 and 7.2.

When enabling the VCE without changing anything else (IS002, Tab. 7.13), it is obvious that the effect from VCE on the global sea level budget is basically negligible and limited to variations in the 0.01 mm/yr level to hydrology, IMV and steric components. These components are all derived based on PCA and require a quite large number of associated fingerprints to represent the high spatial and temporal variabilities. Consequently, these components are also the most variable. The formal errors are affected only in digits after the comma that are not reported, e.g., in table 7.1.

In the following, all further configurations will have the VCE enabled as it generally makes sense to utilize the available co-variance information from GRACE/GRACE-FO and altimetry for deriving optimal results. This will become even more important when including additional data from other altimetry missions, gravity data or steric observations (Sec. 7.4). Therefore, all following comparisons will be made to the base inversion setup with VCE turned on, i.e. IS002 (Tab. 7.12).

7.3.2 Impact of Glacial Isostatic Adjustment Correction

As already found in the context of spherical harmonic gravity data processing, the choice of GIA model utilized for correction will significantly influence the resulting sea level estimates (Sect.

Table 7.12: Tested inversion configurations in table 7.13 relative to base inversion (IS001).

Inversion ID	Configuration Changes
IS001	Base Inversion
IS002	VCE enabled
IS003	GIA replaced by ICE6G_D
IS004	GIA replaced by Klemann and Martinec (2009)
IS005	GIA co-estimated as in Rietbroek (2014) and Rietbroek et al. (2016) based on Klemann and Martinec (2009) model
IS006	Regularization of strongly correlated melting basins from land glaciers, Greenland and Antarctica
IS007	IMB from RADS only without further corrections
IS008	IMB co-estimated as in Rietbroek (2014) and Rietbroek et al. (2016)
IS009	IMB as in Nerem et al. (2018)
IS010	80% of explained variance from all PCA-derived fingerprints (Steric (15 FPs), Hydrology (10 FPs) and IMV (15 FPs))
IS011	90% of explained variance from all PCA-derived fingerprints (Steric (45 FPs), Hydrology (20 FPs) and IMV (40 FPs))
IS012	Greenland and Antarctica patterns without background melting information
IS013	16 Glacier patterns from Rietbroek (2014) and Rietbroek et al. (2016)
IS014	60 hydrology EOF patterns based on WGHM as utilized by Rietbroek (2014) and Rietbroek et al. (2016)
IS015	60 hydrology EOF patterns from the PCRGLOB model
IS016	FESOM version 1.2 steric patterns as in Rietbroek et al. (2016)
IS017	FESOM version 1.4 steric patterns
IS018	Further splitting the upper 700 m steric sea level into thermo- and halosteric contributions (100FPs each) based on the ORAS5 model
IS019	Further splitting the upper 700 m steric sea level into thermo- and halosteric contributions (200FPs each) based on the ORAS5 model
IS027	Steric fingerprints only derived from model data up to 2008
IS028	Steric fingerprints derived from the ORAS5 undisturbed base run until 2020-12
IS029	Same as IS002 but evaluated considering an additional 300 km coastal buffer

Table 7.13: Overview on sea level budget results from different inversion configurations. All values are global mean sea level trends in mm/yr for the period 2005-01 till 2015-12. At first the small effect of applying VCE is investigated (IS002). After that, VCE is kept enabled for all other inversions considered here.

Inversion ID	Total	Mass	Steric	Greenland	Antarctica	Glaciers	Hydrology	IMV	Steric $>700\,\mathrm{m}$	Steric $<700\,\mathrm{m}$	Ocean Dynamics
	VCE effect										
IS001	3.43	1.89	1.41	0.75	0.42	0.64	0.21	−0.11	1.04	0.38	0.13
IS002	3.43	1.89	1.43	0.75	0.42	0.64	0.22	−0.13	1.05	0.37	0.12
	Impact of GIA correction										
IS003	3.47	2.03	1.33	0.75	0.49	0.63	0.18	−0.06	0.96	0.37	0.12
IS004	3.35	1.74	1.47	0.75	0.40	0.60	0.11	−0.12	1.07	0.40	0.14
IS005	3.33	1.75	1.49	0.66	0.35	0.64	0.13	−0.05	1.08	0.41	0.17
	Impact of regularizing correlated Greenland, Antarctic and Glacier basins										
IS006	3.43	1.87	1.44	0.73	0.41	0.64	0.22	−0.12	1.07	0.37	0.12
	Impact of different IMB configurations										
IS007	3.22	1.79	1.34	0.75	0.41	0.63	0.13	−0.13	0.99	0.35	0.09
IS008	3.39	1.83	1.39	0.75	0.40	0.63	0.16	−0.11	1.03	0.36	0.18
IS009	3.32	1.85	1.36	0.75	0.42	0.64	0.17	−0.12	1.00	0.36	0.11
	Impact of different fingerprint setups										
IS010	3.43	1.93	1.28	0.75	0.43	0.65	0.16	−0.06	0.95	0.33	0.23
IS011	3.43	1.90	1.35	0.75	0.42	0.64	0.20	−0.10	0.98	0.36	0.18
IS012	3.46	2.20	1.20	0.78	0.81	0.65	0.12	−0.15	0.89	0.31	0.06
IS013	3.42	1.65	1.60	0.77	0.42	0.35	0.28	−0.16	1.22	0.39	0.16
IS014	3.43	1.88	1.43	0.75	0.42	0.62	0.23	−0.13	1.06	0.37	0.12
IS015	3.44	2.00	1.34	0.76	0.41	0.58	0.37	−0.12	0.99	0.36	0.10
IS016	3.44	2.01	1.28	0.75	0.42	0.66	0.24	−0.05	0.37	0.91	0.15
IS017	3.47	2.48	0.74	0.76	0.43	0.69	0.62	−0.02	0.76	−0.02	0.25
	Impact of steric fingerprint creation time period										
IS027	3.49	2.94	0.16	0.78	0.43	0.73	0.91	0.10	−0.05	0.21	0.39
IS028	3.43	1.82	1.49	0.75	0.42	0.63	0.14	−0.10	1.26	0.23	0.11
	Applying a 300 km ocean buffer										
IS029	3.22	1.76	1.39	0.77	0.41	0.65	0.21	−0.27	1.03	0.36	0.07

5.3.2). Consequently, the impact from different GIA solutions on the inversion is investigated.

The standard inversion (IS001, IS002, Tab. 7.12) always employs the GIA correction by A et al. (2013), which is most consistent with the one provided in the RADS database that is, e.g., utilized by Nerem et al. (2018). It is relatively similar in terms of the global mean ocean mass trend effect to the ICE6G_D GIA model (Peltier et al., 2018), which is nowadays often utilized in GRACE/GRACE-FO data processing. Consequently when used in IS003, one would generally expect a rather small impact on the sea level budget.

However, a shift of about 0.10 mm/yr is observed between mass and steric attributed sea level change, which is mostly driven by the Antarctic sea level contribution. The total sea level change is found to be slightly larger (3.47 mm/yr, Tab. 7.13). Differences in the spatial patterns in modern GIA models are generally most pronounced in Antarctica. This leads to a larger sea level change being attributed to Antarctica based on the choice of ICE6G_D (IS003, Tab. 7.13). This is to a small extent compensated by the hydrology component. Furthermore, a reduced steric sea level contribution from the upper 700 m is found, but, an increased IMV contribution, leading to an overall increase of global mean OMC (2.03 mm/yr). The budget closure remains at the same level. Impacts from the chosen GIA correction can also be seen looking at the Antarctic ice mass changes (Fig. 7.13).

When the A et al. (2013) GIA correction is substituted with the GIA model by Klemann and Martinec (2009), which is also utilized in Rietbroek (2014) and Rietbroek et al. (2016), an even stronger impact is observed as would be expected based on table 5.2. The total sea level compared to the base run (IS001, IS002, Tab. 7.12) is reduced by about 0.10 mm/yr driven by the reduction of OMC to a level of 1.74 mm/yr. This is only partly compensated by a small increase in the steric estimate (1.47 mm/yr). In contrast to the ICE6G_D model the mass loss is rather driven by the glaciers and hydrology components, while the Antarctic contribution remains relatively stable with respect to the reference solution.

When GIA is co-estimated (Rietbroek, 2014; Rietbroek et al., 2016), the budget is significantly impacted. While the glacier component remains stable with respect to the reference solution, sea level contributions from, both, Greenland and Antarctica are found to be significantly smaller compared to the reference solution, indicating reduced ice mass loss (IS005, Tab. 7.13). The overall OMC and steric contributions remain the same as in IS004 (Tab. 7.13). At the same time the residual trend is found to be about 50% larger compared to the reference solution.

Overall it becomes clear that the choice of GIA correction can significantly impact the estimated sea level budget. The impact on the OMC estimate for the inversion (IS002 versus IS003, Tab. 7.13) is about the same as for the directly processing the GRACE data (Tab. 5.2). In the inversion, the resulting change in OMC is compensated by the steric component. While GIA does not contribute directly to the global budget as it is defined as zero over the global ocean, regionally these choices will have a much bigger impact. Furthermore, inconsistencies in the choice of GIA model will directly affect comparisons with other derived or published estimates.

7.3.3 Regularization of Individual Basins

Regularizing the mass change of individual basins can be helpful in case these are highly correlated. From the correlation matrix (Figs. 6.11 and 6.12) mass variations from particular basins show significant statistical correlation. For this thesis, the impact from constraining highly correlated mass changes from individual sub-basins on the sea level budget is investigated by introducing regularization for mass changes of selected Antarctic, Greenland and glaciers basins (IS006, Tab. 7.12).

For Antarctica, mass change from the two smallest basins (26+27) cannot be separated well, due to the spatial resolution of GRACE/GRACE-FO, leading to high correlations. For Greenland cor-

relations between mass change from the above and below 2000 m elevation basins are considered as well as some smaller interconnections between mass changes at the southern tip of Greenland. For the glacier melting contribution, mass changes from neighboring sub-basins in the Arctic Canada North/South regions (Figs. 6.1 and 7.14) as well as two small basins in the Himalayan region (Fig. 6.1) are regularized as in Rietbroek (2014).

From the results in table 7.13 (IS006) it becomes clear that the applied regularization does not significantly affect the global mean sea level budget. The overall mass contribution from Greenland, Antarctica and land glaciers seems to be less affected. The regularization rather leads to a small shift in mass loss attribution between individual sub-basins, resulting in a more similar behavior, as one would expect. With the updated inversion presented in this thesis, the addition of melting background information for Greenland and Antarctica has lead to a significant decrease in inter-basin correlations, compared to earlier inversion versions without the need for further regularization. In this thesis, regularization is not applied, since solving the combined normal equations is possible and the output is usually interpreted as a sum over all sub-basins of a specific region, e.g. Greenland, where inter-basin dependencies do not matter that much.

7.3.4 Impact of Different Altimetry Inter-Mission Bias Configurations

The IMB between individual satellite altimetry missions plays a significant role when combining datasets and evaluating sea level budgets. While the IMB for the Jason missions can be estimated relatively robust due to the tandem mission phases, biases between other missions are even more prone to introducing trend errors into the sea level budget. For this configuration test, the focus is on the IMB of the Jason missions.

First, the impact from directly using the RADS estimates for the Jason-1/-2/-3 missions without additional corrections as described in section 6.2.1 is investigated (IS007, Tab. 7.13). As a result, the hydrological sea level contribution is found at only 60% level compared to the base solution (IS002, Tab. 7.13), reducing the OMC contribution by about 0.10 mm/yr. Similar reduction is found for the steric sea level. While the budget closure is slightly better than for the base solution (0.09 mm/yr), the corresponding total sea level is found too small at a level of 3.22 mm/yr compared to other GMSL estimates (Sect. 7.2.1).

When co-estimating the corrections to the RADS based IMB coefficients similar to Rietbroek (2014) and Rietbroek et al. (2016), the budget closure becomes significantly worse (IS008, Tab. 7.13). The other components remain relatively close within about 0.05 mm/yr to the reference solution. This in combination with the increase in residual trend indicates that the co-estimated IMB parameters do not really represent the correct IMBs, but rather absorb other trend signals.

The third IMB configuration tested (IS009, Tab. 7.13) is by replacing the RADS based IMB with the ones used in Nerem et al. (2018) as described on their website[3]. Both, derived IMBs solely from an altimetry data crossover analysis. One would expect results similar to IS007 since the corresponding offsets are close to the RADS ones. However, the impact is different. While the steric contribution is similarly affected as with the RADS IMBs, the influence on the mass estimate is lower (IS009, Tab. 7.13).

Overall, the three experiments (IS007-IS009) show that even for slightly different IMB estimates just for the Jason-1/-2/-3 nominal missions, the impact on derived trends and, consequently, the corresponding sea level budget is quite significant. This underlines the importance of accurate derivation of altimetry IMBs and the need for consistency when comparing to other published estimates. However, information such as those is only rarely provided and might, thus, pose potential for significant trend errors.

[3] https://sealevel.colorado.edu/data-processing-methods (last accessed: 15.06.2022)

7.3.5 Impact of Different Fingerprint Setups

Reducing the explained variance for the PCA based fingerprints

For the hydrological, IMV and steric component the fingerprints are constructed by applying PCA to corresponding model data in order to extract the dominant EOFs. Generally, all EOFs that explain the model variance up to 99% are fitted in the inversion approach from this thesis (e.g., IS001 or IS002, Tabs. 7.12 and 7.13). This results in a large number of fitted fingerprints for these components. Consequently, it makes sense to investigate whether all of these fingerprints are necessary or a smaller number, i.e. an explained variance of only 80% or 90%, is sufficient to rule out and avoid over-fitting.

For the first experiment, the corresponding EOFs are chosen to only represent 80% of the respective variance, significantly reducing the number of fingerprints (Tab. 7.12). As expected from the resulting budget (IS010, Tab. 7.13), it becomes clear that the mass budget is most significantly affected in the hydrology and IMV components. The smaller hydrological contribution is compensated to an extent by the IMV component. Melting contributions are not severely affected (< 0.01 mm/yr). The largest impact is found for the steric component, where the explained sea level is reduced by about 0.15 mm/yr. At the same time, the ocean dynamics component grows, increasing the budget closure error to 0.23 mm/yr.

Employing EOFs for up to 90% explained variance (IS011, Tab. 7.12), slightly increases the number of fingerprints again. Consequently, the effects observed when utilizing 80% (IS010, Tab. 7.13) are reduced. However, there is still a significant reduction effect of 0.1 mm/yr observed for the steric sea level. On the one hand, the impact from using 90% or 99% for the hydrological and IMV component is negligible, but on the other hand, the steric component is quite sensitive to the reduced explained variance representation. The steric component is by far the most spatio-temporal variable and, consequently, more affected by reducing the available number of base functions for explaining the observed sea level effects.

Upgrading mass fingerprints from earlier inversions

The effect from replacing the melting fingerprints used by Rietbroek (2014) and Rietbroek et al. (2016) is investigated (IS012, IS013 and IS014, Tab. 7.12 and Tab. 7.13). First, the introduction of background melting patterns in Greenland and Antarctica (IS012) is investigated. From table 7.13 it becomes clear that the impact is quite significant. OMC is found at 2.20 mm/yr. The overall change for the Greenland component is minimal (0.03 mm/yr), similar for the glaciers contribution. At the same time, the reported Antarctic melting rate has almost doubled (IS012, Tab. 7.13) and the hydrological trend has been roughly halved. Similarly, steric sea level is found at 1.20 mm/yr level resulting from a reduced upper 700 m contribution. The budget closure is rather good (0.06 mm/yr). But due to the Antarctic component, indicating a significantly wrong sea level contribution, which is not supported by the validation data (Sect. 7.2.4), the overall budget is not reliable.

When the 68 glacier fingerprints (Sect. 6.1.1) are replaced by the old 16 regions from Rietbroek (2014) and Rietbroek et al. (2016), the resulting budget also shows a strong impact. As expected, the glaciers component is affected the most, with the corresponding sea level contribution almost halved (IS013) compared to the reference run (IS002). Melting rates from Greenland and Antarctica are not affected much. Hydrology related sea level and budget closure are found at an about 0.05 mm/yr increased level. The steric sea level is significantly larger (1.60 mm/yr), mostly driven by the upper 700 m ocean.

In a third step, the hydrological EOFs are replaced with the ones employed in Rietbroek (2014) and Rietbroek et al. (2016), which are based on an earlier version of the WGHM model (IS014,

Table 7.14: Effect from further splitting the upper 700 m steric sea level change into thermo- and halo-steric components based on GRACE/GRACE-FO and altimetry data. All values are global mean sea level trends in mm/yr for the period 2005-01 till 2015-12. The result can be compared to the reference solution (IS002, Tab. 7.13).

Inversion ID	Total	Mass	Steric	Steric > 700 m	Thermo-Steric > 700 m	Halo-Steric > 700 m	Steric < 700 m	Ocean Dynamics
IS018	3.45	2.09	1.20	0.86	0.82	0.04	0.34	0.16
IS019	3.45	2.11	1.19	0.85	0.81	0.04	0.33	0.16

Tab. 7.12). The resulting budget is found to be quite similar to the reference solution (IS002). This indicates that the overall information included in the WGHM model has not significantly changed with the newer version and extended time series. This is also supported by the result from IS011 and to some extent IS010 that showed relatively stable results, despite a significant reduction in hydrological fingerprints. When the WGHM is replaced by a different hydrological model, such as PCR-GLOBWB (IS015, Tab. 7.12), the impact is much more severe. Ice sheet melting rates exhibit only minimal changes, while the glaciers and hydrology components change more drastically leading to a significant increase in OMC. At the same time steric sea level is slightly smaller compared to the reference solution.

Choice of steric model data for fingerprint generation

Impacts from employing different steric model data from the FESOM model for generating fingerprints (IS016 and IS017, Tab. 7.12) are investigated. The first configuration (IS016) utilizes the FESOM version 1.2 employed in Rietbroek (2014) and Rietbroek et al. (2016). Replacing the ORAS5 fingerprints affects both, OMC and steric contribution. OMC is found at a level of 2.01 mm/yr mostly driven by a reduced IMV trend. The steric sea level rate (1.28 mm/yr) is smaller than the reference solution. However, a close look at the upper 700 m and deep ocean component reveals that about 70% of steric sea level change is attributed to the deep ocean, which is clearly not meaningful (cf. Sect. 7.2.8). Interestingly, utilizing fingerprints derived from the newer FESOM version 1.4 results in even more severe effects (IS017, Tab. 7.13). The overall steric sea level change is found only at a level of 0.74 mm/yr, which is significantly smaller than comparable estimates (cf. Sect. 7.2.8) nearly 100% of the steric change is attributed to the upper 700 m. At the same time, the terrestrial hydrology driven sea level change is found at a significantly increased level (0.62 mm/yr), which results from the hydrology fingerprints absorbing parts of the steric trend. Consequently, the resulting budget closure error is found quite high with 0.25 mm/yr.

Additionally, it is investigated whether a steric configuration, which further splits the upper 700 m of the water column into a thermo- and halo-steric contribution is feasible (IS018, Tab. 7.12) based on fingerprints derived from ORAS5. The results are shown in table 7.14. OMC is found increased by about 0.15 mm/yr, mainly driven by the hydrological mass component, which compensates the reduced steric sea level to some extent. The upper 700 m steric change is found at 0.86 mm/yr, which is clearly dominated by the thermo-steric sea level (0.82 mm/yr) with a small halo-steric contribution (0.04 mm/yr). The deep steric component is only marginally affected by the modeling change. Closure of the sea level budget is slightly worse (0.16 mm/yr) compared to the reference solution (IS002). From this it can be concluded that the additional split of upper 700 m ocean is feasible and the corresponding thermo- and halo-steric patterns are relatively inde-

pendent from each other and can be fitted. The representation by 100 fingerprints each for IS018 has been chosen to keep the overall number of fingerprints the same. Adding additional fingerprints in order to increase the roughly 95% explained variance for IS018 to 99% at 200 EOFs (IS019, Tab. 7.12) does not significantly change the results. IS018 and IS019 represent a good basis for further expansion of the inversion method by introducing additional in-situ temperature and salinity data to better separate the thermo- and halo-steric contributions (Sect. 7.4.4).

7.3.6 Impact of the steric fingerprint creation period

As has been mentioned before (e.g., Sect. 7.2.9), the time period utilized for the creation of the PCA based fingerprint is the data period for which the fingerprints correspond to EOFs, i.e. ranked eigenmodes of the variability. These are derived for the steric, terrestrial hydrology and IMV contributions. The time period of available model data will significantly affect the ability to correctly reconstruct the respective sea level contribution. This leads to unwanted trend and bias effects, therefore, partly explaining the bias found in the residual component during the GRACE-FO era in the base inversion (Figs. 7.2, D, and 7.23).

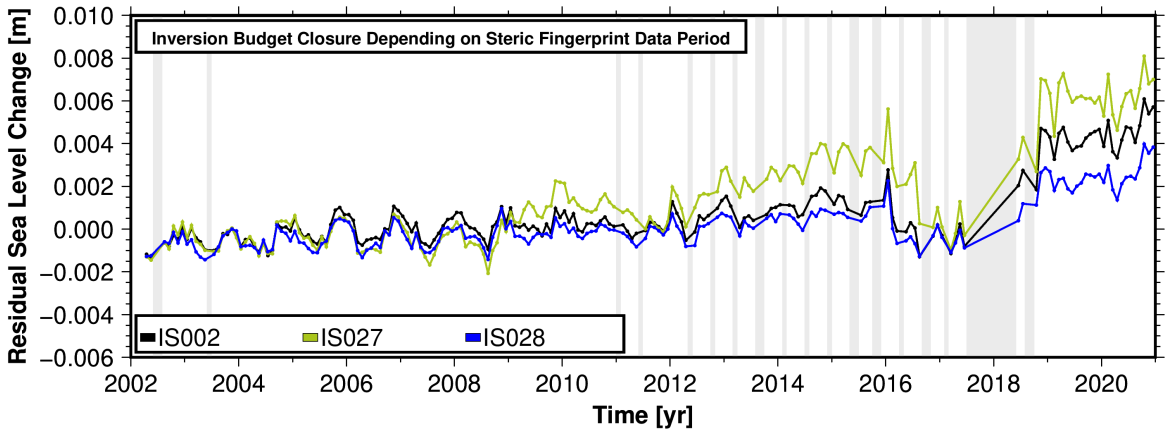


Figure 7.23: Inversion budget closure relative to the data period utilized for creating the steric fingerprints.

In principle, the effect results from extrapolation of a specific sea level component outside of the original time period used for creation of the respective fingerprints. In other words, due to the shorter creation time, the limited number of fingerprints are less representative as a spatial basis outside of the creation time period. For this thesis, ensemble mean ORAS5 data is only available up till 2017-12. This means that the steric sea level after that time is reconstructed assuming that the available steric fingerprints are still valid and sufficient for modeling the spatio-temporal steric variability of the GRACE-FO era. For testing these assumptions, an inversion where the steric fingerprints have been derived based on the period until 2008 is computed (IS027, Tabs. 7.12 and 7.13). The resulting budget is heavily influenced by the inability of the steric fingerprints to correctly model the observed sea level starting shortly after 2008 (Tab. 7.13). The sea level budget is dominated by the mass component accounting for about 85% of the total sea level variation while the steric component is able to explain only 5% of the total trend, with the remaining 10% increasing the budget closure error to 0.39 mm/yr (IS027, Tab. 7.13). Before 2008, the residual and also the other components are found relatively close to the reference solution. But after about 2010, the residuals become noisy and residual trend effects are clearly visible. This also leads to an actual increase of the bias during the GRACE-FO era to 6 mm (Fig. 7.23).

On the other hand, when extending the steric period utilized for derivation of the fingerprints until 2020-12, the sea level budget for the reference time period is much closer to the reference

solution (IS028, Tabs. 7.12 and 7.13). Since not all ensemble members of ORAS5 have been available, the IS028 is based solely on the nominal/operational ORAS5 run. The mass component of IS028 is found differing by about 0.07 mm/yr, resulting from a smaller hydrological sea level that is balanced by the increase in steric sea level to 1.49 mm/yr for 2005-01 till 2015-12. The Budget closure error is at the same level (0.11 mm/yr) as for the reference solution (Tab. 7.13). Effects from the longer time period for the fingerprint creation are also clearly visible in the residuals (Fig. 7.23). Till the end of 2017, the residual time series from IS028 is close to the reference one (IS002). However, the trend over the GRACE-FO era is reduced by about 50% when including the years 2018-2020 in the creation of the steric fingerprints.

This clearly shows the need for good prior information on highly spatio-temporally variable sea level components, such as steric, IMV or terrestrial hydrology. Although not shown here, similar effects occur due to the limited data availability for the fingerprint creation of the hydrological component. For the IMV, which is based on the AOD1B-GAB product that is produced operationally on a regular basis and coupled with the GRACE/GRACE-FO data, this is less of a problem. This experiment also clearly shows a weakness of the inversion method or fingerprints in general, where it is always assumed that the patterns derived for a certain time period are also representative for sea level reconstruction outside that time frame, i.e. extrapolation. For the time periods considered in this thesis, the assumption clearly holds for most components, especially the melting rates for the ice sheets and land glaciers. But for the spatio-temporal variable components, such as steric sea level, meaningful extrapolation is only possible for a short period.

7.3.7 Applying a 300 km ocean buffer

So far, the inversion budget has always been evaluated on the Jason along-track measurement positions that went into the estimation process, without any further mask applied. For deriving OMC from time-variable gravity (Sect. 5.3), a 300 to 500 km coastal buffer zone mask is usually applied in order to reduce the leakage impact from the much larger land hydrology signals into the OMC estimate. Since the inversion approach explicitly models the land hydrology effect, it is assumed that it is possible to exclude that mask for evaluating the inversion results; this has been done here so far. However, when comparing to individually processed GRACE/GRACE-FO based estimates, it makes sense to also consider a coastal buffer zone for the mass estimate.

Consequently, the results from IS002 have been reevaluated while also masking out positions inside a 300 km coastal buffer zone (IS029, Tab. 7.12). For the reduced ocean area, the total sea level change is found lower at 3.22 mm/yr resulting from a slight reduction in the OMC and steric component (1.76 mm/yr and 1.39 mm/yr, respectively) as well as a smaller budget closure error of only 0.07 mm/yr. Since the ocean area is reduced by about 29% (about 38% for a 500 km buffer), the IMV component has larger impact (-0.27 mm/yr) since it is constrained to be zero over the total ocean area. Similarly when considering smaller basins of the ocean, the GIA effect on sea level is no longer zero. For evaluating on the Jason positions the GIA impact is, in fact, basically zero. In contrast, it contributes by about -0.02 mm/yr to the budget when applying the 300 km buffer zone. Generally, the distribution of OMC and steric sea level over the individual sub-components is rather similar to the reference solution (IS002, 7.12).

Overall, reducing the ocean area by applying additional masks, such as a coastal buffer has significant impact on the budget. Especially, sub-contribution of OMC, which are constrained to be zero or close to zero, such as GIA and IMV, respectively, will gain increasing impact on the budget. This is especially important when considering regional sea level budgets in section 7.5. At the same time it is necessary to apply consistent ocean basins to all considered parts of the sea level budget. Considering the 300 km buffer only on the mass estimate, e.g. when evaluating GRACE/GRACE-FO data, but not for the steric or altimetry based sea level change will directly translate into budget closure errors and, generally, invalidate the derived budget. Inconsistencies like these are often found in published sea level budgets (cf. Sect. 7.2).

7.4 Extending the Inversion with Additional Input Data

This section expands the inversion approach with additional input data, such as expansion of the altimetry data base with further satellite missions and phases besides the nominal Jason altimetry period. Furthermore, the GRACE data releases RL05 and RL06 are investigated as well as potential bias effects and their source. So far, the inversion has been limited to OMC observations from GRACE/GRACE-FO and integrated sea level measurements from satellite altimetry. This section examines the potential of additionally constraining the steric sea level contribution by including in-situ temperature and salinity measurements converted to thermo- and halo-steric sea level, respectively. Similarly, potential to derive results in months of missing GRACE/GRACE-FO data, by utilizing time-variable gravity information from SLR and Swarm, is explored.

Table 7.15: Inversion configurations including additional input data relative to base inversions (IS001 and IS002, Tab. 7.12).

Inversion ID	Configuration Changes
IS020	Replacing the GRACE RL06 input data with RL05 data from GFZ utilized by Rietbroek (2014) and Rietbroek et al. (2016)
IS021	Same as IS002 (Tab. 7.12) with additional altimetry observations from the nominal Envisat and Saral/Altika missions
IS022	Same as IS002 (Tab. 7.12) with additional altimetry observations from all available missions and phases, except for ERS-2 and HY-2A
IS023	Same as IS001 (Tab. 7.12) with additional in-situ steric sea level profile observations for the upper 700 m ocean
IS024	Same as IS002 (Tab. 7.12) with additional in-situ steric sea level profile observations for the upper 700 m ocean
IS025	Same as IS018 (Tab. 7.12) with additional in-situ thermo- and halo-steric profile observations from the upper 700 m ocean (VCE disabled)
IS026	Same as IS018 (Tab. 7.12) with additional in-situ thermo- and halo-steric profile observations from the upper 700 m ocean (VCE enabled)
IS030	Same as IS002 (Tab. 7.12) including all altimetry mission data, additional SLR gravity observations and in-situ steric profile data from easyCORA
IS031	Same as IS030, but also solving months with missing GRACE/GRACE-FO data based on SLR and Swarm gravity observations and in-situ steric profile data from easyCORA

7.4.1 Replacing GRACE RL05 with RL06 Data

GRACE RL06 data has been released in 2018, which represented a significant update in background models, as well as observational data handling (e.g., Dobslaw et al., 2017b; Mayer-Gürr et al., 2018). However, earlier published inversion estimates (Rietbroek, 2014; Kusche et al., 2016; Rietbroek et al., 2016; Uebbing et al., 2019) all rely on the RL05a GRACE data by GFZ. Therefore, it is investigated how the resulting global mean sea level budget would change when simply replacing the RL06 data with RL05 data for the reference solution from the previous section (IS020, Tabs. 7.15 and 7.16).

From table 7.16 in combination with the validation results from section 7.2 it becomes clear that the previous release of GRACE data is not able to correctly separate the individual mass and steric components. In fact, the basically zero budget closure error indicates a severe over-fitting, where all signal is absorbed into the available fingerprint parameters. This leads to a significantly large OMC of 2.71 mm/yr, which is about one millimeter above the reference solution. At the same time, the steric contribution is significantly underestimated (0.76 mm/yr).

Table 7.16: Overview on sea level budget results from different inversion configurations based on varying input data. All values are global mean sea level trends in mm/yr for the period 2005-01 till 2015-12. The results from IS002 (Tab. 7.13) are repeated for direct comparison.

Inversion ID	Total	Mass	Steric	Greenland	Antarctica	Glaciers	Hydrology	IMV	Steric > 700 m	Steric < 700 m	Ocean Dynamics
	Repeating the reference solution from table 7.13										
IS002	3.43	1.89	1.43	0.75	0.42	0.64	0.22	−0.13	1.05	0.37	0.12
	GFZ-GRACE RL05a gravity input data										
IS020	3.48	2.71	0.76	0.83	0.53	0.75	0.63	−0.01	0.49	0.28	0.01
	Including high-latitude altimetry data										
IS021 (a)	3.44	2.16	1.24	0.76	0.42	0.68	0.49	−0.19	0.81	0.43	0.04
IS021 (b)	3.64	2.19	1.22	0.76	0.43	0.68	0.49	−0.16	0.80	0.42	0.23
	Including all meaningful available altimetry data										
IS021 (c)	3.63	2.19	1.22	0.76	0.43	0.68	0.49	−0.16	0.80	0.42	0.23
IS022 (a)	3.46	2.70	1.02	0.78	0.43	0.76	1.10	−0.36	0.64	0.38	−0.26
IS022 (c)	3.83	2.73	1.06	0.78	0.43	0.76	1.10	−0.32	0.68	0.38	0.03
IS022 (d)	3.80	2.72	1.04	0.77	0.43	0.75	1.10	−0.32	0.66	0.38	0.04
	Introducing in-situ steric profile data from easyCORA										
IS023	3.44	2.02	1.25	0.75	0.42	0.65	0.30	−0.10	0.77	0.48	0.16
IS024	3.43	1.91	1.39	0.75	0.42	0.64	0.24	−0.12	1.01	0.39	0.13
	Additional SLR and Swarm data and solution of missing months										
IS031	3.93	3.01	0.89	0.33	0.72	−0.20	2.50	−0.33	0.55	0.34	0.02
	Including all altimetry missions, easyCORA in-situ profiles and SLR										
IS030	3.80	2.68	1.07	0.77	0.43	0.78	1.05	−0.32	0.68	0.39	0.05

Consequently, it can be concluded that the new fingerprint setup for the base inversion (Tab. 6.2) is able to leverage the improvements in RL06 data with respect to resolution and the ability to separate individual mass signals. This also means that for earlier GRACE releases, but also for utilizing time-variable gravity from other sources, such as SLR or Swarm that provide information only on low degree coefficients, the fingerprint base has to be simplified in order to derive meaningful separation results (Sect. 7.4.5).

7.4.2 Including GRACE-FO Data

Generally, utilizing GRACE-FO data as input for the inversion method works the same way as with GRACE data. After decommissioning of the GRACE mission there was an one year gap between the two missions, where no high resolution gravity data was available. At the time of writing this thesis, only two years of GRACE-FO data have been available, which limits potential validation efforts due to the short time span, especially in the context of deriving trends (see App. C). In addition, the results from the GRACE-FO era have to be interpreted carefully. As has been noted before (Sect. 7.2.6 and 7.2.8), the fingerprint base is limited due to the EOF modes being derived without including GRACE-FO time period and the high spatio-temporal variability of, both, hydrology and steric changes.

A bias in the residual ocean dynamics component of 3 to 4 mm/yr has been found for the GRACE-FO era (Fig. 7.2), which would introduce a significant artificial trend when deriving sea level budget for the combined GRACE and GRACE-FO period. The origin of this bias is not entirely clear (personal communication with Felix Landerer, JPL). It could be related to the limited

quality of the fingerprint basis for that time period, a bias in the GRACE-FO data or Jason-3 altimetry data utilized for combination.

A bias in the GRACE-FO data seems unlikely as these are processed as a continuation of the GRACE observations in the same manner, with the same processing and background models applied, and one would not expect any biases. In fact, investigations into this matter so far have shown that no GRACE/GRACE-FO bias can be detected (Landerer et al., 2020). In the following section, the bias is further reduced when utilizing all available altimetry missions (Sect. 7.4.3).

7.4.3 Including Additional Altimetry Missions

For all inversion that have been presented up to this point and also published in the past (Jensen et al., 2013; Rietbroek, 2014; Kusche et al., 2016; Rietbroek et al., 2016; Uebbing et al., 2019), altimetry data has been limited to the Jason mission only. In this thesis so far, it has been strictly limited to the nominal orbit phase of the Jason-1/-2/-3 missions in order to be as consistent as possible with other published budgets and global mean sea level time series, which only utilize the Jason reference mission (e.g., Nerem et al., 2018; WCRP-Global-Sea-Level-Budget-Group, 2018; Horwath et al., 2022). However, the Jason nominal orbit is limited to covering only ±66° latitude, which excludes large parts of the Arctic and Antarctic oceans. This is also reflected in the reconstructed total sea level compared to tide gauge data (Fig. 7.5).

Previously, Rietbroek et al. (2016), Kusche et al. (2016) and Uebbing et al. (2019) also considered information from the interleaved mission phase of Jason-1. This affected the derived sea level budget during overlap times due to multiple altimetry sea level observations for the same time period, resulting in a kind of average estimate. In principle, this is not undesired as the additional observations can reduce impacts of errors and, generally, aid the estimation. Consequently, this section will investigate including additional altimetry missions and mission phases in order to improve the spatio-temporal coverage.

Adding Envisat and SARAL/Altika measurements for better high latitude coverage

In a first step, the Jason altimetry data is augmented by additional observations from Envisat and SARAL/Altika (IS021, Tab. 7.15). Both missions flew on the same orbit (Fig. 3.2) and cover most of the main investigation period, except for two years between 2011 and 2013 (Fig. 3.1). The extended mission from Envisat is excluded for now, as it operated on a different orbit. Since this also adds additional observation points for evaluation, the results from IS021 are investigated at three different sets of orbit positions: (a) only Jason nominal mission orbits as for all other inversions introduced so far (IS001-IS020), (b) at the Jason, Envisat and Saral/Altika positions but limited to ±66° latitude and (c) at all available and valid Jason, Envisat and Saral/Altika positions including the Arctic and Antarctic oceans (Tab. 7.16).

From the results (Tab. 7.16), it is obvious that not only the addition of Envisat and Saral/Altika data influences the results, but also the choice of evaluation points. Selecting only the Jason nominal orbit positions for deriving the sea level budget leads to a good agreement in total sea level with the Jason-only reference solution (IS002). However, the mass estimate is found significantly larger at 2.16 mm/yr, while the steric sea level is found smaller at 1.24 mm/yr. The mass increase is mainly driven by a doubling of the hydrological contribution, whereas the IMV component becomes slightly smaller. Similarly the steric sea level in the upper 700 m also becomes smaller, while the deep ocean steric contribution is found to be slightly larger compared to the reference. Budget closure is found to be quite good at a level of 0.04 mm/yr, which, on the first look, would indicate a better sea level budget solution of IS021 (a) compared to IS002. However, a closer look at the corresponding time series (IS021 (a), Fig. 7.24) reveals that this is rather a coincidence as there is first a strong increase in residual that is followed by a sudden drop after no more Envisat data is available in 2010. By coincidence this leads to a very small budget closure

estimate for the selected period.

When considering all points, the difference between solutions IS021 (b) and (c) (Tab. 7.16), i.e. additionally limiting the set of points to the Jason-covered area (±66° latitude), is negligible. Therefore, in the following this limitation is ignored. When comparing the evaluation at only the Jason positions (IS021 (a)) with those, where the budget is derived at all utilized altimetry mission locations for the solution (IS021 (c)), the budget is affected significantly. The total sea level is found at a larger level (3.64 mm/yr). The separation into mass and steric changes reveals larger OMC driven by terrestrial hydrology, which doubles compared to the Jason-based reference solution. The melting contributions remain relatively stable. The steric sea level change is found about 0.20 mm/yr smaller. The budget closure error has also doubled. From this, it becomes clear that inclusion of additional altimetry data will significantly affect the sea level budget. However, the mix of periods with additional data (Envisat and Saral/Altika) and times where there is only Jason-based results available introduce additional effects, which are clearly visible in figure 7.24. During period of no Envisat or Saral/Altika data the monthly solutions and, consequently, the corresponding residuals match those of the reference solution (IS002), indicated by the black and green curve.

Including all available altimetry missions and phases

In the next step, all altimetry missions and phases (Fig. 3.1), except for ERS-2 and HY-2A, are introduced as input to the inversion method. This ensures that for all considered months at least two missions are available. The resulting solution (IS022) is evaluated at (a) the Jason nominal orbits, (c) at all available positions where the reference latitude ϕ_{ref} for inclination weighting (Eq. (5.2.1)) at all locations is set to the Jason reference and (d) where each evaluation location is weighted with ϕ_{ref} of the corresponding mission. Again, the evaluation at the Jason positions results in a matching total sea level change with the reference solution (IS022 (a), Tab. 7.16), but, the separation into mass and steric component is significantly different to the reference solution. Focusing only on the Jason measurement positions for evaluation shows a severe impact in the residual time series (IS022 (a), Fig. 7.24). The residuals become very noisy and the bias found for the GRACE-FO era raises to more than 2 cm.

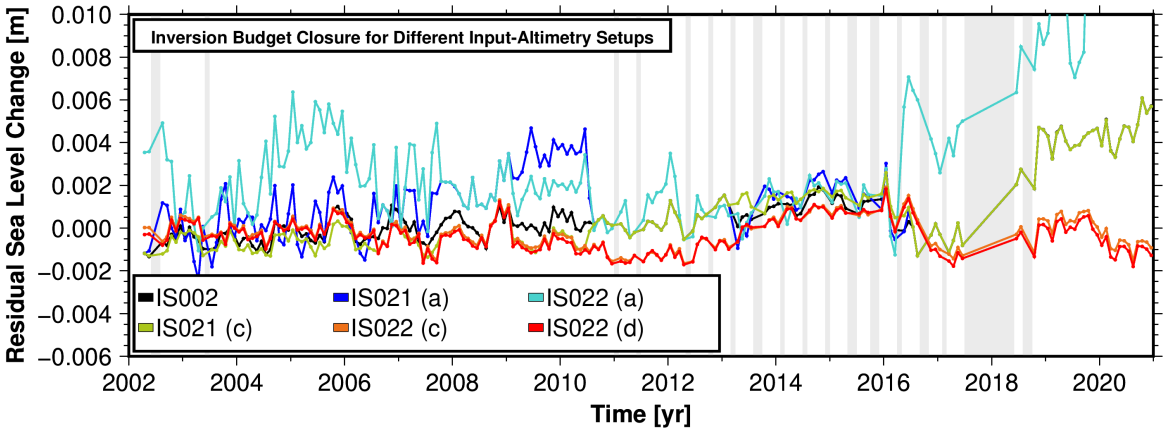


Figure 7.24: Inversion budget closure based on different setups of altimetry input data for the inversion. In addition, the effect from selecting different altimetry positions and corresponding weighting for the budget evaluation is presented.

Evaluating the budget at all locations using inclination weighting with ϕ_{ref} set to the Jason reference inclination or choosing the mission specific ϕ_{ref} has only minor effects on the budget. In addition, the choice of evaluation location seems to predominantly affect the resulting total sea

level and the corresponding residual with altimetry (IS021 and IS022, Tab. 7.16). Consequently, individual budget components can be compared and assessed with respect to the reference solution (IS002). OMC is found 0.81 mm/yr larger compared to the Jason only based solution. While the melting contributions from the Greenland and Antarctic ice sheets are found in close agreement with the reference solution, the glacier contribution from IS022 is found to be 0.75 mm/yr, larger than the reference but closer to published estimates by WCRP-Global-Sea-Level-Budget-Group (2018) or Horwath et al. (2022) (cf. Sect. 7.2.5). The latter is likely related to the additionally available altimetry data at the high latitude glacier regions. Furthermore, the hydrology component is found at 1.10 mm/yr, which is five times the contribution found for the reference solution. This is to some extent compensated by the IMV, which are found at −0.36 mm/yr. The IMV contribution is supposed to be zero on global scales, consequently, the relatively strong negative IMV contribution might indicate some compensation effects with hydrology or steric sea level based on the correlation matrix (Figs. 6.11 and 6.12). In principle, the glacier regions from the glaciers component are removed, i.e. set to zero, in the hydrological data. However, it is possible that other remaining glacier regions, especially in high latitude areas, remain in the hydrology data and translate into the corresponding fingerprints and are then impacted by the additional high latitude altimetry missions. Similarly, sea ice affected measurements should be removed from the altimetry data; here done by utilizing the standard flags in the RADS data. In case some of those observations are still included, they will affect the resulting total estimate and consequently, the separation into mass and steric components.

Another explanation for the significant trend changes with respect to the reference solution could be related to the spatial sampling of the individual altimetry missions. While the Jason only solution (IS002) is based on a relatively homogeneous spatial and temporal sampling, the combination with the other missions introduces different sampling locations. These are not necessarily sampled all at least once during each month since, e.g. the Envisat mission flies on a 35 d repeat orbit, exceeding one month. The steric contribution is found about one third lower compared to the reference solution. This could be connected to the added sampling of the high latitude oceans, containing more cold waters in the upper 700 m, which will reduce the steric component driven by ocean warming in the low latitudes. However, the same sampling issues apply as before.

When evaluating the budget at all utilized and available altimetry measurement locations for each month (IS022 (d), Tab. 7.16), the budget closure improves significantly to 0.04 mm/yr. At the same time, the bias for the GRACE-FO era is basically gone. This indicates that the bias is mainly resulting from the Jason-3 data or, at least, connected to the measurement locations of Jason-3. However, a comparison of the differences in measurement locations between Jason-2 and Jason-3 during their tandem phase revealed no significant differences compared to the measurement locations of Jason-1 and Jason-2. The residuals (IS022 (d), Fig. 7.24) still show some impacts based on the available altimetry missions, but this is expected to some extent. Especially the IMB are not constant in reality and while quite some effort has been undertaken to remove these, residual IMB effect still remain. Nevertheless, the bias seems to be reduced, which in turn strengthens the faith in the quality of the solution including all available altimetry data.

In order to further evaluate the total sea level reconstructed from the inversion, improvement at each tide gauge location relative to the reference solution is investigated in figure 7.25. The results show correlation improvements at most tide gauge locations, where the high latitude gauges in the Arctic improve the most. At other locations, correlation closest to the tide gauge stays more or less the same, but increases at more distant grid points. The largest decrease of correlation is found at the Tenerife and Kerguelen tide gauges where it drops by about 10%. Overall, the reconstructed total sea level when including all available altimetry missions is improved relative to the reference solution, especially at high latitudes.

In summary, the addition of additional altimetry data leads to a significantly changed sea level

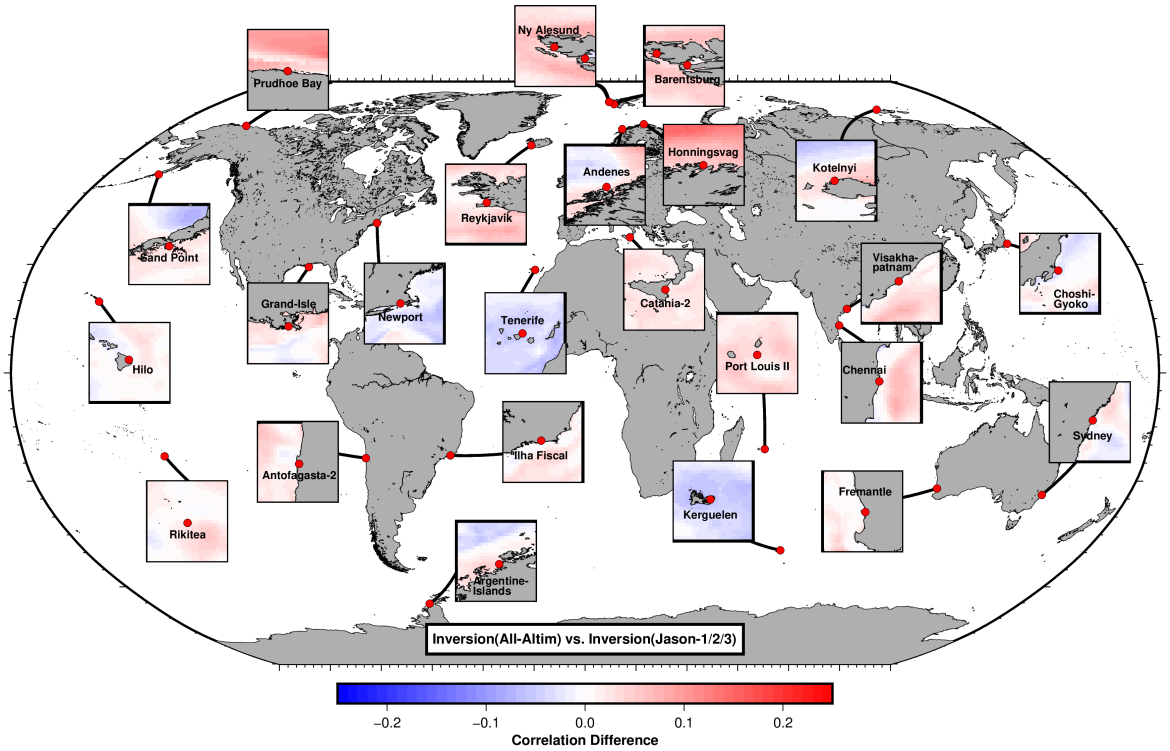


Figure 7.25: Correlation improvement at selected tide gauges of inversion including all available altimetry data (IS022, Tab. 7.15) relative to the base inversion (IS002, Tab. 7.12). Red colors indicate better agreement with tide gauge data while blue represents a reduced correspondence.

budget compared to the reference solution. It has to be noted that the evaluation of the results should be done on all available altimetry mission points in order to reconstruct the correct total sea level and avoid sampling effects in the residuals. However, the retrieved hydrological component seems extremely large, which is somewhat compensated by the IMV in combination with the steric sea level. Again, this shows that the PCA based components are highly variable. Consequently, these need to be further constrained, e.g., by including additional steric observation data from in-situ temperature and salinity profiles (Sect. 7.4.4).

7.4.4 Introducing in-situ Steric Observations from easyCORA

It is investigated whether introducing in-situ steric profile data as additional observable into the inversion will support the separation of mass and steric sea level contributions. Since the majority of profile data is observed in the upper 1000 m of the ocean, only data for the upper 700 m steric sea level contribution is introduced. For this, the data are processed and modeled as described in sections 6.2.1 and 6.2.2. In order to limit other potential influences the profile data are combined with GRACE/GRACE-FO and Jason-only altimetry data.

The resulting inversions (IS023 and IS024, Tab. 7.15) deviate slightly from the corresponding base solutions (IS001 and IS002, Tab. 7.12). Without applying VCE (IS023, Tab. 7.16), the OMC component is found slightly larger (2.02 mm/yr) driven by terrestrial hydrology related sea level change. Steric sea level is found slightly smaller at 1.25 mm/yr. This is somewhat expected since the comparisons in section 7.2.8 showed that the profile data driven estimates were generally found to provide smaller steric sea level rates relative to the other approaches. Budget closure is found slightly worse compared to IS001.

When enabling VCE the estimates (IS024, Tab. 7.16) are relatively close to the reference solu-

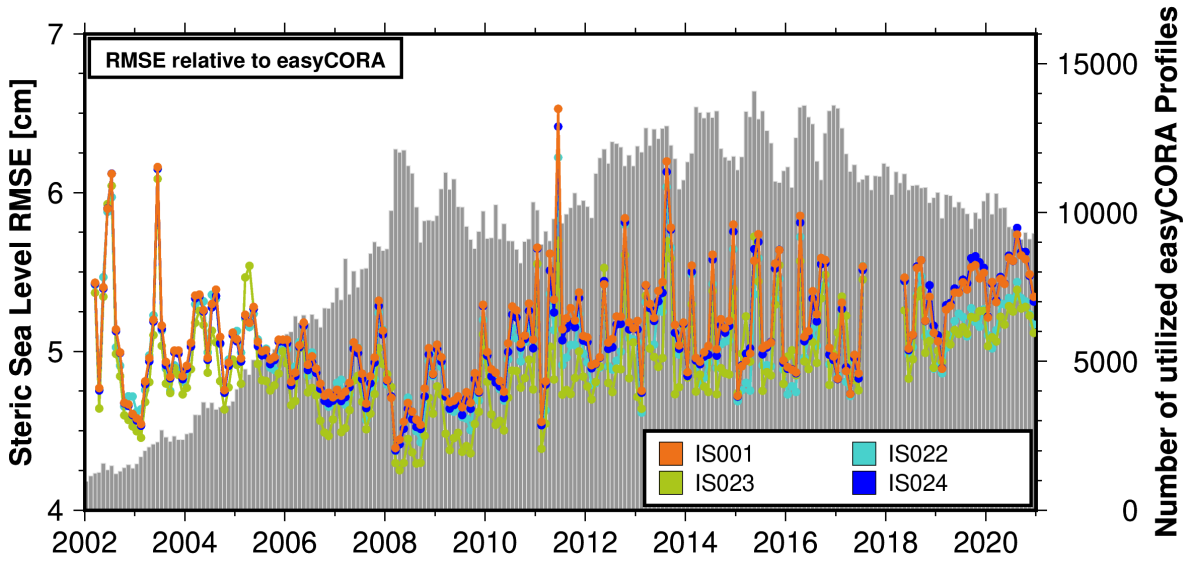


Figure 7.26: Improvement of monthly RMSE relative to the easyCORA time series from including in-situ steric profile observations in the inversion.

tion (IS002). The VCE down-weights the modeled steric profile data error by a factor of about 10 to 35. Consequently, the altimetry data exerts a relatively larger influence on the final parameter estimates compared to the profile data. This is driven by the shear number of several hundred thousand altimetry observations in contrast to a few thousand profile observation for each month. Therefore with VCE enabled, the additional profile data has little to no effect on the budget. Including profile buoy data in the inversion leads to a lower RMSE with the easyCORA, especially when disabling the VCE (IS023, Fig. 7.26). In addition, besides a lower overall budget closure error, including all altimetry missions (IS022, Tab. 7.15) also reduces the residual with the in-situ steric profile observations.

Based on the configuration experiments, IS018 and IS019, the next logical step would be to utilize the temperature and salinity observations converted to thermo- and halo-steric sea level, respectively, in order to further separate the steric contribution in the upper 700 m. Here, this is investigated by computing thermo- and halosteric fingerprints for the upper 700 m from corresponding ORAS5 model output utilizing equation (2.3.11). The corresponding inversion runs with VCE disabled (IS025) and enabled (IS026) are presented in table 7.17.

Table 7.17: Effect from further splitting the upper 700 m steric sea level change into thermo- and halo-steric components including in-situ steric profile data from easyCORA. All values are global mean sea level trends in mm/yr for the period 2005-01 till 2015-12. The result can be compared to the reference solution (IS002, Tab. 7.13).

Inversion ID	Total	Mass	Steric	Steric > 700 m	Thermo-Steric > 700 m	Halo-Steric > 700 m	Steric < 700 m	Ocean Dynamics
IS025	3.45	2.17	1.06	0.14	0.32	−0.18	0.92	0.22
IS026	3.44	2.09	1.18	0.76	0.70	0.05	0.41	0.17

When disabling the VCE, the resulting separation into mass and steric (IS025, Tab.7.17) looks relatively good on first glance, with a slightly increased mass component compared to the reference solution (IS001). However, a closer look at the steric component reveals that most signal is now concentrated in the ocean below 700 m while the upper 700 m ocean is actually found to be very small (0.14 mm/yr) resulting from a small thermo-steric component (0.32 mm/yr) in combination with a relatively large negative halo-steric contribution (−0.18 mm/yr). When enabling the VCE, the resulting budget is more similar to the one from IS018, although, with an, again, smaller upper 700 m steric contribution (0.70 mm/yr, IS026, Tab. 7.17).

The bad performance of the inversion, with the easyCORA input data additionally split into a thermo- and halo-steric contribution, is related to the modeling of both. In fact, the thermo- and halo-steric sea level change are highly correlated due to the non-linear co-dependence on each other for converting to steric sea level, e.g., evident from equation (2.3.9) (cf. Sect. 2.3.1). While the combined (thermo+halo) steric sea level can be easily introduced as an additional observable, utilization of thermo- and halo-steric sea level individually requires further investigation. This includes, at least, modeling of the correlations between the two datasets.

Overall, the inclusion of in-situ profile steric sea level observations from the upper 700 m of the ocean has been found to be beneficial for separating the altimetry observed total sea level into mass and steric contributions. Basically, this adds another constraint to the sea level budget, which limits the non-steric signal that the steric component might absorb. However, further investigation is required regarding weighting of the in-situ profile data with respect to the altimetry observations.

7.4.5 Closing the GRACE/GRACE-FO Gap using Swarm and SLR

Towards the end of it's lifetime, the GRACE mission struggled with several problems impacting data quality (Sect. 3.2.1). This lead to months with degraded data quality, which is why the main investigation time period in this thesis is limited to data up until 2015-12. Furthermore, the about one year long data gap between the GRACE and GRACE-FO missions resulted in no high resolution gravity information being available, thus severely limiting the ability to derive meaningful global and, especially, regional sea level budgets.

With the current base configuration of the inversion (Sect. 6.2), only those months where GRACE and GRACE-FO data is available are processed, despite other datasets from altimetry, SLR or steric in-situ profiles being available. Generally, the idea would be to simply augment GRACE/GRACE-FO data with those from SLR and Swarm, in order to provide inversion results for the missing months as well as the gap between the GRACE missions. However as Lück (2022) has shown, the resulting budget for these months are not entirely meaningful (IS031, Tab. 7.16) due to the lower spatial resolution of SLR and Swarm. For effectively utilizing the SLR and Swarm data, it is, thus, necessary to drastically reduce the number of fingerprints to avoid overfitting, which is clearly happening without the high resolution constraint from the GRACE/GRACE-FO data (Fig. 7.27, B)

Nonetheless, the time series for the total and mass components look rather good (Fig. 7.27, A), since SLR and Swarm are, both, able to retrieve global mean OMC well and even provide decent results for the ice sheets and individual hydrological basins (Löcher and Kusche, 2020; Lück, 2022). This is also confirmed when comparing the corresponding estimates in table C.1 for the whole GRACE/GRACE-FO time period. The steric component seems to be retrieved well (Fig. 7.27, C) and the residuals are not severely affected (Fig. 7.27, D). Consequently, the number of fingerprints needs to be reduced by combining individual mass basins since those can not be separated based on the reduced resolution. In Lück (2022), new fingerprints have been created from a GRACE based inversion run where the mean, trend and seasonal signals were extracted at each grid point of the ice mass change results. These have been combined with a reduced number of PCA based EOF-fingerprints. It has been found that combining mean and trend patterns for the melting of

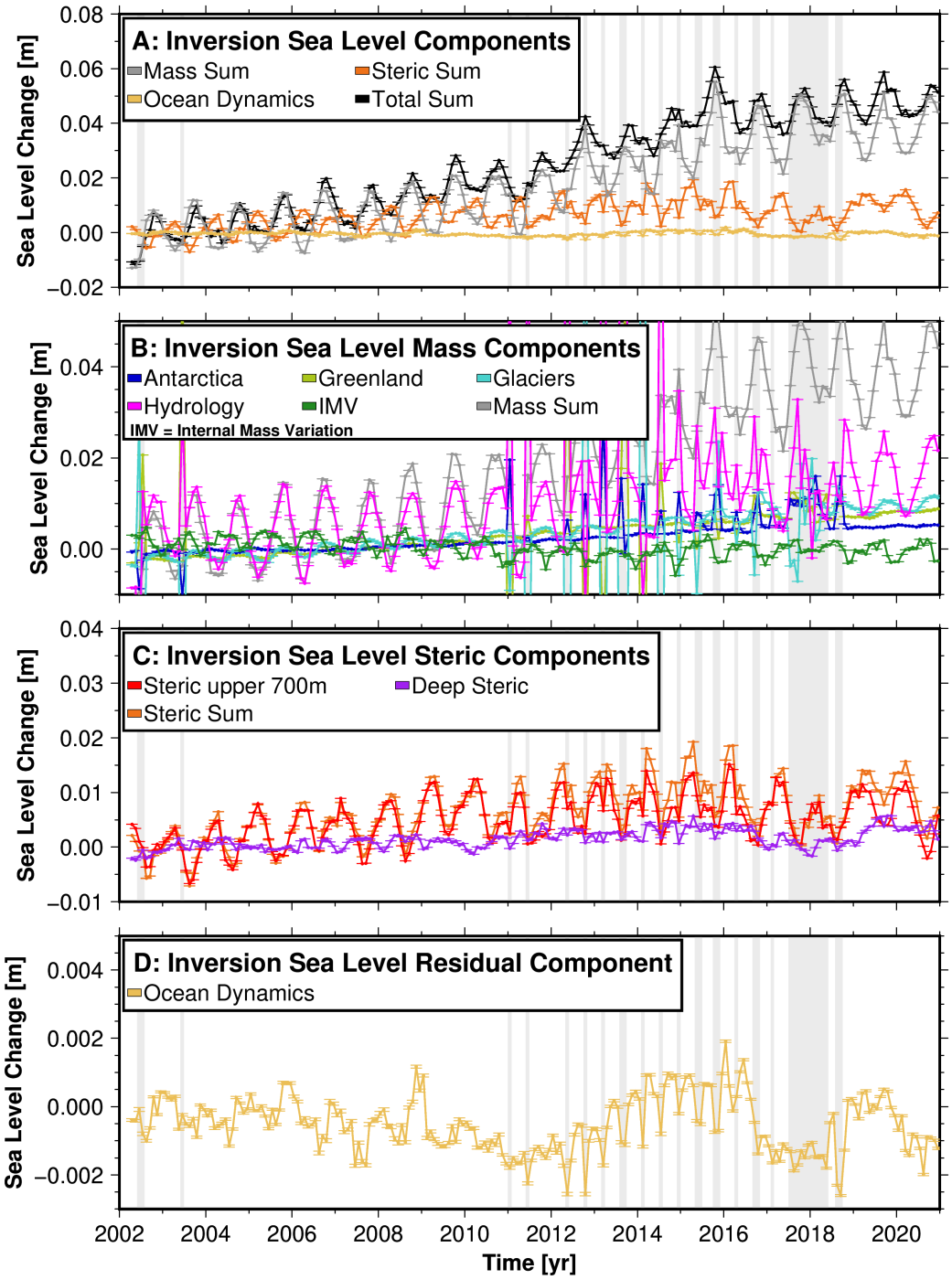


Figure 7.27: Global mean sea level budget time series for inversion IS031 (Tab. 7.15) including SLR and Swarm data to fill missing GRACE months and close the GRACE/GRACE-FO gap. Similar to figure 7.2 for IS001.

the land glaciers as well as the Greenland and Antarctic ice sheets, each, with 10 EOF-based fingerprints enabled a reconstruction of corresponding trends, which were close to the GRACE based solution and also contained the missing months.

However, this approach had some weaknesses, namely, since the mean and trend patterns have been computed from the reference inversion, the result is expected to be close, especially during the GRACE era. In addition, it would make sense to also introduce corresponding patterns for the hydrology, steric, and IMV component in order to further stabilize the Swarm based solution. In the end, these reduced or constrained solutions can only be evaluated on global scales as the regional

behavior is basically pre-defined by the fingerprints. This does not allow for regional flexibility as is the case with the base inversion (Sect. 6.2). A deeper analysis requires further changes to the inversion setup, which is out of the scope of this thesis. However, it is worth to further investigate especially SLR based inversion solutions in the future, as this also allows for an extension backwards in time until the early 1990s.

7.4.6 Combining All Available Input Data

Considering the results from the sections above, it makes sense to derive an inversion containing all available and meaningful datasets in order to utilize all possible observational information. IS030 (Tab. 7.15) basically combines inversion runs IS022, IS024 and the SLR data also employed in IS031 (Tab. 7.15). Swarm data has been excluded in this case as it is more noisy and will be down-weighted by the VCE. In contrast to IS001, which is only based on a combination of GRACE/GRACE-FO and Jason-altimetry data, weighting the input datasets with VCE is necessary for a well-balanced result. Otherwise, noise effects in particular datasets in one month would distort the budget.

The resulting budget of IS030 is close to the one from IS022 with a slightly reduced mass component compensated by an increased steric sea level contribution. This solution will be the basis for investigating regional sea level budgets in section 7.5. In principle, the Jason altimetry spatial resolution is fine for global approaches and looking at large ocean basins, e.g., the Pacific Ocean. However, for smaller regions additional information benefits the budget estimation and avoids sparse data coverage of regions by only a few Jason tracks. While in-situ steric profile data coverage is not optimal in many regions (Fig. 3.7), it is really good in some regions and may still aid the budget estimation in sparsely covered regions.

7.5 Regional Sea Level Budgets

Regional sea level budgets describe the budget for a limited area of the ocean and are essentially a subset from the global inversion results. In this section, inversion IS030 (Tab. 7.15) is the basis for all regional budgets, since it includes all altimetry missions as well as additional gravity information from SLR and in-situ easyCORA steric profiles. For deriving regional budgets, a high data coverage is essential, such as all altimetry missions in contrast to utilizing Jason only. Consequently, the usage of IS030 represents the best inversion data basis available in this thesis.

First, the major ocean basins of the Pacific, Atlantic, Indian and Arctic ocean are examined (Sect. 7.5.1), followed by sea level budgets for selected smaller regions (Sect. 7.5.2), which are driven by different mass and steric contributions.

7.5.1 Major Ocean Basins

This section partitions the total ocean area into the sub-basins of the Pacific, Atlantic, Indian and Arctic Ocean and examines the budget in each of these. The results are based on IS030 (Tab. 7.15) and presented in figure 7.28 and table 7.18. In sum the basins considered in this section cover almost the total ocean surface except for the Mediterranean Sea, the Baltic sea and the shallow ocean region between Australia and Asia.

Pacific Ocean

The Pacific Ocean sea level is mainly driven by OMC explaining about 80% of the sea level change with steric, consequently, accounting for the remaining 20% (Tab. 7.18). Budget closure is found to be 0.07 mm/yr, which is in line with the global closure error. Here, the GIA contribution to sea level change starts to become relevant, showing a slightly negative contribution of -0.07 mm/yr,

Table 7.18: Regional sea level budgets based on inversion IS030 (Tab. 7.15). All values are global mean sea level trends in mm/yr for the period 2005-01 till 2015-12.

Basin	Total	Mass	Steric	Greenland	Antarctica	Glaciers	Hydrology	IMV	Steric > 700 m	Steric < 700 m	Ocean Dynamics	GIA
	Major ocean basins											
Pacific Ocean	3.56	2.80	0.69	0.86	0.37	0.76	1.10	−0.22	0.37	0.31	0.07	−0.07
Atlantic Ocean	3.48	2.32	1.20	0.62	0.47	0.73	0.95	−0.55	0.37	0.83	−0.03	0.10
Indian Ocean	4.49	2.49	1.90	0.81	0.51	0.82	1.07	−0.76	1.80	0.10	0.10	0.04
Arctic Ocean	5.76	5.74	0.21	−0.71	0.44	0.11	0.79	5.00	−0.20	0.40	−0.19	0.11
	Selected regions of interest											
North Sea	3.39	4.20	−0.31	−0.05	0.40	0.44	0.96	2.42	−0.24	−0.07	−0.49	0.03
Baltic Sea	4.41	3.37	0.28	0.13	0.37	0.45	0.80	4.15	0.37	−0.09	0.75	−2.53
Bay of Bengal	6.43	2.32	4.11	0.83	0.44	0.68	0.78	−0.34	3.68	0.44	0.00	−0.06
Mediterranean	4.90	5.64	−0.71	0.48	0.37	0.62	0.83	3.14	−0.15	−0.57	−0.02	0.20
East China Sea	3.65	4.84	−1.31	0.90	0.45	0.71	0.77	2.13	−1.11	−0.20	0.12	−0.13

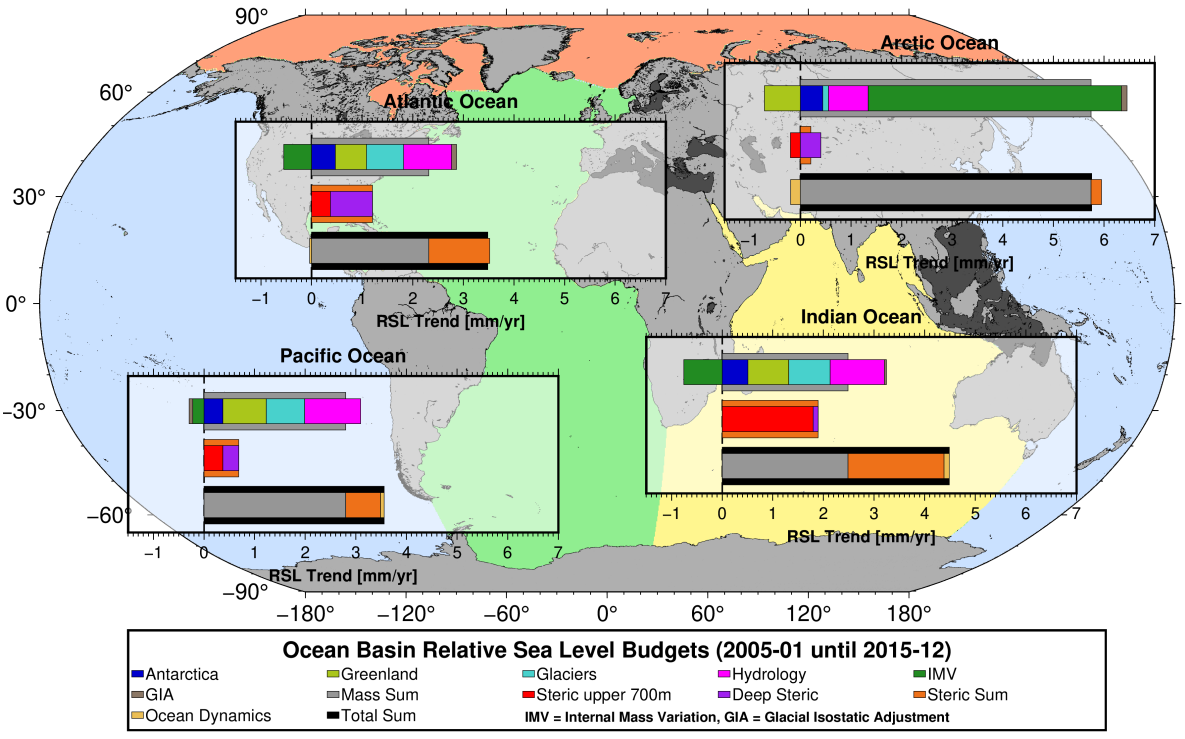


Figure 7.28: Sea level budgets for the Pacific, Atlantic, Indian and Arctic Oceans.

which is basically directly derived form the A et al. (2013) model (Tab. 6.2). The Greenland driven sea level change is found larger compared to the global average, while the Antarctic contribution is slightly smaller compared to the global result (IS030, Tab. 7.16). Hydrology and land glacier melt contribute roughly the same as for the global average.

Atlantic Ocean

For the Atlantic Ocean, total sea level rise is found to be smallest at only 3.48 mm/yr of all the four major ocean basins considered (Tab. 7.18). The OMC is found at 2.32 mm/yr and steric sea level change at 1.20 mm/yr, explaining two thirds and one third, respectively. The budget closure is found close to zero (−0.03 mm/yr). The contribution by Greenland is found significantly smaller compared to the global average since most of the northern Atlantic is close to the ice sheet, resulting in actual sea level fall due to the loss of mass attraction and uplift of the sea floor (Sects. 6.1.2 and 7.2.3). The GIA contribution to sea level is found at 0.10 mm/yr, again, proving that GIA can not be neglected when deriving regional sea level budgets. While the steric sea level from the upper 700 m is found very similar to the Pacific Ocean at 0.37 mm/yr, the deep ocean steric contribution is found significantly stronger in the Atlantic (0.83 mm/yr), more than double the value of the Pacific. This indicates significant deep ocean warming, which has been found to be in part attributed to anthropogenic influence on the climate (Messias and Mercier, 2022).

Indian Ocean

Indian Ocean sea level rise is found to be significantly above the global average (4.49 mm/yr). Here, OMC account for only about 55% of the change, while steric sea level accounts for the rest. The GIA contribution is found close to zero. In contrast to the Atlantic ocean, steric sea level change in the Indian ocean is clearly dominated by warming in the upper 700 m (1.80 mm/yr) explaining 95% of the steric change. In addition, IMV related sea level is found negative at −0.76 mm/yr indicating transport of water masses to other ocean basins. This has been attributed to a see-saw effect (Chambers and Willis, 2009; Wouters et al., 2014) observed by the GRACE mission in the past. But, newer studies suggest a relation between hydrological and atmospheric related water exchange predominantly in the Atlantic and Indian oceans (García-García et al., 2020).

Arctic Ocean

The Arctic ocean basin in this thesis, basically, represents the rest, which is neither covered by the Atlantic or Pacific ocean basins (Fig. 7.28). Due to the relatively bad data coverage despite the inclusion of high latitude altimetry, the resulting sea level budget (Tab. 7.18) has to be interpreted with care (see also Henry et al., 2012; Ludwigsen and Andersen, 2021), since the evaluation points are also limited to the available inversion input altimetry observation points (Morison et al., 2022). The total sea level is found quite large at 5.76 mm/yr, the majority of, which is explained by OMC. Only a small steric sea level contribution (0.21 mm/yr) is found. This could be driven by halo-steric effects, which have been found to dominate especially in the Canadian Arctic (Lyu et al., 2022). In contrast to the other ocean basins, the budget closure error is also found to be significantly larger and negative (−0.19 mm/yr) indicating potentially unmodeled effects.

7.5.2 Selected Regions of Interest

After examining the major ocean basins, further sea level budgets are extracted from IS030 for selected regions of interest. These basins are dominated by different sea level drivers in addition to local phenomena. The individual regions are limited as defined and provided by International Hydrographic Organization[4].

[4] https://www.marineregions.org (last accessed: 03.07.2022)

North Sea

The North Sea (Fig. 7.29, A) is a rather shallow ocean basin with only a few evaluation points providing steric information below 700 m. Consequently, the total sea level change of 3.39 mm/yr mostly contains OMC (4.20 mm/yr) with a small negative steric change (−0.31 mm/yr). The latter is mostly due to the upper 700 m of the water column (−0.24 mm/yr) and related to the cooling period in the north Atlantic (Chafik et al., 2019). Greenland ice melt has only a small influence on sea level in the North Sea due to the vicinity of Greenland leading to an almost zero RSL effect (Fig. 7.10). About 60% of OMC results from IMV transporting water into the North Sea region. This transport results from sea level changes around the Canary Islands and propagates northward along the continental shelf (Dangendorf et al., 2014). A budget closure of −0.49 mm/yr is found for the North Sea indicating unmodeled residual effects, which are likely related to atmospheric wind forcing (Dangendorf et al., 2014). Sea level change due to atmospheric influence is not explicitly modeled in the inversion and, thus, expected to show up in the residual component.

Baltic Sea

In the Baltic Sea (Fig. 7.29, B), total sea level change of 4.41 mm/yr is driven by OMC. The latter contains large contributions (4.15 mm/yr) from the IMV component indicating mass transport into the Baltic basin. In fact, it has been found that about 75% of the mass change in the Baltic Sea is driven by transports from the adjacent North Sea (Gräwe et al., 2019). Together with the ice-melt and hydrology components, this would amount to a mass related RSL of 5.90 mm/yr, which is compensated by GIA causing −2.53 mm/yr of sea level change. The impact of GIA exhibits a north-south gradient where the northern parts of the Baltic are significantly more impacted compared to the southern part (Weisse et al., 2021). Results from this basin stress the importance of considering GIA for regional sea level budgets. Similar to the North Sea, the Baltic is a shallow ocean and, consequently, steric sea level change is mostly limited to the upper 700 m of the water column. The budget closure is at the level of 0.75 mm/yr indicating significant remaining signals that are not associated with any of the inversion components. Due to the relevance of GIA related sea level in this basin, the choice of GIA model applied during the inversion processing plays a crucial role and any errors in the utilized GIA model will theoretically translate into the residuals.

Bay of Bengal

In contrast to the North Sea, sea level change in the Bay of Bengal (Fig. 7.29, C) is dominated by (thermo-)steric variations. The total sea level of 6.43 mm/yr is found at about double the level of GMSL rise. OMC (2.32 mm/yr) accounts for about 35% of that change. 4.11 mm/yr are due to steric sea level rise, where the majority (3.68 mm/yr) is due warming in the upper 700 m, with the deep ocean contribution at roughly the same level as the global average (0.44 mm/yr). Steric sea level change in the Bay of Bengal is driven in part by transport of water from the equatorial Indian ocean in the form of semi-annual alternating upwelling (Jan-Mar and Aug-Sep) and downwelling (Apr-Jul and Oct-Dec) Kelvin waves excited by the IOD and ENSO events, which then propagate northward into the Bay (Sreenivas et al., 2012; Kusche et al., 2016). The budget closure error is found to be zero for the chosen time period, theoretically indicating a perfectly closed budget. This is in part due to the good data coverage of that region from all considered input data products. Besides good coverage by altimetry, the in-situ steric profile data availability is quite good (Fig. 3.7) and the inversion is able to filter the GRACE artifacts caused by the 2004 Sumatra-Andaman earthquake in the region (Han et al., 2006).

The same region has also been investigated in Kusche et al. (2016) utilizing an earlier inversion similar to Rietbroek et al. (2016). The budget by Kusche et al. (2016) reports a closure error of 1.29 mm/yr for the period 2002-04 till 2014-06, whereas this inversion provides closure at about one third of that value (0.42 mm/yr). Similarly, the budget is dominated by steric effects (3.08 mm/yr),

which is in line with the value found from this thesis' inversion (3.16 mm/yr). Differentiation into shallow and deep steric effects has not been possible for the Kusche et al. (2016) inversion. Furthermore, no IMV component has been considered, explaining in part the increased budget closure error. The total sea level values are not comparable since the Kusche et al. (2016) utilized a AOD1B-GAC corrected altimetry input similar to Rietbroek et al. (2016).

Mediterranean Sea

Total sea level change of 4.90 mm/yr in the Mediterranean Sea (Fig. 7.29, D) can be decomposed into an OMC component of 5.64 mm/yr and steric change of −0.71 mm/yr with a budget closure error of −0.02 mm/yr. The OMC is dominated by a rather large IMV component, which is due to the net water inflow from the Black Sea and the Atlantic Ocean (Fenoglio-Marc et al., 2006). Negative steric sea level change has also been reported by Fenoglio-Marc et al. (2012), which has been found to be largely originating from the Ionian Sea (Carillo et al., 2012). About 80% of the steric sea level change is driven by the deep ocean below 700 m resulting from deep-water cooling due to less mixing with warm surface water, where the latter also becomes more saline due to excess evaporation (Carillo et al., 2012; Legeais et al., 2018; Margirier et al., 2020).

The OMC estimate is roughly in agreement with Fenoglio-Marc et al. (2012) who provide a range of 2.8 to 19.2 mm/yr. GIA contributes with 0.20 mm/yr, again, proving that this is a non-negligible component of regional sea level budgets. Similar to the Bay of Bengal, the inversion budget is closed well for the Mediterranean Sea during the reference time period (−0.02 mm/yr), also resulting from quite good data coverage with Argo buoys providing regular measurements in this region (Fig. 3.7).

East China Sea

The East China Sea (Fig. 7.29, E) is a mostly shallow ocean region with depths of less than 200 m and a small swath in the East with depths up to 2000 m. The total sea level change of 3.65 mm/yr is dominated by a mass component (4.84 mm/yr) in combination with negative steric sea level change (−1.31 mm/yr), 85% of which are from the shallow ocean region. A large portion of the detected OMC is attributed to the IMV component (2.13 mm/yr) indicating transport of masses within the ocean due to the Kuroshio current located right outside the eastern boundary of the region. Parts of this transports are also linked to sediment transport (Chang et al., 2019), which are neither explicitly modeled in the AOD1B background model, which serves as a basis for the IMV fingerprints, nor in the inversion method. Consequently, sediment movement will also affect the residual component and regional budget closure (0.12 mm/yr).

7.6 Additional Inversion Output

Besides the sea level budget, the inversion results can also be utilized and further processed for other applications. It is possible to extract gravity coefficients from combining all mass components. In this context, the low degree ones, which are commonly replaced during the direct processing of GRACE/GRACE-FO data, are of interest. In addition, the inversion-updated steric scaling factors can be used to infer variations in global ocean heat content and, thus, EEI.

7.6.1 Low Degree Gravity Coefficients

The mass fingerprints within the inversion framework are generally expressed in spherical harmonics including degree-1, which correspond to the geocenter motion. This refers to the shift between the CM frame of the GRACE/GRACE-FO observations and the CF frame of the altimetry measurements. The GRACE/GRACE-FO mission is insensitive to changes of the Earth's center of mass, effectively only fitting to degrees 2 and above. However, the altimetry measurements are performed and provided in the CF frame and, since the set of fingerprints for both observation

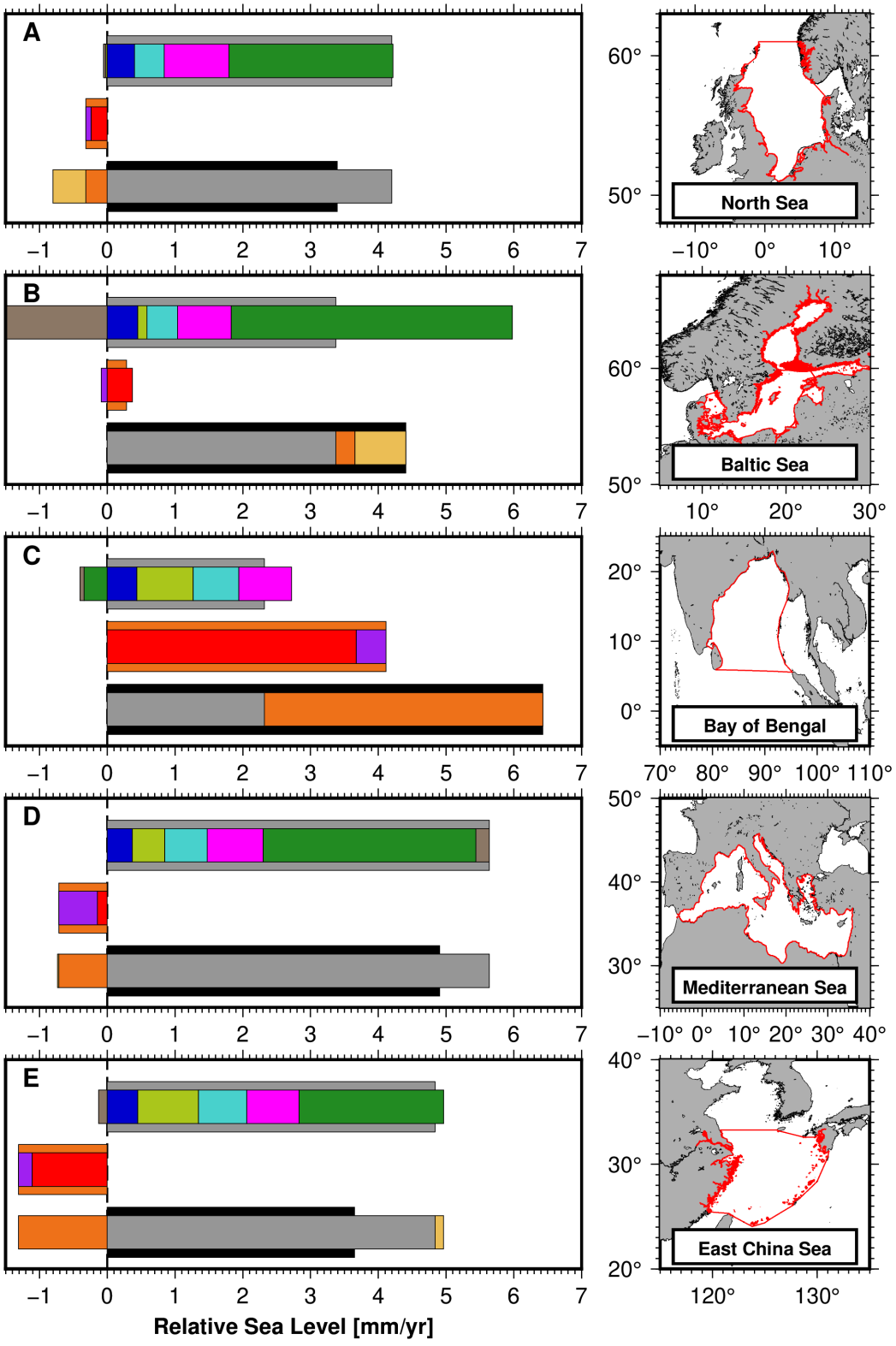


Figure 7.29: Regional relative sea level budgets for selected basins. A: North Sea, B: Baltic Sea, C: Bay of Bengal, D: Mediterranean Sea and E: East China Sea.

types is the same, the geocenter motion is accounted for by the individual fingerprints degree-1 coefficients. Therefore, it is possible to extract the geocenter motion from the inversion results and compare it to other published estimates (Fig. 7.30) or utilize it for consistently processing OMC directly from the gravity spherical harmonics (Sect. 5.3). Similarly, the c_{20} and c_{30} are commonly replaced for directly processing gravity field spherical harmonic data (see Fig. 7.31, Sect. 5.3 and Loomis et al., 2020).

Degree-1: Geocenter Motion

In order to extract geocenter motion from the inversion results, individual degree-1 coefficients, c_{10}, c_{11}, and c_{1-1}, from each fingerprint are scaled with the corresponding estimated factors for each month. These are then summed and converted to geocenter motion in meters based on equation (2.4.23). Similarly geocenter information in Cartesian coordinates based on SLR data (Sect. 3.2.1 and Sect. 3.2.2), which is commonly used for substitution during GRACE processing, is utilized for comparison. For consistency, all investigated geocenter motion estimates in this thesis are relative to the AOD1B background model employed during gravity processing and, thus, do no represent the full geocenter motion effect.

The comparison in figure 7.30 shows that the geocenter motion based purely on SLR is significantly noisier than other estimates (grey and light-blue lines). The additional disagreement between these two SLR solutions is likely due to differences in processing linked to varying arc lengths and force modeling. The variations in X- and Y-direction are smaller compared to the Z-direction. Generally, the inversion results agree well with the independently derived RL05 TN-11 and RL06 TN-13 geocenter estimates, which are commonly substituted when processing gravity data. Before 2005, a visible difference is found between the Y-component from the inversion and from the RL05 TN-11 and RL06 TN-13 data. Similarly the RL05 TN-11 solution differs significantly from the inversion and RL06 TN-13 solution after 2014 for the Z-component. The impact on OMC from selecting the individual solutions has been presented in table 5.3. When introducing additional SLR data in the inversion and solving for the available GRACE month, the impact from the SLR data is small. The combination of all degrees and orders of the spherical harmonic coefficients forms the corresponding fingerprint and, consequently, all are scaled with the same associated scaling factor. This leads to a certain dominance of the GRACE/GRACE-FO data by fitting to the higher degrees, which in turn also limits the potential impact from SLR data with a maximum degree of 5.

From these results in combination with the impacts presented in table 5.3, it is obvious, that for a consistent comparison of OMC from the inversion with independently derived estimates, it is necessary to utilize the correct degree-1 substitutes; as applied to the GRACE-OMC, e.g., in figure 7.1. In addition, the inversion allows to further split the geocenter motion into contributions from individual sea level drivers, such as Greenland or Antarctica, by limiting the degree-1 coefficient summation to the corresponding fingerprints (Tab. 7.19).

While seasonal variability in amplitude and phase of geocenter motion is clearly dominated by the hydrology component (Tab. 7.19), the long term trend is driven by the ice-melt from land glaciers and the ice sheets. In X-direction, the Greenland mass loss (-0.11 mm/yr) leads to a significant shift of the Earth's center of mass, explaining about 85% of the total X-shift (Tab. 7.19), since Greenland is located close to the zero meridian. In comparison, the contributions from other mass sources to the X-direction shift are negligible. However, Rietbroek (2014) found a significant positive hydrological influence on the X-shift, which is not confirmed in this work. The long term shift in Y-direction is driven by all contributions with similar magnitude, indicating an eastward shift of the geocenter (Tab. 7.19), in line with Rietbroek (2014). In Z-direction, negative trends are found from Greenland (-0.34 mm/yr), land glaciers (-0.20 mm/yr) and hydrology (-0.07 mm/yr) contributions while Antarctic mass loss (0.16 mm/yr) induces a positive trend

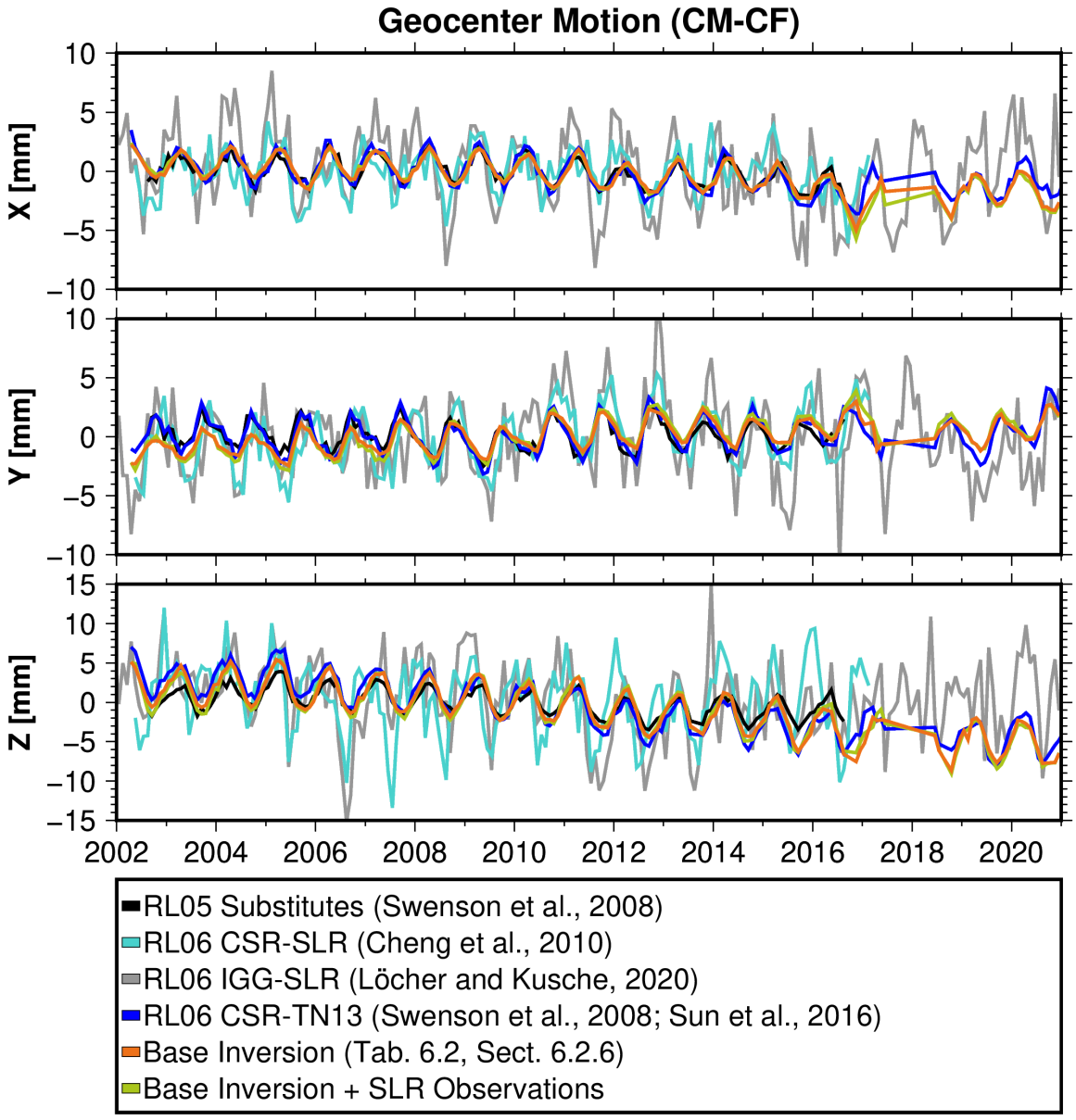


Figure 7.30: Inversion-based geocenter motion compared to other published estimates. The degree-1 coefficients are converted to X-, Y-, and Z-shifts of the Earth's center of mass (CM) relative to the CF frame (Sect. 2.4.1).

(Tab. 7.19). The negative overall shift in Z-direction results from Greenland and most land masses, containing glaciers and hydrological catchments, being located on the Northern hemisphere. These induce a negative Z-shift, while Antarctic mass loss exerts a shift in the opposite direction. When additionally introducing the IGG-SLR observations into the inversion framework, the Y-shift is found even larger while X- and Z-direction roughly stay the same.

From comparing to the other solutions, the seasonal cycle from the SLR-only geocenter shifts is found significantly larger compared to the Swenson et al. (2008), Sun et al. (2016) and inversion method (Fig. 7.30, Tab. 7.19). For the trends, differences are quite significant where the X-direction even switches the sign for the CSR-SLR solution. This solution also attributes almost no trend to the X- and Z-direction but mostly to the Y-direction, contradicting all other solutions, especially in Z-direction. The TN13 (Swenson et al., 2008; Sun et al., 2016) geocenter shift indicates a −0.68 mm/yr trend that is significantly larger compared to other methods especially to the RL05 Swenson et al. (2008) solution, which it is supposed to replace and continue. Addi-

Table 7.19: Trend, annual amplitude and phase (2005-01 till 2015-12) of the geocenter motion from the inversion, compared to external sources. The total geocenter motion from the inversion is further split into contributions from individual contributors to OMC.

Source		**Trend** [mm/yr]	**Amplitude** [mm]	**Phase** [doy]
Greenland:	X	-0.11 ± 0.01	0.061 ± 0.005	112.6 ± 4.5
	Y	0.06 ± 0.01	0.034 ± 0.003	297.0 ± 4.5
	Z	-0.34 ± 0.01	0.172 ± 0.015	111.4 ± 4.8
Antarctica:	X	0.03 ± 0.01	0.008 ± 0.003	178.0 ± 19.0
	Y	0.05 ± 0.01	0.004 ± 0.003	157.7 ± 36.3
	Z	0.16 ± 0.01	0.057 ± 0.012	37.7 ± 12.7
Glaciers:	X	-0.03 ± 0.01	0.051 ± 0.005	165.2 ± 6.0
	Y	0.03 ± 0.01	0.093 ± 0.010	193.0 ± 6.4
	Z	-0.20 ± 0.01	0.540 ± 0.016	114.0 ± 1.7
Hydrology:	X	-0.02 ± 0.02	1.273 ± 0.049	103.2 ± 2.2
	Y	0.02 ± 0.02	1.345 ± 0.056	306.4 ± 2.4
	Z	-0.07 ± 0.02	2.022 ± 0.066	83.7 ± 1.9
Total (Base Inv.):	X	-0.13 ± 0.02	1.361 ± 0.050	105.9 ± 2.1
	Y	0.16 ± 0.02	1.344 ± 0.057	302.3 ± 2.5
	Z	-0.46 ± 0.02	2.700 ± 0.074	90.3 ± 1.6
Total (incl. SLR):	X	-0.14 ± 0.02	1.333 ± 0.054	101.9 ± 2.3
	Y	0.22 ± 0.03	1.472 ± 0.074	303.7 ± 2.9
	Z	-0.44 ± 0.02	2.896 ± 0.077	88.7 ± 1.5
RL05 Substitutes:	X	-0.12 ± 0.02	1.285 ± 0.080	98.3 ± 3.6
	Y	0.00 ± 0.02	1.522 ± 0.089	289.8 ± 3.4
	Z	-0.29 ± 0.02	1.854 ± 0.082	93.0 ± 2.5
RL06 CSR-SLR:	X	0.05 ± 0.05	1.787 ± 0.214	59.1 ± 7.0
	Y	0.19 ± 0.05	2.653 ± 0.201	325.7 ± 4.4
	Z	0.00 ± 0.10	4.593 ± 0.418	19.5 ± 5.3
RL06 IGG-SLR:	X	-0.22 ± 0.07	3.220 ± 0.324	60.5 ± 5.8
	Y	0.04 ± 0.11	2.670 ± 0.451	342.0 ± 9.9
	Z	-0.31 ± 0.18	4.037 ± 0.707	48.5 ± 10.2
RL06 CSR-TN13:	X	-0.16 ± 0.02	1.594 ± 0.093	96.1 ± 3.4
	Y	0.08 ± 0.03	1.751 ± 0.100	300.4 ± 3.3
	Z	-0.68 ± 0.03	2.620 ± 0.107	82.7 ± 2.3

tionally, the large trend difference in Z-direction also leads to a significant effect in OMC (Tab. 5.3).

c_{20} and c_{30} Gravity Coefficients

Similar to the geocenter motion, other spherical harmonic coefficients can be extracted from the inversion and analyzed. Here, the c_{20} and c_{30} coefficients have been selected as both are regularly replaced during the processing of GRACE/GRACE-FO data. For better comparison, the Stokes coefficients have been converted to geoid heights relative to the mean field over 2005-01 till 2010-12.

The c_{20} coefficient from the ITSG-2018 GRACE data appears to be noisier, especially after 2016, compared to the coefficients derived from the inversion and extracted from the TN14 data (Fig. 7.31). Generally, the inversion results agree well with the TN14 data and the coefficients extracted from IGG-SLR data (Tab. 7.20). Before 2005, the IGG-SLR data is biased compared to the other data sources. Similarly, the TN14 solution is slightly biased with respect to the inversion and GRACE coefficients (Fig. 7.31). This behavior is expected since the inversion is fitted against GRACE normal equations including the original c_{20} coefficients, which results in a small

bias between the two. With degradation of individual GRACE months where these are influenced by near-repeat orbit conditions after 2012 the GRACE original c_{20} coefficients are significantly affected. In contrast, the inversion-based coefficients are found to preserve the seasonal cycle also during the GRACE-FO period (Fig. 7.31). The trend estimates from the inversion and TN14 solution (−0.19 mm/yr and −0.11 mm/yr, respectively) agree well while the IGG-SLR trend is slightly larger (−0.11 mm/yr). In contrast the trend from the original GRACE coefficient (−0.27 mm/yr) is found to be significantly smaller (Tab. 7.20). This shows that the inversion, while fitted to the GRACE/GRACE-FO data, is at the same time not completely bound by the input.

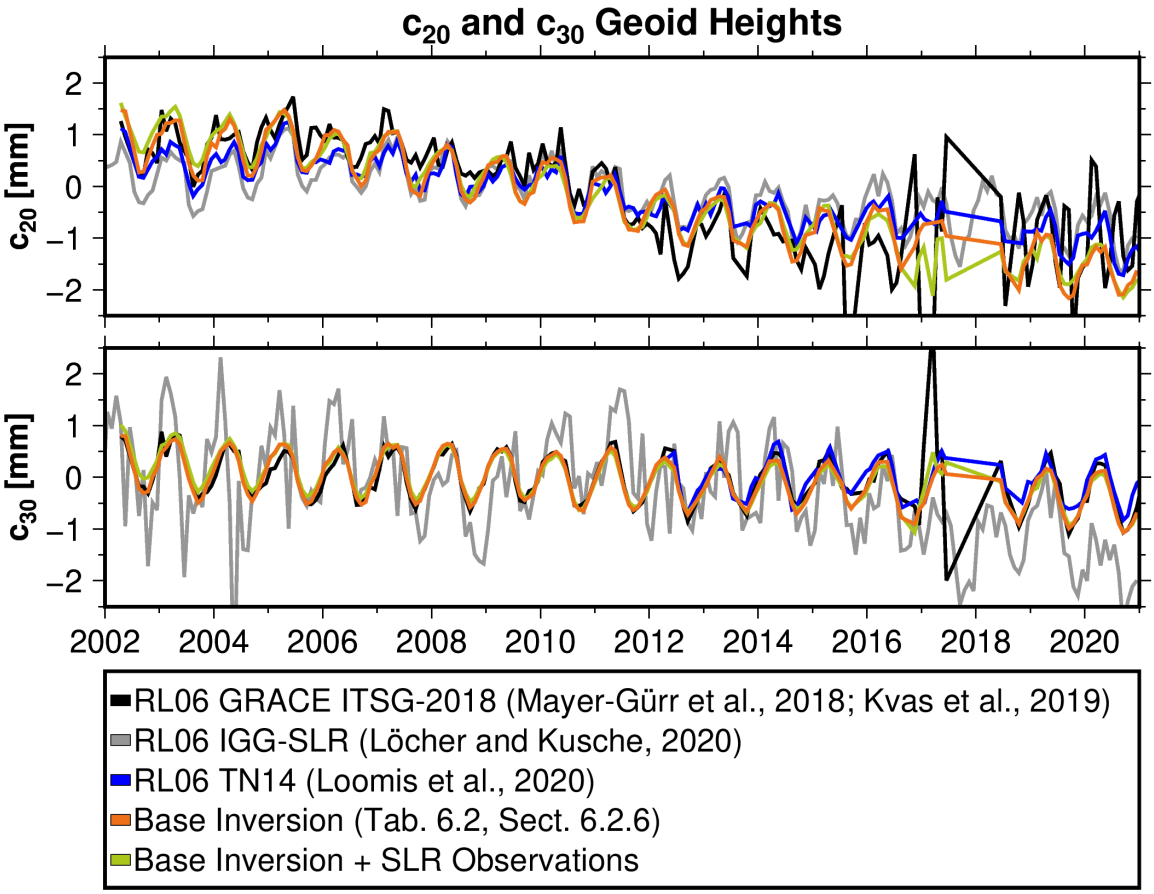


Figure 7.31: Temporal variation of the c_{20} and c_{30} gravity coefficients converted to geoid heights relative to the average over 2005-01 till 2015-12. Inversion results are compared to other sources, including GRACE/GRACE-FO where those coefficients are regularly replaced (Sect. 5.3 and Loomis et al., 2020).

With todays necessity of transplanting accelerometer data from one GRACE/GRACE-FO satellite to the other, the c_{30} coefficient is also routinely replaced during the processing of the L2 spherical harmonic data (Sect. 5.3 and Loomis et al., 2020). The c_{30} coefficients from GRACE/GRACE-FO agree well with the ones extracted from the inversion method. After March 2012, the difference between the two becomes slightly larger, especially during high peak times. While TN14 does not provide c_{30} information before March 2012, it is available afterwards and also agrees relatively well with the GRACE and inversion output. After August 2016, the GRACE coefficient becomes visibly more noisy compared to the other estimates (Fig. 7.31), marking the strong degradation of the available GRACE gravity field data, which also affects the inversion results. The IGG-SLR only solution is overall more noisy and also indicates a negative trend after 2015 (Fig. 7.31), which is not confirmed by the other approaches. This results from the low maximum degree of 5, where improved c_{20} from SLR-only can be derived considering a higher maximum degree and order or a solution augmented with additional EOFs (Loomis et al., 2019b; Löcher and Kusche, 2020). With

Table 7.20: Trend, annual amplitude and phase (2005-01 till 2015-12) of low degree coefficients c_{20} and c_{30}, which are commonly replaced during GRACE/GRACE-FO processing. The potential values have been converted to geoid height changes.

Source	Trend [mm/yr]	Amplitude [mm]	Phase [doy]
Total (Base Inv.): c_{20}	-0.19 ± 0.01	0.441 ± 0.015	80.0 ± 1.9
c_{30}	-0.04 ± 0.01	0.484 ± 0.010	95.4 ± 1.2
Total (incl. SLR): c_{20}	-0.19 ± 0.01	0.511 ± 0.018	79.3 ± 2.0
c_{30}	-0.03 ± 0.01	0.544 ± 0.013	93.4 ± 1.4
RL06 IGG-SLR: c_{20}	-0.11 ± 0.01	0.426 ± 0.023	87.0 ± 4.0
c_{30}	-0.04 ± 0.02	0.677 ± 0.100	123.9 ± 8.6
RL06 TN14: c_{20}	-0.14 ± 0.01	0.274 ± 0.021	94.2 ± 4.5
$^*c_{30}$	0.06 ± 0.02	0.451 ± 0.036	93.2 ± 4.6
RL06 GRACE ITSG-2018: c_{20}	-0.27 ± 0.02	0.272 ± 0.069	77.7 ± 14.6
c_{30}	-0.01 ± 0.01	0.530 ± 0.020	93.2 ± 4.6

$^*c_{30}$ from TN14 is only available starting from 2012-03.

respect to amplitude, phase and trend, the inversion solution including additional SLR information is closer to the GRACE/GRACE-FO coefficient (Tab. 7.20). The trends of the c_{30} coefficients from all solutions agree well with the exception of TN14, which is not available for the whole investigated time period.

In summary, the inversion provides an additional way of deriving low degree coefficients, which can be utilized for generating consistently processed datasets for validation and comparison. While the c_{20} and c_{30} estimates agree rather well with other data sources, the impact of geocenter motion, extracted from the degree-1 coefficients, has to be considered in the context of consistent processing (Tab. 5.3). For this, most differences are found in the Z-direction corresponding to c_{10}, which basically represents a hemispheric zonal component. In this thesis, the geocenter motion extracted from the inversion has always been introduced into the individual processing of the spherical harmonic data, unless stated otherwise (e.g., Fig. 7.1).

7.6.2 Ocean Heat Uptake and Earth Energy Imbalance

The inversion results enable a novel approach to deriving data driven Ocean Heat Uptake (OHU) and estimates of Earth Energy Imbalance (EEI) (Sect. 6.2.8). The long-term global mean net radiative flux at top of the atmosphere (EEI) describes the planet's heat accumulation rate due to radiative forcing. EEI is one of the key indicators of global warming (e.g., Loeb et al., 2012; Trenberth et al., 2016; Loeb et al., 2017; Trenberth et al., 2019; Meyssignac et al., 2019; Hakuba et al., 2021).

The inversion results are converted to OHU following section 6.2.8. Estimates of OHU for the global ocean and the major ocean basins are provided in tables 7.21 and 7.22. The first column in table 7.21 is derived by converting a rescaled OHC trend estimate to OHU, while the first column in table 7.22 is computed from, first, filtering with a derivative filter followed by a smoothing filter (Sect. 6.2.8). All computations are limited to the GRACE era to avoid the gap between GRACE/GRACE-FO and its effect on the sea level budget. Due to filtering effects of the second approach for deriving OHU (Sect. 6.2.8), the valid time period used for comparison in this section is 2005-01 till 2014-12. Furthermore, the OHU estimates are all scaled by 0.71 to refer to m^2 of the total surface of the Earth (Sect. 6.2.8 and, e.g., Meyssignac et al., 2019) in order to be consistent with the EEI representation from the CERES project, used for comparison.

Comparing the two approaches for deriving OHU from OHC (Sect. 6.2.8), the major difference

Table 7.21: OHU derived by directly estimating the OHC trend (first approach, Sect. 6.2.8) and scaled relative to the total surface of the Earth. All estimates are derived for 2005-01 till 2014-12 and based on IS001 (Tab. 7.12). Unscaled estimates are without the factor of 0.71 for referencing to the total Earth surface for consistency with CERES.

Ocean Basin	**Inversion: EOF-scaling**	**Steric Trend 0.52-factor**	**ORAS5**
Atlantic Ocean	0.12	0.11	0.19
Pacific Ocean	0.14	0.14	0.14
Indian Ocean	0.16	0.17	0.23
Remainder	0.02	0.03	0.03
Total Ocean	0.44	0.45	0.59
Unscaled Total IS001	0.61	0.63	0.83
Unscaled Total IS030	0.55	0.50	0.83

between the two approaches (first columns in Tabs. 7.21 and 7.22) is related to the slightly larger noise level of the filtering approach. Both approaches are influenced by noisy inversion-rescaled OHC, resulting from small PC values in the denominator of equation (6.2.12). These results are compared with the steric trend rescaling that uses a constant factor of 0.52 $W/m^2/mm/yr$ (Kuhlbrodt and Gregory, 2012) and with directly utilizing the OHU model estimates. Here, the two inversion-rescaling approaches for deriving OHU perform similar to directly rescaling the steric trend estimate. However, the inversion-rescaling involving filtering (Sect. 6.2.8) provides a smaller OHU value on global scales. The model-based OHU provides generally larger OHU results.

Table 7.22: OHU derived by utilizing a derivative filter (second approach, Sect. 6.2.8) and scaled relative to the total surface of the Earth. All estimates are derived for 2005-01 till 2014-12 and based on IS001 (Tab. 7.12). Unscaled estimates are without the factor of 0.71 for referencing to the total Earth surface for consistency with CERES.

Ocean Basin	**Inversion: EOF-scaling**	**Steric Trend 0.52-factor**	**ORAS5**
Atlantic Ocean	0.09	0.10	0.19
Pacific Ocean	0.11	0.16	0.18
Indian Ocean	0.12	0.16	0.20
Remaining	0.02	0.01	0.03
Total Ocean	0.34	0.44	0.61
Unscaled Total IS001	0.47	0.63	0.86
Unscaled Total IS030	0.36	0.50	0.86

OHC derived directly from the ORAS5 model is rising in all three of the major ocean basins, with the strongest increase observed in the Indian Ocean (Fig. 7.32). This is also confirmed by the trend estimates, i.e. OHU (Tabs. 7.21 and 7.22). Global ocean OHU is found in the range of 0.34 to 0.61 $W\,m^{-2}$. Based on the first approach (Sect. 6.2.8), OHU from the rescaled inversion and from scaling the steric trend with the factor 0.52 $W/m^2/mm/yr$ are about the same. The ORAS5 model estimates from both approaches are generally found larger at about 0.60 $W\,m^{-2}$ (Tabs. 7.21 and 7.22). The smallest OHU is derived from the rescaled-EOF method (0.34 $W\,m^{-2}$) using the second conversion approach (Sect. 6.2.8).

In a first step, the OHU values are compared to estimates of EEI derived from NASA's CERES

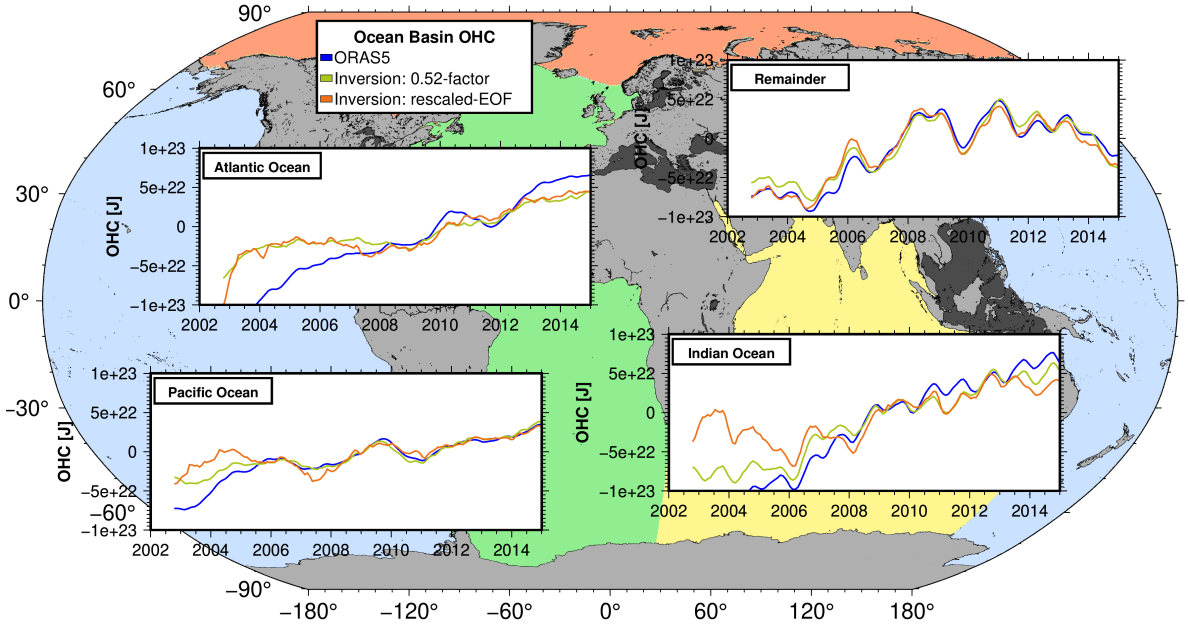


Figure 7.32: OHC for each major ocean basin.

program[5]. The monthly gridded CERES Energy Balanced And Filled (EBAF) v4.1 data products of the long and short term radiation fluxes at the top of atmosphere are utilized to compute residuals of the Earth's radiation budget. Globally averaging these leads to a time series of EEI. Then, the mean over 2005-01 to 2014-12 is computed for comparison, resulting in an EEI estimate of $0.73\,\mathrm{W\,m^{-2}}$. However, this value refers to the top of atmosphere and also includes land and atmosphere contributions. According to literature, about 93% of the excess heat is stored in the global oceans (e.g., Stocker et al., 2013; Trenberth et al., 2016). Furthermore considering the top of atmosphere roughly at an altitude of 100 km, the area is by about 3% larger compared to Earth's surface. Consequently, scaling the CERES derived estimate accordingly leads to corresponding OHU of $0.66\,\mathrm{W\,m^{-2}}$. This scaling is roughly in line with the $0.08\,\mathrm{W\,m^{-2}}$ land contribution to EEI reported in literature (e.g., von Schuckmann et al., 2020). As expected, the CERES-EEI estimate is quite close to the value directly derived from the ORAS5 model (Tabs. 7.21 and 7.22). The CERES EBAF data products are constrained towards an ocean model based OHU estimate, since it is difficult to derive an absolute value from the radiance sensors (Loeb et al., 2012; Loeb et al., 2017). In contrast, data based estimates derived from the inversion EOF-scaling and from the steric inversion result using a constant factor, are both found to be smaller than CERES-based and model-driven OHU values.

Published estimates are generally found in the range of 0.4 to $1.0\,\mathrm{W\,m^{-2}}$ (e.g., Johnson et al., 2016; Hakuba et al., 2019; Meyssignac et al., 2019; von Schuckmann et al., 2020; Hakuba et al., 2021; Marti et al., 2022), which is in agreement with the estimates derived in this thesis. For an overview on methods and results for deriving OHU and EEI estimates see Meyssignac et al. (2019) and von Schuckmann et al. (2020). Recent publications focus on utilizing space geodetic techniques, such as GRACE/GRACE-FO and altimetry, for OHU computation. First, a sea level budget is constructed and then the steric sea level trend is coverted to OHU by simply utilizing the conversion factor of $0.52\,\mathrm{W/m^2/mm/yr}$. Finally for converting to EEI, the OHU is then combined with land contributions, often taken from literature and, not necessarily, consistently derived in terms of covered time period. (e.g., Hakuba et al., 2021; Marti et al., 2022).

Applying the literature approach of multiplying steric trends by $0.52\,\mathrm{W/m^2/mm/yr}$ to the steric estimates from the sea level budgets IS001 (Tab. 7.12) and IS030 (Tab. 7.15) results in OHU values

[5] https://ceres.larc.nasa.gov/data/ (last accessed: 06.07.2022)

of $0.73\,\mathrm{W\,m^{-2}}$ and $0.56\,\mathrm{W\,m^{-2}}$, respectively. Both are in range with the reported estimates (Tabs. 7.21 and 7.22). Since these estimates are tied to the steric sea level trends, correspondence between deriving OHU from different published steric trend estimates based on the constant factor are very similar to steric comparisons in section 7.2.8 and are, thus, not repeated here.

In summary, the inversion based results indicate that a simple global constant conversion factor in combination with a steric sea level trend estimate can only provide a rough estimate of OHU since, both, steric sea level and conversion factor depend on the location. By rescaling model OHC projected on the steric fingerprints of the inversion, it is possible to derive grids of OHC driven by space geodetic techniques in a consistent way. In addition, it enables derivation of observation based regional estimates of OHU. Usage of the global expansion efficiency factor ($0.52\,\mathrm{W/m^2/mm/yr}$) for regional approaches seems questionable, although one could theoretically derive corresponding regional conversion factors adapting the global methodology described, e.g., as employed by Hakuba et al. (2021) based on Kuhlbrodt and Gregory (2012). Based on the wide range of published OHU and EEI estimates, those derived from GRACE/GRACE-FO and altimetry based sea level budgets as well as in-situ steric profile based estimates tend to be smaller than model based values and the model-constrained EEI from the CERES project datasets.

Chapter 8

Conclusions and Outlook

The goal of this thesis was twofold. On the one hand, a novel coastal altimetry algorithm has been introduced and extended in order to provide high quality coastal sea level change. On the other hand, the separation of total sea level change, as measured by satellite altimetry, into OMC and steric-related contributions is investigated for individually processed data sets and in a consistent global fingerprint inversion approach, combining multiple datasets within one estimation.

Results from the altimetry retracking can serve as a future basis for further developments and extensions since the novel retracking approach, developed as part of this thesis, opened up possibilities in other areas for extracting improved parameters and even novel estimates from the altimetry data. Similarly, the inversion framework can be further extended by introducing new and high resolution datasets to better separate smaller basins or connect the sea level changes with variations in other parts of the Earth system.

8.1 Conclusions

Improved Retracking of Coastal Altimetry

As part of the first objective of this thesis (Sect. 1.4), a novel sub-waveform retracking approach for improving coastal altimetry estimations has been developed. Instead of trying to develop the perfect waveform model, which is able to retrieve data from all waveforms, the STAR algorithm shifts the problem to a later stage by, first, computing many potential solutions at each along-track measurement position, which are then further analyzed to select a final estimate. In contrast to the previously utilized method, which extracted a few sub-waveforms from a single waveform, the STAR algorithm partitions the total waveform with different orders of sub-waveform size, providing a multitude of sub-waveforms.

STAR has been developed as part of this thesis. In contrast to the first version (STAR-V1) published in Roscher et al. (2017), I further extended the algorithm that now provides more potential estimates and improved analysis of the point-clouds as part of STAR-V3. It has turned out that for STAR-V1, the Dijkstra approach for analyzing the point-clouds of SLA, SWH and σ° was too simplistic in that the selection of final estimates could get skewed by a single leverage point. Therefore, I replaced the Dijkstra with my own algorithm utilizing the special structure of the point-cloud graph. This allowed for modification of edge-weights as well as inclusion of prior auxiliary information in order to better deal with potential disturbances from erroneous MSS or rain events. This lead to improved selection of the final estimates. Consequently, STAR-V3 significantly outperforms the previous versions and enables retrieval of coastal sea level from conventional altimetry that is of the same quality level as from state-of-the-art DDA. Furthermore, I have transferred the slow Matlab implementation to C++, optimized the program code and included parallelized processing of individual cycles or files.

The validation showed that STAR-V3 is able to retrieve high quality data from an increased number of cycles compared to other state-of-the-art coastal retracking methods, which generally show a severe drop in quality about 5 km off the coast. In contrast, STAR is able to provide high quality SLA, SWH and σ° up to less than 1 km off coast. In contrast to STAR-V1, the improvements in STAR-V3 also reduced the repeatability error, especially in coastal regions.

Application to DDA-based representations of a conventional altimetry waveform for the Cryosat-2 and Sentinel-3 missions also showed that STAR-V3 is able to retrieve more coastal data with better quality compared to other algorithms. When investigating the noise level with respect to distance to coast, the STAR noise level from RDSAR data is of the same quality as for DDA data or even better. This is also confirmed by comparison to tide gauge data, where STAR even provided more data points than DDA of the same quality level. Based on the RDSAR results, STAR is able to provide SLA of the same quality level or even better than DDA.

While STAR is, in principal, developed and tuned to the retrieval of SLA, it also provides estimates of SWH and σ°, where the corresponding point-clouds can be analyzed separately. Comparison of resulting SWH and σ° converted to wind-speed at a gauge station in the North Sea also confirmed the good quality of these estimates in comparison to other retrackers. In particular, STAR is able to significantly reduce the noise level of SWH.

Global Mean Sea Level Changes from Individual Datasets

For the second thesis objective (Sect. 1.4), deriving sea level budgets based on individually and independently processed time series has been examined. Investigating different published time series of GMSL based on the same input data showed different temporal behavior and trends. These have been found to be related to differences in global averaging and corresponding weighting, and the choice of applied IMB. The IMB directly affects trend estimates as these are supposed to correct for, assumed constant, jumps between altimetry missions, related to individual instrumentation delays and other effects. Furthermore, conversion to RSL was found to be largely dependent on the chosen GIA model and the contemporary surface loading driven vertical land motion effect as a consequence from contemporary OMC. The latter is generally considered negligible by most publications as either only a GIA correction is applied or simply -0.3 mm/yr, taken from literature, are subtracted for the conversion to RSL. The benefit of the fingerprint inversion, utilized in this thesis, is that it also allows for the computation of these contemporary mass effects in the order of 0.12 mm/yr, which can then be consistently applied for validation and other applications.

Examining common processing strategies of converting space gravimetry data into OMC revealed impacts of individual processing choices. The choice of GIA correction affects the resulting OMC trends more compared to altimetry-based total sea level trends, since small errors in the GIA model become severely exacerbated by conversion to EWH. These errors directly transfer to global and regional OMC trend estimates. Since GRACE and similar missions are blind to geocenter motion, degree-1 coefficients are commonly substituted during processing. However, these substitutes include significant trend signals and comparison of different degree-1 products, including outputs from this thesis' inversion, revealed strong disagreement in the order of several tens of mm/yr. Following well known processing strategies in literature, I discovered a commonly introduced inconsistency in the restoration of the AOD1B-GAD product related to an erroneously applied ocean mask. Instead of utilizing the total ocean area, a sub-region including a coastal bufferzone was used to convert OBP to OMC resulting in erroneous OMC trends. This lead to the OMC being estimated too large by 0.37 mm/yr and 0.12 mm/yr for RL05 and RL06 data, respectively. The adapted processing is now commonly applied for deriving OMC from satellite gravity.

Converting profiles of ocean temperature and salinity data to steric sea level change, generally follows a predefined processing, which is similar for in-situ Argo buoys, gridded Argo data and

ocean model (re-)analysis. Comparing different data products revealed a strong dependence of the derived trends on the data product.

Utilizing individually processed datasets for generating sea level budgets, like it is commonly done in literature, requires a great deal of attention with respect to consistency that considers strength and, especially, weaknesses of each individual dataset. For example, converting spherical harmonic GRACE data to OMC includes strong leakage effects from terrestrial hydrology, which will translate to the OMC estimate. Most commonly, a 300 km ocean buffer will be applied, which then in turn should also be included in the processing of averaging altimetry or steric data in order to derive consistent time series. However, this is not always the case and combination of inconsistent time series will directly affect the budget closure and interpretations of the budget.

Global Fingerprint Inversion

In this thesis, I have further developed and extended the global fingerprint inversion method as part of the third and fourth objectives (Sect. 1.4) allowing for retrieval of significantly improved and consistently closed sea level budgets on global and regional scales (objective five, Sect. 1.4). First, the input data has been updated with up to date RADS altimetry data and the GFZ RL05 data has been replaced with ITSG2018 gravity data processed following the RL06 standard. This has significantly improved the capabilities for separating individual mass contributors. Afterwards, an updated fingerprint parameterization reduced inter-basin mass change correlations and lead to more realistic OMC estimates for the ice sheets, land glaciers and terrestrial hydrology. In addition, new fingerprints for IMV within the ocean have been added, which significantly reduced the residual signal and, especially, improved regional sea level budget closure. While IMV is constrained to zero over the total ocean area, it becomes relevant for smaller basins, including non global coverage, e.g., by the Jason altimetry missions and, thus, cannot be neglected.

Relative GMSL change from the inversion method (3.43 mm/yr) fits well with published estimates, e.g., by Nerem et al. (2018), while other averaging and weighting methods lead to larger estimates. Similarly, global OMC (1.89 mm/yr) was found in good agreement with individually processed spherical harmonic and mascon-based estimates, after consistently substituting the inversion-based degree-1 coefficients and accounting for the same GIA correction during processing. After converting the inversion based OMC to OBP, comparison to in-situ OBP gauge stations showed the inversion solution quality to be in line with state-of-the-art GRACE mascon solutions or even better. The inversion fingerprint approach is able to filter artifacts in the gravity data, such as from the 2004 Sumatra Andaman earthquake, since these signals cannot be modeled by the fingerprints and, thus, turn up in the GRACE residuals. Similarly, the aliasing stripes found in unfiltered GRACE data, which is used as input for the inversion, is filtered simply by the fact that the fingerprints are not able to represent these patterns. This removes the need for filtering and dealing with corresponding leakage effects, which is especially beneficial for investigating regional sea level budgets.

OMC estimates from the ice sheets in Greenland (0.75 mm/yr) and Antarctica (0.42 mm/yr) were found to be in good agreement with other published estimates on basin-scale and for the integrated ice sheet contributions. The contribution from glaciers (0.64 mm/yr) agrees significantly better with other published glacier sea level contributions, compared to earlier inversions. This is due to extending the glaciers data base to 68 glacier basins, in contrast to only 16 fingerprints utilized by Rietbroek et al. (2016). Updated hydrological model data improved the retrieved terrestrial hydrology signals (0.21 mm/yr) and basin scale mass comparisons revealed good agreement with independent estimates.

An update of the steric model data significantly improved the derived fingerprints, estimated steric sea level change (1.41 mm/yr) and allowed for a generally increased inversion spatial resolu-

tion of 0.25°. Nowadays, the steric sea level is further separated into a shallow part from the upper 700 m and a deep ocean contribution from below 700 m. It turns out that the two contributions are separable using GRACE and altimetry data. Estimation of the upper 700 m steric change was then further augmented by introducing easyCORA in-situ steric profile data as an additional observable into the inversion. While it turned out that the impact on global steric sea level change was small, regions with high in-situ data coverage showed improved budget closure.

It was shown that PCA based fingerprints and their capability to correctly separate individual sea level contributions heavily depend on the time period used for the creation of these fingerprints. While it is generally assumed that these fingerprint are also representative for time periods outside their original creation period, it turned out that the quality of the extrapolated signals degrades rapidly outside the creation period. This lead to biases and unrealistic trends, especially, for the spatio-temporally variable steric contributions. To a certain extent, this limits the inversion capabilities for correctly separating mass and steric signals. Nowadays, steric model data is produced operationally, but other datasets, such as the WGHM hydrological data, although slightly less affected, are only available after delay.

Budget closure largely depends on the utilized input data. For the GRACE-FO period, the base inversion (IS001, Tab. 7.12) residuals showed a few mm bias, which turned out to be in part related to the Jason-3 positions utilized for evaluation of the budget and in part to extrapolating the steric reconstruction beyond the original fingerprint creation period. However, the impact from the Jason-3 positions could be greatly reduced after introducing all available altimetry data in a multi-mission solution (IS030, Tab. 7.15). Globally, the sea level budget could be closed with an error of 0.12 mm/yr for 2005-01 till 2015-12 based on Jason-altimetry and GRACE data only. Including all available altimetry missions, steric in-situ data, GRACE/GRACE-FO and SLR, the budget closure error was further reduced by about 75% resulting in 0.04 mm/yr for the same period. Both estimates represent a significant improvement compared to published budget closures in global sea level budgets.

When investigating strengths and weaknesses of the original inversion method, it was discovered that the co-estimated GIA and IMB parameters posed a problem. The inversion based GIA estimates were found to be significantly smaller compared to published values, raising serious doubts on their validity. Consequently, the co-estimation of GIA has been removed for now and is replaced by an a priori GIA correction applied before the estimation. Similarly, the co-estimated IMB estimates introduced unrealistically large jumps between individual missions, directly impacting the derived budget. Considering this was already a problem when only utilizing Jason data, introduction of multi-mission altimetry data exacerbated the impact. Consequently, IMB corrections, in addition to the RADS ones, have been derived for the along-track input data and are also accounted for before the fingerprint estimation.

The inversion processing itself has also been altered. Previously after a first run, the residuals with respect to altimetry have been decomposed using PCA and the resulting EOFs have been introduced as an additional set of fingerprints in the parameterization during a second estimation step. Due to the improvements described above, the residuals, after the first run, are already significantly reduced and, consequently, the second run is no longer necessary. Furthermore, the introduction of the residual fingerprints also altered the results from the first run and it was difficult to actually attribute these estimated bootstrap signals to either steric or mass related changes; Rietbroek (2014) interpreted these as purely deep ocean steric signal, which in hindsight most likely did not turn out to be correct.

Extending the Jason-only altimetry data to multi-mission altimetry data proved to be beneficial. Significant improvements in agreement with tide gauge data have been found at high latitudes, not covered by the Jason mission. General improvement in spatio-temporal coverage also benefited

other regions of the world, especially on regional scales. However, these datasets made the results less comparable to other published sea level estimates, which are mostly based on the Jason reference missions.

While global sea level budgets are derived on a regular basis, the inversion framework also enables investigation of regional sea level budgets. Based on the results of this thesis, it was possible to consistently close sea level budgets on regional scales, resulting in meaningful separations of the total sea level change into individual contributions. These were found to be in-line with published estimates and local sea level phenomena. In addition, it turned out that IMV and GIA play a significant role for regional sea level budget estimation, e.g., in the Baltic Sea and cannot be neglected, as it is usually done on global scales. For regions with high spatio-temporal multi-mission altimetry coverage as well as good available in-situ steric profile data, such as the Bay of Bengal or the Mediterranean Sea, the inversion-based regional budget could be closed with minimal error. In other regions, such as the North Sea or the East China Sea, local unmodeled effects likely related to wind and sediment influence, respectively, impacted the sea level budget and, thus, lead to larger closure errors.

The inversion results can be used to produce, non-sea level related, additional outputs. As already mentioned, the inversion allows to derive degree-1 as well as c_{20} and c_{30} Stokes coefficient substitutes for the spherical harmonic gravity processing. While accounting of the degree-1 substitutes is paramount for consistent comparisons to other OMC estimates, the other low degree coefficients agree quite well with those from publicly available substitute products. Finally, the estimated scaling factors or PCs for the steric contribution can be utilized in a novel inversion-based rescaling approach for deriving OHC. Assuming certain hypotheses, it is possible to further process OHC to OHU, which is closely related to EEI, representing one of the essential climate variables utilized to monitor global warming. Besides providing global estimates in good agreement with published ones, the latter all depend on a simple constant scaling factor applied to a steric trend estimate. The novel approach introduced in this thesis also allows to attribute basin scale contributions in relation to global OHU.

8.2 Outlook

It is possible to further improve the coastal retracker and the global fingerprint inversion, both of which have been introduced in this thesis. Besides improving the existing methodology, expansion into new data fields or transfer of concepts to other applications can be considered in the future.

The STAR methodology has originally been developed for application to conventional altimetry. Based on the very good validation results against DDA data, the next step would be to utilize the STAR processing scheme with DDA. In theory, this mostly requires replacement of the conventional altimetry retracking model with a DDA model, since the waveforms are different. Steps in this direction have been done by utilizing the SINCS-retracker (Buchhaupt et al., 2018) resulting in the STAR for SAR (STARS) retracker. DDA retrackers usually work on the DDA-stack data and, thus, a sub-waveform detection and retracking, considering the whole stack, is required. Nonetheless, the generated point-clouds of SLA, SWH and σ° can then be analyzed in the same manner as for conventional altimetry. First results look promising, indicating further improvements of the retracked parameters, albeit the increase in performance will be smaller compared to the conventional altimetry application, since DDA itself already produces quite good results.

Considering the STAR point-clouds, these can be utilized for other approaches besides ocean and coastal retracking. Over small inland waters and rivers, the point-clouds provide a multitude of information along the track, including clear hooking effects (Frappart et al., 2006). These can then be exploited to derive robust river heights as has been done manually in S. Schröder et al. (2019). Automation of this analysis would be the next step. However due to the diversity of land effects,

this task requires more effort. For example in coastal regions, the correct points are selected along a, more or less, straight line, while the hooking parabola over rivers highly depends on location and the point-cloud can even contain multiple parabolas at once.

Furthermore, the STAR point-clouds could be utilized to infer snow depth over the ice covered surface areas in Greenland and Antarctica. The radar pulse will penetrate the snow surface reflecting from multiple reflectors in the snow layer. Generally, this is considered as a nuisance when estimating surface heights for ice altimetry applications. However, the thickness of the STAR point-clouds can be utilized to analyze this penetration depth and infer information on the snow layer as well as improve and aid surface height retrieval. Similarly, it might be possible to infer information on vegetation coverage over land surfaces.

The obvious approach for further extending the global fingerprint inversion is the expansion and improvement of the fingerprint database. Introducing spatial prior information for the melting basins in Greenland and Antarctica led to significantly improved separability. Similarly, introducing spatial information on melting hotspots in the glacier (sub-)regions would aid in reducing inter basin mass change correlations and improve separability. Furthermore, expanding the hydrological dataset, which is used as a basis for the corresponding fingerprints, will aid in mitigating extrapolation effects.

On global scales, the residual signal contains mostly ocean dynamics from eddies and currents. While some ocean models provide eddy information, it rarely corresponds to eddies existing in reality. On regional scales, unmodeled effects can contribute significantly to the regional sea level budget. Consequently, introducing local sea level effects by wind forcing or sedimentation would improve separation and budget retrieval in these regions.

So far, the fingerprints utilized are static in time, assuming invariant spatial patterns. This is fine for the relatively small time periods considered in this thesis. However, extrapolation effects from the PCA-based fingerprints have been observed and all spatial patterns will vary over time. Consequently, considering an inversion approach, which accounts for these pattern variations, might be necessary when expanding the time frames.

Expanding the inversion with additional datasets would also aid separability and even open up new possibilities for improving spatial resolution or connecting physical processes on an observational basis. Currently, first steps are made towards including ice altimetry into the inversion approach, in order to aid separating smaller basins in Antarctica based on the higher spatial resolution of the altimetry data. This also enables an increased spatial resolution of the retrieved mass changes by further splitting the basins into sub-basins down to a few km^2 of area. At the same time, inclusion of ice-altimetry together with firn data will potentially re-enable the possibility for co-estimating GIA changes as the inversion currently depends to a certain extent on the a priori selected GIA correction.

Introducing data from the CERES project and linking these to the OHU and OHC requires careful modeling of the atmospheric energy fluxes in order to avoid inconsistencies and improve the recovery of OHU and EEI estimates. Further exploiting in-situ profile data may enable a finer depth discretization for steric contributions. Tide gauge measurements are mainly driven by sea level, but also include vertical land motion signals, which needs to be carefully modeled before usage in combination with other datasets. This thesis has shown that there is certain potential in utilizing time-variable gravity data from other missions, such as SLR or Swarm. Besides filling only missing months in the GRACE data, these datasets could be utilized to extend the inversion backwards in time for analyzing sea level budget variations before the GRACE era.

Most of the inversion processing nowadays is implemented in C++, leading to significantly

improved run-time and more flexibility. The estimation procedure is still based on a combination of earlier implementations of programs in Fortran, which limit the possibilities to a certain extent, especially with respect to the combination of the individual datasets on normal equation level. Consequently, reworking those parts will allow for higher performance and also allows accounting for potential expansions, such as implementing the inversion as part of a Kalman filter framework.

While the time-variable gravity data employed in the inversion is provided with full error covariance information, the other datasets lack of these covariance information. Altimetry and in-situ steric profile data consider only a diagonal error covariance. However, both data types are affected by spatio-temporal correlations. For example, modeling along-track altimetry correlations is an ongoing field of research and incorporation into the inversion will aid in weighting of individual observation types as well as improving retrieved sea level budgets.

Finally, the general inversion methodology can be transferred to investigating other phenomena. For example, Uebbing et al. (2017) employed a fingerprint-based approach to retrieve along-track soil moisture information from altimetry. This could be further expanded to a gridded approach in the future. Furthermore, the fingerprint methodology can be applied to other areas, where spatial prior information is available, but the temporal evolution is less well known due to limited availability of observations.

Appendix A

Least Squares Estimation and Modification of Normal Equation Systems

A.1 Least Squares Estimation

This appendix describes the basic least squares approach, utilized in this thesis, as well as several operations applied to normal equation systems in order to eliminate parameters, change parameters or the a priori solution. The described methods are fairly standard and can be found from several sources (e.g., Koch, 1999; Niemeier, 2008) where the parts most relevant for this thesis are included here for completeness.

Observations, such as satellite measurements from GRACE and altimetry or waveform values (Sect. 4.2), can be stacked in the $m \times 1$ observation vector $\boldsymbol{l}$. The individual observation l_i $(i = 1 \dots m)$ is related to the set of p unknown parameters stacked in the $p \times 1$ parameter vector, $\boldsymbol{x}$, by a functional model (e.g., Koch, 1999; Niemeier, 2008)

$$l_i = f_i(x_1, x_2, \dots, x_p). \tag{A.1.1}$$

For the least squares estimation, it is assumed that the functional relationship between observations and parameters is linear and can be written as

$$\boldsymbol{l} + \boldsymbol{v} = \mathbf{A}\boldsymbol{x}, \tag{A.1.2}$$

with the design (or Jacobi) matrix, $\mathbf{A}$ containing the functional relations and with $\boldsymbol{v}$ accounting for the residual. In case of a non-linear functional relationship it is necessary to first linearize the function by expansion into a tailor series

$$f_i(\boldsymbol{x}_0 + \boldsymbol{\Delta x}) = f_i(\boldsymbol{x}_0) + \left(\frac{\partial f}{\partial \boldsymbol{x}}\right)_{\boldsymbol{x}=\boldsymbol{x}_0} \boldsymbol{\Delta x} + O(x^2), \tag{A.1.3}$$

requiring approximate values, $\boldsymbol{x}_0$, of the desired parameters. The design matrix, $\mathbf{A}$, contains the partial derivatives of each observation with respect to the individual parameters in its columns. In matrix-vector form this becomes

$$\boldsymbol{l} + \boldsymbol{v} = \mathbf{A}(\boldsymbol{x}_0 + \boldsymbol{\Delta x}), \tag{A.1.4}$$

which can be further simplified using the computed observation $\boldsymbol{l}_0 = \mathbf{A}\boldsymbol{x}_0$ and introducing reduced observations $\boldsymbol{\Delta l} = \boldsymbol{l} - \boldsymbol{l}_0$ resulting in

$$\boldsymbol{\Delta l} + \boldsymbol{v} = \mathbf{A}\boldsymbol{\Delta x}. \tag{A.1.5}$$

Since the observations do not correspond to true values but are assumed as realizations of a random variable due to measurement errors, it is necessary to account for the stochastic model in form of the covariance matrix of the observations, $\mathbf{\Sigma}_{ll}$ (e.g., Niemeier, 2008)

$$\mathbf{\Sigma}_{ll} = \begin{bmatrix} \sigma_1^2 & \rho_{12}\sigma_1\sigma_2 & \cdots & \rho_{1m}\sigma_1\sigma_m \\ \rho_{21}\sigma_1\sigma_2 & \sigma_2^2 & \cdots & \rho_{2m}\sigma_2\sigma_m \\ \vdots & \vdots & \ddots & \vdots \\ \rho_{m1}\sigma_1\sigma_m & \rho_{m2}\sigma_2\sigma_m & \cdots & \sigma_m^2 \end{bmatrix}. \tag{A.1.6}$$

Here, σ_i represents the standard deviation of the ith observation and ρ_{mp} describes the correlation between individual observations. The covariance matrix can be further split by $\mathbf{\Sigma}_{ll} = \sigma_0^2\mathbf{Q}_{ll}$ into the variance factor σ_0^2 and the co-factor matrix $\mathbf{Q}_{ll}$. The inverse of the co-factor matrix formally describes the weight matrix of the observations $\mathbf{P}_{ll} = \mathbf{Q}_{ll}^{-1}$.

The optimal solution in a least squares sense for the parameters, $\boldsymbol{x} = \boldsymbol{x}_0 + \Delta x$, is found by minimizing the residuals $\boldsymbol{v} = \mathbf{A}(\boldsymbol{x}_0 + \Delta\boldsymbol{x}) - \boldsymbol{l}$ weighted with the covariance information

$$\boldsymbol{v}^T\mathbf{Q}_{ll}^{-1}\boldsymbol{v} = \boldsymbol{v}^T\mathbf{P}_{ll}\boldsymbol{v} \rightarrow \min. \tag{A.1.7}$$

In case of a linear least squares approach, approximate values for the parameters are not necessary and one usually assumes $\boldsymbol{x}_0 = \mathbf{0}$. Expanding equation (A.1.7) and computing the first derivative with respect to $\boldsymbol{x}$ and setting it to zero, leads to (e.g., Niemeier, 2008)

$$\begin{aligned} (\mathbf{A}^T\mathbf{P}_{ll}\mathbf{A})\boldsymbol{x} - \mathbf{A}^T\mathbf{P}_{ll}(\mathbf{A}(\boldsymbol{x}_0 + \Delta\boldsymbol{x}) - \boldsymbol{l}) &= \mathbf{0}, \\ (\mathbf{A}^T\mathbf{P}_{ll}\mathbf{A})\boldsymbol{x} &= \mathbf{A}^T\mathbf{P}_{ll}(\mathbf{A}(\boldsymbol{x}_0 + \Delta\boldsymbol{x}) - \boldsymbol{l}). \end{aligned} \tag{A.1.8}$$

Introducing the normal equation matrix $\mathbf{N} = \mathbf{A}^T\mathbf{P}\mathbf{A}$ and the corresponding right hand side $\boldsymbol{n} = \mathbf{A}^T\mathbf{P}(\boldsymbol{l} - \mathbf{A}\boldsymbol{x}_0)$, the normal equation system from equation (A.1.7) is given by

$$\mathbf{N}\widetilde{\boldsymbol{x}} = \boldsymbol{n}. \tag{A.1.9}$$

Solving the linear equation system leads to an optimal estimate, $\widetilde{\boldsymbol{x}}$, in the least squares sense ($\min \boldsymbol{v}^T\mathbf{P}\boldsymbol{v}$). The corresponding covariance matrix of the parameters, $\mathbf{\Sigma}_{\widetilde{x}\widetilde{x}}$, can be derived following the laws of error propagation (Niemeier, 2008) as

$$\mathbf{\Sigma}_{\widetilde{x}\widetilde{x}} = \widetilde{\sigma}_0^2\mathbf{Q}_{\widetilde{x}\widetilde{x}} = \widetilde{\sigma}_0^2\mathbf{N}^{-1}. \tag{A.1.10}$$

An estimate for the a-posteriori variance factor can be obtained from

$$\widetilde{\sigma}_0^2 = \frac{\boldsymbol{v}^T\mathbf{P}_{ll}\boldsymbol{v}}{m - p}, \tag{A.1.11}$$

where the difference of the number of observations, m, and the number of parameters, p, describes the degrees of freedom of the overdetermined system.

In case of a given normal equation system, such as for the inversion GRACE/GRACE-FO input, the value of the quadratic optimization functional from equation (A.1.7) can be obtained without knowledge of the original observations or design matrix by

$$\boldsymbol{v}^T\mathbf{P}\boldsymbol{v} = \boldsymbol{v}_0^T\mathbf{P}\boldsymbol{v}_0 - 2\widetilde{\boldsymbol{x}}^T\boldsymbol{n} + \widetilde{\boldsymbol{x}}^T\mathbf{N}\widetilde{\boldsymbol{x}} = \boldsymbol{v}_0^T\mathbf{P}\boldsymbol{v}_0 - \widetilde{\boldsymbol{x}}^T\boldsymbol{n}, \tag{A.1.12}$$

assuming the scalar $\boldsymbol{v}_0^T\mathbf{P}\boldsymbol{v}_0$ is provided.

A.2 Modification of Normal Equation Systems

A.2.1 Reducing Parameters

Normal equation systems often contain parameters, which are necessary in order to solve the problem, but are not of interest for further investigation, e.g. scale and bias orbit parameters for estimating gravity fields. It is possible to eliminate these parameters from the solution space, while still solving those implicitly. This leads to reduced and modified normal equations (e.g., Niemeier, 2008).

First, the normal equation matrix, $\mathbf{N}$, the corresponding right hand side, $\boldsymbol{n}$, and the parameter vector $\boldsymbol{x}$ are sorted into blocks of parameters to keep, k, and parameters to reduce, r, as

$$\mathbf{N} = \begin{bmatrix} \mathbf{N}_{rr} & \mathbf{N}_{rk} \\ \mathbf{N}_{kr} & \mathbf{N}_{kk} \end{bmatrix} \widetilde{\boldsymbol{x}} = \begin{bmatrix} \widetilde{\boldsymbol{x}_r} \\ \widetilde{\boldsymbol{x}_k} \end{bmatrix} = \boldsymbol{n} = \begin{bmatrix} \boldsymbol{n}_r \\ \boldsymbol{n}_k \end{bmatrix}. \tag{A.2.1}$$

To solve this linear equation system, the first row of equation (A.2.1) is first solved for $\widetilde{\boldsymbol{x}_r}$ leading to

$$\widetilde{\boldsymbol{x}_r} = \mathbf{N}_{rr}^{-1}(\boldsymbol{n}_r - \mathbf{N}_{rk}^{-1}\widetilde{\boldsymbol{x}_k}). \tag{A.2.2}$$

Insertion into the second row results in

$$\mathbf{N}_{kk}\widetilde{\boldsymbol{x}_k} + \mathbf{N}_{kr}\mathbf{N}_{rr}^{-1}(\boldsymbol{n}_r - \mathbf{N}_{rk}\widetilde{\boldsymbol{x}_k}) = \boldsymbol{n}_k, \tag{A.2.3}$$

which sorted for $\widetilde{\boldsymbol{x}_k}$ becomes

$$(\mathbf{N}_{kk} - \mathbf{N}_{kr}\mathbf{N}_{rr}^{-1}\mathbf{N}_{rk})\widetilde{\boldsymbol{x}_k} = \boldsymbol{n}_k - \mathbf{N}_{kr}\mathbf{N}_{rr}^{-1}\boldsymbol{n}_r, \tag{A.2.4}$$

where the term in the brackets on the left hand side is called "Schur form". Solving for $\widetilde{\boldsymbol{x}_k}$ results in

$$\widetilde{\boldsymbol{x}_k} = (\mathbf{N}_{kk} - \mathbf{N}_{kr}\mathbf{N}_{rr}^{-1}\mathbf{N}_{rk})^{-1}(\boldsymbol{n}_k - \mathbf{N}_{kr}\mathbf{N}_{rr}^{-1}\boldsymbol{n}_r). \tag{A.2.5}$$

This can be rearranged to again adapt the form of a linear equation system

$$\begin{aligned} \widehat{\mathbf{N}}\widetilde{\boldsymbol{x}_k} &= \widehat{\boldsymbol{n}}, \\ \widehat{\mathbf{N}} &= (\mathbf{N}_{kk} - \mathbf{N}_{kr}\mathbf{N}_{rr}^{-1}\mathbf{N}_{rk}), \\ \widehat{\boldsymbol{n}} &= \boldsymbol{n}_k - \mathbf{N}_{kr}\mathbf{N}_{rr}^{-1}\boldsymbol{n}_r, \\ \widehat{\boldsymbol{v}_0^T\mathbf{P}\boldsymbol{v}_0} &= \boldsymbol{v}_0^T\mathbf{P}\boldsymbol{v}_0 - \boldsymbol{n}_r^T\mathbf{N}_{rr}^{-1}\boldsymbol{n}_r, \\ \widehat{m} &= m, \\ \widehat{p} &= p. \end{aligned} \tag{A.2.6}$$

Since the parameters are only eliminated implicitly, the degrees of freedom of the normal equation system does not change from the above operations.

A.2.2 Changing the a priori Information

For the inversion described in this thesis, it is necessary to modify the normal equations from GRACE and altimetry in order to be consistent in signal content. Consequently, one needs to adapt the a priori signal content, e.g., applied corrections, before further combination.

Given system of normal equations with an a priori solution, $\boldsymbol{x}_0$, is then modified by adding a small change $\boldsymbol{\delta x}$ resulting in $\widehat{\boldsymbol{x}}_0 = \boldsymbol{x}_0 + \boldsymbol{\delta x}_0$. Only the right hand side and the minimization cost

function need to be modified, while keeping the degrees of freedom constant:

$$\begin{aligned}
\widehat{\mathbf{N}}\widetilde{\boldsymbol{x}} &= \widehat{\boldsymbol{n}}, \\
\widehat{\mathbf{N}} &= \mathbf{N}, \\
\widehat{\boldsymbol{n}} &= \mathbf{A}^T\mathbf{P}(\boldsymbol{l} - \mathbf{A}\widehat{\boldsymbol{x}}_0) = \boldsymbol{n} - \mathbf{N}\boldsymbol{\delta x}_0, \\
\widehat{\boldsymbol{v}_0^T\mathbf{P}\boldsymbol{v}_0} &= \boldsymbol{v}_0^T\mathbf{P}\boldsymbol{v}_0 - 2\boldsymbol{\delta x}_0^T\boldsymbol{n} + \boldsymbol{\delta x}_0^T\mathbf{N}\boldsymbol{\delta x}_0, \\
\widehat{m} &= m, \\
\widehat{p} &= p.
\end{aligned} \tag{A.2.7}$$

A.2.3 Fixing Parameters to a priori Values

In case some parameters of a normal equation system are to be removed completely from the estimation, it is possible to simply fix those parameters to their a priori values. Assuming that p_f parameters are to be fixed and p_k parameters are kept for estimation, the system can be rearranged into blocks

$$\begin{bmatrix} \mathbf{N}_{kk} & \mathbf{N}_{kf} \\ \mathbf{N}_{kf}^T & \mathbf{N}_{ff} \end{bmatrix} \begin{bmatrix} \boldsymbol{x}_k \\ \boldsymbol{x}_f \end{bmatrix} = \begin{bmatrix} \boldsymbol{n}_k \\ \boldsymbol{n}_f \end{bmatrix}. \tag{A.2.8}$$

For the resulting system, the degrees of freedom increases and this becomes:

$$\begin{aligned}
\widehat{\mathbf{N}}\widetilde{\boldsymbol{x}_k} &= \widehat{\boldsymbol{n}}, \\
\widehat{\mathbf{N}} &= \mathbf{N}_{kk}, \\
\widehat{\boldsymbol{n}} &= \boldsymbol{n}_k, \\
\widehat{\boldsymbol{v}_0^T\mathbf{P}\boldsymbol{v}_0} &= \boldsymbol{v}_0^T\mathbf{P}\boldsymbol{v}_0, \\
\widehat{m} &= m, \\
\widehat{p} &= p_k.
\end{aligned} \tag{A.2.9}$$

A.2.4 Linear Transformation of Estimation Parameters

For transforming the inversion related normal equations, e.g., from the GRACE mission, from the gravity field solution space, described by the $p \times 1$ vector $\widetilde{\boldsymbol{x}}$, to the solution space of the fingerprints, represented by the $p_t \times 1$ vector $\widehat{\boldsymbol{x}}$, is possible in case the transformed state is linearly dependent on the unknowns of the original system itself:

$$\widetilde{\boldsymbol{x}} = \mathbf{B}\widehat{\boldsymbol{x}}. \tag{A.2.10}$$

The transformation matrix $\mathbf{B}$ is a $p \times p_t$ matrix where p_t is the size of the transformed solution space. Consequently the transformed observation equation from (A.1.2) becomes

$$\boldsymbol{l} - \mathbf{A}\boldsymbol{x}_0 + \boldsymbol{v} = \mathbf{AB}\boldsymbol{x}. \tag{A.2.11}$$

The resulting transformed system is then given by

$$\begin{aligned}
\widehat{\mathbf{N}}\widetilde{\boldsymbol{x}} &= \widehat{\boldsymbol{n}}, \\
\widehat{\mathbf{N}} &= \mathbf{B}^T\mathbf{A}^T\mathbf{PAB} = \mathbf{B}^T\mathbf{NB}, \\
\widehat{\boldsymbol{n}} &= \mathbf{B}^T\mathbf{A}^T\mathbf{P}(\boldsymbol{l} - \mathbf{A}\boldsymbol{x}_0) = \mathbf{B}^T\boldsymbol{n}, \\
\widehat{\boldsymbol{v}_0^T\mathbf{P}\boldsymbol{v}_0} &= \boldsymbol{v}_0^T\mathbf{P}\boldsymbol{v}_0, \\
\widehat{m} &= m, \\
\widehat{p} &= p_t.
\end{aligned} \tag{A.2.12}$$

The modified a priori vector, $\widehat{\boldsymbol{x}}_0$, follows from solving

$$\mathbf{B}\widehat{\boldsymbol{x}}_0 = \boldsymbol{x}_0. \tag{A.2.13}$$

A.2.5 Variance Component Estimation

Variance Component Estimation (VCE) is a technique to weight normal equation systems with similar parameters from different sources against each other as described, e.g., in Förstner (1979) and Koch and Kusche (2002). In the context of this thesis this refers to weighting normal equation systems from K sources, such as GRACE and altimetry data and potentially other data sets from SLR or Argo. The individual input systems are combined based on the same (sub-)set of parameters which is connected to their individual observations.

The combined normal equation system is given by

$$\widehat{\mathbf{N}}\widetilde{\boldsymbol{x}} = \widehat{\boldsymbol{n}}, \tag{A.2.14}$$

with

$$\begin{aligned}
\widehat{\mathbf{N}} &= \sum_{i=1}^{K} \frac{1}{\sigma_i^2}\mathbf{N}_i, \\
\widehat{\boldsymbol{n}} &= \sum_{i=1}^{K} \frac{1}{\sigma_i^2}\boldsymbol{n}_i, \\
\widehat{\boldsymbol{v}_0^T\mathbf{P}\boldsymbol{v}_0} &= \sum_{i=1}^{K} \frac{1}{\sigma_i^2}\left[v_0^T\mathbf{P}\boldsymbol{v}_0\right]_i, \\
\widehat{m} &= \sum_{i=1}^{K} m_i, \\
\widehat{p} &= p,
\end{aligned} \tag{A.2.15}$$

where σ_i is the a priori variance factor. The posteriori variance component $\widetilde{\sigma}_i$ is estimated from

$$\widetilde{\sigma}_i^2 = \frac{\left[\boldsymbol{v}_i^T\mathbf{P}_{ii}\boldsymbol{v}_i\right]}{r_i}, \tag{A.2.16}$$

where the redundancy number, r_i, refers to the contribution of each individual set of observations to the total estimation result and is given by (e.g, Koch and Kusche, 2002)

$$r_i = m_i - \operatorname{trace}\left(\frac{1}{\sigma_i^2}\mathbf{N}_i\widehat{\mathbf{N}}^{-1}\right). \tag{A.2.17}$$

Note that for large systems $\widehat{\mathbf{N}}^{-1}$ might not be available requiring modified solution approaches (see e.g., Koch and Kusche, 2002). However in the context of this thesis, this is usually not necessary since the number of parameters is relatively small.

Since the posteriori $\widetilde{\sigma}_i^2$ from (A.2.16) and the a priori σ_i^2 generally do not agree, the VCE can be applied iteratively converging usually after a few iterations (e.g., Rietbroek, 2014):

1. Approximate $\sigma_i^2 = 1$, for $i = 1 \ldots K$; better approximations lead to faster convergence
2. Solve the combined normal equation system ($\widehat{\mathbf{N}}$, $\widehat{\boldsymbol{n}}$, $\widehat{\boldsymbol{v}_0^T\mathbf{P}\boldsymbol{v}_0}$, …)
3. Compute an update of the optimization functional from Eq. (A.1.12) using the combined solution $\widetilde{\widetilde{\boldsymbol{x}}}$.
4. Compute the corresponding posteriori variance factors, $\widetilde{\sigma}_i^2$
5. Check for convergence ($\widetilde{\sigma_i^2}/\sigma_i^2 \approx 1$) and update $\sigma_i^2 = \widetilde{\sigma}_i^2$, for all K observation groups if necessary.

A.3 Autoregressive Process

This section generally follows Schuh et al. (2014), Schuh (2016), and Schuh and Brockmann (2019) for introducing autoregressive processes for modeling covariance information, decorrelation of the observation and enhancing the estimated parameters.

The observation model for a discrete time $t \in \mathbb{Z}$ from equation (A.1.2) is not perfect and the residual can be interpreted as a combination of deterministic and stochastic processes (Schuh et al., 2014)

$$\mathcal{S}_t = \mathcal{L}_t - \mathbf{A}_t\boldsymbol{\xi}, \tag{A.3.1}$$

where $\boldsymbol{\xi}$ are the true parameters and $\mathcal{L}_t$ and $\mathcal{S}_t$, respectively, describe random processes of the observation and unmodeled additional signal content including noise. Stochastic processes are considered to be stationary and possess a probability density function with corresponding expectation, $E[.]$ and variance $\Sigma[.]$. The observation at time t is usually not independent, but, rather correlated with observations at $t-1$, $t-2$, ..., $t-p$. This can be expressed by interpreting $\mathcal{S}_t$ as the result from an autoregressive process of order p or short AR(p) (Schuh et al., 2014), which is defined as

$$\mathcal{S}_t = \alpha_1\mathcal{S}_{t-1} + \alpha_2\mathcal{S}_{t-2} + \cdots + \mathcal{E}_t = \mathcal{E}_t + \sum_{j=1}^{p}\alpha_j\mathcal{S}_{t-j}, \tag{A.3.2}$$

where $\mathcal{E}_t$ is a random white noise process with expectation $E[\mathcal{E}_t] = 0$ and variance $\Sigma[\mathcal{E}_t] = \sigma_{\mathcal{E}}^2$. The parameters α_j, $j = 1 \dots p$ are the process parameters of the autoregressive process. Applying the expectation operator to equation (A.3.1) results in $E[\mathcal{S}_t] = 0$. Following Schuh et al. (2014) and Schuh (2016), the auto-covariances are defined by $\gamma^{\mathcal{S}}_{|t-j|} := E[\mathcal{S}_{u-j}\mathcal{S}_{u-t}]$, which allows to connect these with the process coefficients, α_j, resulting in the so called Yule-Walker equations (Schuh et al., 2014)

$$\sum_{j=1}^{p}\alpha_j\gamma^{\mathcal{S}}_{|t-j|} = \begin{cases}\gamma^{\mathcal{S}}_0 - \sigma^2_{\mathcal{E}} & \text{for } k = 0\\ \gamma^{\mathcal{S}}_k & \text{for } k > 0.\end{cases} \tag{A.3.3}$$

Due to the assumption of stationarity and regularly sampled data, the covariances only depend on the lag k. Sorting for the autoregressive coefficients and rewriting equation (A.3.3) in matrix-vector this becomes (Schuh et al., 2014)

$$\begin{bmatrix}\gamma^{\mathcal{S}}_0\\ \gamma^{\mathcal{S}}_1\\ \vdots\\ \gamma^{\mathcal{S}}_p\\ \gamma^{\mathcal{S}}_{p+1}\\ \vdots\end{bmatrix} = \begin{bmatrix}\gamma^{\mathcal{S}}_1 & \gamma^{\mathcal{S}}_2 & \cdots & \gamma^{\mathcal{S}}_p\\ \gamma^{\mathcal{S}}_0 & \gamma^{\mathcal{S}}_1 & \cdots & \gamma^{\mathcal{S}}_{p-1}\\ \vdots & \vdots & & \vdots\\ \gamma^{\mathcal{S}}_{p-1} & \gamma^{\mathcal{S}}_{p-2} & \cdots & \gamma^{\mathcal{S}}_0\\ \gamma^{\mathcal{S}}_p & \gamma^{\mathcal{S}}_{p-1} & \cdots & \gamma^{\mathcal{S}}_1\\ \vdots & \vdots & & \vdots\end{bmatrix}\begin{bmatrix}\alpha_1\\ \alpha_2\\ \vdots\\ \alpha_p\end{bmatrix} + \begin{bmatrix}\sigma^2_{\mathcal{E}}\\ 0\\ \vdots\\ 0\\ 0\\ \vdots\end{bmatrix}. \tag{A.3.4}$$

Utilizing the empirical covariances allows to estimate the process parameters α. Reordering the first $p+1$ equations in equation (A.3.4) according to the order of covariances (Schuh, 2016) leads to

$$\left(\begin{bmatrix}-1 & & & & & \\ \alpha_1 & -1 & & & & \\ \alpha_1 & \alpha_2 & -1 & & & \\ \vdots & \vdots & \vdots & \ddots & & \\ \alpha_{p-1} & \alpha_{p-2} & \alpha_{p-3} & \cdots & -1 & \\ \alpha_p & \alpha_{p-1} & \alpha_{p-2} & \cdots & \alpha_1 & -1\end{bmatrix} + \begin{bmatrix}0 & \alpha_1 & \cdots & \alpha_{p-2} & \alpha_{p-1} & \alpha_p\\ 0 & \alpha_2 & \cdots & \alpha_{p-1} & \alpha_p & \\ 0 & \alpha_3 & \cdots & \alpha_p & & \\ \vdots & \vdots & \iddots & & & \\ 0 & \alpha_p & & & & \\ 0 & & & & & \end{bmatrix}\right)\begin{bmatrix}\gamma^{\mathcal{S}}_0\\ \gamma^{\mathcal{S}}_1\\ \gamma^{\mathcal{S}}_2\\ \vdots\\ \gamma^{\mathcal{S}}_{p-1}\\ \gamma^{\mathcal{S}}_p\end{bmatrix} = \begin{bmatrix}-\sigma^2_{\mathcal{E}}\\ 0\\ 0\\ \vdots\\ 0\\ 0\end{bmatrix}, \tag{A.3.5}$$

which can be solved for the first p auto-covariances. The remaining covariances can be derived from the recursive relation

$$\begin{aligned}\gamma^{\mathcal{S}}_{p+1} &= \alpha_1\gamma^{\mathcal{S}}_{p} \quad + \alpha_2\gamma^{\mathcal{S}}_{p-1} + \ldots + \alpha_p\gamma^{\mathcal{S}}_{1} \\ \gamma^{\mathcal{S}}_{p+1} &= \alpha_1\gamma^{\mathcal{S}}_{p+1} + \alpha_2\gamma^{\mathcal{S}}_{p} \quad + \ldots + \alpha_p\gamma^{\mathcal{S}}_{2} \\ \gamma^{\mathcal{S}}_{p+2} &= \ldots\end{aligned} \tag{A.3.6}$$

Together, equations (A.3.5) and (A.3.6) form the reorganized Yule-Walker equations which allow to derive the auto-covariances for each lag $k \in \mathbb{N}$ based on the process parameters, α.

The covariances are then used to decorrelate the observations, which means the corresponding covariance matrix will be an identity matrix $\mathbf{\Sigma}_{ll} = \mathbf{I}$, before re-estimating the parameters $\boldsymbol{x}$. This is achieved by decomposing the signal covariance matrix, $\mathbf{\Sigma}_{\mathcal{SS}}$, by applying the Cholesky decomposition

$$\mathbf{\Sigma} = \mathbf{R}^T\mathbf{R}, \tag{A.3.7}$$

where $\mathbf{R}$ is an upper triangular matrix. From

$$\mathbf{H\Sigma H}^T = \mathbf{HR}^T\mathbf{RH}^T \stackrel{!}{=} \mathbf{I} \tag{A.3.8}$$

it becomes clear that the decorrelation matrix is given by $\mathbf{H} = (\mathbf{R}^T)^{-1}$ (Schuh et al., 2014). This leads to a system of linear equations which can then be easily solved for the decorrelated observations, $\bar{\boldsymbol{l}}$, and corresponding design matrix, $\bar{\mathbf{A}}$, utilizing the triangular structure of $\mathbf{R}$

$$\begin{aligned}\mathbf{R}^T\bar{\boldsymbol{l}} &= \boldsymbol{l}, \\ \mathbf{R}^T\bar{\mathbf{A}} &= \mathbf{A}.\end{aligned} \tag{A.3.9}$$

The decorrelated observations and design matrix are then used for re-estimating the parameters of interest following Section A.1.

In this thesis, the AR(p) process is used to model covariances of the individual sea level time series leading to more realistic error estimates for the derived mean, trend, and seasonal parameters. In general, time series rarely include error or covariance information resulting in unrealistically small errors for estimated parameters, such as trend estimates in the context of sea level budgets. However for real data, the assumptions of stationarity and regular sampling are generally not true, e.g., due to missing months of GRACE, leading to data gaps. Consequently, these have to be considered for the individual lags when deriving the covariances, $\gamma^{\mathcal{S}}_k$ (Schuh and Brockmann, 2019).

Appendix B

Principal Component Analysis

Structured data on p numerical variables, given for each of n individual entities, can be analyzed by finding the best fitting linear combination of defined base functions, which represent the data in its entirety using Principal Component Analysis (PCA) (Jolliffe and Cadima, 2016). In the context of this thesis, this transfers to a $p \times n$ data matrix $\mathbf{X}$ containing data on p well defined positions, such as grid points, and n (regular) points in time, e.g. in the case of monthly observations and model data. In other words, the rows of the matrix contain the time series of data for an individual location whereas the columns contain data from all location at a certain epoch.

Before any further analysis is applied to the data, it is possible to weight the data, e.g., based on accuracy information or based on location dependent factors $\bar{\mathbf{X}} = \mathbf{XW}$ with the weight matrix $\mathbf{WW}^T = \mathbf{P}$. Usually, the data is analyzed as time series per location, which leads to the $n \times n$ signal covariance matrix

$$\mathbf{\Sigma}_{nn} = \frac{1}{n}\mathbf{X}^T\mathbf{X}. \tag{B.0.1}$$

Similarly, the $p \times p$ spatial covariance matrix $\mathbf{\Sigma}_{pp}$ of the positions can be defined. However in this thesis, the focus is on $\mathbf{\Sigma}_{nn}$ for finding time independent spatial patterns and temporally varying scaling factors.

As part of the Empirical Orthogonal Function (EOF) or PCA method, the data matrix can be decomposed using eigenvalue decomposition

$$\mathbf{\Sigma}_{nn} = \mathbf{U\Lambda U}^T, \tag{B.0.2}$$

where $\mathbf{\Lambda}$ contains the n eigenvalues λ_i $(i = 1...n)$ on its diagonal. The matrix $\mathbf{U}$ contains the corresponding eigenvectors as its columns. The eigenvalue matrix, $\mathbf{U}$, is an ortho-normal matrix, i.e. it fulfills $\mathbf{UU}^T = \mathbf{I}$, with the identity matrix $\mathbf{I}$. The sum of all eigenvalues, i.e. the trace of $\mathbf{\Lambda}$, equals the trace of $\mathbf{\Sigma}_{nn}$, representing the total signal variance. Consequently, it is possible to derive the percentage of variance explained by each eigenvalue from

$$\nu_i = \frac{\lambda_i}{\sum_{k=1}^{n} \lambda_k} = \frac{\lambda_i}{\text{trace}(\mathbf{\Lambda})}. \tag{B.0.3}$$

Conventionally, the eigenvalues and corresponding eigenvectors are sorted from largest to smallest explained variance.

Similarly, it is often convenient to decompose the data matrix, $\mathbf{X}$, directly using Singular Value Decomposition (SVD)

$$\mathbf{X} = \mathbf{USV}^T, \tag{B.0.4}$$

where $\mathbf{S}$ is the $p \times n$ contains the singular values s_i on its main diagonal, which are related to the eigenvalues by $s_i = \sqrt{\lambda_i}$. Since $\mathbf{X}$ is generally not a square matrix, $\mathbf{S}$ will contain at most

$m = \min(p, n)$ distinct singular values. The columns of $\mathbf{U}$ are the eigenvectors of $\mathbf{\Sigma}_{nn}$, while the columns of $\mathbf{V}$ are the eigenvectors of $\mathbf{\Sigma}_{pp}$.

The columns of the eigenvector matrix $\mathbf{U}$ represent common (spatial) patterns within the entire dataset. These patterns are generally called EOFs or "modes". Due to the conventional sorting of the eigenvalues, the corresponding EOFs will also be sorted from the most dominant patterns to less distinct or small scale patterns. Since each EOF consists of p entries it is easily possible to visualize individual EOFs on a grid. The EOFs can be considered a basis for representing the dataset of interest

$$\boldsymbol{x}_i = \mathbf{U}\boldsymbol{d}_i, \tag{B.0.5}$$

where $\boldsymbol{d}_i$ are the corresponding Principal Component (PC). From comparing equations (B.0.4) and (B.0.5) it is obvious that the PCs, $\mathbf{D}$, are derived from

$$\mathbf{D} = \mathbf{S}\mathbf{V}^T, \tag{B.0.6}$$

and can be interpreted as the temporal evolution of scaling factors needed in order to reconstruct the input data, $\mathbf{X}$, from the orthonormal basis, $\mathbf{U}$, defined by the EOFs. Given the EOF basis vectors, it is possible to derive PCs by projecting the data matrix $\mathbf{X}$ onto the basis. Furthermore, the known EOF basis vectors derived from $\mathbf{X}$ can be utilized to project other datasets $\mathbf{Y}$ onto the same basis in a least squares sense ($y_i + v_i = \mathbf{U}\widetilde{\boldsymbol{d}}_i$)

$$\widetilde{\boldsymbol{d}}_i = (\mathbf{U}^T\mathbf{U})^{-1}\mathbf{U}^T\boldsymbol{y}_i. \tag{B.0.7}$$

Besides limiting the number of EOFs and PCs by the rank of the data matrix, it is possible to further manually limit the number of EOFs, effectively filtering the dataset; based on the represented total variance of each EOF one could, e.g., decide to only reconstruct the data to up to 90% of the total variance, discarding the high frequency noise.

In the context of this thesis, the PCA method is used to decompose auxiliary datasets into sets of (time invariant) spatial patterns, i.e. EOFs, which are then introduced as empirical spatial basis functions, called fingerprints (see Sect. 6.1), into the inversion method and fitted to gravity and altimetry observations in order to derive the best fitting scaling factors (similar to Eq. (B.0.7)). This includes the assumption that the utilized auxiliary data, such as ocean model data, includes valid spatial information, but insufficient information on temporal variations (PCs), which are then (re-)estimated based on the observations.

Appendix C

Additional Global Sea Level Budget Results

This section includes additional global mean sea level budget results from different time periods based on inversions presented in Chapter 7.

Table C.1: Sea level budgets from the main inversion solutions IS001 (Tab. 7.12) and IS030 (Tab. 7.15) in this thesis, evaluated for different commonly used time periods. Budgets are evaluated at the input altimetry positions and inclination weights (Eq. (5.2.1)) are utilized for averaging. However, it should be noted that trends are most stable estimated from full time periods, i.e. full years.

Inversion ID	Total	Mass	Steric	Greenland	Antarctica	Glaciers	Hydrology	IMV	Steric $> 700\,\mathrm{m}$	Steric $< 700\,\mathrm{m}$	Ocean Dynamics
	2005-01 until 2015-12										
IS001	3.43	1.89	1.41	0.75	0.42	0.64	0.21	−0.11	1.04	0.38	0.12
IS030	3.80	2.68	1.07	0.77	0.43	0.78	1.05	−0.32	0.68	0.39	0.05
	2002-04 until 2015-12										
IS001	3.21	1.68	1.40	0.69	0.36	0.62	0.10	−0.08	1.07	0.33	0.13
IS030	3.38	2.27	1.10	0.70	0.37	0.70	0.77	−0.26	0.77	0.33	0.01
	2002-04 until 2016-08										
IS001	3.34	1.83	1.40	0.69	0.36	0.64	0.23	−0.08	1.05	0.35	0.11
IS030	3.47	2.38	1.05	0.69	0.37	0.71	0.85	−0.23	0.73	0.33	0.04
	2002-04 until 2020-12, excluding bad GRACE data after 2016-08										
IS001	3.58	2.14	1.21	0.64	0.36	0.67	0.53	−0.06	0.90	0.31	0.23
IS030	3.12	2.45	0.67	0.64	0.36	0.71	0.89	−0.15	0.42	0.24	0.01
	2005-01 until 2020-12, excluding bad GRACE data after 2016-08										
IS001	3.78	2.35	1.16	0.65	0.38	0.69	0.70	−0.06	0.84	0.32	0.27
IS030	3.22	2.67	0.53	0.66	0.39	0.74	1.04	−0.15	0.29	0.25	0.02
	2002-04 until 2020-12, GRACE/GRACE-FO gap filled with SLR and Swarm										
IS031	3.16	2.63	0.55	0.53	0.53	0.68	1.03	−0.14	0.36	0.19	−0.02

Appendix D

Acronyms

σ°	Backscatter Coefficient 9, 38, 40, 49, 51, 55–60, 63, 65–67, 70, 71, 74–76, 185, 186, 189
ALES	Adaptive Leading Edge Subwaveform 58
AMOC	Atlantic Meridional Overturning Circulation 147, 150
AOD1B	Atmosphere and Ocean De-aliasing Level-1B 43, 48, 87, 88, 90, 91, 99, 100, 105, 115, 116, 131, 132, 147, 161, 175, 177, 186
AVISO	Archiving, Validation and Interpretation of Satellite Oceanographic data 39, 41, 82, 84, 123–127
AWI	Alfred Wegener Institute, Bremerhaven 47
CERES	Clouds and the Earth's Radiant Energy System 28, 181–184, 190
CMEMS	Copernicus Marine Environment Monitoring Service 45, 126
CNES	Centre national d'études spatiales 35, 39
CORA	Coriolis Ocean database for ReAnalysis 45, 46
CRF	Conditional Random Field 60, 61
CSIRO	Commonwealth Scientific and Industrial Research Organisation 41, 82, 84, 123, 124
CSR	Center for Space Research 42, 43, 89, 178
DBSCAN	Density-Based Spatial Clustering of Applications with Noise 66–68, 71
DDA	Delay Doppler Altimetry 3, 5, 7, 9, 10, 35, 40, 49, 58, 72, 76–78, 185, 186, 189
DEM	Digital Elevation Model 52
DLR	Deutsches Zentrum für Luft- und Raumfahrt e.V. 41
DORIS	Doppler Orbitography and Radio-positioning Integrated by Satellite 29, 38
ECMWF	European Centre for Medium-Range Weather Forecasts 37, 40, 145
EEI	Earth Energy Imbalance 3, 5, 25, 28, 81, 119, 175, 181–184, 189, 190
ENSO	El Niño Southern Oscillation 4, 99, 147, 150, 174
EOF	Empirical Orthogonal Function 98–104, 110, 115–118, 129, 144, 145, 150, 152–154, 158, 160, 163, 169, 170, 180, 182, 183, 188, 201, 202
ESA	European Space Agency 35, 40, 44, 56
EWH	Equivalent Water Height 16, 19–21, 42, 86–89, 91, 100, 102, 131, 133, 145, 186
FESOM	Finite Element Sea Ice-Ocean Model 47, 101, 150, 154, 159

GDR Geophyiscal Data Records 56, 57
GFZ Deutsches GeoForschungsZentrum 42, 43, 162, 163, 187
GIA Glacial Isostatic Adjustment 2, 7, 9, 13, 47, 81, 82, 85, 86, 88–90, 102–105, 116, 117, 119, 121, 124, 128, 153–156, 161, 171, 173–175, 186–190
GMSL Global Mean Sea Level 2, 4, 6, 7, 9, 11, 41, 82–85, 123–125, 157, 174, 186, 187
GNSS Global Navigation Satellite System 38, 44
GPS Global Positioning System 29, 37, 41, 42
GRACE Gravity Recovery And Climate Experiment 3–5, 7–10, 41–44, 47, 48, 85, 86, 88, 89, 95, 97, 99, 102, 104, 105, 109, 111–115, 117–121, 126, 128–132, 134–142, 144–147, 149, 151, 153, 156, 159, 161–164, 167, 169–171, 173–175, 177, 179–181, 183, 184, 186–188, 190, 193–197, 199, 203
GRACE-FO Gravity Recovery And Climate Experiment Follow On 3, 4, 10, 41–44, 47, 48, 85, 86, 88, 105, 109, 112, 113, 115, 117–121, 125, 128–131, 134–137, 139–151, 153, 156, 159–167, 169–171, 175, 177, 179–181, 183, 184, 188, 194, 203
GSFC Goddard Space Flight Center 43, 88, 128, 129, 134, 135, 137, 138
GSL Geocentric Sea Level 2, 20, 82, 85, 151
GSM GRACE Satellite-only Model 43

IB Inverse Barometric 39, 48, 88, 90, 91
IGG Institut für Geodäsie und Geoinformation 129, 130, 178–181
IMB Inter-Mission Bias 9, 82–84, 105–108, 110, 116, 117, 154, 155, 157, 166, 186, 188
IMV Internal Mass Variations 3, 5, 9, 19, 48, 81, 82, 99, 100, 110, 113–115, 120–122, 128, 146, 147, 153, 154, 156, 158–161, 164, 166, 167, 170, 173–175, 187, 189
IOD Indian Ocean Dipole 4, 147, 150, 174
IPRC International Pacific Research Center 46, 92, 93, 149
ITR Improved Threshold Retracker 57
ITRF International Terrestrial Reference Frame 29, 33
ITRS International Terrestrial Reference System 29

JPL Jet Propulsion Laboratory 42, 43, 48, 88, 128, 129, 133–135, 137, 138, 145, 163

KBR K-Band Ranging System 112

MAD Median Absolute Deviation 69
MDT Mean Dynamic Topography 101
MSS Mean Sea Surface 39, 65, 66, 74, 79, 185

NASA National Aeronautics and Space Administration 35, 41, 56, 182
NCEP U.S. National Centers for Environmental Prediction 37
NEQ Normal EQuation 43, 44, 117
NOAA National Oceanic and Atmospheric Administration 40

OBP Ocean Bottom Pressure 48, 87, 88, 90, 91, 99, 100, 115, 131–133, 186, 187
OHC Ocean Heat Content 3, 10, 25, 28, 29, 118, 181–184, 189, 190
OHU Ocean Heat Uptake 28, 29, 118, 181–184, 189, 190
OMC Ocean Mass Change 3, 4, 7–11, 44, 82, 85–91, 105, 119–123, 125, 127–133, 136, 137, 140, 142, 144, 151, 156–159, 161, 162, 165–167, 169, 171, 173–175, 177, 179, 185–187, 189

ORAP5	Ocean ReAnalysis Pilot 5 47
ORAS4	ECMWF Ocean ReAnalysis System 4 46, 101
ORAS5	ECMWF Ocean ReAnalysis System 5 46, 47, 93, 101, 103, 104, 108, 115, 116, 118, 120, 123, 149, 150, 153, 154, 159–161, 168, 182, 183
PC	Principal Component 98–101, 103, 104, 118, 145, 152, 153, 182, 189, 202
PCA	Principal Component Analysis 95, 99, 101, 102, 110, 116, 150–154, 158, 160, 167, 169, 188, 190, 201, 202
PCR-GLOBWB	PCRaster Global Water Balance 48, 144, 145, 159
PDF	Probability Density Function 53, 55
RADS	Radar Altimetry Database System 35, 40, 84, 105, 106, 108, 110, 112, 115, 117, 154, 156, 157, 166, 187, 188
RANSAC	RANdom SAmple Consensus 58, 66–69
RDSAR	Reduced Synthetic Aperture Radar 10, 40, 58, 72, 76–79, 186
RMSE	Root Mean Square Error 149, 168
RSL	Relative Sea Level 2, 20, 81, 82, 85, 102, 103, 124, 174, 186
SAR	Synthetic Aperture Radar 35, 40, 76–79, 189
SGDR	Sensory Geophysical Data Records 39, 40, 72
SIO	Scripps Institute of Oceanography 46, 92, 149
SLA	Sea Level Anomaly 9, 39, 59, 63, 65–67, 70, 71, 74, 76–79, 82–84, 105, 185, 186, 189
SLE	Sea Level Equation 19–22, 25, 95, 97, 99
SLR	Satellite Laser Ranging 10, 29, 33, 38, 41–44, 85, 86, 88, 89, 91, 105, 109, 118, 119, 128, 129, 162, 163, 169–171, 177–181, 188, 190, 197, 203
SNREI	Spherically-symmetric Non-rotating Elastic Isotropic 16, 18, 29, 32
SSH	Sea Surface Height 35, 38–40, 49, 59, 60, 62–64, 66, 67, 70, 73, 74
STAR	Spatio-Temporal Altimetry Retracker 3, 5, 7–11, 49, 58–60, 62–67, 69–79, 185, 186, 189, 190
SVD	Singular Value Decomposition 201
SWH	Significant Wave Height 9, 38, 40, 49, 51, 53, 55, 57–60, 63, 65–67, 70, 71, 74–76, 185, 186, 189
TALES	TU-Darmstadt Adaptive Leading Edge Subwaveform 58
TEOS-10	Thermodynamic Equation of Seawater - 2010 25–28
TWS	Total Water Storage 47, 48, 88, 98, 99
VCE	Variance Component Estimation 111, 112, 116, 117, 153–155, 162, 167–169, 171, 197
VLBI	Very Long Baseline Interferometry 29
WGHM	WaterGAP Global Hydrological Model 47, 48, 82, 98, 99, 115, 144–146, 154, 158, 159, 188

List of Figures

1.1 General overview of the global fingerprint inversion framework. 5
1.2 Published regional sea level budgets in the northern Atlantic Ocean region. 6

2.1 Thin shell approximation for deriving equivalent water heights. 16
2.2 Self-consistent sea level theory. 20

3.1 Overview of individual altimetry missions and corresponding mission phases since 2000. 36
3.2 Nominal orbits for individual altimetry missions. 37
3.3 Altimetry measurement principle. 38
3.4 GRACE/GRACE-FO measurement principle. 42
3.5 Satellite laser ranging measurement principle. 43
3.6 Argo in-situ profile measurement principle. 45
3.7 Argo spatial measurement density. 46

4.1 Interaction of the emitted radar pulse with the backscattering surface and the corresponding footprint and part of the return waveform measured by the altimeter. . . 50
4.2 Theoretical altimeter return waveform over the ocean corresponding to the Brown (1977) model. 51
4.3 Exemplary waveforms along-track Jason-3, pass 213, passing over the North Sea. . . 52
4.4 STARS sub-waveform partitioning framework. 61
4.5 STAR-V3 point-cloud processing example for arbitrarily chosen Jason-3 track. 64
4.6 SLA point-cloud and straight line assumption. 67
4.7 Effect of a leverage point on the selection of final heights for STAR. 70
4.8 Study sites from Roscher et al. (2017) utilized for validation of STAR-V3. 72
4.9 Percentage of cycles retained to achieve a correlation of at least 0.9 with hourly tide gauge data from a total number of 227 available cycles. 73
4.10 Repeatability of STAR-V1 and STAR-V3. 74
4.11 Comparison of STAR-derived SWH estimates. 75
4.12 Comparison of STAR-derived wind speed estimates. 76
4.13 Comparison of RDSAR-SLA from the TALES and STAR retrackers against DDA-SLA from the SAMOSA+ method. 77
4.14 Comparison of RDSAR TALES and STAR-V3 as well as SAR-SAM+ retrackers against tide gauge data at the station Helgoland. 78
4.15 20 Hz SLA variation depending on the distance to coast. 79

5.1 Impact of processing choices on the GMSL time series based on the reference missions Topex/Poseidon and Jason-1/-2/-3. 83
5.2 Overview of individual processing steps for deriving OMC from RL06 monthly time-variable gravity data given either as spherical harmonics or in the form of mascons. . 86
5.3 Ocean mask including a 300 km buffer zone along the coastlines. 87
5.4 Steric sea level derived from different datasets. 93

6.1 Glacier locations and sub-regions extracted from the Randolph Glacier Inventory version 6. . . . 96
6.2 Drainage basins for Greenland and Antarctica. . . . 97
6.3 First three EOFs, PCs and corresponding explained variances based on the WGHM model. . . . 98
6.4 First three EOFs, converted to geoid height, PCs and corresponding explained variances based on the AOD1B-GAB product. . . . 100
6.5 Global mean steric sea level model comparison. . . . 102
6.6 First three EOFs, PCs and corresponding explained variances based on the ORAS5 ensemble mean steric sea level change of the upper 700 m ocean depth. . . . 103
6.7 First three EOFs, PCs and corresponding explained variances based on the ORAS5 ensemble mean steric sea level change from below 700 m ocean depth. . . . 104
6.8 IMB effect for the nominal Jason missions. . . . 106
6.9 IMB effect in addition to the RADS-based IMB correction from all missions considered in this thesis with respect to the combined Jason time series. . . . 108
6.10 Square roots of the estimated VCE components from the standard inversion run. . . . 112
6.11 Exemplary formal error correlation of the estimated parameter scales for 2006-06 for the standard inversion run. . . . 113
6.12 Exemplary formal error correlation of the estimated mass parameters from glaciers, Antarctica, Greenland and Hydrology for 2006-06. . . . 114

7.1 Global mean relative sea level budget overview from the base inversion for 2005-01 till 2015-12 with budget closure of 0.12 mm/yr. . . . 120
7.2 Global mean sea level budget time series. . . . 122
7.3 Comparison of GMSL derived from the inversion with other independently computed or published time series. . . . 124
7.4 Spatial trend maps of total (relative) sea level change for the period 2005-01 till 2015-12. . . . 125
7.5 Correlation with tide gauge data for selected globally distributed tide gauges. . . . 126
7.6 Correlation improvement of inversion gridded total sea level change relative to gridded monthly mean AVISO altimetry data at selected tide gauge stations. . . . 127
7.7 Spatial trend maps of OMC derived from the inversion and two mascon solutions by JPL and GSFC for the period 2005-01 till 2015-12. . . . 128
7.8 Comparison of global mean OMC time series from different data sources. . . . 129
7.9 Comparison of OBP from selected gauge stations, including at least five years of data, with OBP derived from the inversion and indivudally processed GRACE data. 132
7.10 Spatial trend map of inversion-based ice mass change over the Greenland ice sheet together with corresponding spatial trend map of induced sea level change for the period 2005-01 till 2015-12. . . . 133
7.11 Time series of inversion results from individual Greenland basins compared to external GRACE-based results and ice-altimetry. . . . 134
7.12 Spatial trend map of inversion-based ice mass change over the Antarctic ice sheet together with corresponding spatial trend map of induced sea level change for the period 2005-01 till 2015-12. . . . 136
7.13 Time series of inversion results from selected Antarctic basins compared to external GRACE-based results and ice-altimetry. . . . 138
7.14 Spatial trend maps of sea level change induced by melting from individual glacier mass regions for the period 2005-01 till 2015-12. . . . 140
7.15 Trend patterns of hydrological mass change and corresponding sea level change trends over the period 2005-01 till 2015-12. . . . 143
7.16 Comparison of inversion-based mass change in selected hydrological basins with mass changes from models and individually derived GRACE/GRACE-FO-based results. . 144
7.17 Comparison of original WGHM PC and inversion scaling factor for the first EOF mainly representing the annual signal. . . . 145

7.18 Trend map of IMV within the ocean for the period 2005-01 till 2015-12. 146
7.19 Steric sea level change trend maps for the period 2005-01 till 2015-12. 148
7.20 Comparison of model, re-analysis and inversion-based steric sea level change from the upper 700 m with in-situ profile data extracted from the easyCORA dataset. . . 149
7.21 Comparison of the Multivariate ENSO Index (MEI.v2) against the scaling factor of the EOF, which is generally associated with the ENSO phenomenon from the inversion as well as the ORAS5 and FESOM models. 150
7.22 First three EOFs, PCs and corresponding explained variances based on the residuals of total sea level change between the inversion and altimetry. 152
7.23 Inversion budget closure relative to the data period utilized for creating the steric fingerprints. 160
7.24 Inversion budget closure based on different setups of altimetry input data for the inversion. 165
7.25 Correlation improvement at selected tide gauges of inversion including all available altimetry data (IS022, Tab. 7.15) relative to the base inversion (IS002, Tab. 7.12). . 167
7.26 Improvement of monthly RMSE relative to the easyCORA time series from including in-situ steric profile observations in the inversion. 168
7.27 Global mean sea level budget time series for inversion IS031 (Tab. 7.15) including SLR and Swarm data to fill missing GRACE months and close the GRACE/GRACE-FO gap. 170
7.28 Sea level budgets for the Pacific, Atlantic, Indian and Arctic Oceans. 172
7.29 Regional relative sea level budgets for selected basins. 176
7.30 Inversion-based geocenter motion compared to other published estimates. 178
7.31 Temporal variation of the c_{20} and c_{30} gravity coefficients converted to geoid heights relative to the average over 2005-01 till 2015-12. 180
7.32 OHC for each major ocean basin. 183

List of Tables

3.1 Satellite altimetry mission overview during the GRACE/GRACE-FO era (extended from Quartly et al., 2001). . . . 36
3.2 Chosen RADS orbits and corrections. . . . 40

4.1 Conventional altimeter characteristic parameters (extended from Quartly et al., 2001). 54
4.2 Comparison of major differences between STAR versions 1,2 and 3. . . . 59
4.3 Comparison of the STAR and TALES retrackers at the European Coast. . . . 78

5.1 Inter-mission biases for the Jason-1/-2/-3 reference missions. . . . 84
5.2 GIA effect on global mean ocean mass change. . . . 88
5.3 Effect of choosing different degree-1 substitutes for deriving OMC. . . . 89
5.4 Effect of inconsistencies in the AOD1B-GAD product restoration. . . . 91

6.1 Nominal errors of the easyCORA profile data. . . . 109
6.2 Comparison of the inversion setup by Rietbroek (2014) / Rietbroek et al. (2016) and the base inversion in this thesis. . . . 116

7.1 Sea level component trends and (semi-)annual amplitude and phase for the time frame 2005-01 till 2015-12. . . . 121
7.2 GMSL trends and (semi-)annual amplitude and phase for the time frame 2005-01 till 2015-12. . . . 124
7.3 Comparison of global mean OMC trends from different data sources for the time periods 2005-01 till 2015-12 and 2018-06 till 2020-12. . . . 130
7.4 Effect on the OMC trend estimate (2005-01 till 2015-12) from choosing different "global" ocean regions for averaging. . . . 130
7.5 Standard deviation of the differences between the monthly averaged OBP gauge data and different solutions of GRACE-based OBP evaluated at the in-situ OBP gauge positions . . . 131
7.6 Greenland ice mass loss trends for the period 2005-01 till 2015-12 for the Greenland ice sheet and eight sub-basins. . . . 135
7.7 Greenland ice mass loss trends for the period 2005-01 till 2015-12 for the Antarctic ice sheet, the Antarctic Peninsula, the East Antarctic Ice Sheet (EAIS) and the West Antarctic Ice Sheet (WAIS). . . . 137
7.8 Antarctic ice mass loss trends for the period 2005-01 till 2015-12 for the 27 Antarctic basins. . . . 139
7.9 Trend, annual amplitude and phase of the major glacier regions defined by RGIv6.0 and shown in figure 6.1. . . . 141
7.10 Trend, annual amplitude and phase of the Arctic Canadian glaciers. . . . 142
7.11 Mass trends from 2005-01 till 2015-12 from different solutions for selected hydrological catchments (Fig. 7.15) ordered by basin-size. . . . 145
7.12 Tested inversion configurations in table 7.13 relative to base inversion (IS001). . . . 154
7.13 Overview on sea level budget results from different inversion configurations. . . . 155
7.14 Effect from further splitting the upper 700 m steric sea level change into thermo- and halo-steric components based on GRACE and altimetry data. . . . 159

7.15 Inversion configurations including additional input data relative to base inversions (IS001 and IS002). . . . 162
7.16 Overview on sea level budget results from different inversion configurations based on varying input data. . . . 163
7.17 Effect from further splitting the upper 700 m steric sea level change into thermo- and halo-steric components including in-situ steric profile data from easyCORA. . . . 168
7.18 Regional sea level budgets based on inversion IS030 (Tab. 7.15). . . . 172
7.19 Trend, annual amplitude and phase (2005-01 till 2015-12) of the geocenter motion from the inversion, compared to external sources. . . . 179
7.20 Trend, annual amplitude and phase (2005-01 till 2015-12) of low degree coefficients c_{20} and c_{30}, which are commonly replaced during GRACE/GRACE-FO processing. . . 181
7.21 OHU derived by directly estimating the OHC trend (first approach, Sect. 6.2.8) and scaled relative to the total surface of the Earth. . . . 182
7.22 OHU derived by utilizing a derivative filter (second approach, Sect. 6.2.8) and scaled relative to the total surface of the Earth. . . . 182

C.1 Sea level budgets from the main inversion solutions IS001 (Tab. 7.12) and IS030 (Tab. 7.15) in this thesis, evaluated for different commonly used time periods. . . . 203

Bibliography

A, G., J. Wahr, and S. Zhong. "Computations of the Viscoelastic Response of a 3-D Compressible Earth to Surface Loading: An Application to Glacial Isostatic Adjustment in Antarctica and Canada". In: *Geophysical Journal International* 192.2 (Feb. 1, 2013), pp. 557–572. ISSN: 0956-540X. DOI: 10.1093/gji/ggs030.

Ablain, M., A. Cazenave, G. Larnicol, M. Balmaseda, P. Cipollini, Y. Faugère, M. J. Fernandes, O. Henry, J. A. Johannessen, P. Knudsen, O. Andersen, J. Legeais, B. Meyssignac, N. Picot, M. Roca, S. Rudenko, M. G. Scharffenberg, D. Stammer, G. Timms, and J. Benveniste. "Improved Sea Level Record over the Satellite Altimetry Era (1993–2010) from the Climate Change Initiative Project". In: *Ocean Science* 11.1 (Jan. 13, 2015), pp. 67–82. ISSN: 1812-0784. DOI: 10.5194/os-11-67-2015.

Ablain, M., B. Meyssignac, L. Zawadzki, R. Jugier, A. Ribes, G. Spada, J. Benveniste, A. Cazenave, and N. Picot. "Uncertainty in Satellite Estimates of Global Mean Sea-Level Changes, Trend and Acceleration". In: *Earth System Science Data* 11.3 (Aug. 7, 2019), pp. 1189–1202. ISSN: 1866-3508. DOI: 10.5194/essd-11-1189-2019.

Altamimi, Z., X. Collilieux, and L. Métivier. "ITRF Combination: Theoretical and Practical Considerations and Lessons from ITRF2008". In: *Reference Frames for Applications in Geosciences*. Ed. by Z. Altamimi and X. Collilieux. International Association of Geodesy Symposia. Berlin, Heidelberg: Springer, 2013, pp. 7–12. ISBN: 978-3-642-32998-2. DOI: 10.1007/978-3-642-32998-2_2.

Amarouche, L., P. Thibaut, O. Z. ZaZanife, J.-P. Dumont, P. Vincent, and N. Steunou. "Improving the Jason-1 Ground Retracking to Better Account for Attitude Effects". In: *Marine Geodesy* 27.1-2 (2004), pp. 171–197. DOI: 10.1080/01490410490465210.

Andersen, O. and R. Scharroo. "Range and Geophysical Corrections in Coastal Regions: And Implications for Mean Sea Surface Determination". In: ed. by S. Vignudelli, A. G. Kostianoy, P. Cipollini, and J. Benveniste. Springer, 2011, pp. 103–104. DOI: 10.1007/978-3-642-12796-0.

Andersen, O. B., L. Stenseng, G. Piccioni, and P. Knudsen. "The DTU15 MSS (Mean Sea Surface) and DTU15LAT (Lowest Astronomical Tide) Reference Surface". In: ESA Living Planet Symposium 2016 ; Conference Date: 09-05-2016 Through 13-05-2016. 2016.

Balmaseda, M. A. et al. "The Ocean Reanalyses Intercomparison Project (ORA-IP)". In: *Journal of Operational Oceanography* 8 (sup1 Apr. 17, 2015), s80–s97. ISSN: 1755-876X. DOI: 10.1080/1755876X.2015.1022329.

Balmaseda, M. A., K. Mogensen, and A. T. Weaver. "Evaluation of the ECMWF Ocean Reanalysis System ORAS4". In: *Quarterly Journal of the Royal Meteorological Society* 139.674 (July 1, 2013), pp. 1132–1161. ISSN: 1477-870X. DOI: 10.1002/qj.2063.

Bandikova, T., C. McCullough, G. L. Kruizinga, H. Save, and B. Christophe. "GRACE Accelerometer Data Transplant". In: *Advances in Space Research* 64.3 (Aug. 1, 2019), pp. 623–644. ISSN: 0273-1177. DOI: 10.1016/j.asr.2019.05.021.

Barletta, V. R., M. Bevis, B. E. Smith, T. Wilson, A. Brown, A. Bordoni, M. Willis, S. A. Khan, M. Rovira-Navarro, I. Dalziel, R. Smalley, E. Kendrick, S. Konfal, D. J. Caccamise, R. C. Aster, A. Nyblade, and D. A. Wiens. "Observed Rapid Bedrock Uplift in Amundsen Sea Embayment Promotes Ice-Sheet Stability". In: *Science* 360.6395 (June 22, 2018), pp. 1335–1339. ISSN: 0036-8075, 1095-9203. DOI: 10.1126/science.aao1447. pmid: 29930133.

Barnoud, A., J. Pfeffer, A. Guérou, M.-L. Frery, M. Siméon, A. Cazenave, J. Chen, W. Llovel, V. Thierry, J.-F. Legeais, and M. Ablain. "Contributions of Altimetry and Argo to Non-Closure of the Global Mean Sea Level Budget Since 2016". In: *Geophysical Research Letters* 48.14 (2021), e2021GL092824. ISSN: 1944-8007. DOI: 10.1029/2021GL092824.

Becker, S. "Konsistente Kombination von Schwerefeld, Altimetrie und hydrographischen Daten zur Modellierung der dynamischen Ozeantopographie". PhD thesis. Bonn, Germany: Rheinische Friedrich-Wilhelms-Universität Bonn, July 18, 2012.

Berry, P. A. M. "Topography from Land Radar Altimeter Data: Possibilities and Restrictions". In: *Physics and Chemistry of the Earth, Part A: Solid Earth and Geodesy* 25.1 (Jan. 1, 2000), pp. 81–88. ISSN: 1464-1895. DOI: 10.1016/S1464-1895(00)00014-4.

Berry, P. A. M., J. D. Garlick, and R. G. Smith. "Near-Global Validation of the SRTM DEM Using Satellite Radar Altimetry". In: *Remote Sensing of Environment* 106.1 (Jan. 15, 2007), pp. 17–27. ISSN: 0034-4257. DOI: 10.1016/j.rse.2006.07.011.

Berry, P. A. M., R. F. Sanders, C. Leenmans, and E. Bron. "Generating Orthometric Heights from the ERS-1 Altimeter Geodetic Mission Dataset: Results from an Expert Systems Approach". In: *Geodesy on the Move*. Ed. by R. Forsberg, M. Feissel, and R. Dietrich. International Association of Geodesy Symposia. Berlin, Heidelberg: Springer, 1998, pp. 113–118. ISBN: 978-3-642-72245-5. DOI: 10.1007/978-3-642-72245-5_14.

Binder, K. and D. Heermann. *Monte Carlo Simulation in Statistical Physics: An Introduction*. 5th ed. Graduate Texts in Physics. Berlin Heidelberg: Springer-Verlag, 2010. ISBN: 978-3-642-03162-5. DOI: 10.1007/978-3-642-03163-2.

Blewitt, G. "Self-Consistency in Reference Frames, Geocenter Definition, and Surface Loading of the Solid Earth". In: *Journal of Geophysical Research: Solid Earth* 108.B2 (2003). ISSN: 2156-2202. DOI: 10.1029/2002JB002082.

Blewitt, G. and P. Clarke. "Inversion of Earth's Changing Shape to Weigh Sea Level in Static Equilibrium with Surface Mass Redistribution". In: *Journal of Geophysical Research: Solid Earth* 108.B6 (2003). ISSN: 2156-2202. DOI: 10.1029/2002JB002290.

Boening, C., J. K. Willis, F. W. Landerer, R. S. Nerem, and J. Fasullo. "The 2011 La Niña: So Strong, the Oceans Fell". In: *Geophysical Research Letters* 39.19 (2012). ISSN: 1944-8007. DOI: 10.1029/2012GL053055.

Boergens, E., D. Dettmering, C. Schwatke, and F. Seitz. "Treating the Hooking Effect in Satellite Altimetry Data: A Case Study along the Mekong River and Its Tributaries". In: *Remote Sensing* 8.2 (Feb. 2016), p. 91. DOI: 10.3390/rs8020091.

Boyer, T., C. M. Domingues, S. A. Good, G. C. Johnson, J. M. Lyman, M. Ishii, V. Gouretski, J. K. Willis, J. Antonov, S. Wijffels, J. A. Church, R. Cowley, and N. L. Bindoff. "Sensitivity of Global Upper-Ocean Heat Content Estimates to Mapping Methods, XBT Bias Corrections, and Baseline Climatologies". In: *Journal of Climate* 29.13 (July 1, 2016), pp. 4817–4842. ISSN: 0894-8755, 1520-0442. DOI: 10.1175/JCLI-D-15-0801.1.

Brown, G. S. "The Average Impulse Response of a Rough Surface and Its Applications". In: *IEEE Transactions on Antennas and Propagation* AP-25.1 (1977), pp. 67–74.

Brunnabend, S.-E., J. Schröter, R. Timmermann, R. Rietbroek, and J. Kusche. "Modeled Steric and Mass-Driven Sea Level Change Caused by Greenland Ice Sheet Melting". In: *Journal of Geodynamics*. Mass Transport and Mass Distribution in the System Earth 59–60 (Sept. 1, 2012), pp. 219–225. ISSN: 0264-3707. DOI: 10.1016/j.jog.2011.06.001.

Buchhaupt, C., L. Fenoglio-Marc, S. Dinardo, R. Scharroo, and M. Becker. "A Fast Convolution Based Waveform Model for Conventional and Unfocused SAR Altimetry". In: *Advances in Space Research*. The CryoSat Satellite Altimetry Mission: Eight Years of Scientific Exploitation 62.6 (Sept. 15, 2018), pp. 1445–1463. ISSN: 0273-1177. DOI: 10.1016/j.asr.2017.11.039.

Cabanes, C., A. Grouazel, K. von Schuckmann, M. Hamon, V. Turpin, C. Coatanoan, F. Paris, S. Guinehut, C. Boone, N. Ferry, C. de Boyer Montégut, T. Carval, G. Reverdin, S. Pouliquen, and P.-Y. L. Traon. "The CORA Dataset: Validation and Diagnostics of in-Situ Ocean Temperature and Salinity Measurements". In: *Ocean Science* 9.1 (Jan. 10, 2013), pp. 1–18. ISSN: 1812-0784. DOI: 10.5194/os-9-1-2013.

Calafat, F. M., T. Wahl, M. G. Tadesse, and S. N. Sparrow. "Trends in Europe Storm Surge Extremes Match the Rate of Sea-Level Rise". In: *Nature* 603.7903 (7903 Mar. 2022), pp. 841–845. ISSN: 1476-4687. DOI: 10.1038/s41586-022-04426-5.

Carillo, A., G. Sannino, V. Artale, P. M. Ruti, S. Calmanti, and A. Dell'Aquila. "Steric Sea Level Rise over the Mediterranean Sea: Present Climate and Scenario Simulations". In: *Climate Dynamics* 39.9 (Nov. 1, 2012), pp. 2167–2184. ISSN: 1432-0894. DOI: 10.1007/s00382-012-1369-1.

Caron, L., E. R. Ivins, E. Larour, S. Adhikari, J. Nilsson, and G. Blewitt. "GIA Model Statistics for GRACE Hydrology, Cryosphere, and Ocean Science". In: *Geophysical Research Letters* 45.5 (Mar. 6, 2018), pp. 2203–2212. ISSN: 0094-8276. DOI: 10.1002/2017GL076644.

Carrère, L. and F. Lyard. "Modeling the Barotropic Response of the Global Ocean to Atmospheric Wind and Pressure Forcing - Comparisons with Observations". In: *Geophysical Research Letters* 30.6 (2003). ISSN: 1944-8007. DOI: 10.1029/2002GL016473.

Cartwright, D. E. and A. C. Edden. "Corrected Tables of Tidal Harmonics". In: *Geophysical Journal International* 33.3 (Sept. 1, 1973), pp. 253–264. ISSN: 0956-540X. DOI: 10.1111/j.1365-246X.1973.tb03420.x.

Cartwright, D. E. and R. J. Tayler. "New Computations of the Tide-generating Potential". In: *Geophysical Journal International* 23.1 (June 1, 1971), pp. 45–73. ISSN: 0956-540X. DOI: 10.1111/j.1365-246X.1971.tb01803.x.

Cazenave, A., K. Dominh, S. Guinehut, E. Berthier, W. Llovel, G. Ramillien, M. Ablain, and G. Larnicol. "Sea Level Budget over 2003–2008: A Reevaluation from GRACE Space Gravimetry, Satellite Altimetry and Argo". In: *Global and Planetary Change* 65.1 (Jan. 1, 2009), pp. 83–88. ISSN: 0921-8181. DOI: 10.1016/j.gloplacha.2008.10.004.

Cazenave, A. and W. Llovel. "Contemporary Sea Level Rise". In: *Annual Review of Marine Science* 2.1 (2010), pp. 145–173. DOI: 10.1146/annurev-marine-120308-081105. eprint: https://doi.org/10.1146/annurev-marine-120308-081105.

Chafik, L., J. E. Ø. Nilsen, S. Dangendorf, G. Reverdin, and T. Frederikse. "North Atlantic Ocean Circulation and Decadal Sea Level Change During the Altimetry Era". In: *Scientific Reports* 9.1 (1 Jan. 31, 2019), p. 1041. ISSN: 2045-2322. DOI: 10.1038/s41598-018-37603-6.

Chambers, D. P. and J. A. Bonin. "Evaluation of Release-05 GGRACE Time-Variable Gravity Coefficients over the Ocean". In: *Ocean Science* 8 (2012), pp. 859–868. DOI: 10.5194/os-8-859-2012.

Chambers, D. P., A. Cazenave, N. Champollion, H. Dieng, W. Llovel, R. Forsberg, K. von Schuckmann, and Y. Wada. "Evaluation of the Global Mean Sea Level Budget between 1993 and 2014". In: *Surveys in Geophysics* 38.1 (Jan. 1, 2017), pp. 309–327. ISSN: 0169-3298, 1573-0956. DOI: 10.1007/s10712-016-9381-3.

Chambers, D. P. and J. K. Willis. "Low-frequency Exchange of Mass between Ocean Basins". In: *Journal of Geophysical Research: Oceans* 114.C11 (Nov. 5, 2009). ISSN: 0148-0227. DOI: 10.1029/2009JC005518.

Chang, L., H. Tang, S. Yi, and W. Sun. "The Trend and Seasonal Change of Sediment in the East China Sea Detected by GRACE". In: *Geophysical Research Letters* 46.3 (2019), pp. 1250–1258. ISSN: 1944-8007. DOI: 10.1029/2018GL081652.

Chao, B. F. "Caveats on the Equivalent Water Thickness and Surface Mascon Solutions Derived from the GRACE Satellite-Observed Time-Variable Gravity". In: *Journal of Geodesy* 90.9 (Sept. 1, 2016), pp. 807–813. ISSN: 0949-7714, 1432-1394. DOI: 10.1007/s00190-016-0912-y.

Chelton, D. B., J. C. Ries, B. J. Haines, Lee-Lueng Fu, and P. S. Callahan. "Satellite Altimetry". In: *Satellite Altimetry and Earth Sciences: A Handbook of Techniques and Applications*. Ed. by L.-L. Fu and A. Cazenave. 2001, pp. 1–132.

Chelton, D. B., E. J. Walsh, and J. L. MacArthur. "Pulse Compression and Sea Level Tracking in Satellite Altimetry". In: *J. Atmos. Oceanic Technol.* 6 (Oct. 1989), pp. 407–438.

Chen, J. L., C. R. Wilson, and B. D. Tapley. "Contribution of Ice Sheet and Mountain Glacier Melt to Recent Sea Level Rise". In: *Nature Geoscience* 6.7 (July 2013), pp. 549–552. ISSN: 1752-0908. DOI: 10.1038/ngeo1829.

Cheng, M., B. Tapley, and J. Ries. "Geocenter Variations from Analysis of SLR Data". In: *Reference Frames for Applications in Geosciences (REFAG2010)*. IAG Commission 1 Symposium 2010. Springer Berlin Heidelberg, Oct. 4–8, 2010. ISBN: 978-3-642-32997-5.

Church, J., N. White, K. L.F, C. Domingues, C. J.G, E. Rignot, J. Gregory, M. v.d.Broeke, A. Monaghan, and I. Velicogna. "Revisiting the Earth's Sea-Level and Energy Budgets from 1961 to 2008". In: *Geophysical Research Letters* 38 (2011).

Church, J. A., D. Roemmich, C. M. Domingues, J. K. Willis, N. J. White, J. E. Gilson, D. Stammer, A. Köhl, D. P. Chambers, F. W. Landerer, J. Marotzke, J. M. Gregory, T. Suzuki, A. Cazenave, and P.-Y. L. Traon. "Ocean Temperature and Salinity Contributions to Global and Regional Sea-Level Change". In: *Understanding Sea-Level Rise and Variability*. John Wiley & Sons, Ltd, 2010, pp. 143–176. ISBN: 978-1-4443-2327-6. DOI: 10.1002/9781444323276.ch6.

Church, J. A. and N. J. White. "A 20th Century Acceleration in Global Sea-Level Rise". In: *Geophysical Research Letters* 33.1 (2006). ISSN: 1944-8007. DOI: 10.1029/2005GL024826.

Church, J. A., N. J. White, R. Coleman, K. Lambeck, and J. X. Mitrovica. "Estimates of the Regional Distribution of Sea Level Rise over the 1950–2000 Period". In: *Journal of Climate* 17.13 (July 1, 2004), pp. 2609–2625. ISSN: 0894-8755, 1520-0442. DOI: 10.1175/1520-0442(2004)017<2609:EOTRDO>2.0.CO;2.

Dahlen, F. A. "The Passive Influence of the Oceans upon the Rotation of the Earth". In: *Geophysical Journal International* 46.2 (Aug. 1, 1976), pp. 363–406. ISSN: 0956-540X. DOI: 10.1111/j.1365-246X.1976.tb04163.x.

Dangendorf, S., F. M. Calafat, A. Arns, T. Wahl, I. D. Haigh, and J. Jensen. "Mean Sea Level Variability in the North Sea: Processes and Implications". In: *Journal of Geophysical Research: Oceans* 119.10 (2014). ISSN: 2169-9291. DOI: 10.1002/2014JC009901.

Davis, C. H. "A Robust Threshold Retracking Algorithm for Measuring Ice-Sheet Surface Elevation Change from Satellite Radar Altimeters". In: *IEEE Trans. Geosci. Remote Sens.* 35.4 (July 1997), pp. 974–979.

Davis, C. H. "Growth of the Greenland Ice Sheet: A Performance Assessment of Altimeter Retracking Algorithms". In: *IEEE Trans. Geosci. Remote Sens.* 33.5 (Sept. 1995), pp. 1108–1116.

Deng, X. "Improvement of Geodetic Parameter Estimation in Coastal Regions from Satellite Radar Altimetry". PhD thesis. Curtin University of Technology, Aug. 2003.

Dick, S., E. Kleine, N. Müller, H. Klein, and H. Komo. *The Operational Circulation Model of BSH (BSHcmod)*. Technical Report, BSH. ISNN 0956-6010. 2001.

Dieng, H. B., A. Cazenave, B. Meyssignac, and M. Ablain. "New Estimate of the Current Rate of Sea Level Rise from a Sea Level Budget Approach". In: *Geophysical Research Letters* 44.8 (Apr. 5, 2017), pp. 3744–3751. ISSN: 0094-8276. DOI: 10.1002/2017GL073308.

Dieng, H. B., H. Palanisamy, A. Cazenave, B. Meyssignac, and K. von Schuckmann. "The Sea Level Budget Since 2003: Inference on the Deep Ocean Heat Content". In: *Surveys in Geophysics* 36.2 (Mar. 1, 2015), pp. 209–229. ISSN: 0169-3298, 1573-0956. DOI: 10.1007/s10712-015-9314-6.

Dijkstra, E. W. "A Note on Two Problems in Connexion with Graphs". In: *Numerische Mathematik* 1.1 (Dec. 1, 1959), pp. 269–271. ISSN: 0945-3245. DOI: 10.1007/BF01386390.

Dinardo, S., L. Fenoglio-Marc, C. Buchhaupt, M. Becker, R. Scharroo, M. Joana Fernandes, and J. Benveniste. "Coastal SAR and PLRM Altimetry in German Bight and West Baltic Sea". In: *Advances in Space Research*. The CryoSat Satellite Altimetry Mission: Eight Years of Scientific Exploitation 62.6 (Sept. 15, 2018), pp. 1371–1404. ISSN: 0273-1177. DOI: 10.1016/j.asr.2017.12.018.

Dobslaw, H., I. Bergmann-Wolf, R. Dill, L. Poropat, M. Thomas, C. Dahle, S. Esselborn, R. König, and F. Flechtner. "A New High-Resolution Model of Non-Tidal Atmosphere and Ocean Mass Variability for de-Aliasing of Satellite Gravity Observations: AOD1B RL06". In: *Geophysical Journal International* 211.1 (Oct. 1, 2017), pp. 263–269. ISSN: 0956-540X. DOI: 10.1093/gji/ggx302.

Dobslaw, H., F. Flechtner, I. Bergmann-Wolf, C. Dahle, R. Dill, S. Esselborn, I. Sasgen, and M. Thomas. "Simulating High-Frequency Atmosphere-Ocean Mmass Variability for Dealiasing of

Satellite Gravity Observations: AOD1B RL05". In: *Jornal of Geophysical Research: Oceans* 118 (2013), pp. 3704–3711. DOI: 10.1002/jgrc.20271.

Dobslaw, H., I. Bergmann-Wolf, R. Dill, L. Poropat, and F. Flechtner. *Product Description Document for AOD1B Release 06, Rev. 6.1*. Potsdam, Germany: GFZ German Research Centre for Geosciences, Department 1: Geodesy and Remote Sensing, 2017.

Döll, P., F. Kaspar, and B. Lehner. "A Global Hydrological Model for Deriving Water Availability Indicators: Model Tuning and Validation". In: *Journal of Hydrology* 270.1 (Jan. 10, 2003), pp. 105–134. ISSN: 0022-1694. DOI: 10.1016/S0022-1694(02)00283-4.

Döll, P., H. M. Schmied, C. Schuh, F. T. Portmann, and A. Eicker. "Global-Scale Assessment of Groundwater Depletion and Related Groundwater Abstractions: Combining Hydrological Modeling with Information from Well Observations and GRACE Satellites". In: *Water Resources Research* 50.7 (2014), pp. 5698–5720. ISSN: 1944-7973. DOI: 10.1002/2014WR015595.

Döll, P., T. Trautmann, M. Göllner, and H. M. Schmied. "A Global-Scale Analysis of Water Storage Dynamics of Inland Wetlands: Quantifying the Impacts of Human Water Use and Man-Made Reservoirs as Well as the Unavoidable and Avoidable Impacts of Climate Change". In: *Ecohydrology* 13.1 (2020), e2175. ISSN: 1936-0592. DOI: 10.1002/eco.2175.

Dziewonski, A. M. and D. L. Anderson. "Preliminary Reference Earth Model". In: *Physics of the Earth and Planetary Interiors* 25.4 (June 1, 1981), pp. 297–356. ISSN: 0031-9201. DOI: 10.1016/0031-9201(81)90046-7.

Ester, M., H.-P. Kriegel, J. Sander, and X. Xu. "A Density-Based Algorithm for Discovering Clusters a Density-Based Algorithm for Discovering Clusters in Large Spatial Databases with Noise". In: *Proceedings of the Second International Conference on Knowledge Discovery and Data Mining*. (Portland, Oregon). KDD'96. AAAI Press, 1996, pp. 226–231.

Farrell, W. E. "Deformation of the Earth by Surface Loads". In: *Reviews of Geophysics* 10.3 (1972), pp. 761–797. ISSN: 1944-9208. DOI: 10.1029/RG010i003p00761.

Farrell, W. E. and J. A. Clark. "On Postglacial Sea Level". In: *Geophysical Journal of the Royal Astronomical Society* 46.3 (Sept. 1, 1976), pp. 647–667. ISSN: 1365-246X. DOI: 10.1111/j.1365-246X.1976.tb01252.x.

Feistel, R. "A Gibbs Function for Seawater Thermodynamics for −6 to 80°C and Salinity up to 120gkg–1". In: *Deep Sea Research Part I: Oceanographic Research Papers* 55.12 (Dec. 1, 2008), pp. 1639–1671. ISSN: 0967-0637. DOI: 10.1016/j.dsr.2008.07.004.

Feistel, R. "A New Extended Gibbs Thermodynamic Potential of Seawater". In: *Progress in Oceanography* 58.1 (July 1, 2003), pp. 43–114. ISSN: 0079-6611. DOI: 10.1016/S0079-6611(03)00088-0.

Feng, W. and M. Zhong. "Global Sea Level Variations from Altimetry, GRACE and Argo Data over 2005–2014". In: *Geodesy and Geodynamics* 6.4 (July 1, 2015), pp. 274–279. ISSN: 1674-9847. DOI: 10.1016/j.geog.2015.07.001.

Fenoglio, L., S. Dinardo, C. Buchhaupt, B. Uebbing, R. Scharroo, J. Kusche, M. Becker, and J. Benveniste. "Calibrating CryoSat-2 and Sentinel-3A Sea Surface Heights Along the German Coast". In: (2019), pp. 1–8. DOI: 10.1007/1345_2019_73.

Fenoglio, L., S. Dinardo, B. Uebbing, C. Buchhaupt, M. Gärtner, J. Staneva, M. Becker, A. Klos, and J. Kusche. "Advances in NE-Atlantic Coastal Sea Level Change Monitoring by Delay Doppler Altimetry". In: *Advances in Space Research*. 25 Years of Progress in Radar Altimetry 68.2 (July 15, 2021), pp. 571–592. ISSN: 0273-1177. DOI: 10.1016/j.asr.2020.10.041.

Fenoglio-Marc, L., M. Fehlau, L. Ferri, M. Becker, Y. Gao, and S. Vignudelli. "Coastal Sea Surface Heights from Improved Altimeter Data in the Mediterranean Sea". In: *Gravity, Geoid and Earth Observation*. Ed. by S. P. Mertikas. International Association of Geodesy Symposia. Berlin, Heidelberg: Springer, 2010, pp. 253–261. ISBN: 978-3-642-10634-7. DOI: 10.1007/978-3-642-10634-7_33.

Fenoglio-Marc, L., J. Kusche, and M. Becker. "Mass Variation in the Mediterranean Sea from GRACE and Its Validation by Altimetry, Steric and Hydrologic Fields". In: *Geophysical Research Letters* 33.19 (Oct. 6, 2006). ISSN: 0094-8276. DOI: 10.1029/2006GL026851.

Fenoglio-Marc, L., R. Rietbroek, S. Grayek, M. Becker, J. Kusche, and E. Stanev. "Water Mass Variation in the Mediterranean and Black Seas". In: *Journal of Geodynamics*. Mass Transport

and Mass Distribution in the System Earth 59–60 (Sept. 1, 2012), pp. 168–182. ISSN: 0264-3707. DOI: 10.1016/j.jog.2012.04.001.

Fischler, M. A. and R. C. Bolles. "Random Sample Consensus: A Paradigm for Model Fitting with Applications to Image Analysis and Automated Cartography". In: *Commun. ACM* 24.6 (June 1981), pp. 381–395. ISSN: 0001-0782. DOI: 10.1145/358669.358692.

Flechtner, F., H. Dobslaw, and E. Fagiolini. *AOD1B Product Description Document for Product Release 05*. GFZ German Research Centre for Geosciences, Department 1: Geodesy and Remote Sensing, 2015.

Förstner, W. "Ein Verfahren zur Schätzung von Varianz- und Kovarianzkomponenten". In: *Allgemeine Vermessungsnachrichten* 86.11–12 (1979), pp. 446–453.

Frappart, F., S. Calmant, M. Cauhopé, F. Seyler, and A. Cazenave. "Preliminary Results of ENVISAT RA-2-derived Water Levels Validation over the Amazon Basin". In: *Remote Sensing of Environment* 100.2 (Jan. 30, 2006), pp. 252–264. ISSN: 0034-4257. DOI: 10.1016/j.rse.2005.10.027.

Frederikse, T., F. Landerer, L. Caron, S. Adhikari, D. Parkes, V. W. Humphrey, S. Dangendorf, P. Hogarth, L. Zanna, L. Cheng, and Y.-H. Wu. "The Causes of Sea-Level Rise since 1900". In: *Nature* 584.7821 (7821 Aug. 2020), pp. 393–397. ISSN: 1476-4687. DOI: 10.1038/s41586-020-2591-3.

Frederikse, T., R. E. M. Riva, and M. A. King. "Ocean Bottom Deformation Due To Present-Day Mass Redistribution and Its Impact on Sea Level Observations". In: *Geophysical Research Letters* 44.24 (Dec. 28, 2017), pp. 12, 306–12, 314. ISSN: 1944-8007. DOI: 10.1002/2017GL075419.

Frederikse, T., R. Riva, M. Kleinherenbrink, Y. Wada, M. van den Broeke, and B. Marzeion. "Closing the Sea Level Budget on a Regional Scale: Trends and Variability on the Northwestern European Continental Shelf". In: *Geophysical Research Letters* 43.20 (2016), pp. 10, 864–10, 872. ISSN: 1944-8007. DOI: 10.1002/2016GL070750.

Frederikse, T., K. Simon, C. A. Katsman, and R. Riva. "The Sea-Level Budget along the Northwest Atlantic Coast: GIA, Mass Changes, and Large-Scale Ocean Dynamics". In: *Journal of Geophysical Research: Oceans* 122.7 (2017), pp. 5486–5501. ISSN: 2169-9291. DOI: 10.1002/2017JC012699.

Friis-Christensen, E., H. Lühr, D. Knudsen, and R. Haagmans. "Swarm – An Earth Observation Mission Investigating Geospace". In: *Advances in Space Research* 41.1 (Jan. 1, 2008), pp. 210–216. ISSN: 0273-1177. DOI: 10.1016/j.asr.2006.10.008.

García-García, D., I. Vigo, and M. Trottini. "Water Transport among the World Ocean Basins within the Water Cycle". In: *Earth System Dynamics* 11.4 (Dec. 7, 2020), pp. 1089–1106. ISSN: 2190-4979. DOI: 10.5194/esd-11-1089-2020.

Gill, A. E. and P. P. Niller. "The Theory of the Seasonal Variability in the Ocean". In: *Deep Sea Research and Oceanographic Abstracts* 20.2 (Feb. 1, 1973), pp. 141–177. ISSN: 0011-7471. DOI: 10.1016/0011-7471(73)90049-1.

Gill, A. E. *Atmosphere-Ocean Dynamics*. International Geophysics Series, v. 30. New York: Academic Press, 1982. ISBN: 978-0-08-057052-5 978-0-12-283522-3 978-1-281-71335-3.

Gommenginger, C., P. Thibaut, L. Fenoglio-Marc, G. D. Quartly, X. Deng, J. Gómez-Enri, P. Challenor, and Y. Gao. "Retracking Altimeter Waveforms Near the Coasts: A Review of Retracking Methods and Some Applications to Coastal Waveforms". In: *Coastal Altimetry*. Ed. by S. Vignudelli, A. G. Kostianoy, P. Cipollini, and J. Benveniste. Springer-Verlag Berlin Heidelberg, 2011.

Good, S. A., M. J. Martin, and N. A. Rayner. "EN4: Quality Controlled Ocean Temperature and Salinity Profiles and Monthly Objective Analyses with Uncertainty Estimates". In: *Journal of Geophysical Research: Oceans* 118.12 (2013), pp. 6704–6716. ISSN: 2169-9291. DOI: 10.1002/2013JC009067.

Gouzenes, Y., F. Léger, A. Cazenave, F. Birol, P. Bonnefond, M. Passaro, F. Nino, R. Almar, O. Laurain, C. Schwatke, J.-F. Legeais, and J. Benveniste. "Coastal Sea Level Rise at Senetosa (Corsica) during the Jason Altimetry Missions". In: *Ocean Science* 16.5 (Oct. 7, 2020), pp. 1165–1182. ISSN: 1812-0784. DOI: 10.5194/os-16-1165-2020.

Gräwe, U., K. Klingbeil, J. Kelln, and S. Dangendorf. "Decomposing Mean Sea Level Rise in a Semi-Enclosed Basin, the Baltic Sea". In: *Journal of Climate* 32.11 (June 1, 2019), pp. 3089–3108. ISSN: 0894-8755, 1520-0442. DOI: 10.1175/JCLI-D-18-0174.1.

Gregory, J. M. and J. A. Lowe. "Predictions of Global and Regional Sea-Level Rise Using AOGCMs with and without Flux Adjustment". In: *Geophysical Research Letters* 27.19 (2000), pp. 3069–3072. ISSN: 1944-8007. DOI: 10.1029/1999GL011228.

Gregory, J. M., N. J. White, J. A. Church, M. F. P. Bierkens, J. E. Box, M. R. van den Broeke, J. G. Cogley, X. Fettweis, E. Hanna, P. Huybrechts, L. F. Konikow, P. W. Leclercq, B. Marzeion, J. Oerlemans, M. E. Tamisiea, Y. Wada, L. M. Wake, and R. S. W. van de Wal. "Twentieth-Century Global-Mean Sea Level Rise: Is the Whole Greater than the Sum of the Parts?" In: *Journal of Climate* 26.13 (July 1, 2013), pp. 4476–4499. ISSN: 0894-8755, 1520-0442. DOI: 10.1175/JCLI-D-12-00319.1.

Groh, A. and M. Horwath. "The Method of Tailored Sensitivity Kernels for GRACE Mass Change Estimates". In: Geophysical Research Abstracts, 18, EGU2016-12065, EGU General Assembly 2016. Vienna, Austria, 2016.

Groh, A. and M. Horwath. "Antarctic Ice Mass Change Products from GRACE/GRACE-FO Using Tailored Sensitivity Kernels". In: *Remote Sensing* 13.9 (9 Jan. 2021), p. 1736. ISSN: 2072-4292. DOI: 10.3390/rs13091736.

Gunter, B. C., O. Didova, R. E. M. Riva, S. R. M. Ligtenberg, J. T. M. Lenaerts, M. A. King, M. R. van den Broeke, and T. Urban. "Empirical Estimation of Present-Day Antarctic Glacial Isostatic Adjustment and Ice Mass Change". In: *The Cryosphere* 8.2 (Apr. 28, 2014), pp. 743–760. ISSN: 1994-0416. DOI: 10.5194/tc-8-743-2014.

Guo, J., X. Chang, Y. Gao, J. Sun, and C. Hwang. "Lake Level Variations Monitored With Satellite Altimetry Waveform Retracking". In: *IEEE Journal of Selected Topics in applied Earth Observations and Remote Sensing* 2.2 (June 2009), pp. 80–86.

Hakuba, M. Z., T. Frederikse, and F. W. Landerer. "Earth's Energy Imbalance From the Ocean Perspective (2005–2019)". In: *Geophysical Research Letters* 48.16 (2021), e2021GL093624. ISSN: 1944-8007. DOI: 10.1029/2021GL093624.

Hakuba, M. Z., G. L. Stephens, B. Christophe, A. E. Nash, B. Foulon, S. V. Bettadpur, B. D. Tapley, and F. H. Webb. "Earth's Energy Imbalance Measured From Space". In: *IEEE Transactions on Geoscience and Remote Sensing* 57.1 (Jan. 2019), pp. 32–45. ISSN: 1558-0644. DOI: 10.1109/TGRS.2018.2851976.

Halimi, A., C. Mailhes, J.-Y. Tourneret, and H. Snoussi. "Bayesian Estimation of Smooth Altimetric Parameters: Application to Conventional and Delay/Doppler Altimetry". In: *IEEE Transactions on Geoscience and Remote Sensing* 54.4 (Apr. 2016), pp. 2207–2219. ISSN: 1558-0644. DOI: 10.1109/TGRS.2015.2497583.

Halimi, A., C. Mailhes, J.-Y. Tourneret, P. Thibaut, and F. Boy. "Parameter Estimation for Peaky Altimetric Waveforms". In: *IEEE Transactions on Geoscience and Remote Sensing* 51.3 (Mar. 2013), pp. 1568–1577. ISSN: 1558-0644. DOI: 10.1109/TGRS.2012.2205697.

Hallegatte, S., C. Green, R. J. Nicholls, and J. Corfee-Morlot. "Future Flood Losses in Major Coastal Cities". In: *Nature Climate Change* 3.9 (9 Sept. 2013), pp. 802–806. ISSN: 1758-6798. DOI: 10.1038/nclimate1979.

Han, S.-C., C. K. Shum, M. Bevis, C. Ji, and C.-Y. Kuo. "Crustal Dilatation Observed by GRACE After the 2004 Sumatra-Andaman Earthquake". In: *Science* 313.5787 (Aug. 4, 2006), pp. 658–662. DOI: 10.1126/science.1128661.

Hay, C. C., E. Morrow, R. E. Kopp, and J. X. Mitrovica. "Probabilistic Reanalysis of Twentieth-Century Sea-Level Rise". In: *Nature* 517.7535 (7535 Jan. 2015), pp. 481–484. ISSN: 1476-4687. DOI: 10.1038/nature14093.

Hayne, G. S. "Radar Altimeter Mean Retun Waveforms from Near-Normal-Incidence Ocean Surface Scattering". In: *IEEE Transactions on Antennas and Propagation* AP-28.5 (Sept. 1980), pp. 687–692.

Heiskanen, W. A. and H. Moritz. *Physical Geodesy*. Ed. by J. Gilluly and A. O. Woodford. San Francisco, CA, USA: Freeman, 1967.

Henry, O., P. Prandi, W. Llovel, A. Cazenave, S. Jevrejeva, D. Stammer, B. Meyssignac, and N. Koldunov. "Tide Gauge-Based Sea Level Variations since 1950 along the Norwegian and Russian Coasts of the Arctic Ocean: Contribution of the Steric and Mass Components". In: *Journal of Geophysical Research: Oceans* 117.C6 (2012). ISSN: 2156-2202. DOI: 10.1029/2011JC007706.

Hibbert, F. D., E. J. Rohling, A. Dutton, F. H. Williams, P. M. Chutcharavan, C. Zhao, and M. E. Tamisiea. "Coral Indicators of Past Sea-Level Change: A Global Repository of U-series Dated Benchmarks". In: *Quaternary Science Reviews* 145 (Aug. 1, 2016), pp. 1–56. ISSN: 0277-3791. DOI: 10.1016/j.quascirev.2016.04.019.

Holgate, S. J. and P. L. Woodworth. "Evidence for Enhanced Coastal Sea Level Rise during the 1990s". In: *Geophysical Research Letters* 31.7 (2004). ISSN: 1944-8007. DOI: 10.1029/2004GL019626.

Holgate, S. J., A. Matthews, P. L. Woodworth, L. J. Rickards, M. E. Tamisiea, E. Bradshaw, P. R. Foden, K. M. Gordon, S. Jevrejeva, and J. Pugh. "New Data Systems and Products at the Permanent Service for Mean Sea Level". In: *Journal of Coastal Research* 29.3 (May 2013), pp. 493–504. ISSN: 0749-0208, 1551-5036. DOI: 10.2112/JCOASTRES-D-12-00175.1.

Horwath, M. et al. "Global Sea-Level Budget and Ocean-Mass Budget, with a Focus on Advanced Data Products and Uncertainty Characterisation". In: *Earth System Science Data* 14.2 (Feb. 7, 2022), pp. 411–447. ISSN: 1866-3508. DOI: 10.5194/essd-14-411-2022.

Hosoda, S., T. Ohira, K. Sato, and T. Suga. "Improved Description of Global Mixed-Layer Depth Using Argo Profiling Floats". In: *Journal of Oceanography* 66.6 (Dec. 1, 2010), pp. 773–787. ISSN: 1573-868X. DOI: 10.1007/s10872-010-0063-3.

Hsu, S. A., E. A. Meindl, and D. B. Gilhousen. "Determining the Power-Law Wind-Profile Exponent under Near-Neutral Stability Conditions at Sea". In: *Journal of Applied Meteorology and Climatology* 33.6 (June 1, 1994), pp. 757–765. ISSN: 1520-0450, 0894-8763. DOI: 10.1175/1520-0450(1994)033<0757:DTPLWP>2.0.CO;2.

Humphrey, V. and L. Gudmundsson. "GRACE-REC: A Reconstruction of Climate-Driven Water Storage Changes over the Last Century". In: *Earth System Science Data* 11.3 (Aug. 2, 2019), pp. 1153–1170. ISSN: 1866-3508. DOI: 10.5194/essd-11-1153-2019.

Huybers, K. and G. H. Roe. "Spatial Patterns of Glaciers in Response to Spatial Patterns in Regional Climate". In: *Journal of Climate* 22.17 (Sept. 1, 2009), pp. 4606–4620. ISSN: 0894-8755, 1520-0442. DOI: 10.1175/2009JCLI2857.1.

Hwang, C., J. Guo, X. Deng, H.-Y. Hsu, and Y. Liu. "Coastal Gravity Anomalies from Retracked Geosat/GM Altimetry: Improvement, Limitation and the Role of Airborne Gravity Data". In: *Journal of Geodesy* 80.4 (July 1, 2006), pp. 204–216. ISSN: 1432-1394. DOI: 10.1007/s00190-006-0052-x.

International-Altimetry-Team. "Altimetry for the Future: Building on 25 Years of Progress". In: *Advances in Space Research*. 25 Years of Progress in Radar Altimetry 68.2 (July 15, 2021), pp. 319–363. ISSN: 0273-1177. DOI: 10.1016/j.asr.2021.01.022.

IOC, SCOR, and IAPSO. *The International Thermodynamic Equation of Seawater - 2010: Calculation and Use of Thermodynamic Properties*. 56. Intergovernmental Oceanographic Commission, Manuals and Guides No. UNESCO (English), 2010, p. 196.

Ishii, M. and M. Kimoto. "Reevaluation of Historical Ocean Heat Content Variations with Time-Varying XBT and MBT Depth Bias Corrections". In: *Journal of Oceanography* 65.3 (June 1, 2009), pp. 287–299. ISSN: 1573-868X. DOI: 10.1007/s10872-009-0027-7.

Jensen, L., R. Rietbroek, and J. Kusche. "Land Water Contribution to Sea Level from GRACE and Jason-1measurements". In: *Journal of Geophysical Research: Oceans* 118.1 (Jan. 17, 2013), pp. 212–226. ISSN: 2169-9275. DOI: 10.1002/jgrc.20058.

Jevrejeva, S., J. C. Moore, A. Grinsted, A. P. Matthews, and G. Spada. "Trends and Acceleration in Global and Regional Sea Levels since 1807". In: *Global and Planetary Change* 113 (Feb. 1, 2014), pp. 11–22. ISSN: 0921-8181. DOI: 10.1016/j.gloplacha.2013.12.004.

Jevrejeva, S., J. C. Moore, A. Grinsted, and P. L. Woodworth. "Recent Global Sea Level Acceleration Started over 200 Years Ago?" In: *Geophysical Research Letters* 35.8 (2008). ISSN: 1944-8007. DOI: 10.1029/2008GL033611.

Johnson, G. C. and D. P. Chambers. "Ocean Bottom Pressure Seasonal Cycles and Decadal Trends from GRACE Release-05: Ocean Circulation Implications". In: *Journal of Geophysical Research: Oceans* 118.9 (2013), pp. 4228–4240. DOI: 10.1002/jgrc.20307.

Johnson, G. C., J. M. Lyman, and N. G. Loeb. "Improving Estimates of Earth's Energy Imbalance". In: *Nature Climate Change* 6.7 (7 July 2016), pp. 639–640. ISSN: 1758-6798. DOI: 10.1038/nclimate3043.

Jolliffe, I. T. and J. Cadima. "Principal Component Analysis: A Review and Recent Developments". In: *Philosophical Transactions of the Royal Society A: Mathematical, Physical and Engineering Sciences* 374.2065 (Apr. 13, 2016), p. 20150202. DOI: 10.1098/rsta.2015.0202.

Jordà, G. "Detection Time for Global and Regional Sea Level Trends and Accelerations". In: *Journal of Geophysical Research: Oceans* 119.10 (2014), pp. 7164–7174. ISSN: 2169-9291. DOI: 10.1002/2014JC010005.

Jungclaus, J. H., N. Fischer, H. Haak, K. Lohmann, J. Marotzke, D. Matei, U. Mikolajewicz, D. Notz, and J. S. von Storch. "Characteristics of the Ocean Simulations in the Max Planck Institute Ocean Model (MPIOM) the Ocean Component of the MPI-Earth System Model". In: *Journal of Advances in Modeling Earth Systems* 5.2 (2013), pp. 422–446. ISSN: 1942-2466. DOI: 10.1002/jame.20023.

Kirezci, E., I. R. Young, R. Ranasinghe, S. Muis, R. J. Nicholls, D. Lincke, and J. Hinkel. "Projections of Global-Scale Extreme Sea Levels and Resulting Episodic Coastal Flooding over the 21st Century". In: *Scientific Reports* 10.1 (1 July 30, 2020), p. 11629. ISSN: 2045-2322. DOI: 10.1038/s41598-020-67736-6.

Klemann, V. and Z. Martinec. "Contribution of Glacial-Isostatic Adjustment to the Geocenter Motion". In: *Tectonophysics*. Special Section on Observation and Modeling of Glacial Isostatic Adjustment 511.3 (Sept. 10, 2009), pp. 99–108. ISSN: 0040-1951. DOI: 10.1016/j.tecto.2009.08.031.

Kobayashi, S., Y. Ota, Y. Harada, A. Ebita, M. Moriya, H. Onoda, K. Onogi, H. Kamahori, C. Kobayashi, H. Endo, K. Miyaoka, and K. Takahashi. "The JRA-55 Reanalysis: General Specifications and Basic Characteristics". In: *Journal of the Meteorological Society of Japan. Ser. II* 93.1 (2015), pp. 5–48. DOI: 10.2151/jmsj.2015-001.

Koch, K.-R. *Parameter Estimation and Hypothesis Testing in Linear Models*. 2nd ed. Berlin Heidelberg: Springer-Verlag, 1999. ISBN: 978-3-540-65257-1. DOI: 10.1007/978-3-662-03976-2.

Koch, K.-R. and J. Kusche. "Regularization of Geopotential Determination from Satellite Data by Variance Components". In: *Journal of Geodesy* 76.5 (May 1, 2002), pp. 259–268. ISSN: 1432-1394. DOI: 10.1007/s00190-002-0245-x.

Komjathy, A., L. Sparks, B. D. Wilson, and A. J. Mannucci. "Automated Daily Processing of More than 1000 Ground-Based GPS Receivers for Studying Intense Ionospheric Storms". In: *Radio Science* 40.6 (2005). ISSN: 1944-799X. DOI: 10.1029/2005RS003279.

Kornfeld, R. P., B. W. Arnold, M. A. Gross, N. T. Dahya, W. M. Klipstein, P. F. Gath, and S. Bettadpur. "GRACE-FO: The Gravity Recovery and Climate Experiment Follow-On Mission". In: *Journal of Spacecraft and Rockets* 56.3 (2019), pp. 931–951. ISSN: 0022-4650. DOI: 10.2514/1.A34326.

Kuhlbrodt, T. and J. M. Gregory. "Ocean Heat Uptake and Its Consequences for the Magnitude of Sea Level Rise and Climate Change". In: *Geophysical Research Letters* 39.18 (2012). ISSN: 1944-8007. DOI: 10.1029/2012GL052952.

Kuhlmann, J., H. Dobslaw, and M. Thomas. "Improved Modeling of Sea Level Patterns by Incorporating Self-Attraction and Loading". In: *Journal of Geophysical Research: Oceans* 116.C11 (2011). ISSN: 2156-2202. DOI: 10.1029/2011JC007399.

Kusche, J., R. Schmidt, S. Petrovic, and R. Rietbroek. "Decorrelated GRACE Time-Variable Gravity Solutions by GFZ, and Their Validation Using a Hydrological Model". In: *Journal of Geodesy* 83.10 (Oct. 1, 2009), pp. 903–913. ISSN: 1432-1394. DOI: 10.1007/s00190-009-0308-3.

Kusche, J., B. Uebbing, R. Rietbroek, C. K. Shum, and Z. H. Khan. "Sea Level Budget in the Bay of Bengal (2002–2014) from GRACE and Altimetry". In: *Journal of Geophysical Research: Oceans* 121.2 (Jan. 27, 2016), pp. 1194–1217. ISSN: 2169-9291. DOI: 10.1002/2015JC011471.

Kusche, J. "Approximate Decorrelation and Non-Isotropic Smoothing of Time-Variable GRACE-type Gravity Field Models". In: *Journal of Geodesy* 81.11 (Nov. 1, 2007), pp. 733–749. ISSN: 0949-7714, 1432-1394. DOI: 10.1007/s00190-007-0143-3.

Kvas, A., S. Behzadpour, M. Ellmer, B. Klinger, S. Strasser, N. Zehentner, and T. Mayer-Gürr. "ITSG-Grace2018: Overview and Evaluation of a New GRACE-Only Gravity Field Time Series". In: *Journal of Geophysical Research: Solid Earth* 124.8 (2019), pp. 9332–9344. ISSN: 2169-9356. DOI: 10.1029/2019JB017415.

Labroue, S., P. Gaspar, J. Dorandeu, O. Z. Zanifé, F. Mertz, P. V. Vincent, and D. Choquet. "Nonparametric Estimates of the Sea State Bias for the Jason-1 Radar Altimeter". In: *Marine Geodesy* 27.3-4 (July 1, 2004), pp. 453–481. ISSN: 0149-0419. DOI: 10.1080/01490410490902089.

Lafferty, J. D., A. McCallum, and F. C. N. Pereira. "Conditional Random Fields: Probabilistic Models for Segmenting and Labeling Sequence Data". In: *Proceedings of the Eighteenth International Conference on Machine Learning*. ICML '01. San Francisco, CA, USA: Morgan Kaufmann Publishers Inc., 2001, pp. 282–289. ISBN: 978-1-55860-778-1.

Lambeck, K., C. D. Woodroffe, F. Antonioli, M. Anzidei, W. R. Gehrels, J. Laborel, and A. J. Wright. "Paleoenvironmental Records, Geophysical Modeling, and Reconstruction of Sea-Level Trends and Variability on Centennial and Longer Timescales". In: *Understanding Sea-Level Rise and Variability*. John Wiley & Sons, Ltd, 2010, pp. 61–121. ISBN: 978-1-4443-2327-6. DOI: 10.1002/9781444323276.ch4.

Landerer, F. W., J. H. Jungclaus, and J. Marotzke. "Regional Dynamic and Steric Sea Level Change in Response to the IPCC-A1B Scenario". In: *Journal of Physical Oceanography* 37.2 (Feb. 1, 2007), pp. 296–312. ISSN: 0022-3670, 1520-0485. DOI: 10.1175/JPO3013.1.

Landerer, F. W. et al. "Extending the Global Mass Change Data Record: GRACE Follow-On Instrument and Science Data Performance". In: *Geophysical Research Letters* 47.12 (2020), e2020GL088306. ISSN: 1944-8007. DOI: 10.1029/2020GL088306.

Lebedev, K. V., H. Yoshinari, N. A. Maximenko, and P. W. Hacker. *YoMaHa'07: Velocity Data Assessed from Trajectories of Argo Floats at Parking Level and at the Sea Surface*. IPRC Technical Note No. 4. June 12, 2007.

Legeais, J.-F., M. Ablain, L. Zawadzki, H. Zuo, J. A. Johannessen, M. G. Scharffenberg, L. Fenoglio-Marc, M. J. Fernandes, O. B. Andersen, S. Rudenko, P. Cipollini, G. D. Quartly, M. Passaro, A. Cazenave, and J. Benveniste. "An Improved and Homogeneous Altimeter Sea Level Record from the ESA Climate Change Initiative". In: *Earth System Science Data* 10.1 (Feb. 12, 2018), pp. 281–301. ISSN: 1866-3508. DOI: 10.5194/essd-10-281-2018.

Lenaerts, J. T. M., E. van Meijgaard, M. R. van den Broeke, S. R. M. Ligtenberg, M. Horwath, and E. Isaksson. "Recent Snowfall Anomalies in Dronning Maud Land, East Antarctica, in a Historical and Future Climate Perspective". In: *Geophysical Research Letters* 40.11 (2013), pp. 2684–2688. ISSN: 1944-8007. DOI: 10.1002/grl.50559.

Leuliette, E. and J. Willis. "Balancing the Sea Level Budget". In: *Oceanography* 24.2 (June 1, 2011), pp. 122–129. ISSN: 10428275. DOI: 10.5670/oceanog.2011.32.

Lillibridge, J., R. Scharroo, S. Abdalla, and D. Vandemark. "One- and Two-Dimensional Wind Speed Models for Ka-Band Altimetry". In: *Journal of Atmospheric and Oceanic Technology* 31.3 (Mar. 1, 2014), pp. 630–638. ISSN: 0739-0572, 1520-0426. DOI: 10.1175/JTECH-D-13-00167.1.

Llovel, W., J. Willis, F. Landerer, and I. Fukumori. "Deep-Ocean Contribution to Sea Level and Energy Budget Not Detectable over the Past Decade". In: *Nature Climate Change* 4 (2014). DOI: 10.1038/nclimate2387.

Llovel, W., M. Becker, A. Cazenave, J.-F. Crétaux, and G. Ramillien. "Global Land Water Storage Change from GRACE over 2002–2009; Inference on Sea Level". In: *Comptes Rendus Geoscience* 342.3 (Mar. 1, 2010), pp. 179–188. ISSN: 1631-0713. DOI: 10.1016/j.crte.2009.12.004.

Löcher, A. and J. Kusche. "A Hybrid Approach for Recovering High-Resolution Temporal Gravity Fields from Satellite Laser Ranging". In: *Journal of Geodesy* 95.1 (Dec. 23, 2020), p. 6. ISSN: 1432-1394. DOI: 10.1007/s00190-020-01460-x.

Loeb, N. G., D. R. Doelling, H. Wang, W. Su, C. Nguyen, J. G. Corbett, L. Liang, C. Mitrescu, F. G. Rose, and S. Kato. "Clouds and the Earth's Radiant Energy System (CERES) Energy

Balanced and Filled (EBAF) Top-of-Atmosphere (TOA) Edition-4.0 Data Product". In: *Journal of Climate* 31.2 (Nov. 20, 2017), pp. 895–918. ISSN: 0894-8755. DOI: 10.1175/JCLI-D-17-0208.1.

Loeb, N. G., J. M. Lyman, G. C. Johnson, R. P. Allan, D. R. Doelling, T. Wong, B. J. Soden, and G. L. Stephens. "Observed Changes in Top-of-the-Atmosphere Radiation and Upper-Ocean Heating Consistent within Uncertainty". In: *Nature Geoscience* 5.2 (2 Feb. 2012), pp. 110–113. ISSN: 1752-0908. DOI: 10.1038/ngeo1375.

Lombard, A., D. Garcia, G. Ramillien, A. Cazenave, R. Biancale, J. M. Lemoine, F. Flechtner, R. Schmidt, and M. Ishii. "Estimation of Steric Sea Level Variations from Combined GRACE and Jason-1 Data". In: *Earth and Planetary Science Letters* 254.1 (Feb. 15, 2007), pp. 194–202. ISSN: 0012-821X. DOI: 10.1016/j.epsl.2006.11.035.

Loomis, B. D., S. B. Luthcke, and T. J. Sabaka. "Regularization and Error Characterization of GRACE Mascons". In: *Journal of Geodesy* 93.9 (Sept. 1, 2019), pp. 1381–1398. ISSN: 1432-1394. DOI: 10.1007/s00190-019-01252-y.

Loomis, B. D., K. E. Rachlin, and S. B. Luthcke. "Improved Earth Oblateness Rate Reveals Increased Ice Sheet Losses and Mass-Driven Sea Level Rise". In: *Geophysical Research Letters* 46.12 (2019), pp. 6910–6917. ISSN: 1944-8007. DOI: 10.1029/2019GL082929.

Loomis, B. D., K. E. Rachlin, D. N. Wiese, F. W. Landerer, and S. B. Luthcke. "Replacing GRACE/GRACE-FO With Satellite Laser Ranging: Impacts on Antarctic Ice Sheet Mass Change". In: *Geophysical Research Letters* 47.3 (2020), e2019GL085488. ISSN: 1944-8007. DOI: 10.1029/2019GL085488.

Love, A. E. H. "The Yielding of the Earth to Disturbing Forces". In: *Proceedings of the Royal Society of London. Series A, Containing Papers of a Mathematical and Physical Character* 82.551 (Feb. 16, 1909), pp. 73–88. DOI: 10.1098/rspa.1909.0008.

Lowe, J. A., P. L. Woodworth, T. Knutson, R. E. McDonald, K. L. McInnes, K. Woth, H. von Storch, J. Wolf, V. Swail, N. B. Bernier, S. Gulev, K. J. Horsburgh, A. S. Unnikrishnan, J. R. Hunter, and R. Weisse. "Past and Future Changes in Extreme Sea Levels and Waves". In: *Understanding Sea-Level Rise and Variability*. John Wiley & Sons, Ltd, 2010, pp. 326–375. ISBN: 978-1-4443-2327-6. DOI: 10.1002/9781444323276.ch11.

Lück, C. "Large-Scale Mass Redistribution in the Earth System from Synergistic Use of Swarm Data". Thesis. Universitäts- und Landesbibliothek Bonn, Jan. 26, 2022.

Lück, C., J. Kusche, R. Rietbroek, and A. Löcher. "Time-Variable Gravity Fields and Ocean Mass Change from 37 Months of Kinematic Swarm Orbits". In: *Solid Earth* 9.2 (Mar. 23, 2018), pp. 323–339. ISSN: 1869-9510. DOI: 10.5194/se-9-323-2018.

Ludwigsen, C. A. and O. B. Andersen. "Contributions to Arctic Sea Level from 2003 to 2015". In: *Advances in Space Research*. 25 Years of Progress in Radar Altimetry 68.2 (July 15, 2021), pp. 703–710. ISSN: 0273-1177. DOI: 10.1016/j.asr.2019.12.027.

Lyard, F. H., D. J. Allain, M. Cancet, L. Carrère, and N. Picot. "FES2014 Global Ocean Tide Atlas: Design and Performance". In: *Ocean Science* 17.3 (May 5, 2021), pp. 615–649. ISSN: 1812-0784. DOI: 10.5194/os-17-615-2021.

Lyu, G., N. Serra, M. Zhou, and D. Stammer. "Arctic Sea Level Variability from High-Resolution Model Simulations and Implications for the Arctic Observing System". In: *Ocean Science* 18.1 (Jan. 6, 2022), pp. 51–66. ISSN: 1812-0784. DOI: 10.5194/os-18-51-2022.

Margirier, F., P. Testor, E. Heslop, K. Mallil, A. Bosse, L. Houpert, L. Mortier, M.-N. Bouin, L. Coppola, F. D'Ortenzio, X. Durrieu de Madron, B. Mourre, L. Prieur, P. Raimbault, and V. Taillandier. "Abrupt Warming and Salinification of Intermediate Waters Interplays with Decline of Deep Convection in the Northwestern Mediterranean Sea". In: *Scientific Reports* 10.1 (1 Dec. 1, 2020), p. 20923. ISSN: 2045-2322. DOI: 10.1038/s41598-020-77859-5.

Marti, F., A. Blazquez, B. Meyssignac, M. Ablain, A. Barnoud, R. Fraudeau, R. Jugier, J. Chenal, G. Larnicol, J. Pfeffer, M. Restano, and J. Benveniste. "Monitoring the Ocean Heat Content Change and the Earth Energy Imbalance from Space Altimetry and Space Gravimetry". In: *Earth System Science Data* 14.1 (Jan. 26, 2022), pp. 229–249. ISSN: 1866-3508. DOI: 10.5194/essd-14-229-2022.

Marti, F., A. Cazenave, F. Birol, M. Passaro, F. Léger, F. Niño, R. Almar, J. Benveniste, and J. F. Legeais. "Altimetry-Based Sea Level Trends along the Coasts of Western Africa". In: *Advances in Space Research*. 25 Years of Progress in Radar Altimetry 68.2 (July 15, 2021), pp. 504–522. ISSN: 0273-1177. DOI: 10.1016/j.asr.2019.05.033.

Martin, T. V., H. J. Zwally, A. C. Brenner, and R. A. Bindschadler. "Analysis and Retracking of Continental Ice Sheet Radar Altimeter Waveforms". In: *J. Geophys. Res.* 88 (1983), pp. 1608–1616.

Martín-Español, A., M. A. King, A. Zammit-Mangion, S. B. Andrews, P. Moore, and J. L. Bamber. "An Assessment of Forward and Inverse GIA Solutions for Antarctica". In: *Journal of Geophysical Research: Solid Earth* 121.9 (Sept. 16, 2016), pp. 6947–6965. ISSN: 2169-9356. DOI: 10.1002/2016JB013154.

Marzeion, B., A. H. Jarosch, and M. Hofer. "Past and Future Sea-Level Change from the Surface Mass Balance of Glaciers". In: *The Cryosphere* 6.6 (Nov. 12, 2012), pp. 1295–1322. ISSN: 1994-0416. DOI: 10.5194/tc-6-1295-2012.

Marzeion, B., R. Hock, B. Anderson, A. Bliss, N. Champollion, K. Fujita, M. Huss, W. W. Immerzeel, P. Kraaijenbrink, J.-H. Malles, F. Maussion, V. Radić, D. R. Rounce, A. Sakai, S. Shannon, R. van de Wal, and H. Zekollari. "Partitioning the Uncertainty of Ensemble Projections of Global Glacier Mass Change". In: *Earth's Future* 8.7 (2020), e2019EF001470. ISSN: 2328-4277. DOI: 10.1029/2019EF001470.

Mathers, E. L. and P. L. Woodworth. "A Study of Departures from the Inverse-Barometer Response of Sea Level to Air-Pressure Forcing at a Period of 5 Days". In: *Quarterly Journal of the Royal Meteorological Society* 130.597 (Dec. 29, 2006), pp. 725–738. ISSN: 1477-870X. DOI: 10.1256/qj.03.46.

Mayer-Gürr, T., S. Behzadpour, M. Ellmer, A. Kvas, B. Klinger, S. Strasser, and N. Zehentner. "ITSG-Grace2018 - Monthly, Daily and Static Gravity Field Solutions from GRACE". In: *GFZ Data Services* (2018). DOI: 10.5880/ICGEM.2018.003.

McDougall, T. J., D. R. Jackett, F. J. Millero, R. Pawlowicz, and P. M. Barker. "A Global Algorithm for Estimating Absolute Salinity". In: *Ocean Science* 8.6 (Dec. 21, 2012), pp. 1123–1134. ISSN: 1812-0784. DOI: 10.5194/os-8-1123-2012.

McDougall, T. J. and S. J. Wotherspoon. "A Simple Modification of Newton's Method to Achieve Convergence of Order 1+2". In: *Applied Mathematics Letters* 29 (Mar. 1, 2014), pp. 20–25. ISSN: 0893-9659. DOI: 10.1016/j.aml.2013.10.008.

McGranahan, G., D. Balk, and B. Anderson. "The Rising Tide: Assessing the Risks of Climate Change and Human Settlements in Low Elevation Coastal Zones". In: *Environment and Urbanization* 19.1 (Apr. 1, 2007), pp. 17–37. ISSN: 0956-2478. DOI: 10.1177/0956247807076960.

Messias, M.-J. and H. Mercier. "The Redistribution of Anthropogenic Excess Heat Is a Key Driver of Warming in the North Atlantic". In: *Communications Earth & Environment* 3.1 (1 May 17, 2022), pp. 1–14. ISSN: 2662-4435. DOI: 10.1038/s43247-022-00443-4.

Meyssignac, B. et al. "Measuring Global Ocean Heat Content to Estimate the Earth Energy Imbalance". In: *Frontiers in Marine Science* 6 (2019). ISSN: 2296-7745. DOI: 10.3389/fmars.2019.00432.

Millero, F. J., R. Feistel, D. G. Wright, and T. J. McDougall. "The Composition of Standard Seawater and the Definition of the Reference-Composition Salinity Scale". In: *Deep Sea Research Part I: Oceanographic Research Papers* 55.1 (Jan. 1, 2008), pp. 50–72. ISSN: 0967-0637. DOI: 10.1016/j.dsr.2007.10.001.

Milly, P. C. D. (, A. Cazenave, J. S. Famiglietti, V. Gornitz, K. Laval, D. P. Lettenmaier, D. L. Sahagian, J. M. Wahr, and C. R. Wilson. "Terrestrial Water-Storage Contributions to Sea-Level Rise and Variability". In: *Understanding Sea-Level Rise and Variability*. John Wiley & Sons, Ltd, 2010, pp. 226–255. ISBN: 978-1-4443-2327-6. DOI: 10.1002/9781444323276.ch8.

Milne A., G. and J. Mitrovica X. "Postglacial Sea-Level Change on a Rotating Earth". In: *Geophysical Journal International* 133.1 (1998), pp. 1–19. ISSN: 1365-246X. DOI: 10.1046/j.1365-246X.1998.1331455.x.

Mitchum, G. T., R. S. Nerem, M. A. Merrifield, and W. R. Gehrels. "Modern Sea-Level-Change Estimates". In: *Understanding Sea-Level Rise and Variability*. John Wiley & Sons, Ltd, 2010, pp. 122–142. ISBN: 978-1-4443-2327-6. DOI: 10.1002/9781444323276.ch5.

Mitrovica, J. X., J. Wahr, I. Matsuyama, and A. Paulson. "The Rotational Stability of an Ice-Age Earth". In: *Geophysical Journal International* 161.2 (May 1, 2005), pp. 491–506. ISSN: 0956-540X. DOI: 10.1111/j.1365-246X.2005.02609.x.

Morison, J., R. Kwok, and I. Rigor. "Changes in Arctic Ocean Circulation from In Situ and Remotely Sensed Observations: Synergies and Sampling Challenges". In: *Oceanography* (2022). ISSN: 10428275. DOI: 10.5670/oceanog.2022.111.

Munk, W. H. and G. J. MacDonald. *The Rotation of the Earth; a Geophysical Discussion,* Cambridge Monographs on Mechanics and Applied Mathematics. Cambridge [England] : Cambridge University Press, 1960., 1960.

Nakada, M. and J. Okuno. "Perturbations of the Earth's Rotation and Their Implications for the Present-Day Mass Balance of Both Polar Ice Caps". In: *Geophysical Journal International* 152.1 (Jan. 1, 2003), pp. 124–138. ISSN: 0956-540X. DOI: 10.1046/j.1365-246X.2003.01831.x.

Nerem, R. S., B. D. Beckley, J. T. Fasullo, B. D. Hamlington, D. Masters, and G. T. Mitchum. "Climate-Change–Driven Accelerated Sea-Level Rise Detected in the Altimeter Era". In: *Proceedings of the National Academy of Sciences* (Feb. 7, 2018), p. 201717312. ISSN: 0027-8424, 1091-6490. DOI: 10.1073/pnas.1717312115. pmid: 29440401.

Nerem, R. S., D. P. Chambers, C. Choe, and G. T. Mitchum. "Estimating Mean Sea Level Change from the TOPEX and Jason Altimeter Missions". In: *Marine Geodesy* 33 (sup1 Aug. 16, 2010), pp. 435–446. ISSN: 0149-0419. DOI: 10.1080/01490419.2010.491031.

Nicholls, R. J. and A. Cazenave. "Sea-Level Rise and Its Impact on Coastal Zones". In: *Science* 328.5985 (June 18, 2010), pp. 1517–1520. ISSN: 0036-8075, 1095-9203. DOI: 10.1126/science.1185782. pmid: 20558707.

Niemeier, W. *Ausgleichungsrechnung*. De Gruyter, Sept. 25, 2008. ISBN: 978-3-11-020678-4.

NSIDC, N. S. a. I. D. C. *World Glacier Inventory, Version 1*. WGMS, and National Snow and Ice Data Center (comps.), updated 2012. 1999. URL: https://doi.org/10.7265/N5/NSIDC-WGI-2012-02 (visited on 12/30/2020).

Olshausen, B. A. and D. J. Field. "Sparse Coding with an Overcomplete Basis Set: A Strategy Employed by V1?" In: *Vision Research* 37.23 (Dec. 1, 1997), pp. 3311–3325. ISSN: 0042-6989. DOI: 10.1016/S0042-6989(97)00169-7.

Pagiatakis, S. D. "The Response of a Realistic Earth to Ocean Tide Loading". In: *Geophysical Journal International* 103.2 (1990), pp. 541–560. ISSN: 1365-246X. DOI: 10.1111/j.1365-246X.1990.tb01790.x.

Passaro, M., P. Cipollini, S. Vignudelli, G. D. Quartly, and H. M. Snaith. "ALES: A Multi-Mission Adaptive Subwaveform Retracker for Coastal and Open Ocean Altimetry". In: *Remote Sensing of Environment* 145 (Apr. 5, 2014), pp. 173–189. ISSN: 0034-4257. DOI: 10.1016/j.rse.2014.02.008.

Passaro, M., S. K. Rose, O. B. Andersen, E. Boergens, F. M. Calafat, D. Dettmering, and J. Benveniste. "ALES+: Adapting a Homogenous Ocean Retracker for Satellite Altimetry to Sea Ice Leads, Coastal and Inland Waters". In: *Remote Sensing of Environment* 211 (June 15, 2018), pp. 456–471. ISSN: 0034-4257. DOI: 10.1016/j.rse.2018.02.074.

Paulson, A., S. Zhong, and J. Wahr. "Inference of Mantle Viscosity from GRACE and Relative Sea Level Data". In: *Geophysical Journal International* 171.2 (Nov. 1, 2007), pp. 497–508. ISSN: 1365-246X. DOI: 10.1111/j.1365-246X.2007.03556.x.

Peltier, W. R., D. F. Argus, and R. Drummond. "Space Geodesy Constrains Ice Age Terminal Deglaciation: The Global ICE-6G_C (VM5a) Model". In: *Journal of Geophysical Research: Solid Earth* 120.1 (Feb. 20, 2015), pp. 450–487. ISSN: 2169-9313. DOI: 10.1002/2014JB011176.

Peltier, W. R. and S. B. Luthcke. "On the Origins of Earth Rotation Anomalies: New Insights on the Basis of Both "Paleogeodetic" Data and Gravity Recovery and Climate Experiment (GRACE) Data". In: *Journal of Geophysical Research: Solid Earth* 114.B11 (Nov. 18, 2009). ISSN: 0148-0227. DOI: 10.1029/2009JB006352.

Peltier, W. R., D. F. Argus, and R. Drummond. "Comment on "An Assessment of the ICE-6G_C (VM5a) Glacial Isostatic Adjustment Model" by Purcell et Al." In: *Journal of Geophysical Research: Solid Earth* 123.2 (2018), pp. 2019–2028. ISSN: 2169-9356. DOI: 10.1002/2016JB013844.

Peltier, W. "GLOBAL GLACIAL ISOSTASY AND THE SURFACE OF THE ICE-AGE EARTH: The ICE-5G (VM2) Model and GRACE". In: *Annual Review of Earth and Planetary Sciences* 32.1 (2004), pp. 111–149. DOI: 10.1146/annurev.earth.32.082503.144359.

Petit, G. and B. Luzum. *IERS Conventions (2010)*. IERS Technical Note ; 36. Frankfurt am Main: Verlag des Bundesamts für Kartographie und Geodäsie, ISBN 3-89888-989-6, 2010, p. 179.

Picot, N., C. Marechal, A. Couhert, S. Desai, R. Scharroo, and A. Egido. *Jason-3 Products Handbook*. 1.5. CNES / NASA, Sept. 2018.

Piecuch, C. G. and K. J. Quinn. "El Niño, La Niña, and the Global Sea Level Budget". In: *Ocean Sci.* 12.6 (Nov. 11, 2016), pp. 1165–1177. ISSN: 1812-0792. DOI: 10.5194/os-12-1165-2016.

Ponte, R. M. "Low-Frequency Sea Level Variability and the Inverted Barometer Effect". In: *Journal of Atmospheric and Oceanic Technology* 23.4 (Apr. 1, 2006), pp. 619–629. ISSN: 0739-0572. DOI: 10.1175/JTECH1864.1.

Ponte, R. M. et al. "Towards Comprehensive Observing and Modeling Systems for Monitoring and Predicting Regional to Coastal Sea Level". In: *Frontiers in Marine Science* 6 (2019). ISSN: 2296-7745.

Pujol, M.-I., Y. Faugère, G. Taburet, S. Dupuy, C. Pelloquin, M. Ablain, and N. Picot. "DUACS DT2014: The New Multi-Mission Altimeter Data Set Reprocessed over 20 Years". In: *Ocean Science* 12.5 (Sept. 9, 2016), pp. 1067–1090. ISSN: 1812-0784. DOI: 10.5194/os-12-1067-2016.

Pujol, M.-I., P. Schaeffer, Y. Faugère, M. Raynal, G. Dibarboure, and N. Picot. "Gauging the Improvement of Recent Mean Sea Surface Models: A New Approach for Identifying and Quantifying Their Errors". In: *Journal of Geophysical Research: Oceans* 123.8 (2018), pp. 5889–5911. ISSN: 2169-9291. DOI: 10.1029/2017JC013503.

Quartly, G. D., M. A. Srokosz, and A. C. McMillan. "Analyzing Altimeter Artifacts: Statistical Properties of Ocean Waveforms". In: *Journal of Atmospheric and Oceanic Technology* 18 (2001), pp. 2074–2091.

Quartly, G. D. and A. A. Kurekin. "Sensitivity of Altimeter Wave Height Assessment to Data Selection". In: *Remote Sensing* 12.16 (16 Jan. 2020), p. 2608. DOI: 10.3390/rs12162608.

Raney, R. "The Delay/Doppler Radar Altimeter". In: *IEEE Transactions on Geoscience and Remote Sensing* 36.5 (Sept. 1998), pp. 1578–1588. ISSN: 1558-0644. DOI: 10.1109/36.718861.

Raup, B., A. Racoviteanu, S. J. S. Khalsa, C. Helm, R. Armstrong, and Y. Arnaud. "The GLIMS Geospatial Glacier Database: A New Tool for Studying Glacier Change". In: *Global and Planetary Change*. Climate Change Impacts on Mountain Glaciers and Permafrost 56.1 (Mar. 1, 2007), pp. 101–110. ISSN: 0921-8181. DOI: 10.1016/j.gloplacha.2006.07.018.

Rayner, R. and B. MacKenzie. "A First-Order Assessment of the Impact of Long-Term Trends in Extreme Sea Levels on Offshore Structures and Coastal Refineries". In: *Understanding Sea-Level Rise and Variability*. John Wiley & Sons, Ltd, 2010, pp. 52–60. ISBN: 978-1-4443-2327-6. DOI: 10.1002/9781444323276.ch3.

Reager, J. T., A. S. Gardner, J. S. Famiglietti, D. N. Wiese, A. Eicker, and M.-H. Lo. "A Decade of Sea Level Rise Slowed by Climate-Driven Hydrology". In: *Science* 351.6274 (Feb. 12, 2016), pp. 699–703. ISSN: 0036-8075, 1095-9203. DOI: 10.1126/science.aad8386. pmid: 26912856.

RGI Consortium. *Randolph Glacier Inventory – A Dataset of Global Glacier Outlines: Version 6.0*. Technical Report, Global Land Ice Measurements from Space. Colorado, USA: Digital Media, DOI: https://doi.org/10.7265/N5-RGI-60, 2017.

Rhein, M., S. Rintoul, S. Aoki, E. Campos, D. Chambers, R. Feely, S. Gulev, G. Johnson, S. Josey, A. Kostianoy, C. Mauritzen, D. Roemmich, L. Talley, and F. Wang. "Observations: Ocean". In: *Climate Change 2013: The Physical Science Basis. Contribution of Working Group I to the Fifth Assessment Report of the Intergovernmental Panel on Climate Change*. Ed. by T. Stocker, D. Qin, G.-K. Plattner, M. Tignor, S. Allen, J. Boschung, A. Nauels, Y. Xia, V. Bex, and P. Midgley. Cambridge University Press, Cambridge, United Kingdom and New York, NY, USA, 2013.

Rieck, J. K., C. W. Böning, R. J. Greatbatch, and M. Scheinert. "Seasonal Variability of Eddy Kinetic Energy in a Global High-Resolution Ocean Model". In: *Geophysical Research Letters* 42.21 (2015), pp. 9379–9386. ISSN: 1944-8007. DOI: 10.1002/2015GL066152.

Rietbroek, R. "Retrieval of Sea Level and Surface Loading Variations from Geodetic Observations and Model Simulations: An Integrated Approach". PhD thesis. Rheinische Friedrich-Wilhelms-Universität Bonn, 2014.

Rietbroek, R., S. .-.-E. Brunnabend, J. Kusche, and J. Schröter. "Resolving Sea Level Contributions by Identifying Fingerprints in Time-Variable Gravity and Altimetry". In: *Journal of Geodynamics*. Mass Transport and Mass Distribution in the System Earth 59–60 (Sept. 1, 2012), pp. 72–81. ISSN: 0264-3707. DOI: 10.1016/j.jog.2011.06.007.

Rietbroek, R., S.-E. Brunnabend, C. Dahle, J. Kusche, F. Flechtner, J. Schröter, and R. Timmermann. "Changes in Total Ocean Mass Derived from GRACE, GPS, and Ocean Modeling with Weekly Resolution". In: *Journal of Geophysical Research: Oceans* 114.C11 (2009). ISSN: 2156-2202. DOI: 10.1029/2009JC005449.

Rietbroek, R., S.-E. Brunnabend, J. Kusche, J. Schröter, and C. Dahle. "Revisiting the Contemporary Sea-Level Budget on Global and Regional Scales". In: *Proceedings of the National Academy of Sciences* 113.6 (Feb. 9, 2016), pp. 1504–1509. ISSN: 0027-8424, 1091-6490. DOI: 10.1073/pnas.1519132113. pmid: 26811469.

Riva, R. E. M., J. L. Bamber, D. A. Lavallée, and B. Wouters. "Sea-Level Fingerprint of Continental Water and Ice Mass Change from GRACE". In: *Geophysical Research Letters* 37.19 (2010). ISSN: 1944-8007. DOI: 10.1029/2010GL044770.

Rodell, M., J. S. Famiglietti, D. N. Wiese, J. T. Reager, H. K. Beaudoing, F. W. Landerer, and M.-H. Lo. "Emerging Trends in Global Freshwater Availability". In: *Nature* 557.7707 (7707 May 2018), pp. 651–659. ISSN: 1476-4687. DOI: 10.1038/s41586-018-0123-1.

Rodell, M., P. Houser, U. Jambor, J. Gottschalck, K. Mitchell, C.-J. Meng, K. Arsenault, B. Cosgrove, J. Radakovich, M. Bosilovich, J. Entin, J. Walker, D. Lohmann, and D. Toll. "The Global Land Data Assimilation System". In: *Bulletin of the American Meteorological Society* 85(3) (2004), pp. 381–394.

Roemmich, D. and J. Gilson. "The 2004–2008 Mean and Annual Cycle of Temperature, Salinity, and Steric Height in the Global Ocean from the Argo Program". In: *Progress in Oceanography* 82.2 (Aug. 1, 2009), pp. 81–100. ISSN: 0079-6611. DOI: 10.1016/j.pocean.2009.03.004.

Roemmich, D. et al. "Argo: The Challenge of Continuing 10 Years of Progress". In: *Oceanography* 22.3 (Sept. 1, 2009), pp. 46–55. ISSN: 10428275. DOI: 10.5670/oceanog.2009.65.

Roscher, R., B. Uebbing, and J. Kusche. "STAR: Spatio-temporal Altimeter Waveform Retracking Using Sparse Representation and Conditional Random Fields". In: *Remote Sensing of Environment* 201 (Nov. 1, 2017), pp. 148–164. ISSN: 0034-4257. DOI: 10.1016/j.rse.2017.07.024.

Royston, S., B. D. Vishwakarma, R. Westaway, J. Rougier, Z. Sha, and J. Bamber. "Can We Resolve the Basin-Scale Sea Level Trend Budget From GRACE Ocean Mass?" In: *Journal of Geophysical Research: Oceans* 125.1 (2020), e2019JC015535. ISSN: 2169-9291. DOI: 10.1029/2019JC015535.

Sabadini, R. and B. Vermeersen. *Global Dynamics of the Earth: Applications of Normal Mode Relaxation Theory to Solid-Earth Geophysics*. Modern Approaches in Geophysics. Springer Netherlands, 2004. ISBN: 978-1-4020-1267-9. DOI: 10.1007/978-94-017-1709-0.

Sandwell, D. T. and W. H. F. Smith. "Marine Gravity Anomaly from Geosat and ERS-1 Satellite Altimetry". In: *Journal of Geophysical Research* 102.B5 (May 1997), pp. 10, 039–10, 054.

Scanlon, B. R., Z. Zhang, H. Save, A. Y. Sun, H. M. Schmied, L. P. H. van Beek, D. N. Wiese, Y. Wada, D. Long, R. C. Reedy, L. Longuevergne, P. Döll, and M. F. P. Bierkens. "Global Models Underestimate Large Decadal Declining and Rising Water Storage Trends Relative to GRACE Satellite Data". In: *Proceedings of the National Academy of Sciences* (Jan. 17, 2018), p. 201704665. ISSN: 0027-8424, 1091-6490. DOI: 10.1073/pnas.1704665115. pmid: 29358394.

Scharroo, R., E. Leuliette, J. Lillibridge, D. Byrne, M. Naeije, and G. Mitchum. "RADS: Consistent Multi-Mission Products". In: 20 Years of Progress in Radar Altimatry. Vol. 710. Sept. 1, 2013, p. 69.

Schlembach, F., M. Passaro, G. D. Quartly, A. Kurekin, F. Nencioli, G. Dodet, J.-F. Piollé, F. Ardhuin, J. Bidlot, C. Schwatke, F. Seitz, P. Cipollini, and C. Donlon. "Round Robin Assessment of Radar Altimeter Low Resolution Mode and Delay-Doppler Retracking Algorithms for Significant Wave Height". In: *Remote Sensing* 12.8 (8 Jan. 2020), p. 1254. DOI: 10.3390/rs12081254.

Schröder, L., M. Horwath, R. Dietrich, V. Helm, M. R. van den Broeke, and S. R. M. Ligtenberg. "Four Decades of Antarctic Surface Elevation Changes from Multi-Mission Satellite Altimetry". In: *The Cryosphere* 13.2 (Feb. 5, 2019), pp. 427–449. ISSN: 1994-0416. DOI: 10.5194/tc-13-427-2019.

Schröder, S., A. Springer, J. Kusche, B. Uebbing, L. Fenoglio-Marc, B. Diekkrüger, and T. Poméon. "Niger Discharge from Radar Altimetry: Bridging Gaps between Gauge and Altimetry Time Series". In: *Hydrology and Earth System Sciences* 23.10 (Oct. 2, 2019), pp. 4113–4128. ISSN: 1027-5606. DOI: 10.5194/hess-23-4113-2019.

Schuh, W.-D., I. Krasbutter, and B. Kargoll. "Korrelierte Messungen - Was Nun?" In: *Zeitabhängige Messgrößen - Ihre Daten Haben (Mehr-) Wert*. DVW-Schriftenreihe 74. Neuner, H. (Hrsg.), 2014, pp. 85–101. ISBN: 978-3-89639-970-0.

Schuh, W.-D. "Signalverarbeitung in der Physikalischen Geodäsie". In: *Handbuch der Geodäsie: 5 Bände*. Ed. by W. Freeden and R. Rummel. Springer Reference Naturwissenschaften. Berlin, Heidelberg: Springer, 2016, pp. 1–49. ISBN: 978-3-662-46900-2. DOI: 10.1007/978-3-662-46900-2_15-1.

Schuh, W.-D. and J. M. Brockmann. "Numerical Treatment of Covariance Stationary Processes in Least Squares Collocation". In: *Handbuch der Geodäsie: 6 Bände*. Ed. by W. Freeden and R. Rummel. Springer Reference Naturwissenschaften. Berlin, Heidelberg: Springer, 2019, pp. 1–37. ISBN: 978-3-662-46900-2. DOI: 10.1007/978-3-662-46900-2_95-1.

Siemes, C., J. de Teixeira da Encarnação, E. Doornbos, J. van den IJssel, J. Kraus, R. Pereštý, L. Grunwaldt, G. Apelbaum, J. Flury, and P. E. Holmdahl Olsen. "Swarm Accelerometer Data Processing from Raw Accelerations to Thermospheric Neutral Densities". In: *Earth, Planets and Space* 68.1 (May 28, 2016), p. 92. ISSN: 1880-5981. DOI: 10.1186/s40623-016-0474-5.

Sreenivas, P., C. Gnanaseelan, and K. V. S. R. Prasad. "Influence of El Niño and Indian Ocean Dipole on Sea Level Variability in the Bay of Bengal". In: *Global and Planetary Change* 80–81 (Jan. 1, 2012), pp. 215–225. ISSN: 0921-8181. DOI: 10.1016/j.gloplacha.2011.11.001.

Steffen, K., R. H. Thomas, E. Rignot, J. G. Cogley, M. B. Dyurgerov, S. C. B. Raper, P. Huybrechts, and E. Hanna. "Cryospheric Contributions to Sea-Level Rise and Variability". In: *Understanding Sea-Level Rise and Variability*. John Wiley & Sons, Ltd, 2010, pp. 177–225. ISBN: 978-1-4443-2327-6. DOI: 10.1002/9781444323276.ch7.

Stewart, R. H. *Introduction to Physical Oceanography*. 2008.

Stocker, T., D. Qin, G.-K. Plattner, M. Tignor, S. Allen, J. Boschung, A. Nauels, Y. Xia, V. Bex, and P. Midgley, eds. *Climate Change 2013: The Physical Science Basis. Contribution of Working Group I to the Fifth Assessment Report of the Intergovernmental Panel on Climate Change*. Cambridge University Press, Cambride, United Kingdom and New York, NY, USA, 2013. 1585 pp.

Strößenreuther, U., M. Horwath, and L. Schröder. "How Different Analysis and Interpolation Methods Affect the Accuracy of Ice Surface Elevation Changes Inferred from Satellite Altimetry". In: *Mathematical Geosciences* 52.4 (May 1, 2020), pp. 499–525. ISSN: 1874-8953. DOI: 10.1007/s11004-019-09851-3.

Sun, Y. and R. E. M. Riva. "A Global Semi-Empirical Glacial Isostatic Adjustment (GIA) Model Based on Gravity Recovery and Climate Experiment (GRACE) Data". In: *Earth System Dynamics* 11.1 (Feb. 14, 2020), pp. 129–137. ISSN: 2190-4979. DOI: 10.5194/esd-11-129-2020.

Sun, Y., R. Riva, and P. Ditmar. "Optimizing Estimates of Annual Variations and Trends in Geocenter Motion and J2 from a Combination of GRACE Data and Geophysical Models". In: *Journal of Geophysical Research: Solid Earth* 121.11 (Nov. 8, 2016), pp. 8352–8370. ISSN: 2169-9356. DOI: 10.1002/2016JB013073.

Sutanudjaja, E. H., R. van Beek, N. Wanders, Y. Wada, J. H. C. Bosmans, N. Drost, R. J. van der Ent, I. E. M. de Graaf, J. M. Hoch, K. de Jong, D. Karssenberg, P. López López, S. Peßenteiner,

O. Schmitz, M. W. Straatsma, E. Vannametee, D. Wisser, and M. F. P. Bierkens. "PCR-GLOBWB 2: A 5 Arcmin Global Hydrological and Water Resources Model". In: *Geoscientific Model Development* 11.6 (June 20, 2018), pp. 2429–2453. ISSN: 1991-959X. DOI: 10.5194/gmd-11-2429-2018.

Swenson, S., D. Chambers, and J. Wahr. "Estimating Geocenter Variations from a Combination of GRACE and Ocean Model Output". In: *Journal of Geophysical Research: Solid Earth* 113.B8 (Aug. 1, 2008). ISSN: 2156-2202. DOI: 10.1029/2007JB005338.

Tamisiea, M. E. "Ongoing Glacial Isostatic Contributions to Observations of Sea Level Change". In: *Geophysical Journal International* 186.3 (Sept. 1, 2011), pp. 1036–1044. ISSN: 0956-540X. DOI: 10.1111/j.1365-246X.2011.05116.x.

Tapley, B. D., S. Bettadpur, M. Watkins, and C. Reigber. "The Gravity Recovery and Climate Experiment: Mission Overview and Early Results". In: *Geophysical Research Letters* 31.9 (2004). ISSN: 1944-8007. DOI: 10.1029/2004GL019920.

Timmermann, R., S. Danilov, J. Schröter, C. Böning, D. Sidorenko, and K. Rollenhagen. "Ocean Circulation and Sea Ice Distribution in a Finite Element Global Sea Ice–Ocean Model". In: *Ocean Modelling* 27.3 (Jan. 1, 2009), pp. 114–129. ISSN: 1463-5003. DOI: 10.1016/j.ocemod.2008.10.009.

Tourian, M. J., A. Tarpanelli, O. Elmi, T. Qin, L. Brocca, T. Moramarco, and N. Sneeuw. "Spatiotemporal Densification of River Water Level Time Series by Multimission Satellite Altimetry". In: *Water Resources Research* 52.2 (2016), pp. 1140–1159. ISSN: 1944-7973. DOI: 10.1002/2015WR017654.

Trenberth, K. E., J. T. Fasullo, K. von Schuckmann, and L. Cheng. "Insights into Earth's Energy Imbalance from Multiple Sources". In: *Journal of Climate* 29.20 (July 7, 2016), pp. 7495–7505. ISSN: 0894-8755. DOI: 10.1175/JCLI-D-16-0339.1.

Trenberth, K. E., Y. Zhang, J. T. Fasullo, and L. Cheng. "Observation-Based Estimates of Global and Basin Ocean Meridional Heat Transport Time Series". In: *Journal of Climate* 32.14 (July 15, 2019), pp. 4567–4583. ISSN: 0894-8755. DOI: 10.1175/JCLI-D-18-0872.1.

Tropp, J. A., A. C. Gilbert, and M. J. Strauss. "Algorithms for Simultaneous Sparse Approximation. Part I: Greedy Pursuit". In: *Signal Processing*. Sparse Approximations in Signal and Image Processing 86.3 (Mar. 1, 2006), pp. 572–588. ISSN: 0165-1684. DOI: 10.1016/j.sigpro.2005.05.030.

Uebbing, B., E. Forootan, A. Braakmann-Folgmann, and J. Kusche. "Inverting Surface Soil Moisture Information from Satellite Altimetry over Arid and Semi-Arid Regions". In: *Remote Sensing of Environment* 196 (Supplement C 2017), pp. 205–223. ISSN: 0034-4257. DOI: 10.1016/j.rse.2017.05.004.

Uebbing, B., J. Kusche, R. Rietbroek, and F. W. Landerer. "Processing Choices Affect Ocean Mass Estimates From GRACE". In: *Journal of Geophysical Research: Oceans* 124.2 (2019), pp. 1029–1044. ISSN: 2169-9291. DOI: 10.1029/2018JC014341.

Uebbing, B., J. Kusche, and E. Forootan. "Waveform Retracking for Improving Level Estimations From TOPEX/Poseidon, Jason-1, and Jason-2 Altimetry Observations Over African Lakes". In: *IEEE Transactions on Geoscience and Remote Sensing* 53.4 (Apr. 2015), pp. 2211–2224. ISSN: 1558-0644. DOI: 10.1109/TGRS.2014.2357893.

UNESCO. *The Practical Salinity Scale 1978 and the International Equation of State of Seawater 1980*. UNESCO Technical papers in Marine Science, vol. 36. 1981.

Van der Wal, W., P. L. Whitehouse, and E. J. O. Schrama. "Effect of GIA Models with 3D Composite Mantle Viscosity on GRACE Mass Balance Estimates for Antarctica". In: *Earth and Planetary Science Letters* 414 (Mar. 15, 2015), pp. 134–143. ISSN: 0012-821X. DOI: 10.1016/j.epsl.2015.01.001.

Von Schuckmann, K., M. D. Palmer, K. E. Trenberth, A. Cazenave, D. Chambers, N. Champollion, J. Hansen, S. A. Josey, N. Loeb, P.-P. Mathieu, B. Meyssignac, and M. Wild. "An Imperative to Monitor Earth's Energy Imbalance". In: *Nature Climate Change* 6.2 (2 Feb. 2016), pp. 138–144. ISSN: 1758-6798. DOI: 10.1038/nclimate2876.

Von Schuckmann, K., J.-B. Sallée, D. Chambers, P.-Y. Le Traon, C. Cabanes, F. Gaillard, S. Speich, and M. Hamon. "Consistency of the Current Global Ocean Observing Systems from an Argo Perspective". In: *Ocean Sci.* 10.3 (June 24, 2014), pp. 547–557. ISSN: 1812-0792. DOI: 10.5194/os-10-547-2014.

Von Schuckmann, K. et al. "Heat Stored in the Earth System: Where Does the Energy Go?" In: *Earth System Science Data* 12.3 (Sept. 7, 2020), pp. 2013–2041. ISSN: 1866-3508. DOI: 10.5194/essd-12-2013-2020.

Wagner, W. and A. Pruß. "The IAPWS Formulation 1995 for the Thermodynamic Properties of Ordinary Water Substance for General and Scientific Use". In: *Journal of Physical and Chemical Reference Data* 31.2 (June 1, 2002), pp. 387–535. ISSN: 0047-2689. DOI: 10.1063/1.1461829.

Wahr, J., R. S. Nerem, and S. V. Bettadpur. "The Pole Tide and Its Effect on GRACE Time-Variable Gravity Measurements: Implications for Estimates of Surface Mass Variations". In: *Journal of Geophysical Research: Solid Earth* 120.6 (May 27, 2015), pp. 4597–4615. ISSN: 2169-9356. DOI: 10.1002/2015JB011986.

Wang, Q., S. Danilov, D. Sidorenko, R. Timmermann, C. Wekerle, X. Wang, T. Jung, and J. Schröter. "The Finite Element Sea Ice-Ocean Model (FESOM) v.1.4: Formulation of an Ocean General Circulation Model". In: *Geoscientific Model Development* 7.2 (Apr. 30, 2014), pp. 663–693. ISSN: 1991-959X. DOI: 10.5194/gmd-7-663-2014.

Watkins, M. M., D. N. Wiese, D.-N. Yuan, C. Boening, and F. W. Landerer. "Improved Methods for Observing Earth's Time Variable Mass Distribution with GRACE Using Spherical Cap Mascons". In: *Journal of Geophysical Research: Solid Earth* 120.4 (2015), pp. 2648–2671. ISSN: 2169-9356. DOI: 10.1002/2014JB011547.

Watson, C. S., N. J. White, J. A. Church, M. A. King, R. J. Burgette, and B. Legresy. "Unabated Global Mean Sea-Level Rise over the Satellite Altimeter Era". In: *Nature Climate Change* 5.6 (June 2015), pp. 565–568. ISSN: 1758-6798. DOI: 10.1038/nclimate2635.

WCRP-Global-Sea-Level-Budget-Group. "Global Sea-Level Budget 1993–Present". In: *Earth System Science Data* 10.3 (Aug. 28, 2018), pp. 1551–1590. ISSN: 1866-3508. DOI: 10.5194/essd-10-1551-2018.

Weisse, R., I. Dailidienė, B. Hünicke, K. Kahma, K. Madsen, A. Omstedt, K. Parnell, T. Schöne, T. Soomere, W. Zhang, and E. Zorita. "Sea Level Dynamics and Coastal Erosion in the Baltic Sea Region". In: *Earth System Dynamics* 12.3 (Aug. 17, 2021), pp. 871–898. ISSN: 2190-4979. DOI: 10.5194/esd-12-871-2021.

Whitehouse, P. L., M. J. Bentley, G. A. Milne, M. A. King, and I. D. Thomas. "A New Glacial Isostatic Adjustment Model for Antarctica: Calibrated and Tested Using Observations of Relative Sea-Level Change and Present-Day Uplift Rates". In: *Geophysical Journal International* 190.3 (Sept. 1, 2012), pp. 1464–1482. ISSN: 1365-246X. DOI: 10.1111/j.1365-246X.2012.05557.x.

Wiese, D. N., F. W. Landerer, and M. M. Watkins. "Quantifying and Reducing Leakage Errors in the JPL RL05M GRACE Mascon Solution". In: *Water Resources Research* 52.9 (2016), pp. 7490–7502. ISSN: 1944-7973. DOI: 10.1002/2016WR019344.

Wingham, D. J., C. G. Rapley, and H. Griffiths. "New Techniques in Satellite Altimeter Tracking Systems". In: *Proceedings of IGARSS' 88 Symposium*. Zurich, Switzerland, Sept. 1986, pp. 1339–1344.

Winton, M., S. M. Griffies, B. L. Samuels, J. L. Sarmiento, and T. L. Frölicher. "Connecting Changing Ocean Circulation with Changing Climate". In: *Journal of Climate* 26.7 (Apr. 1, 2013), pp. 2268–2278. ISSN: 0894-8755, 1520-0442. DOI: 10.1175/JCLI-D-12-00296.1.

Wong, A. P. S. et al. "Argo Data 1999–2019: Two Million Temperature-Salinity Profiles and Subsurface Velocity Observations From a Global Array of Profiling Floats". In: *Frontiers in Marine Science* 7 (2020). ISSN: 2296-7745.

Woodward, R. S. *On the Form and Position of the Sea Level with Special References to Its Dependence on Superficial Masses Symmetrically Disposed about a Normal to the Earth's Surface*. 48. Govt. Print. Off., 1888. DOI: 10.3133/b48.

Woodworth, P. L., N. Pouvreau, and G. Wöppelmann. "The Gyre-Scale Circulation of the North Atlantic and Sea Level at Brest". In: *Ocean Science* 6.1 (Feb. 8, 2010), pp. 185–190. ISSN: 1812-0784. DOI: 10.5194/os-6-185-2010.

Woodworth, P. L., A. Melet, M. Marcos, R. D. Ray, G. Wöppelmann, Y. N. Sasaki, M. Cirano, A. Hibbert, J. M. Huthnance, S. Monserrat, and M. A. Merrifield. "Forcing Factors Affecting Sea Level Changes at the Coast". In: *Surveys in Geophysics* 40.6 (Nov. 1, 2019), pp. 1351–1397. ISSN: 1573-0956. DOI: 10.1007/s10712-019-09531-1.

Wouters, B., J. A. Bonin, D. P. Chambers, R. E. M. Riva, I. Sasgen, and J. Wahr. "GRACE, Time-Varying Gravity, Earth System Dynamics and Climate Change". In: *Reports on Progress in Physics* 77.11 (Oct. 2014), p. 116801. ISSN: 0034-4885. DOI: 10.1088/0034-4885/77/11/116801.

Wouters, B., D. Chambers, and E. J. O. Schrama. "GRACE Observes Small-Scale Mass Loss in Greenland". In: *Geophysical Research Letters* 35.20 (2008). ISSN: 1944-8007. DOI: 10.1029/2008GL034816.

Wouters, B., A. S. Gardner, and G. Moholdt. "Global Glacier Mass Loss During the GRACE Satellite Mission (2002-2016)". In: *Frontiers in Earth Science* 7 (2019). ISSN: 2296-6463.

Wright, D. G., R. Pawlowicz, T. J. McDougall, R. Feistel, and G. M. Marion. "Absolute Salinity, "Density Salinity" and the Reference-Composition Salinity Scale: Present and Future Use in the Seawater Standard TEOS-10". In: *Ocean Science* 7.1 (Jan. 6, 2011), pp. 1–26. ISSN: 1812-0784. DOI: 10.5194/os-7-1-2011.

Wu, P. and W. R. Peltier. "Pleistocene Deglaciation and the Earth's Rotation: A New Analysis". In: *Geophysical Journal International* 76.3 (Mar. 1, 1984), pp. 753–791. ISSN: 0956-540X. DOI: 10.1111/j.1365-246X.1984.tb01920.x.

Wu, P.-C., M. Wei, and S. D'Hondt. "Subsidence in Coastal Cities Throughout the World Observed by InSAR". In: *Geophysical Research Letters* 49.7 (2022), e2022GL098477. ISSN: 1944-8007. DOI: 10.1029/2022GL098477.

Yamaguchi, R. and T. Suga. "Trend and Variability in Global Upper-Ocean Stratification Since the 1960s". In: *Journal of Geophysical Research: Oceans* 124.12 (2019), pp. 8933–8948. ISSN: 2169-9291. DOI: 10.1029/2019JC015439.

Yaplee, B. S., A. Shapiro, D. L. Hammond, B. D. Au, and E. A. Uliana. "Nanosecond Radar Observations of the Ocean Surface from a Stable Platform". In: *IEEE Transactions on Geoscience Electronics* 9.3 (July 1971), pp. 170–174. ISSN: 0018-9413. DOI: 10.1109/TGE.1971.271490.

Zuo, H., M. A. Balmaseda, and K. Mogensen. "The New Eddy-Permitting ORAP5 Ocean Reanalysis: Description, Evaluation and Uncertainties in Climate Signals". In: *Climate Dynamics* 49.3 (Aug. 1, 2017), pp. 791–811. ISSN: 0930-7575, 1432-0894. DOI: 10.1007/s00382-015-2675-1.

Zuo, H., M. A. Balmaseda, S. Tietsche, K. Mogensen, and M. Mayer. "The ECMWF Operational Ensemble Reanalysis-Analysis System for Ocean and Sea-Ice: A Description of the System and Assessment". In: *Ocean Science Discussions* (Jan. 8, 2019), pp. 1–44. ISSN: 1812-0784. DOI: 10.5194/os-2018-154.

Zwally, H. J. and M. B. Giovinetto. "Overview and Assessment of Antarctic Ice-Sheet Mass Balance Estimates: 1992–2009". In: *Surveys in Geophysics* 32.4 (Sept. 1, 2011), pp. 351–376. ISSN: 1573-0956. DOI: 10.1007/s10712-011-9123-5.